Improving Accuracy of Polyoxometalate Computational Models

Daniel Malcolm

A thesis submitted to the University of Glasgow for the degree of Doctor of Philosophy

School of Chemistry

College of Science and Engineering

May 2024

Acknowledgements

The work contained in this thesis was carried out in the LVN group at the University of Glasgow between October 2020 and May 2024. This work would not have been possible without the generosity and help of many people, both within and outside of the university. I am especially grateful to:

Dr. Laia Vilà-Nadal for welcoming me into her burgeoning research group in the trying time of 2020, for her endless patience and for always making the time to discuss what's been on my mind, scientific and otherwise. Her passion for science is unparalleled and has helped me to rediscover the fun in science. I've also learned the invaluable lesson that science if often just as much about being a decent, understanding person as it is graphs and data.

Jake Thompson for being a crucial colleague and friend during the last 4 years. His enormous knowledge of chemistry has helped me on many an occasion and his sense of humour has helped raise my spirits throughout some of the most difficult times of my PhD. Agar.io?

Jake Jacobs for being such a warm, friendly presence in the office. I've immensely enjoyed our debates and respect him enormously for his willingness to help others and be an all-round decent bloke. I have never felt self-conscious or judged floating an idea with Jake J., and for this I am incredibly grateful.

Michael Nicolaou for always being ready to help out his colleagues and being the reason why all my python graphs look so pretty.

Prof. Lee Cronin for challenging me to think more about the 'why' behind my research and coming away from every Annual Progression Review with a drastically different perspective on my work. I am also very grateful to him for allowing me to join the Device-X project within

his group during 2021, being able to function like a normal PhD during COVID was a lifesaver. I would also like to thank **Dr. Diana Castro, Jim McIver, and Alasdair MacLeod** within the Cronin group for their help with Device-X, I would have been lost or stumped many a time without them.

Stuart Mackay for his vast computational knowledge; from helping with ethernet connection to setting up our HPC cluster, I honestly can't remember all the myriad ways Stuart has helped myself and the group over the years but without him this project would have been significantly harder to accomplish.

Dr. Maria Jose Aliaga for helping proofread and grilling me at that one presentation I gave; my work would not be of the standard it has reached without that early viva.

Finally, I would like to thank my **family, friends, and partner** for their continued support and encouragement throughout this PhD start to finish. I can't express how grateful I am for my community and can't wait to see more of you once this thesis is finally written.

Table of Contents

List of Publications

The following book chapters have been published over the course of this PhD:

[1.] – Malcolm, D., and Vilà-Nadal, L. "**Transition Metal Oxide-based Storage Materials**", In: Ruiz Rubio, L., Vilas Vilela, J. L., Artetxe, B. and Gutiérrez-Zorrilla, J. M. (eds.) *Polyoxometalates: Advances, Properties, and Applications.* **2022**, Jenny Stanford Publishing: Singapore, pp. 243-274. ISBN 9789814968140 (doi:10.1201/9781003277446-6)

The following research articles have been published over the course of this PhD:

[1.] - Archived paper: Malcolm D, Vilà-Nadal L. "**First steps in the inverse design of porous metal oxide materials: lacunary Wells-Dawson anion**" *ChemRxiv*. **2022** (doi:10.26434/chemrxiv-2022-db0z9) This content is a preprint and has not been peer-reviewed.

[2.] - Malcolm, D., and Vilà-Nadal, L. "**Computational Study into the Effects of Countercations on the $[P_8W_{48}O_{184}]^{40-}$ Polyoxometalate Wheel**", *ACS Org. Inorg. Au* **2023**, *3*, (5), 274-282 (doi:10.1021/acsorginorgau.3c00014)

[3.] – Malcolm, D., and Vilà-Nadal, L. "**Exploring the Theoretical Landscape of the Hexalacunary $[\alpha\text{-}H_2P_2W_{12}O_{48}]^{12-}$ Wells-Dawson Anion: A Comprehensive Study**" – awaiting submission

[4.] - Malcolm, D., Jacobs, J., Thompson, J., and Vilà-Nadal, L. "**Improving Benchmarking of Polyoxometalate Frontier Orbitals using Hybrid Functionals**" – awaiting submission

The following posters have been presented over the course of this PhD:

[1.] - Malcolm, D., and Vilà-Nadal, L. "**Investigating the Fundamental Building Units of POMzites**", *RSCPoster Twitter Conference* **3/3/2021**

[2.] – Malcolm, D. "**Exploring Electrochemistry of POM Building Blocks**", *UK-Young InPOMers Conference* **9/12/2021**, Newcastle

[3.] - Malcolm, D., and Vilà-Nadal, L. "**Computationally based Predictions of New POM Species**", *POM Basics Conference* **14/6/2022**, La Rochelle

[4.] - Malcolm, D., and Vilà-Nadal, L. "**Effects of Countercations on the $[P_8W_{48}O_{184}]^{40-}$ POM Wheel**", *ScotCHEM Conference* **19/6/2023**, Glasgow

Abbreviations

ADF	Amsterdam Density Functional
AO	Atomic Orbital
BHEP	*N*,*N*-bis-(2-hyrdoxyethyl)-piperazine
BZ	Belousov-Zhabotinsky
COSMO	Conductor-like Screening Model
CV	Cyclic Voltammetry
DFT	Density Functional Theory
DMACl	Dimethylammonium Chloride
GGA	Generalized Gradient Approximation
GTO	Gaussian Type Orbital
H-L	HOMO-LUMO
HDMF	Hydrogenated Dimethylformamide
HF	Hartree-Fock Theory
HMTA	Hexamethylenetetramine
HOMO	Highest Occupied Molecular Orbital
HPOM	Heteropolyoxometalate
IR	Infrared Spectroscopy
IsoPOM	Isopolyoxometalate
LCAO	Linear Combination of Atomic Orbitals
LDA	Local Density Approximation
LFC	Large Frozen Core
LUMO	Lowest Unoccupied Molecular Orbital
MAC	Mean Atomic Charge
MAE	Mean Absolute Error
MD	Molecular Dynamics
MEP	Molecular Electrostatic Potential maps

MOF	Metal-Organic Framework
MS	Mass Spectrometry
NFC	No Frozen Core
NMR	Nuclear Magnetic Resonance
POM	Polyoxometalate
POMOF	POM-Organic Framework
RFB	Redox Flow Battery
SBB	Secondary Building Block
SCF	Self Consistent Field
SCRF	Self-Consistent Reaction Field
SD	Standard Deviation
SFC	Small Frozen Core
SMM	Single Molecule Magnets
STO	Slater Type Orbital
TBA	Tetrabutylammonium
TD-DFT	Time Dependent Density Functional Theory
TEA	Triethanol Amine
TI-DFT	Time Independent Density Functional Theory
TM	Transition Metal
TMSP	Transition Metal Substituted Polyoxometalate
UV-Vis	UV-Visible Light Spectroscopy
VdW	Van der Waals
WD	Wells-Dawson
WFT	Wavefunction Theory

$K_n\{P_2W_{12}\}$	$K_n[P_2W_{12}O_{48}]^{n-14}$
$K_8\{P_8W_{48}\}$	$K_8[P_8W_{48}O_{184}]^{32-}$
$\{As_2W_{12}\}$	$[As_2W_{12}O_{46}]^{14-}$

ABBREVIATIONS

{As$_8$W$_{48}$}	$[As_8W_{48}O_{184}]^{40-}$
{K$_3$H$_2$}	$K_3[H_2X_2W_{12}O_m]^{n-}$
{K$_{12}$H$_2$}	$K_{12}[H_2X_2W_{12}O_{48}]$
{Mo$_{132}$}	$[Mo_{132}O_{372}(CH_3COO)_{30}(H_2O)_{72}]^{42-}$
{Mo$_{154}$}	$[Mo_{154}(NO)_{14}O_{448}H_{14}(H_2O)_{70}]^{28-}$
{P$_2$W$_{12}$}	$[P_2W_{12}O_{48}]^{14-}$
{P$_8$W$_{48}$}	$[P_8W_{48}O_{184}]^{40-}$
{Se$_2$W$_{12}$}	$[Se_2W_{12}O_{46}]^{12-}$
{Se$_8$W$_{48}$}	$[Se_8W_{48}O_{176}]^{32-}$
{W$_{48}$}	$[X_8W_{48}O_m]^{n-}$ (X = P or As, Se) (m = 184, 176)
{X$_2$W$_{12}$}	$[X_2W_{12}O_m]^{n-}$ (X = P or As, Se) (m = 48, 46)
{X$_8$W$_{48}$}	$[X_8W_{48}O_m]^{n-}$ (emphasis on possible identity of ‘X’)

Formulae Notation

If a formula is presented with square brackets, it is shown in its' fullest and complete form, such as $[P_2W_{18}O_{62}]^{6-}$ or $[P_8W_{48}O_{184}]^{40-}$. Due to the clunkiness of presenting the formula in this format and the fact that many formulae will be repeated multiple times, a couple of abbreviated forms will be additionally utilised:

1. Curly brackets highlight the number of heteroatoms and metal atoms within the POM, without including the number of oxygen atoms, charge (if present), and the nature and number of countercations (if present)

   An example would be shortening $K_6[P_2W_{18}O_{62}]$ to **{P_2W_{18}}** or $[P_8W_{48}O_{184}]^{40-}$ to **{P_8W_{48}}**

2. Regular brackets are used to show the configuration of heteroatom present within the POM.

   (XO_3) – a single templating anion is located within one cap cavity of the POM, connected to the closest belt regions via 3 O-W(-W) bridging bonds.
   (XO_3)$_2$ – a single templating anion is located within each cap cavity of the POM, connected to the closest belt regions via 3 O-W(-W) bridging bonds.
   (XO_4)$_2$ – a single templating anion is located within each cap cavity of the POM, connected to the closest belt regions via 3 O-W(-W) bridging bonds and to the nearest cap region via 1 O-W(-W,-W) bond.
   (XO_6) – a single templating anion is located within the centre of the POM cavity, connected to both belt regions via 6 O-W(-W) bridging bonds, 3 to each belt region.

Abstract

Given the growing materials and energy crises, where the Earth's stock of precious, non-renewable metals and fuels being consumed by an ever-bigger population of human beings, it is more imperative than ever that we design smarter technology that is not only versatile, but also relevant to the problems we currently face; from being able to store renewable energy for long periods of time to finding alternative batteries to power our transportation, there is an ever greater need to develop electrochemically based methods of storing energy. Polyoxometalates (POMs) as a family of molecules are well-known for their ability to reversibly store large number of electrons per unit cage, solubility and structural durability under a wide range of environmental conditions, and studies show that alteration of the central heteroatom can further tune the oxidizing power of the species.[1]

One of the main issues holding POMs back from being specially designed to exhibit the most desirable properties allowing for optimal deployment in key fields such as redox flow batteries is the lack of understanding surrounding their self-assembly mechanisms and, therefore, synthetic methods. Without this fundamental knowledge of how metal oxide reagents interact to yield unique structures under particular environmental conditions, we are left to rely on change discoveries to provide us with innovation. The first step towards building a greater wealth of knowledge is to refine our ability to simulate POM characteristics and properties using DFT, iteratively improving our calculations by benchmarking against empirical data; with this theory behind us, it should be easier to elucidate the mysteries hiding within the synthetic mixture.

With this investigation, we set out to establish how one can accurately model three species of POM: the well-known $[X_2W_{18}O_m]^{n-}$ Wells-Dawson (X = As, P, Se m = 60, 62), its hexalacunary variant $[X_2W_{12}O_m]^{n-}$ (X = As, P, Se m = 46, 48), and the wheel-shaped $[X_8W_{48}O_m]^{n-}$ framework these hexalacunaries can self-aggregate to form (X = As, P, Se m = 176, 184). After detailing the POM, computational chemistry, inverse design basics, and experimental details relevant to this work (**Chapters 1, 2,** and **3** respectively), we discuss our

strategies and results with modelling the $[X_8W_{48}O_{184}]^{n-}$ POM wheel, highlighting how inclusion of only a few of the total number of countercations is sufficient for good empirical comparison (**Chapter 5**). Likewise, we repeat the same premise with the $[X_2W_{18}O_{62}]^{n-}$ Wells-Dawson and $[X_2W_{12}O_{48}]^{n-}$ hexalacunary species (**Chapter 6**), concluding that presence of several (but not all) countercations is essential for accurate replication of the POM structure but additional inclusion of protons within the framework will provide the best model for analysing regions of electron density and frontier orbital data. Finally, we review the available literature regarding computational modelling of POM UV-Vis spectra, arguing that the current level of theory is insufficient for accurate results and reviewing the available options (**Chapter 7**).

We also included results from a brief organic chemistry project we conducted over the course of this PhD thesis relating to the Ugi reaction which we, in the end, were not able to see through to completion (**Chapter 8)**. Following this are the appendices for **Chapters 10-13** (**Appendix:1 – Appendix:4 respectively**), collecting the vast number of tables, figures, and graphs produced by this work.

Declaration of Originality

University of Glasgow | School of Chemistry

Declaration of Originality Form

This form **must** be completed and signed and submitted with all assignments.

Please complete the information below (using BLOCK CAPITALS).

Name DANIEL MALCOLM

Student Number.....

Course Name CHEMISTRY

Assignment Number/Name DOCTORAL THESIS

A link to the University's Statement on Plagiarism is provided at the end of this form. Please read the Statement on Plagiarism carefully THEN read and sign the declaration below.

I confirm that this assignment is my own work and that I have:

Read and understood the guidance on plagiarism in the Student Handbook, including the University of Glasgow Statement on Plagiarism	☑
Clearly referenced, in both the text and the bibliography or references, **all sources** used in the work	☑
Fully referenced (including page numbers) and used inverted commas for **all text quoted** from books, journals, web etc. (Please check with your School which referencing style is to be used)	☑
Provided the sources for all tables, figures, data etc. that are not my own work	☑
Not made use of the work of any other student(s) past or present without acknowledgement. This includes any of my own work, that has been previously, or concurrently, submitted for assessment, either at this or any other educational institution, including school (see overleaf at 31.2)	☑
Not sought or used the services of any professional agencies, or any artificial intelligence to produce this work	☑
In addition, I understand that any false claim in respect of this work will result in conduct action in accordance with University regulations	☑

DECLARATION:

I am aware of and understand the University's policy on plagiarism and I certify that this assignment is my own work, except where indicated by referencing, and that I have followed the good academic practices noted above

Signed.....

Chapter 1: Polyoxometalate Basics

In this chapter we will briefly summarize what a polyoxometalate framework is, specifically how they are formed, basic chemistry, and the main groups and sub-species, the history behind these inorganic compounds, and finally their current and potential applications in the future.

Polyoxometalates (POMs) are ordered, inorganic metal-oxide clusters,[2,3] with the general formula $[MO_x]_n^{p-}$ (where M = Mo, W, V, Nb, Ta…; x = 3-7; n = 6-368)[4] for isoPOMs and $[X_mM_nO_x]^{p-}$ (where X = P, As, Se…; m 1-8; M = Mo, W, V; n = 12-48; x = 40-184) for heteroPOMs, that spontaneously self-assemble from oxometallate monomers under appropriate, usually acidic, reaction conditions.[5] The library of known POM species is large and keeps on expanding, with variation arising from the transition metal element used in the framework, the number or size of oxometallate monomers, and the presence or absence of a heteroatom housed within the central cavity, which also opens up a large range of possibilities for tuning redox functions (**Fig. 1.1**).[6,7,8]

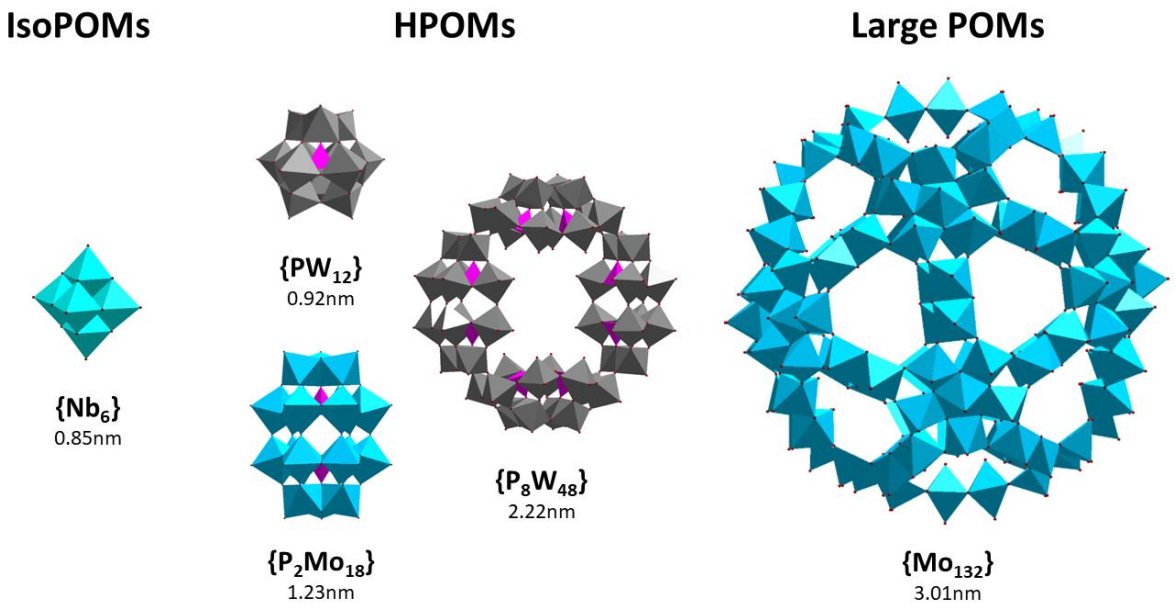

Figure 1.1. {Nb$_6$} Lindqvist, $[Nb_6O_{19}]^{8-}$, **{PW$_{12}$}** Keggin, $[PW_{12}O_{40}]^{3-}$, **{P$_2$Mo$_{18}$}** Wells Dawson $[P_2Mo_{18}O_{62}]^{6-}$, **{P$_8$W$_{48}$}** W_{48} Wheel, $[P_8W_{48}O_{184}]^{40-}$, and **{Mo$_{132}$}** Müller Sphere, $[Mo_{132}O_{372}X_{30}(H_2O)_{72}]^{n-}$, arranged by diameter magnitude from smallest to largest.

Most POMs are synthesized from Molybdenum- or Tungsten-based oxide salts, which offer a reasonable choice in customisability; the bonds in Mo-based POMs tend to be more flexible, yielding a greater range of structures, especially very sizeable ones, whilst those in W-based POMs are more thermally stable yet rigid, resulting in smaller cages.[9] Those frameworks composed of Vanadium, Niobium, Tantalum, or other Transition Metal elements are relatively scarce in the literature; vanadium usually crops up when substituted with another metal atom in a mixed addenda framework[10] and not as a pure $[V_nO_x]$-type POM.

1.1 History

The field of polyoxometalates extends back surprisingly far; although first reported in 1783 by C.W. Scheele,[11] it is clear that the Native Americans living in the region of Colorado which would come to be known as Idaho Springs noticed the unusual blue colouration of the water in that area countless years prior, if not centuries.[12]

This effect was caused by the natural formation of Ilsemannite, $Na_{14}[Mo^{VI}_{126}Mo^{V}_{28}O_{462}H_{14}(H_2O)_{70}]$ 'Blue' POMs, which was probably triggered by oxidation of molybdenite deposits in the region (**Fig. 1.2**). It would be almost 200 years before the structure was fully characterized, but this hasn't stopped scientists from puzzling over this most fundamental of riddles right from the start.

J. J. Berzelius synthesized the first POM, a $(NH_4)_3[PMo_{12}O_{40}]$ Keggin species, in 1826,[13] although the exact structure wouldn't be determined until decades later.[14] Due to the inherent complexity associated with a POM framework, simply determining the formula for the cluster will only get one so far in gaining a true understanding of the structure and its capabilities; leaving aside the fact that isomers can be readily formed under certain conditions, the shape of the POM, including the presence or absence of features, such as a pore, within the architecture, will have significant effects on the properties and applications available to the POM.

Thus, it wasn't until the development of the new spectroscopic techniques x-ray diffraction[15,16] and x-ray crystallization,[16] during the first and second halves of the 20th century respectively that the field of POM chemistry could properly gain traction.[17] Over the last two centuries since Berzelius's initial paper, the size of the POM library has ballooned and these molecules are finding increased relevance in tackling many of the major chemical problems of the present day.

Figure 1.2. Postcard with photo of Lucania Tunnel mine. This Colorado mine in Idaho Springs was primarily focused on the excavation of gold seams, but more than half a dozen other minerals, including Ilsemannite, are also present within the rock.

1.2 General Synthesis

As previously alluded to, POMs spontaneously form using self-assembly mechanisms driven by a series of condensation reactions. Self-assembly is something of a marvel in the natural world; in a universe fundamentally governed by the second law of thermodynamics, it seems counterintuitive that basic building block molecules can grow into larger, more complex structures. Nevertheless, there exist countless examples of self-assembly in nature, ranging from inorganic salts and crystals to organic proteins and DNA. Being able to harness this phenomenon and direct it to reliably produce new species with desirable properties can provide one with an efficient and energetically cheap method of synthesis but requires a deep

understanding into how the myriad molecular and environmental factors interact with each other for one to claim to possess even a modicum of control over.

In the case of POMs, synthesis begins with acidification of the initial tetra-coordinate [MO_4], converting it to the 'active monomer' [MO_6].[18] [MO_6] units then react with each via a condensation reaction, aggregating into larger structures block by block. After each [MO_6] unit has been integrated into the growing cage, water is expelled from the dimer unit via interaction with a hydronium cation; this loss of oxygen via condensation forces the monomer units to stay bound together via a shared oxygen atom(s). See **equations (1.1)** and **(1.2)** for the simplified process of how POMs grow by monomer addition.

$$[M_{x1}O_{y1}H]^{z1-} + [M_{x2}O_{y2}H]^{z2-} \rightarrow [M_{(x1+x2)}O_{(y1+y2)}H_2]^{(z1+z2)-} \quad \textbf{(eq. 1.1)}$$

$$[M_{(x1+x2)}O_{(y1+y2)}H_2]^{(z1+z2)-} + H_3O^+ \rightarrow [M_{(x1+x2)}O_{([y1+y2]-1)}H]^{([z1+z2]-1)-} + 2H_2O \quad \textbf{(eq. 1.2)}$$

For any chemical reaction to be spontaneous, it must exhibit a negative Gibbs free energy value; in order to achieve this, there must exist a balance between the entropy and enthalpy values for the system, whereby the formation of bonds (enthalpy) and loss of energy (entropy) must yield an overall negative Gibbs free energy value. With regards to POMs specifically, the relatively low enthalpy associated with making or breaking metal oxide bonds combined with the large number of water molecules released by the condensation reactions, which increases the number of intermolecular interactions within the system, and thereby the entropy of the system as a whole, complement each other and allows POM synthesis to be spontaneous at temperatures under ~370K.

POM synthesis is generally favoured in acidic mixtures with a pH lower than 5.0, as this allows the metal oxide 'monomers' to increase their nuclearity towards each other;[5] it can be useful to

regard the acidic conditions as providing an activating environment for the metal oxide complexes. The reason why acids are key for POM synthesis lies in their enabling and promoting the condensation reactions by which POM structures are able to grow and aggregate; as acidity of the solvent increases and protons are made increasingly available to the system, water molecules are more easily produced via metal oxide bond cleavage and the number of bridging M-O-M bonds formed as a result increases.

As the reaction proceeds, each POM eventually reaches a cut-off point where it stops growing and becomes a defined, distinct framework. Bridging oxygen atoms (M-O-M) tend to form longer bonds than their terminal counterparts (M=O), which has the effect of the terminal atoms being more polarized and nucleophilic; as these terminal oxygens are located on the exterior of the framework, they act to repel further monomers from binding to the POM. It's also worth noting that terminal bonds are shorter than their bridging counterparts; this has the effect of weakening the metal-oxide bond located opposite the terminal bond with respect to the metal centre and making it more susceptible to cleavage via a condensation reaction.[17,19]

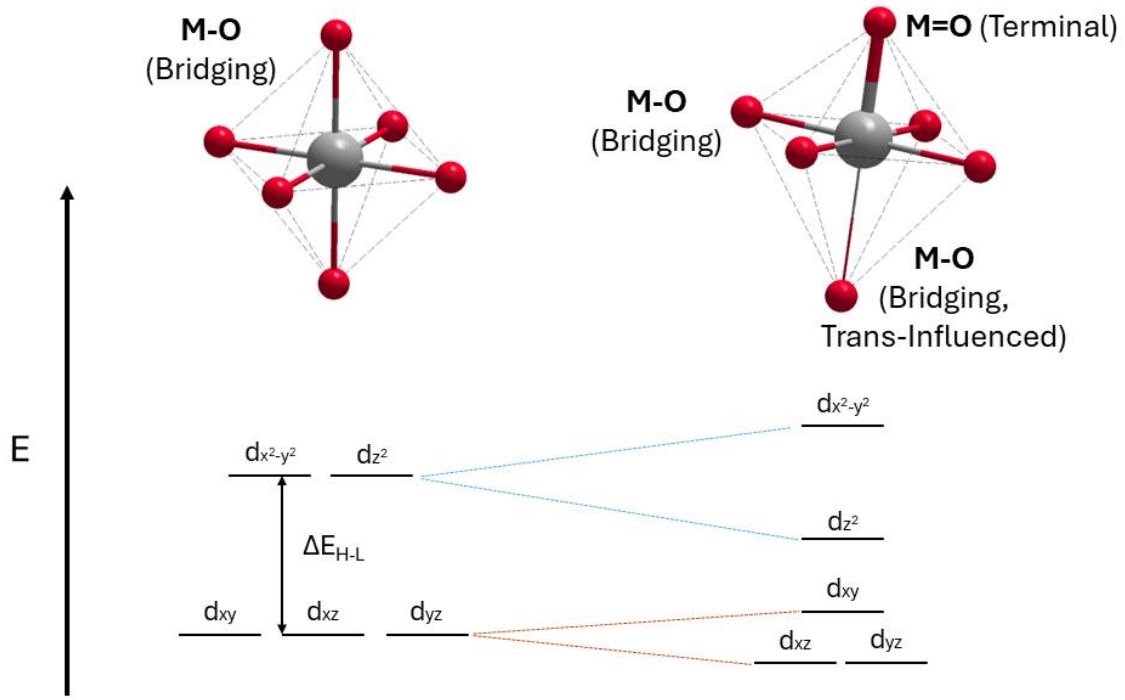

Figure 1.3. Splitting of d-orbital degeneracy as a result of Jahn-Teller distortion. Orbitals with a 'z' component are stabilized, whereas those without are destabilized.

This Jahn-Teller distortion (**Fig. 1.3**) is responsible for the formation of discrete POM units; without terminal oxygen groups repelling other oxometallate reagents in solution, polymerization would continue until one created a bulk metal oxide sheet. It is worth noting this distortion is more prominent in polyoxomolybdates than polyoxotungstates.[20] Jahn-Teller distortion is also present in the final POM framework, not just during synthesis; depending on the nature of metal in the framework (Mo, W…) and the degree of alternating bond length distortion, the frontier orbital energies and favourability of particular isomers will be affected.[21]

Therefore, from the simple [MO_6] building block is the entire POM library created, with each species and family defined and synthesized by exposing this single metal complex to a different set of environmental conditions. As to the nature of 'M', not every metal element is suitable to form a POM. The element must feature several unoccupied d-orbitals when present in a high oxidation state in order to interact well with up to 6 oxygen atoms, as well as featuring an octahedral ionic radius value between 0.65-0.80Å. The most common elements to fall within these rules are molybdenum (5+/6+), tungsten (5+/6+), and vanadium (4+/5+), although examples of POM composed of niobium (5+), tantalum (5+), chromium (5+/6+), and platinum (2+) metal atoms have also been reported. The major variables at play in the synthesis are pH, temperature, countercation utilised, presence of structure directing agents, and the ratios or concentrations of reactants relative to each other. Structure directing agents are ligands which have been identified as especially useful at improving the yield of a specific species and isomer.[22,23,24]

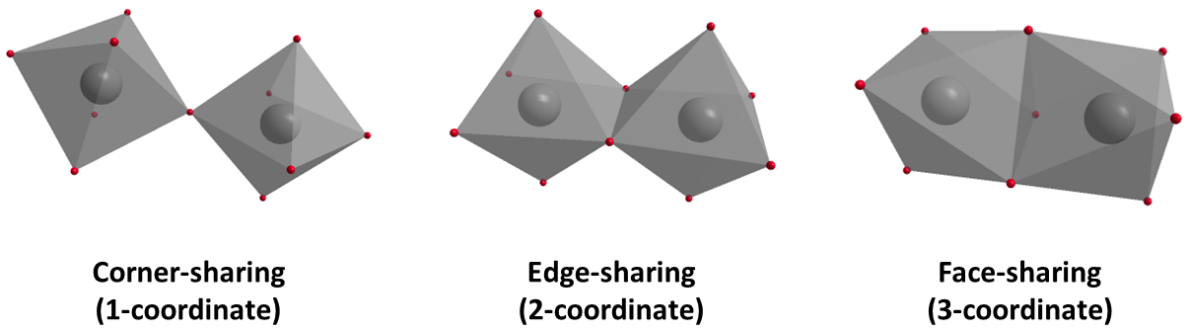

Figure 1.4. Metal oxide binding configurations present during polyoxometalate self-assembly reaction

There exist a few different methods of binding between monomer units within the POM, depending on where in the framework the metal centres are located. These bond configurations

are referred to as corner-sharing, edge-sharing, and face-sharing, each with its own set of characteristics (**Fig. 1.4**); corner-sharing configurations are the most flexible, due to the degree of rotation afforded by only being connected by a single oxygen atom, whilst edge- and face-sharing are stronger due to their being bound by multiple oxygens (two or three oxygen atoms respectively). Each POM species will be characterized by a different combination of these bond configurations.

Although straightforward and repetitive in principle, attempts to discern the most thermodynamically favourable, and therefore the likeliest, path taken by the growing cage quickly becomes drowned out by the sheer complexity of the task; past the stage at which a trimer is formed the number of possible combinations for assembly skyrockets, stymieing progress into understanding why certain metal atoms in the polymer become more attractive in growing the molecule than others. Nevertheless, the single-pot nature of the reaction renders it highly appealing for a multitude of different applications, where the POM can be easily made without the need for expensive lab equipment once the synthetic method has been optimized to a sufficiently good degree.

1.3 IsoPOMs

IsoPOMs are a small family of POMs which don't contain any heteroatoms, exhibiting the formula $[M_xO_y]^{n-}$.[2] They can range in size from the smallest known POM, Lindqvist ($[W_6O_{19}]^{2-}$),[25] to containing up to 36 metal centres for the 'Celtic-Ring' structure ($[H_{12}W_{36}O_{120}]^{12-}$);[26] without a heteroatom present, these POMs are limited in the sizes they can grow to on account of the high anionic charge they inevitably exhibit.[22] It is also easier for rarer POM-metals, such as V,[27] Nb,[28] and Ta,[29] to form pure IsoPOM structures than HPOM, with Lindqvist-type frameworks being identified for all these elements.[30,31] Although Lindqvist is the most well-known IsoPOM, other commonly known species include Decatungstates ($[W_{10}O_{32}]^{4-}$)[32] and Paratungstates ($[H_2W_{12}O_{42}]^{10-}$).[33] Some IsoPOM derivatives of traditionally HPOM species have also been identified, such as Metatungstate ($[H_2W_{12}O_{42}]^{10-}$)[34] and

($[H_4W_{19}O_{62}]^{6-}$)[35] for Keggin and Wells-Dawson respectively. See **Fig. 1.5** for selected IsoPOM geometries.

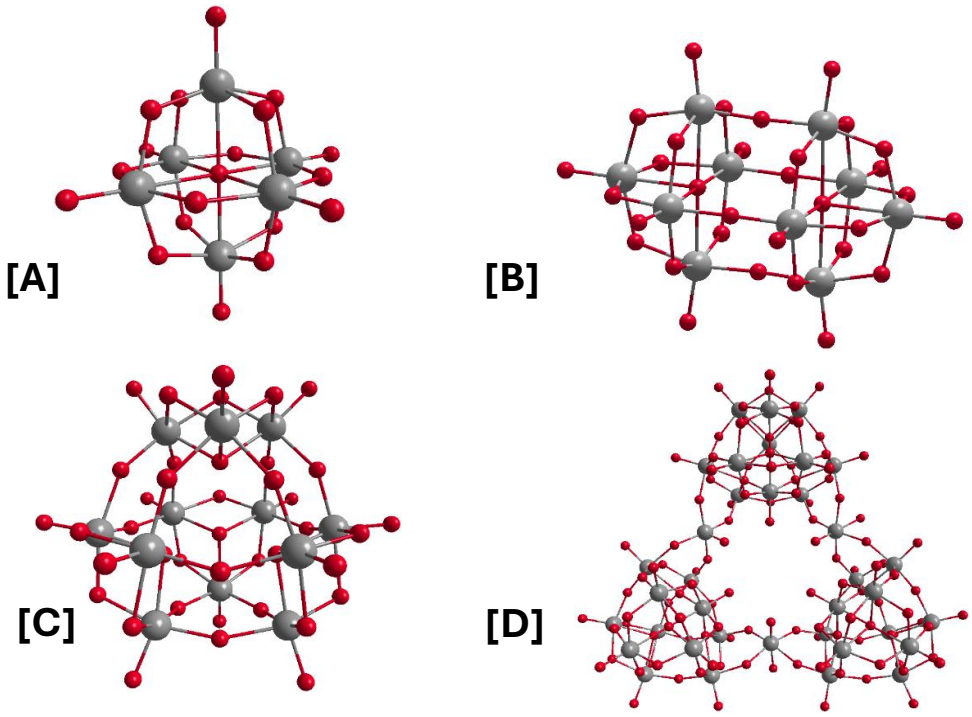

Figure 1.5. Ball and Stick representations of IsoPOM frameworks **[A]** Lindqvist, $[W_6O_{19}]^{2-}$, **[B]** Decatungstate, $[W_{10}O_{32}]^{4-}$, **[C]** Metatungstate, $[W_{12}O_{42}]^{12-}$, and **[D]** Celtic-Ring, $[W_{36}O_{120}]^{24-}$. W: grey, O: red.

While the applications for many species of IsoPOMs are limited, being mostly used to justify POM theory on a small-scale and extrapolating these theories onto larger POMs which are harder to work with, $[W_{10}O_{32}]^{4-}$ decatungstate is one of the most widely used POMs in the literature due to their key photocatalytic abilities,[36,37] where these POMs have proven themselves capable of activating and functionalizing inert C-H bonds.[38,39,40] Some other areas IsoPOMs have been applied to include the formation of organic-inorganic hybrids,[41,42] and SBBs to from larger frameworks.[43,44,45]

1.4 HeteroPOMs

HeteroPOMs (HPOMs), general formula $[X_wM_xO_y]^{n-}$, are generally more stable, and subsequently bigger, than their IsoPOM counterparts, with the heteroatom-containing template anion acting to direct synthesis towards a certain product structure and, as a cation, lowering the overall anionic charge. This templating anion, general formula $[XO_y]^{n-}$, is usually a non-metal p-block element, such as $[PO_4]^{3-}$,[46] $[SiO_4]^{4-}$,[47] $[SO_4]^{4-}$,[48] and $[AsO_4]^{3-}$,[49] but examples of POMs containing metal templating anions outside of the p-block have also been reported, including $[WO_6]^{6-}$[35] and $[VO_4]^{3-}$.[50]

The species of heteroatom can have a major impact on the redox properties of the POM framework, allowing us to divide HPOMs into two main categories: classical and non-classical. Classical is the more well studied of the two and is characterized as redox-inactive, with the POM housing a XO_4 anion, such as $[(XO_4)_2W_{18}O_{54}]^{n-}$, whereas non-classical HPOMs contain either a redox activity XO_3 or XO_6 anion, example formulae $[(XO_3)_2W_{18}O_{54}]^{n-}$ and $[(XO_6)W_{18}O_{56}]^{n-}$ respectively. It is worth noting that non-classical HPOMs only become present in frameworks that contain at least 18 metal atoms (Wells-Dawson or larger); Keggin, for example, only features classical structures. This may be due to the fact that heteroatoms that are part of a XO_3 configuration often feature a lone pair which requires a bigger internal cavity to avoid disrupting the stability of the surrounding POM cage, or that XO_6 templating anions are simply too big for a Keggin structure to accommodate. See **Fig. 1.6** for examples of different heteroatom configurations for WD.

This difference in redox activity between classical and non-classical (XO_3) POMs appears to arise from the differences in oxidation state; heteroatoms in a XO_4 species tend to be present in the highest oxidation state possible, which is not the case for those with the XO_3 configuration, allowing for further oxidation and subsequent reduction reactions to take place. XO_6 manages to avoid redox inactivity due to the greater number of oxygen species present, which increase the electronegativity of the central heteroatom and transform it into a powerful oxidizing agent. Inclusion within a highly anionic POM helps to protect the often-catalytic XO_6 core from being immediately reduced, as a further increase in electron density would

destabilize the framework.[51] It's worth noting that this change in redox activity is localized on the heteroatom specifically, as opposed to altering the chemistry of the POM cage as a whole.

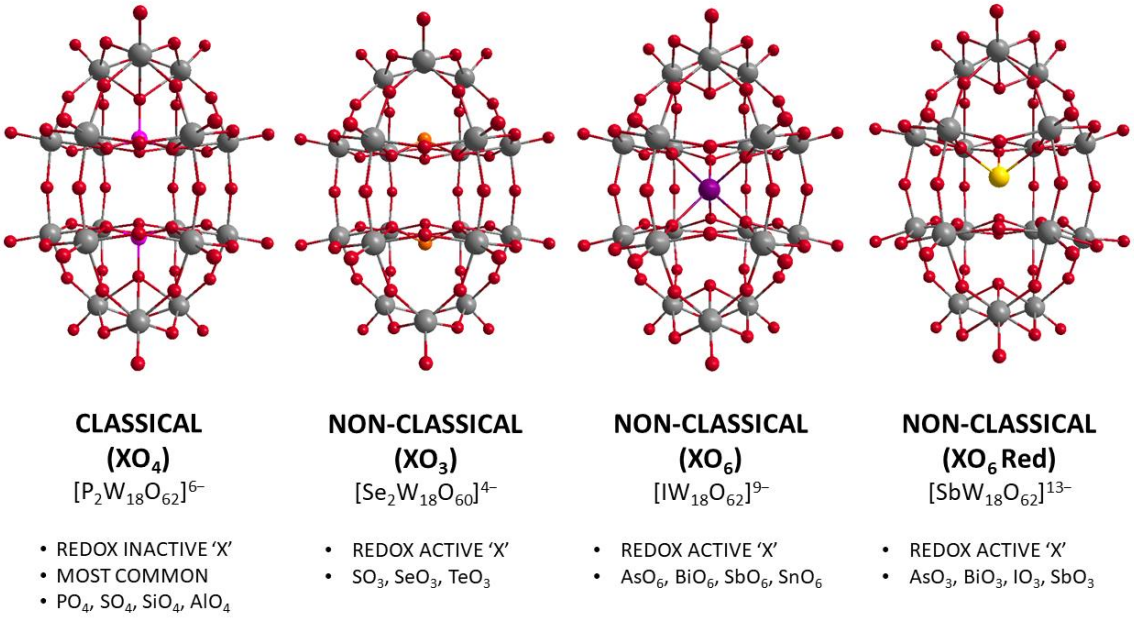

Figure 1.6. Ball and Stick representations of Wells-Dawson POMs with a range of different heteroatom configurations. W: grey, O: red, P: pink, Se: orange, I: purple, Sb: yellow

There exists a third species of non-classical HPOM, in which a XO_6 species is reduced by 2 electrons, converting it to a XO_3 anion configuration, general formula $[(XO_3)W_{18}O_{59}]^{n-}$. This HPOM sub-family is still largely under-researched in the literature, but available reports include work by Jeannin, Y. *et al*,[52] Wang, J. *et al*,[53] and Long, D.L. *et al*.[54]

Given the immense variety of HPOMs which have been identified thus far, we will highlight the most well-known examples in addition to the species we have examined in the course of this work. POMs are referred to by their common names, when available, for the sake of ease.

Keggin POMs, for example, have the general formula $[XM_{12}O_{40}]^{n-}$, where M = W, Mo, V, Nb, and are one of the most well-known and reported POM species in the literature.[16,55] Keggin frameworks have been deployed in a variety of different fields, finding application in fields such as catalysts,[56] molecular memory devices,[57] redox flow batteries,[58] and secondary building blocks (SBBs) for larger frameworks.[59] The main factor that enables this high rate of

applicability is the wide degree of customization the Keggin structure can be subjected to. The nature of the heteroatom (X), for example, can vary widely in the choice of element; species have been identified that contain As, Ge, P, and Si heteroatoms.[60]

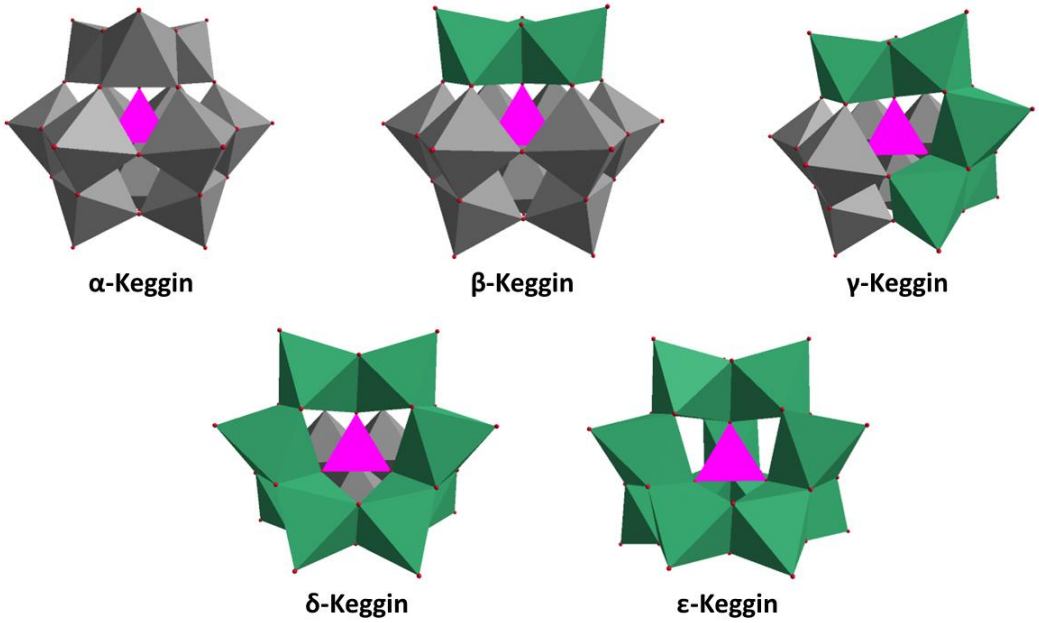

Figure 1.7. Polyhedron representations of Keggin isomers alpha through epsilon. Non-rotated W section: grey; rotated W section: green; O: red; P: pink.

The Keggin anion can be synthesized as one out of several different isomers, each of which is characterized by a different structural geometry, reactive properties, and stability. Each of the 4 $\{M_3O_{13}\}$ units within the framework can be rotated by 60 degrees, exposing the heteroatom-containing core more with each rotated unit (**Fig. 1.7**).[61] The **ε** isomer, where all 4 units have been rotated, is the only species too unstable to have been synthesized; this is due to an increase in the number of short-range W-W electrostatic repulsion interactions within the framework, triggered by each successive rotation.[62]

The final point of structural diversity in Keggin anions we shall touch on is that of the ability for these species, specifically those composed of tungsten atoms, to form lacunary structures.[63] When exposed to basic conditions, tungsten-POMs can lose $[WO_6]^{6-}$ complexes from their frameworks, leaving behind a very nucleophilic, vacant site in the structure. This lacunary site can easily react with a different metal element or electrophile, introducing a method for fine

tuning the redox properties and reactivity of the POM. The degree of controlled degradation can be controlled based on the strength of the basic reagent the POM species is exposed to. We will discuss the formation of lacunary POM species in greater detail later.

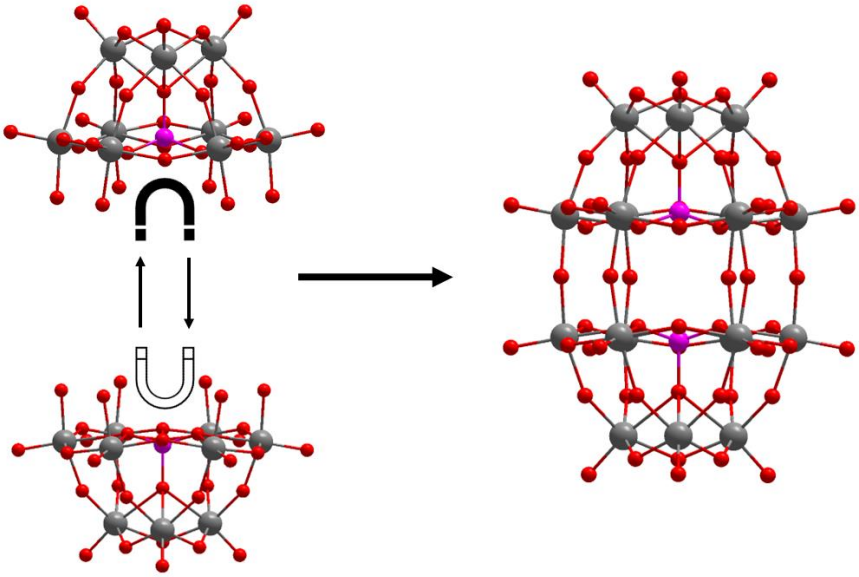

Figure 1.8. Ball and Stick representation of synthesis of Wells-Dawson POM from two tri-lacunarised Keggin frameworks. W: grey; O: red; P: pink

In tandem with the Keggin anion, the Wells-Dawson POM (WD) is the most recognisable example of a POM in the literature, general formula $[X_nM_{18}O_m]^{p-}$, where M = W, Mo; n = 1, 2; m = 60, 62. The two POM species are relatively similar in structural arrangement, with the WD essentially being composed of two tri-lacunarised Keggin sub-sections (**Fig. 1.8**). As with Keggin, the WD can be present as one of half a dozen different and distinct isomer configurations (α, β, γ, α*, β*, γ*) based on rotation of one or both trimer 'cap' M_3O_{13} units located at either end of the POM and/or rotation of one or both central 'belt' M_6O_{15} units.[64,65]

Another HPOM is the Preyssler anion framework, $[NaP_5W_{30}O_{110}]^{14-}$, which is the smallest of a number of wheel-shaped POMs we shall discuss in this work (**Fig. 1.9**).[66] Initially discovered as a by-product in the synthesis of the $[P_2W_{18}O_{62}]^{6-}$ Wells-Dawson framework,[67] the Preyssler POM is primarily known for its 'crown-ether-like' constitution, in which the interior of the 'wheel' traps a countercation; this countercation, traditionally sodium, can be exchanged with a wide range of different elements, including various transition metal and lanthanide elements,[68,69] under the correct hydrothermal conditions.

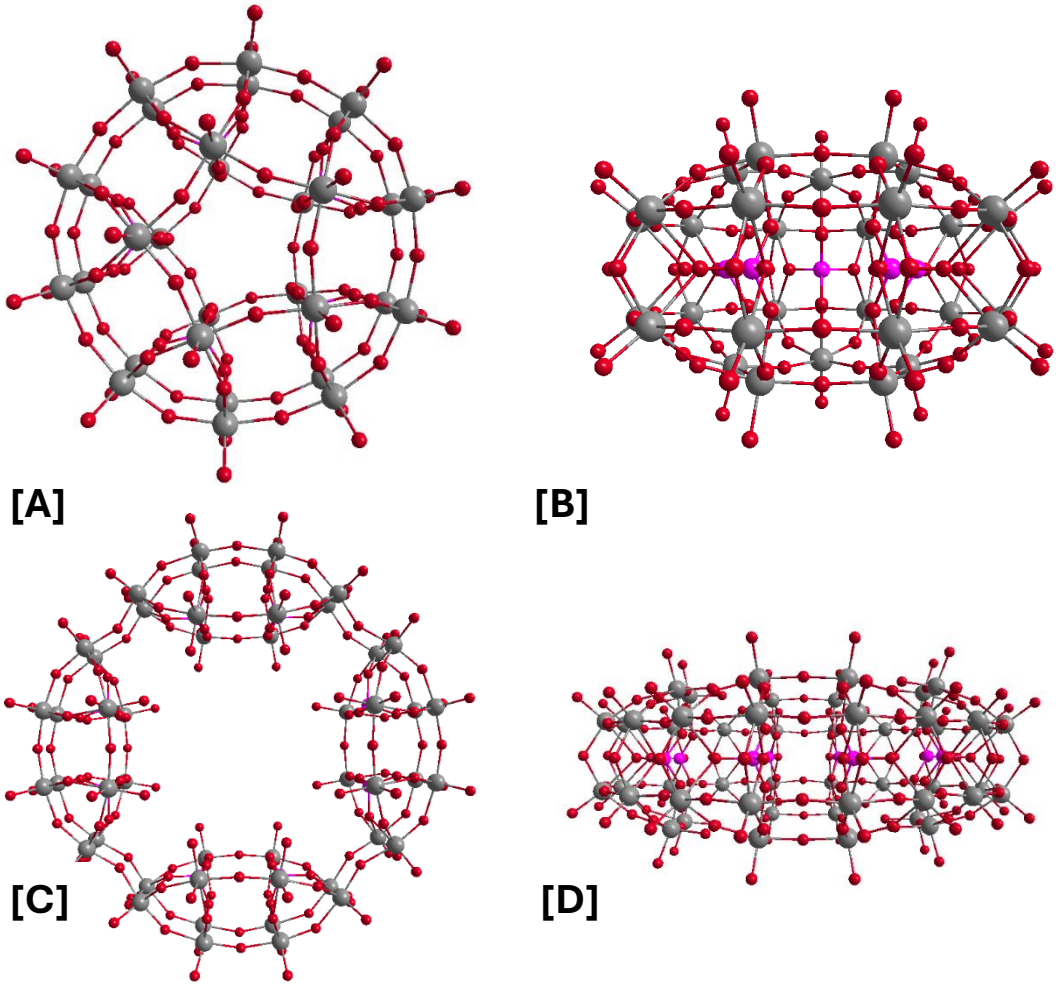

Figure 1.9. Ball and Stick geometries of $[P_5W_{30}O_{110}]^{15-}$ (**[A]** Top and **[B]** Side) 'Preyssler' and $[P_8W_{48}O_{184}]^{40-}$ (**[C]** Top and **[D]** Side) 'W_{48}' POM anions. W: grey, O: red, P: pink.

Preyssler's ability to act as a crown-ether has resulted in being applied within the fields of waste metal adsorption[68] and trapping of specific cations, such as cerium.[70] More recently, Preyssler POMs have been used as building block units as part of a larger porous POMzite network, with notable work being carried out by the research group of Prof. A.M. Schimpf,[71,72] which we shall discuss further later. Other applications include incorporation into POM-based silica surfaces,[73] catalysis,[74] and virus staining.[75]

There exist several, wheel shaped HPOMs composed of 48 tungsten framework atoms. (see **Fig. 1.9** and **1.10**). These HPOMs are: $[As_8W_{48}O_{184}]^{40-}$, $[P_8W_{48}O_{184}]^{40-}$, and $[Se_8W_{48}O_{176}]^{32-}$, which can be abbreviated as **{As_8W_{48}}**, **{P_8W_{48}}**, and **{Se_8W_{48}}** respectively.[76,77,78] Out of these,

{P8W48} is the most widely known within the literature. The remaining two POMs were discovered relatively recently and thus only have a handful of publications between them.

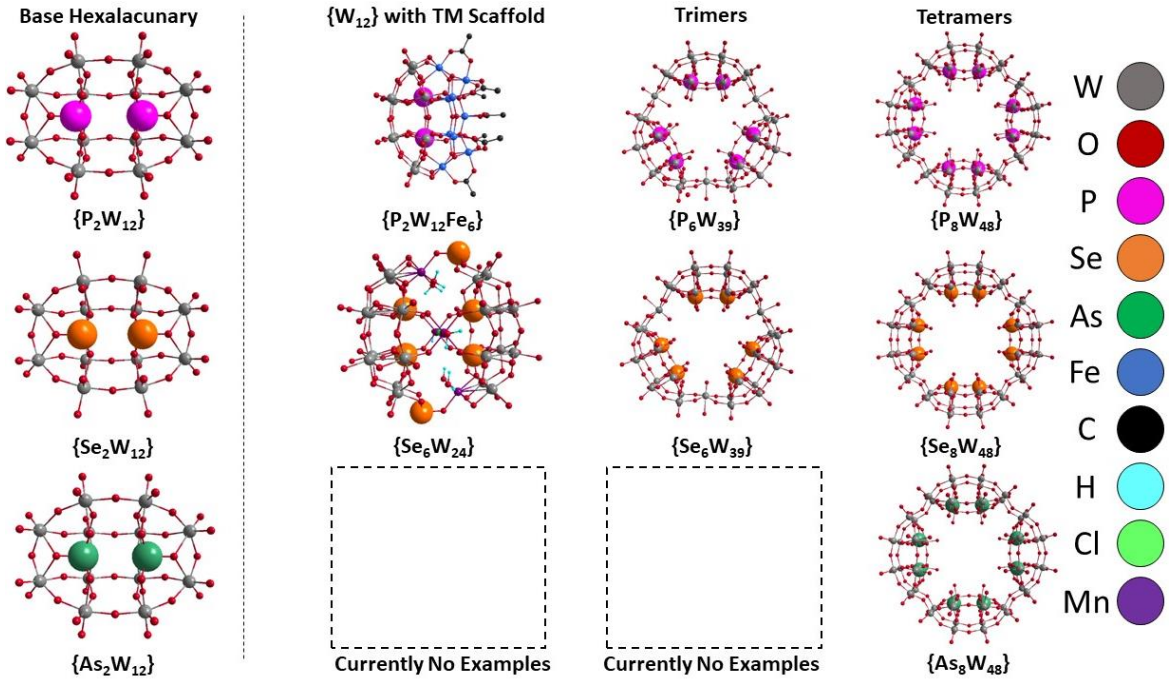

Figure 1.10. Ball-and-stick geometries for known hexalacunary species $[P_2W_{12}O_{48}]^{14-}$, $[Se_2W_{12}O_{46}]^{12-}$, and $[As_2W_{12}O_{48}]^{14-}$, as well as a few examples of further species they can form (where available), divided into TM-scaffold structures $[H_4P_2W_{12}Fe_9O_{56}(OAc)_7]^{6-}$, see in[79], and $[Mn_3Se_6W_{24}O_{94}Cl(H_2O)_2]^{15-}$, see in[78], (abbreviated as **{P2W12Fe6}** and **{Se6W24}** respectively), timers $[\{WO(H_2O)\}_3P_6W_{36}O_{144}]^{30-}$, see in[80], and $[Se_6W_{39}O_{141}(H_2O)_3]^{24-}$, see in[78], (abbreviated as **{P6W39}** and **{Se6W39}** respectively), and tetramers $[P_8W_{48}O_{184}]^{40-}$, see in[77], $[Se_8W_{48}O_{176}]^{32-}$, see in[78], and $[As_8W_{48}O_{184}]^{40-}$, see in[76], (abbreviated as **{P8W48}**, **{Se8W48}**, and **{As8W48}** respectively). Heteroatoms are enlarged for clarity.

All the **{W48}** POMs self-assemble by a multi-step process, beginning with an appropriate WD cage. This WD is subsequently exposed to very basic conditions, forming a hexalacunary structure by 'peeling off' roughly one third of the total framework (**Fig. 1.11**).[81] When the pH is decreased to mildly acidic levels, four of these hexalacunaries spontaneously self-aggregate to form the final **{W48}** wheel.[81,82] The hexalacunaries **{As2W12}**[83] and **{P2W12}**[81] have been isolated as intermediates whilst **{Se2W12}** currently exists as a theoretical transition state. It is unusual that, although many macrocycles exist in the wider chemical landscape, {W_{48}} POMs are relatively rare amongst the current library of polyoxometalates.

{P₈W₄₈} is considered an especially promising POM due to its intrinsic porosity, ability to reversibly store up to 28 electrons per cage, remarkable stability over a wide pH range (pH 1-8), unusually high anionic charge, and robust synthetic route (**Fig. 1.11**).[84,81] As previously mentioned, **{P₈W₄₈}** occupies the spotlight amongst the current W_{48} structures; first discovered in 1985 by R. Contant and A. Tézé., it received very little attention for 30 years, as the original report described the ring as relatively inert, stating "*... P_8W_{48} [does] not give complexes with divalent or trivalent transition-metal ion*.".[77] This changed in 2005, when S.S. Mal and U. Kortz published work detailing how it was possible to assemble a Cu_{20} 'core' within the pore of the larger **{P₈W₄₈}** wheel.[85]

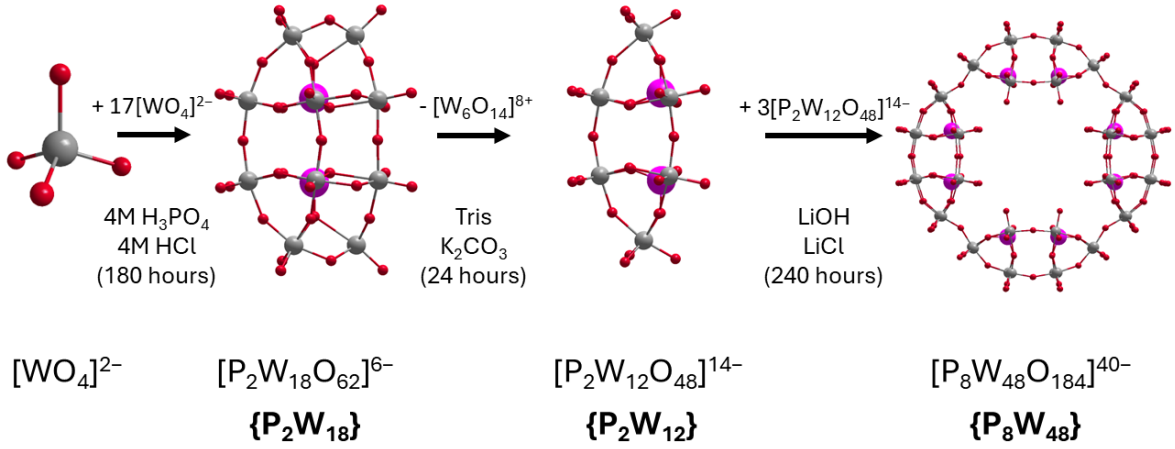

Figure 1.11. Ball and Stick representation of synthetic process for formation of $[P_8W_{48}O_{184}]^{40-}$ POM species by initial self-assembly of $[P_2W_{18}O_{62}]^{6-}$, followed by degradation in the presence of basic conditions to form the appropriate $[P_2W_{12}O_{48}]^{14-}$ hexalacunary species. Phosphorus heteroatoms are enlarged for clarity. W: grey, O: red, P: pink.

This is partly what makes W_{48}'s such a key member of the wider POM family, with the central pore able to be utilized for several different purposes. These include housing countercations,[82] commonly Na^+ or K^+, that aid in balancing the high anionic charge of the ring, capturing a desired cation in a similar manner to that observed in a crown ether, and construction of a multi-metal scaffold, where the metal is Cu,[86,85] Fe,[87] or U,[88] that confers magnetic properties, ideally ground state paramagnetic as this is a rare chemical property, to the POM as a whole. The interior face of the POM is much more nucleophilic than the exterior, which explains why cations are drawn into and trapped within the pore.

In cases where the symmetry of the wheel is broken, additional tungstate monomers can bind to the hinge regions.[89] It is unclear whether these 'growth points' originate from impurities from within the reaction mixture, which could be from unreacted reagents or, more likely, remnants of degraded POMs which didn't survive the strongly basic conditions associated with formation of lacunary structures.[90]

1.5 Large POMs

Beyond 100 metal framework atoms, POMs are only formed from Mo atoms, as only Mo-POMs have the inherent flexibility required to grow so large. The most common of these huge POMs can be classified as either Blue or Brown POMs.[91] Blue and Brown POMs are differentiated based on their shape; Blues have a wheel-like structure while Browns are more spherical and enclosed (**Fig. 1.12**).

Blue POMs are characterised by a well-structured nano-surface, pocked with numerous pores that smaller molecules can bind and react with. The Bielefeld Wheel, the previously mentioned and original 'Molybdenum Blue', is a prime example of a Blue POM. This class of POMs is generally formed through reduction of Mo(VI)-based salts under very acidic conditions.[12]

Brown POMs were discovered soon after the Bielefeld Wheel and share many similarities with Blue POMs.[91] They are in fact obtained from continuing to reduce already heavily reduced Blue POMs.[12] Due to their spherical structure and regulated internal environment, they have been compared to and show promise in being used to gain a deeper understanding of biological cells.

Whilst these POMs undoubtedly dwarf their common counterparts, they are themselves rendered modest in comparison to the largest POM discovered to date: the gargantuan 'lemon'

framework $Na_{48}[H_xMo_{368}O_{1032}(H_2O)_{240}(SO_4)_{48}]\cdot$ca. 1000 H_2O, abbreviated as **{Mo_{368}}**, which reaches 5.4nm in length.[9,91,92]

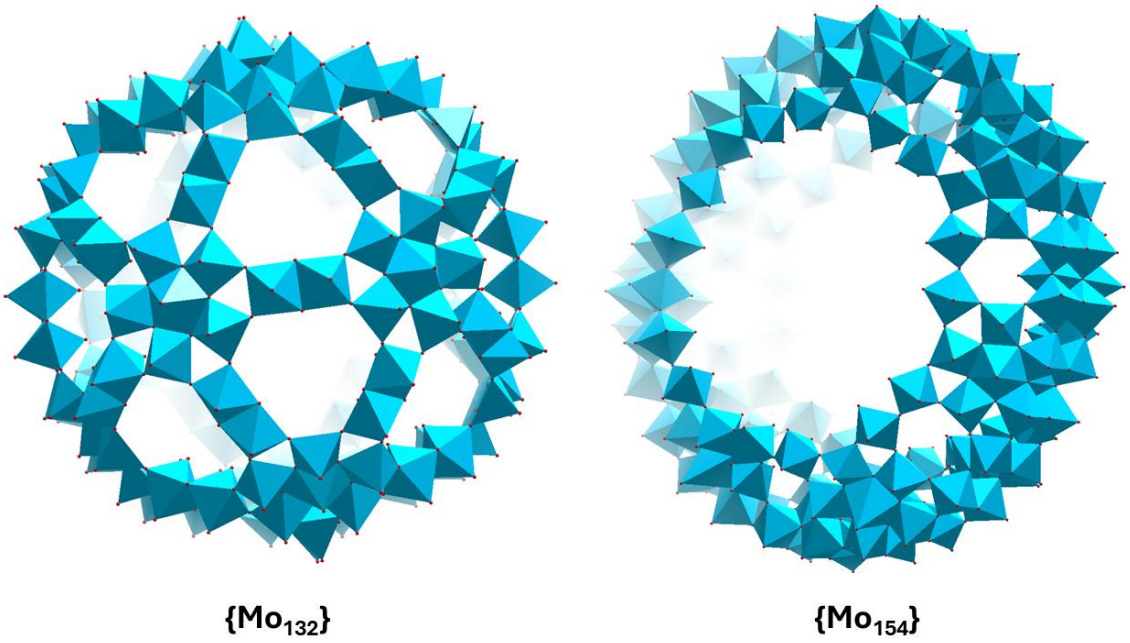

Figure 1.12. Polyhedron representation of differences in structures and characteristics between Blue and Brown POMs, represented using Bielefeld Wheel, $[Mo_{154}(NO)_{14}O_{462}H_{14}(H_2O)_{70}]^{28-}$, and Müller Sphere, $[Mo_{132}O_{372}(CH_3COO)_{30}(H_2O)_{72}]^{42-}$, frameworks respectively.

1.6 Countercations

Due to their, sometimes strongly, anionic nature, POMs are always isolated as salts in tandem with charge balancing countercations. These cations play a much more significant role than merely balancing the charge, with evidence indicating that they can play a direct role in the self-assembly process. Additionally, an appropriate cation must be chosen to facilitate formation, precipitation and subsequent crystallization of the desired POM.[93,94] Selection of an appropriate countercation is therefore vital and opens up a new method of conducting crystal engineering. Alkali Metal elements, such as potassium and sodium, are commonly featured as countercations for POMs; these can be substituted with each other in solution to alter the

properties of the POM substantially, altering framework solubility depending on the radius of the cation.

Bulky, organic cations, such as protonated hexamethylenetetramine (HMTAH),[22] protonated triethanol amine (TEAH),[95] and protonated *N*,*N*-bis-(2-hyrdoxyethyl)-piperazine (HBHEP),[96] are also regularly deployed. In contrast to their 'simple' Alkali Metal counterparts, these organic cations can guide self-assembly via a 'Shrink-wrapping' method.[22,94] To use the work of Long D.-L. *et al*[22] as an example, a group of Mo-based IsoPOMs can only be formed in the presence of the HMTAH countercation; in this case, each cation is big enough so that collectively, the surface area of the framework is completely surrounded and enclosed by the cations (**Fig. 1.13**). In cases where the choice of countercation influences selection of the final product, cryospray mass spectrometry (CSI-MS) studies can be utilized to quantify the degree of selection at play in solution.[97]

In addition to improving selectivity, cation selection can also influence the construction of larger POM-based frameworks, including POMzites. In the case of $[Ag_2\{Mo_5O_{13}(OMe)_4(NO)\}_2]^{4-}$,[98] the choice of cation affects the configuration and dimensionality of the final POMzite network, with inclusion of HTBA forming a 1-D sheet and HDMF allowing construction of a 2-D network.[99] Chirality can also be influenced, with chiral cations leading to the synthesis of chiral POM-based materials.[100,101]

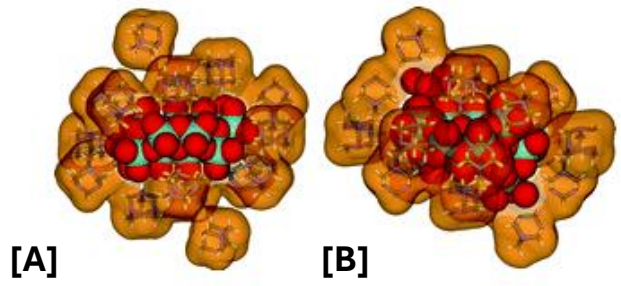

Figure 1.13. Shrink-wrapping effect of HMTA cations surrounding a POM in the cases of $(C_6H_{13}N_4)_{10}[H_2Mo_{16}O_{52}]$ **[A]** and $(C_6H_{13}N_4)_6[Fe_2(H_2O)_8H_2Mo_{16}O_{52}]$ **[B]**. Image borrowed from **Liang, D.L. *et al*.**[22]

1.7 Porous Materials

A porous material can be defined as any framework that allows or, via entrapment, arrests the passage of small molecules through its structure. Porous materials have been used by humanity as far back as the time of the Romans, who used zeolites formed from deposits of volcanic ash as cheap, lightweight, and durable building blocks for construction.[102] Since then, they have been utilised for a wide range of applications, with the library of structures burgeoning to meet this demand; examples include usage in medicine,[103] dentistry,[104] and synthesis of eco-friendly[105] and adsorptive materials. [106]

Zeolites are one of the most well-known porous materials, the most common of which are aluminosilicates; these zeolites have the general formula of $M_{x/n}[(AlO_2)_x(SiO_2)_y]\,wH_2O$, where M = Group 1 or 2 cation, n = valence of M, w = number of H_2O molecules, and x and y are the total number of tetrahedra within a given unit cell.[107] The ratio of y:x usually ranges between 1 and 5, but can be as large as 100 for silica zeolites. Additionally, zeolites display pores between 3-12Å in diameter, with water or cations loosely bound within.[108]

Zeolites were first identified by science more than 200 years ago by A.F. Cronstedt[109] but the field didn't take off until the 1940's, at which point zeolite structures could be accurately solved, allowing for effective modification of the network or, as is now possible for many species, being synthesized in the lab from scratch.[108] Since the 50's the use of zeolites has become even more widespread, in no small part due to their availability and porous abilities. This is showcased in the large variety of applications they can be utilised for; the main areas of catalysis[110,111] and adsorptive selectivity[112,113] are accompanied by water treatment for standard contaminants and radioactive material,[114,115] green chemistry,[116,117] and additives in animal feed.[118]

In contrast to zeolites, Metal-Organic Frameworks (MOFs) are inorganic-organic hybrids, with the inorganic metal oxide centres being connected by organic 'linker' molecules.[119] The field of MOFs became more widespread during the 90's, when they were first identified as a separate entity from coordination polymers[120,121,122] and some of their most well-known species, including MOF-5[123] and HKUST-1,[124] were synthesized. The immense range of MOF frameworks are registered in the Cambridge Structural Database, more than 10,000,[125] is due to the wide array of linkers that can be employed, as well as the connections they can form between metal centres.

MOFs offer a greater degree of control over the crystal structure and inherent framework properties than is possible for zeolites, allowing the network to structurally transform in the presence of external stimuli whilst maintaining crystallinity, which improves selectivity capabilities when it comes to gas adsorption applications.[126,127] This comes at the cost of structural tolerance for high temperature and pressure, with pores losing integrity under more extreme conditions, or simply if a guest molecule is removed (**Fig. 1.14**).[123] This renders MOFs unsuitable for many standard industrial processes, limiting their wide-spread deployment despite being financially viable.[128]

One exciting new type of porous material, referred to as 'POMzites',[89] can combine the thermal stability of zeolites with the modularity and customizability of MOFs without exhibiting the drawbacks associated with either network.[9] POMzites are composed of multiple discrete POM units, connected to each other via transition metal (TM) oxide 'linker' units of the form $[MO_x]$[129] (where M = Mn,[130] Co,[129] V,[129] Ni,[89] Ag,[90] x = 4-6) in the general configuration of POM – TM – POM.

The earliest work we have identified as a POMzite is a series of works conducted by Khan M.I. in 1999 working with Vanadium-based POMs,[131,132,133] but the field laid dormant for another decade before a number of works from within the Cronin group were published. These series of papers from the Cronin group covered a wide range of topics, including proving the **{P_8W_{48}}** POM is not inert, and can therefore absorb molecules[82] or form POMzite networks,[84] in addition to detailing new POMzite configurations, based on **{P_8W_{48}}**[134, 130] or other POMs.[135]

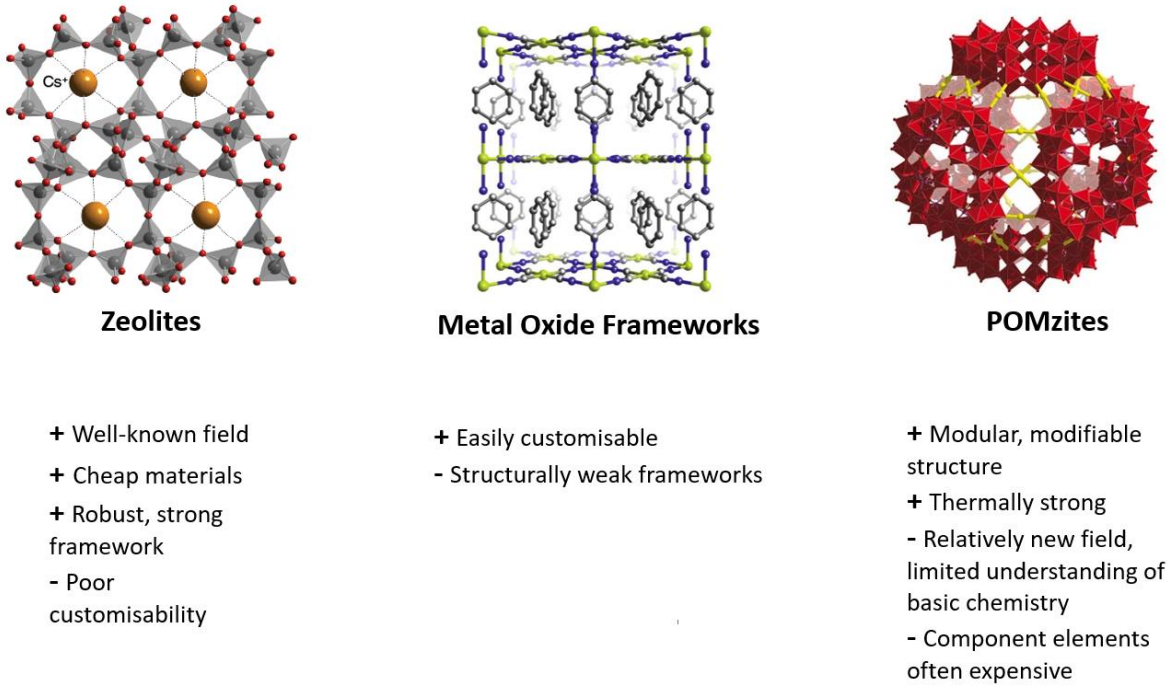

Figure 1.14. Comparison of properties between several different species of porous networks. Images for the Clinoptilolite zeolite, Hofmann-type clathrate MOF, and POMzite, are borrowed from **Weller, M. *et al***,[136] **Otsubo, K. *et al***,[137] and **Mitchell, S.G. *et al***.[134]

POMzite materials have two distinct benefits over MOFs and zeolites respectively: firstly, each POM building block serves as an easily identifiable secondary building block (SBU), allowing for easy identification and differentiation between different networks, and secondly the modular fashion in which **{P_8W_{48}}** is built up from its base $[WO_4]^{2-}$ monomer, through the WD and hexalacunary to the final product, allows for a great degree of control over not just the POM but also the final POMzite product.

One work by Zhan C. *et al* encapsulates the benefits of the new materials over their counterparts perfectly, where the POMzite synthesized was capable of existing as and reversibly transforming between one of 8 distinct states.[138] This incredible pairing of flexibility and ongoing structural stability is only possible through the ability of the TM anion linking unit to easily exchange ligands or repeatedly form new bonds with the POM node unit based on changes in the environment and the integrity of the POM used as a building block for the

network. Only 3 POMs have thus far been utilized as building blocks for a POMzite network: $[P_8W_{48}O_{184}]^{40-}$, $[P_5W_{30}O_{110}]^{15-}$, and $[SV_{18}O_{46}]^{14-}$.

The types of molecules that can be encapsulated within the POMzite network vary; at the high end range is the absorption of close to 35 Cu(II) cations within the cube structure of POMzite-3(Mn).[134] These cations can be, additionally, reversibly desorbed; uptake or loss of cations can be controlled via electrochemically switching the oxidation state of the TM linkers or by physically blocking the pores of the POMs using large organic cations once the POMzite has reached its absorption capacity.

$[P_8W_{48}O_{184}]^{40-}$, as previously mentioned, is an ideal scaffold for extended structures due to its stability across a wide range of pH values, exemplary redox properties, and high anionic charge and intrinsic porosity, which make it perfect for attracting and trapping small cationic molecules or ions. Out of the currently available POMzite building blocks, this POM yields the greatest range of structures in terms of variety and dimensionality.[89]

Just as with their POM constituents, POMzite formation is determinant on a very complex interplay of numerous synthetic variables. Several of these are common to all POM-related synthesis, most prominently pH and temperature control;[130] a more acidic solution, for example, generally results in a more porous material, whilst a temperature between room temperature (20-30°C) and 70-90°C acts as a sweet spot where a sufficient number of TM linkers bind to the SBB POM unit to allow for POMzite network growth. Other variables, such as the choice and concentration of TM linker for the network,[90] are specific to POMzites only.

The disadvantage to using POMzites that will limit their widespread use is that of their elemental composition; the metals employed, particularly those employed as TM linker units, are many magnitudes of order rarer, and therefore more expensive, than the abundant elements of Al and Si that zeolites are composed of.[139] Combined with the same lack of a comprehensive understanding pertaining to their self-assembly processes shared with POMs themselves, this acts to severely hamstring the widespread deployability of this material. Zeolites and MOFs,

by comparison, tend to be synthesized from more abundant elements; this, coupled with the trove of literature available for these materials, continues to give them a monopoly in the market of porous networks, zeolites especially (**Fig. 1.14**).

1.8 POM Applications

The variety of applications POMs have been utilised for is immense, ranging from electrochemical fields of study through to novel uses in relation to biological systems. In this sub-section we will aim to cover several of the most prevalent fields of study from the literature, highlighting why research into polyoxometalates is not only worthwhile but also potentially crucial for solving many of the major issues facing the scientific community today.

1.8.1 Biomedical

With the rise of both drug-resistant bacteria and viruses, as well as cancer rates, there is an ever-growing need for new methods of tackling these sicknesses. The literature reports POMs as able to block replication of several well-known bacteria and viruses, including influenza, HIV, and HSV, as well as helping construct nanocomposites at the affected site to improve drug delivery and activity.[140,141] Polyoxotungstates, specifically, have been identified as the most effective POM sub-species for neutralizing these microorganisms.[142]

Additionally, POMs can be used to target cancerous cells in a few different approaches such as acting as nanoprobes, whereby POMs can form coloured compounds by reacting with tumour-associated molecules and allowing for easy cancer detection, or by relying on redox reactions native to tumorous regions to protonate the framework to an active, ‘toxic’ species.[140,141] This second tactic is especially exciting because it allows for cancer medicine to

only target tumorous areas of the body and massively reduce chemotherapy associated side effects.

POMs are ideal drug molecules or delivery systems for other drugs due to exhibiting low toxicity towards the human body and good solubility in water. The ease with which POMs can be functionalized to bind to a wide range of different organic molecules, such as amino acids and dopamine, lends these frameworks well to being utilised for many different treatments.

Of final note is the ability of the well-known $[P_2W_{18}O_{62}]^{6-}$ Wells-Dawson to improve quality of crystallization of ribosomes; for this discovery Yonath, A.E., Ramakrishnan V., and Steitz T.A. were presented with the Chemical Nobel Prize in 2009 due to the unlocked capability for researchers to finally map ribosome sections to a high degree of accuracy, allowing for information on amino acid sequencing and subsequent protein transcription.[143]

1.8.2 Catalysis

Polyoxometalates are ideal candidates for use as catalysts, containing both acidic or electrophilic and basic or nucleophilic sites in their terminal oxygen and metal framework atoms respectively; combined with their tuneable redox properties, very stable structures, and ability to be photo- and electroactive, they can easily be applied to a range of different problems.[144] Use of POMs as catalysts for oxidation reactions specifically has been widely reported,[145,146,147] but if one takes time to properly activate the POM, they can be effectively used for reduction reactions too;[148,149] some species are even bifunctional, facilitating both the oxidation and reduction components of the catalytic cycle.[150]

POM-organic hybrids have also shown promise due to their photoactivity when exposed to visible light. Photoactivity can be tuned to a specific wavelength of light based on the choice of organic ligand within the hybrid; ligands such as cationic chromophores have been identified

as suitable for this task.[151] Compared with their semiconductor competitors, POM-based photocatalysts are deemed more desirable due to being cheaper, more environmentally friendly, very redox active, and significantly more customisable in their design. Current photocatalytic applications for POMs include CO_2 and N_2 reduction,[148,149] photochromism,[152,153] and water purification[154] and splitting.[155,156,157]

Water splitting POM catalysts, such as $[\{Ru_4O_4(OH)_2(H_2O)_4\}(\gamma\text{-}SiW_{10}O_{36})_2]$, are of particular interest due to their ability to generate hydrogen fuel;[155] this source of fuel is being extensively researched due to its capability of revolutionizing the energy industry if it can be commercially deployed on a large scale. POMs are well suited to operate as water splitting catalysts due to the high number of active sites in their framework, and ability to incorporate non-POM components, such as noble metal cations or organic ligands, further improving catalytic efficiency.[158]

Ammonia synthesis accounts for almost 2% of worldwide annual energy consumption and still heavily relies on the energy intensive Haber-Bosch process.[159] Any material which can act as a catalyst for this reaction therefore stands to free up a monumental amount of energy for other uses. POMs have been identified as suitable catalysts for the electrocatalytic nitrogen reduction reaction, as they are able to inject electrons directly into nitrogen, overcoming its infamously inert nature.[160,161,162] POMs are also well suited as CO_2 activating catalysts due to the high basicity of their terminal oxygen atoms;[163] one hybrid species, $\{P_4Mo_6\}$/Ru(bpy), is a photocatalytic system which, in tandem with Co^{2+} cations, has been shown to produce 322.7nm CO from the parent CO_2 in a time span of 10 hours.[164]

1.8.3 Gas Adsorption

POMs have proven especially well-suited to trapping select elements and small molecules, especially when incorporated into a larger MOF network.[165] These POMOF materials are well

referenced in the literature, with multiple examples of the selective trapping of gases such as O_2 and CO_2,[166,167] as well as larger organic compounds including benzene[168] and formaldehyde.[169] A relatively new support material, known as ionic crystals, have also been used to enhance the adsorptive properties of POMs.[170,171] Unlike MOFs, these crystals can 'flex' after absorption, allowing for uptake of a larger range of compounds than the relatively inflexible MOFs.[171]

A crucial aspect to absorption and separation is that of the removal of contaminants from the chemical mixture. Everyday applications, like that of wastewater purification,[154] are contrasted with less obvious uses, such as trapping and removing radioactive elements from the environment.[172] Capture of CO_2 has been highlighted in several works,[166,167,173] with preferential absorption over other gas molecules; despite this initially proving a possible solution for removing excess, man-made CO_2 from the atmosphere, we believe POMs too expensive a material to be deployed widely enough to make a difference, especially when compared with available bio-alternatives.

1.8.4 Molecular Memory

Improving the storage capacity of metal-oxide semiconductors is hampered by the principles of Moore's Law, which prevents increased storage density at our current level of technology due to the effects of quantum mechanics.[174,175] One solution is to use individual molecules to store memory, thus allowing us to improve storage density whilst still abiding by Moore's Law. POMs are specifically well suited to this task as the metal framework can encase and protect the oxidizable heteroatom 'core' against extreme environmental conditions; a tungsten POM can withstand temperatures of up to 600K.

Work carried out by Vilà-Nadal *et. al.*[176] demonstrated how a $[Se_2W_{18}O_{60}]^{4-}$ POM can be used to store a new type of rewritable memory; reduction of the POM causes a shift in the oxidation state of the selenium heteroatoms and subsequently fosters reversible bond formation between

the two atoms. This bond can be regarded as representing a byte of information, with absence or presence representing 0 or 1 binary code respectively.

1.8.5 Redox Flow Batteries

The storing of renewably generated energy is one of the most pertinent issues of this century; despite the many benefits of substituting the burning of fossil fuels by harnessing the power of the elements, the unpredictable nature of said elements means that without the ability to store energy in times of plenty and release it in times of scarcity, it is not viable for our energy needs to be wholly satisfied by renewables.[177]

Redox active POMs have been identified as especially well suited to the reversible storage of electrons, showing promise as a potential solution for solving our renewable problem; able to undergo numerous, distinct redox steps at room temperature and without decomposition over sufficiently long periods of time in aqueous[178] and non-aqueous[179] solutions, they have already found applications as fuel cells and Redox Flow Batteries (RFBs).[1]

As previously mentioned, redox ability in POMs is dependent on the choice of element for both the metal framework and heteroatom, as well as the family and size of POM (Keggin, WD…) used, and the nature of countercations present.[6,180,181] $Li_6[P_2W_{18}O_{62}]$, for instance, can be reduced by up to 18 electrons per cage, or 1 electron per metal centre.[182] This translates to a potential maximum of 2.46 x 10^{21} electrons which can be stored per gram of WD material. Other highly reducible species include $[NaP_5W_{30}O_{110}]^{14-}$ and $[H_7P_8W_{48}O_{184}]^{33-}$, which can be reduced up to 23 or 28 times per POM cluster respectively.[183]

Whilst other chemical species exist which can match (ferrocene can store up to 18 electrons per unit molecule)[184] or even exceed POMs in electrons stored per metal centre (permanganate can be reduced up to a maximum of 5 times per metal centre), POMs shine as candidates for

redox flow batteries due to the following factors: good solubility in a range of solvents, modular synthesis which allows one to easily tune the redox abilities of the species to suit specific applications, a relatively durable structure that allows for withstanding harsh temperatures and acidities, and their nature as discrete 0-D clusters; the last point in particular prevents POMs from exhibiting the properties of bulk materials and being subsequently affected by electron tunnelling, which would reduce the ability for POMs to reliably store electrons for longer periods of time.

Finally, one of the main problems in the field of redox flow batteries is how to improve energy density and incorporation of organic components to improve charge carrier rate has yielded poor results. Organic-POM hybrids have demonstrated better performance as organic-redox flow batteries due to their high solubility and good framework stability. Additionally, non-hybrid POMs are also suitable for use in aqueous RFBs, where they can operate effectively at much colder temperatures than standard electrolytes.

1.9 References

(1) Han, Y.; Lan, J.; Li, K.; Yang, L.; Zhu, C.; Chen, J. The Cluster Design and Redox Behavior Characterization of Polyoxometalates for Redox Flow Batteries. *Chem. – An Asian J.* **2022**, *17* (24), 1–14. https://doi.org/10.1002/asia.202200950.

(2) Pope, M. T. *Heteropoly and Isopoly Oxometalates*, 1st ed.; Springer Berlin, Heidelberg, 1983.

(3) Hill, C. L. Polyoxometalates [Special Issue]. *Chem. Rev.* **1998**, *98*, 1–390.

(4) Pope, M. T.; Muller, A. *Polyoxometalate Chemisty From Topology via Self-Assembly to Applications*, 1st ed.; Springer Netherlands, 2001. https://doi.org/10.1007/0-306-47625-8.

(5) Long, D. L.; Burkholder, E.; Cronin, L. Polyoxometalate Clusters, Nanostructures and Materials: From Self Assembly to Designer Materials and Devices. *Chem. Soc. Rev.* **2007**, *36* (1), 105–121. https://doi.org/10.1039/b502666k.

(6) Streb, C. New Trends in Polyoxometalate Photoredox Chemistry: From Photosensitisation to Water Oxidation Catalysis. *Dalt. Trans.* **2012**, *41* (6), 1651–1659. https://doi.org/10.1039/c1dt11220a.

(7) Walsh, J. J.; Bond, A. M.; Forster, R. J.; Keyes, T. E. Hybrid Polyoxometalate Materials for Photo(Electro-) Chemical Applications. *Coord. Chem. Rev.* **2016**, *306* (Part 1), 217–234. https://doi.org/10.1016/j.ccr.2015.06.016.

(8) Blasco-Ahicart, M.; Soriano-Lopez, J.; Carbo, J. J.; Poblet, J. M.; Galan-Mascaros, J. R. Polyoxometalate Electrocatalysts Based on Earth-Abundant Metals for Efficient Water Oxidation in Acidic Media. *Nat. Chem.* **2017**, *10*, 24–30. https://doi.org/10.1038/nchem.2874.

(9) Vilà-Nadal, L.; Cronin, L. Design and Synthesis of Polyoxometalate-Framework Materials from Cluster Precursors. *Nat. Rev. Mater.* **2017**, *2*, 1–15. https://doi.org/10.1038/natrevmats.2017.54.

(10) Wang, Z.; Xin, X.; Zhang, M.; Li, Z.; Lv, H.; Yang, G. Y. Recent Advances of Mixed-Transition-Metal-Substituted Polyoxometalates. *Sci. China Chem.* **2022**, *65* (8), 1515–1525. https://doi.org/10.1007/s11426-022-1276-4.

(11) Scheele, C. W. *Sämtliche Physische Und Chemische Werke*; Hermannstadt, 1793.

(12) Muller, A.; Serain, C. Soluble Molybdenum Blues - "Des Pudels Kern." *Acc. Chem. Res.* **2000**, *33* (1), 2–10. https://doi.org/10.1021/ar9601510.

(13) Berzelius, J. J. Beitrag Zur Näheren Kenntnis Des Molybdäns. *Poggend. Ann. Phys. Chem.* **1826**, *6*, 369–392.

(14) Galissard de Marignac, J.-C. Recherches Sur Les Acides Silicotungstiques. *C. Ann. Chim. Phys.* **1864**, *3* (1).

(15) Keggin, J. F. Structure of the Crystals of 12-Phosphotungstic Acid. *Nature* **1933**, *132*, 351.

(16) Keggin, J. F. The Structure and Formula of 12-Phosphotungstic Acid. *Proc. R. Soc. A.* **1934**, *144* (851), 75–100. https://doi.org/10.1098/rspa.1934.0035.

(17) Baker, L. C. W.; Glick, D. C. Present General Status of Understanding of Heteropoly Electrolytes and a Tracing of Some Major Highlights in the History of Their Elucidation. *Chem. Rev.* **1998**, *98* (1), 3–49. https://doi.org/10.1021/cr960392l.

(18) Vilà-Nadal, L.; Wilson, E. F.; Miras, H. N.; Rodríguez-Fortea, A.; Cronin, L.; Poblet, J. M. Combined Theoretical and Mass Spectrometry Study of the Formation-Fragmentation of Small Polyoxomolybdates. *Inorg. Chem.* **2011**, *50* (16), 7811–7819. https://doi.org/10.1021/ic200969h.

(19) Müller, A.; Roy, S. En Route from the Mystery of Molybdenum Blue via Related Manipulatable Building Blocks to Aspects of Materials Science. *Coord. Chem. Rev.* **2003**, *245* (1–2), 153–166. https://doi.org/10.1016/S0010-8545(03)00110-3.

(20) López, X.; Vilà-Nadal, L.; Aparicio-Anglès, X.; Poblet, J. M. Theoretical View on the Origin and Implications of Structural Distortions in Polyoxometalates. *Phys. Procedia* **2010**, *8*, 94–103. https://doi.org/10.1016/j.phpro.2010.10.018.

(21) Yan, L.; López, X.; Carbó, J. J.; Sniatynsky, R.; Duncan, D. C.; Poblet, J. M. On the Origin of Alternating Bond Distortions and the Emergence of Chirality in Polyoxometalate Anions. *J. Am. Chem. Soc.* **2008**, *130* (26), 8223–8233. https://doi.org/10.1021/ja711008n.

(22) Long, D. L.; Kögerler, P.; Farrugia, L. J.; Cronin, L. Restraining Symmetry in the Formation of Small Polyoxomolybdates: Building Blocks of Unprecedented Topology Resulting from "Shrink-Wrapping" [H2Mo16O52]10- -Type Clusters. *Angew. Chemie - Int. Ed.* **2003**, *42* (35), 4180–4183. https://doi.org/10.1002/anie.200351615.

(23) Ritchie, C.; Streb, C.; Thiel, J.; Mitchell, S. G.; Miras, H. N.; Long, D. L.; Boyd, T.; Peacock, R. D.; McGlone, T.; Cronin, L. Reversible Redox Reactions in an Extended Polyoxometalate Framework Solid. *Angew. Chemie - Int. Ed.* **2008**, *47* (36), 6881–6884. https://doi.org/10.1002/anie.200802594.

(24) Janusson, E.; De Kler, N.; Vilà-Nadal, L.; Long, D. L.; Cronin, L. Synthesis of Polyoxometalate Clusters Using Carbohydrates as Reducing Agents Leads to Isomer-Selection. *Chem. Commun.* **2019**, *55* (41), 5797–5800. https://doi.org/10.1039/c9cc02361e.

(25) Bhattacharyya, R.; Biswas, S.; Armstrong, J.; Holt, E. M. New and General Route to the Synthesis of Oxopolymetalates via Peroxometalates in Aqueous Medium: Synthesis and Crystal and Molecular Structure of Bis[Bis(Triphenylphosphine)Nitrogen(1+)]Nonadecaoxohexatungstate(2-). *Inorg. Chem.* **1989**, *28* (23), 4297–4300. https://doi.org/10.1021/ic00322a024.

(26) Long, D. L.; Brücher, O.; Streb, C.; Cronin, L. Inorganic Crown: The Host-Guest Chemistry of a High Nuclearity "Celtic-Ring" Isopolyoxotungstate [H12W36O120]12-. *Dalt. Trans.* **2006**, No. 23, 2852–2860. https://doi.org/10.1039/b515935k.

(27) Khan, M. I.; Chen, Q.; Höpe, H.; Parkin, S.; O'Connor, C. J.; Zubieta, J. Hydrothermal Synthesis and Characterization of Hexavanadium Polyoxo Alkoxide Anion Clusters: Crystal Structures of the Vanadium(IV) Species Ba[V6O7(OH)3{(OCH2)3CCH3}3]·3H2O and Na2[V6O7{(OCH2)3CCH2CH3}4], of the Mixed-Valence Complex (Me3NH)[VIV5VVO7(OH)3. *Inorg. Chem.* **1993**, *32* (13), 2929–2937. https://doi.org/10.1021/ic00065a022.

(28) Dale, B. W.; Pope, M. T. The Heteropoly-12-Niobomanganate(IV) Anion. *Chem. Commun.* **1967**, No. 16, 792–792. https://doi.org/10.1039/C19670000792.

(29) Anderson, T. M.; Rodriguez, M. A.; Bonhomme, F.; Bixler, J. N.; Alam, T. M.; Nyman, M. An Aqueous Route to [Ta6O19] 8- and Solid-State Studies of Isostructural Niobium and Tantalum Oxide Complexes. *Dalt. Trans.* **2007**, *9226* (40), 4517–4522. https://doi.org/10.1039/b707636c.

(30) Pope, M. T.; Dale, B. W. Isopoly-Vanadates, -Niobates, and -Tantalates. *Q. Rev. Chem. Soc.* **1968**, *22* (4), 527–548. https://doi.org/10.1039/QR9682200527.

(31) Hartl, H.; Pickhard, F.; Emmerling, F.; Röhr, C. Rubidium- Und Caesium-Verbindungen Mit Dem Isopolyanion [Ta6O19]8- - Synthesen, Kristallstrukturen, Thermische Und Schwingungsspektroskopische Untersichingen Der Oxotantalate A8[Ta6O19] * n H2O (A = Rb, Cs; n = 0,4,14). *J. Inorg. Gen. Chem.* **2001**, *627* (12), 2630–2638. https://doi.org/10.7868/s0132344x16050017.

(32) Fuchs, J.; Hartl, H.; Schiller, W.; Gerlach, U. Die Kristallstruktur Des Tributylammoniumdekawolframats [(C4H9)3NH]4W10O32. *Acta Crystallogr. Sect. B Struct. Crystallogr. Cryst. Chem.* **1976**, *32* (3), 740–749. https://doi.org/10.1107/S0567740876003907.

(33) Cruywagen, J. J.; Van der Merwe, I. F. J.; Nassimbeni, L. R.; Niven, M. L.; Symonds, E. A. Crystal and Molecular Structure of Sodium Paratungstate 26 Hydrate. *J. Crystallogr. Spectrosc. Res.* **1986**, *16* (4), 525–535. https://doi.org/10.1007/BF01161041.

(34) Fuchs, J.; Flindt, E.-P. Preparation and Structure Investigation of Polytungstates. A Contribution to the Paratungstate A Problem. *Z. Naturforsch. B* **1979**, *34* (3), 412–422. https://doi.org/10.1515/znb-1979-0311.

(35) Long, D. L.; Kögerler, P.; Parenty, A. D. C.; Fielden, J.; Cronin, L. Discovery of a Family of Isopolyoxotungstates [H4W 19O62]6- Encapsulating a {WO6} Moiety within a {W18} Dawson-like Cluster Cage. *Angew. Chemie - Int. Ed.* **2006**, *45* (29), 4798–4803. https://doi.org/10.1002/anie.200504600.

(36) Tzirakis, M. D.; Lykakis, I. N.; Orfanopoulos, M. Decatungstate as an Efficient Photocatalyst in Organic Chemistry. *Chem. Soc. Rev.* **2009**, *38* (9), 2609–2621. https://doi.org/10.1039/b812100c.

(37) Ravelli, D.; Protti, S.; Fagnoni, M. Decatungstate Anion for Photocatalyzed "Window Ledge" Reactions. *Acc. Chem. Res.* **2016**, *49* (10), 2232–2242. https://doi.org/10.1021/acs.accounts.6b00339.

(38) Ravelli, D.; Fagnoni, M.; Fukuyama, T.; Nishikawa, T.; Ryu, I. Site-Selective C-H Functionalization by Decatungstate Anion Photocatalysis: Synergistic Control by Polar and Steric Effects Expands the Reaction Scope. *ACS Catal.* **2018**, *8* (1), 701–713. https://doi.org/10.1021/acscatal.7b03354.

(39) Perry, I. B.; Brewer, T. F.; Sarver, P. J.; Schultz, D. M.; DiRocco, D. A.; MacMillan, D. W. C. Direct Arylation of Strong Aliphatic C–H Bonds. *Nature* **2018**, *560* (7716), 70–75. https://doi.org/10.1038/s41586-018-0366-x.

(40) Capaldo, L.; Ravelli, D. Hydrogen Atom Transfer (HAT): A Versatile Strategy for Substrate Activation in Photocatalyzed Organic Synthesis. *European J. Org. Chem.* **2017**, *2017* (15), 2056–2071. https://doi.org/10.1002/ejoc.201601485.

(41) Kibler, A. J.; Newton, G. N. Tuning the Electronic Structure of Organic–Inorganic Hybrid Polyoxometalates: The Crucial Role of the Covalent Linkage. *Polyhedron* **2018**, *154*, 1–20. https://doi.org/10.1016/j.poly.2018.06.027.

(42) Cameron, J. M.; Guillemot, G.; Galambos, T.; Amin, S. S.; Hampson, E.; Mall Haidaraly, K.; Newton, G. N.; Izzet, G. Supramolecular Assemblies of Organo-Functionalised Hybrid Polyoxometalates: From Functional Building Blocks to Hierarchical Nanomaterials. *Chem. Soc. Rev.* **2022**, *51* (1), 293–328. https://doi.org/10.1039/d1cs00832c.

(43) Long, D. L.; Cronin, L. Towards Polyoxometalate-Integrated Nanosystems. *Chem. - A Eur. J.* **2006**, *12* (14), 3698–3706. https://doi.org/10.1002/chem.200501002.

(44) Dutta, D.; Dolai, M.; Biswas, S.; Dutta, A.; Ali, M. Multidimensional CuII Incorporated POMs [KI2CuII(En)2(β-Mo8O26)]n and [KI2CuII3(H2O)10(W12O40)0.2(H2O)]n: Syntheses, Structures and Catalytic Epoxidation. *Polyhedron* **2020**, *176*. https://doi.org/10.1016/j.poly.2019.114204.

(45) Jassal, A. K.; Mudsainiyan, R. K.; Shankar, R. A Rational Assembly of Paradodecatungstate Anions from Clusters to Morphology-Controlled Nanomaterials. *Mater. Chem. Front.* **2021**, *5* (3), 1090–1125. https://doi.org/10.1039/d0qm00646g.

(46) Mbomekalle, I. M.; Lu, Y. W.; Keita, B.; Nadjo, L. Simple, High Yield and Reagent-Saving Synthesis of Pure α-K 6P2W18O62 · 14H2O. *Inorg. Chem. Commun.* **2004**, *7* (1), 86–90. https://doi.org/10.1016/j.inoche.2003.10.011.

(47) Minato, T.; Suzuki, K.; Kamata, K.; Mizuno, N. Synthesis of α-Dawson-Type Silicotungstate [α-Si 2W18O62]8- and Protonation and Deprotonation inside the Aperture through Intramolecular Hydrogen Bonds. *Chem. - A Eur. J.* **2014**, *20* (20), 5946–5952. https://doi.org/10.1002/chem.201400390.

(48) Long, D. L.; Abbas, H.; Kögerler, P.; Cronin, L. Confined Electron-Transfer Reactions within a

Molecular Metal Oxide "Trojan Horse." *Angew. Chemie - Int. Ed.* **2005**, *44* (22), 3415–3419. https://doi.org/10.1002/anie.200500541.

(49) Contant, R.; Thouvenot, R. A Reinvestigation of Isomerism in the Dawson Structure: Syntheses and 183W NMR Structural Characterization of Three New Polyoxotungstates [X2W18O62]6- (X=PV, AsV). *Inorganica Chim. Acta* **1993**, *212* (1–2), 41–50. https://doi.org/10.1016/S0020-1693(00)92306-5.

(50) Miras, H. N.; Stone, D.; Long, D. L.; McInnes, E. J. L.; Kögerler, P.; Cronin, L. Exploring the Structure and Properties of Transition Metal Templated {VM17(VO4)2} Dawson-like Capsules. *Inorg. Chem.* **2011**, *50* (17), 8384–8391. https://doi.org/10.1021/ic200943s.

(51) Long, D. L.; Song, Y. F.; Wilson, E. F.; Kögerler, P.; Guo, S. X.; Bond, A. M.; Hargreaves, J. S. J.; Cronin, L. Capture of Periodate in a {W18O54} Cluster Cage Yielding a Catalytically Active Polyoxometalate [H3W 18O56(IO6)]6- Embedded with High-Valent Iodine. *Angew. Chemie - Int. Ed.* **2008**, *47* (23), 4384–4387. https://doi.org/10.1002/anie.200800041.

(52) Jeannin, Y.; Martin-Frere, J. X-Ray Study of (NH4)7[H2AsW18O60]'16H2O: First Example of a Heteropolyanion Containing Protons and Arsenic(III). *Inorg. Chem.* **1979**, *18* (11), 3010–3014. https://doi.org/10.1021/ic50201a013.

(53) Wang, J. P.; Ma, P. T.; Niu, J. Y. Synthesis, Crystal Structure and Properties of a New Organic-Inorganic Hybrid Dawson-like Polyoxotungstate [Co(2,2'-Bpy)3] 2[Co(2,2'-Bpy)2Cl][Co(2,2'-Bpy) 2]H2[SbW18O60]•4H2O. *Sci. China, Ser. B Chem.* **2007**, *50* (6), 784–789. https://doi.org/10.1007/s11426-007-0140-7.

(54) Long, D. L.; Yan, J.; de la Oliva, A. R.; Busche, C.; Miras, H. N.; Errington, R. J.; Cronin, L. A Redox-Triggered Structural Rearrangement in an Iodate-Templated Polyoxotungstate Cluster Cage. *Chem. Commun.* **2013**, *49* (84), 9731–9733. https://doi.org/10.1039/c3cc45659e.

(55) Pope, M. T. Happy Birthday Keggin Structure! *Eur. J. Inorg. Chem.* **2013**, *2013* (10–11), 1561–1561. https://doi.org/10.1002/ejic.201300282.

(56) Malmir, M.; Heravi, M. M.; Yekke-Ghasemi, Z.; Mirzaei, M. Incorporating Heterogeneous Lacunary Keggin Anions as Efficient Catalysts for Solvent-Free Cyanosilylation of Aldehydes and Ketones. *Sci. Rep.* **2022**, *12* (1), 1–9. https://doi.org/10.1038/s41598-022-15831-1.

(57) Chen, X.; Huang, P.; Zhu, X.; Zhuang, S.; Zhu, H.; Fu, J.; Nissimagoudar, A. S.; Li, W.; Zhang, X.; Zhou, L.; Wang, Y.; Lv, Z.; Zhou, Y.; Han, S. T. Keggin-Type Polyoxometalate Cluster as an Active Component for Redox-Based Nonvolatile Memory. *Nanoscale Horizons* **2019**, *4* (3), 697–704. https://doi.org/10.1039/c8nh00366a.

(58) Friedl, J.; Pfanschilling, F. L.; Holland-Cunz, M. V.; Fleck, R.; Schricker, B.; Wolfschmidt, H.; Stimming, U. A Polyoxometalate Redox Flow Battery: Functionality and Upscale. *Clean Energy* **2019**, *3* (4), 278–287. https://doi.org/10.1093/ce/zkz019.

(59) Fotović, L.; Bedeković, N.; Stilinović, V. Keggin-Type Anions as Halogen Bond Acceptors. *Cryst. Growth Des.* **2023**, *23* (5), 3384–3392. https://doi.org/10.1021/acs.cgd.2c01509.

(60) Steffler, F.; De Lima, G. F.; Duarte, H. A. The Effect of the Heteroatom (X=P, As, Si and Ge) on the Geometrical and Electronic Properties of α-Keggin Polyoxometalates (M=Mo, W and Nb) – A DFT Investigation. *J. Mol. Struct.* **2020**, *1213*, 1–6. https://doi.org/10.1016/j.molstruc.2020.128159.

(61) Weinstock, I. A.; Cowan, J. J.; Barbuzzi, E. M. G.; Zeng, H.; Hill, C. L. Equilibria between α and β Isomers of Keggin Heteropolytungstates. *J. Am. Chem. Soc.* **1999**, *121* (19), 4608–4617. https://doi.org/10.1021/ja982908j.

(62) López, X.; Poblet, J. M. DFT Study on the Five Isomers of PW12O403-: Relative Stabilization upon Reduction. *Inorg. Chem.* **2004**, *43* (22), 6863–6865. https://doi.org/10.1021/ic049119p.

(63) Kondinski, A.; Parac-Vogt, T. N. Keggin Structure, Quō Vadis? *Front. Chem.* **2018**, *6* (AUG), 1–7. https://doi.org/10.3389/fchem.2018.00346.

(64) Zhang, F. Q.; Guan, W.; Yan, L. K.; Zhang, Y. T.; Xu, M. T.; Hayfron-Benjamin, E.; Su, Z. M. On the Origin of the Relative Stability of Wells-Dawson Isomers: A DFT Study of α-, β-, γ-, A*-, B*-, and Γ*-[(PO4)2W18O54] 6-Anions. *Inorg. Chem.* **2011**, *50* (11), 4967–4977. https://doi.org/10.1021/ic200203s.

(65) Vilà-Nadal, L.; Mitchell, S. G.; Long, D. L.; Rodríguez-Fortea, A.; López, X.; Poblet, J. M.; Cronin, L. Exploring the Rotational Isomerism in Non-Classical Wells-Dawson Anions {W 18X}: A Combined Theoretical and Mass Spectrometry Study. *Dalt. Trans.* **2012**, *41* (8), 2264–2271. https://doi.org/10.1039/c2dt11919f.

(66) Neogi, O. Preyssler Polyoxometalate an Overview. *Int. J. Innov. Sci. Res. Technol.* **2023**, *8* (2), 142–160. https://doi.org/10.5281/zenodo.7645910.

(67) Alizadeh, M. H.; Harmalker, S. P.; Jeannin, Y.; Martin-Frer, J.; Pope, M. T. A Heteropolyanion with Fivefold Molecular Symmetry That Contains a Nonlabile Encapsulated Sodium Ion. The Structure and Chemistry of [NaP5W30O110]14-. *J. Am. Chem. Soc.* **1985**, *107* (9), 2662–2669. https://doi.org/10.1021/ja00295a019.

(68) Takahashi, K.; Sano, T.; Sadakane, M. Preparation and Characterization of Preyssler-Type Phosphotungstic Acid, H15-n[P5W30O110Mn+], with Different Encapsulated Cations (M = Na, Ca, Bi, Eu, Y, or Ce), and Their Thermal Stability and Acid Catalyst Properties. *Zeitschrift fur Anorg. und Allg. Chemie* **2014**, *640* (7), 1314–1321. https://doi.org/10.1002/zaac.201400038.

(69) Fernández, J. A.; López, X.; Bo, C.; de Graaf, C.; Baerends, E. J.; Poblet, J. M. Polyoxometalates with Internal Cavities: Redox Activity, Basicity, and Cation Encapsulation in [Xn+P5W30O110](15-n)- Preyssler Complexes, with X = Na+, Ca2+, Y3+, La3+, Ce3+, and Th4+. *J. Am. Chem. Soc.* **2007**, *129* (3), 12244–12253. https://doi.org/10.1021/ja0737321.

(70) Shitamatsu, K.; Kojima, T.; Waddell, P. G.; Sugiarto; Ooyama, H. E.; Errington, R. J.; Sadakane, M. Structural Characterization of Cerium-Encapsulated Preyssler-Type Phosphotungstate: Additional Evidence of Ce(III) in the Cavity. *Zeitschrift fur Anorg. und Allg. Chemie* **2021**, *647* (11), 1239–1244. https://doi.org/10.1002/zaac.202100075.

(71) Turo, M. J.; Chen, L.; Moore, C. E.; Schimpf, A. M. Co2+-Linked [NaP5W30O110]14-: A Redox-Active Metal Oxide Framework with High Electron Density. *J. Am. Chem. Soc.* **2019**, *141* (11), 4553–4557. https://doi.org/10.1021/jacs.9b00866.

(72) Alves, L. S.; Chen, L.; Lemmon, C. E.; Gembicky, M.; Xu, M.; Schimpf, A. M. PEG-Infiltrated Polyoxometalate Frameworks with Flexible Form-Factors. *ACS Mater. Lett.* **2022**, *4* (10), 1937–1943. https://doi.org/10.1021/acsmaterialslett.2c00393.

(73) Yang, B.; Picchetti, P.; Wang, Y.; Wang, W.; Seeger, C.; Bozov, K.; Malik, S.; Mallach, D.; Schäfer, A. H.; Ibrahim, M.; Hirtz, M.; Powell, A. K. Patterned Immobilization of Polyoxometalate-Loaded Mesoporous Silica Particles via Amine-Ene Michael Additions on Alkene Functionalized Surfaces. *Sci. Rep.* **2024**, *14* (1), 1–12. https://doi.org/10.1038/s41598-023-50846-2.

(74) Bamoharram, F. F.; Heravi, M. M.; Roshani, M.; Tavakoli, N. N-Oxidation of Pyridine Carboxylic Acids Using Hydrogen Peroxide Catalyzed by a Green Heteropolyacid Catalyst: Preyssler's Anion, [NaP5W30O110]14-. *J. Mol. Catal. A Chem.* **2006**, *252* (1–2), 219–225. https://doi.org/10.1016/j.molcata.2006.02.059.

(75) Sahiro, K.; Kawato, Y.; Koike, K.; Sano, T.; Nakai, T.; Sadakane, M. Preyssler-Type Phosphotungstate Is a New Family of Negative-Staining Reagents for the TEM Observation of Viruses. *Sci. Rep.* **2022**, *12* (1), 1–8. https://doi.org/10.1038/s41598-022-11405-3.

(76) Ammam, M.; Mbomekalle, I. M.; Keita, B.; Nadjo, L.; Fransaer, J. [As8W48O184]40-, a New Crown-Shaped Heteropolyanion: Electrochemistry and Electrocatalytic Properties towards Reduction of Nitrite. *Electrochim. Acta* **2010**, *55* (9), 3118–3122. https://doi.org/10.1016/j.electacta.2010.01.067.

(77) Contant, R.; Teze, A. A New Crown Heteropolyanion, K28Li5H7P8W48O184.92H2O: Synthesis,

Structure, and Properties. *Inorg. Chem.* **1985**, *24* (26), 4610–4614. https://doi.org/10.1021/ic00220a036.

(78) Cameron, J. M.; Gao, J.; Vilà-Nadal, L.; Long, D. L.; Cronin, L. Formation, Self-Assembly and Transformation of a Transient Selenotungstate Building Block into Clusters, Chains and Macrocycles. *Chem. Commun.* **2014**, *50* (17), 2155–2157. https://doi.org/10.1039/c3cc49293a.

(79) Godin, B.; Chen, Y. G.; Vaissermann, J.; Ruhlmann, L.; Verdaguer, M.; Gouzerh, P. Coordination Chemistry of the Hexavacant Tungstophosphate [H2P2W12O48]12- with FeIII Ions: Towards Original Structures of Increasing Size and Complexity. *Angew. Chemie - Int. Ed.* **2005**, *44* (20), 3072–3075. https://doi.org/10.1002/anie.200463033.

(80) Yao, S.; Zhang, Z.; Li, Y.; Lu, Y.; Wang, E.; Su, Z. Two Heterometallic Aggregates Constructed from the {P2W 12}-Based Trimeric Polyoxotungstates and 3d-4f Heterometals. *Cryst. Growth Des.* **2010**, *10* (1), 135–139. https://doi.org/10.1021/cg900745z.

(81) Contant, R. *Inorganic Syntheses*, 1st ed.; Ginsberg, A. P., Ed.; Wiley-Interscience: New York, 1990. https://doi.org/10.1002/9780470132586.

(82) Boyd, T.; Mitchell, S. G.; Gabb, D.; Long, D. L.; Cronin, L. Investigating Cation Binding in the Polyoxometalate-Super-Crown [P 8W48O184]40-. *Chem. - A Eur. J.* **2011**, *17* (43), 12010–12014. https://doi.org/10.1002/chem.201101666.

(83) Contant, R.; Thouvenot, R. Hétéropolyanions de Type Dawson. 2. Synthèses de Polyoxotungstoarsénates Lacunaires Dérivant de l'octadécatungstodiarsénate. Étude Structurale Par RMN Du Tungstène-183 Des Octadéca(Mo1ybdotungstovanado)Diarsénates Apparentés. *Can. J. Chem.* **1991**, *69* (10), 1498–1506. https://doi.org/10.1139/v91-221.

(84) Mitchell, S. G.; Gabb, D.; Ritchie, C.; Hazel, N.; Long, D. L.; Cronin, L. Controlling Nucleation of the Cyclic Heteropolyanion {P8W 48}: A Cobalt-Substituted Phosphotungstate Chain and Network. *CrystEngComm* **2009**, *11* (1), 36–39. https://doi.org/10.1039/b813066c.

(85) Mal, S. S.; Kortz, U. The Wheel-Shaped Cu20 Tungstophosphate [Cu20Cl(OH) 24(H2O)12(P8W48O 184)]25- Ion. *Angew. Chemie - Int. Ed.* **2005**, *44* (24), 3777–3780. https://doi.org/10.1002/anie.200500682.

(86) Liu, G.; Liu, T.; Mal, S. S.; Kortz, U. Wheel-Shaped Polyoxotungstate Supramolecular " Blackberry " Structure in Aqueous Solution. *J. Am. Chem. Soc.* **2006**, *24* (2), 10103–10110. https://doi.org/10.1021/ja0610840.

(87) Mal, S. S.; Dickman, M. H.; Kortz, U.; Todea, A. M.; Merca, A.; Bogge, H.; Glaser, T.; Muller, A.; Nellutla, S.; Kaur, N.; Van Tol, J.; Dalal, N. S.; Keita, B.; Nadjo, L. Nucleation Process in the Cavity of a 48-Tungstophosphate Wheel Resulting in a 16-Metal-Centre Iron Oxide Nanocluster. *Chem. - A Eur. J.* **2008**, *14* (4), 1186–1195. https://doi.org/10.1002/chem.200701424.

(88) Goura, J.; Sundar, A.; Bassil, B. S.; Ćirić-Marjanović, G.; Bajuk-Bogdanović, D.; Kortz, U. Peroxouranyl-Containing W48 Wheel: Synthesis, Structure, and Detailed Infrared and Raman Spectroscopy Study. *Inorg. Chem.* **2020**, *59* (23), 16789–16794. https://doi.org/10.1021/acs.inorgchem.0c02858.

(89) Boyd, T.; Mitchell, S. G.; Gabb, D.; Long, D. L.; Song, Y. F.; Cronin, L. POMzites: A Family of Zeolitic Polyoxometalate Frameworks from a Minimal Building Block Library. *J. Am. Chem. Soc.* **2017**, *139* (16), 5930–5938. https://doi.org/10.1021/jacs.7b01807.

(90) Zhan, C. H.; Zheng, Q.; Long, D. L.; Vilà-Nadal, L.; Cronin, L. Controlling the Reactivity of the [P8W48O184]40− Inorganic Ring and Its Assembly into POMZite Inorganic Frameworks with Silver Ions. *Angew. Chemie - Int. Ed.* **2019**, *58* (48), 17282–17286. https://doi.org/10.1002/anie.201911170.

(91) Gouzerh, P.; Che, M. Polyoxometalates (POMs) Revisited and the "Missing Link" between the Bottom up and Top down Approaches. *Actual. Chim.* **2006**, *298*, 1–14.

(92) Müller, A.; Beckmann, E.; Bögge, H.; Schmidtmann, M.; Dress, A. Inorganic Chemistry Goes Protein Size: A Mo368 Nano-Hedgehod Initiating Nanochemistry by Symmetry Breaking. *Angew. Chemie - Int. Ed.* **2002**, *41* (7), 1162–1167. https://doi.org/10.1002/1521-3773(20020402)41:7<1162::AID-ANIE1162>3.0.CO;2-8.

(93) Pope, M. T.; Müller, A. Polyoxometalate Chemistry: An Old Field with New Dimensions in Several Disciplines. *Angew. Chemie Int. Ed. English* **1991**, *30* (1), 34–48. https://doi.org/10.1002/anie.199100341.

(94) Pradeep, C. P.; Long, D. L.; Cronin, L. Cations in Control: Crystal Engineering Polyoxometalate Clusters Using Cation Directed Self-Assembly. *Dalt. Trans.* **2010**, *39* (40), 9443–9457. https://doi.org/10.1039/c0dt00325e.

(95) Long, D.-L.; Kögerler, P.; Cronin, L. Old Clusters with New Tricks: Engineering S···S Interactions and Novel Physical Properties in Sulfite-Based Dawson Clusters. *Angew. Chemie* **2004**, *116* (14), 1853–1856. https://doi.org/10.1002/ange.200352896.

(96) Ritchie, C.; Burkholder, E. M.; Long, D. L.; Adam, D.; Kögerler, P.; Cronin, L. Exploiting the Multifunctionality of Organocations in the Assembly of Hybrid Polyoxometalate Clusters and Networks. *Chem. Commun.* **2007**, No. 5, 468–470. https://doi.org/10.1039/b612741j.

(97) Wilson, E. F.; Abbas, H.; Duncombe, B. J.; Strebe, C.; Long, D. L.; Cronin, L. Probing the Self-Assembly of Inorganic Cluster Architectures in Solution with Cryospray Mass Spectrometry: Growth of Polyoxomolybdate Clusters and Polymers Mediated by Silver(I) Ions. *J. Am. Chem. Soc.* **2008**, *130* (42), 13876–13884. https://doi.org/10.1021/ja802514q.

(98) Villanneau, R.; Proust, A.; Robert, F.; Gouzerh, P. Synthesis and Characterization of [NBu4]4[Ag2{Mo5O13(OMe)4(NO)}2], a Novel Polyoxomolybdate Complex with a Short Ag I ··· Ag I Distance. *Chem. Commun.* **1998**, *13* (419), 1491–1492. https://doi.org/10.1039/A802548G.

(99) Boulay, A. G.; Cooper, G. J. T.; Cronin, L. Directed Assembly of Polyoxometalates Across Length Scales: From Macro-Molecules to Microsystems and ICHELLs. In *Polyoxometalate Chemistry: Some Recent Trends*; 2013; pp 101–153. https://doi.org/10.1142/9789814458986 0003.

(100) Fang, X.; Anderson, T. M.; Hill, C. L. Enantiomerically Pure Polytungstates: Chirality Transfer through Zirconium Coordination Centers to Nanosized Inorganic Clusters. *Angew. Chemie - Int. Ed.* **2005**, *44* (23), 3540–3544. https://doi.org/10.1002/anie.200500415.

(101) Zhu, Z.; Wei, M.; Li, B.; Wu, L. Constructing Chiral Polyoxometalate Assembliesviasupramolecular Approaches. *Dalt. Trans.* **2021**, *50* (15), 5080–5098. https://doi.org/10.1039/d1dt00182e.

(102) Mumpton, F. A. La Roca Magica: Uses of Natural Zeolites in Agriculture and Industry. *Proc. Natl. Acad. Sci. U. S. A.* **1999**, *96* (7), 3463–3470. https://doi.org/10.1073/pnas.96.7.3463.

(103) Pavelić, S. K.; Medica, J. S.; Gumbarević, D.; Filošević, A.; Pržulj, N.; Pavelić, K. Critical Review on Zeolite Clinoptilolite Safety and Medical Applications in Vivo. *Front. Pharmacol.* **2018**, *9* (NOV), 1–15. https://doi.org/10.3389/fphar.2018.01350.

(104) Deshpande, S.; Kheur, S.; Kheur, M.; Eyüboğlu, T. F.; Özcan, M. A Review on Zeolites and Their Applications in Dentistry. *Curr. Oral Heal. Reports* **2023**, *10* (2), 36–42. https://doi.org/10.1007/s40496-023-00330-7.

(105) Khaleque, A.; Alam, M. M.; Hoque, M.; Mondal, S.; Haider, J. Bin; Xu, B.; Johir, M. A. H.; Karmakar, A. K.; Zhou, J. L.; Ahmed, M. B.; Moni, M. A. Zeolite Synthesis from Low-Cost Materials and Environmental Applications: A Review. *Environ. Adv.* **2020**, *2* (October). https://doi.org/10.1016/j.envadv.2020.100019.

(106) Pérez-Botella, E.; Valencia, S.; Rey, F. Zeolites in Adsorption Processes: State of the Art and Future Prospects. *Chem. Rev.* **2022**, *122* (24), 17647–17695. https://doi.org/10.1021/acs.chemrev.2c00140.

(107) Petrov, I.; Michalev, T. Synthesis of Zeolite A: A Review. *НАУЧНИ ТРУДОВЕ НА РУСЕНСКИЯ*

УНИВЕРСИТЕТ (Proceedings - Chem. Technol. **2012**, No. 51, Book 9.1, 30–35.

(108) Millini, R.; Bellussi, G. *Zeolites in Catalysis: Properties and Applications*; 2017. https://doi.org/10.1039/9781788010610-00001.

(109) Cronstedt, A. Natural Zeolite and Minerals. *Kongl Vetenskaps Akad. Handl. Stock.* **1756**, No. 17, 120.

(110) Vermeiren, W.; Gilson, J. P. Impact of Zeolites on the Petroleum and Petrochemical Industry. *Top. Catal.* **2009**, *52* (9), 1131–1161. https://doi.org/10.1007/s11244-009-9271-8.

(111) Degnan, T. F. The Implications of the Fundamentals of Shape Selectivity for the Development of Catalysts for the Petroleum and Petrochemical Industries. *J. Catal.* **2003**, *216* (1–2), 32–46. https://doi.org/10.1016/S0021-9517(02)00105-7.

(112) Humphrey, J. L.; Keller II, G. E. *Separation Process Technology*; McGraw-Hill: New York, 1997.

(113) Granato, M. A.; Vlugt, T. J. H.; Rodrigues, A. E. Molecular Simulation of Propane-Propylene Binary Adsorption Equilibrium in Zeolite 13X. *Ind. Eng. Chem. Res.* **2007**, *46* (22), 7239–7245. https://doi.org/10.1021/ie0705655.

(114) Misaelides, P. Application of Natural Zeolites in Environmental Remediation: A Short Review. *Microporous Mesoporous Mater.* **2011**, *144* (1–3), 15–18. https://doi.org/10.1016/j.micromeso.2011.03.024.

(115) Borai, E. H.; Harjula, R.; malinen, L.; Paajanen, A. Efficient Removal of Cesium from Low-Level Radioactive Liquid Waste Using Natural and Impregnated Zeolite Minerals. *J. Hazard. Mater.* **2009**, *172* (1), 416–422. https://doi.org/10.1016/j.jhazmat.2009.07.033.

(116) Lima, C. G. S.; Moreira, N. M.; Paixão, M. W.; Corrêa, A. G. Heterogenous Green Catalysis: Application of Zeolites on Multicomponent Reactions. *Curr. Opin. Green Sustain. Chem.* **2019**, *15*, 7–12. https://doi.org/10.1016/j.cogsc.2018.07.006.

(117) Li, Y.; Li, L.; Yu, J. Applications of Zeolites in Sustainable Chemistry. *Chem* **2017**, *3* (6), 928–949. https://doi.org/10.1016/j.chempr.2017.10.009.

(118) Menyakina, A. G.; Gamko, L. N.; Streltsov, V. A.; Talyzina, T. L. Productivity of Breeding Pigs during Marl Feeding in Areas with High Density of Soil Pollution with Radiocesium. *BIO Web Conf.* **2020**, *27*, 00033. https://doi.org/10.1051/bioconf/20202700033.

(119) Furukawa, H.; Cordova, K. E.; O'Keeffe, M.; Yaghi, O. M. The Chemistry and Applications of Metal-Organic Frameworks. *Science (80-.).* **2013**, *341* (6149). https://doi.org/10.1126/science.1230444.

(120) Yaghi, O. M.; Li Hailian. Hydrothermal Synthesis of a Metal-Organic Framework Containing Large Rectangular Channels. *J. Am. Chem. Soc.* **1995**, *117*, 10401–10402. https://doi.org/10.1021/JA00146A033.

(121) Yaghi, O. M.; Li, G.; Li Hailian. Selective Binding and Removal of Guests in a Imcroporous Metal-Organic Framework. *Nature* **1995**, *378*, 703–706. https://doi.org/10.1038/378703a0.

(122) Batten, S. R.; Champness, N. R.; Chen, X.-M.; Garcia-Martinez, J.; Kitagawa, S.; Öhrström, L.; O'Keeffe, M.; Suh, M. P.; Reedijk, J. Terminology of Metal-Organic Frameworks and Coordination Polymers. *Pure Appl. Chem.* **2013**, *85* (8), 1715–1724. https://doi.org/10.1351/PAC-REC-12-11-20.

(123) Li, H.; Eddaoudi, M.; O'Keeffe, M.; Yaghi, O. M. Design and Synthesis of an Exceptionally Stable and Highly Porous Metal-Organic Framework. *Nature* **1999**, *402*, 276–279. https://doi.org/10.1038/46248.

(124) Chui, S. S. Y.; Lo, S. M. F.; Charmant, J. P. H.; Orpen, A. G.; Williams, I. D. A Chemically Functionalizable Nanoporous Material [Cu3(TMA)2 (H2O)3](N). *Science (80-.).* **1999**, *283* (5405), 1148–1150. https://doi.org/10.1126/science.283.5405.1148.

(125) Moghadam, P. Z.; Li, A.; Wiggin, S. B.; Tao, A.; Maloney, A. G. P.; Wood, P. A.; Ward, S. C.; Fairen-Jimenez, D. Development of a Cambridge Structural Database Subset: A Collection of Metal-Organic Frameworks for Past, Present, and Future. *Chem. Mater.* **2017**, *29* (7), 2618–2625. https://doi.org/10.1021/acs.chemmater.7b00441.

(126) Schneemann, A.; Bon, V.; Schwedler, I.; Senkovska, I.; Kaskel, S.; Fischer, R. A. Flexible Metal-Organic Frameworks. *Chem. Soc. Rev.* **2014**, *43* (16), 6062–6096. https://doi.org/10.1039/c4cs00101j.

(127) Lin, Z. J.; Lü, J.; Hong, M.; Cao, R. Metal-Organic Frameworks Based on Flexible Ligands (FL-MOFs): Structures and Applications. *Chem. Soc. Rev.* **2014**, *43* (16), 5867–5895. https://doi.org/10.1039/c3cs60483g.

(128) Severino, M. I.; Gkaniatsou, E.; Nouar, F.; Pinto, M. L.; Serre, C. MOFs Industrialization: A Complete Assessment of Production Costs. *Faraday Discuss.* **2021**, *231*, 326–341. https://doi.org/10.1039/d1fd00018g.

(129) Bassil, B. S.; Ibrahim, M.; Mal, S. S.; Suchopar, A.; Biboum, R. N.; Keita, B.; Nadjo, L.; Nellutla, S.; Van Tol, J.; Dalal, N. S.; Kortz, U. Cobalt, Manganese, Nickel, and Vanadium Derivatives of the Cyclic 48-Tungsto-8-Phosphate [H7P8W48O 184]33-. *Inorg. Chem.* **2010**, *49* (11), 4949–4959. https://doi.org/10.1021/ic100050r.

(130) Mitchell, S. G.; Boyd, T.; Miras, H. N.; Long, D. L.; Cronin, L. Extended Polyoxometalate Framework Solids: Two Mn(II)-Linked {P 8W48} Network Arrays. *Inorg. Chem.* **2011**, *50* (1), 136–143. https://doi.org/10.1021/ic101472s.

(131) Khan, M. I.; Yohannes, E.; Doedens, R. J. [M3V18O42(H2O) 12(XO4)]·24H2O (M = Fe, Co; X = V, S): Metal Oxide Based Framework Materials Composed of Polyoxovanadate Clusters. *Angew. Chemie - Int. Ed.* **1999**, *38* (9), 1292–1294. https://doi.org/10.1002/(SICI)1521-3773(19990503)38:9<1292::AID-ANIE1292>3.0.CO;2-2.

(132) Ishaque Khan, M.; Yohannes, E.; Powell, D. Vanadium Oxide Clusters as Building Blocks for the Synthesis of Metal Oxide Surfaces and Framework Materials: Synthesis and x-Ray Crystal Structure of [H6Mn3VIV15VV4O46(H2O)12]·30H2O. *Inorg. Chem.* **1999**, *38* (2), 212–213. https://doi.org/10.1021/ic981077f.

(133) Khan, M. I.; Powell, D. Synthesis and Characterization of a New Mixed-Metal Oxide Framework Material Composed of Vanadium Oxide Clusters : X-Ray Crystal Structure of (N 2 H 5) 2 [Zn 3 V IV12 V V6 O 42 (SO 4)(H 2 O) 12]· 24H 2 O The Reaction of a Slurry of V 2 O 5 with Li. **1999**, *42*, 23–24. https://doi.org/10.1039/A807503D.

(134) Mitchell, S. G.; Streb, C.; Miras, H. N.; Boyd, T.; Long, D. L.; Cronin, L. Face-Directed Self-Assembly of an Electronically Active Archimedean Polyoxometalate Architecture. *Nat. Chem.* **2010**, *2* (4), 308–312. https://doi.org/10.1038/nchem.581.

(135) Gao, J.; Yan, J.; Mitchell, S. G.; Miras, H. N.; Boulay, A. G.; Long, D. L.; Cronin, L. Self-Assembly of a Family of Macrocyclic Polyoxotungstates with Emergent Material Properties. *Chem. Sci.* **2011**, *2* (8), 1502–1508. https://doi.org/10.1039/c1sc00150g.

(136) Weller, M.; Overton, T.; Rourke, J.; Armstrong, F. *Inorganic Chemistry*, Seventh ed.; Oxford University Press: Oxford, 2018.

(137) Otsubo, K.; Haraguchi, T.; Kitagawa, H. Nanoscale Crystalline Architectures of Hofmann-Type Metal–Organic Frameworks. *Coord. Chem. Rev.* **2017**, *346*, 123–138. https://doi.org/10.1016/j.ccr.2017.03.022.

(138) Zhan, C.; Cameron, J. M.; Gabb, D.; Boyd, T.; Winter, R. S.; Vilà-Nadal, L.; Mitchell, S. G.; Glatzel, S.; Breternitz, J.; Gregory, D. H.; Long, D. L.; MacDonell, A.; Cronin, L. A Metamorphic Inorganic Framework That Can Be Switched between Eight Single-Crystalline States. *Nat. Commun.* **2017**, *8*. https://doi.org/10.1038/ncomms14185.

(139) Bruno, T. J.; Lide, D. R.; Rumble, J. R. *CRC Handbook of Chemistry and Physics: A Ready-Reference Book of Chemical and Physical Data*, 100th ed.; CRC Press, 2019.

(140) Yanagie, H.; Ogata, A.; Mitsui, S.; Hisa, T.; Yamase, T.; Eriguchi, M. Anticancer Activity of Polyoxomolybdate. *Biomed. Pharmacother.* **2006**, *60* (7), 349–352. https://doi.org/10.1016/j.biopha.2006.06.018.

(141) Chang, D.; Li, Y.; Chen, Y.; Wang, X.; Zang, D.; Liu, T. Polyoxometalate-Based Nanocomposites for Antitumor and Antibacterial Applications. *Nanoscale Adv.* **2022**, *4* (18), 3689–3706. https://doi.org/10.1039/d2na00391k.

(142) Inoue, M.; Segawa, K.; Matsunaga, S.; Matsumoto, N.; Oda, M.; Yamase, T. Antibacterial Activity of Highly Negative Charged Polyoxotungstates, K 27[KAs4W40O140] and K 18[KSb9W21O86], and Keggin-Structural Polyoxotungstates against Helicobacter Pylori. *J. Inorg. Biochem.* **2005**, *99* (5), 1023–1031. https://doi.org/10.1016/j.jinorgbio.2005.01.010.

(143) Tocilj, A.; Schlünzen, F.; Janell, D.; Glühmann, M.; Hansen, H. A. S.; Harms, J.; Bashan, A.; Bartels, H.; Agmon, I.; Franceschi, F.; Yonath, A. The Small Ribosomal Subunit from Thermus Thermophilus at 4.5 Å Resolution: Pattern Fittings and the Identification of a Functional Site. *Proc. Natl. Acad. Sci. U. S. A.* **1999**, *96* (25), 14252–14257. https://doi.org/10.1073/pnas.96.25.14252.

(144) Wang, S. S.; Yang, G. Y. Recent Advances in Polyoxometalate-Catalyzed Reactions. *Chem. Rev.* **2015**, *115* (11), 4893–4962. https://doi.org/10.1021/cr500390v.

(145) Neumann, R. Activation of Molecular Oxygen, Polyoxometalates, and Liquid-Phase Catalytic Oxidation. *Inorg. Chem.* **2010**, *49* (8), 3594–3601. https://doi.org/10.1021/ic9015383.

(146) Lechner, M.; Güttel, R.; Streb, C. Challenges in Polyoxometalate-Mediated Aerobic Oxidation Catalysis: Catalyst Development Meets Reactor Design. *Dalt. Trans.* **2016**, *45* (42), 16716–16726. https://doi.org/10.1039/c6dt03051c.

(147) Qin, K.; Zang, D.; Wei, Y. Polyoxometalates Based Compounds for Green Synthesis of Aldehydes and Ketones. *Chinese Chem. Lett.* **2023**, *34* (8). https://doi.org/10.1016/j.cclet.2022.107999.

(148) Gu, J.; Chen, W.; Shan, G. G.; Li, G.; Sun, C.; Wang, X. L.; Su, Z. The Roles of Polyoxometalates in Photocatalytic Reduction of Carbon Dioxide. *Mater. Today Energy* **2021**, *21*. https://doi.org/10.1016/j.mtener.2021.100760.

(149) Zang, D.; Wang, H. Polyoxometalate-Based Nanostructures for Electrocatalytic and Photocatalytic CO 2 Reduction . *Polyoxometalates* **2022**, *1* (1), 9140006. https://doi.org/10.26599/pom.2022.9140006.

(150) Kikukawa, Y.; Suzuki, K.; Sugawa, M.; Hirano, T.; Kamata, K.; Yamaguchi, K.; Mizuno, N. Cyanosilylation of Carbonyl Compounds with Trimethylsilyl Cyanide Catalyzed by an Yttrium-Pillared Silicotungstate Dimer. *Angew. Chemie - Int. Ed.* **2012**, *51* (15), 3686–3690. https://doi.org/10.1002/anie.201200486.

(151) Kibler, A. J.; Souza, V. S.; Fernandes, J. A.; Lewis, W.; Argent, S. P.; Dupont, J.; Newton, G. N. A Cooperative Photoactive Class-I Hybrid Polyoxometalate With Benzothiadiazole–Imidazolium Cations. *Front. Chem.* **2021**, *8*, 1–10. https://doi.org/10.3389/fchem.2020.612535.

(152) Xu, J.; Volfova, H.; Mulder, R. J.; Goerigk, L.; Bryant, G.; Riedle, E.; Ritchie, C. Visible-Light-Driven “on”/"Off" Photochromism of a Polyoxometalate Diarylethene Coordination Complex. *J. Am. Chem. Soc.* **2018**, *140* (33), 10482–10487. https://doi.org/10.1021/jacs.8b04900.

(153) Xu, X.; Yang, M.; Lu, Q.; Yu, S.; Ma, S.; Tian, A.; Ying, J. Three Photochromic Materials Based on POMs and Viologens for UV Probing, Visual Detection of Metal Ions and Amine Detection. *CrystEngComm* **2022**, *24* (43), 7677–7685. https://doi.org/10.1039/d2ce01244h.

(154) Recepoglu, Y. K.; Goren, A. Y.; Orooji, Y.; Vatanpour, V.; Kudaibergenov, N.; Khataee, A. Polyoxometalate-Based Hybrid Composites in Multi-Functional Wastewater Treatment Applications. *J. Water Process Eng.* **2023**, *53* (May), 103863.

https://doi.org/10.1016/j.jwpe.2023.103863.

(155) Geletii, Y. V.; Botar, B.; Kögerler, P.; Hillesheim, D. A.; Musaev, D. G.; Hill, C. L. An All-Inorganic, Stable, and Highly Active Tetraruthenium Homogeneous Catalyst for Water Oxidation. *Angewandte Chemie - International Edition*. 2008, pp 3896–3899. https://doi.org/10.1002/anie.200705652.

(156) Wang, M.; Zhong, W.; Zhang, S.; Liu, R.; Xing, J.; Zhang, G. An Overall Water-Splitting Polyoxometalate Catalyst for the Electromicrobial Conversion of CO2 in Neutral Water. *J. Mater. Chem. A* **2018**, *6* (21), 9915–9921. https://doi.org/10.1039/c8ta01902a.

(157) Ullah, I.; Munir, A.; Haider, A.; Ullah, N.; Hussain, I. Supported Polyoxometalates as Emerging Nanohybrid Materials for Photochemical and Photoelectrochemical Water Splitting. *Nanophotonics* **2021**, *10* (6), 1595–1620. https://doi.org/10.1515/nanoph-2020-0542.

(158) Zeb, Z.; Huang, Y.; Chen, L.; Zhou, W.; Liao, M.; Jiang, Y.; Li, H.; Wang, L.; Wang, L.; Wang, H.; Wei, T.; Zang, D.; Fan, Z.; Wei, Y. Comprehensive Overview of Polyoxometalates for Electrocatalytic Hydrogen Evolution Reaction. *Coord. Chem. Rev.* **2023**, *482*, 215058. https://doi.org/10.1016/j.ccr.2023.215058.

(159) Qing, G.; Ghazfar, R.; Jackowski, S. T.; Habibzadeh, F.; Ashtiani, M. M.; Chen, C. P.; Smith, M. R.; Hamann, T. W. Recent Advances and Challenges of Electrocatalytic N2Reduction to Ammonia. *Chem. Rev.* **2020**, *120* (12), 5437–5516. https://doi.org/10.1021/acs.chemrev.9b00659.

(160) Liao, W.; Qi, L.; Wang, Y.; Qin, J.; Liu, G.; Liang, S.; He, H.; Jiang, L. Interfacial Engineering Promoting Electrosynthesis of Ammonia over Mo/Phosphotungstic Acid with High Performance. *Adv. Funct. Mater.* **2021**, *31* (22), 1–9. https://doi.org/10.1002/adfm.202009151.

(161) Hui, X.; Wang, L.; Yao, Z.; Hao, L.; Sun, Z. Recent Progress of Photocatalysts Based on Tungsten and Related Metals for Nitrogen Reduction to Ammonia. *Front. Chem.* **2022**, *10* (August), 1–26. https://doi.org/10.3389/fchem.2022.978078.

(162) Yang, M.; Wang, X.; Gómez-García, C. J.; Jin, Z.; Xin, J.; Cao, X.; Ma, H.; Pang, H.; Tan, L.; Yang, G.; Kan, Y. Efficient Electron Transfer from an Electron-Reservoir Polyoxometalate to Dual-Metal-Site Metal-Organic Frameworks for Highly Efficient Electroreduction of Nitrogen. *Adv. Funct. Mater.* **2023**, *33* (28), 1–13. https://doi.org/10.1002/adfm.202214495.

(163) Du, J.; Ma, Y. Y.; Tan, H.; Kang, Z. H.; Li, Y. Progress of Electrochemical CO2 Reduction Reactions over Polyoxometalate-Based Materials. *Chinese J. Catal.* **2021**, *42* (6), 920–937. https://doi.org/10.1016/S1872-2067(20)63718-4.

(164) Du, J.; Ma, Y.; Xin, X.; Na, H.; Zhao, Y.; Tan, H.; Han, Z.; Li, Y.; Kang, Z. Reduced Polyoxometalates and Bipyridine Ruthenium Complex Forming a Tunable Photocatalytic System for High Efficient CO2 Reduction. *Chem. Eng. J.* **2020**, *398*. https://doi.org/10.1016/j.cej.2020.125518.

(165) Sun, J.; Abednatanzi, S.; Van Der Voort, P.; Liu, Y. Y.; Leus, K. POM@MOF Hybrids: Synthesis and Applications. *Catalysts* **2020**, *10* (5). https://doi.org/10.3390/catal10050578.

(166) Duan, F.; Liu, X.; Qu, D.; Li, B.; Wu, L. Polyoxometalate-Based Ionic Frameworks for Highly Selective CO2 Capture and Separation. *CCS Chem.* **2020**, *3* (11), 2676–2687. https://doi.org/10.31635/ccschem.020.202000498.

(167) Deng, L.; Dong, X.; Zhou, Z.-H. Intrinsic Molybdenum-Based POMOFs with Impressive Gas Adsorptions and Phtochromism. *Chem. Eur. J.* **2021**, *27* (37), 9643–9653. https://doi.org/10.1002/chem.202100745.

(168) Ma, F. J.; Liu, S. X.; Liang, D. D.; Ren, G. J.; Wei, F.; Chen, Y. G.; Su, Z. M. Adsorption of Volatile Organic Compounds in Porous Metal-Organic Frameworks Functionalized by Polyoxometalates. *J. Solid State Chem.* **2011**, *184* (11), 3034–3039. https://doi.org/10.1016/j.jssc.2011.09.002.

(169) Delen, G.; Monai, M.; Stančiaková, K.; Baumgartner, B.; Meirer, F.; Weckhuysen, B. M. Structure Sensitivity in Gas Sorption and Conversion on Metal-Organic Frameworks. *Nat. Commun.* **2023**,

14 (1), 1–11. https://doi.org/10.1038/s41467-022-35762-9.

(170) Dey, C.; Banerjee, R. Structure and Selective Gas Adsorption Study on POM-Based Ionic Salts. *Acta Crystallogr.* **2011**, *A67*, C369. https://doi.org/10.1107/S0108767311090714.

(171) Dey, C.; Das, R.; Pachfule, P.; Poddar, P.; Banerjee, R. Structural and Selective Gas Adsorption Studies of Polyoxometalate and Tris(Ethylenediamine) Cobalt(III) Based Ionic Crystals. *Cryst. Growth Des.* **2011**, *11* (1), 139–146. https://doi.org/10.1021/cg101201b.

(172) Zhang, H.; Li, A.; Li, K.; Wang, Z.; Xu, X.; Wang, Y.; Sheridan, M. V; Hu, H.; Xu, C.; Alekseev, E. V; Zhang, Z.; Yan, P.; Cao, K.; Chai, Z.; Albrecht-Schönzart, T. E.; Wang, S. Ultrafiltration Separation of Am(VI)-Polyoxometalate from Lanthanides. **2023**, *616* (April), 482–491. https://doi.org/10.1038/s41586-023-05840-z.

(173) Deng, L.; Lin, R. Y.; Zhou, Z. H. Isolated Molybdenum-Based Microporous POMs for Selective Adsorption of Gases. *Dalt. Trans.* **2022**, *51* (13), 5239–5249. https://doi.org/10.1039/d2dt00134a.

(174) Moore, G. E. Progress In Digital Integrated Electronics. *IEDM Tech. Dig.* **1975**, *21*, 11–13.

(175) Nowak, E. J. Maintaining the Benefits of CMOS Scaling When Scaling Bogs Down. *IBM J. Res. Dev.* **2002**, *46* (2–3), 169–180. https://doi.org/10.1147/rd.462.0169.

(176) Busche, C.; Vilà-Nadal, L.; Yan, J.; Miras, H. N.; Long, D. L.; Georgiev, V. P.; Asenov, A.; Pedersen, R. H.; Gadegaard, N.; Mirza, M. M.; Paul, D. J.; Poblet, J. M.; Cronin, L. Design and Fabrication of Memory Devices Based on Nanoscale Polyoxometalate Clusters. *Nature* **2014**, *515* (7528), 545–549. https://doi.org/10.1038/nature13951.

(177) Liu, Y.; Zhang, J.; Lu, S.; Xiang, Y. Polyoxometalate-Based Electrolyte Materials in Redox Flow Batteries: Current Trends and Emerging Opportunities. *Mater. Reports Energy* **2022**, *2* (2), 100094. https://doi.org/10.1016/j.matre.2022.100094.

(178) Ai, F.; Wang, Z.; Lai, N. C.; Zou, Q.; Liang, Z.; Lu, Y. C. Heteropoly Acid Negolytes for High-Power-Density Aqueous Redox Flow Batteries at Low Temperatures. *Nat. Energy* **2022**, *7* (5), 417–426. https://doi.org/10.1038/s41560-022-01011-y.

(179) Cao, Y.; Chen, J. J. J.; Barteau, M. A. Systematic Approaches to Improving the Performance of Polyoxometalates in Non-Aqueous Redox Flow Batteries. *J. Energy Chem.* **2020**, *50*, 115–124. https://doi.org/10.1016/j.jechem.2020.03.009.

(180) Vilà-Nadal, L.; Peuntinger, K.; Busche, C.; Yan, J.; Lüders, D.; Long, D.; Poblet, J. M.; Guldi, D. M.; Cronin, L. Polyoxometalate {W18O56XO6} Clusters with Embedded Redox-Active Main-Group Templates as Localized Inner-Cluster Radicals. *Angew. Chemie* **2013**, *125*, 9877–9881. https://doi.org/ange.201303126.

(181) Ueda, T. Electrochemistry of Polyoxometalates: From Fundamental Aspects to Applications. *ChemElectroChem* **2018**, *5* (6), 823–838. https://doi.org/10.1002/celc.201701170.

(182) Chen, J. J.; Symes, M. D.; Cronin, L. Highly Reduced and Protonated Aqueous Solutions of [P2W18O62]6− for on-Demand Hydrogen Generation and Energy Storage. *Nat. Chem.* **2018**, *10* (10), 1042–1047. https://doi.org/10.1038/s41557-018-0109-5.

(183) Zhao, T.; Bell, N. L.; Chisholm, G.; Kandasamy, B.; Long, D. L.; Cronin, L. Aqueous Solutions of Super Reduced Polyoxotungstates as Electron Storage Systems. *Energy Environ. Sci.* **2023**, 2603–2610. https://doi.org/10.1039/d3ee00569k.

Chapter 2: Computational Chemistry

In this section we will review the field of quantum mechanics as it pertains to the description of atomic orbitals, with emphasis on Schrödinger's equation, before detailing how it has been deployed as part of computational chemistry, such as part of Hartree-Fock or Density Functional Theory methods. Finally, we will discuss the tenets of inverse design and how it can improve the usefulness of computational chemistry in accelerating the developmental life cycles of new chemicals and materials.

2.1 Quantum Mechanics

The birth of quantum mechanics can be traced back to the famous Double-Slit experiment in 1801, where it was established that electrons could behave as either solid particles or waves depending on if the electrons are being observed.[185] From there the field has steadily grown, particularly throughout the 20th century, with such major discoveries as general relativity and the Higgs Boson revolutionising our understanding of the universe, making scientists such as Albert Einstein and Erwin Schrödinger household names.

Most relevant to us is the work surrounding how electrons behave within atoms. It was originally believed that electrons orbited the atomic nucleus at variable distances akin to planets around a star but this was eventually disproved by Niel Bohr's model of the atom,[186] in which electrons could only orbit at specific, quantized distances; each distance and the subsequent path each electron could take in its orbit are referred to as orbitals. This builds off the work of other key researchers, including Boltzmann,[187] Planck,[188] and Einstein.[189]

One of the issues with Bohr's model is that it doesn't take into consideration the uncertainty principle identified by the Double-Slit experiment. Atomic orbitals must be treated differently

than classical orbitals as the electrons, when acting as waves, can be distributed over a range of positions instead of the classical single point. Using Schrödinger's equation (**eq. 2.1**), which describes electrons using wavefunctions, we can properly describe the positions of electrons using probability; there a 100% chance of finding the electron within its atomic orbital but we can make no other predictions as to where within the orbital the electron will be at any one point in time.[190]

$$\Psi(r,\theta,\varphi) = R(r),Y(\theta,\varphi) = NR_{n,l}(r)P_l^m(Cos\theta)e^{im\varphi} \quad \textbf{(eq. 2.1)}$$

where:

$\Psi(r,\theta,\varphi)$ = complete description of 3-D electron wavefunction

$R(r) = R_{n,l}(r)$ = radial component (z-axis contribution)

$Y(\theta,\varphi) = P_l^m(Cos\theta)e^{im\varphi}$ = angular component (x- and y-axis contribution)

N = total collection of constants

n = principal quantum number (1, 2, …)

l = azimuthal quantum number (0, 1, 2, … , n-1)

m = magnetic quantum number (-n-1, … -2, -1, 0, 1, 2, …, n-1)

Expressing the radial components as full equations, we can solve for specific n and l values:

$$R_{n,l}(r) = \frac{1}{r}e^{-\varsigma}\varsigma^{l+1}V(\varsigma) \quad \textbf{(eq. 2.2)}$$

$$\varsigma = \frac{r}{0.529n} \quad \textbf{(eq. 2.3)}$$

For the angular component, we need to further separate $Y(\theta,\varphi)$ into the polar and azimuth equations before solving for l and m:

$$Y(\theta,\varphi) = \Theta(\theta)\cdot\Phi(\varphi) \quad \textbf{(eq. 2.4)}$$

$$\Theta(\theta) = P_l^m(Cos\theta) \quad \textbf{(eq. 2.5)}$$

$$P_l^m(x) = (1-x)^{|m/2|}\left(\frac{d}{dx}\right)^{|m|} P_l(x) \quad \textbf{(eq. 2.6)}$$

$$\Phi(\varphi) = c_1 e^{im\varphi} \quad \textbf{(eq. 2.7)}$$

The easiest method for solving Schrödinger's equation is to remove time from the equation; this time-independent form treats each wavefunction as a standing or stationary wave, in contrast to the time-dependent equation where the probability of finding an electron at a specific point is constantly changing and requires oscillating wavefunctions.

Other than accurately representing an electron as a wave, Schrödinger's equation also describes the path electrons will take as they orbit the atom, also referred to as the shape of the orbital. Higher energy orbitals, especially d and f orbitals, become increasingly complex and Schrödinger's equation is therefore only practical to solve by hand for the simplest of elements, namely hydrogen and helium; calculation of heavier elements necessitates use of computational aid.

Another facet of Bohr's model which ties into UV-Vis absorption is that of explaining why certain elements or molecules emit light at specific wavelengths. As electrons occupy discrete orbitals, they require absorption of a quantized packet of light to promote themselves to a higher order orbital. These excited electrons invariably return to their orbital of origin but not before releasing the absorbed energy as an emission of electromagnetic radiation. The wavelength of light emitted is therefore determined by **equation 2.8**.

$$E = h / \lambda \quad \textbf{(eq. 2.8)}$$

where:

$h = 1.24 \times 10^{-6}$ eV nm^{-1}

λ = wavelength (nm)

The first/ lowest energy absorption band is associated with the excitation of an electron from the Highest Occupied Molecular Orbital (HOMO) to the Lowest Unoccupied Molecular Orbital (LUMO), across a dimension of energy commonly referred to as the HOMO-LUMO gap. In the case of POMs, this HOMO-LUMO gap usually emits light in the UV-region of the electromagnetic spectrum but can be blue-shifted upon reduction.

2.2 Computational Chemistry History and Software

There has been a growing trend towards the use of computational simulations of chemical systems in recent years, mostly brought about by the introduction of a wide range of accessible computer programs. This has allowed for theory to take a more prominent role in describing the interactions within the beaker whilst not requiring researchers to obtain a degree in theoretical chemistry.[191] That being said, it is essential that one cultivate at least a basic understanding of the mathematics underpinning these calculations, lest one build their work on less-than-sound foundations.

Though there were rudimentary attempts to mechanically solve Schrödinger's equation during the 1920's, with the advent of electronic computers in the Second World War the field truly gained traction; there was now the computational power available to make decent approximations of the Schrödinger's equation for multi-electron elements. In the decades to follow, researchers would learn how to fully utilise this new technology.[192,193,194] The 1970's brought about an explosion in new publications as a direct result of the first accessible software packages being made available, including ATMOL[195], IBMOL[196], and Gaussian[197], the latter being the most famous example still in use today.

Today there exists a wide range of different computational chemistry software programmes, many of which are free and easily accessible.[198,199] An example that we utilised towards the start of this project was ORCA,[200] an open system software that can run a number of different

calculation types, including DFT, semi-empirical methods, and force-field methods, and featuring more than 22,000 users in 2020.[201] Another successful project worth mention is the Libxc library, which provides access to more than 600 DFT functionals and tasks and is seeing increased incorporation into other commercial programmes.[202]

The literature, however, indicates that the old adage of 'you get what you pay for' is still the law of the land; most publications tend towards the usage of paid programmes, such as Gaussian,[197] ADF,[203,204] and Turbomole,[205] to name only those used over the duration of this project. Of these, Gaussian has seen the most usage by researchers and to this day remains the quintessential computational chemistry programme, with its easy-to-use interface, intuitive molecule builder/ editor, and wide array of tasks it can run.

All these programmes utilise the more efficient Gaussian orbitals over the more precise Slater orbitals, with the exception of ADF which gives one the option to use Slater instead of Gaussian. We will discuss these orbitals in more detail in the **Basis Sets (2.6)** section. ADF also tends to be more accurate when it comes to molecules containing transition metals, making it essential for running calculations on POMs. The other main downside to using Gaussian is the cost, which is where cheaper programmes such as TURBOMOLE find their niche; although their results may be less accurate, as long as it is stipulated which programme was used for the research project researchers can still get a good idea of the relative stabilities, energy level values etc of the chemical system.

If further proof is required as to the significant impact computational chemistry is beginning to have in the field, one need only look to the two Nobel prizes that have been awarded to researchers in the field: one in 1998 for Walter Kohn and John Pople for their work towards making financially viable DFT computational calculations, and the other in 2013 to Martin Karplus, Michael Levitt, and Arieh Warshel for making possible the simulation of extended chemical systems by quantum mechanical or molecular mechanical methods.[206]

2.3 Schrödinger Equation Methods

Computational methods can be classified into one of three main families: *ab initio methods*, semi-empirical and empirical. They exist on a scale ranging from utilising purely theoretical data (*ab initio*) to sourcing their parameter values solely from experimental data (empirical). Semi-empirical exists as a compromise between the two, being based on *ab initio* but obtaining some parameters from experimental sources. When talking about using *ab initio*, it is usually implied that this will take the form of Hartree-Fock calculations, which aim to exactly solve the wavefunction.

We will now briefly outline the two main methods of determining Schrödinger's equation in commercial packages, Hartree-Fock Theory and Density Functional Theory, and the main types of functionals and basis sets one will encounter when carrying out computational work; the aim is not to engage in deep discussion as to the intricate inner workings of these methods so much as it is to give one a working knowledge of each method and be able to discern the differences between them. We will start with Hartree-Fock, as it is the foundation upon which Density Functional Theory was designed and informs as to why the latter was a gamechanger for the field.

2.3.1 Hartree-Fock Theory

As previously discussed, electronic wavefunctions give the probability of finding an electron at a given point in space. Hartree-Fock (HF) Theory aims to solve Schrödinger's equation as a linear combination of atomic orbitals (LCAO), each orbital composed of a number of electronic wavefunctions. By a self-iterative process, the electronic model is steadily built up until it reaches a sufficient degree of accuracy to be considered as converged.

The theory was first employed in the late 1920's when Dr. Douglas Hartree developed the method to approximately determine the wavefunctions and energy values for a range of atoms.[207] Fock's contribution came in the early 1930's, when he pointed out and devised a solution to the apparent lack of consideration in Hartree's initial equations for electronic asymmetry;[208,209] without the inclusion of this asymmetry, Pauli's exclusion principle is essentially omitted. This culminated in the inclusion of Slater Determinants in HF theory in the 1950's, which we will soon discuss in greater detail.[210]

HF theory took until the 1950's to gain prominence in the field due to the lack of computational power required to run the calculations, and even after this point was mostly restricted to working with spherical atoms with a high degree of symmetry.

$$\mathrm{H} = -\sum_l^M \frac{1}{2M_l}\nabla_l^2 - \sum_i^N \frac{1}{2}\nabla_i^2 - \sum_i^N \sum_A^M \frac{Z_A}{r_{iA}} + \sum_i^N \sum_{j>i}^N \frac{1}{r_{ij}} + \sum_A^M \sum_{A<B}^M \frac{Z_A Z_B}{R_{AB}} \quad \textbf{(eq. 2.9)}$$

Utilising such approximations as Born-Oppenheimer, wherein the nucleus is stationary relative to the electron(s),[211] the full HF equation (**eq. 2.9**) can be separated into two distinct parts: the nuclear contributions and the solely electronic ones. The nuclear part, the left-most and right-most terms respectively, can be solved exactly but the electronic component (**eq. 2.10**) must be approximated to a certain degree.

$$\mathrm{H_{el}} = -\sum_i^N \frac{1}{2}\nabla_i^2 - \sum_i^N \sum_A^M \frac{Z_A}{r_{iA}} + \sum_i^N \sum_{j>i}^N \frac{1}{r_{ij}} \quad \textbf{(eq. 2.10)}$$

The electronic terms represent (from left to right): the sum of electron kinetic energies, the sum of electron-nuclei attractions, and the sum of electron-electron repulsions. These terms can be collected into a single electron equation (**eq. 2.11**), where electron-electron repulsion is grouped into a single term, in which repulsion between any given electron and all other

electrons in the system is an average value (υ^{HF}). **f(x)** is referred to as the Fock operator, which can be used to break the Schrödinger equation down into a set of single electron equations suitable for representation as Slater determinants.

$$H_{el} = \sum_i^N f(x_i), \quad f(x_i) = -\frac{1}{2}\nabla_i^2 - \sum_A^M \frac{Z_A}{r_{iA}} + \upsilon^{HF}(x_i), \quad \upsilon^{HF}(x_i) = \sum_{j>i}^N \frac{1}{r_{ij}} \qquad \textbf{(eq. 2.11)}$$

To approximate the total electron-electron repulsion energy within the atom, we can represent the total set of electron coordinates within the following Slater determinant (**eq. 2.12**). First envisioned for this purpose by J.C. Slater in 1929, the determinant treats every electron as independent within the atom, therefore enabling us to satisfy Pauli's exclusion principle and allowing for solving of Schrödinger's equation for multi-electron systems (albeit approximately).

$$\psi(x_1, x_2, \ldots, x_{n,}) = \frac{1}{\sqrt{n!}} \begin{vmatrix} \chi_i(x_1) & \chi_j(x_1) & \cdots & \chi_k(x_1) \\ \chi_i(x_2) & \chi_j(x_2) & \cdots & \chi_k(x_2) \\ \vdots & \vdots & \ddots & \vdots \\ \chi_i(x_n) & \chi_j(x_n) & \cdots & \chi_k(x_n) \end{vmatrix} \qquad \textbf{(eq. 2.12)}$$

For the Slater determinant to be appropriate for this purpose, $\psi(x_1, x_2)$ must be equivalent to $-\psi(x_2, x_1)$, which we can prove in (**eq. 2.13**) and (**eq. 2.14**).

$$\psi(x_1, x_2) = \frac{1}{\sqrt{2!}} \begin{vmatrix} \chi_1(x_1) & \chi_2(x_1) \\ \chi_1(x_2) & \chi_2(x_2) \end{vmatrix} = \frac{1}{\sqrt{2!}} [\{\chi_1(x_1)\chi_2(x_2)\} - \{\chi_2(x_1)\chi_1(x_2)\}] \qquad \textbf{(eq. 2.13)}$$

$$-\psi(x_2, x_1) = \frac{1}{\sqrt{2!}} \begin{vmatrix} -\chi_2(x_2) & -\chi_1(x_2) \\ -\chi_2(x_1) & -\chi_1(x_1) \end{vmatrix} = \frac{1}{\sqrt{2!}} [\{-\chi_2(x_2) - \chi_1(x_1)\} - \{-\chi_2(x_1) - \chi_1(x_2)\}] \qquad \textbf{(eq. 2.14)}$$

It's worth noting that Slater determinants can only be used for representing simple electron wavefunctions and fail in more complex applications, such as with describing fermionic wavefunctions.[212] Additionally, as the Slater determinant only provides one with an approximation, Hartree-Fock will not provide completely accurate solutions when they are used. This last point is the result of electron correlation being omitted from the determinant by the particular method it utilizes in satisfying Pauli's exclusion principle.

Returning to Hartree-Fock theory: by treating the whole Slater determinant as a wavefunction we can optimize the electronic contribution as a single package, with the minima representing a solution that takes the energies and spin states of all electrons within the system into account (**eq. 2.15**).

$$E_{elec}(\{\chi_a\}) = \langle\psi_{elec}|\, H_{elec}\, |\psi_{elec}\rangle \qquad \textbf{(eq. 2.15)}$$

Substitution and expansion of (**eq. 2.15**) is a long process but it eventually arranges itself in terms of the Fock operator **f(x)** (**eq. 2.16**):

$$f\chi_a(x_1) = \sum_b^N \varepsilon_{ab}\chi_b(x_1) = \chi_a(x_1)[h_{one}(x_1) + \sum_b^N J_b(x_1) - K_b(x_1)],$$

$$h_{one} = -\frac{1}{2}\nabla_i^2 - \sum_A^M \frac{Z_A}{r_{iA}} \qquad \textbf{(eq. 2.16)}$$

The most important terms from (**eq. 2.16**) are $\mathbf{J_b}$ and $\mathbf{K_b}$, the Coulomb and Exchange operators respectively. In practical terms, the Coulomb operator describes electron-electron repulsion between electrons in orbitals '**a**' and '**b**', whilst the Exchange operator elucidates the energy required for electron exchange, suggesting that Pauli's exclusion principle is taken into account after all.

The final form of the HF equation can be simplified as:

$$f(x_1) = h_{one}(x_1) + \sum_b^N [J_b(x_1) - K_b(x_1)] \qquad \textbf{(eq. 2.17)}$$

While HF theory can easily solve a single electron system (elemental Hydrogen), it quickly becomes more complex as more electrons must be considered. υ^{HF} depends on the wavefunctions of the other occupied orbitals in the system, which all act on and influence each other. To solve this issue, a process referred to as the Self-Consistent Field (SCF) approach is utilised; the total effect of all the wavefunctions is estimated, to a reasonable degree of accuracy, and the Schrödinger equation thus solved for the desired orbital. This process is then repeated for the rest of the orbitals, with each new result feeding into and improving the initial estimation until the system reaches an equilibrium of sorts and further repetitions don't lead to a significant change in the results; this is referred to as the point of convergence, where the minima of the system has been identified.

With a basic understanding of HF under our belts, it's now time to move on to DFT. It's worth a final mention that although sole use of HF is outdated and easily outcompeted by other methods, such as DFT, it still remains a basis off of which these new methods are built and also typically operates as part of a larger whole in many DFT functionals.

2.3.2 Density Functional Theory

Density Functional Theory (DFT) acts as a more elegant solution for Schrödinger's equation than the HF theorem, especially when dealing with larger molecular systems. Rather than solving multiple electron wavefunctions, which rapidly becomes unwieldy to solve, DFT instead focusses on calculating distribution of the total electron density, regardless of which specific electrons are contributing to that density in a given space.[213] This results in DFT being much less computationally demanding than HF, as there are now only 3 spatial coordinates that

have to be taken into account for the total density, instead of 3N, where N is the number of electrons in the system.

Developed in its current state almost 60 years ago, the origins of DFT stretch back almost as far as those of HF theory; building off the back of the Thomas-Fermi model from the late 1920's,[214] the Hohenberg-Kohn theorems have provided, at least in theory, the possibility of coupling the ground state electron density and ground state molecular wavefunction from 1964 onwards.[215] Just the following year, Kohn and Sham introduced their set of equations which would become essentially the definitive method of conducting DFT up to and including the present day.[216]

With regards to the Kohn-Sham equations, the energy of the ground state is expressed as follows:

$$E(\rho) = V_{ext}[\rho] + F[\rho] \qquad \textbf{(eq. 2.18)}$$

In contrast to HF theory, where there is $\mathbf{x_n}$ number of terms, with DFT there is just one: **ρ(r)**, the electron density at coordinate '**r**'. (**eq. 2.18**) can be separated into terms which can be exactly determined (**eq. 2.19**) and those which must be approximated (**eq. 2.20**).

$$V_{ext}[\rho] = \int \hat{V}_{ext}\, \rho(r) dr \qquad \textbf{(eq. 2.19)}$$

$$F[\rho] = T[\rho] + V_{coul}[\rho] + V_{xc}[\rho] \qquad \textbf{(eq. 2.20)}$$

Kinetic energy (**T[ρ]**) is obtained directly from the electron density, where x number of non-interacting electrons are collected into one determinant wavefunction with 'i' number of ϕ_i orbitals, replicating the correct ground state electron density when minimized. Coulombic interaction is slightly tweaked to take electron density into account.

The final term to define is the exchange-correlation potential, which collects the non-classical contributions for $\mathbf{V_{ext}}$ and $\mathbf{V_{coul}}$ into a single term, $\mathbf{V_{xc}}$. $\mathbf{V_{xc}}$ can be thought of as describing a 'XC hole' that each electron within the system creates to repulse other electrons. Whilst only a small term in the complete Kohn-Sham equation, it is the most critical for determining accuracy of the model; a quantum improvement of the DFT method is currently bottlenecked due to a lack of understanding as to how $\mathbf{V_{xc}}$ operates under the hood.

Theoretically speaking, the ground state energy could be exactly calculated if $\mathbf{E_{xc}}$ is known; this has only been achieved for a handful of the simplest molecules thus far however, and so approximation is the standard method of approach.

For the sake of brevity, we will conclude the theory discussion of this chapter and move on to discuss the applications of DFT.

2.4 DFT Applications

Due to the high accuracy of results obtained from DFT coupled with its reasonable cost, it's no wonder that the method has been utilised throughout the STEM community as a whole.[217,218,219] Within the biology community, for example, small sections of proteins or enzymes are analysed for potential binding mechanisms[220] and electronic properties.[221] Biological applications have only appeared relatively recently, due to the size and complexity of the associated molecules or systems, which is partly why DFT has historically seen more utilisation in the field of chemistry.

Within the field of chemistry specifically, there is a longstanding tradition of DFT use that goes back to its earliest origins;[222] this in part explains the wide range of different fields that have

found a problem which is solved in part by DFT. Some key examples include *ab initio* molecular dynamics (MD),[223,224] and solid-state[225] and redox chemistry,[226] see **Table 2.1.** for a more comprehensive list. Within the last 10 years multiple databases for DFT-based calculations have been created to allow for easy access to and comparison against the work of other researchers around the world, some of which have more than 130,000 reported entries,[227] emphasising how widespread the use of DFT has become amongst researchers.[228,229,230]

Within the field of POM chemistry specifically, DFT is able to describe redox activity via electronic energies, and HOMO-LUMO energy values and orbitals.[231,180,176] This is key information and essential for informed POM design, where the structure and isomeric configuration of the framework play a significant part in deciding the final redox properties for the cage.[62] The ability to fine tune in this manner is useful in a manner of different areas, such as nitrogen[232] and hydrogen-evolution catalysis.[233] The redox activity of POMs is particularly desirable due to their ability to store and release large numbers of electrons;[234] DFT allows for detailed analysis of how POMs in different redox states interact within their environment, such as with solvent and reagent molecules.[235]

Carles Bo and his research group have been at the forefront of utilising DFT to further our knowledge of POM chemistry for more than 20 years,[236,69] particularly with a series of works centred around the Keggin structure during the 00's which analysed a wide range of electronic and structural properties; in these publications the effect a number of different variables, such as a different heteroatom species,[237] isomer identity,[238] and framework composition (TM-sub POMs),[239] have on the reduction potential, as well as the interactions between POM and solvent.[240]

Other key researchers include Josep Poblet,[8] who has published computational work on a range of subjects such as chirality[21] and reaction mechanisms,[241] and Stephan Irle, who is associated with a couple of theoretical works gaining insight into the capabilities of POMs to acts as electron sponges.[242,234]

Table 2.1. Key examples of DFT application for a chemical problem at varying levels of theory

Field	Level of Theory Employed (Functional)	Reference
Ab initio Molecular Dynamics	GGA (**PBE**)	He, X. *et al.*[224]
Catalysis	GGA (**PW91**)	Chen, Y. *et al.*[243]
EPR	Hybrid (**B3LYP**)	Sciortino, G. *et al.*[244]
NMR	Hybrid (**B3LYP**)	Yesiltepe, Y. *et al.*[245]
Photovoltaics	GGA (**PBE**)	Elegbeleye, I.F. *et al.*[246]
Redox Chemistry	GGA-D (**B97-3c**), post-HF (**MP2**)	Neugebauer, H. *et al.*[226]
Solid-state Chemistry (POMs)	Hybrid (**B3LYP**)	Busche, C. *et al.*[176]
Surface Chemistry	GGA (**RPBE)**	Hensley, A.J.R. *et al.*[247]
Thermochemistry	Hybrid (**B3LYP, PBE1PBE, B98…**)	Zhao, Y. *et al.*[248]

Despite some doubts concerning the accuracy of functionals developed post 2000,[249] DFT remains the best general method for determining many fundamental molecular properties and providing us with accurate, optimized geometries from which we can make educated assertions as to the underlying chemistry.

2.5 Functionals

A functional is essentially the function by which you attempt to solve Schrödinger's eigenfunction at the DFT level; these vary in the level of complexity they operate at and therefore the computational power they require to successfully reach the point of convergence. The categorization of functionals based on complexity is beautifully illustrated by the concept

of Jacob's ladder, see **Fig. 2.1**, first put forth by John Perdew and Karla Schmidt in a 2001 paper.[250]

As you 'climb the rungs' of the ladder, the accuracy of your results improves but this is offset by the associated increase in computational time; there exists a crossover point where using a more accurate functional is no longer effective. It is important to benchmark several different functionals against available experimental results, as sometimes the less theoretically accurate functionals are the most accurate in practice; no functional is appropriate in every situation.

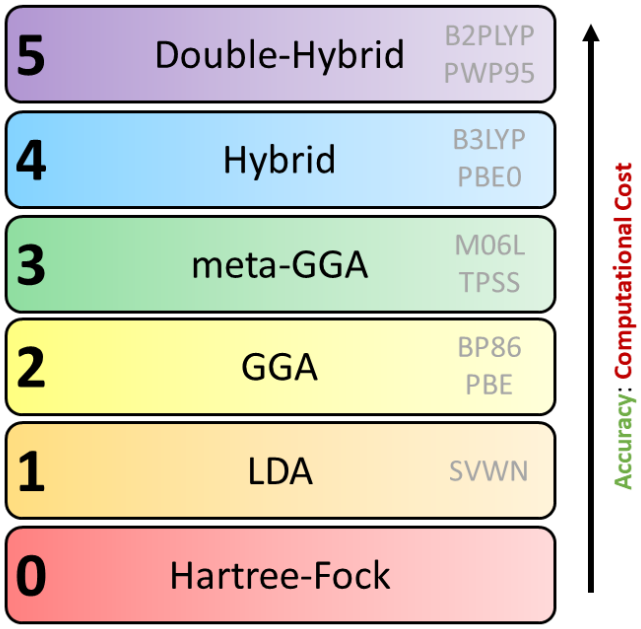

Figure 2.1. Graphical representation of Jacob's ladder, with 'Hartree "hell"' as the lowest rung of the ladder and '"heaven" of chemical accuracy' at the top.

A recent paper by Markus Bursch *et al* acts as an essential guide for not only functional benchmarking, but also for deducing which functional is best suited for a specific application; examples include frequency calculations, reaction barrier energies, and conformers.[251] Another great source for choosing the initial functionals to benchmark with is the DFT poll run by the Swart Lab every year;[252] this survey essentially collects the most popular functional choices by the computational community and gives one an idea of which functionals are the most effective in a general setting. Some functionals may have been designed for a specific application, such as working with TM-containing molecules, and may be more suitable for the type of

calculations you want to run; this will become evident after becoming familiar with the relevant literature.

Local Density Approximation (LDA) is the least complex DFT functional. It assumes local electron density is essentially uniform and only calculates the exchange energy component. (**eq. 2.21**)

$$E_x^{LDA}[\rho] = \int \rho(\mathbf{r})\, \varepsilon_{xc}(\rho)\, d\mathbf{r} \qquad \textbf{(eq. 2.21)}$$

While this lack of complexity has its benefits when working with very simple molecular systems with relatively homogenous electron distribution, predominantly atoms, it is considered unsuitable when working with most molecules.

The next step up from LDA is that of the Generalized Gradient Approximation (GGA); which is a functional for both the electron density and electron density gradient (∇_ρ); instead of calculating the density at a single point ($\rho(\mathbf{r})$), a GGA functional takes the density from several different points to create a more realistic picture of the electron distribution (**eq. 2.22**).

$$E_{xc}^{GGA} = \int f_{xc}\left(\rho_\alpha(\boldsymbol{r}), \rho_\beta(\boldsymbol{r}), \nabla\rho_\alpha(\boldsymbol{r}), \nabla\rho_\beta(\boldsymbol{r})\right) d\boldsymbol{r} \qquad \textbf{(eq. 2.22)}$$

Apart from more accurately portraying electron distribution, GGA also correctly estimates molecular binding energy, something that LDA overestimates. Both factors result in a significant improvement when using GGA over LDA. The most popular function for the last 5 years, according to Swart Lab's DFT poll, is PBE,[253] a well-known GGA functional.[254,255,256,257,252] It uses solely *ab initio* parameters but exhibits only a minute error value when compared with empirical evidence, especially when compared against PW91,[258] a semi-empirical GGA functional.

BP86 is another commonly used functional,[259,260] combining two less complex functionals, Becke 1988 exchange functional and Perdew 86 correlation functional respectively; it is a common characteristic of functionals to combine several other functionals, as it is a relatively straightforward method of increasing the accuracy of a calculation without having to develop a novel functional from scratch. The benefits of this will be expounded upon in the next section.

Thus far we have covered both the pros and cons of utilising Hartree-Fock theory and DFT-based GGA functionals separately; HF theory attempts to exactly solve the Schrödinger equation at great computational cost, whereas DFT at the GGA functional level makes cheaper approximations.

Hybrid functionals act to combine the best of both worlds, linearly combining the exact exchange energy from HF and the exchange and correlation energies for DFT. The ratio to which these components are utilised in the functional differs; PBE0,[261,262,263] for example, has a 3:1 character of PBE:HF inclusion, whilst B3LYP[264] combines several different elements and weighs them against each other using 3 parameters (**eq. 2.23**). B3LYP, which stands for "Becke, 3-parameter, Lee–Yang–Parr", reigned supreme as somewhat of the gold standard for DFT functionals for a number of years[265] and is still very popular to this day (**Fig. 2.2**).[252]

$$E_{xc}^{B3LYP} = 0.8E_z^{LSDA} + 0.2E_x^{exact} + 0.72E_x^{B88} + 0.19E_c^{VWN} + 0.81E_c^{LYP}$$

(eq. 2.23)

By only exactly describing part of the whole molecular system using HF theory and approximating the rest, hybrid functionals are designed to deliver a more accurate result in a timely manner than would be possible if the HF and DT elements were working in isolation. By introducing HF, and therefore wavefunction theory (WFT), the functional ceases to be a

purely non-empirical system, which is a theme for all functionals with at least this level of complexity. As is to be expected when an exact exchange (HF) element is included, there is a marked increase in functional complexity from the hybrid functional rung onwards, in conjunction with a switch from local to non-local electron density.

Building off a hybrid functional base, the range-separate exchange component describes electron-electron correlation/ charge transfer and can be tuned based on the ratio of DFT:WFT elements one intends to utilise in its operation. This branch of functional occupies the grey zone between rungs four and five in the Jacob's ladder (**see Fig. 2.2**). Standard hybrid functionals, such as B3LYP, only take short-range interactions intro account, whereas a range-separated functional can capture short- and/or long-range; it is this long-range component which usually holds the key to accurately depicting charge transfer.[266]

The best-known example of a range-separated functional is ωB97x, which captures both short- and long-range HF exchange.[267] Building on top of the B97 exchange functional, the 'ω' term is the empirical parameter, which is tuned to align the functional as closely to empirical data as possible, whilst the final 'x' term discloses short-range interactions are taken into account as well as long-range; ωB97 would contain long-range only.

Functional	Functional Type	Year Released	Usage (%)
B3LYP	Hybrid	1994	80
B3PW91	Hybrid	1993	4
BLYP	GGA	1988	5
BP86	GGA	1988	3
BPW91	GGA	1991	1
Other	---	---	4
PBE	GGA	1996	2
TPSS	m-GGA	2003	1

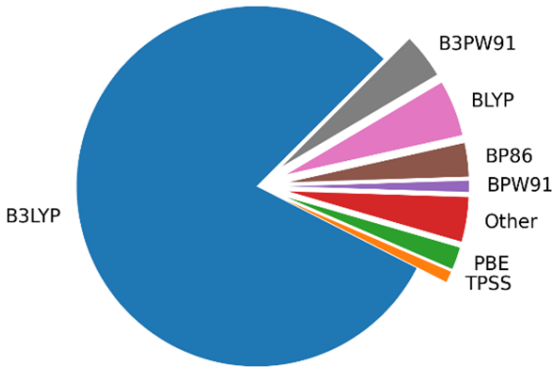

Figure 2.2. Pie chart showcasing the immense popularity of B3LYP in 2007. Data collected from and figure inspired by **Sousa, S.F. *et al.***[265]

Dispersion correlated, or DFT-D, functionals aim to incorporate long-range (Van der Waals) VdW forces into the existing molecular model by introducing an empirical correction to the original DFT functional.[268] This is important for large, biological molecules that have scores of independent degrees of freedom, as VdW forces have a much larger impact on the final geometry.[269]

Two commonly used dispersion correlated functionals are PBE-D and B3LYP-D, both of which improve upon their respective predecessors. PBE-D is especially accurate as a dispersion functional as it already takes dispersive interactions into account as the core PBE functional.[268]

Occupying the fifth, and at present highest, rung of Jacob's ladder are the double hybrid functionals. Unlike previous rungs, *ab initio* DFT methods are applied to great advantage; long-range dispersion and VdW interactions which have to be accounted for at lower levels of complexity are intrinsic to this level of theory.[270] Unoccupied, virtual orbitals are also included, something distinctly lacking up to this point.

Whilst mixing GGA and HF components as with standard hybrid functionals, a perturbative second order (PT2) correlation is included which results in the creation of a new class of functional, namely the double hybrid.[271,272] This PT2 term significantly improves the relationship between GGA and HF, including reducing the self-interaction error and increasing the degree of exact exchange.

Needless to say, that the highest rung of Jacob's ladder is also by far the most computationally expensive and is currently only viable for very small molecular systems and in specific cases, namely analysis of excited state.

2.6 Basis Sets

A basis set is a set of basis functions, with each basis function describing the spatial component of spin for a single electron, see (**eq. 2.24**) for the general form of a basis function equation, where ϕ_i is the spatial orbital term and χ_s represents the basis function. Having these constant functions present for a functional to use makes solving Schrödinger's equation significantly easier. A wide range of different basis sets have been developed over the years, each tailored for a specific application and providing a different level of accuracy for the final solution.

$$\phi_i = \sum_s c_{si}\chi_s \qquad \textbf{(eq. 2.24)}$$

Basis sets can be categorized as minimal or extended based on the number of basis functions they contain; minimal basis sets contain basis functions that describe occupied orbitals within the desired molecular system whilst an extended basis set, by definition, provides the calculation with a greater number of basis functions, which will allow for description of excited states or virtual orbitals. Generally speaking, extended basis sets will improve the accuracy of the result, but this practically comes at the cost of exponentially more computational cost; carefully choosing a smaller number of key basis functions for your basis set can prove the more prudent decision.

Basis functions come in two varieties: Slater-type orbitals (STOs) and Gaussian-type orbitals (GTOs), see **Figure 2.3**. STOs more accurately describe the hydrogen atom but this comes with the caveat of being more computationally expensive. GTOs are conversely less accurate but with the help of a particular technique, whereby several different GTOs are linearly combined and yielding an overall function with a shape more akin to a STO, they can be used to construct a basis function as accurate as an STO while reducing the associated computational cost, see **Figure 2.4**.

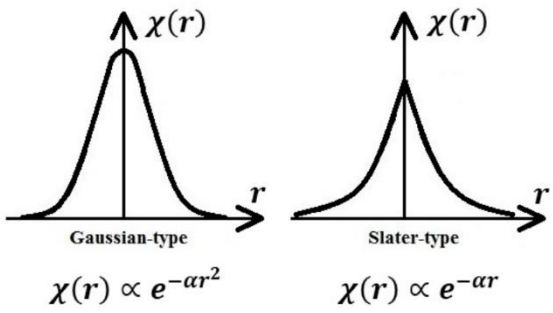

Figure 2.3. Slater- and Gaussian-type functions for a 1s orbital. The sharp point at apex of the Slater function is what makes it an accurate representation for a Hydrogen atom. Image obtained from Moradabadi, A (2017).[273] Gaussian code typically uses Gaussian type functions, whereas SCM-ADF uses STOs

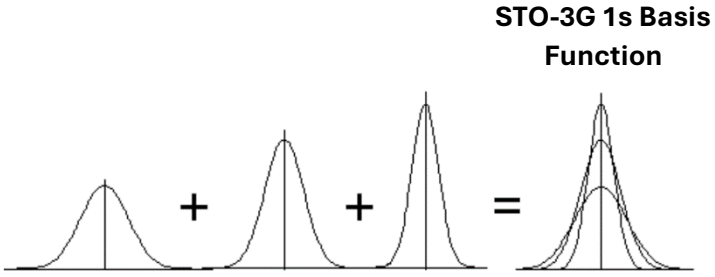

Figure 2.4. Combination of Gaussian-type functions, creating a pseudo-Slater function. Image obtained from LibreTexts Chemistry[274]

Given that GTOs have this advantage over STOs in terms of efficiency, it should be no surprise that all the main DFT software packages utilise GTOs, ADF being the exception. It's worth mentioning that STOs are still a viable choice of basis function due to the relatively high abundance of economical numerical integration schemes, providing one with the flexibility of multiple different methods to achieve convergence.

Although STOs are more accurate than GTOs at describing atomic orbitals (AOs), they still fall short of matching the empirical data. An easy method of vastly improving the margin of accuracy is to expand the number of STOs within a single basis function. In this case, each STO has a different orbital exponent (ζ_n) value, which yields 'n' number of unique variational coefficient (C_n) values, with the exponent with the smallest 'n' value describing charge density further from the nucleus than the others and vice versa; from the selection of coefficients the

computational software chooses the one which best models electron density for the molecular ground state at a given point.

For the simplest level of STO basis set we shall examine, DZP, there are 2 STOs (**D**i) and 1 polarization function per basis function (**P**) (**eq. 2.25**) The polarization functions inclusion is necessitated by the nature of asymmetric AOs within a molecule; an AO will polarize if bonded to another AO with an angular momentum quantum number that is 1 value greater than the original AO. Polarization functions therefore become integral to describing systems containing a mix of metal and non-metal atoms bound together within the same molecule.

$$R_{2s}(r) = C_1 r e^{-\zeta_1 r} + C_2 r e^{-\zeta_2 r} \qquad \textbf{(eq. 2.25)}$$

For Karlsruhe basis sets, there are a couple of methods to increase complexity of the basis set further: increase the number of STOs and/or polarization functions within the basis function. In terms of the number of STOs, either 1 or 2 more functions can be included, creating a TZP- or QZP-type basis set. For polarization functions, the total number can be brought up to 4 within ADF. The most complex basis set available within the software is QZ4P, which is considered to be near to the complete basis set limit for molecules at the DFT level; this limit is the point at which a molecule can't be described with any greater degree of accuracy.

2.7 Solvation Simulation Methods

Unless specified, DFT-calculations are run in a gaseous environment. While this is satisfactory for simplified systems, inclusion of a simulated solvent around the molecule is essential for any serious benchmarking effort. Although viable for very small molecular systems, a niche within which Molecular Dynamics (MD) simulations has proven useful, it would be near impossible to converge a starting geometry that included hundreds of individual solvent molecules around the main solute due to the trillions of possible geometry combinations; it was

therefore essential for researchers to develop inspired methods of simulating the solvent environment despite the inherent loss of accuracy associated with using an implicit model of solvation over an explicit one.[275]

Such an inspired method is that of the implicit or continuum solvent model; instead of generating individual solvent molecules, the solvent is treated as a bulk quantity, or sheet, that the solute is present within. Said solute occupies a cavity within the solvent, see **Fig. 2.5**. Interactions between solute and bulk solvent are averaged out relative to an explicit solvent model; thus, loss in true accuracy is more than made for by the significant increase in accuracy associated with the implicit model.[276]

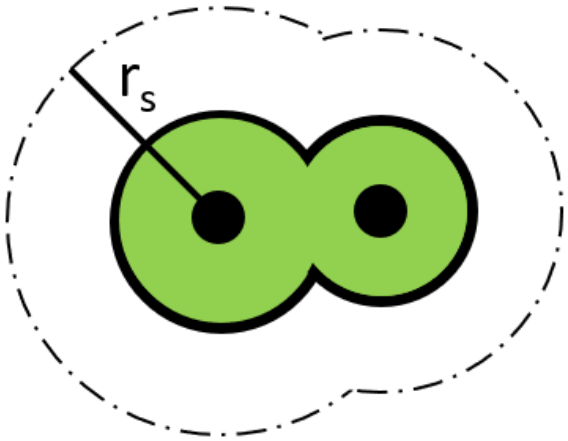

Figure 2.5. Green molecule encapsulated inside a cavity of radius 'r_s'

Calculations utilising a solvent model converge with the aid of a Self-Consistent Reaction Field (SCRF).[277] This field acts in a straightforward fashion: the solute polarizes the surrounding solvent. The polarized solvent now polarizes the solute and so on until a point of convergence is reached. This is particularly vital for calculations with POMs, as the interactions between the polarized terminal oxygen atoms and solvent can be accurately characterized.[231] All implicit solvent models, including PCM,[276] aim to solve the Poisson equation, which describes the dielectric solvent medium encapsulating a charged solute molecule within a cavity at point r_s (**eq. 2.26**).[276] The shape of the cavity determines how easy this equation is to solve, with less symmetrical cavities requiring more computational time and effort.

$$4\pi\varepsilon\sigma(r_s) = (\varepsilon - 1)F(r_s) \qquad \textbf{(eq. 2.26)}$$

The total energy required to create a cavity, or, more accurately, to remove the appropriate solvent-solvent interactions, is represented by ΔG_{cav}. The interactions between the solute occupying the pore and the surrounding solvent are then characterized by either an electrostatic (ΔG_{elec}) or a non-electrostatic contribution ($\Delta G_{non\text{-}elec}$); summation of all these components amounts to the total energy of solvation, represented by (**eq. 2.27**).

$$\Delta G_{solvation} = \Delta G_{elec} + \Delta G_{non-elec} + \Delta G_{cav} \qquad \textbf{(eq. 2.27)}$$

There exist several solvent models open to the computational chemist, including QM/MM methods and the supermolecule model, but the option with the best accuracy to cost ratio, and consequently the most widely used model, is the conductor-like screening model (COSMO).[278,279,280] COSMO simulates a continuous conductive medium to stand in for the solvent, with the solute occupying a cavity within the medium.

In contrast to a dielectric medium, the conductive medium significantly simplifies the mathematics involved with finding the correct solution to the iterative problem whilst also avoiding the significant problem with incorrectly placement of the charge.[281] COSMO can also operate well across a wide range of solvent species, using metrics other than the dielectric constant (ε) to characterize the solvent, which is important as some solvent species have identical ε values and dielectric mediums are unable to differentiate between them if this is the case.[282] Note that for a conductive medium, which take charged solutes into account, a derivative of the Poisson equation, referred to as the Poisson-Boltzmann equation, is used instead of the standard version.

Due to the large anionic charge usually associated with POMs, a solvation model is usually required to stabilize the energy of the frontier orbitals. This model tends to be the implicit

solvation model COSMO, on account of POMs already being relatively large and complex structures to run calculations on;[283,284,285] though some attempts of explicitly representing the solvent have been conducted (**Fig. 2.6**),[286] COSMO remains the predominant method of modelling solvent to this day due to the simplicity with which it can be applied.

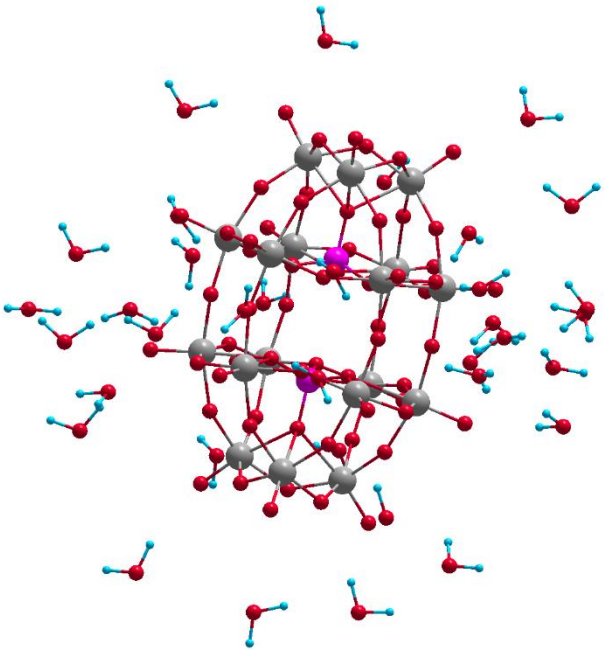

Figure 2.6. Example of explicit solvation model, where a $[P_2W_{18}O_{62}]^{6-}$ Wells-Dawson POM is surrounded by water molecules. Hydrogen visualized blue for clarity.

2.8 UV-Vis Calculations

Frontier orbital properties can be calculated using Time-Independent (TI-DFT) or Time-Dependent (TD-DFT); TI-DFT relies on simply reading the orbital energies from the DFT output file, subtracting between the two, and thereby determining the HOMO-LUMO gap, whilst TD-DFT allows for examination of exciton identity in greater detail.

As of AMS2023, TD-DFT can be substituted with the GW-Bethe-Salpeter method (GW-BSM)[287] to achieve description of excitons to a greater degree of accuracy.[288,289] This method has been tested on organic systems with a couple thousand electrons,[290,287] indicating it is appropriate to use with most common POM species, up to a cluster of the size of a Wells-Dawson cluster ($K_6[P_2W_{18}O_{62}]$).

2.9 Inverse Design

Given the increasing demand on time and resources in the modern day to solve key existential problems to continued human survival and flourishing, new methods for chemical discovery must be devised and utilised over previous brute force or serendipitous roads to scientific innovation. These previous routes rely on an application for a new material being evident, which relies heavily on the discovering researcher being aware of the ideal area for applying their new compound and that area being one of the main topics of research of a given era.

Instead of crossing ones fingers and hoping for the best when setting out to discover new, world-changing materials, inverse design[291,292] is a method that has the potential to provide a work around; designing a molecule or material in this manner requires a theoretical model of the product, one that is expected to fulfil a specific role, followed by working backwards along the synthetic route until the reagents and reaction conditions necessary to yield the desired product are elucidated. It also allows for easy experimentation with novel ideas in the computational realm, testing the waters to determine if an approach is feasible before expensive lab work is undertaken.[82,293] In other words, inverse design has the capability to save researchers a great deal of lab time and money, finding the best solution to a pertinent research question instead of the other way around (**Fig. 2.7**).

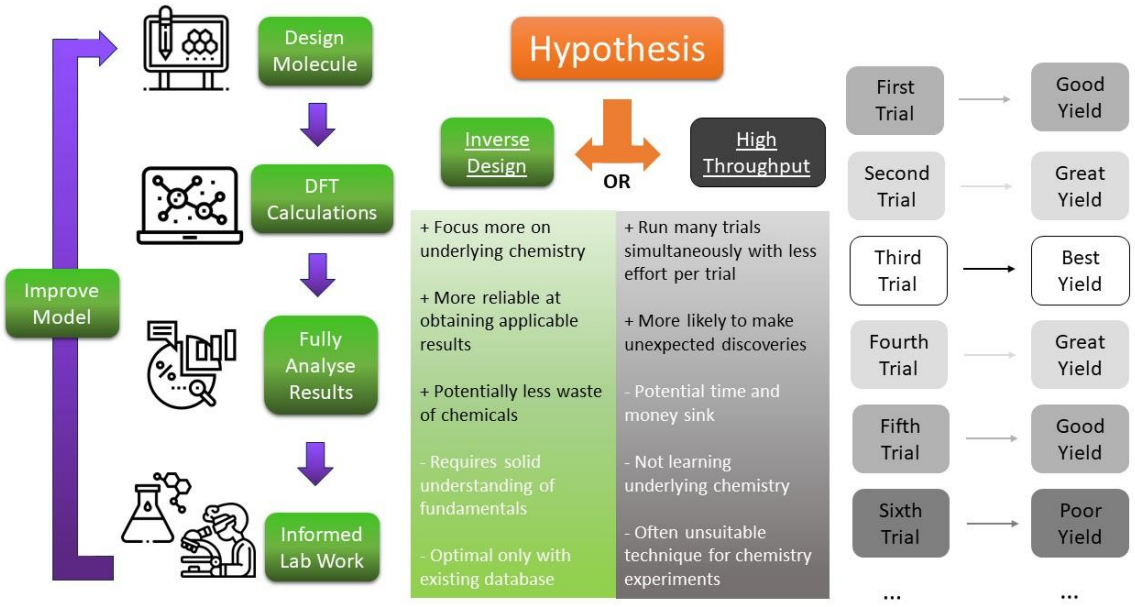

Figure 2.7. Diagram explaining differences between High Throughput and Inverse Design development methods.

Fully realising the potential of inverse design, that of finding a solution to a problem out of countless possible answers, naturally necessitates collaboration with a machine learning programme.[294] While machine learning can be something of a 'black box', with only a select few with the knowledge to understand and run the programme properly, it remains a very exciting avenue of research, with the programme learning from past experiences and adapting based on those experiences or new parameters set by the researcher.[295] Only a machine learning computer programme has the complexity and power necessary to parse through the multitude of possibilities to arrive with a relevant compound for the desired application, drastically reducing the length of the development cycle in the process.[296]

To use POMzites as an example,[292] this relatively new material is easily customised during synthesis using a variety of variables (temperature, pH, choice and concentration of TM anions…) but the lack of comprehensive understanding into their self-assembly processes acts to drive up the costs associated with researching these materials;[297] simply creating 100 new species of POMzite doesn't guarantee any are optimal for a given application. With a big enough database of POMzite structures with which to train a machine learning programme and a better understanding into the underlying chemistry behind POMzite self-assembly, we could

parse through less relevant species and only synthesize the select few which exhibit the greatest promise.[298]

If we are to properly apply the tenets of inverse design, we must have the capabilities to build and analyse complex computational models of POMzite and their POM aggregates, in tandem with having a deep knowledge of their self-assembly processes.[299] It is currently not feasible to run DFT-level optimization calculations on POMzite subsections, due to the large level of complexity associated with these structures; we can only optimize their POM constituents with the computational theory and power at our disposal. Additionally, we need to establish the correct set of parameters or descriptors to sufficiently characterize each POM species, allowing us to identify the most useful POM species for our use.[300]

2.10 Computational Details

To round out this chapter, we will report the computational details used in our research. All calculations were performed using the Amsterdam Modelling Suite (AMS 2023.1).[203,301] In this work we have been comparing the results from using several different functionals: the non-empirical Perdew-Burke-Ernzerhof (PBE), the generalized gradient approximation (GGA) exchange-correlation functional,[253] the empirical exchange-correlation functionals of Becke and Perdew,[259,302] the B3LYP hybrid functionals,[264] the PBE0 functional of Adamo and Barone,[303,268] a dispersion correction in the form of DFT-D2,[304] which was applied to PBE (PBE-D) and B3LYP (B3LYP-D), the range separated functional wB97X,[267] the Minnesota 2006 local functional (M06-L),[305] the Moller-Plesset perturbation theory (MP2),[306,307] and HF.[207,208,209]

Relativistic corrections were included by means of the ZORA formalism.[308] Double-ζ polarization (def2-DZP), triple-ζ polarization (def2- TZP),[309,] triple-ζ plus polarization (def2-TZ2P), and (def2-QZ4P) basis sets were employed to describe the valence electrons of all

atoms, all of which were from the ADF basis set library.[310] Structures were optimized in the presence of a continuous model solvent by means of the conductor-like screening model (COSMO), with water , methane, dichloromethane, and hexane being utilised as solvents.[278,279]

The OPBE[311] functional and TZ2P-J[312] basis set were selected for NMR calculations, as the literature indicated this would give the most accurate results.

The solvation radii values used were the standard Van der Waals values for ADF, determined by Alvarez S. Computational results were obtained using the ARCHIE-WeSt High-Performance Computer (see www.archie-west.ac.uk) based at the University of Strathclyde.

2.11 References

(8) Blasco-Ahicart, M.; Soriano-Lopez, J.; Carbo, J. J.; Poblet, J. M.; Galan-Mascaros, J. R. Polyoxometalate Electrocatalysts Based on Earth-Abundant Metals for Efficient Water Oxidation in Acidic Media. *Nat. Chem.* **2017**, *10*, 24–30. https://doi.org/10.1038/nchem.2874.

(21) Yan, L.; López, X.; Carbó, J. J.; Sniatynsky, R.; Duncan, D. C.; Poblet, J. M. On the Origin of Alternating Bond Distortions and the Emergence of Chirality in Polyoxometalate Anions. *J. Am. Chem. Soc.* **2008**, *130* (26), 8223–8233. https://doi.org/10.1021/ja711008n.

(62) López, X.; Poblet, J. M. DFT Study on the Five Isomers of PW12O403-: Relative Stabilization upon Reduction. *Inorg. Chem.* **2004**, *43* (22), 6863–6865. https://doi.org/10.1021/ic049119p.

(69) Fernández, J. A.; López, X.; Bo, C.; de Graaf, C.; Baerends, E. J.; Poblet, J. M. Polyoxometalates with Internal Cavities: Redox Activity, Basicity, and Cation Encapsulation in [Xn+P5W30O110](15-n)-Preyssler Complexes, with X = Na+, Ca2+, Y3+, La3+, Ce3+, and Th4+. *J. Am. Chem. Soc.* **2007**, *129* (3), 12244–12253. https://doi.org/10.1021/ja0737321.

(176) Busche, C.; Vilà-Nadal, L.; Yan, J.; Miras, H. N.; Long, D. L.; Georgiev, V. P.; Asenov, A.; Pedersen, R. H.; Gadegaard, N.; Mirza, M. M.; Paul, D. J.; Poblet, J. M.; Cronin, L. Design and Fabrication of Memory Devices Based on Nanoscale Polyoxometalate Clusters. *Nature* **2014**, *515* (7528), 545–549. https://doi.org/10.1038/nature13951.

(180) Vilà-Nadal, L.; Peuntinger, K.; Busche, C.; Yan, J.; Lüders, D.; Long, D.; Poblet, J. M.; Guldi, D. M.; Cronin, L. Polyoxometalate {W18O56XO6} Clusters with Embedded Redox-Active Main-Group Templates as Localized Inner-Cluster Radicals. *Angew. Chemie* **2013**, *125*, 9877–9881. https://doi.org/ange.201303126.

(185) Young, T. 1. The Bakerian Lecture. Experiments and Calculations Relative to Physical Optics. *Philos. Trans. R. Soc. London* **1804**, *94* (94), 1–16. https://doi.org/10.1098/rstl.1804.0001.

(186) Bohr, N. I. On the Constitution of Atoms and Molecules. *London, Edinburgh, Dublin Philos. Mag. J. Sci.* **1913**, *26* (151), 1–25. https://doi.org/10.1080/14786441308634955.

(187) Flamm, D. Ludwig Boltzmann -- A Pioneer of Modern Physics. **1997**. https://doi.org/10.48550/arXiv.physics/9710007.

(188) Planck, M. Ueber Das Gesetz Der Energieverteilung Im Normalspectrum. *Ann. Phys.* **1901**, *309* (3), 553–563. https://doi.org/10.1002/andp.19013090310.

(189) Einstein, A. Über Einen Die Erzeugung Und Verwandlung Des Lichtes Betreffenden Heuristischen Gesichtspunkt. *Ann. Phys.* **1905**, *322* (6), 132–148. https://doi.org/10.1002/andp.19053220607.

(190) Schrödinger, E. An Undulatory Theory of the Mechanics of Atoms and Molecules. *Phys. Rev.* **1926**, *28* (6), 1049–1070. https://doi.org/10.1103/PhysRev.28.1049.

(191) Krylov, A.; Windus, T. L.; Barnes, T.; Marin-Rimoldi, E.; Nash, J. A.; Pritchard, B.; Smith, D. G. A.; Altarawy, D.; Saxe, P.; Clementi, C.; Crawford, T. D.; Harrison, R. J.; Jha, S.; Pande, V. S.; Head-Gordon, T. Perspective: Computational Chemistry Software and Its Advancement as Illustrated through Three Grand Challenge Cases for Molecular Science. *J. Chem. Phys.* **2018**, *149* (18). https://doi.org/10.1063/1.5052551.

(192) Roothaan, C. C. J. New Developments in Molecular Orbital Theory. *Rev. Mod. Phys.* **1951**, *23* (2), 69–89. https://doi.org/10.1103/RevModPhys.23.69.

(193) Parr, R. G.; Craig, D. P.; Ross, I. G. Molecular Orbital Calculations of the Lower Excited Electronic Levels of Benzene, Configuration Interaction Included. *J. Chem. Phys.* **1950**, *18* (12), 1561–1563. https://doi.org/10.1063/1.1747540.

(194) Streitwieser, A.; Brauman, J.; Coulson, C. *Supplemental Tables of Molecular Orbital Calculations with a Dictionary of Pi-Electron Calculations*; Pergamon Press, 1965.

(195) Moncrieff, D.; Saunders, V. R. ATMOL-SCF Program.

(196) Davis, D. R.; Clementi, E. *IBMOL: Computation of Wave Functions for Molecules of General Geometry. An IBM 7090 Program Using the LCAO-MO-SCF Method; IBM Research Report, December, 1965*.

(197) Frisch, J.; Trucks, G.; Schlegel, H.; Scuseria, G.; Robb, M.; Cheeseman, J.; Scalmani, G.; Barone, V.; Mennucci, B.; Petersson, G.; Nakatsuji, H.; Caricato, M.; Li, X.; Hratchian, H.; Izmaylov, A.; Bloino, J.; Zheng, G.; Sonnennberg, J.; Hada, M.; Ehara, M.; Toyota, K.; Fukuda, R.; Hasegawa, J.; Ishida, M.; Nakajima, T.; Honda, Y.; Kitao, O.; Nakai, H.; Vreven, T.; Montgomery, JA, J.; Peralta, J.; Ogliaro, F.; Bearpark, M.; Heyd, J.; Brothers, E.; Kudin, K.; Staroverov, V.; Kobayashi, R.; Normand, J.; Raghavachari, K.; Rendell, A.; Burant, J.; Iyengar, S.; Tomasi, J.; Cossi, M.; Rega, N.; Millam, J.; Klene, M.; Knox, J.; Cross, J.; Bakken, V.; Adamo, C.; Jaramillo, J.; Gomperts, R.; Stratmann, R.; Yazyev, O.; Austin, A.; Cammi, R.; Pomelli, C.; Ochterski, J.; Martin, R.; Morokuma, K.; Zakrzewski, V.; Voth, G.; Salvador, P.; Dannenberg, J.; Dapprich, S.; Daniels, A.; Farkas, O.; Foresman, J.; Ortiz, J.; Cioslowski, J.; Fox, D. *GAUSSIAN*. Gaussian, Inc., Wallingford CT. https://gaussian.com/g09citation/ (accessed 2021-05-09).

(198) Lehtola, S.; Karttunen, A. J. Free and Open Source Software for Computational Chemistry Education. *Wiley Interdiscip. Rev. Comput. Mol. Sci.* **2022**, *12* (5), 1–33. https://doi.org/10.1002/wcms.1610.

(199) *List of Quantum Chemistry and Solid-States Physics Software*. https://en.wikipedia.org/wiki/List_of_quantum_chemistry_and_solid-state_physics_software (accessed 2023-02-01).

(200) Neese, F.; Wennmohs, F.; Becker, U.; Riplinger, C. The ORCA Quantum Chemistry Program Package. *J. Chem. Phys.* **2020**, *152* (22). https://doi.org/10.1063/5.0004608.

(201) Wennmohs, F.; Neese, F. *ORCA Forum*. https://orcaforum.kofo.mpg.de/app.php/portal (accessed 2023-02-01).

(202) Lehtola, S.; Steigemann, C.; Oliveira, M. J. T.; Marques, M. A. L. Recent Developments in LIBXC — A Comprehensive Library of Functionals for Density Functional Theory. *SoftwareX* **2018**, *7*, 1–5. https://doi.org/10.1016/j.softx.2017.11.002.

(203) Rüger, R.; Franchini, M.; Trnka, T.; Yakovlev, A.; E, van L.; Philipsen, P.; van Vuren, T.; Klumpers, B.; Soini, T. *AMS 2020, SCM, Theoretical Chemistry, Vrije Universiteit, Amsterdam, The Netherlands*. http://www.scm.com.

(204) te Velde, G.; Bickelhaupt, F. M.; Baerends, E. J.; Fonseca Guerra, C.; van Gisbergen, S. J. A.; Snijders, J. G.; Ziegler, T. Chemistry with ADF. *J. Comput. Chem.* **2001**, *22* (9), 931–967. https://doi.org/10.1002/jcc.1056.

(205) Balasubramani, S. G.; Chen, G. P.; Coriani, S.; Diedenhofen, M.; Frank, M. S.; Franzke, Y. J.; Furche, F.; Grotjahn, R.; Harding, M. E.; Hättig, C.; Hellweg, A.; Helmich-Paris, B.; Holzer, C.; Huniar, U.; Kaupp, M.; Marefat Khah, A.; Karbalaei Khani, S.; Müller, T.; Mack, F.; Nguyen, B. D.; Parker, S. M.; Perlt, E.; Rappoport, D.; Reiter, K.; Roy, S.; Rückert, M.; Schmitz, G.; Sierka, M.; Tapavicza, E.; Tew, D. P.; Van Wüllen, C.; Voora, V. K.; Weigend, F.; Wodyński, A.; Yu, J. M. TURBOMOLE: Modular Program Suite for Ab Initio Quantum-Chemical and Condensed-Matter Simulations. *J. Chem. Phys.* **2020**, *152* (18). https://doi.org/10.1063/5.0004635.

(206) Prize, N. A Computational Perspective on the Nobel Prize. *Nat. Comput. Sci.* **2022**, *2* (9), 527–528. https://doi.org/10.1038/s43588-022-00325-x.

(207) Hartree, D. R. The Wave Mechanics of an Atom with a Non-Coulomb Central Field Part I Theory and Methods. *Math. Proc. Cambridge Philos. Soc.* **1928**, *24* (1), 89–110. https://doi.org/10.1017/S0305004100011919.

(208) Fock, V. Näherungsmethode Zur Lösung Des Quantenmechanischen Mehrkörperproblems. *Zeitschrift für Phys.* **1930**, *61* (1–2), 126–148. https://doi.org/10.1007/BF01340294.

(209) February, R. Self-Consistent Field, with Exchange, for Beryllium. *Proc. R. Soc. London. Ser. A - Math. Phys. Sci.* **1935**, *150* (869), 9–33. https://doi.org/10.1098/rspa.1935.0085.

(210) Slater, J. A Simplification of the Hartree-Fock Method. *Phys. Rev.* **1951**, *81*, 385–390.

(211) Born, M.; Oppenheimer, R. Zur Quantentheorie Der Molekeln. *Ann. Phys.* **1927**, *389* (20), 457–484. https://doi.org/10.1002/andp.19273892002.

(212) Zhang, J. M.; Kollar, M. Optimal Multiconfiguration Approximation of an N -Fermion Wave Function. *Phys. Rev. A - At. Mol. Opt. Phys.* **2014**, *89* (1), 1–11. https://doi.org/10.1103/PhysRevA.89.012504.

(213) Parr, R. G.; Weitao, Y. *Density-Functional Theory of Atoms and Molecules*; Oxford University Press, 1994. https://doi.org/10.1093/oso/9780195092769.001.0001.

(214) Thomas, L. H. The Calculation of Atomic Fields. *Math. Proc. Cambridge Philos. Soc.* **1927**, *23* (5), 542–548. https://doi.org/10.1017/S0305004100011683.

(215) Hohenberg, P.; Kohn, W. Inhomogeneous Electron Gas. *Phys. Rev.* **1964**, *136* (3B), 864–871. https://doi.org/10.1007/BF01198136.

(216) Kohn, W.; Sham, L. Self-Consistent Equations Including Exchange and Correlation Effects. *Phys. Rev.* **1965**, *140* (4A), 1133–1138. https://doi.org/10.1103/PHYSREV.140.A1133.

(217) Peverati, R.; Truhlar, D. G. Quest for a Universal Density Functional: The Accuracy of Density Functionals across a Broad Spectrum of Databases in Chemistry and Physics. *Philos. Trans. R. Soc. A Math. Phys. Eng. Sci.* **2014**, *372* (2011). https://doi.org/10.1098/rsta.2012.0476.

(218) Van Mourik, T.; Bühl, M.; Gaigeot, M. P. Density Functional Theory across Chemistry, Physics and Biology. *Philos. Trans. R. Soc. A Math. Phys. Eng. Sci.* **2014**, *372* (2011). https://doi.org/10.1098/rsta.2012.0488.

(219) Andreoni, W.; Curioni, A.; Mordasini, T. DFT-Based Molecular Dynamics as a New Tool for Computational Biology: First Applications and Perspective. *IBM J. Res. Dev.* **2001**, *45* (3–4), 397–407. https://doi.org/10.1147/rd.453.0397.

(220) Assis, L. C.; De Castro, A. A.; De Jesus, J. P. A.; Da Cunha, E. F. F.; Nepovimova, E.; Krejcar, O.; Kuca, K.; Ramalho, T. C.; La Porta, F. D. A. Theoretical Insights into the Effect of Halogenated Substituent on the Electronic Structure and Spectroscopic Properties of the Favipiravir Tautomeric Forms and Its Implications for the Treatment of COVID-19. *RSC Adv.* **2021**, *11* (56), 35228–35244. https://doi.org/10.1039/d1ra06309j.

(221) Mahmoudi, S.; Dehkordi, M. M.; Asgarshamsi, M. H. Density Functional Theory Studies of the Antioxidants—a Review. *J. Mol. Model.* **2021**, *27* (9). https://doi.org/10.1007/s00894-021-04891-1.

(222) Laird, B. B.; Ross, R. B.; Ziegler, T. Density-Functional Methods in Chemistry : An Overview. In *Chemical Applications of Density-Functional Theory*; Laird, B. B., Ross, R. B., Ziegler, T., Eds.; American Chemical Society, 1996; pp 1–17. https://doi.org/10.1021/bk-1996-0629.

(223) Rosen, A. S.; Fung, V.; Huck, P.; O'Donnell, C. T.; Horton, M. K.; Truhlar, D. G.; Persson, K. A.; Notestein, J. M.; Snurr, R. Q. High-Throughput Predictions of Metal–Organic Framework Electronic Properties: Theoretical Challenges, Graph Neural Networks, and Data Exploration. *npj Comput. Mater.* **2022**, *8* (1), 1–10. https://doi.org/10.1038/s41524-022-00796-6.

(224) He, X.; Zhu, Y.; Epstein, A.; Mo, Y. Statistical Variances of Diffusional Properties from Ab Initio Molecular Dynamics Simulations. *npj Comput. Mater.* **2018**, *4* (1). https://doi.org/10.1038/s41524-018-0074-y.

(225) Hasnip, P. J.; Refson, K.; Probert, M. I. J.; Yates, J. R.; Clark, S. J.; Pickard, C. J. Density Functional Theory in the Solid State. *Philos. Trans. R. Soc. A Math. Phys. Eng. Sci.* **2014**, *372* (2011). https://doi.org/10.1098/rsta.2013.0270.

(226) Neugebauer, H.; Bohle, F.; Bursch, M.; Hansen, A.; Grimme, S. Benchmark Study of Electrochemical Redox Potentials Calculated with Semiempirical and DFT Methods. *J. Phys. Chem. A* **2020**, *124* (35),

7166–7176. https://doi.org/10.1021/acs.jpca.0c05052.

(227) Winther, K. T.; Hoffmann, M. J.; Boes, J. R.; Mamun, O.; Bajdich, M.; Bligaard, T. Catalysis-Hub.Org, an Open Electronic Structure Database for Surface Reactions. *Sci. Data* **2019**, *6* (1), 1–10. https://doi.org/10.1038/s41597-019-0081-y.

(228) Curtarolo, S.; Setyawan, W.; Hart, G. L. W.; Jahnatek, M.; Chepulskii, R. V.; Taylor, R. H.; Wang, S.; Xue, J.; Yang, K.; Levy, O.; Mehl, M. J.; Stokes, H. T.; Demchenko, D. O.; Morgan, D. AFLOW: An Automatic Framework for High-Throughput Materials Discovery. *Comput. Mater. Sci.* **2012**, *58*, 218–226. https://doi.org/10.1016/j.commatsci.2012.02.005.

(229) Kirklin, S.; Saal, J. E.; Meredig, B.; Thompson, A.; Doak, J. W.; Aykol, M.; Rühl, S.; Wolverton, C. The Open Quantum Materials Database (OQMD): Assessing the Accuracy of DFT Formation Energies. *npj Comput. Mater.* **2015**, *1* (September). https://doi.org/10.1038/npjcompumats.2015.10.

(230) Haastrup, S.; Strange, M.; Pandey, M.; Deilmann, T.; Schmidt, P. S.; Hinsche, N. F.; Gjerding, M. N.; Torelli, D.; Larsen, P. M.; Riis-Jensen, A. C.; Gath, J.; Jacobsen, K. W.; Mortensen, J. J.; Olsen, T.; Thygesen, K. S. The Computational 2D Materials Database: High-Throughput Modeling and Discovery of Atomically Thin Crystals. *2D Mater.* **2018**, *5* (4). https://doi.org/10.1088/2053-1583/aacfc1.

(231) López, X.; Carbó, J. J.; Bo, C.; Poblet, J. M. Structure, Properties and Reactivity of Polyoxometalates: A Theoretical Perspective. *Chem. Soc. Rev.* **2012**, *41* (22), 7537–7571. https://doi.org/10.1039/c2cs35168d.

(232) González-Cabaleiro, R.; Thompson, J. A.; Vilà-Nadal, L. Looking for Options to Sustainably Fixate Nitrogen. Are Molecular Metal Oxides Catalysts a Viable Avenue? *Front. Chem.* **2021**, *9* (September), 1–7. https://doi.org/10.3389/fchem.2021.742565.

(233) McAllister, J.; Bandeira, N. A. G.; McGlynn, J. C.; Ganin, A. Y.; Song, Y. F.; Bo, C.; Miras, H. N. Tuning and Mechanistic Insights of Metal Chalcogenide Molecular Catalysts for the Hydrogen-Evolution Reaction. *Nat. Commun.* **2019**, *10* (1). https://doi.org/10.1038/s41467-018-08208-4.

(234) Nishimoto, Y.; Yokogawa, D.; Yoshikawa, H.; Awaga, K.; Irle, S. Super-Reduced Polyoxometalates: Excellent Molecular Cluster Battery Components and Semipermeable Molecular Capacitors. *J. Am. Chem. Soc.* **2014**, *136* (25), 9042–9052. https://doi.org/10.1021/ja5032369.

(235) Solé-Daura, A.; Notario-Estévez, A.; Carbó, J. J.; Poblet, J. M.; De Graaf, C.; Monakhov, K. Y.; López, X. How Does the Redox State of Polyoxovanadates Influence the Collective Behavior in Solution? A Case Study with [I@V 18 O 42] q- (q = 3, 5, 7, 11, and 13). *Inorg. Chem.* **2019**, No. Md. https://doi.org/10.1021/acs.inorgchem.8b03508.

(236) Sartorel, A.; Miró, P.; Salvadori, E.; Romain, S.; Carraro, M.; Scorrano, G.; Di Valentin, M.; Llobet, A.; Bo, C.; Bonchio, M. Water Oxidation at a Tetraruthenate Core Stabilized by Polyoxometalate Ligands: Experimental and Computational Evidence to Trace the Competent Intermediates. *J. Am. Chem. Soc.* **2009**, *131* (44), 16051–16053. https://doi.org/10.1021/ja905067u.

(237) Maestre, J. M.; Lopez, X.; Bo, C.; Poblet, J. Electronic and Magnetic Properties of R -Keggin Anions : A DFT Study of [XM12O40]n-, (M = W, Mo; X = AlIII, SiIV, PV, FeIII, CoII, CoIII) and [SiM11VO40]m- (M = Mo and W). *J. Am. Chem. Soc.* **2001**, *123* (16), 3749–3758. https://doi.org/10.1021/ja003563j.

(238) López, X.; Maestre, J. M.; Bo, C.; Poblet, J. M. Electronic Properties of Polyoxometalates: A DFT Study of α/β-[XM12O40]n- Relative Stability (M=W, Mo and X a Main Group Element). *J. Am. Chem. Soc.* **2001**, *123* (39), 9571–9576. https://doi.org/10.1021/ja010768z.

(239) López, X.; Bo, C.; Poblet, J. M. Electronic Properties of Polyoxometalates: Electron and Proton Affinity of Mixed-Addenda Keggin and Wells-Dawson Anions. *J. Am. Chem. Soc.* **2002**, *124* (42), 12574–12582. https://doi.org/10.1021/ja020407z.

(240) Lo, X.; Nieto-draghi, C.; Bo, C.; Avalos, J. B.; Poblet, J. M. Polyoxometalates in Solution: Molecular Dynamics Simulations on the Alpha-PW12O40 3- Keggin Anion in Aqueous Media. *J. Phys. Chem. A* **2005**, *109* (6), 1216–1222. https://doi.org/10.1021/jp046862u.

(241) Antonova, N. S.; Carbo, J. J.; Kortz, U.; Kholdeeva, O. A.; Poblet, J. M.; Uni, V.; Ro, V. Mechanistic Insights into Alkene Epoxidation with H 2 O 2 by Ti- and Other TM-Containing Polyoxometalates : Role of the Metal Nature and Coordination Environment. *J. Am. Chem. Soc.* **2010**, *132* (21), 7488–7497. https://doi.org/10.1021/ja1023157.

(242) Yoshikawa, H.; Awaga, K. In Operando X-Ray Absorption Fine Structure Studies of Polyoxometalate Molecular Cluster Batteries: Polyoxometalates as Electron Sponges. *J. Am* **2012**, *134*, 4918–4924. https://doi.org/10.1021/ja2117206.

(243) Chen, Y.; Gao, Y.; Wang, L.; Gong, H. The Mechanism of MOF as a Heterogeneous Catalyst for Propene Hydroformylation: A DFT Study. *React. Chem. Eng.* **2022**, *7* (5), 1156–1167. https://doi.org/10.1039/d1re00527h.

(244) Sciortino, G.; Lubinu, G.; Maréchal, J. D.; Garribba, E. Dft Protocol for Epr Prediction of Paramagnetic Cu(Ii) Complexes and Application to Protein Binding Sites. *Magnetochemistry* **2018**, *4* (4). https://doi.org/10.3390/magnetochemistry4040055.

(245) Yesiltepe, Y.; Nuñez, J. R.; Colby, S. M.; Thomas, D. G.; Borkum, M. I.; Reardon, P. N.; Washton, N. M.; Metz, T. O.; Teeguarden, J. G.; Govind, N.; Renslow, R. S. An Automated Framework for NMR Chemical Shift Calculations of Small Organic Molecules. *J. Cheminform.* **2018**, *10* (1), 1–16. https://doi.org/10.1186/s13321-018-0305-8.

(246) Elegbeleye, I. F.; Maluta, N. E.; Maphanga, R. R. Density Functional Theory Study of Optical and Electronic Properties of (TiO2)N=5,8,68 Clusters for Application in Solar Cells. *Molecules* **2021**, *26* (4). https://doi.org/10.3390/molecules26040955.

(247) Hensley, A. J. R.; Ghale, K.; Rieg, C.; Dang, T.; Anderst, E.; Studt, F.; Campbell, C. T.; McEwen, J. S.; Xu, Y. DFT-Based Method for More Accurate Adsorption Energies: An Adaptive Sum of Energies from RPBE and VdW Density Functionals. *J. Phys. Chem. C* **2017**, *121* (9), 4937–4945.

https://doi.org/10.1021/acs.jpcc.6b10187.

(248) Zhao, Y.; Truhlar, D. G. Infinite-Basis Calculations of Binding Energies for the Hydrogen Bonded and Stacked Tetramers of Formic Acid and Formamide and Their Use for Validation of Hybrid DFT and Ab Initio Methods. *J. Phys. Chem. A* **2005**, *109* (30), 6624–6627. https://doi.org/10.1021/jp052571p.

(249) Medvedev, M. G.; Bushmarinov, I. S.; Sun, J.; Perdew, J. P.; Lyssenko, K. A. Density Functional Theory Is Straying from the Path toward the Exact Functional. *Science (80-.).* **2017**, *356* (6337), 496c. https://doi.org/10.1126/science.aam9550.

(250) Perdew; Schmidt, K. Jacob ’s Ladder of Density Functional Approximations for the Exchange-Correlation Energy. *AIP Conf. Proc.* **2001**, *577*, 1–20. https://doi.org/10.1063/1.1390175.

(251) Bursch, M.; Mewes, J. M.; Hansen, A.; Grimme, S. Best-Practice DFT Protocols for Basic Molecular Computational Chemistry**. *Angew. Chemie - Int. Ed.* **2022**, *61* (42). https://doi.org/10.1002/anie.202205735.

(252) Swart, M.; Bickelhaupt, F. M.; Duran, M. *DFT2022 Poll*; 2022.

(253) Perdew, J.; Burke, K.; Ernzerhof, M. Generalized Gradient Approximation Made Simple. *Phys. Rev. Lett.* **1996**, *77* (18), 3865–3868. https://doi.org/10.1103/PhysRevLett.77.3865.

(254) Swart, M.; Bickelhaupt, F. M.; Duran, M. *DFT2018 Poll*; 2018.

(255) Swart, M.; Bickelhaupt, F. M.; Duran, M. *DFT2019 Poll*; 2019.

(256) Swart, M.; Bickelhaupt, F. M.; Duran, M. *DFT2020 Poll*; 2020.

(257) Swart, M.; Duran, M.; Bickelhaupt, F. M. DFT2021 Poll. **2021**.

(258) Ziesche, P.; Eschrig, H. *Electronic Structure of Solids ’91 : Proceedings of the 75. WE-Heraeus-Seminar and 21st Annual International Symposium on Electronic Structure of Solids, Held in Gaussig (Germany), March 11-15, 1991*, 1st ed.; Ziesche, P., Eschrig, H., Eds.; Akademie Verlag: Berlin, 1991.

(259) Becke, A. Density-Functional Exchange-Energy Approximation with Correct Asymptotic Behavior. *Phys. Rev. A* **1988**, *38* (6), 3098–3100. https://doi.org/10.1103/PhysRevA.38.3098.

(260) Cartier, E.; Pfluger, P. Transport and Relaxation of Hot Conduction Electrons in an Organic Dielectric. *Phys. Rev. B* **1986**, *34* (12), 8822–8828. https://doi.org/10.1103/PhysRevB.34.8822.

(261) Perdew, J.; Ernzerhof, M.; Burke, K. Rationale for Mixing Exact Exchange with Density Functional Approximations. *J. Chem. Phys.* **1996**, *105* (22), 9982–9985. https://doi.org/10.1063/1.472933.

(262) Ernzerhof, M.; Scuseria, G. Assessment of the Perdew–Burke–Ernzerhof Exchange-Correlation Functional. *J. Chem. Phys.* **1999**, *110* (11), 5029–5036. https://doi.org/10.1063/1.478401.

(263) Adamo, C.; Barone, V. Toward Reliable Density Functional Methods without Adjustable Parameters: The PBE0 Model. *J. Chem. Phys.* **1999**, *110* (13), 6158–6169. https://doi.org/10.1063/1.478522.

(264) Stephens, P.; Devlin, F.; Chabalowski, C.; Frisch, M. Ab Initio Calculation of Vibrational Absorption and Circular Dichroism Spectra Using Density Functional Force Fields. *J. Phys. Chem.* **1994**, *98* (45), 11623–11627. https://doi.org/10.1021/j100096a001.

(265) Sousa, S. F.; Fernandes, P. A.; Ramos, M. J. General Performance of Density Functionals. *J. Phys. Chem. A* **2007**, *111* (42), 10439–10452. https://doi.org/10.1021/jp0734474.

(266) Begam, K.; Bhandari, S.; Maiti, B.; Dunietz, B. D. Screened Range-Separated Hybrid Functional with Polarizable Continuum Model Overcomes Challenges in Describing Triplet Excitations in the Condensed Phase Using TDDFT. *J. Chem. Theory Comput.* **2020**, *16* (5), 3287–3293. https://doi.org/10.1021/acs.jctc.0c00086.

(267) Chai, J. Da; Head-Gordon, M. Systematic Optimization of Long-Range Corrected Hybrid Density Functionals. *J. Chem. Phys.* **2008**, *128* (8). https://doi.org/10.1063/1.2834918.

(268) Grimme, S. Accurate Description of van Der Waals Complexes by Density Functional Theory Including Empirical Corrections. *J. Comput. Chem.* **2004**, *25* (12), 1463–1473. https://doi.org/10.1002/jcc.20078.

(269) Antony, J.; Grimme, S. Density Functional Theory Including Dispersion Corrections for Intermolecular Interactions in a Large Benchmark Set of Biologically Relevant Molecules. *Phys. Chem. Chem. Phys.* **2006**, *8* (45), 5287–5293. https://doi.org/10.1039/b612585a.

(270) Bartlett, R. J.; Lotrich, V. F.; Schweigert, I. V. Ab Initio Density Functional Theory: The Best of Both Worlds? *J. Chem. Phys.* **2005**, *123* (6). https://doi.org/10.1063/1.1904585.

(271) Grimme, S. Semiempirical Hybrid Density Functional with Perturbative Second-Order Correlation. *J. Chem. Phys.* **2006**, *124* (3). https://doi.org/10.1063/1.2148954.

(272) Grimme, S.; Neese, F. Double-Hybrid Density Functional Theory for Excited Electronic States of Molecules. *J. Chem. Phys.* **2007**, *127* (15). https://doi.org/10.1063/1.2772854.

(273) Moradabadi, A. Theoretical Study of Charge Transport in Li-Based Batteries, Freie Universität Berlin, 2017. https://doi.org/10.13140/RG.2.2.20292.12161.

(274) *11.2: Gaussian Basis Sets*. LibreTexts Chemistry. https://chem.libretexts.org/Courses/Pacific_Union_College/Quantum_Chemistry/11%3A_Computational_Quantum_Chemistry/11.02%3A_Gaussian_Basis_Sets (accessed 2023-03-14).

(275) Zhang, J.; Zhang, H.; Wu, T.; Wang, Q.; Van Der Spoel, D. Comparison of Implicit and Explicit Solvent Models for the Calculation of Solvation Free Energy in Organic Solvents. *J. Chem. Theory Comput.* **2017**, *13* (3), 1034–1043. https://doi.org/10.1021/acs.jctc.7b00169.

(276) Tomasi, J.; Mennucci, B.; Cammi, R. Quantum Mechanical Continuum Solvation Models. *Chem. Rev.* **2005**, *105* (8), 2999–3093. https://doi.org/10.1021/cr9904009.

(277) Tapia, O.; Goscinski, O. Self-Consistent Reaction Field Theory of Solvent Effects. *Mol. Phys.* **1975**, *29* (6), 1653–1661. https://doi.org/10.1080/00268977500101461.

(278) Marsh, K. N. COSMO-RS From Quantum Chemistry to Fluid Phase Thermodynamics and Drug Design. *J. Chem. Eng. Data* **2006**, *51* (4), 1480. https://doi.org/10.1021/je0602317.

(279) Pye, C.; Ziegler, T.; van Lenthe, E.; Louwen, J. An Implementation of the Conductor-like Screening Model of Solvation within the Amsterdam Density Functional Package. Part II. COSMO for Real Solvents. *Can. J. Chem.* **2009**, *87* (7), 790. https://doi.org/10.1139/V09-008.

(280) Klamt, A. The COSMO and COSMO-RS Solvation Models. *WIREs Comput. Mol. Sci.* **2011**, *1* (5), 699–709. https://doi.org/10.1002/wcms.56.

(281) Klamt, A. *COSMO-RS: From Quantum Chemistry to Fluid Phase Thermodynamics and Drug Design*; Elsevier Science, 2005.

(282) Durand, M.; Molinier, V.; Kunz, W.; Aubry, J. M. Classification of Organic Solvents Revisited by Using the COSMO-RS APPROACH. *Chemistry - A European Journal*. 2011, pp 5155–5164. https://doi.org/10.1002/chem.201001743.

(283) Miro, P.; Ling, J.; Qiu, J.; Burns, P. C.; Gagliardi, L.; Cramer, C. J. Experimental and Computational Study of a New Wheel-Shaped {[W5O21]3[(UVIO2)2(M-O2)]3}30− Polyoxometalate. *Inorg. Chem.* **2012**, *2*, 8784–8790. https://doi.org/10.1021/ic3005536.

(284) Vilà-Nadal, L.; Mitchell, S. G.; Markov, S.; Busche, C.; Georgiev, V.; Asenov, A.; Cronin, L. Towards Polyoxometalate-Cluster-Based Nano-Electronics. *Chem. - A Eur. J.* **2013**, *19* (49), 16502–16511. https://doi.org/10.1002/chem.201301631.

(285) Cameron, J. M.; Fujimoto, S.; Kastner, K.; Wei, R. J.; Robinson, D.; Sans, V.; Newton, G. N.; Oshio, H. H. Orbital Engineering: Photoactivation of an Organofunctionalized Polyoxotungstate. *Chem. - A Eur. J.* **2017**, *23* (1), 47–50. https://doi.org/10.1002/chem.201605021.

(286) Miró, P.; Poblet, J. M.; Ávalos, J. B.; Bo, C. Towards a Computational Treatment of Polyoxometalates in Solution Using QM Methods and Explicit Solvent Molecules. *Can. J. Chem.* **2009**, *87* (10), 1296–1301. https://doi.org/10.1139/V09-059.

(287) Förster, A.; Visscher, L. Quasiparticle Self-Consistent GW-Bethe-Salpeter Equation Calculations for Large Chromophoric Systems. *J. Chem. Theory Comput.* **2022**, *18* (11), 6779–6793. https://doi.org/10.1021/acs.jctc.2c00531.

(288) Gui, X.; Holzer, C.; Klopper, W. Accuracy Assessment of GW Starting Points for Calculating Molecular Excitation Energies Using the Bethe-Salpeter Formalism. *J. Chem. Theory Comput.* **2018**, *14* (4), 2127–2136. https://doi.org/10.1021/acs.jctc.8b00014.

(289) Blase, X.; Duchemin, I.; Jacquemin, D.; Loos, P. F. The Bethe-Salpeter Equation Formalism: From Physics to Chemistry. *J. Phys. Chem. Lett.* **2020**, *11* (17), 7371–7382. https://doi.org/10.1021/acs.jpclett.0c01875.

(290) Förster, A.; Visscher, L. Low-Order Scaling Quasiparticle Self-Consistent GW for Molecules. *Front. Chem.* **2021**, *9* (September), 1–14. https://doi.org/10.3389/fchem.2021.736591.

(291) Kim, B.; Lee, S.; Kim, J. Inverse Design of Porous Materials Using Artificial Neural Networks. *Sci. Adv.* **2020**, *6* (1). https://doi.org/10.1126/sciadv.aax9324.

(292) Vilà-Nadal, L. POMzites: A Roadmap for Inverse Design in Metal Oxide Chemistry. *Int. J. Quantum Chem.* **2021**, *121* (5), 1–8. https://doi.org/10.1002/qua.26493.

(293) Boyd, T.; Mitchell, S. G.; Miras, H. N.; Long, D. L.; Cronin, L. Understanding and Mapping the Assembly of a Family of Trimeric Polyoxometalates: Transition Metal Mediated Wells-Dawson (M18)-Trimers. *Dalt. Trans.* **2010**, *39* (28), 6460–6465. https://doi.org/10.1039/c002633f.

(294) Sanchez-Lengeling, B.; Aspuru-Guzik, A. Inverse Molecular Design Using Machine Learning: Generative Models for Matter Engineering. *Science (80-.).* **2018**, *361* (6400), 360–365. https://doi.org/10.1126/science.aat2663.

(295) Molesky, S.; Lin, Z.; Piggott, A. Y.; Jin, W.; Vucković, J.; Rodriguez, A. W. Inverse Design in Nanophotonics. *Nat. Photonics* **2018**, *12* (11), 659–670. https://doi.org/10.1038/s41566-018-0246-9.

(296) Schlexer Lamoureux, P.; Winther, K. T.; Garrido Torres, J. A.; Streibel, V.; Zhao, M.; Bajdich, M.; Abild-Pedersen, F.; Bligaard, T. Machine Learning for Computational Heterogeneous Catalysis. *ChemCatChem* **2019**, *11* (16), 3581–3601. https://doi.org/10.1002/cctc.201900595.

(297) De La Oliva, A. R.; Sans, V.; Miras, H. N.; Yan, J.; Zang, H.; Richmond, C. J.; Long, D. L.; Cronin, L. Assembly of a Gigantic Polyoxometalate Cluster {W200Co 8O660} in a Networked Reactor System. *Angew. Chemie - Int. Ed.* **2012**, *51* (51), 12759–12762. https://doi.org/10.1002/anie.201206572.

(298) Wang, M.; Hu, X.; Beratan, D. N.; Yang, W. Designing Molecules by Optimizing Potentials. *J. Am. Chem. Soc.* **2006**, *128* (10), 3228–3232. https://doi.org/10.1021/ja0572046.

(299) Petrus, E.; Segado, M.; Bo, C. Nucleation Mechanisms and Speciation of Metal Oxide Clusters. *Chem. Sci.* **2020**, *11* (32), 8448–8456. https://doi.org/10.1039/d0sc03530k.

(300) Claussen, N.; Bernevig, B. A.; Regnault, N. Detection of Topological Materials with Machine Learning. *Phys. Rev. B* **2020**, *101* (24), 1–15. https://doi.org/10.1103/PhysRevB.101.245117.

(301) *AMS 2023.1, SCM, Theoretical Chemistry, Vrije Universiteit, Amsterdam, The Netherlands. http://www.scm.com*.

(302) Perdew, J. P. Density-Functional Approximation for the Correlation Energy of the Inhomogeneous Electron Gas. *Phys. Rev. B* **1986**, *33* (12), 8822–8824. https://doi.org/10.1103/PhysRevB.33.8822.

(303) Ernzerhof, M.; Scuseria, G. E. Assessment of the Perdew–Burke–Ernzerhof Exchange-Correlation Functional. *J. Chem. Phys.* **1999**, *110* (11), 5029–5036. https://doi.org/10.1063/1.478401.

(304) Grimme, S. Semiempirical GGA-type Density Functional Constructed with a Long-range Dispersion Correction. *J Comput Chem* **2006**, *27* (15), 1787–1799. https://doi.org/10.1002/jcc.20495.

(305) Zhao, Y.; Truhlar, D. G. A New Local Density Functional for Main-Group Thermochemistry, Transition Metal Bonding, Thermochemical Kinetics, and Noncovalent Interactions. *J. Chem. Phys.* **2006**, *125*

(19). https://doi.org/10.1063/1.2370993.

(306) Møller, C.; Plesset, M. S. Note on an Approximation Treatment for Many-Electron Systems. *Phys. Rev.* **1934**, *46* (7), 618–622. https://doi.org/10.1103/PhysRev.46.618.

(307) Pople, J. A.; Binkley, J. S.; Seeger, R. Theoretical Models Incorporating Electron Correlation. *Int. J. Quantum Chem.* **1976**, *10*, 1–19. https://doi.org/10.1002/qua.560100802.

(308) van Lenthe, E.; Ehlers, A.; Baerends, E. J. Geometry Optimization in the Zero Order Regular Approximation for Relativistic Effects. *J. Chem. Phys.* **1999**, *110* (18), 8943–8953. https://doi.org/10.1063/1.478813.

(309) Sure, R.; Brandenburg, J.; Gimme, S. Small Atomic Orbital Basis Set First-Principles Quantum Chemical Methods for Large Molecular and Periodic Systems: A Critical Analysis of Error Sources. *ChemistryOpen* **2016**, *5* (2), 94–109. https://doi.org/10.1002/open.201500192.

(310) Van Lenthe, E.; Baerends, E. J. Optimized Slater-Type Basis Sets for the Elements 1-118. *J. Comput. Chem.* **2003**, *24* (9), 1142–1156. https://doi.org/10.1002/jcc.10255.

(311) Swart, M.; Ehlers, A. W.; Lammertsma, K. Performance of the OPBE Exchange-Correlation Functional. *Mol. Phys.* **2004**, *102* (23–24), 2467–2474. https://doi.org/10.1080/00268970420002750 17.

(312) Bryce, D. L.; Autschbach, J. Relativistic Hybrid Density Functional Calculations of Indirect Nuclear Spin-Spin Coupling Tensors - Comparison with Experiment for Diatomic Alkali Metal Halides. *Can. J. Chem.* **2009**, *87* (7), 927–941. https://doi.org/10.1139/V09-040.

Chapter 3: Experimental Details

In this chapter we will detail the synthetic recipes used over the course of this investigation, dividing the sections into POM synthesis carried out in chapters 4-6, two separate sections containing work conducted as part of the Device-X and Ugi projects respectively, and a final section with the spectroscopy details for the techniques and equipment used for analysis.

3.1 Main POM Synthesis

$K_6[P_2W_{18}O_{62}]$: The classical Wells-Dawson POM was synthesized following the method reported by Mbomekalle I. *et al.*[44] 300g $Na_2WO_4 \cdot 2H_2O$ was dissolved in 350ml H_2O, followed by addition of 250ml of 4M HCl under intense stirring. Once the solution became transparent, 250ml 4M H_3PO_4 was transferred to the mixture dropwise. The reaction was then left for 24 hours under reflux. A strong yellow colour was observed after the time had elapsed. After cooling to room temperature, 150g KCl was dissolved in the solution. Next, the mixture was divided into 3 250ml beakers and left to crystallize for 48 hours. Crystals were collected and the remaining liquid filtered twice to obtain further α-$K_6[P_2W_{18}O_{62}] \cdot 14H_2O$ product (70.099g; 28.64%). NMR: -13.02ppm. UV-Vis: 250nm, 310nm

$K_{12}[H_2P_2W_{12}O_{48}]$: The hexalacunary POM was formed using the synthetic procedure of Contant R.[80] 4.148g of $K_6[P_2W_{18}O_{62}] \cdot 14H_2O$ was dissolved in 15ml H_2O, to which 2.42g tris(hydroxymethyl)aminomethane, dissolved in 10ml H_2O, was added. After leaving under stirring for 30 minutes, 3.994 KCl and 2.77 K_2CO_3, dissolved in 12ml H_2O, were mixed with the solution. Following this, the mixture was left for 1 hour under vigorous stirring. The previously milky white solution had separated into a solid white precipitate and a pale solution. The solution was filtered 3 times under suction and the precipitate dried for 3 days. White α-$K_{12}[H_2P_2W_{12}O_{48}] \cdot 24H_2O$ crystals were obtained (2.169g, 64.32%). NMR: -10.12ppm.

3.2 Ugi Reaction Synthetic Procedures

Preparation of $C_{32}H_{35}N_3O_4$ (P3): A 100ml three-neck round-bottom flask was clamped in place above a magnetic stirrer hot plate. To the flask was added a magnetic stirrer bar and methanol (40ml). Following this, a reflux condenser was inserted into the middle neck and the remaining two were stoppered. From this point on, reagents were introduced to the mixture via one of the stoppered necks; after addition of the reagent(s), the neck was re-stoppered. Next, benzaldehyde (40.4µl) and aniline (36µl) were added to the reaction mixture, after which the solution was left for one hour under stirring. Following this, 7-(diethylamino) coumarin-3-carboxylic acid (100mg) and *tert*-butyl isocyanide (41µl) were introduced to the solution. Finally, the reaction was left for 72 hours under stirring and the methanol solvent removed via rotary evaporator to yield **Product 3** (**P3**).

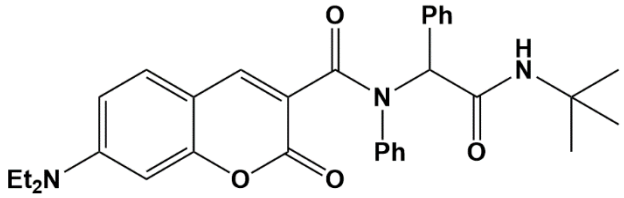

Product 3

$C_{32}H_{35}N_3O_4$ – 525.64g mol^{-1}

Preparation of $C_{34}H_{35}N_3O_4$ (P6): A 100ml three-neck round-bottom flask was clamped in place above a magnetic stirrer hot plate. To the flask was added a magnetic stirrer bar and methanol (40ml). Following this, a reflux condenser was inserted into the middle neck and the remaining two were stoppered. From this point on, reagents were introduced to the mixture via one of the stoppered necks; after addition of the reagent(s), the neck was re-stoppered. Next, benzaldehyde (75µl) and aniline (65µl) were added to the reaction mixture, after which the solution was left for one hour under stirring. Following this, COUMARIN 343 (200mg) and *tert*-butyl isocyanide (80µl) were introduced to the solution. Finally, the reaction was left for 72 hours under stirring and the methanol solvent removed via rotary evaporator to yield **Product 6** (**P6**).

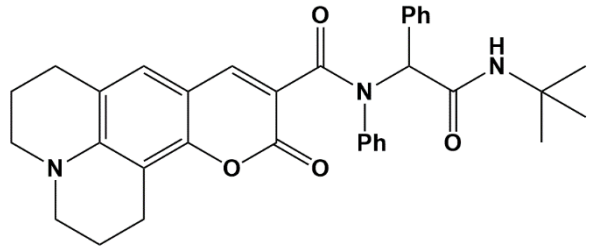

Product 6

$C_{34}H_{35}N_3O_4$ – 549.66g mol^{-1}

Preparation of $C_{36}H_{37}N_3O_4$ (P9): A 100ml three-neck round-bottom flask was clamped in place above a magnetic stirrer hot plate. To the flask was added a magnetic stirrer bar and methanol (40ml). Following this, a reflux condenser was inserted into the middle neck and the remaining two were stoppered. From this point on, reagents were introduced to the mixture via one of the stoppered necks; after addition of the reagent(s), the neck was re-stoppered. Next, cinnamaldehyde (90µl) and aniline (65µl) were added to the reaction mixture, after which the solution was left for one hour under stirring. Following this, COUMARIN 343 (200mg) and *tert*-butyl isocyanide (80µl) were introduced to the solution. Finally, the reaction was left for 72 hours under stirring and the methanol solvent removed via rotary evaporator to yield **Product 9** (**P9**).

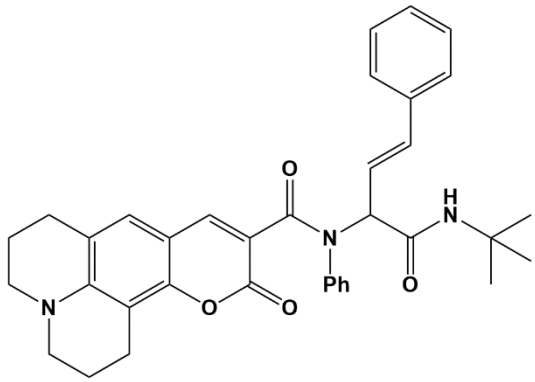

Product 9

$C_{36}H_{37}N_3O_4$ – 575.70g mol^{-1}

Preparation of $C_{28}H_{26}N_2O_4$ (P15): A 100ml three-neck round-bottom flask was clamped in place above a magnetic stirrer hot plate. To the flask was added a magnetic stirrer bar and methanol (40ml). Following this, a reflux condenser was inserted into the middle neck and the remaining two were stoppered. From this point on, reagents were introduced to the mixture via one of the stoppered necks; after addition of the reagent(s), the neck was re-stoppered. Next, benzaldehyde (120µl) and aniline (100µl) were added to the reaction mixture, after which the solution was left for one hour under stirring. Following this, coumarin-3-carboxylic acid (190mg) and *tert*-butyl isocyanide (120µl) were introduced to the solution. Finally, the reaction was left for 72 hours under stirring and the methanol solvent removed via rotary evaporator to yield **Product 15** (**P15**).

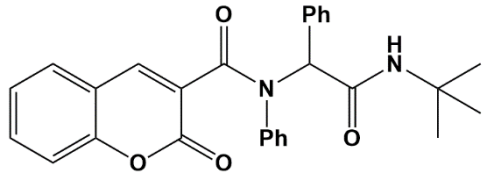

Product 15

$C_{28}H_{26}N_2O_4$ – 454.52g mol^{-1}

Preparation of $C_{30}H_{27}N_2O_4$ (P18): A 100ml three-neck round-bottom flask was clamped in place above a magnetic stirrer hot plate. To the flask was added a magnetic stirrer bar and methanol (40ml). Following this, a reflux condenser was inserted into the middle neck and the remaining two were stoppered. From this point on, reagents were introduced to the mixture via one of the stoppered necks; after addition of the reagent(s), the neck was re-stoppered. Next, cinnamaldehyde (120µl) and aniline (91.5µl) were added to the reaction mixture, after which the solution was left for one hour under stirring. Following this, coumarin-3-carboxylic acid (190mg) and *tert*-butyl isocyanide (104.5µl) were introduced to the solution. Finally, the reaction was left for 72 hours under stirring and the methanol solvent removed via rotary evaporator to yield Product 18 (**P18**).

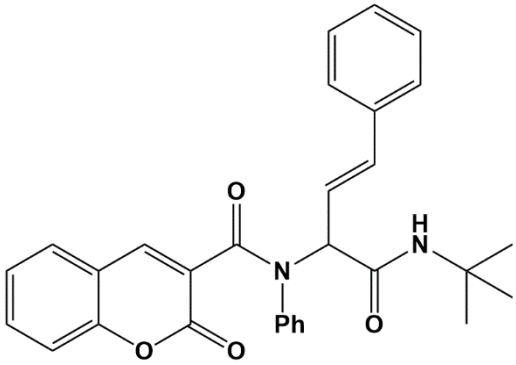

Product 18

$C_{30}H_{28}N_2O_4$ – 480.55g mol^{-1}

Preparation of $C_{28}H_{26}N_2O_6$ (P19): A 100ml three-neck round-bottom flask was clamped in place above a magnetic stirrer hot plate. To the flask was added a magnetic stirrer bar and methanol (40ml). Following this, a reflux condenser was inserted into the middle neck and the remaining two were stoppered. From this point on, reagents were introduced to the mixture via one of the stoppered necks; after addition of the reagent(s), the neck was re-stoppered. Next, benzaldehyde (115µl) and aniline (105µl) were added to the reaction mixture, after which the solution was left for one hour under stirring. Following this, 6,7-dihydroxycoumarin-3-carboxylic acid (250mg) and *tert*-butyl isocyanide (130µl) were introduced to the solution. Finally, the reaction was left for 72 hours under stirring and the methanol solvent removed via rotary evaporator to yield **Product 19** (**P19**).

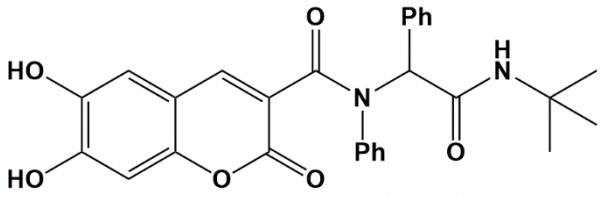

Product 19

$C_{28}H_{26}N_2O_6$ – 486.51g mol^{-1}

Preparation of $C_{30}H_{28}N_2O_6$ (P20): A 100ml three-neck round-bottom flask was clamped in place above a magnetic stirrer hot plate. To the flask was added a magnetic stirrer bar and methanol (40ml). Following this, a reflux condenser was inserted into the middle neck and the remaining two were stoppered. From this point on, reagents were introduced to the mixture via one of the stoppered necks; after addition of the reagent(s), the neck was re-stoppered. Next, cinnamaldehyde (145µl) and aniline (105µl) were added to the reaction mixture, after which the solution was left for one hour under stirring. Following this, 6,7-dihydroxycoumarin-3-carboxylic acid (250mg) and *tert*-butyl isocyanide (130µl) were introduced to the solution. Finally, the reaction was left for 72 hours under stirring and the methanol solvent removed via rotary evaporator to yield **Product 20** (**P20**).

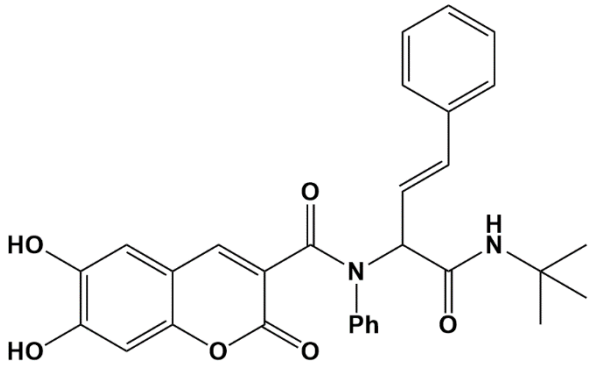

Product 20

$C_{30}H_{28}N_2O_6$ – 512.55g mol^{-1}

Preparation of $C_{36}H_{31}N_5O_7$ (P21-a): A 100ml three-neck round-bottom flask was clamped in place above a magnetic stirrer hot plate. To the flask was added a magnetic stirrer bar and methanol (40ml). Following this, a reflux condenser was inserted into the middle neck and the remaining two were stoppered. From this point on, reagents were introduced to the mixture via one of the stoppered necks; after addition of the reagent(s), the neck was re-stoppered. Next, benzaldehyde (120µl) and Disperse Blue 1 (300mg) were added to the reaction mixture, after which the solution was left for one hour under stirring. Following this, 6,7-dihydroxycoumarin-3-carboxylic acid (190mg) and *tert*-butyl isocyanide (120µl) were introduced to the solution.

Finally, the reaction was left for 72 hours under stirring and the methanol solvent removed via rotary evaporator to yield **Product 21** (**P21**).

Preparation of $C_{36}H_{31}N_5O_7$ (P21-b): A variant of the previous **P21-a** synthesis where only 20mg Disperse Blue 1 was added to the reaction mixture to allow small changes in colour to be more observable. Disperse Blue in **P21-a** completely saturated the mixture with blue colour.

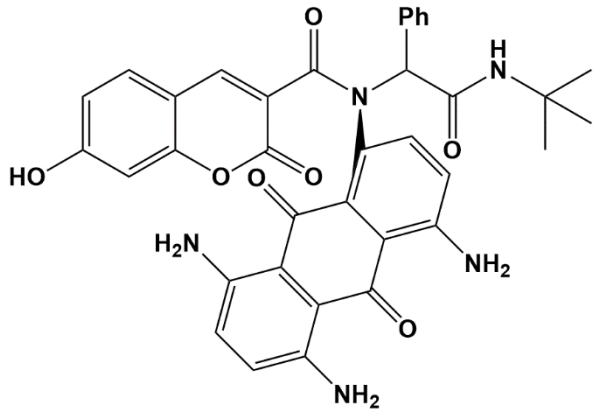

Product 21

$C_{36}H_{30}N_5O_7$ – 644.65g mol^{-1}

Competition between COUMARIN 343 and Coumarin-3-carboxylic acid: A 100ml three-neck round-bottom flask was clamped in place above a magnetic stirrer hot plate. To the flask was added a magnetic stirrer bar and methanol (40ml). Following this, a reflux condenser was inserted into the middle neck and the remaining two were stoppered. From this point on, reagents were introduced to the mixture via one of the stoppered necks; after addition of the reagent(s), the neck was re-stoppered. Next, benzaldehyde (40.4µl) and aniline (36 µl) were added to the reaction mixture, after which the solution was left for one hour under stirring. Following this, COUMARIN 343 (100mg), Coumarin-3-carboxylic acid (100mg) and *tert*-butyl isocyanide (41µl) were introduced to the solution. Finally, the reaction was left for 72 hours under stirring and the methanol solvent removed via rotary evaporator to yield a mixture of **Products 6** and **15** (**P6, P15**).

Quenching of Isocyanide: Needles and gloves that came into contact with any of the isocyanide reagents were quenched using a 10:1 MeOH:HCl solution in a plastic bucket at the rear of the fume hood.

3.3 Spectroscopy Details

NMR: ^{31}P NMR was collected using a Bruker DPX 400 spectrometer, with 85% phosphoric acid as the external standard. 50mg of POM sample were dissolved in D_2O to make up NMR samples.

IR: For FT-IR, a Nicolet 170SX-FT/IR spectrometer was utilised between the ranges of 400-2600cm^{-1}.

UV-Vis: UV-Vis data was obtained using 30µM solutions of our POM in distilled water and a Shimadzu 1800 spectrophotometer matched quartz cell, scanning within the range of 200-400nm.

3.4 References

(44) Mbomekalle, I. M.; Lu, Y. W.; Keita, B.; Nadjo, L. Simple, High Yield and Reagent-Saving Synthesis of Pure α-K 6P2W18O62 · 14H2O. *Inorg. Chem. Commun.* **2004**, *7* (1), 86–90. https://doi.org/10.1016/j.inoche.2003.10.011.

(80) Contant, R. *Inorganic Syntheses*, 1st ed.; Ginsberg, A. P., Ed.; Wiley-Interscience: New York, 1990. https://doi.org/10.1002/9780470132586.

Chapter 4: Hypothesis and Objectives

POM chemistry is very promising with regards to providing solutions to numerous pertinent problems facing the scientific community today, such as effective storage of renewably sourced energy and improving storage capacity of molecular memory devices. Computational chemistry has a big part to play in the design of novel POMs with relevant applications, preventing valuable lab time and money being wasted in the creation of new POM species which are of less use to the scientific community. Proper deployment of computational methods, such as use of DFT, necessitates a rigorous, well-defined set of standards at which to carry out research.

Over the course of this thesis, we aim to elaborate on and set what we believe to be an accurate, yet computationally practical, standard of theoretical modelling at which to operate when working with POMs, as well as present data for large POM species, primarily $[P_8W_{48}O_{184}]^{40-}$. Despite their ability to act as secondary building blocks in the assembly of larger POMzite networks, these POMs have yet to be modelled computationally due to their size. We believe that with current capabilities we can set a good standard for modelling **{P_8W_{48}}** POM wheels moving forward, especially in the context of creating small POMzite sub-sections in the future.

By additionally investigating the viability of modelling the smaller hexalacunary POM, $[P_2W_{12}O_{48}]^{14-}$, which acts as a SBB unit for the larger **{P_8W_{48}}** wheel, we can investigate the effect of alternating elements of the structure, such as different framework metal or heteroatom elements, at a fraction of the computational cost. We believe this to be the optimal POM species we can currently work at with the computational power at our disposal and several key modelling questions, such as the effects of including relevant countercations and protons on the calculation results, can be easily answered.

Finally, we seek to further investigate what we believe to be previous inaccuracies in the reporting of frontier orbital properties for POMs within the literature and establish a more

accurate, yet practical, level of theory with which to obtain this data computationally that is more empirically valid. The nature and magnitude of the HOMO-LUMO gap is a frequently referenced and studied parameter within the literature but, if not modelled correctly, can lead to great confusion and discord between the results of researchers.

Chapter 5: Computational Study into the Effects of Countercations on the $[P_8W_{48}O_{184}]^{40-}$ Polyoxometalate Wheel

This chapter is based on the following publication: Malcolm, D., and Vilà-Nadal, L. "**Computational Study into the Effects of Countercations on the $[P_8W_{48}O_{184}]^{40-}$ Polyoxometalate Wheel**", *ACS Org. Inorg. Au*, 2023, *3*, (5), 274-282.

Over the course of this chapter, we aim to , using the available empirical data, report an accurate, DFT-based computational model for the **$\{P_8W_{48}\}$** POM and similar W_{48}-type POMs. Due to the significant number of countercations present in the empirical molecule, we will take great care determining how many of these cations have to be present in the computational structure to yield an accurate model.

5.1 Introduction

As previously discussed in **Chapter 2.**, the wheel-shaped POM **$\{P_8W_{48}\}$** is an excellent Secondary Building Block (SBB) unit with which to construct larger, porous networks referred to as POMzites. These POMzites have the potential to act as a customisable, robust material, combining the benefits of zeolites and MOFs whilst exhibiting the associated downsides of using either. Additionally, POMzites have been shown to display reversible, metamorphic behaviour, altering their structure and adsorption capabilities based on specific environmental triggers; this has the potential to allow for multifunctional porous networks which reliably change between states when influenced to do so.[138]

Despite this, widespread deployment is hindered by a poor understanding of fundamental POMzite chemistry. Compared with zeolites, the elements that compose POMzites are rarer,[139]

which, combined with the lack of a comprehensive understanding of their self-assembly processes, acts to drive up the costs associated with researching these materials. Tackling this problem in a brute force manner in the lab promises to therefore be a costly endeavor,[297] with no guarantee of yielding an optimal POMzite capable of recuperating financial losses. Consequently, an alternate method is required that reduces the fiscal burden by either limiting synthetic costs[313] or by employing a computational approach which reduces lab time.

Inverse design[291, 314] is such a method, whereby the synthetic route for a theoretical model of the product molecule or material, one that is expected to fulfil a specific role, is devised by working backwards along the synthesis until the reagents and reaction conditions necessary to yield the desired product are elucidated. It also allows for easy experimentation with novel ideas, testing the waters to determine if an approach is feasible before expensive lab work is undertaken.[82, 293] This approach, however, requires a greater understanding of the self-assembly process in order to accurately simulate both real and hypothetical structures.[315] If we are to properly apply the tenets of inverse design, we must have the capabilities to build and analyse complex computational models of POMs and have a deep knowledge of their self-assembly processes.[299]

Ideally, one could build a subsection of a POMzite, containing at least 2 POM units connected by transition metal linkers, and run DFT calculations to examine how altering specific parameters, such as the element present in the linker and the binding configurations between linker and POM, affect the electronic and absorption properties of the network as a whole. The complexity of such a model at the DFT level, however, requires computational power far beyond our current capabilities.

This complexity arises from sheer size of the POMzite subsection; for the POMzites we are interested in modelling, which use $[P_8W_{48}O_{184}]^{40-}$ as the POM building-block for the network, the number of electrons present in the smallest possible subsection, where only 2 POMs without countercations are present, almost exceeds 10,000. Additionally, in some preliminary work we

conducted, we found the presence of the transition metal linker units in particular significantly increased the likelihood of the calculation failing to converge.

Being able to simplify our models of POMzite sub-sections and reduce this complexity is therefore critical if we are to examine these materials at the DFT level. We therefore chose to model the $[P_8W_{48}O_{184}]^{40-}$ POM in isolation and observe the effect of including potassium cations on the dimensions of the cage. If we can reduce the number of cations present in the POM model, and therefore in the larger POMzite subsection, this would be a solid first step in approaching the dream of examining computational POMzite models at the DFT level.

Even if the main issue to modelling POMzite networks is a lack of computational processing power that doesn't currently exist, by establishing modelling tenets at our current level of calculation we can hit the ground running when that technology becomes accessible to researchers. Additionally, potentially reducing the size of the system in terms of atoms and electrons is an avenue worth exploring as it brings the day we can conduct DFT level calculations of POMzites that little bit closer.

Herein we present our **{X_8W_{48}}** wheel, **{X_2W_{18}}** WD and **{X_2W_{12}}** hexalacunary calculation-based data, complete with HOMO-LUMO gap energy values, molecular electrostatic potential maps (MEPs), and standard deviation (STD) calculations. This is intended to deepen our fundamental understanding of these molecules so as to simulate them and currently theoretical, but chemically promising, derivatives more accurately.

5.2 Results and Discussion

Initially, we tested the accuracy and time effectiveness of the computational methods available in SCM-ADF.[41] We chose our functionals and basis sets from a broad range, some of which had been previously used in other computational POM studies. The most used functional in the literature was PBE,[299,283,316,317] as established by Swart and co-workers in their 2021 review;[257] in terms of basis sets, the literature indicated that def2-TZVP, to be the best choice, although TZP acts as a substitute due to def2-TZVP not being included in the ADF package.[78,318,319] We also compared the effects of using either small, large, or no frozen cores and of single point vs optimization tasks.

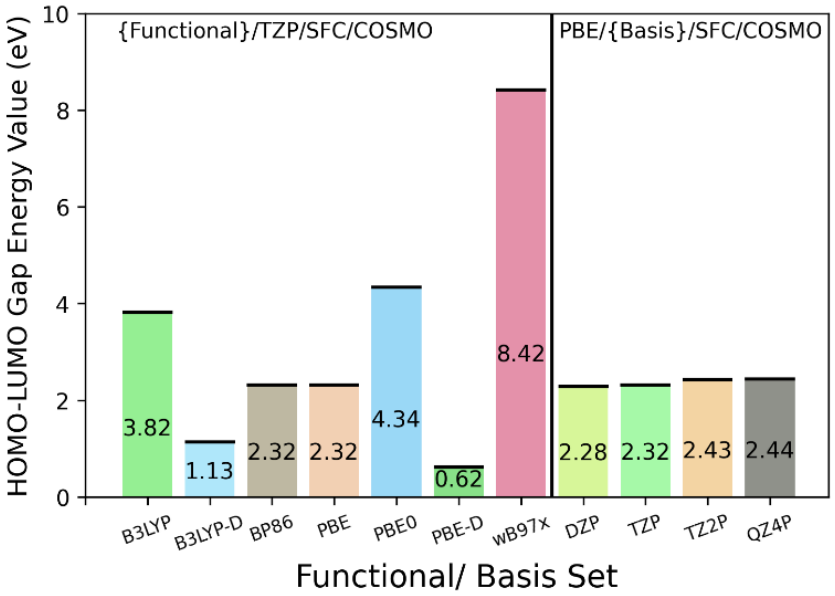

Figure 5.1. HOMO-LUMO gap energy values for a range of functionals and basis sets. The data presented here is for **{P_2W_{18}}**. Functional calculations were run with a TZP basis set, small frozen cores, and the COSMO model with water as a solvent; these conditions were maintained for the basis set calculations, the only difference being PBE as the functional.

To this end, we utilized GGA (PBE, BP86[299]), GGA-D (PBE-D), hybrid (B3LYP,[299] B3LYP-D, PBE0[299,320]), and range separated functional(s) (wB97x), and a few basis sets (TZP,[317,320] TZ2P,[320] QZ4P[320]) to obtain a broad distribution of results and to aid in selecting the appropriate level of theory for our purposes (**Fig. 5.1 and Table A-1.1**). We used the Wells-

Dawson species $[P_2W_{18}O_{62}]^{6-}$ for our benchmarks as it is one of the most widely documented POM species and will thus have plenty of literature to compare our results against.

The functionals which most closely corresponded to the empirical data out of the range tested were PBE and BP86; going forward we chose to use a GGA (PBE) functional and TZP basis set, paired with a small frozen core and a COSMO solvation model[286] as part of an optimization task. (**see Appendix-1.1 for full results of benchmarking, as well as Appendix-1.2 for details on the structural configuration of $[Se_2W_{12}O_{46}]^{12-}$ used**). We found that GGA functionals were also the highest level of theory we could feasibly apply to POMs of the magnitude of **$\{P_8W_{48}\}$**; though we later found GGA functionals ineffective at correctly describing frontier orbital energy values (**see Chapter 7**), these results are still valid for what we set out to achieve, namely: correct structural representation and visualizing the HOMO and LUMO orbitals irrespective of their energy values. Our results from **Chapter 7** demonstrate that using GGA functionals doesn't significantly affect the quality of these results.

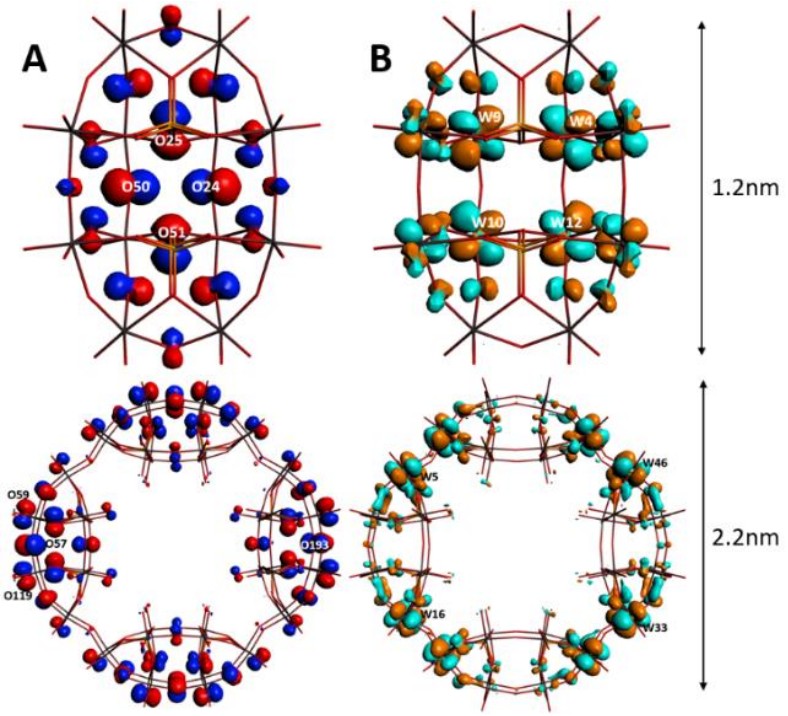

Figure 5.2. Visualisation of HOMO and LUMO orbitals for $[P_2W_{12}O_{48}]^{14-}$ (**A**) and $[P_8W_{48}O_{184}]^{40-}$ (**B**), with labelling of the 4 atoms that contribute most to their respective orbital band. **PBE/TZP/COSMO/Small Frozen Cores**

To complete our benchmarking, we also compared the accuracy of our results against work done by Cameron *et al.*,[78] Zhang *et al.*,[64] and Vilà-Nadal *et al.*[284,180] Our results were very close in value to those of Vilà-Nadal and Zhang, and were, despite a larger difference in values caused by different computational software, were in good agreement with the Cameron work as well. Our optimization calculations of **{P_8W_{48}}** and **{P_2W_{12}}** yielded the nature of the HOMO and LUMO orbitals, (**Fig. 5.2-5.4**), as well the energy gap between them,[285,321] and the molecular electrostatic potentials (MEPs) (**Fig. 5.5-5.6**). The HOMOs for both hexalacunary and W_{48} POMs receive their greatest collective atomic contribution from the framework oxygens, specifically the P_Y orbitals of oxygen atoms located in the belt region nearest to the templating anion. This is a typical distribution observed in POMs, as described in an RSC paper by Poblet *et al.*[231] In addition to **{P_8W_{48}}**, we also ran calculations on $[Se_8W_{48}O_{176}]^{32-}$ and $[As_8W_{48}O_{184}]^{40-}$, both of which have been previously reported in the literature (**see Appendix-1.3 for the electronic values for all POMs featured in this work**).[78,76,322]

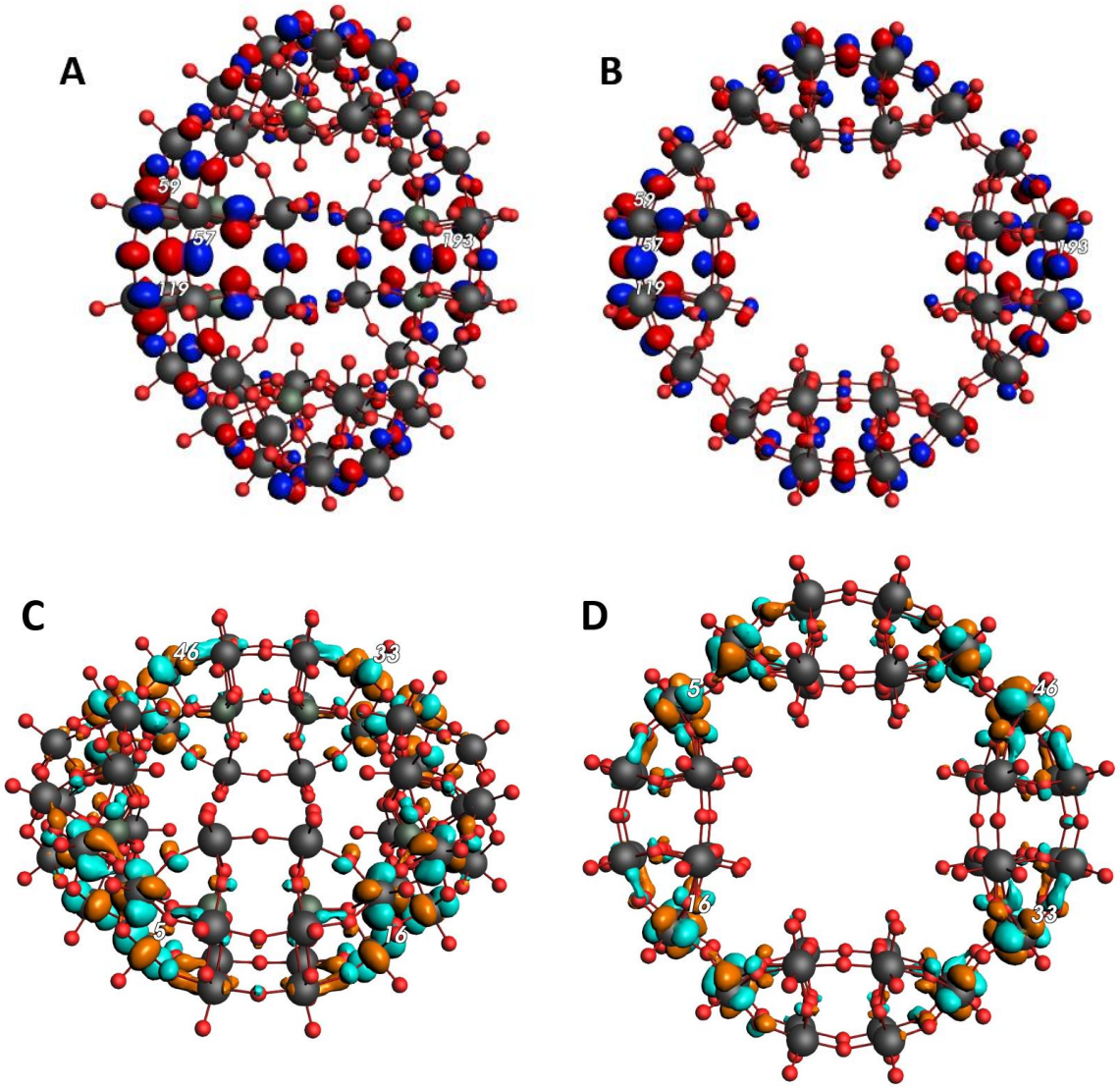

Figure 5.3. HOMO (**A**), (**B**) and LUMO (**C**), (**D**) visualisations for $[As_8W_{48}O_{184}]^{40-}$. The 4 atoms which contribute most to the HOMO or LUMO molecular orbitals respectively are highlighted. **PBE/TZP/COSMO/Small Frozen Cores**

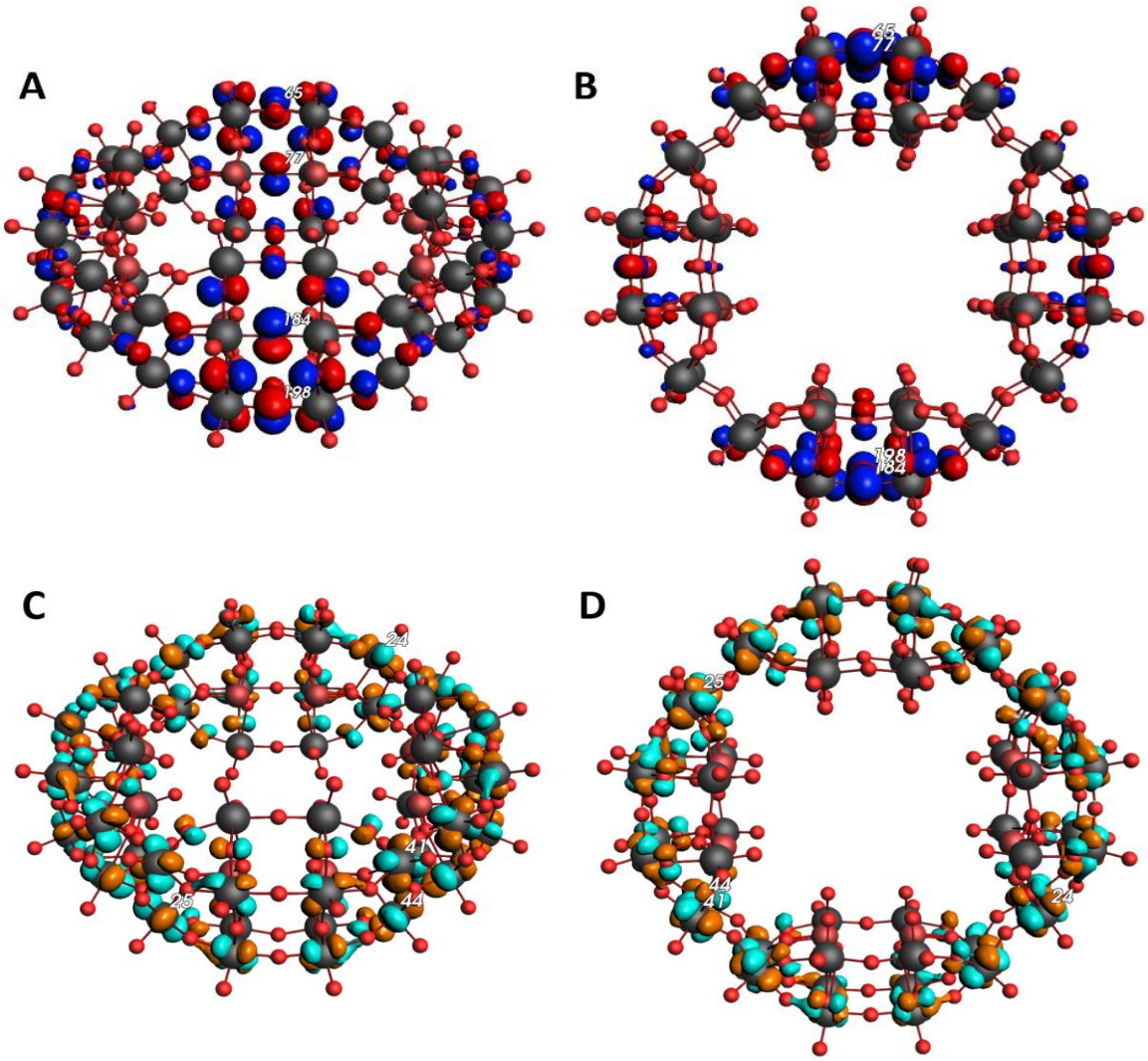

Figure 5.4. HOMO (**A**), (**B**) and LUMO (**C**), (**D**) visualisations for $[Se_8W_{48}O_{176}]^{32-}$. The 4 atoms which contribute most to the HOMO or LUMO molecular orbitals respectively are highlighted. **PBE/TZP/COSMO/Small Frozen Cores**

In contrast, the position of the LUMO orbitals differs between the **$\{P_2W_{12}\}$** and **$\{P_8W_{48}\}$** structures; in the lacunary (**Fig. 5.2B**) they are localized on the tungsten atoms, the D_{YZ} orbital specifically, connected to the main HOMO oxygens, forming a complete square at the back of the lacunary. With the full **$\{P_8W_{48}\}$** wheel however, the LUMO shift onto the tungsten atoms which link each lacunary quarter of the wheel together (**Fig. 5.3C, 5.3D**). The fact that successive reductions will increase electron density in these areas is key to understanding the effect addition of electrons will have to localized POM reactivity. The threshold at which this disintegration will occur is currently unknown but appears to be high, allowing for at least 18 or 27 successive reductions of **$\{P_2W_{18}\}$** or **$\{P_8W_{48}\}$** respectively.[323]

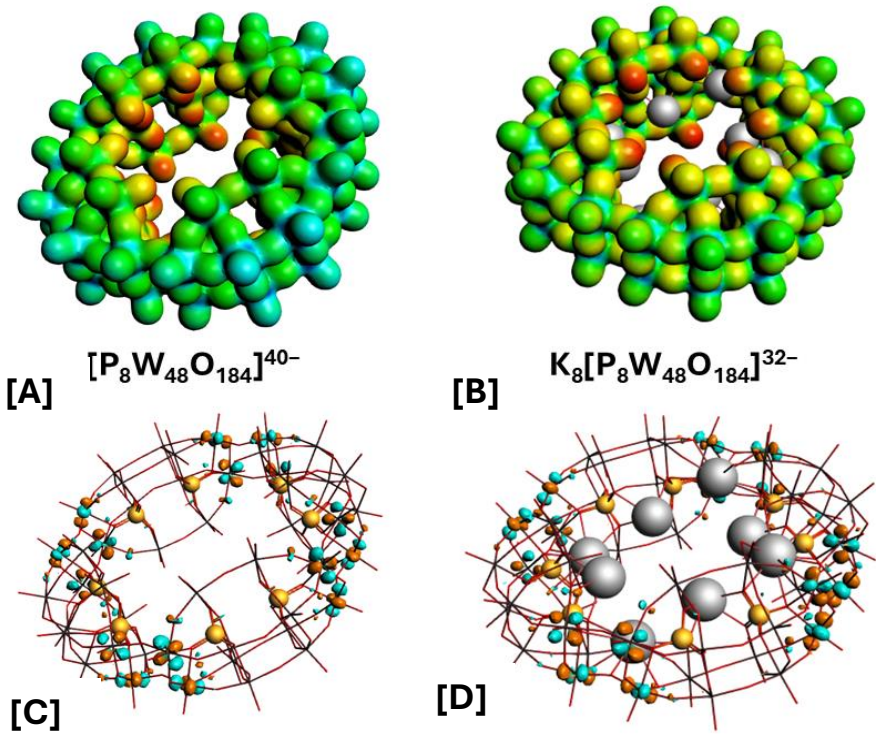

Figure 5.5. MEPs for $[P_8W_{48}O_{184}]^{40-}$ (**A**), $K_8[P_8W_{48}O_{184}]^{32-}$ **(B),** and LUMO visualisations for $[P_8W_{48}O_{184}]^{40-}$ (**C**), $K_8[P_8W_{48}O_{184}]^{32-}$ (**D**). Geometries were optimized and MEP generated with **PBE/TZP/COSMO/Small Frozen Cores**. More nucleophilic (negative) regions are visualised in red, and more electrophilic (positive) in blue. The colour ranges for the MEPs are: -2.40 to -1.50 (**A**), and -1.90 to -1.20 (**B**).

The MEPs revealed that the interior of the ring is more nucleophilic than the exterior, which explains why this POM is exceptionally good at trapping cations within its central pore (**Fig 5.5A and 5.6A**). This polarization of electrons is likely due to the heteroatom, which is in closest proximity to terminal oxygen atoms along the interior face.

Countercations, such as those present in $K_8[P_8W_{48}O_{184}]^{32-}$, are introduced during synthesis to stabilize the highly anionic charge of the framework; they achieve this by situating themselves near the highly nucleophilic oxygen atoms, thereby reducing the high degree of polarization and increasing the overall electrophilicity of the POM. This is clearly visible in **Fig. 5.5B** and **5.6B**, where the 'red hot' nucleophilic region in the centre diffuses over more of the POM, visible as an orange section. A small reduction in nucleophilicity is visible for **$\{Se_8W_{48}\}$** around the 'hinge' areas where the lacunary POMs link up compared to **$\{P_8W_{48}\}$**; this is due to the

{Se_8W_{48}} lacking 2 oxygens per hinge region in these areas. With **K_8{P_8W_{48}}**, the presence of the countercations in the high nucleophilicity in the interior face being reduced in intensity, closer to that of the surrounding areas.

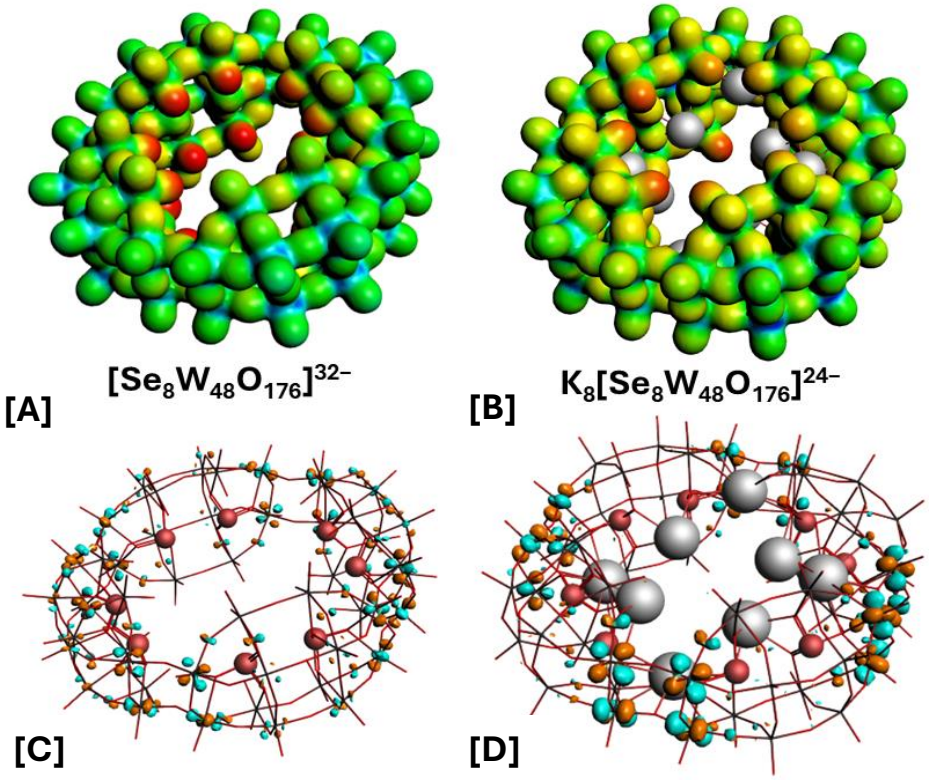

Figure 5.6. MEPs for $[Se_8W_{48}O_{176}]^{32-}$ (**A**), and $K_8[Se_8W_{48}O_{176}]^{24-}$ (**B**) and LUMO visualisations for $[Se_8W_{48}O_{176}]^{32-}$ (**C**), and $K_8[Se_8W_{48}O_{176}]^{24-}$ (**D**). Geometries were optimized and MEP generated with **PBE/TZP/COSMO/Small Frozen Cores**. More nucleophilic (negative) regions are visualised in red, and more electrophilic (positive) in blue. The colour ranges for the MEPs are: -1.80 to -1.20 (**A**), and -1.40 to -0.73 (**B**).

The MEPs we obtained were in good agreement with the literature, where cations or cationic scaffolds assemble within the pore specifically; the works of Ulrich Kortz,[85,88] and Thomas Boyd,[82] springs to mind. Thus, we can prove that we can reproduce an accurate DFT-level model of **{P_8W_{48}}**. LUMO visualizations in **Fig. 5.5C** and **5.5D** are almost identical, indicating that inclusion of countercations has minimal effect on the positions and intensity of the LUMO orbitals. There is, however, an observable, if slight, difference in LUMO localization between **Fig. 5.5C** and **5.6C**, implying that the choice of heteroatom can help tune where in the POM reduction occurs.

Using these MEPs, we are able to observe electron distribution throughout the POM framework and identify the most and least reactive sites. See **Fig. 5.7-5.9** for the MEPs for the Wells-Dawson species, $[As_2W_{18}O_{62}]^{6-}$, $[P_2W_{18}O_{62}]^{6-}$, and $[Se_2W_{18}O_{60}]^{4-}$ respectively, **Fig. 5.10-5.12** for the MEPs for the hexalacunary species, $[As_2W_{12}O_{48}]^{14-}$, $[P_2W_{12}O_{48}]^{14-}$, and $[Se_2W_{12}O_{46}]^{12-}$ respectively, and **Fig. 5.13-5.15** for the MEPs for the W_{48} ring species, $[As_8W_{48}O_{184}]^{40-}$, $[P_8W_{48}O_{184}]^{40-}$, and $[Se_8W_{48}O_{176}]^{32-}$ respectively.

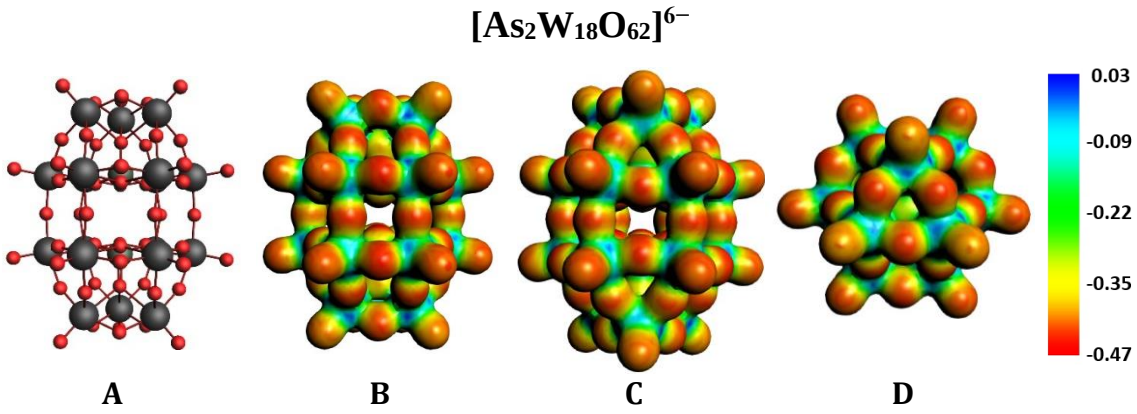

Figure 5.7. PBE MEPs for $[As_2W_{18}O_{62}]^{6-}$ representing (**A**) Side 1 with no MEP, (**B**) Side 1 with MEP, (**C**) Side 2 with MEP, and (**D**) Top with MEP. MEP sensitivity is 0.03. **PBE/TZP/COSMO/Small Frozen Cores**

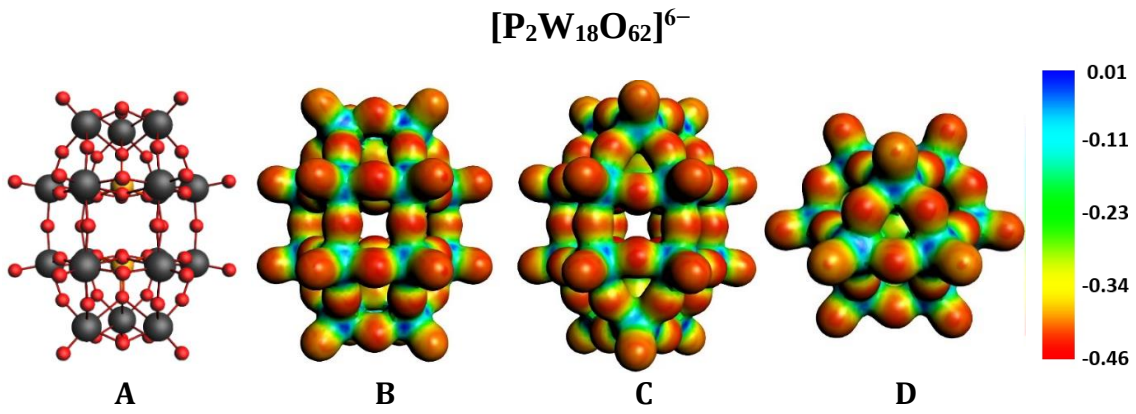

Figure 5.8. PBE MEPs for $[P_2W_{18}O_{62}]^{6-}$ representing (**A**) Side 1 with no MEP, (**B**) Side 1 with MEP, (**C**) Side 2 with MEP, and (**D**) Top with MEP. MEP sensitivity is 0.037. **PBE/TZP/COSMO/Small Frozen Cores**

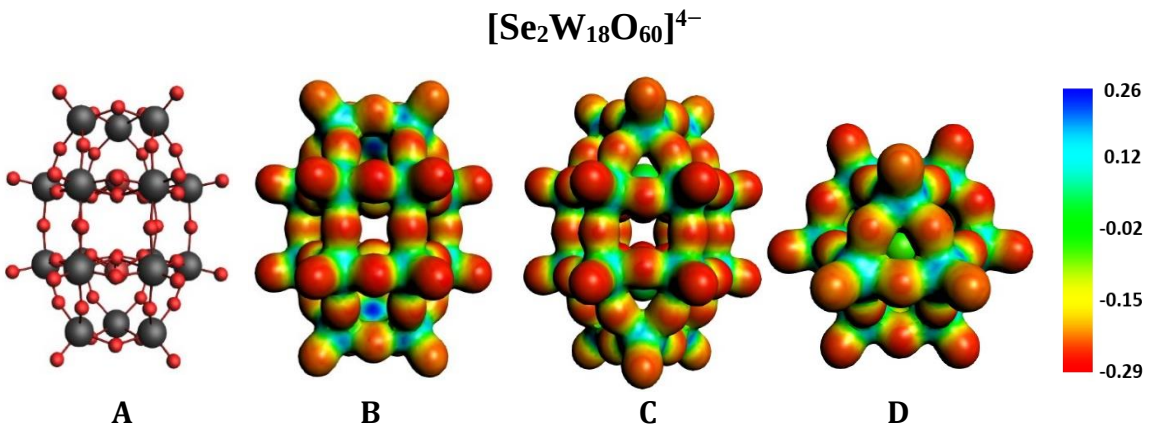

Figure 5.9. PBE MEPs for $[Se_2W_{18}O_{60}]^{4-}$ representing (**A**) Side 1 with no MEP, (**B**) Side 1 with MEP, (**C**) Side 2 with MEP, and (**D**) Top with MEP. MEP sensitivity is 0.037. **PBE/TZP/COSMO/Small Frozen Cores**

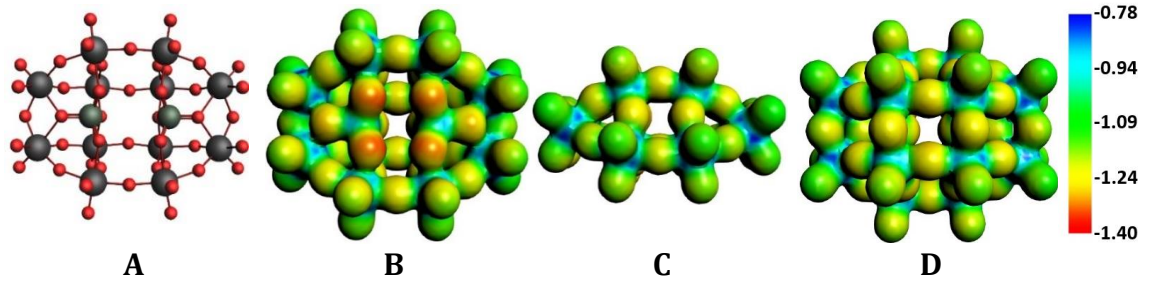

Figure 5.10. PBE MEPs for $[As_2W_{12}O_{48}]^{14-}$ representing (**A**) Front with no MEP, (**B**) Front with MEP, (**C**) Top with MEP, and (**D**) Back with MEP. MEP sensitivity is 0.03. **PBE/TZP/COSMO/Small Frozen Cores**

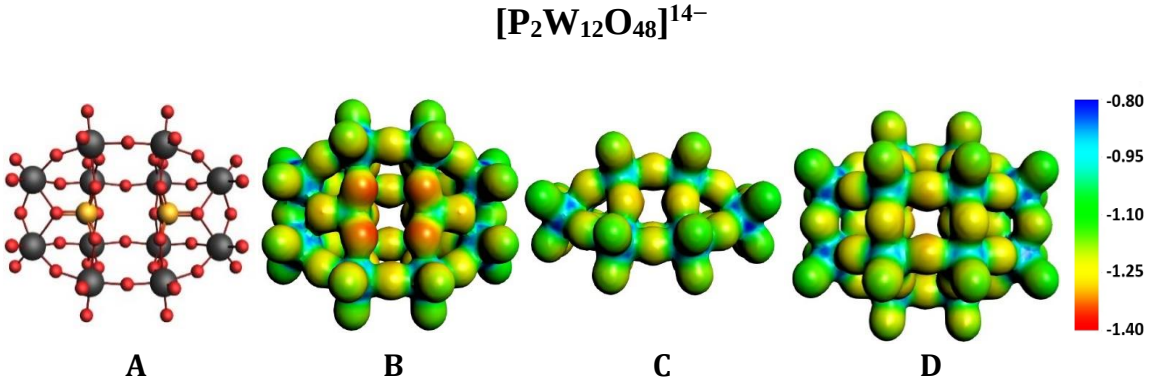

Figure 5.11. PBE MEPs for $[P_2W_{12}O_{48}]^{14-}$ representing (**A**) Front with no MEP, (**B**) Front with MEP, (**C**) Top with MEP, and (**D**) Back with MEP. MEP sensitivity is 0.03. **PBE/TZP/COSMO/Small Frozen Cores**

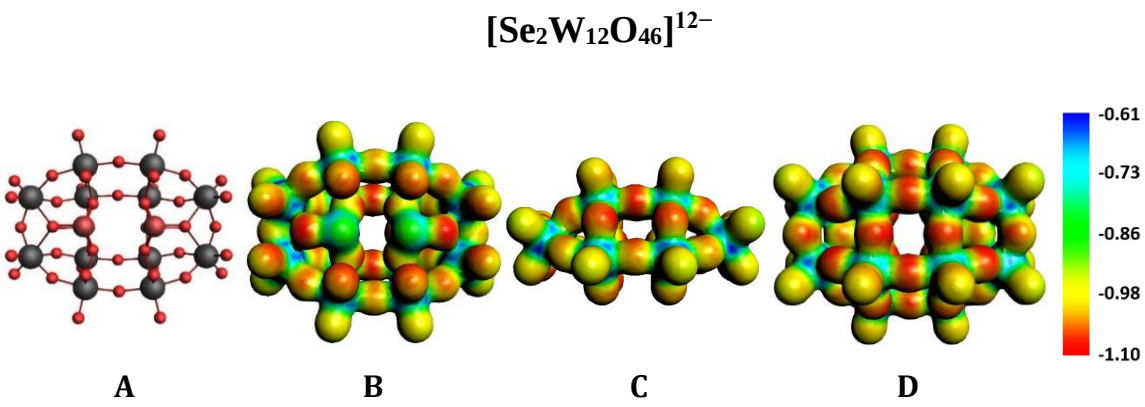

Figure 5.12. PBE MEPs for $[Se_2W_{12}O_{46}]^{12-}$ representing (**A**) Front with no MEP, (**B**) Front with MEP, (**C**) Top with MEP, and (**D**) Back with MEP. MEP sensitivity is 0.03. **PBE/TZP/COSMO/Small Frozen Cores**

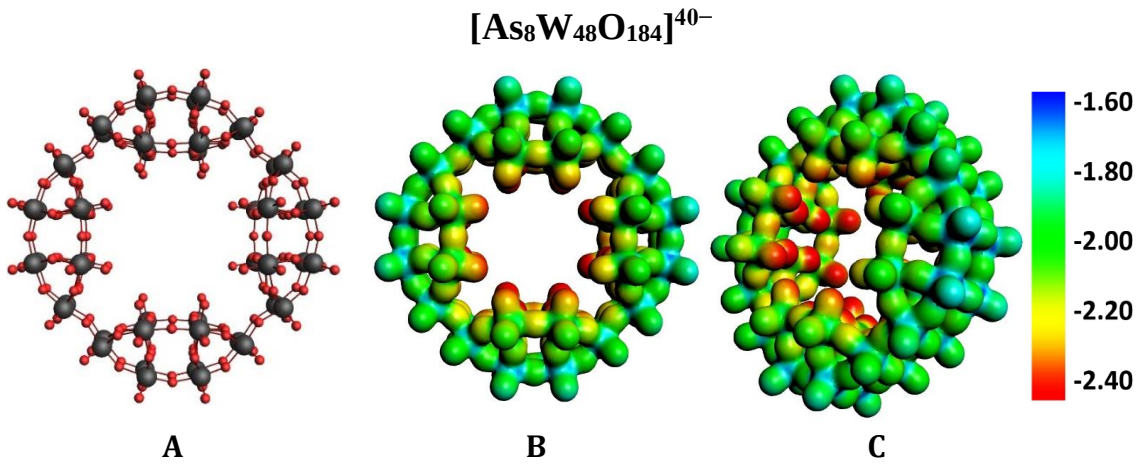

Figure 5.13. MEPs for $[As_8W_{48}O_{184}]^{40-}$ representing (**A**) Front with no MEP, (**B**) Front with MEP, (**C**) Angled Side view with MEP. MEP sensitivity is 0.03. **PBE/TZP/COSMO/Small Frozen Cores**

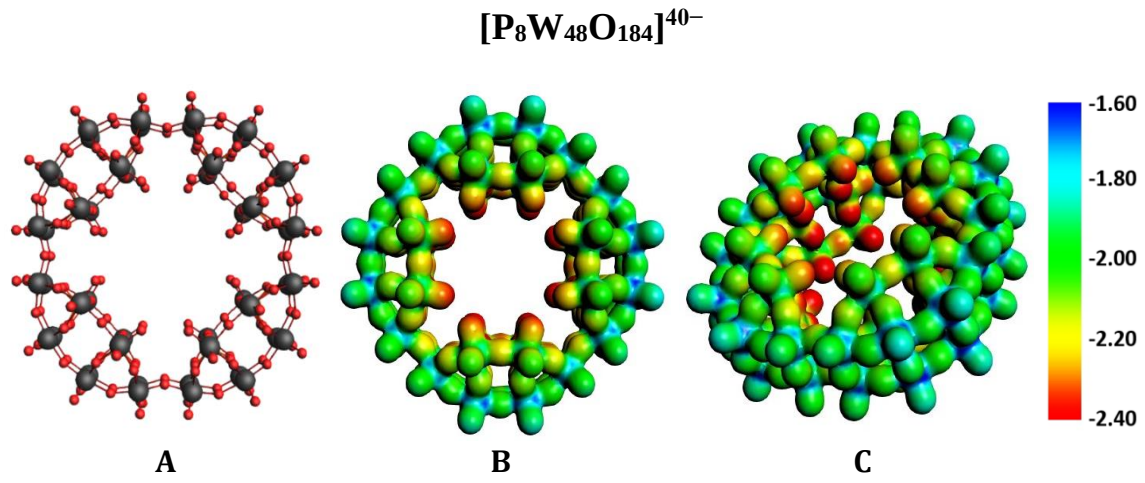

Figure 5.14. MEPs for $[P_8W_{48}O_{184}]^{40-}$ representing (**A**) Front with no MEP, (**B**) Front with MEP, (**C**) Angled Side view with MEP. MEP sensitivity is 0.03. **PBE/TZP/COSMO/Small Frozen Cores**

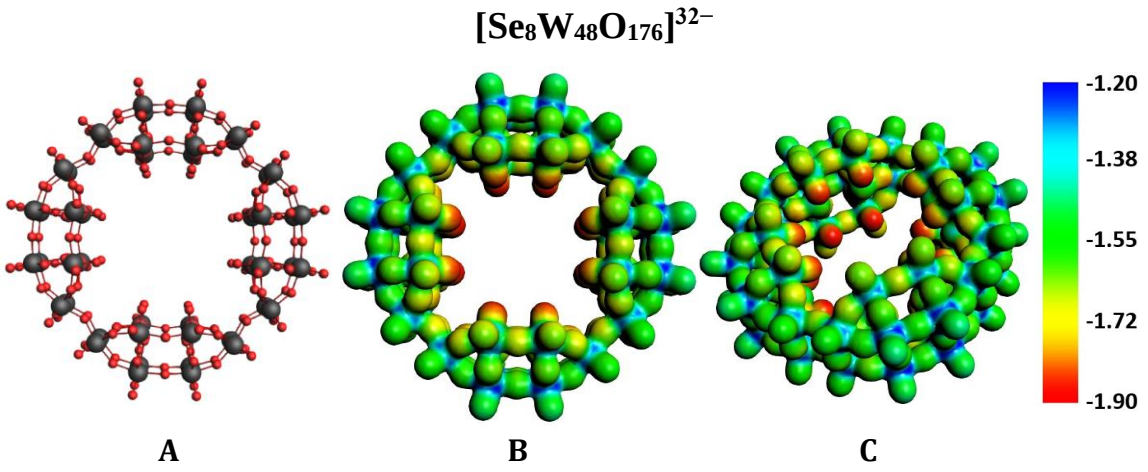

Figure 5.15. MEPs for $[Se_8W_{48}O_{176}]^{32-}$ representing (**A**) Front with no MEP, (**B**) Front with MEP, (**C**) Angled Side view with MEP. MEP sensitivity is 0.03. **PBE/TZP/COSMO/Small Frozen Core**

We initially utilised only 8 K countercations in our geometry as this was the xyz data we had access to, yet the full formula for **{P_8W_{48}}** is $K_{28}Li_5H_7[P_8W_{48}O_{184}]$; the structures we have constructed thus far may be less than accurate at modelling the true structure, especially given that our benchmarking for **{P_8W_{48}}** has not been conducted against empirical data. To rectify this, we first collected a dozen different sets of **{P_8W_{48}}** xyz data from the literature, thus developing a set of 'mean' angles and diameter dimensions with which to compare our calculations against. We based the positions of each potassium cation on available POMzite xyz files,[89,324] which can include up to 18 K cations per **{P_8W_{48}}** wheel, and added in the rest based on the principle of maintaining or improving symmetry of the overall structure (**Figs. 5.16-5.18**). Symmetry is a key factor to keep in mind when designing a molecular model, as a more symmetrical system will take less effort to converge due to there being fewer unique interactions throughout the molecule to consider.

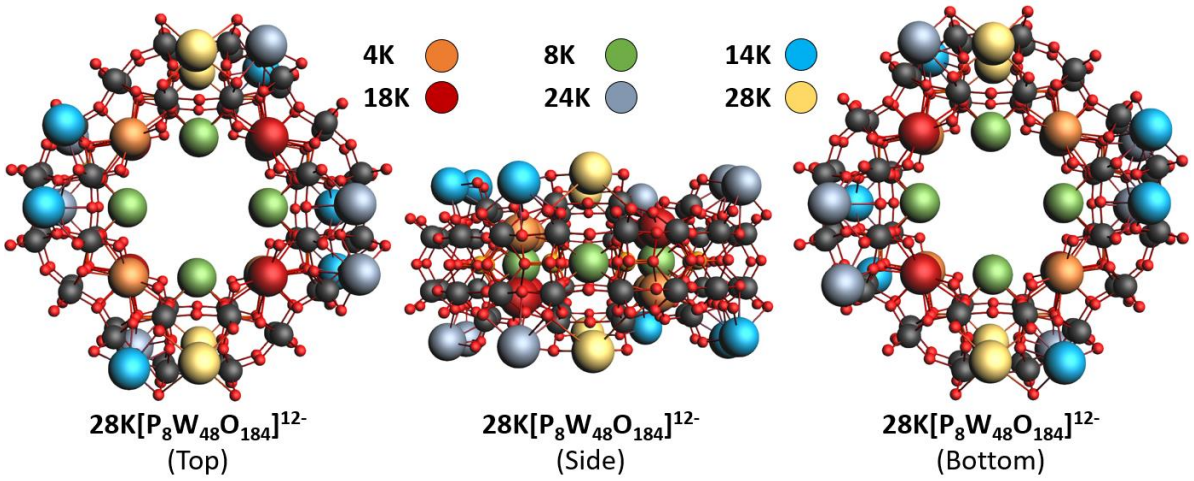

Figure 5.16. Geometry of $K_{28}[P_8W_{48}O_{184}]^{12-}$ with K cations coloured in order of their addition to the initial $[P_8W_{48}O_{184}]^{40-}$ structure. The orange K atoms were added first, followed by the green, and so on; in this way $K_8[P_8W_{48}O_{184}]^{32-}$ contains the atoms coloured orange and green in the above image.

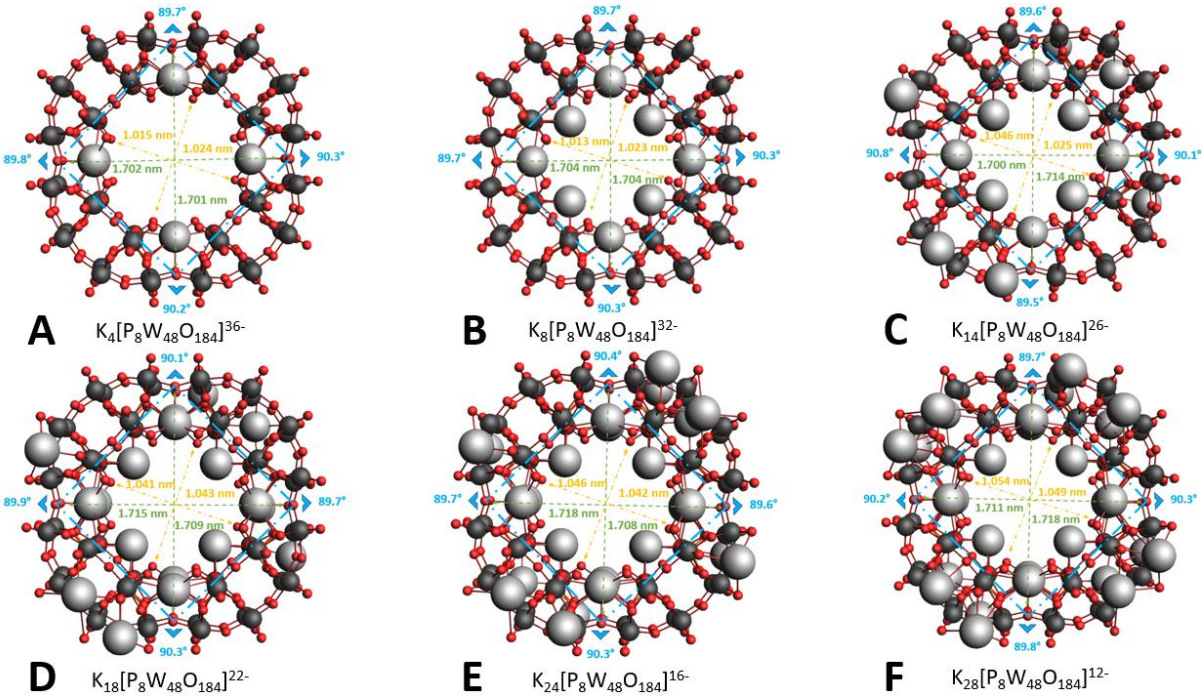

Figure 5.17. Stepwise addition of K cations to **{P_8W_{48}}**. Angles (blue), inner diameters (green), and outer diameters (yellow) are all visualized

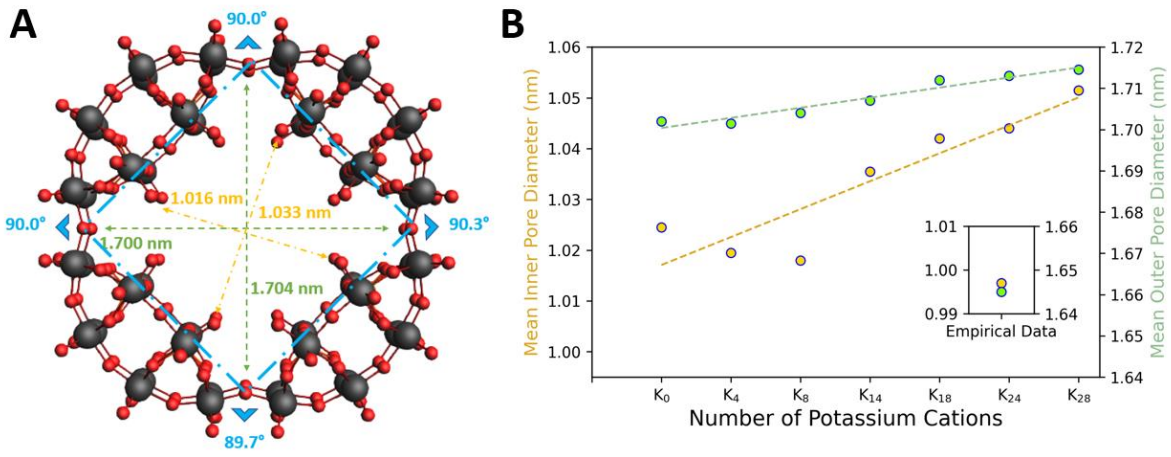

Figure 5.18. Measurement of angles and diameters within the $[P_8W_{48}O_{184}]^{40-}$(**A**) wheel, with angles (blue), the smaller, 'inner' pore diameter (yellow), and the larger, 'outer', pore diameter (green). (**B**) portrays the trend of the pore diameter to increase as more cations are included in the **{P_8W_{48}}** structure. A subplot is included which shows the experimentally obtained values in relation to those measured from calculations.

Determining the mean diameter of the **{P_8W_{48}}** from several points of experimental data, we compared this value against that from our optimized geometries (**see Appendix-1.4 and 1.7 for the full list of structures used and the data extracted from them**); we discovered that the structure with 8 countercations was the closest in diameter to the experimental mean. Inclusion or exclusion of more cations increased this diameter value. When also compared against the computational effort required to converge each geometry, (**Fig. 5.19.**) it becomes clear that 8 K countercations yields the best reflection of reality whilst still being computationally efficient; an efficient calculation is able reach the convergence point for a structure within a reasonable amount of time given the number of cores used. For molecules of a size akin to **{P_8W_{48}}**, a total calculation time of less than a week when 30 cores are used is considered efficient. Additionally, we compared our converged geometries for **{As_8W_{48}}** and **{Se_8W_{48}}** against the available empirical data, and both were in good agreement (**see Appendix-1.5 and -1.6 for the full {As_8W_{48}} and {Se_8W_{48}} benchmarking data**).

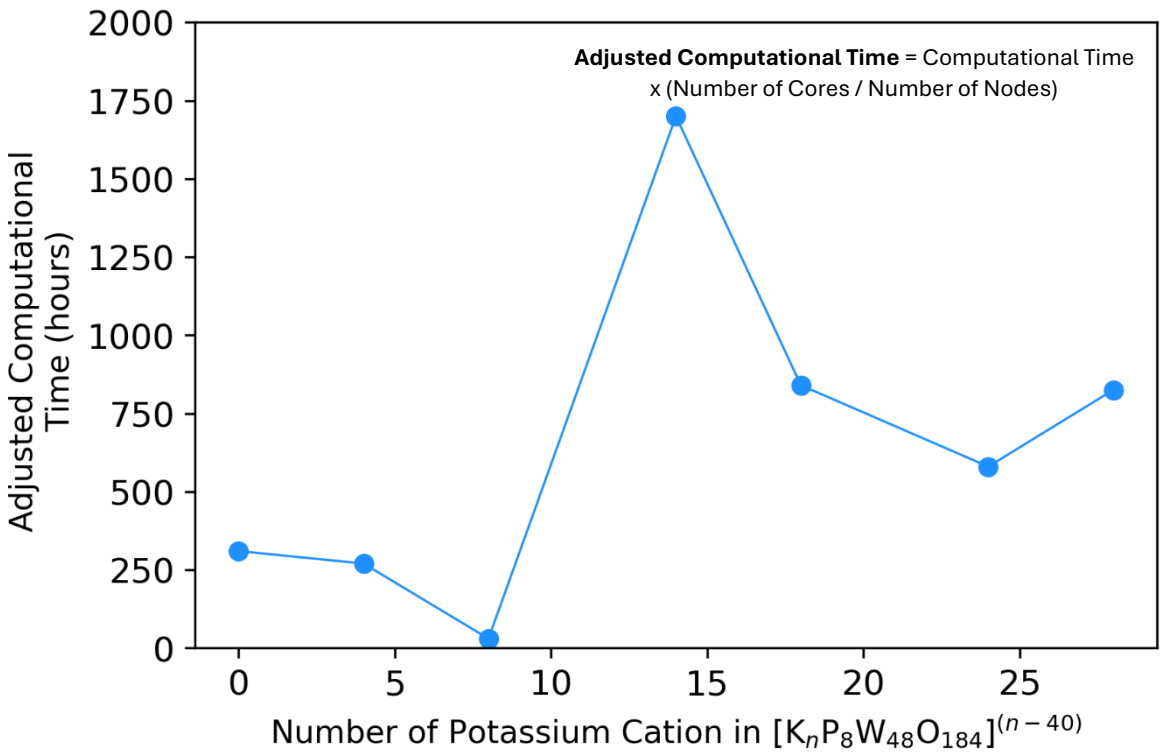

Figure 5.19. Trend of computational time required to converge the structure to increase as more potassium cations are included in the structure.

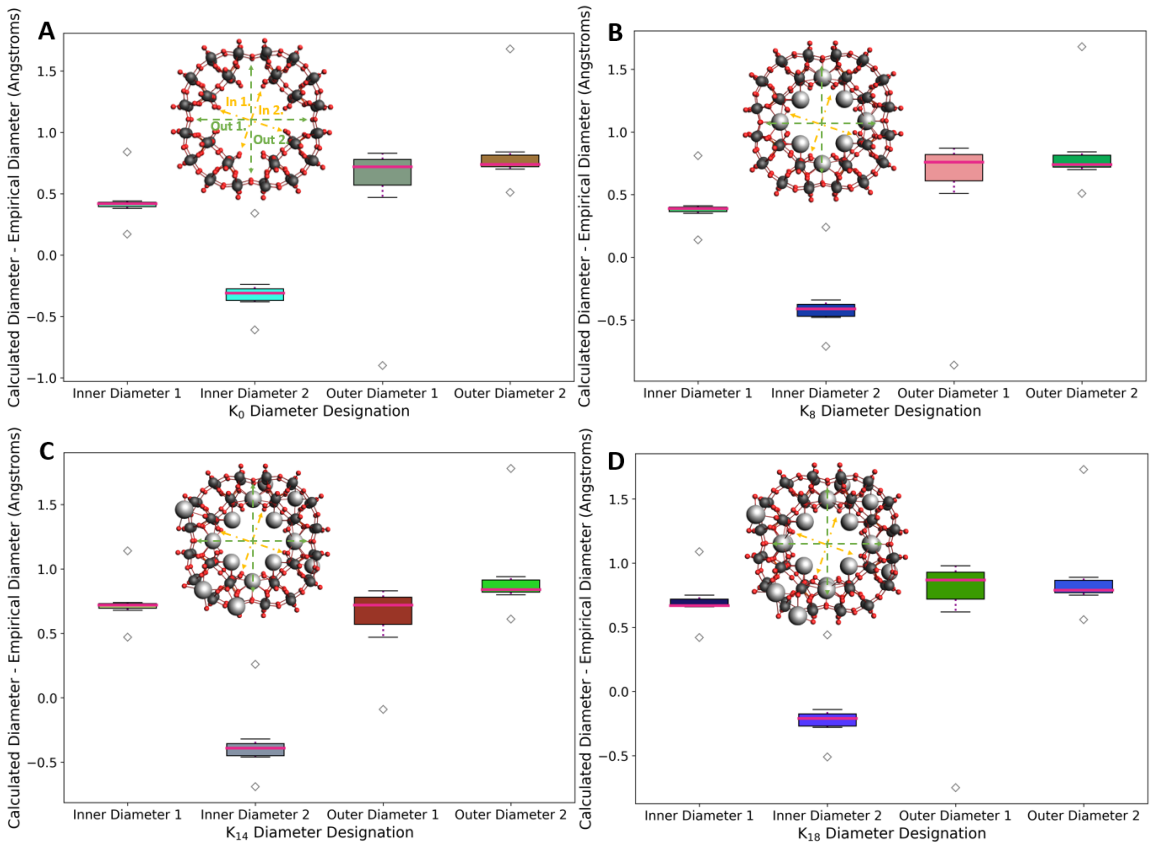

Figure 5.20. Boxplots showing difference between calculated and empirical diameters across a range of 4 distinct diameters for a $[P_8W_{48}O_{184}]^{40-}$ (**A**), $K_8[P_8W_{48}O_{184}]^{32-}$ (**B**), $K_{14}[P_8W_{48}O_{184}]^{26-}$ (**C**), and $K_{18}[P_8W_{48}O_{184}]^{22-}$ (**D**) framework respectively.

We theorise that the ideal model only contains 8 K cations due to the implicit limitations imposed by this computational modelling. Cations such as K are surrounded by a score of solvent molecules in solution, which prevents tight bonding occurring between the cation and POM; when using an effective solvation model such as COSMO however, where the solvent is simulated via a medium, this aspect of solvent interaction is lost. The significance of this is that each cation in a theoretical model now exerts a much greater influence over the overall electron distribution and stability of the molecule than would be observed in solution, and thus a smaller number of cations has a greater impact on the model.

When the difference in diameter values between our theoretical models and the available empirical data is arranged into a boxplot, we can observe several points of interest (**Fig 5.20**). Firstly, that there is little change in the proportions of the differences between calculated and

empirical diameters as more cations are included in the structure; *'inner diameter 2'*, and *'outer diameters 1 and 2'* barely change across the four boxplots. The exception is *'inner diameter 1'*, which experiences an increase in diameter between the addition of 8 and 14 potassium cations (**see Appendix-1.7 for the full list of potassium countercation data, including the error values**).

We theorise that this increase in the value of '*inner diameter 1*' is caused by the uneven addition of cations to the exterior of the POM; two hexalacunary sections receive 2 K cations whilst the other two only benefit from one. This configuration results in a pinched geometry, with the two sections featuring 2 cations repelling more strongly from the similarly cationic pore than the other two.

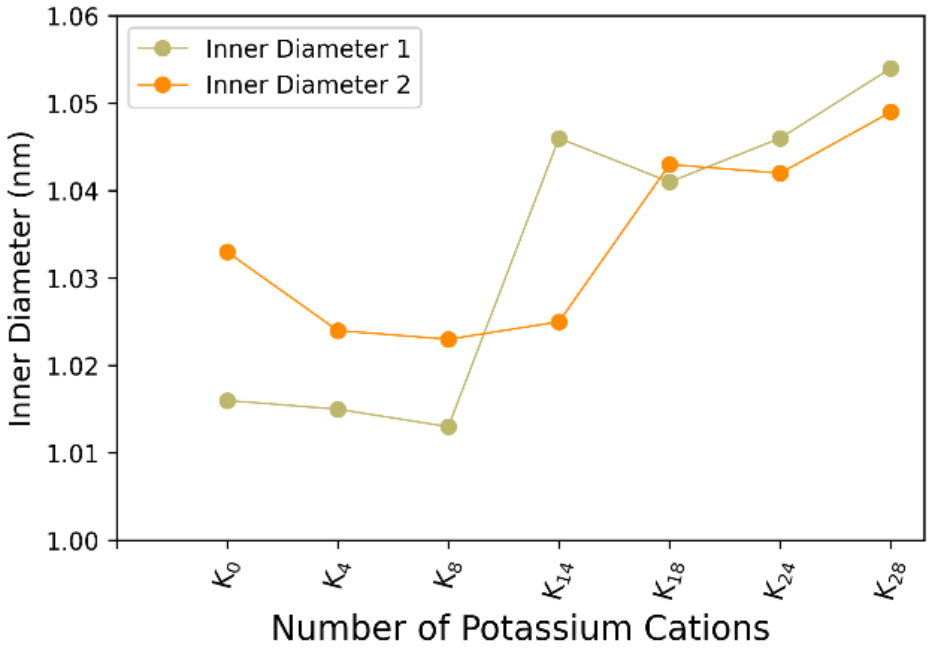

Figure 5.21. Comparison of values for the two inner diameter measurements in various $K_n[P_8W_{48}O_{184}]^{(40-n)-}$ POM structures. There is a large uptick in pore diameter between the addition of 8 and 18 Potassium cations.

This increase in the value of *'inner diameter 1'*, oddly, increases symmetry throughout the POM; the 'default' structure without any cations is slightly ovular, with one inner diameter longer than the other. The addition of cations aids in decreasing the difference between these two diameter values, with a crossover point occurring between the inclusion of 8 and 14 potassium cations and the inner diameter values only coming within 5 pm of each other

between the addition of 14 and 18 cations (**Fig. 5.21)**. The inclusion of cations is therefore essential for maintaining symmetry throughout the POM.

It is worth noting that cations 9-14 are added to the exterior of the POM, instead of within the pore. This arrangement of cations outside the pore as well as within is key for enforcing symmetry in a computational model, as all areas of the POM are now stabilized and prevented from becoming too electron dense.

This enforcement of symmetry, however, comes at the cost of an increasing divergence from the empirical data. As can be seen in **Fig 5.18.**, there is a difference of roughly 5 Angstroms for the inner diameter and 8 Angstroms for the outer equivalent. While this difference is relatively small, it will likely continue to increase if one wanted to completely charge neutralize the POM or if TM oxides were bound to the framework to simulate a portion of a wider POMzite network.

Coupled with the standard increase in computational nodes and time required when one adds more atoms to a molecular system, there most likely exists a crossover point where, in most instances, the accuracy of results obtained from the model is of a suitable quality to not necessitate a more complex molecular model be utilised.

Taking all our results into account, we have determined $K_8[P_8W_{48}O_{184}]^{32-}$ to be the best all-round representation of the full $K_{28}H_7Li_5[P_8W_{48}O_{184}]$ POM framework. It is relatively easy to converge the structure with DFT, with the computational effort rising sharply upon inclusion of additional cations, and the POM exhibits pore dimensions that are more closely in line with the empirical data than the other models we tested.

Finally, we decided to run a small experiment looking at whether countercations other than K could alter the HOMO-LUMO gap or change electron distribution or polarization for the **{P_2W_{12}}** and **{P_8W_{48}}** POMs. Based on trends outlined in the literature,[325] we expect tungsten-based POMs to be less polarised and reactive when exposed to smaller cations, thereby exhibiting a larger HOMO-LUMO gap. Based on our models, we found that more cationic

ions, such as Mg^{2+} or Ca^{2+}, tended to stabilize the HOMO and LUMO orbitals relative to their monocationic counterparts, though the HOMO-LUMO gap was reduced in magnitude. We also observed that the size of the HOMO-LUMO gap decreased slightly overall as the size of the monocation increased, **see Figure 5.22**. (**see Appendix-1.8, specifically Table A-1.22., for the full list of details**).

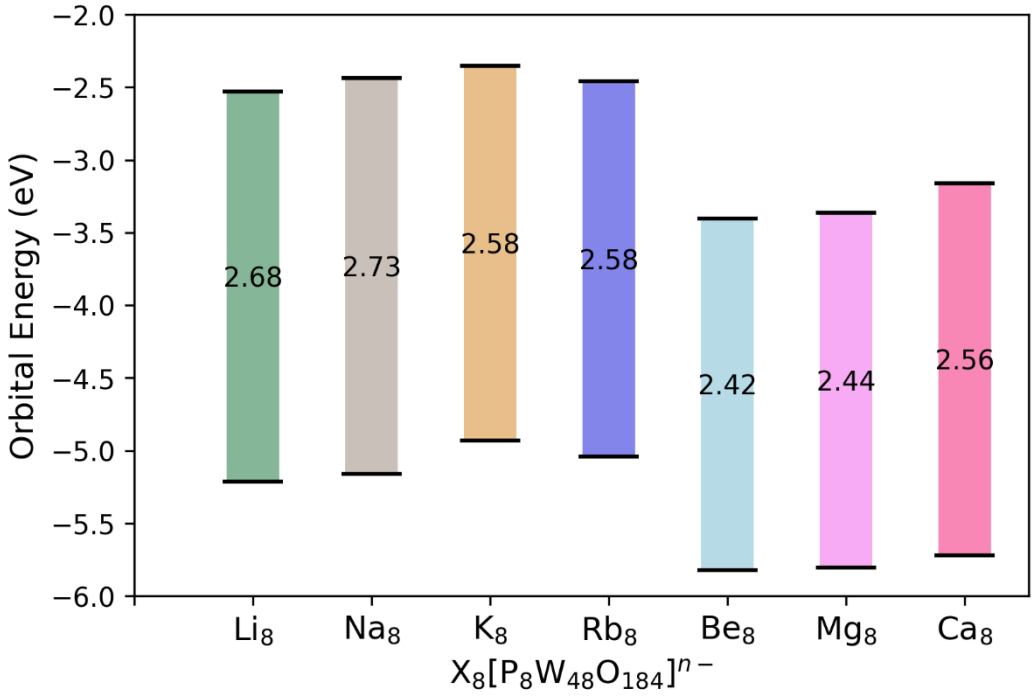

Figure 5.22. Visualization of variations in HOMO and LUMO stabilization as the identity of countercation in a within a $X_8[P_8W_{48}O_{184}]^{n-}$ POM changes, where X=Li^+, Na^+, K^+, Rb^+, Be^{2+}, Mg^{2+}, Ca^{2+}.

Standard deviation (SD) and mean atomic charge (MAC) calculations conducted for each POM species proved more enlightening with respect to the effect different cation elements; the alkali metal and earth cations with the smallest ionic radius displayed the lowest SD value for the molecule as a whole and relatively low values when the constituent elements were examined individually. A small SD value in this context signifies a less polarized POM, which will in turn be less reactive and therefore more stable overall.

We can observe the magnitude of the SD value using the boxplot provided by **Figure 5.23.** A smaller box represents a smaller SD value with regards to the atomic charge of the POM species. Separating the countercations into monocations (Li^+, Na^+, K^+, and Rb^+) and dications

(Be^{2+}, Mg^{2+}, and Ca^{2+}), we can see SD increases as you progress down a group or across a row in the periodic table. This indicates that the best countercations for **$\{P_8W_{48}\}$** are small monocations.

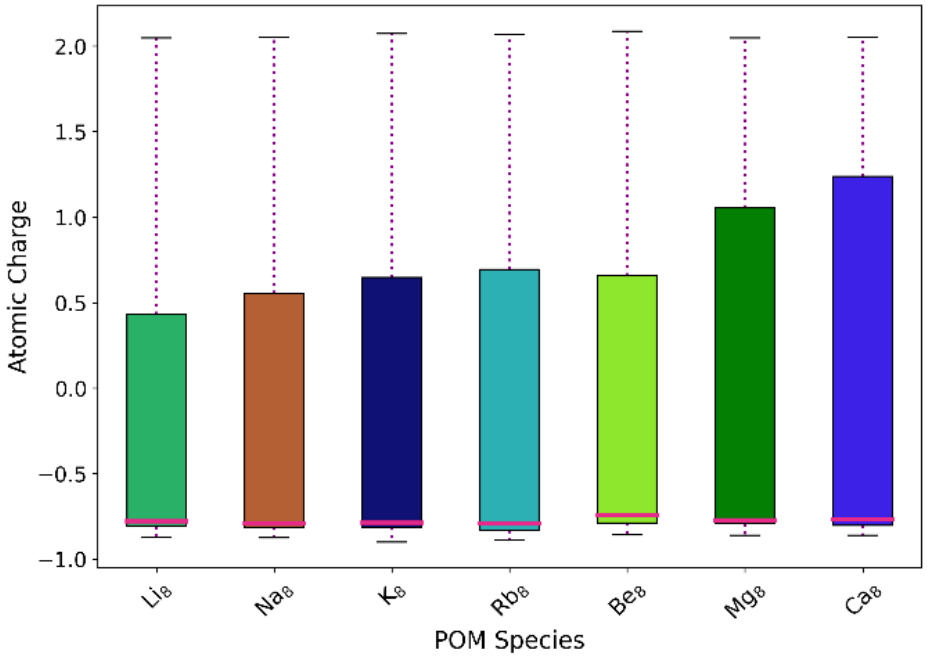

Figure 5.23. Variation in range of atomic charges within a $X_8[P_8W_{48}O_{184}]^{n-}$ POM, where X=Li^+, Na^+, K^+, Rb^+, Be^{2+}, Mg^{2+}, Ca^{2+}.

MAC data similarly placed smaller cations as promoting delocalisation of the framework electrons, and therefore framework stability, by moving the mean elemental charge towards neutral zero more than their larger counterparts (**see Fig. 5.23 and Appendix-1.12, specifically Tables A-1.23. and A-1.26.**).

5.3 Conclusions

In this work we have conducted DFT-level computational research into **{X_8W_{48}}**-type POMs and their precursor species, WD and hexalacunaries, and using the data collected to identify the structural characteristics in the molecule responsible for key chemical and electronic properties. We have also determined $K_8[P_8W_{48}O_{184}]^{32-}$ to be the simplest representation of the full $K_{28}Li_5H_7[P_8W_{48}O_{184}]$ molecule, whilst still being accurate to the empirical data present. Unless one wishes to model a POMzite subsection, for instance, or another molecular system that uses the **{P_8W_{48}}** POM as a building block that sees the overall anionic charge far exceed the original, already high, value of −40, **K_8{P_8W_{48}}** is a very suitable model. Finally, we conducted some preliminary theoretical work into the effect of using countercations other than potassium for **{P_8W_{48}}** POMs, with indication that there are subtle trends down an elemental group or across a row, but overall, the presence of any countercation plays a bigger role in altering molecular properties than the species deployed. In the future, we hope to gain a better understanding of the dynamics of cation-POM interactions by studying cation mobility on the POM surface.

5.4 References

(64) Zhang, F. Q.; Guan, W.; Yan, L. K.; Zhang, Y. T.; Xu, M. T.; Hayfron-Benjamin, E.; Su, Z. M. On the Origin of the Relative Stability of Wells-Dawson Isomers: A DFT Study of α-, β-, γ-, A*-, B*-, and Γ*-[(PO4)2W18O54] 6-Anions. *Inorg. Chem.* **2011**, *50* (11), 4967–4977. https://doi.org/10.1021/ic200203s.

(76) Ammam, M.; Mbomekalle, I. M.; Keita, B.; Nadjo, L.; Fransaer, J. [As8W48O184]40-, a New Crown-Shaped Heteropolyanion: Electrochemistry and Electrocatalytic Properties towards Reduction of Nitrite. *Electrochim. Acta* **2010**, *55* (9), 3118–3122. https://doi.org/10.1016/j.electacta.2010.01.067.

(78) Cameron, J. M.; Gao, J.; Vilà-Nadal, L.; Long, D. L.; Cronin, L. Formation, Self-Assembly and Transformation of a Transient Selenotungstate Building Block into Clusters, Chains and Macrocycles. *Chem. Commun.* **2014**, *50* (17), 2155–2157. https://doi.org/10.1039/c3cc49293a.

(82) Boyd, T.; Mitchell, S. G.; Gabb, D.; Long, D. L.; Cronin, L. Investigating Cation Binding in the Polyoxometalate-Super-Crown [P 8W48O184]40-. *Chem. - A Eur. J.* **2011**, *17* (43), 12010–12014. https://doi.org/10.1002/chem.201101666.

(85) Mal, S. S.; Kortz, U. The Wheel-Shaped Cu20 Tungstophosphate [Cu20Cl(OH) 24(H2O)12(P8W48O 184)]25- Ion. *Angew. Chemie - Int. Ed.* **2005**, *44* (24), 3777–3780. https://doi.org/10.1002/anie.200500682.

(88) Goura, J.; Sundar, A.; Bassil, B. S.; Ćirić-Marjanović, G.; Bajuk-Bogdanović, D.; Kortz, U. Peroxouranyl-Containing W48 Wheel: Synthesis, Structure, and Detailed Infrared and Raman Spectroscopy Study. *Inorg. Chem.* **2020**, *59* (23), 16789–16794. https://doi.org/10.1021/acs.inorgchem.0c02858.

(89) Boyd, T.; Mitchell, S. G.; Gabb, D.; Long, D. L.; Song, Y. F.; Cronin, L. POMzites: A Family of Zeolitic Polyoxometalate Frameworks from a Minimal Building Block Library. *J. Am. Chem. Soc.* **2017**, *139* (16), 5930–5938. https://doi.org/10.1021/jacs.7b01807.

(138) Zhan, C.; Cameron, J. M.; Gabb, D.; Boyd, T.; Winter, R. S.; Vilà-Nadal, L.; Mitchell, S. G.; Glatzel, S.; Breternitz, J.; Gregory, D. H.; Long, D. L.; MacDonell, A.; Cronin, L. A Metamorphic Inorganic Framework That Can Be Switched between Eight Single-Crystalline States. *Nat. Commun.* **2017**, *8*. https://doi.org/10.1038/ncomms14185.

(139) Bruno, T. J.; Lide, D. R.; Rumble, J. R. *CRC Handbook of Chemistry and Physics: A Ready-Reference Book of Chemical and Physical Data*, 100th ed.; CRC Press, 2019.

(180) Vilà-Nadal, L.; Peuntinger, K.; Busche, C.; Yan, J.; Lüders, D.; Long, D.; Poblet, J. M.; Guldi, D. M.; Cronin, L. Polyoxometalate {W18O56XO6} Clusters with Embedded Redox-Active Main-Group Templates as Localized Inner-Cluster Radicals. *Angew. Chemie* **2013**, *125*, 9877–9881. https://doi.org/ange.201303126.

(231) López, X.; Carbó, J. J.; Bo, C.; Poblet, J. M. Structure, Properties and Reactivity of Polyoxometalates: A Theoretical Perspective. *Chem. Soc. Rev.* **2012**, *41* (22), 7537–7571. https://doi.org/10.1039/c2cs35168d.

(257) Swart, M.; Duran, M.; Bickelhaupt, F. M. DFT2021 Poll. **2021**.

(283) Miro, P.; Ling, J.; Qiu, J.; Burns, P. C.; Gagliardi, L.; Cramer, C. J. Experimental and Computational Study of a New Wheel-Shaped {[W5O21]3[(UVIO2)2(M-O2)]3}30− Polyoxometalate. *Inorg. Chem.* **2012**, *2*, 8784–8790. https://doi.org/10.1021/ic3005536.

(284) Vilà-Nadal, L.; Mitchell, S. G.; Markov, S.; Busche, C.; Georgiev, V.; Asenov, A.; Cronin, L. Towards Polyoxometalate-Cluster-Based Nano-Electronics. *Chem. - A Eur. J.* **2013**, *19* (49), 16502–16511. https://doi.org/10.1002/chem.201301631.

(285) Cameron, J. M.; Fujimoto, S.; Kastner, K.; Wei, R. J.; Robinson, D.; Sans, V.; Newton, G. N.; Oshio, H. H. Orbital Engineering: Photoactivation of an Organofunctionalized Polyoxotungstate. *Chem. - A Eur. J.* **2017**, *23* (1), 47–50. https://doi.org/10.1002/chem.201605021.

(286) Miró, P.; Poblet, J. M.; Ávalos, J. B.; Bo, C. Towards a Computational Treatment of Polyoxometalates in Solution Using QM Methods and Explicit Solvent Molecules. *Can. J. Chem.* **2009**, *87* (10), 1296–1301. https://doi.org/10.1139/V09-059.

(291) Kim, B.; Lee, S.; Kim, J. Inverse Design of Porous Materials Using Artificial Neural Networks. *Sci. Adv.* **2020**, *6* (1). https://doi.org/10.1126/sciadv.aax9324.

(293) Boyd, T.; Mitchell, S. G.; Miras, H. N.; Long, D. L.; Cronin, L. Understanding and Mapping the Assembly of a Family of Trimeric Polyoxometalates: Transition Metal Mediated Wells-Dawson (M18)-Trimers. *Dalt. Trans.* **2010**, *39* (28), 6460–6465. https://doi.org/10.1039/c002633f.

(297) De La Oliva, A. R.; Sans, V.; Miras, H. N.; Yan, J.; Zang, H.; Richmond, C. J.; Long, D. L.; Cronin, L. Assembly of a Gigantic Polyoxometalate Cluster {W200Co 8O660} in a Networked Reactor System. *Angew. Chemie - Int. Ed.* **2012**, *51* (51), 12759–12762. https://doi.org/10.1002/anie.201206572.

(299) Petrus, E.; Segado, M.; Bo, C. Nucleation Mechanisms and Speciation of Metal Oxide Clusters. *Chem. Sci.* **2020**, *11* (32), 8448–8456. https://doi.org/10.1039/d0sc03530k.

(313) Zalesskiy, S. S.; Kitson, P. J.; Frei, P.; Bubliauskas, A.; Cronin, L. 3D Designed and Printed Chemical Generators for on Demand Reagent Synthesis. *Nat. Commun.* **2019**, *10* (1), 6–13. https://doi.org/10.1038/s41467-019-13328-6.

(314) Vila-Nadal, L. POMzites: A Roadmap for Inverse Design in Metal Oxide Chemistry. *Int. J. Quantum Chem.* **2020**, *121* (5), e26493. https://doi.org/10.22541/au.159103665.51733499.

(315) Bergman, R. G.; Danheiser, R. L. Reproducibility in Chemical Research. *Angew. Chemie - Int. Ed.* **2016**, *55* (41), 12548–12549. https://doi.org/10.1002/anie.201606591.

(316) Gulam Rabbani, S. M.; Miró, P. Computational Insights into Iron Heterometal Installation in

Polyoxovanadate-Alkoxide Clusters. *Inorg. Chem.* **2021**, 1–7. https://doi.org/10.1021/acs.inorgchem.1c03589.

(317) Petrus, E.; Bo, C. Unlocking Phase Diagrams for Molybdenum and Tungsten Nanoclusters and Prediction of Their Formation Constants. *J. Phys. Chem. A* **2021**, *125* (23), 5212–5219. https://doi.org/10.1021/acs.jpca.1c03292.

(318) Lapham, P.; Vilà-Nadal, L.; Cronin, L.; Georgiev, V. P. Influence of the Contact Geometry and Counterions on the Current Flow and Charge Transfer in Polyoxometalate Molecular Junctions: A Density Functional Theory Study. *J. Phys. Chem. C* **2021**, *125* (6), 3599–3610. https://doi.org/10.1021/acs.jpcc.0c11038.

(319) Ly, H. G. T.; Mihaylov, T.; Absillis, G.; Pierloot, K.; Parac-Vogt, T. N. Reactivity of Dimeric Tetrazirconium(IV) Wells-Dawson Polyoxometalate toward Dipeptide Hydrolysis Studied by a Combined Experimental and Density Functional Theory Approach. *Inorg. Chem.* **2015**, *54* (23), 11477–11492. https://doi.org/10.1021/acs.inorgchem.5b02122.

(320) Ravelli, D.; Dondi, D.; Fagnoni, M.; Albini, A.; Bagno, A. Predicting the UV Spectrum of Polyoxometalates by TD-DFT. *J. Comput. Chem.* **2011**, *32* (14), 2983–2987. https://doi.org/10.1002/jcc.21879.

(321) Amin, S. S.; Cameron, J. M.; Winslow, M.; Davies, E. S.; Argent, S. P.; Robinson, D.; Newton, G. N. A Mixed-Addenda Mo/W Organofunctionalised Hybrid Polyoxometalate. *Eur. J. Inorg. Chem.* **2022**, *2022* (10). https://doi.org/10.1002/ejic.202200019.

(322) Mbomekallé, I. M.; Bassil, B. S.; Suchopar, A.; Keita, B.; Nadjo, L.; Ammam, M.; Haouas, M.; Taulelle, F.; Kortz, U. Improved Synthesis, Structure, and Solution Characterization of the Cyclic 48-Tungsto-8-Arsenate(V), [H4As8W48O184]36-. *J. Clust. Sci.* **2014**, *25* (1), 277–285. https://doi.org/10.1007/s10876-013-0656-2.

(323) Chen, J. J.; Vilà-Nadal, L.; Solé-Daura, A.; Chisholm, G.; Minato, T.; Busche, C.; Zhao, T.; Kandasamy, B.; Ganin, A. Y.; Smith, R. M.; Colliard, I.; Carbó, J. J.; Poblet, J. M.; Nyman, M.; Cronin, L. Effective Storage of Electrons in Water by the Formation of Highly Reduced Polyoxometalate Clusters. *J. Am. Chem. Soc.* **2022**, *144* (20), 8951–8960. https://doi.org/10.1021/jacs.1c10584.

(324) Zhang, L. C.; Xue, H.; Zhu, Z. M.; Zhang, Z. M.; Li, Y. G.; Wang, E. B. Two New {P8W49} Wheel-Shaped Tungstophosphates Decorated by Co(II), Ni(II) Ions. *J. Clust. Sci.* **2010**, *21* (4), 679–689. https://doi.org/10.1007/s10876-010-0286-x.

(325) Misra, A.; Kozma, K.; Streb, C.; Nyman, M. Beyond Charge Balance: Counter-Cations in Polyoxometalate Chemistry. *Angew. Chemie - Int. Ed.* **2020**, *59* (2), 596–612. https://doi.org/10.1002/anie.201905600.

Chapter 6: Exploring the Theoretical Landscape of the Hexalacunary $[\alpha\text{-}H_2P_2W_{12}O_{48}]^{12-}$ Wells-Dawson Anion: A Comprehensive Study

This chapter is based on the following publication: Malcolm, D., and Vilà-Nadal, L. "**Exploring the Theoretical Landscape of the Hexalacunary $[\alpha\text{-}H_2P_2W_{12}O_{48}]^{12-}$ Wells-Dawson Anion: A Comprehensive Study"**, which has been submitted for publication.

In this chapter, we will attempt to construct an accurate, computationally based $[P_2W_{12}O_{48}]^{14-}$ POM using the available empirical data. We will examine how inclusion of potassium countercations and protons affects the model, taking care to note if we can simplify the structure without losing accuracy relative to the literature.

6.1 Introduction

In the last chapter, we looked extensively at methods of modelling the $[P_8W_{48}O_{184}]^{40-}$ POM, exchanging heteroatoms and countercations as part of our investigation. Moving on from the full POM wheel, we shall now dive into the $[P_2W_{12}O_{48}]^{14-}$ hexalacunary species which assemble to form the larger **{P_8W_{48}}** wheel.

The hexalacunary fragment $[\alpha\text{-}H_2P_2W_{12}O_{48}]^{12-}$ anion (abbreviated, **{P_2W_{12}}**) is the hydrolysis product of the WD anion $[P_2W_{18}O_{62}]^{6-}$ in $(HOCH_2)_3CNH_2/K_2CO_3$ solution and was initially documented by Contant and Ciabrini in 1977 as a potassium salt.[326] The structure of **{P_2W_{12}}**

was originally believed to stem from $[P_2W_{18}O_{62}]^{6-}$ by eliminating six **{WO$_x$}** units from the polar caps (formulated as $[H_6P_2W_{12}O_{50}]^{12-}$). However, a ^{183}W NMR study conducted by Baker *et al.* in 1984[327] on $[P_2Mo_6W_{12}O_{62}]^{6-}$ revealed that **{P$_2$W$_{12}$}** has a boat-shaped structure, achieved by removing a longitudinal third (referred to as the "W_6O_{14}" fragment) from an [α-$P_2W_{18}O_{62}]^{6-}$ anion, as illustrated in **Figure 6.1**. After its discovery, **{P$_2$W$_{12}$}** has played a pivotal role as a precursor in synthesizing various polyoxotungstates. One such aggregate is the wheel-shaped POM $[P_8W_{48}O_{184}]^{40-}$, shortened to **{P$_8$W$_{48}$}**,[77] which is formed from four **{P$_2$W$_{12}$}** hexa-vacant lacunary species.[81,82]

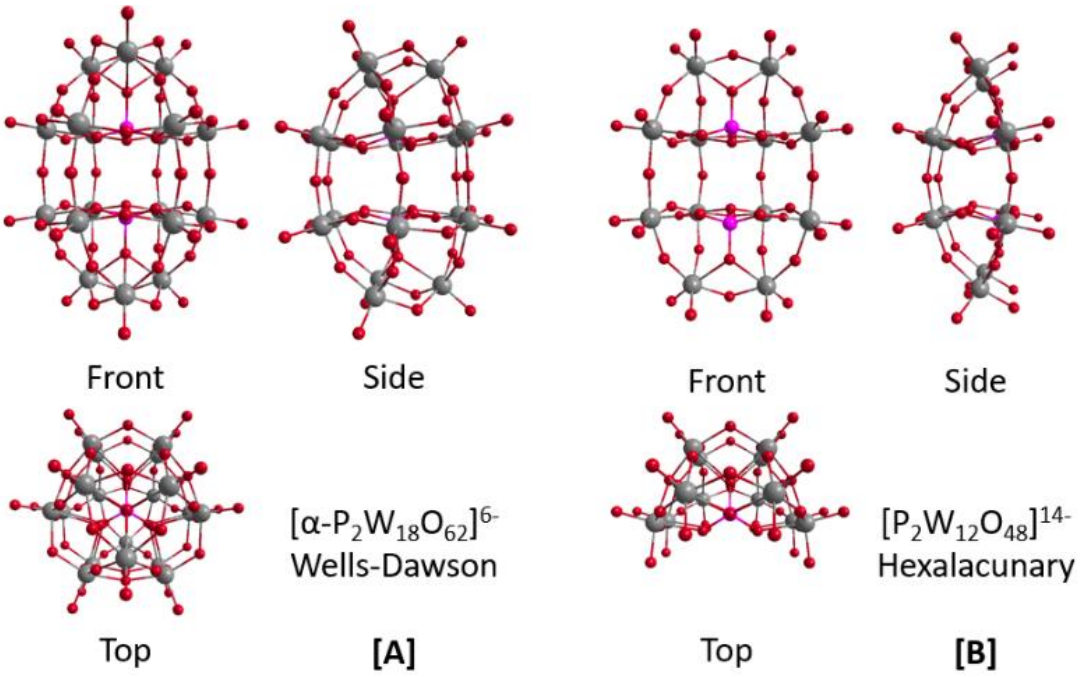

Figure 6.1. Ball-and-stick geometries (front, side, and top views) of the $[\alpha\text{-}P_2W_{18}O_{62}]^{6-}$ Wells-Dawson **[A]** and $[P_2W_{12}O_{48}]^{14-}$ hexalacunary POMs **[B]**. Colour scheme: W: grey, O: red, P: pink.

However, despite its synthetic relevance the experimental determination of the structure of [α-$H_2P_2W_{12}O_{48}]^{12-}$ has been elusive until recently; Suigarto and Sadakane managed to structurally resolve single crystals of **{P$_2$W$_{12}$}** in 2023 using an excess of KCl,[328] answering a lingering question several decades old: **{P$_2$W$_{12}$}** is definitely an alpha isomer, formed from the removal of six **{WO$_x$}** units from the alpha isomer of the Wells-Dawson parent.[64]

There are only two other species of hexalacunary POM that have been demonstrated to form a **{X$_8$W$_{48}$}** POM wheel: these are $[As_2W_{12}O_{48}]^{6-}$, ref[83], and $[Se_2W_{12}O_{46}]^{4-}$, which form $[As_8W_{48}O_{184}]^{40-}$, ref[76], and $[Se_8W_{48}O_{176}]^{32-}$, ref[78], respectively. There is even less data on these hexalacunaries than for the phosphorus analogue, and the selenium species has never been isolated as a stable product; its existence is inferred only through its presence within the **{Se$_8$W$_{48}$}** wheel. See **Figure 6.2.** for the list of families of POM aggregates which can be formed from these few hexalacunary building blocks.

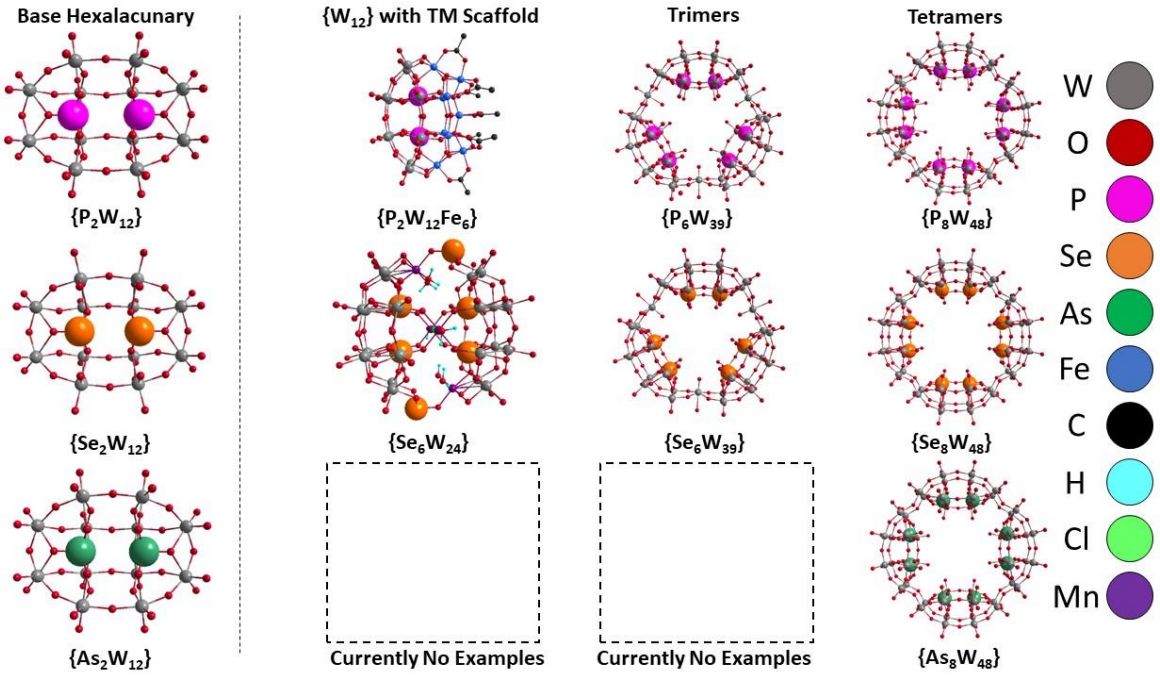

Figure 6.2. Ball-and-stick geometries for known hexalacunary species $[P_2W_{12}O_{48}]^{14-}$, $[Se_2W_{12}O_{46}]^{12-}$, and $[As_2W_{12}O_{48}]^{14-}$, as well as a few examples of further species they can form (where available), divided into TM-scaffold structures $[H_4P_2W_{12}Fe_9O_{56}(OAc)_7]^{6-}$, ref[79], and $[Mn_3Se_6W_{24}O_{94}Cl(H_2O)_2]^{15-}$, ref[78], (abbreviated as **{P$_2$W$_{12}$Fe$_6$}** and **{Se$_6$W$_{24}$}** respectively), timers $[\{WO(H_2O)\}_3P_6W_{36}O_{144}]^{30-}$, ref[80], and $[Se_6W_{39}O_{141}(H_2O)_3]^{24-}$, ref[78], (abbreviated as **{P$_6$W$_{39}$}** and **{Se$_6$W$_{39}$}** respectively), and tetramers $[P_8W_{48}O_{184}]^{40-}$, ref[77], $[Se_8W_{48}O_{176}]^{32-}$, ref[78], and $[As_8W_{48}O_{184}]^{40-}$, ref[76] (abbreviated as **{P$_8$W$_{48}$}**, **{Se$_8$W$_{48}$}**, and **{As$_8$W$_{48}$}** respectively). Heteroatoms are enlarged for clarity.

Herein we present our hexalacunary-based **{X$_2$W$_{12}$}** computational data, highlighting several key areas including benchmarking the theoretical modelling of $K_{12}[H_2P_2W_{12}O_{48}]\cdot 24H_2O$,[328] $K_{12}[H_2As_2W_{12}O_{48}]\cdot 24H_2O$,[83] and the hypothesized $[Se_2W_{12}O_{46}]^{12-}$[78] structures, observing how

their geometries are altered by the inclusion of protons and/or countercations, and finally determining which type of model is the best representation of the empirical data.

6.2 Results and Discussion

6.2.1 Hexalacunary Benchmarking

We initially compared the dimensions of our DFT model with the empirical xyz data. As with our previous work we chose to use the PBE functional,[329] as it provides results at a good level of accuracy whilst remaining relatively cheap in computational terms. We found there to only be a very small degree of error between the empirical dimensions and our computational ones, never exceeding 0.17Å (**Table 6.1.**).

Table 6.1. Comparison in dimensions between empirical and theoretical $[P_2W_{18}O_{62}]^{6-}$ frameworks. Relevant atoms are labelled on the molecular diagram. Colour scheme: W: grey, O: red, P: pink **OPT/PBE/TZP/SFC/COSMO**

Diameter Identifier (nm)	Empirical Fragment Length {Kato, C. *et al*[330]} (Å)	Theoretical Length (Å)	Theor. – Emp. Difference (Å)
HEIGHT			
O_A-O_E	11.27	11.40	+0.13
P-P	3.98	4.00	+0.02
W_A-W_E	9.82	9.93	+0.11
LENGTH			
O_B-O_D	7.23	7.39	+0.16
W_C-W_D	7.06	7.14	+0.08
WIDTH			
O_C-O_D	4.25	4.28	+0.03
W_B-W_D	3.68	3.72	+0.04

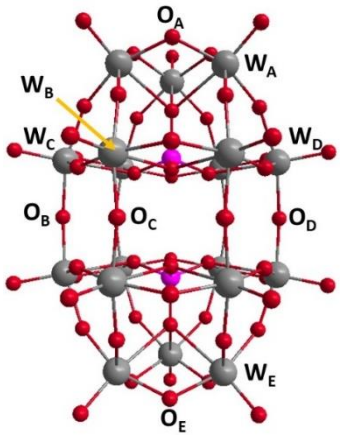

To truly represent the empirical WD with our model, we decided to include countercations to charge neutralize the cluster. We chose potassium cations, as these are one of the most common choices for synthesis, but before presenting our findings we need to discuss the effect the distance between cation and phosphorus heteroatom has on the electronic properties of the WD model. Previous work by Kaledin *et. al*[331] indicated that countercations tend to over stabilize HOMO and LUMO energy levels; an implicit solvent model, such as COSMO, does not correctly simulate the solvent molecules, which would usually surround each countercation in an empirical system, as this significantly reduces the complexity of the calculation. Without constraints on cation-POM distance, optimization calculations tend to converge with the countercations closer to the POM consequently, at a distance of 3-6Å from the nearest Phosphorus heteroatom.

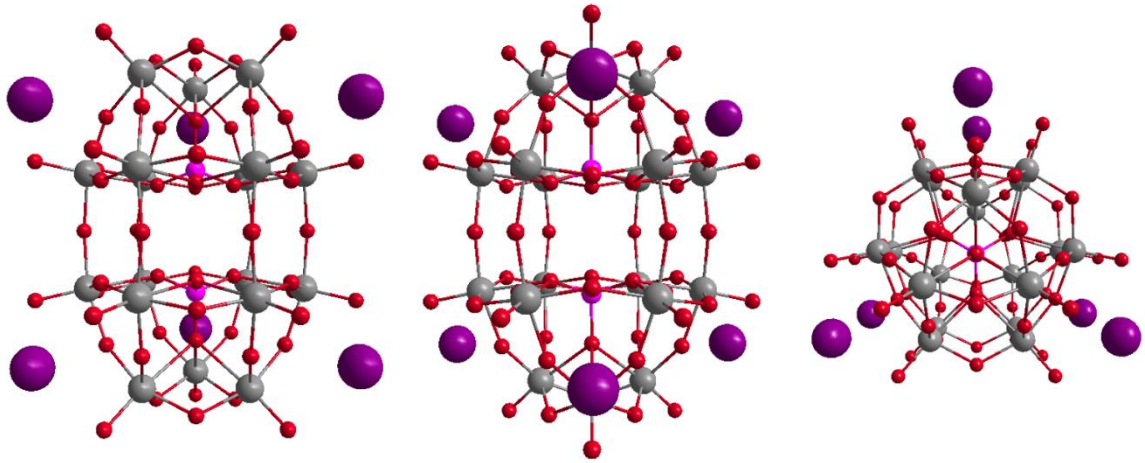

Figure 6.3. $K_6[P_2W_{18}O_{62}]$ framework, where the cations are 5.5Å from the nearest phosphorus heteroatom, from 3 different perspectives. Colour scheme: W: grey, O: red, P: pink, K: purple **OPT/PBE/TZP/SFC/COSMO**

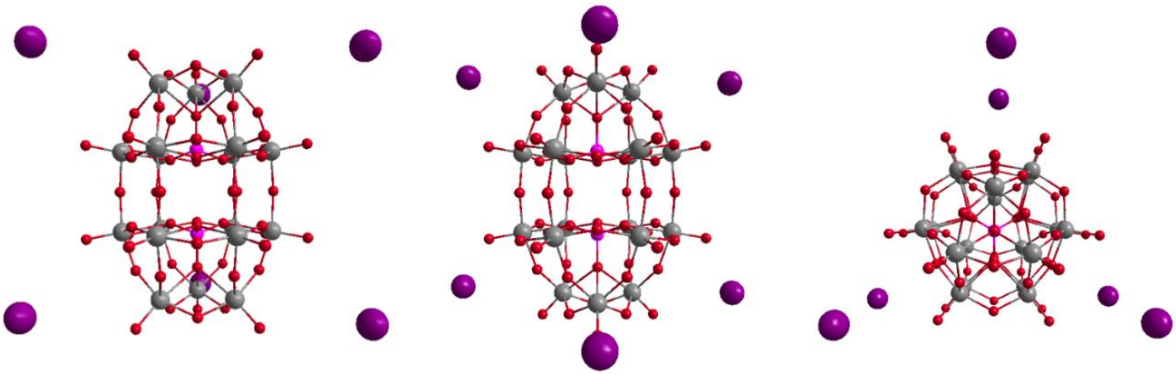

Figure 6.4. $K_6[P_2W_{18}O_{62}]$ framework, where the cations are 9.0Å from the nearest phosphorus heteroatom, from 3 different perspectives. Colour scheme: W: grey, O: red, P: pink, K: purple **SP/PBE/TZP/SFC/COSMO**

We therefore ran single point UV-Vis calculations on $K_6[P_2W_{18}O_{62}]$, where the distance between potassium and phosphorus was constrained at almost a dozen different values. See **Figures 6.3, 6.4** to observe what a difference in cation-heteroatom distance looks like, as well as **Table A-2.2** and **Figure 6.5**, which detail how framework dimensions change with cation-heteroatom distance.

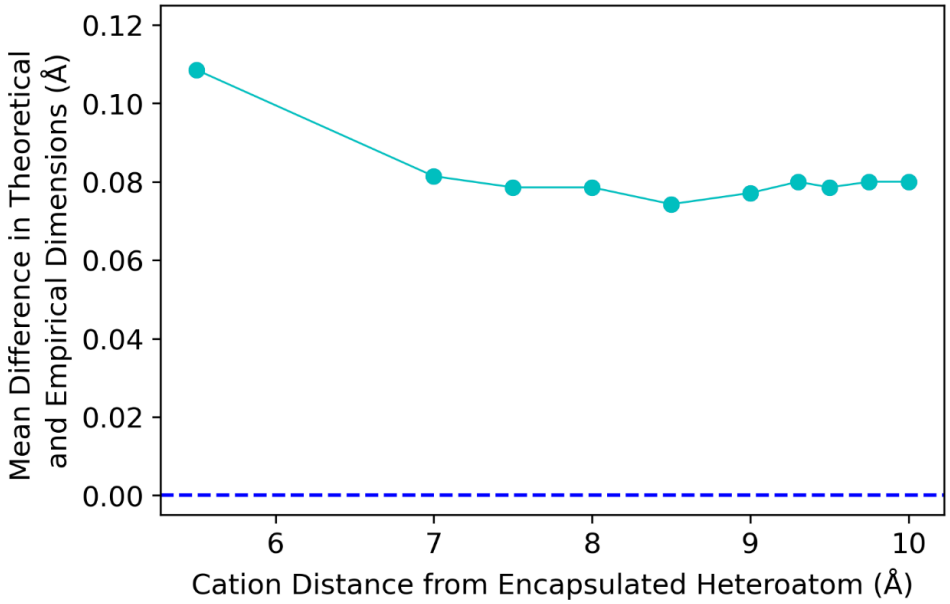

Figure 6.5. Trend of computationally obtained $K_6[P_2W_{18}O_{62}]$ framework to deviate less from the empirical xyz dimensions as the distance between cation and heteroatom increases. A dashed line is provided at 0pm to illustrate relative differences of error. **OPT/PBE/TZP/SFC/COSMO**

We observed minimal differences in error after the distance between cation and heteroatom exceeded 7.0Å. Combining our results with the work carried out by Kaledin *et. al.*,[331] we determined a constrained distance of 9.0Å between cation and heteroatom to be the most accurate model; from this point on, a model with constraints will feature K cations at 9.0Å from the heteroatom.

Having established that we can accurately replicate the WD POM in terms of framework dimensions and the distance between cation and heteroatom, we wanted to compare simulated

spectra against the available empirical data. Additionally, we synthesized the POM and carried out NMR and UV-Vis spectroscopy on the compound to verify the existing spectroscopy literature. We were able to replicate the empirical spectroscopy to a high degree of accuracy, see **Appendix 2.1** for the full details.

Having established the appropriate level of theory required for accurate spectroscopic calculations of medium-sized POMs, we move on to the primary focus of this paper: DFT-modelling of $[P_2W_{12}O_{48}]^{14-}$. Compared with its parent **{P_2W_{18}}**, there is significantly less reported spectroscopy for the hexalacunary; there exists only one crystal structure for $[P_2W_{12}O_{48}]^{14-}$, which was not determined until 2023,[328] and there is no UV-Vis data for this species, unfortunately. There is even less data available for the arsenic and selenium analogs.

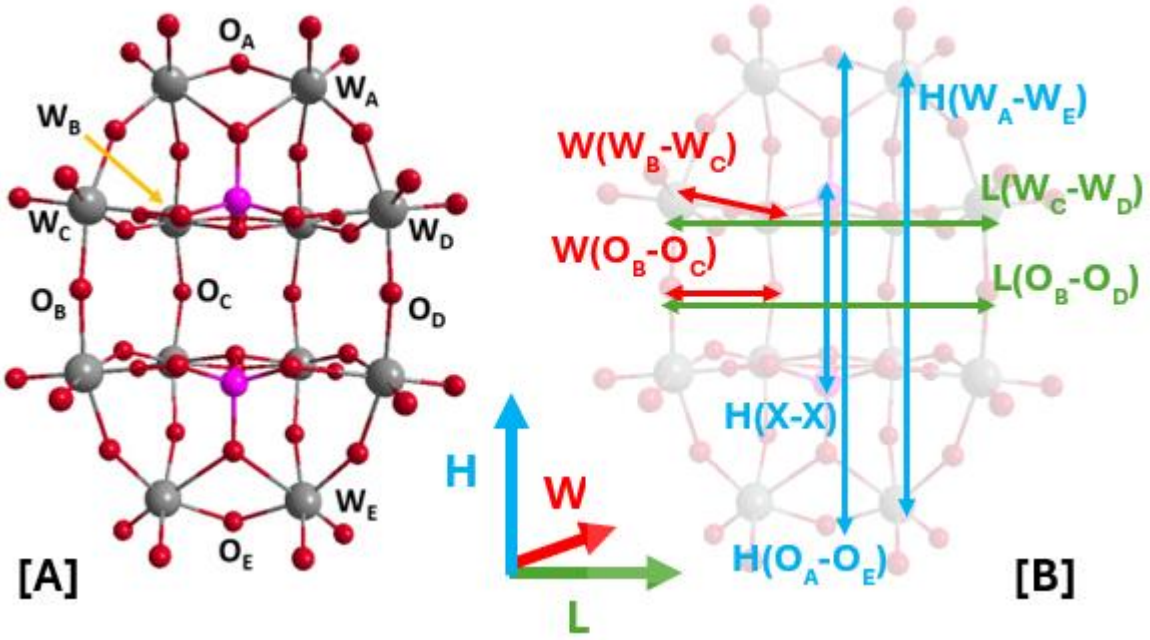

Figure 6.6 Atoms are labelled **(A)** and the dimensions between them specified **(B)** for hexalacunary POMs. Colour scheme: W: grey, O: red, P: pink

We initially compared the recently determined crystal structure for **{P_2W_{12}}**[328] with our converged DFT model and observed that the deviation in structure dimensions between the two was small, with a mean deviation value of only 0.11Å (**see Fig. 6.6.-6.7.**).

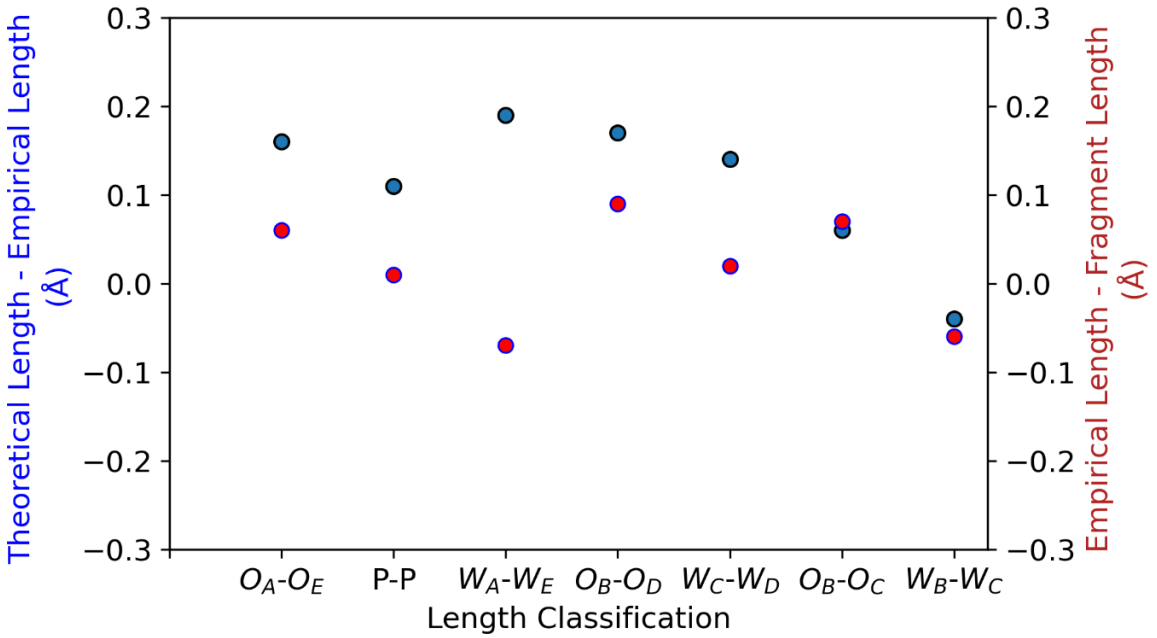

Figure 6.7 Comparison in dimensions between empirical and theoretical $[P_2W_{12}O_{48}]^{14-}$ frameworks. Empirical data is split into $[P_2W_{12}O_{48}]^{6-}$ xyz and the $[P_2W_{12}O_{48}]^{6-}$ segment of a full $[P_8W_{48}O_{184}]^{40-}$ POM wheel. **OPT/PBE/TZP/SFC/COSMO**

We repeated this process for the As and Se hexalacunary variants **(see Figure 6.8 for the full results for all 3 hexalacunaries)**. Despite the absence of available crystal structures for the individual species, there was data for the full **{As_8W_{48}}** and **{Se_8W_{48}}** POM wheels. In this case we took a single hexalacunary quarter from the W_{48} wheel and we were able to compare it against our DFT calculations **(see Appendix-2.2 for dimensions and spectra for {As_2W_{12}}, {P_2W_{12}}, and {Se_2W_{12}})**.

Repeating the process with **{P_8W_{48}}** to act as a control, we deduced that, with a couple exceptions, the dimensions of hexalacunaries, regardless of the heteroatom displayed, tended to remain within a deviation of 0.2Å (between our computational model and the experimental data) when sampled from a **{X_8W_{48}}**-type POM instead of as a separate POM species. We are therefore able to take a hexalacunary section from a **{X_8W_{48}}** wheel and treat it as a distinct, individual hexalacunary species **(see Appendix-1.2 for further details on how we chose to model {Se_2W_{12}} specifically)**.

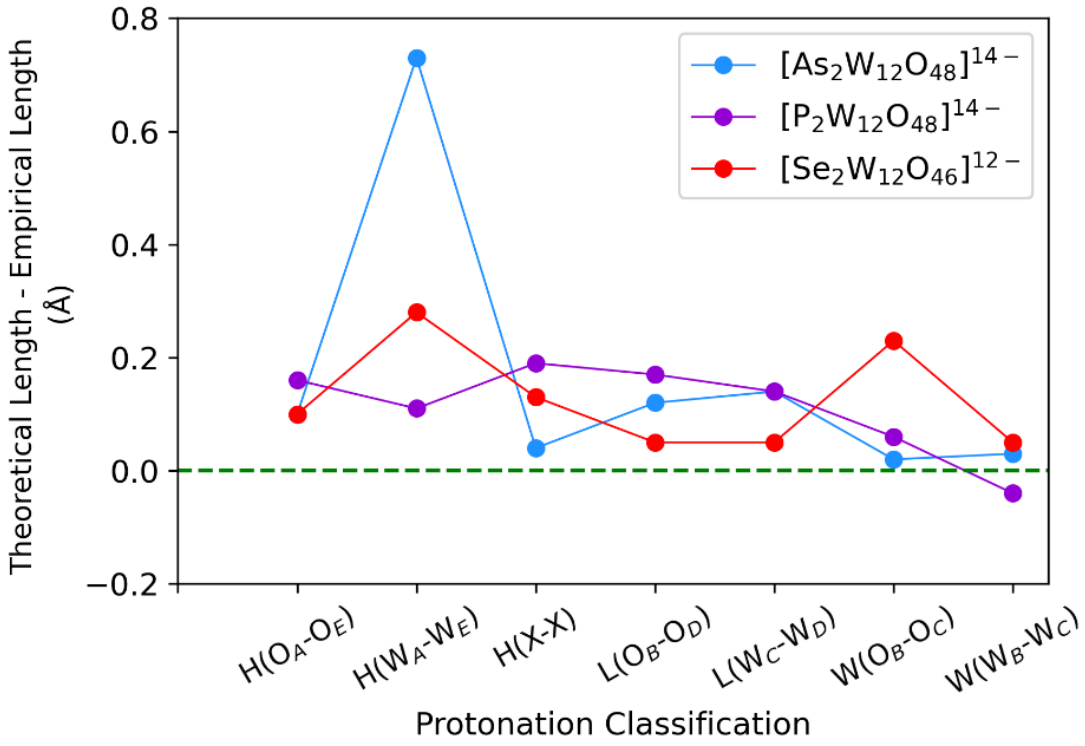

Figure 6.8. Using our specified dimensions, mean structural deviation is determined by subtracting the theoretical dimension from the empirical counterpart for the Arsenic-,[83] Phosphorus-,[328] and Selenium-containing[78] species **(C)**. A deviation of 0.0Å represents an identical value for both empirical and theoretical dimensions. **OPT/PBE/TZP/SFC/COSMO**

By far the biggest deviation, 0.73Å, occurs in the H(W-W) dimension for **{As$_2$W$_{12}$}**, which is a lot shorter in the empirical structure than the DFT model. This is due to the empirical dimensions originating from a W$_{48}$-type POM; the hexalacunary units within this structure curve inwards to form the wheel shape, leading to a shortening of the H(W-W) dimension. The structural tension which causes this is absent when the hexalacunary exists as an individual POM framework. It is unclear why this stretching is only present when the templating anion is $[AsO_4]^{3-}$, but it could be related to the radius of arsenic, which is larger than both phosphorus and selenium. Regardless, the total deviation amounts to less than 1.0Å, a relatively small distance, and in any case, is ultimately irrelevant as we are focussing on discrete hexalacunary clusters, not those which are contained within **{W$_{48}$}** POM wheels.

We shall seek to improve the accuracy of our hexalacunary model by breaking our modelling into 3 sections: inclusion of only the potassium cations, only the protons, and finally combining both cations and protons to construct as full a structure as possible.

6.2.2 Inclusion of Potassium Cations with Hexalacunary POM

We based the positions of the 12 potassium countercations around the **{P_2W_{12}}** POM using our previous work,[329] where we established the positions of potassium cations around the **{P_8W_{48}}** POM using existing crystallographic data; from this we determined the positions of 9 of the cations and added the remaining 3 in such a way as to maximise symmetry, theorising that these chosen vacant sites would be the most likely to be occupied upon successive addition of potassium cations. See **Fig 6.9.** for the geometries of the countercation configurations.

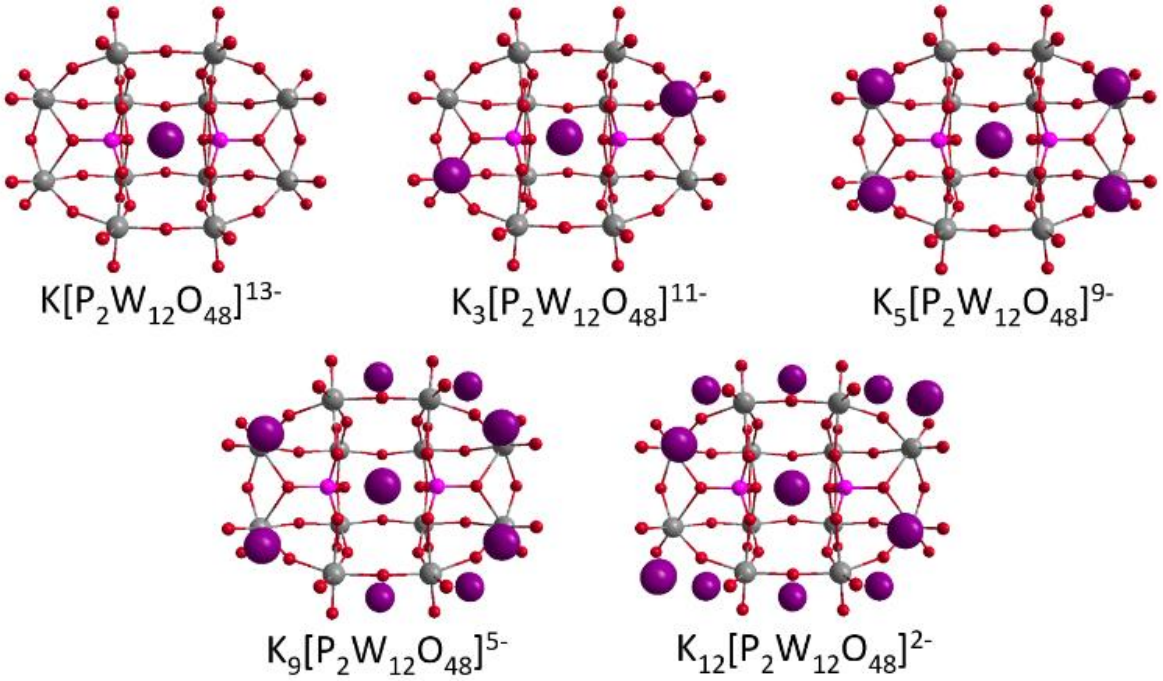

Figure 6.9. Ball and stick models of the $[P_2W_{12}O_{48}]^{14-}$ hexalacunary framework, specifically highlighting the position of potassium countercations around the structure. In the instance of $K_{12}[P_2W_{12}O_{48}]^{2-}$, the twelfth cation is located at the 'back' of the hexalacunary and is thus obscured behind the central cation in this figure.

Previous work by Kaledin *et. al.*[331] indicated that countercations tend to over stabilize HOMO and LUMO energy levels; an implicit solvent model, such as COSMO, does not correctly simulate the solvent molecules, which would usually surround each countercation in an empirical system, as this significantly reduces the complexity of the calculation. Without constraints on cation-POM distance, optimization calculations tend to converge with the countercations closer to the POM consequently, at a distance of 3-6Å from the nearest phosphorus heteroatom. Based on our findings for the Wells-Dawson structure outlined earlier (**see Appendix-2.1**) combined with the work of *Pasucal-Borràs, M. et al.*[331,332] we determined a constrained distance of 9.0Å between cation and heteroatom to be the most accurate model; from this point on, a model with constraints will feature K cations at 9.0Å from the heteroatom.

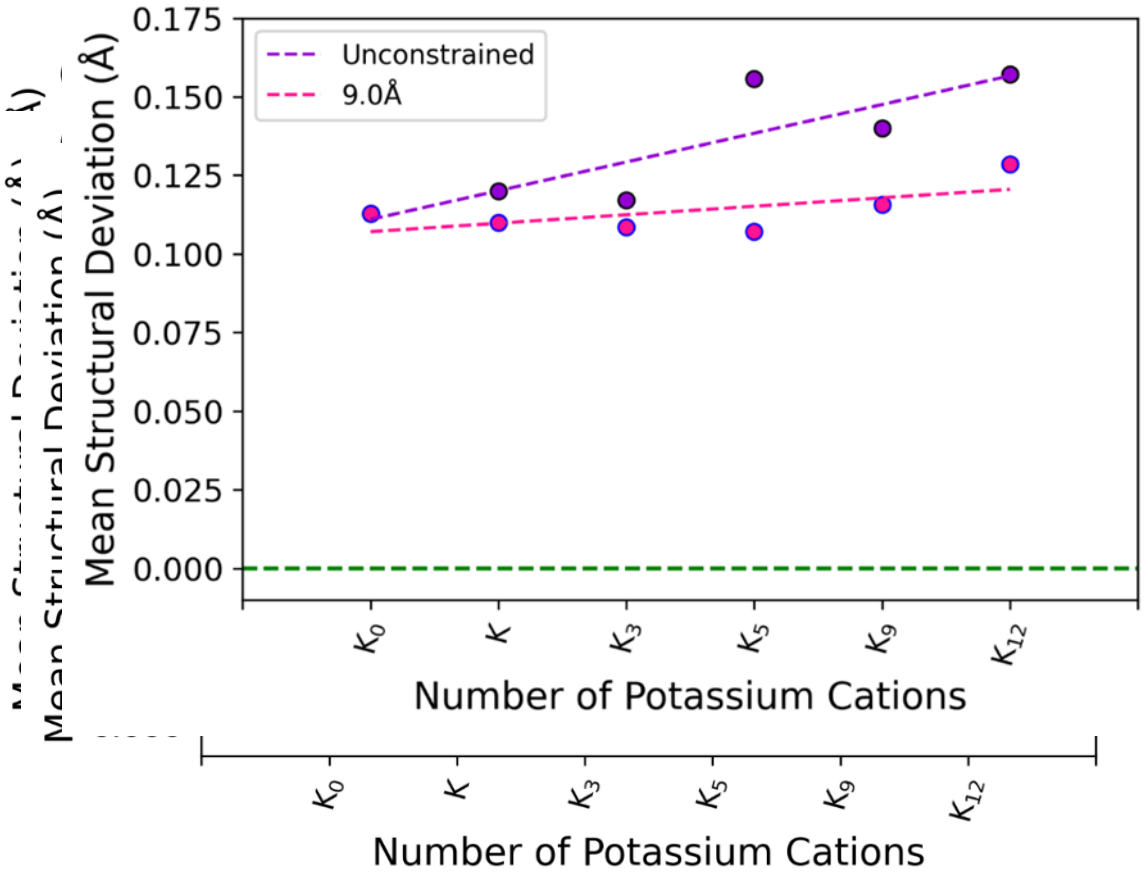

Figure 6.10. Comparison in dimensions between empirical and theoretical $K_n[P_2W_{12}O_{48}]^{(n-14)}$ frameworks across a range of different n values for K. Distances between the cation and heteroatom are either unconstrained or constrained at 9.0Å. A dashed line is provided at 0pm to illustrate relative differences of error. **OPT/PBE/TZP/SFC/COSMO**

Compared to when the **K_n{P_2W_{12}}** models are unconstrained, the deviation in the constrained models from the empirical dimensions increased less rapidly as cations were successively added (see **Table A-2.11** for unconstrained and **Table A-2.12** for constrained). The difference in deviation between constrained and unconstrained models was minimal, never exceeding a difference of 0.05Å. There exists no substantial correlation between adding more potassium countercations to the hexalacunary model and the dimensions of the hexalacunary significantly changing as a result, although structural warping is less prevalent when the cations are further away from the framework (**Figure 6.10.**).

Deviation is slightly greater for the arsenic and selenium counterparts, maxing out at -0.07Å (**Figure 6.11.**) and 0.12Å (**Figure 6.12.**) respectively. For the phosphorus and selenium species, the constrained model almost always deviates less from the empirical xyz crystal than the unconstrained model; this is to be expected as the countercations are further from the POM in the constrained version. Curiously, **{As_2W_{12}}** features greater geometry distortion in the constrained model than the unconstrained one, specifically in the O_B-O_D and W_C-W_D dimensions.

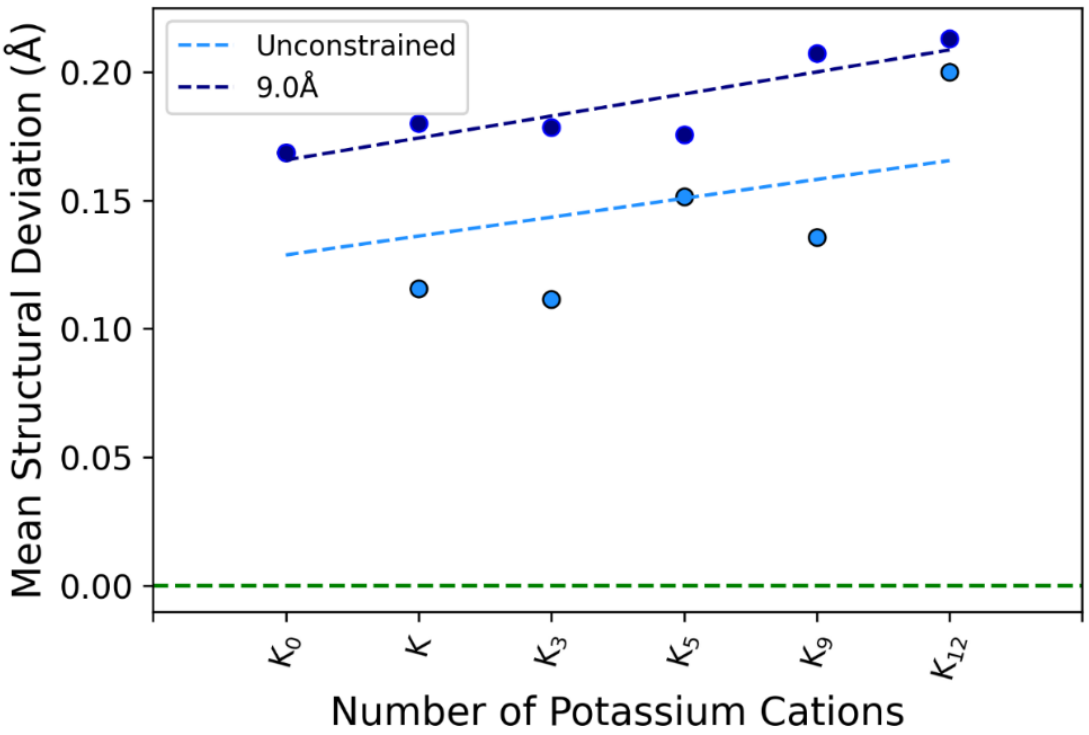

Figure 6.11. Comparison in dimensions between empirical and theoretical $K_n[As_2W_{12}O_{48}]^{(n-14)}$ frameworks across a range of different n values for K. Distances between the cation and heteroatom are either unconstrained or constrained at 9.0Å. A dashed line is provided at 0pm to illustrate relative differences of error. **OPT/PBE/TZP/SFC/COSMO**

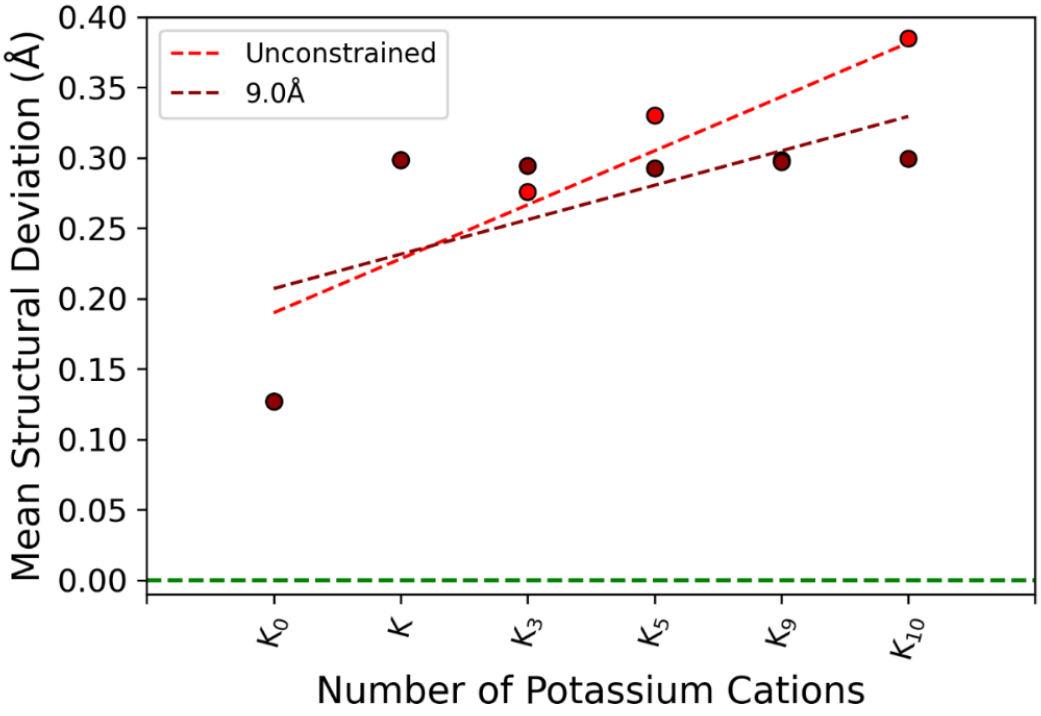

Figure 6.12. Comparison in dimensions between empirical and theoretical $K_n[Se_2W_{12}O_{46}]^{(n-12)}$ frameworks across a range of different n values for K. There are 3 different possible configurations for $K_{10}[Se_2W_{12}O_{46}]^{2-}$, designated as 'Front', 'Side', and 'Top'; the value given in the figure is the average structural deviation across all 3 configurations. Distances between the cation and heteroatom are either unconstrained or constrained at 9.0Å. A dashed line is provided at 0pm to illustrate relative differences of error. **OPT/PBE/TZP/SFC/COSMO**

After compiling all our results, we found that including more potassium cations in the geometry generally led to a greater degree of structural deviation in our computational model when compared to the empirical dimensions (**Figure 6.13, 6.14**). The selenium hexalacunary displayed by far the greatest magnitude of structural deviation, followed by arsenic and finally phosphorus. When comparing the difference between the unconstrained (**Figure 6.13**) and constrained (**Figure 6.14**) models, we found this difference to be generally within a limit of 0.1Å, with constrained models suffering from less distortion due to the cations being kept further from the geometry (**Figure 6.15**). From this, we observed structures with either 3 or 9 countercations featured the smallest deviation in dimensions between the empirical and simulated geometries, but 3 was chosen as the ideal number due to the reduction in complexity

inherent in omitting 6 countercations (**see Appendix 2.3 for the full list of dimensions and spectra gathered for $K_m[X_2W_{12}O_{48}]^{n-}$**).

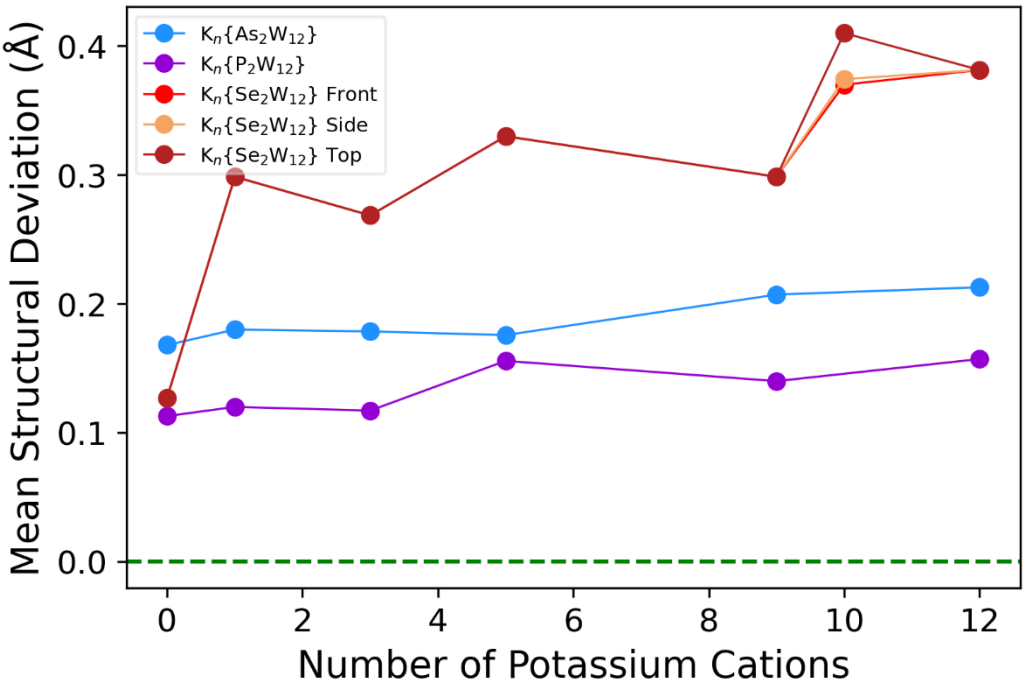

Figure 6.13. Comparison in dimensions between empirical and theoretical $K_n[As_2W_{12}O_{48}]^{(n-14)}$, $K_n[P_2W_{12}O_{48}]^{(n-14)}$, and $K_n[Se_2W_{12}O_{46}]^{(n-12)}$ frameworks across a range of different n values for K. Distances between the cation and heteroatom are unconstrained. **OPT/PBE/TZP/SFC/COSMO**

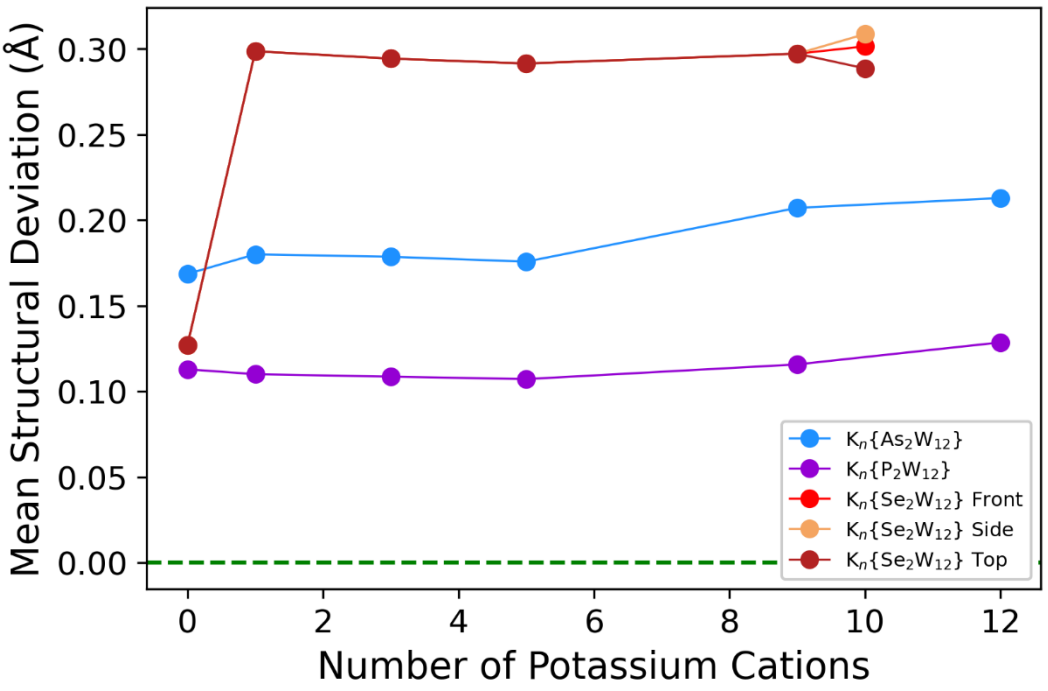

Figure 6.14. Comparison in dimensions between empirical and theoretical $K_n[As_2W_{12}O_{48}]^{(n-14)}$, $K_n[P_2W_{12}O_{48}]^{(n-14)}$, and $K_n[Se_2W_{12}O_{46}]^{(n-12)}$ frameworks across a range of different n values for K. Distances between the cation and heteroatom are constrained at 9.0Å. **OPT/PBE/TZP/SFC/COSMO**

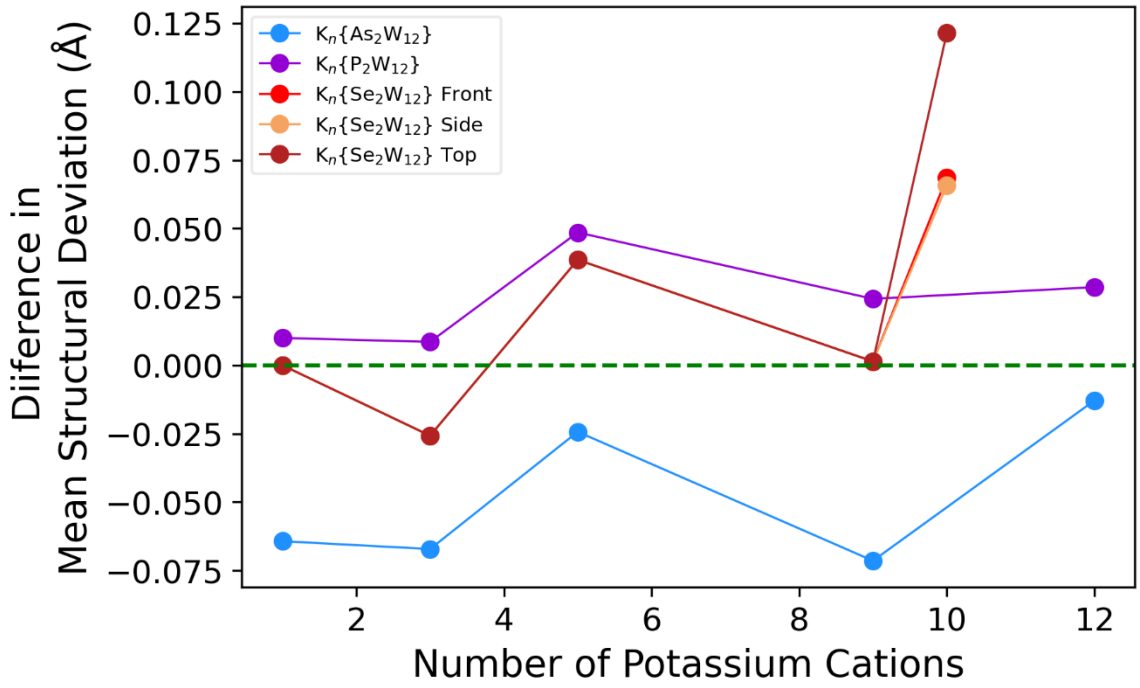

Figure 6.15. Comparison in dimensions between $K_n[As_2W_{12}O_{48}]^{(n-14)}$, $K_n[P_2W_{12}O_{48}]^{(n-14)}$, and $K_n[Se_2W_{12}O_{46}]^{(n-12)}$ frameworks across a range of different n values for K when the distances between the cation and heteroatom are either unconstrained or constrained at 9.0Å. **OPT/PBE/TZP/SFC/COSMO)**

6.2.3 Inclusion of Protons with Hexalacunary POM

Determining the likely regions of protonation is more difficult than with the countercations, as there is no crystal structure data to aid us; as x-ray diffraction works by detecting x-rays scattered by electron dense nuclei, the least dense element, hydrogen, is the most difficult to pick up, especially if in close proximity to much heavier elements. The only method open to us is to simply model and run an optimization calculation for every possible configuration of protonation. From this we will observe which geometries have the lowest electronic energy,

and the general effect of protonation on structural deviation and HOMO-LUMO gap magnitudes to determine the most likely geometries to be present in solution.

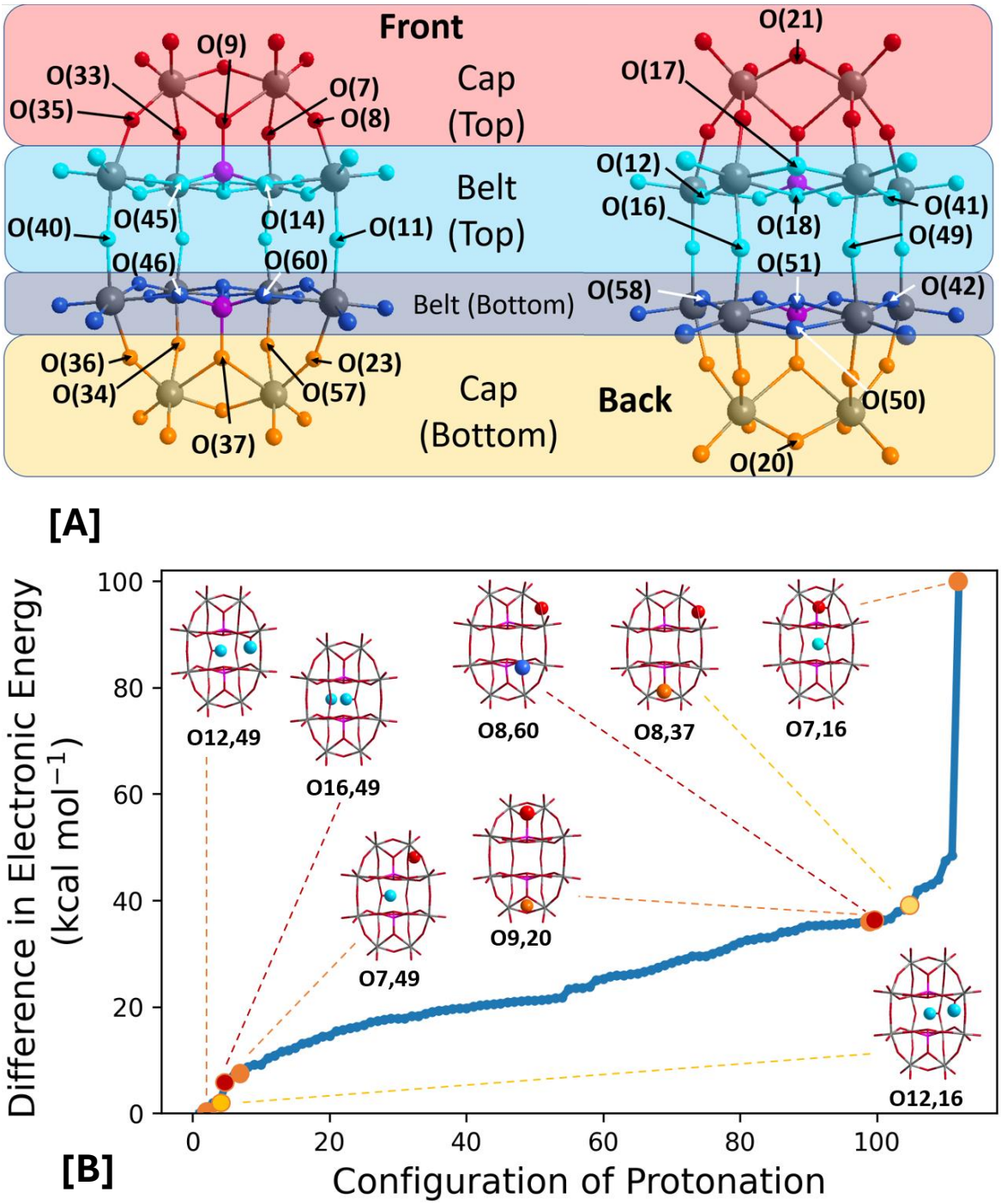

Figure 6.16. Protonation configurations (**A**) and electronic energy values (**B**) for $[H_2P_2W_{12}O_{48}]^{12-}$, the protonation configurations for both in ascending order of electronic energy. All energies are relative to the lowest electronic energy, which is associated with the configuration O12,42. Energies of selected configurations are highlighted in yellow, orange, and red.

There are several types of oxygens within a POM framework, which we differentiate based on their binding configuration: terminal [W=O] tungsten bridging [W-O-W], and heteroatom bridging, which can be either bind to 1 [X-O-W] or 2 [X-O-W(-W)] tungsten atoms. Taking into account that only bridging oxygens (no matter what other elements they bridge) are suitable for protonation,[2] the total number of possible configurations amounts to 112; see **Figure 6.16 [A].** for the guide on how to assign each configuration and **Appendix-2.4** for the full list of geometries for all protonation configurations. The range of electronic energies across the different configuration is surprisingly high, with a 48.4kcal mol^{-1} difference between the highest and lowest energy values, **see Figure 6.16 [B].** Though geometries with at least 1 proton located in the belt region tended to have a more negative electronic energy and a larger HOMO-LUMO gap, there is little correlation between the location of the proton with relation to the cap or belt, how far apart the protons are from each other, or in how negative the electronic energy value ties with the size of the HOMO-LUMO gap, **see Figure 6.17.**

We selected four geometries which ranked within the top 10 for both low electronic energy and large HOMO-LUMO gap, and four which ranked highest in electronic energy with a small HOMO-LUMO gap (lowest 10). These were **O7,49**, **O12,16**, **O12,49**, and **O16,49** for the top 10, and **O8,37**, **O8,60**, **O9,20,** and **O7,16** for the bottom 10 respectively. In this way a handful of configurations can act as representatives of the full library.

When comparing the HOMO-LUMO gaps for the selected protonated geometries, we found that the gap could vary by as much as 0.9eV, a not inconsiderable deviation, though variance was mostly confined to a roughly 0.3eV window ranging from 2.85-3.12eV. This wide range in potential HOMO-LUMO gap values has little to no difference on the dimensions of the hexalacunary structure; we observed that the mean difference in structural dimensions between the large and small H-L groups respectively was 0.0025Å – a truly miniscule value, even on a molecular scale.

Determining the handful of protonation configurations the structure is most likely to adopt is therefore more dependent on having the empirical HOMO and LUMO orbital energies than it

is on the framework dimensions, sourced from crystallographic data. Without UV-Vis spectroscopy, we can only speculate as to the geometry configurations featured by the hexalacunary when in solution.

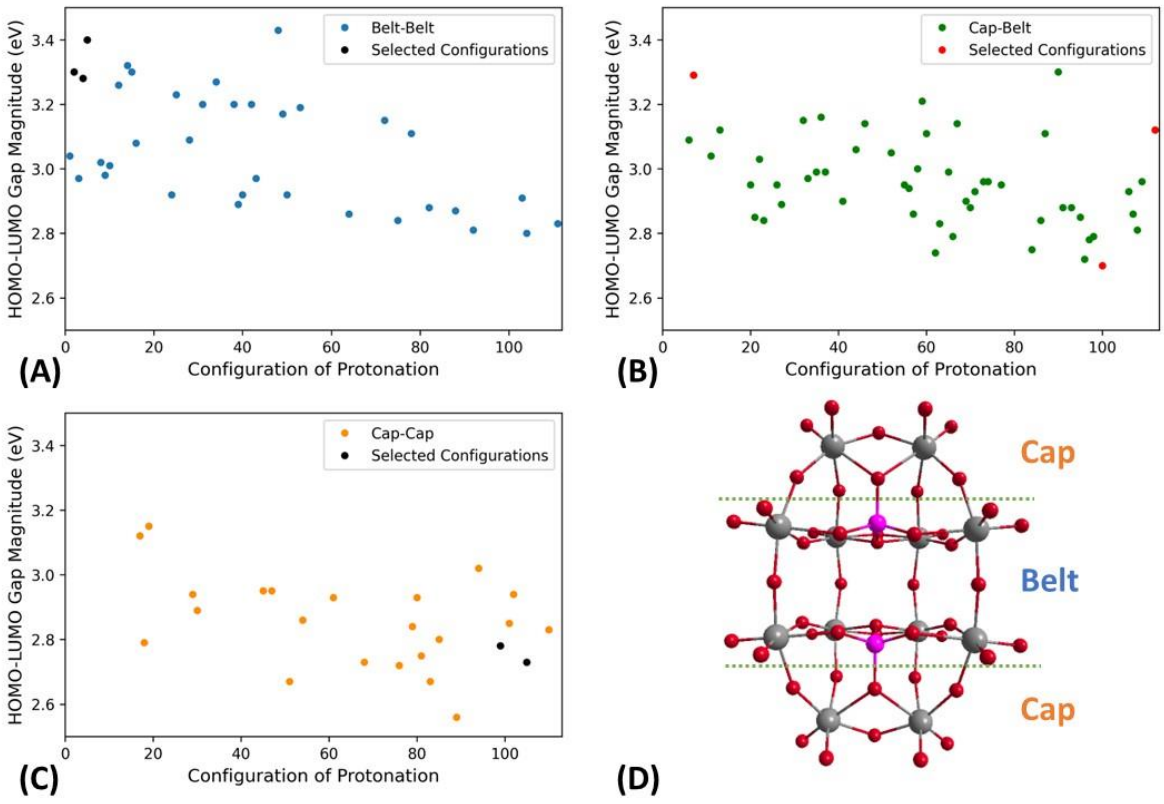

Figure 6.17. HOMO-LUMO gap values for $[H_2P_2W_{12}O_{48}]^{12-}$ frameworks in ascending order of electronic energy. All energies are relative to the lowest electronic energy, which is associated with the configuration O12,42. Different configurations are collected into three separate groups based on the type of bridging atoms the protons are bound to: Belt-Belt **(A)**, Cap-Belt **(B)**, and Cap-Cap **(C)**. Configurations are coloured according to their respective group **(D).** Configurations we examine in further detail later are highlighted black or red (**O12,49, O12,16,** and **O16,49** for Belt-Belt**, O7,49, O8,60,** and **O7,16** for Cap-Belt, and finally **O9,20** and **O8,37** for Cap-Cap).

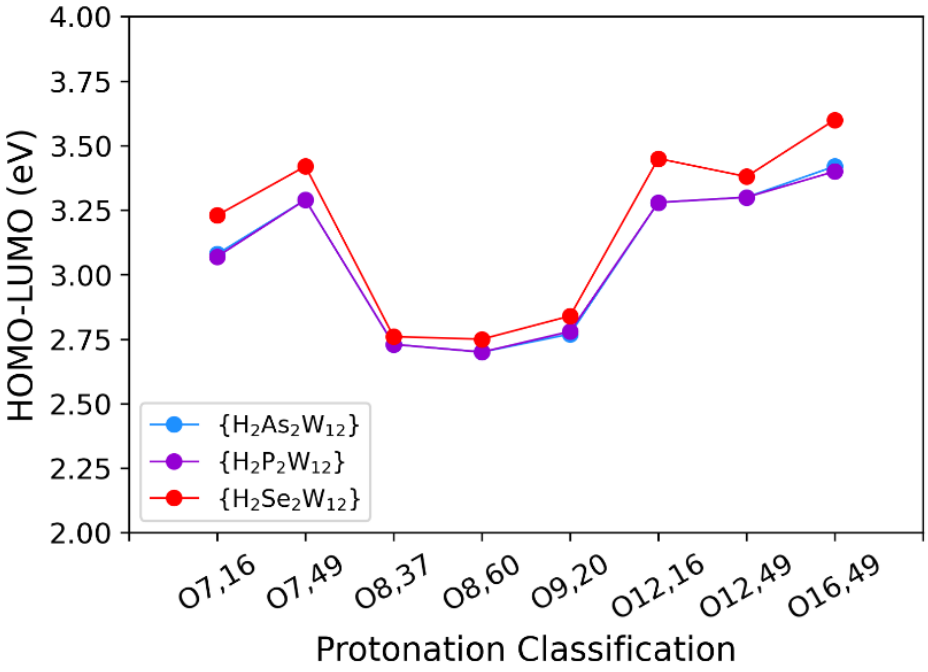

Figure 6.18. Comparison in HOMO-LUMO energy gap values between $[H_2As_2W_{12}O_{48}]^{12-}$, $[H_2P_2W_{12}O_{48}]^{12-}$, and $[H_2Se_2W_{12}O_{46}]^{10-}$ configurations. **OPT/PBE/TZP/SFC/COSMO**

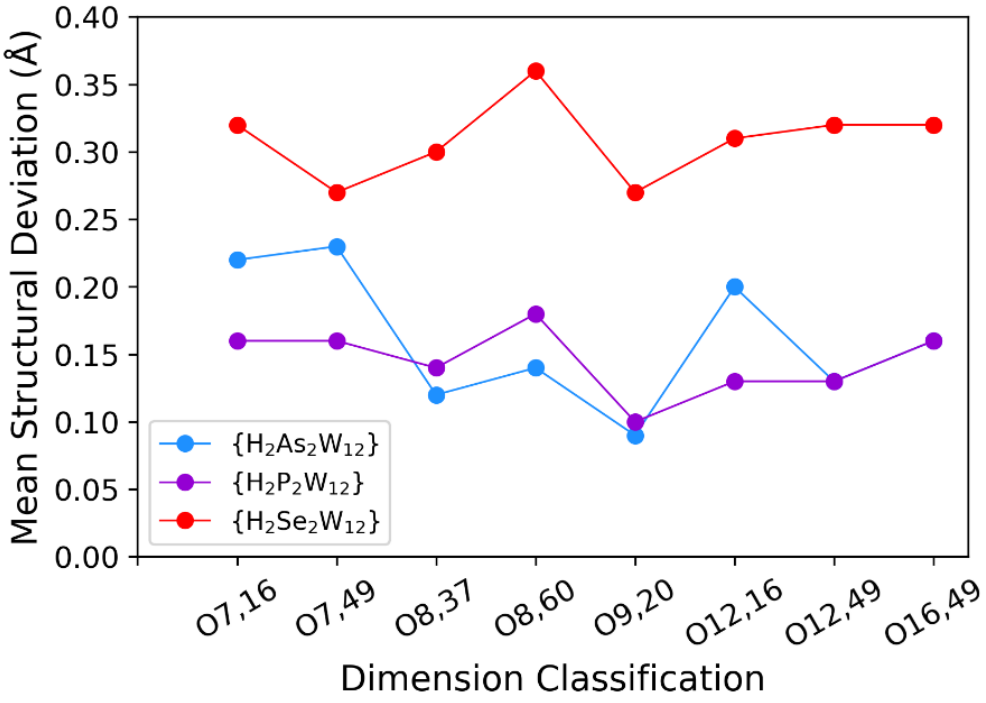

Figure 6.19. Comparison in values for standard deviation of framework dimensions between $[H_2As_2W_{12}O_{48}]^{12-}$, $[H_2P_2W_{12}O_{48}]^{12-}$, and $[H_2Se_2W_{12}O_{46}]^{10-}$ configurations. **OPT/PBE/TZP/SFC/COSMO**

This trend mostly follows for Arsenic and Selenium, with large variance in the HOMO-LUMO gap value (**Fig 6.18.**) and small deviation in the structural dimensions (**Fig 6.19.**). It is worth noting that deviation between theoretical and empirical dimensions is greater in the Selenium-containing hexalacunary, with an XO_3 heteroatom, than the Arsenic- or Phosphorus-containing species, both with XO_4 heteroatoms; this is true whether the cations or protons are present or absent.

We theorise this to be caused by the oxidation state of the heteroatom species; the two missing oxygen atoms would usually aid in holding the structure together, but without them stretching of the POM cage becomes a greater factor. While this warping is still relatively small, it may partially explain why **{Se_2W_{12}}** has yet to be isolated, as it is less structurally robust than its **{As_2W_{12}}** and **{P_2W_{12}}** counterparts.

6.2.4 Inclusion of both Potassium Cations and Protons in Hexalacunary Model

For the final section of this paper, where we combine our established cation and proton geometries, we created 2 families of structures, these being hexalacunaries which are completely charge neutral, $K_{12}[H_2P_2W_{12}O_{48}]$, and those which learn from the findings of earlier sections of this paper; the latter features only 3 potassium cations as this was earlier established to be the ideal number, $K_3[H_2P_2W_{12}O_{48}]^{9-}$. All the structures within each family share the same number of potassium countercations, the only difference is in the proton configurations utilised; these are the **O7,49**, **O12,16**, **O12,49**, and **O16,49** configs already described (**see Figure 6.20. (A-D)**).

With respect to deviation in molecular dimensions between the theoretical and empirical structures for **{K_3H_2}** and **{$K_{12}H_2$}** hexalacunaries, there is minimal difference in deviation. There is little point including all 12 potassium cations as this does not lead to a substantial improvement in this deviation value (**see Figure 6.20. (E)**). See **Appendix-2.5** for collection

of key parameters and variables for when cations and/or protons are either present or absent in a hexalacunary $K_m[H_nX_2W_{12}O_{48}]^{q-}$ POM.

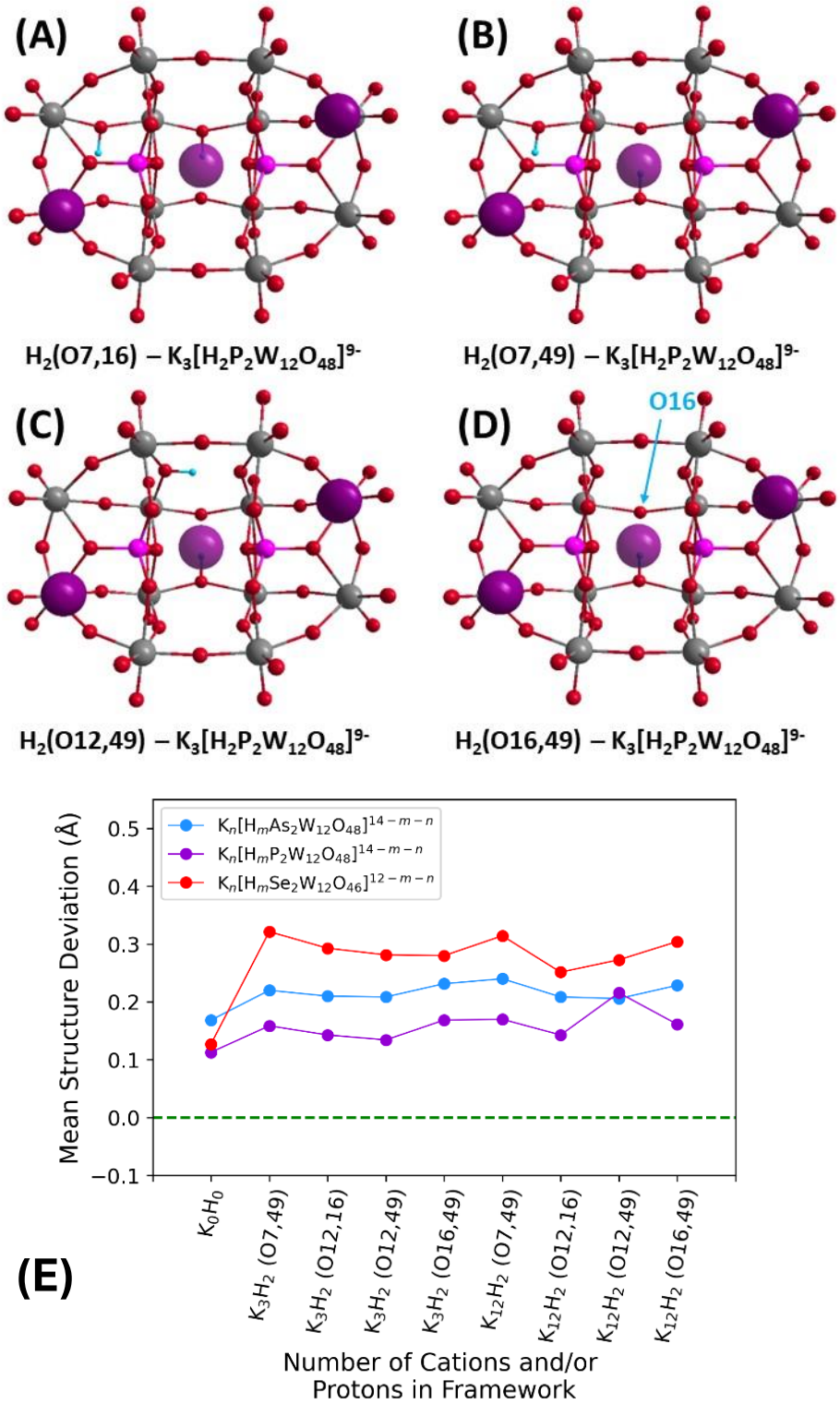

Figure 6.20. Selection of $K_3[H_2P_2W_{12}O_{48}]^{9-}$ **(A-D)** and $K_{12}[H_2P_2W_{12}O_{48}]^{9-}$ structures, each with a unique proton configuration which is designated by the specific oxygens protonated. Using the same dimensions outlined in **Fig. 6.3**, we determined the mean difference between empirical and theoretical dimension magnitude, collecting this as a single deviation value for the geometry **(E)**.

6.2.5 Charge Distribution Analysis

One parameter we have yet to touch upon is that of charge distribution; the combined atomic charge value for all atoms is determined and from this, the standard deviation in electron distribution throughout the framework is calculated. Considering that a large standard deviation (SD) value represents a large degree of difference between all the populations examined, a large SD value in the context of atomic charge indicates a polarized molecule; electrons are localized in one area, rendering the rest of the structure relatively electron deficient. Likewise, a smaller SD value equates to more electron delocalization throughout the POM framework, as the electrons are more evenly spread out, therefore indicating the POM species is less reactive than a more polarized molecule.

While we cannot empirically validate how polarized a molecule is, we can use the charge distribution to observe how introducing different elements to our structure affects polarization and where other molecular species are most likely to bind to the POM. By testing the reactivity of several different compounds with a given hexalacunary POM in the lab, or vice versa, and attempting to computationally rationalize relative reactivities, we may be able to justify, albeit indirectly, our calculated SD values for various POM species. This, however, is beyond the scope of this paper, though we can at least report our computational findings.

In order to calculate SD for a calculated molecule, we wrote and used a python script which parsed out the relevant MDC-q charge values we needed from the output file. The scripts used can be found in the following github repository: https://github.com/POM-Wheel/AMS-Molecule-Electron-Distribution. The Charge-Density-Code-Operate.py script utilizes functions from Charge-Density-Code-Functions.py, separated into two files to present a tidier user interface.

With regards to the progressive addition of countercations, we found that electronic standard deviation tended to decrease as more cations were included in the structure. This makes sense, as the anionic charge is being steadily reduced to zero and the cations are arranged in such a

way so as to be placed in polarized areas, reducing polarization throughout the structure, see **Table A-2.30** and **Figure 6.21**.

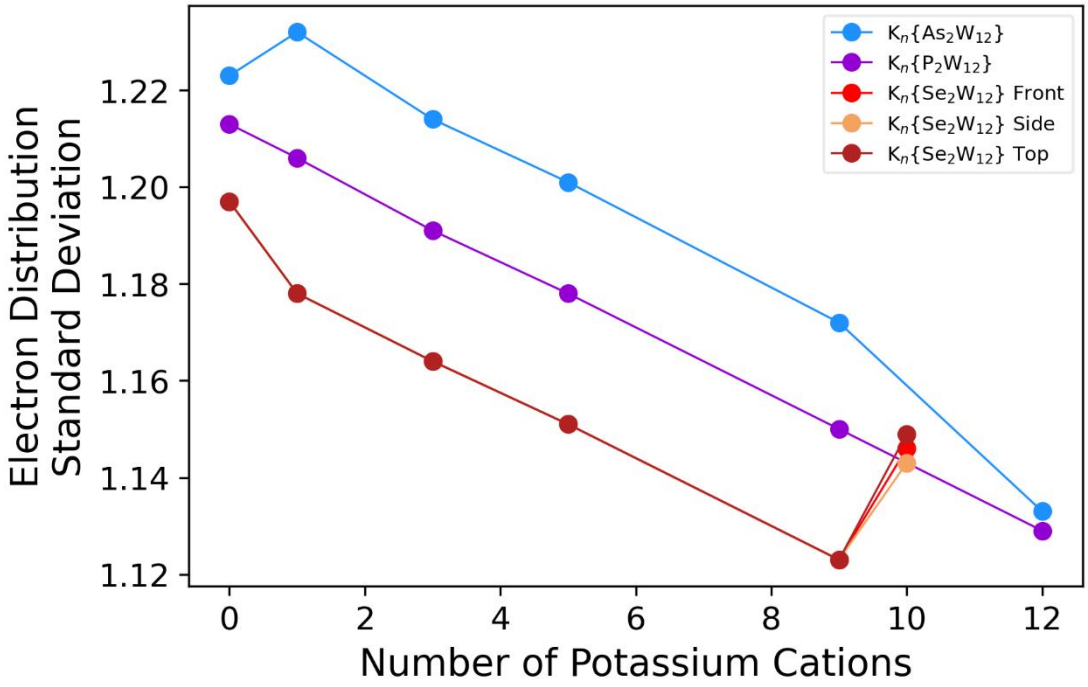

Figure 6.21. Comparison in values for standard deviation of electron distribution between $K_n[As_2W_{12}O_{48}]^{n-14}$, $K_n[P_2W_{12}O_{48}]^{n-14}$, and $K_n[Se_2W_{12}O_{46}]^{n-12}$ configurations. **OPT/PBE/TZP/SFC/COSMO**

Standard deviation dips markedly once hydrogen in included in the structure compared to potassium, and then remains at a consistent level, regardless of the specific protonation configuration present, see **Table A-2.31** and **Figure 6.22**. The inclusion of protons, however, has a greater stabilizing effect on charge distribution than cations do. The presence of 2 protons in absence of any other cations reduces total SD by 0.032, whereas including 5 potassium cations only reduces SD by 0.035. Completely charge neutralizing our model with both cations and protons does not yield the smallest degree of delocalisation, intriguingly, and instead levels off deviation around 1.16. This trend in charge distribution is replicated almost identically with the **{As_2W_{12}}** and **{Se_2W_{12}}** POMs.

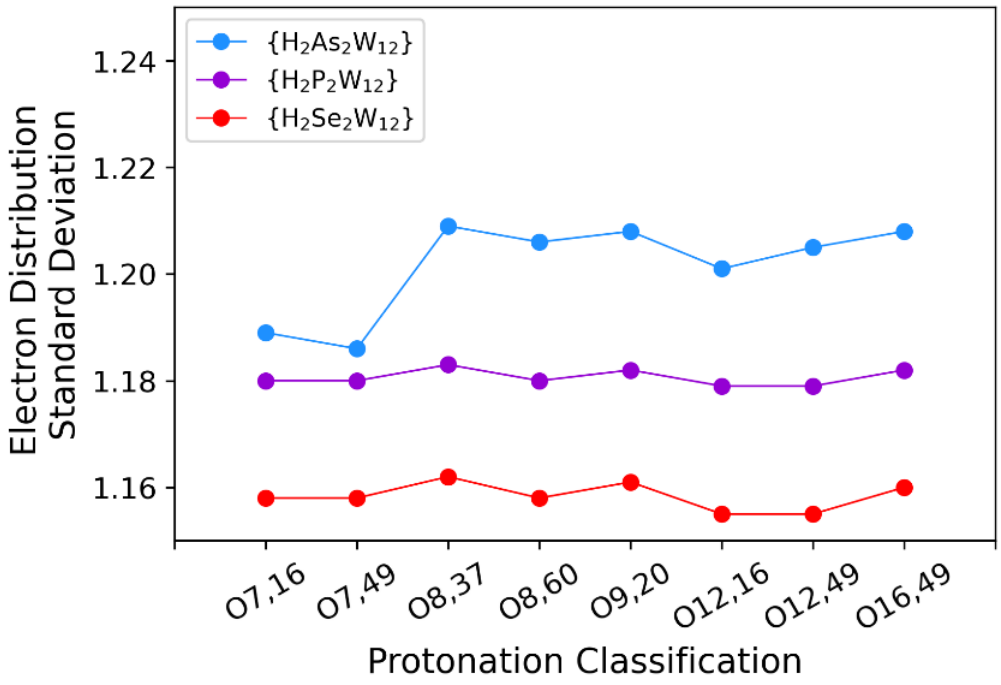

Figure 6.22. Comparison in values for standard deviation of electron distribution between $[H_2As_2W_{12}O_{48}]^{12-}$, $[H_2P_2W_{12}O_{48}]^{12-}$, and $[H_2Se_2W_{12}O_{46}]^{10-}$ configurations. **OPT/PBE/TZP/SFC/COSMO**

Taking **{P_2W_{12}}** as an overall example, we observed that successively adding potassium cations to the structure lead to a gradual decrease in charge distribution for the POM, from 1.213 to 1.129; this makes sense, as addition of more cations aids in spreading out the electron density, as well as reducing the overall anionic charge. The inclusion of protons, however, has a greater stabilizing effect on charge distribution than cations do. The presence of 2 protons in absence of any other cations reduces total SD by 0.032, whereas including 5 potassium cations only reduces SD by 0.035. We theorise that the size of protons causes these results; they are able to move much closer to the framework than larger countercations, such as potassium, and therefore are able to have a greater influence on stabilizing electron distribution throughout the cage.

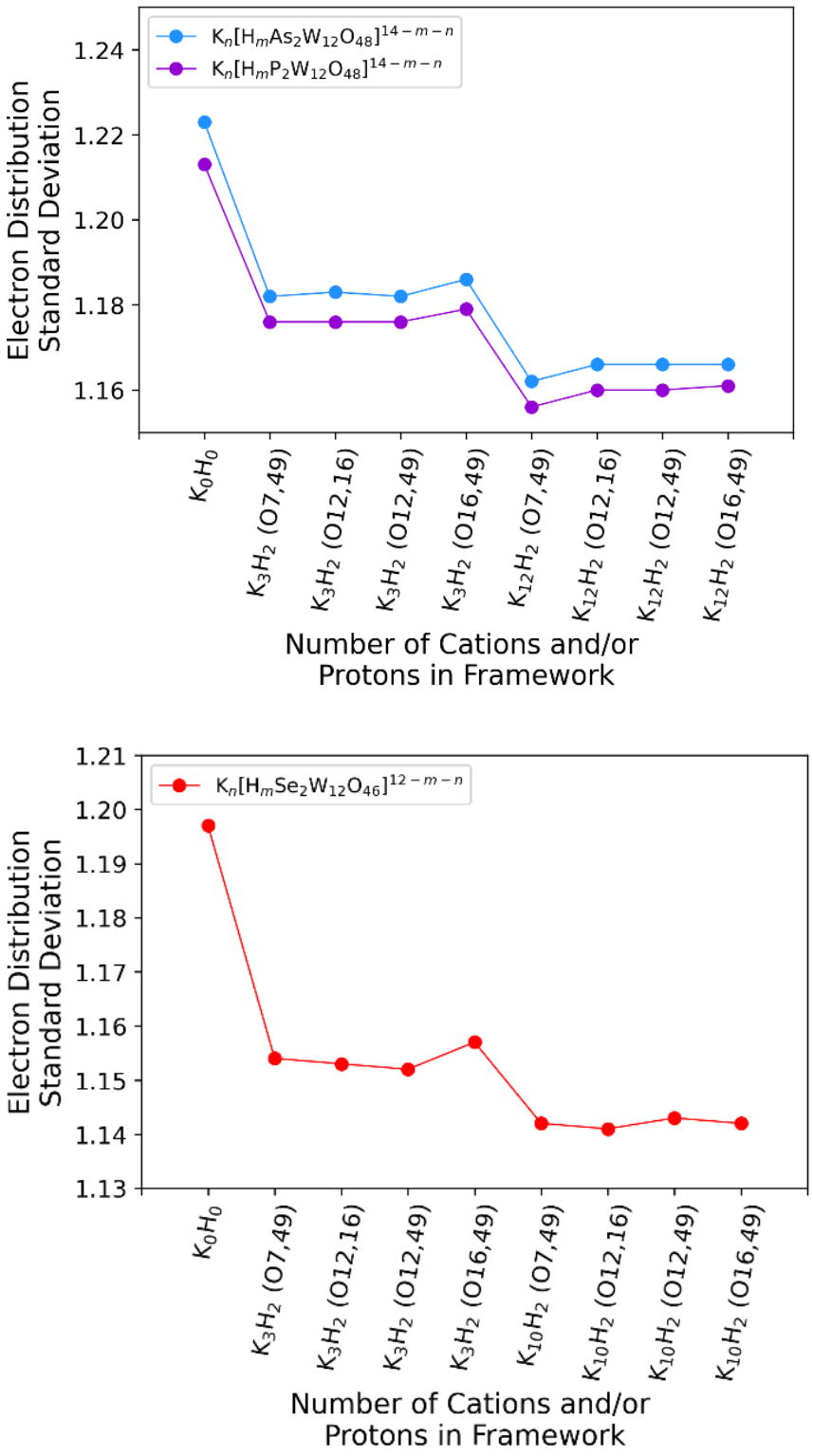

Figure 6.23. Comparison in values for standard deviation of electron distribution between $[H_2As_2W_{12}O_{48}]^{12-}$, $[H_2P_2W_{12}O_{48}]^{12-}$, and $[H_2Se_2W_{12}O_{46}]^{10-}$ configurations. **OPT/PBE/TZP/SFC/COSMO**

Completely charge neutralizing our model with both cations and protons does not yield the smallest degree of delocalisation, intriguingly, and instead levels off deviation around 1.16. This trend in charge distribution is replicated almost identically with the **{As_2W_{12}}** and **{Se_2W_{12}}** POMs **(see Figure 6.23 and Appendix-2.6 for the full summation of our findings)**.

This allows us to produce a less polarized model for a fraction of the complexity and computational cost associated with incorporating large countercations into the structure. Assuming a model with less polarization is more in line with the empirical structure than a more polarized model, a protonated model would be the favoured method of modelling the hexalacunary than only including countercations.

6.2.6 Theoretical Spectroscopy

Finally, we sought to determine if DFT-based spectroscopy, NMR specifically, could provide an accurate match to available empirical data. If in good agreement with, it could provide an extra level of verification for determining an empirical product while also, in the vein of promoting inverse design, giving us an idea of where identifying peaks for a theoretical molecule would lie.

Running our own empirical NMR spectroscopy on $K_{12}[H_2P_2W_{12}O_{48}]\cdot 14H_2O$, we produced the spectra in **Figure 6.24**, with the primary hexalacunary peak at -10.12ppm. This spectra is in good agreement with the literature, where the NMR peak is reported at -9.69ppm; we found our calculated NMR spectra for $[P_2W_{12}O_{48}]^{14-}$ to be relatively inaccurate by comparison, with a calculated shift at -3.58ppm (see **Table A-2.33**).

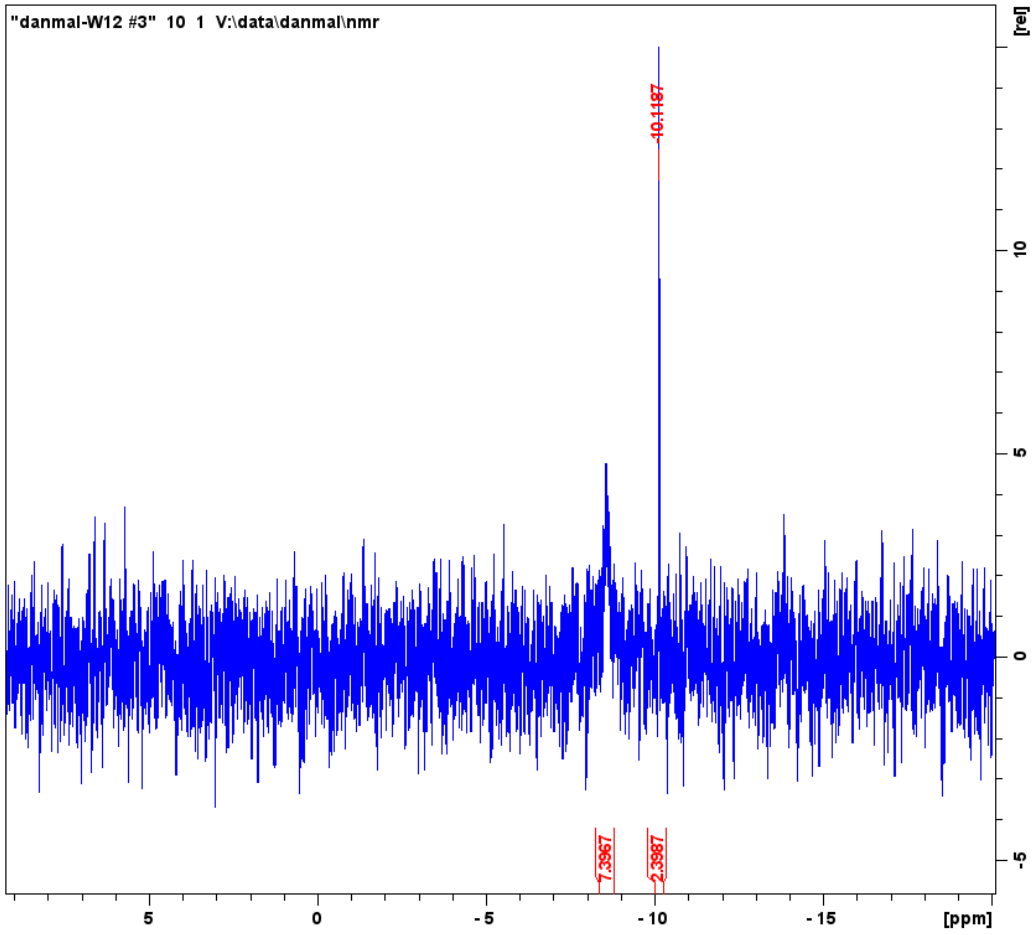

Figure 6.24. ^{31}P NMR spectra for $K_{12}[H_2P_2W_{12}O_{48}]\cdot 14H_2O$, following the synthetic method of Contant, R.[81] Primary peak at -10.12ppm is the hexalacunary.

Theoretical NMR spectra for $[P_2W_{12}O_{48}]^{14-}$ places the major peak at -3.58ppm. This deviates from the empirical data carried out by other researchers[328] and ourselves, where the peak is roughly -9.90ppm. It is unclear why there is such a difference in accuracy when hexalacunaries are the POM of choice instead of the WD framework, but we hypothesize the large anionic charge may play a part; the **{P_2W_{12}}** is surrounded by 12 potassium and 2 proton cations in solution, which may increase the accuracy of the simulated spectra if included in the computational structure.

When potassium countercations are included, theoretical NMR spectra tends to deviate more from the empirical data for hexalacunary POMs; it is worth noting that this deviation does not

increase as more cations are included but stays between the values of 2.0-3.2ppm for unconstrained models and 4.5-4.7ppm for the constrained models. The exception to this rule is the unconstrained $K_3[P_2W_{12}O_{48}]^{11-}$ geometry, which displays two peaks at -1.79 and -1.37ppm, by far the closest chemical shift values to the empirical range of -10.12 to -9.69ppm; despite this, it performs worse than when all cations are excluded from the hexalacunary (**see Fig. 6.25**).

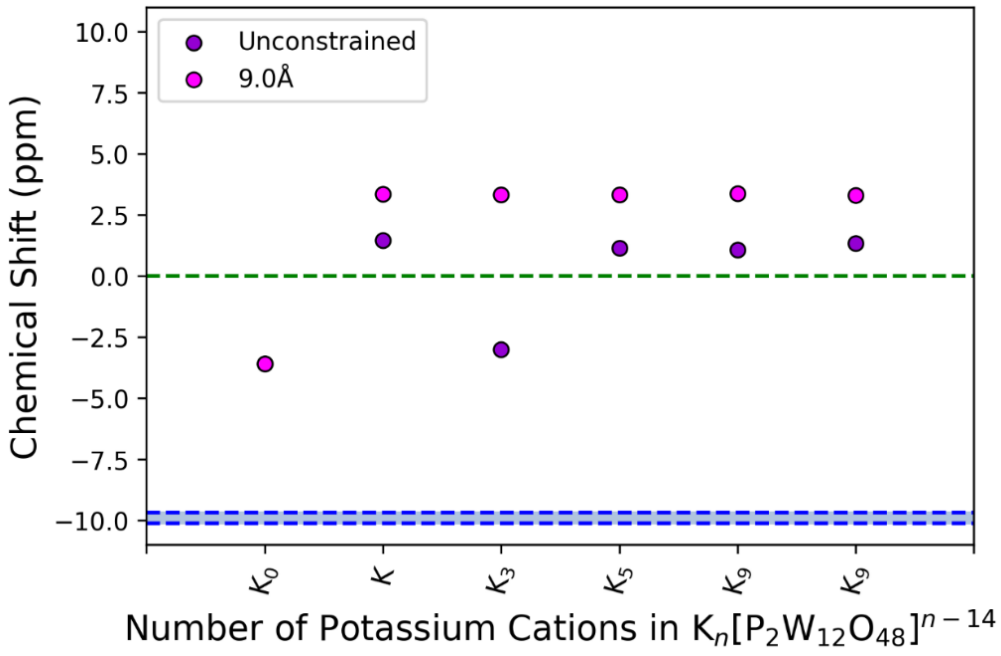

Figure 6.25. Theoretical $K_n[P_2W_{12}O_{48}]^{(n-14)}$ ^{31}P NMR spectra, with constrained and unconstrained models visualized. Where multiple peaks are reported in the calculation, a single mean chemical shift value is reported here. The empirical range for chemical shift is encapsulated between the dashed blue lines. A dashed green line at 0.0ppm is included for reference. **SP/PBE/TZP/SFC/COSMO/Spin-Orbit Relativity**

There is no protonation configuration from the 8 selected that improves over the base $[P_2W_{12}O_{48}]^{14-}$ structure with regards to the ^{31}P NMR spectra, with the peaks generally situated around 0ppm. It is worth mentioning that there is a great degree of variance in chemical shift values. There is no connection between electronic energy or size of the HOMO-LUMO gap and the corresponding chemical shift either (**see Fig. 6.26**).

When protons and 3 potassium countercations are included in the model, we found the chemical shift peaks to be roughly the same as for the solely protonated structures. Our calculations also

show that the predicted spectra worsens when 12 cations are included in the structure instead of only 3, by a margin of almost +7.0ppm (**see Fig. 6.27**).

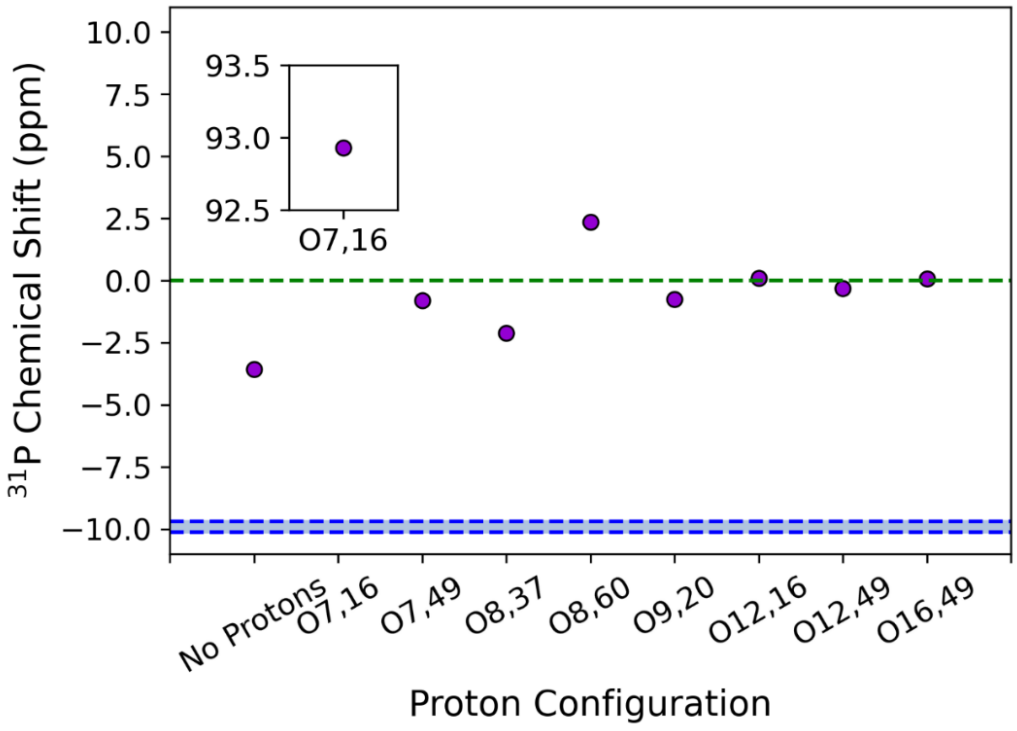

Figure 6.26. Theoretical $[H_2P_2W_{12}O_{48}]^{12-}$ ^{31}P NMR spectra across several different protonation configurations. Where multiple peaks are reported in the calculation, a single mean chemical shift value is reported here. The empirical range for chemical shift is encapsulated between the dashed blue lines. A dashed green line at 0.0ppm is included for reference. **SP/PBE/TZP/SFC/COSMO/Spin-Orbit Relativity**

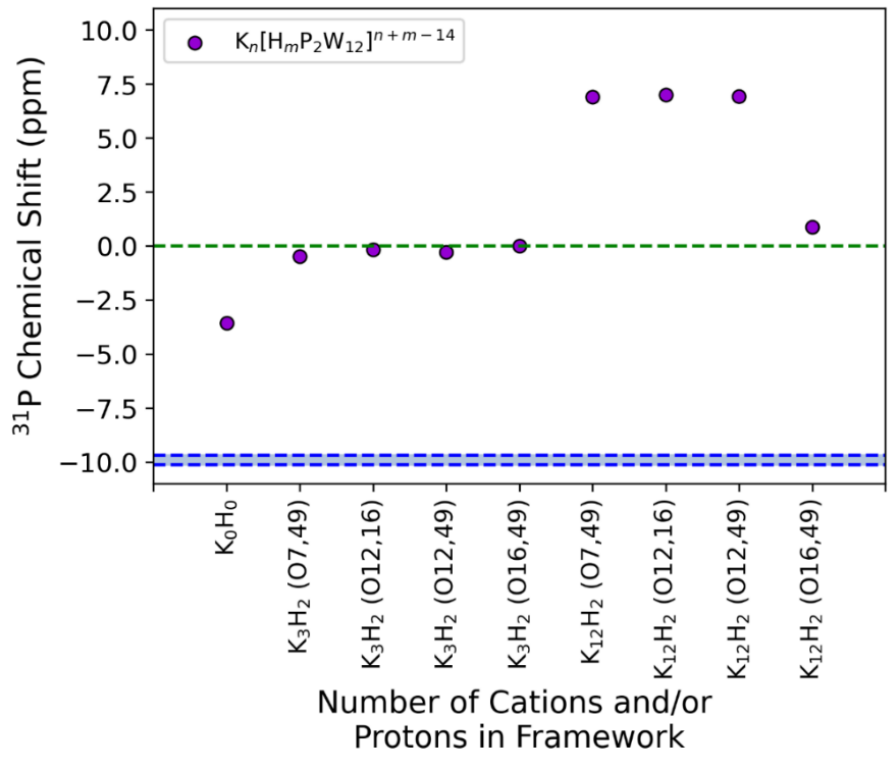

Figure 6.27. Theoretical $K_n[H_mP_2W_{12}O_{48}]^{n+m-14}$ ^{31}P NMR spectra across several different protonation configurations. Where multiple peaks are reported in the calculation, a single mean chemical shift value is reported here. The empirical range for chemical shift is encapsulated between the dashed blue lines. A dashed green line at 0.0ppm is included for reference. **SP/PBE/TZP/SFC/COSMO/Spin-Orbit Relativity**

6.2.7 Summary

Collecting the core hours required to converge each model, see **Figure 6.28** and **Table A-2.41**, we can observe that the number of core hours trends upwards after the structure contains at least 3 countercations. Unless there is a substantial increase in accuracy past this level of complexity, it would be prudent to limit the number of cations to a maximum of 3 countercations with/ or without protons present. A core hour requirement value under 10,000 is deemed acceptable, as this equates to a 5-core job taking 48 hours to complete.

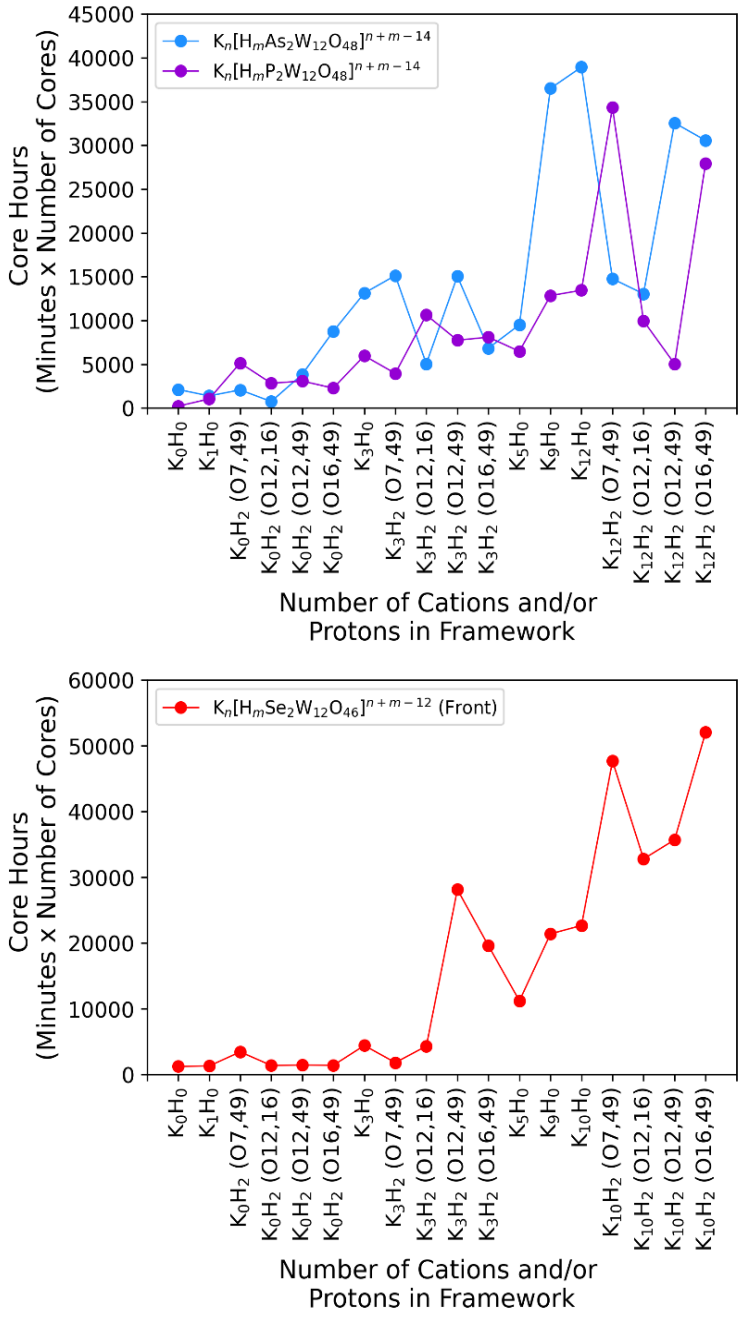

Figure 6.28. Core hours required to converge $K_n[H_mAs_2W_{12}O_{48}]^{14-m-n}$, $K_n[H_mP_2W_{12}O_{48}]^{14-m-n}$, and $K_n[H_mSe_2W_{12}O_{46}]^{12-m-n}$ hexalacunary structures. The number of core hours is defined by the number of cores utilised multiplied by the total job time in minutes.

Deviation in the dimensions of the model relative to the empirical molecule has been a large focus in this paper. We've determined that addition of countercations and/or protons didn't help improve the accuracy of the model and, especially in the case of **{Se_2W_{12}}**, substantially warped the dimensions of the model, (**see Figure 6.29**).

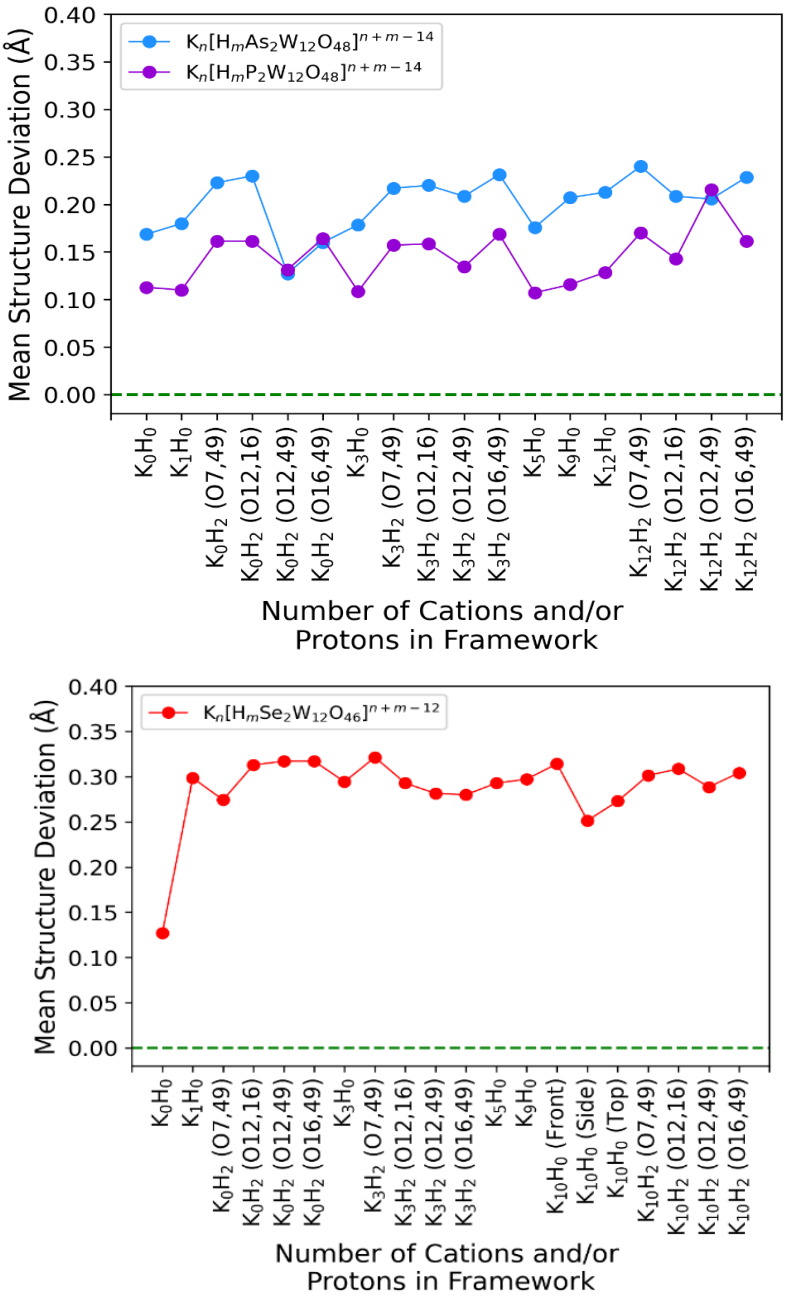

Figure 6.29. Differences in the mean structure deviation value for $[As_2W_{12}O_{48}]^{14-}$, $[P_2W_{12}O_{48}]^{14-}$ and $[Se_2W_{12}O_{46}]^{12-}$ with and without protons and cations. Proton configuration is included where appropriate. For $K_{10}[Se_2W_{12}O_{46}]^{2-}$, the cation arrangement is the same as **K_{12}{P_2W_{12}}** but minus 2 cations; the position these cations are missing from is referred to in the structure designation. **OPT/PBE/TZP/SFC/COSMO**

Given this, we see no reason to include these extra cations if ones aim is to replicate the existing xyz data, despite the fact that these cations are present in the empirical molecule. Why this is the case, as it seems paradoxical that including all 12 potassium and 2 hydrogen cations

included in the molecule would increase structural deviation when this is the 'true molecule', is unknown and may require either increasing the distance between cation and POM and/or operating at a higher level of computational theory than is currently feasible.

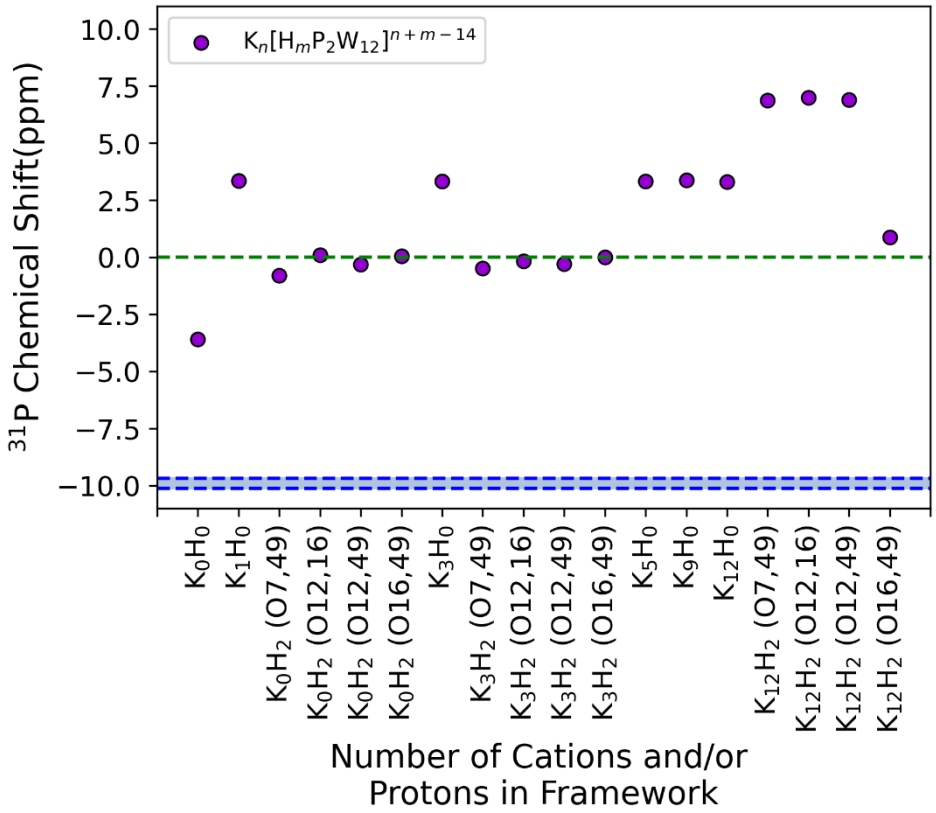

Figure 6.30. Theoretical $K_n[H_mP_2W_{12}O_{48}]^{m+n-14}$ ^{31}P NMR spectra across several different protonation configurations. The empirical range for chemical shift is encapsulated between the dashed blue lines. A dashed green line at 0.0ppm is included for reference. Proton configuration is included where appropriate. **SP/PBE/TZP/SFC/COSMO/Spin-Orbit Relativity**

NMR yielded similar results, with the most accurate model being the base $[P_2W_{12}O_{48}]^{14-}$ geometry without any additional cations, see **Figure 6.30**. Note that only ^{31}P NMR was examined by this work and ^{1}H is generally much less informative, yielding only a single broad peak. This correlates well with our charting of proton configurations, as the configurations are constantly alternating amongst the 112 possibilities.

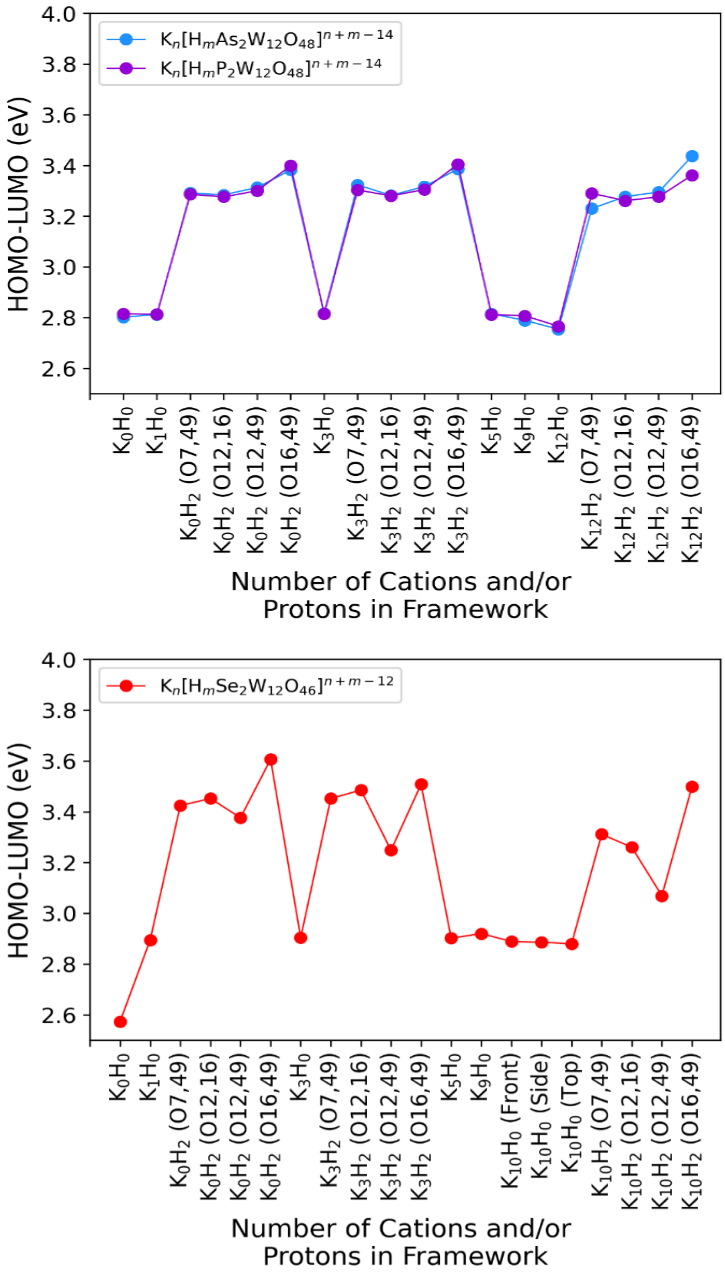

Figure 6.31. Comparison in HOMO-LUMO energy gap values between $K_n[H_mAs_2W_{12}O_{48}]^{m+n-14}$, $K_n[H_mP_2W_{12}O_{48}]^{m+n-14}$ and $K_n[H_mSe_2W_{12}O_{46}]^{m+n-12}$ configurations. **OPT/PBE/TZP/SFC/COSMO**

Though there isn't an empirical value for the HOMO-LUMO gap of $K_{12}[H_2P_2W_{12}O_{48}]$ or the other hexalacunaries, we collected theoretical band gap values for all the species investigated during this work, see **Tables A-2.42** to **A-2.44** and **Figure 6.31**. Even without the empirical gap size, we can observe how introducing different elements to the hexalacunary affects the gap.

From this we can draw two conclusions: firstly, that the presence of countercations (without additional protons) in the model keeps the HOMO-LUMO gap relatively similar to the initial gap size without the cations. The exception is $[Se_2W_{12}O_{46}]^{12-}$, whose inherently weaker framework is more susceptible to structural warping, with the gap shifting +0.3eV before remaining consistently at around 2.9eV. Secondly, addition of protons not only increases the magnitude of the gap by as much as 1.0eV but also exhibits more variation between different proton configurations than adding more countercations does. It is surprising that altering the specific oxygen atoms which experience protonation can have such a significant effect on the size of the associated HOMO-LUMO gap and warrants further investigation.

Finally, we come to atomic charge distribution, or electronic standard deviation. A very desirable application of DFT is to examine how different molecules interact each other and to gain some insight into reactions that occur in the lab. For this practice to be accurate, however, it is vital that our molecules accurately emulate the empirical species. Atomic charge distribution is a key parameter for this, as it determines where nucleophilic and electrophilic regions will reside around the POM and the intensity of their polarity.

We found, somewhat unsurprisingly, that as more cations were included in the geometry, that charge distribution around the anionic POM was reduced as electrons became more delocalised within the structure; in this instance it is worth including as many cations as possible as this has a discernible effect on the model. This approach, however, can be very computationally demanding, as established with **Table A-2.60**. We recommend including protons over cations, as the presence of 2 protons is able to yield a charge distribution value that requires 5 larger potassium countercations to replicate without the associated increase in complexity and computational cost.

6.3 Conclusion

We have converged more than a hundred different hexalacunary POM structures, divided into several distinct families (without countercations or protons, with countercations, with protons, and with both countercations and protons), to determine which provides the most accurate representation of the empirical framework in solution. We determined the quality of our models using a handful of different parameters, including dimension deviation (Å), electron distribution, and simulated NMR and IR spectra.

From these, we were able to establish that, although the full formula of a hexalacunary such as $K_{12}[H_2P_2W_{12}O_{48}]$ is charge neutral, accuracy of the simulated data was not substantially improved by including all these cations. Beyond including both protons and 3 countercations, there was not any significant change in accuracy warranting the additional computational cost required to converge the calculation. Additionally, there is no 'best' model for hexalacunary POMs. For each parameter or variable we have used to obtain information from our models, there are some which perform better than others in specific categories but poorly in others.

If one wants to build a model that is close in dimensions to the available crystallographic data, we advise the usage of a countercation only model ($K_n[X_2W_{12}O_{48}]^{m-}$), with n = 0,1,3 and X =As, P, Se, and the distance between K and X constrained at 9.0Å. The exact value of 'n' depends on the nature of the heteroatom (n = 0 for As, Se; n = 3 for P), especially for a non-classical POM where even a single cation will severely affect the model.

For determining the most reactive site of the POM, a model with both countercations and protons is key, though the protons appear more important than the countercations in replicating the fully charge neutral hexalacunary. In this instance, a model such as $K_m[H_2X_2W_{12}O_n]^{x-}$, (where m = 0-3, and n = 48 when X = As, P or n = 46 when X = Se). will provide the most accurate representation. The specific configuration of protons is irrelevant.

The main limitation that hindered us during this investigation was our inability to accurately replicate the available empirical NMR spectra, even when the structure used for the spectra calculation was crystallographically obtained. It is unclear whether there is a more suitable functional or basis set that could have been employed, or if our models were inherently inaccurate relative to their empirical counterparts, but it is crucial that we discover what causes this issue and how to resolve it if we are to fully realize our vision for inverse design.

6.4 References

(2) Pope, M. T. *Heteropoly and Isopoly Oxometalates*, 1st ed.; Springer Berlin, Heidelberg, 1983.

(64) Zhang, F. Q.; Guan, W.; Yan, L. K.; Zhang, Y. T.; Xu, M. T.; Hayfron-Benjamin, E.; Su, Z. M. On the Origin of the Relative Stability of Wells-Dawson Isomers: A DFT Study of α-, β-, γ-, A*-, B*-, and Γ*-[(PO4)2W18O54] 6-Anions. *Inorg. Chem.* **2011**, *50* (11), 4967–4977. https://doi.org/10.1021/ic200203s.

(76) Ammam, M.; Mbomekalle, I. M.; Keita, B.; Nadjo, L.; Fransaer, J. [As8W48O184]40-, a New Crown-Shaped Heteropolyanion: Electrochemistry and Electrocatalytic Properties towards Reduction of Nitrite. *Electrochim. Acta* **2010**, *55* (9), 3118–3122. https://doi.org/10.1016/j.electacta.2010.01.067.

(77) Contant, R.; Teze, A. A New Crown Heteropolyanion, K28Li5H7P8W48O184.92H2O: Synthesis, Structure, and Properties. *Inorg. Chem.* **1985**, *24* (26), 4610–4614. https://doi.org/10.1021/ic00220a036.

(78) Cameron, J. M.; Gao, J.; Vilà-Nadal, L.; Long, D. L.; Cronin, L. Formation, Self-Assembly and Transformation of a Transient Selenotungstate Building Block into Clusters, Chains and Macrocycles. *Chem. Commun.* **2014**, *50* (17), 2155–2157. https://doi.org/10.1039/c3cc49293a.

(79) Godin, B.; Chen, Y. G.; Vaissermann, J.; Ruhlmann, L.; Verdaguer, M.; Gouzerh, P. Coordination Chemistry of the Hexavacant Tungstophosphate [H2P2W12O48]12- with FeIII Ions: Towards Original Structures of Increasing Size and Complexity. *Angew. Chemie - Int. Ed.* **2005**, *44* (20), 3072–3075. https://doi.org/10.1002/anie.200463033.

(80) Yao, S.; Zhang, Z.; Li, Y.; Lu, Y.; Wang, E.; Su, Z. Two Heterometallic Aggregates Constructed from the {P2W 12}-Based Trimeric Polyoxotungstates and 3d-4f Heterometals. *Cryst. Growth Des.* **2010**, *10* (1), 135–139. https://doi.org/10.1021/cg900745z.

(81) Contant, R. *Inorganic Syntheses*, 1st ed.; Ginsberg, A. P., Ed.; Wiley-Interscience: New York, 1990. https://doi.org/10.1002/9780470132586.

(82) Boyd, T.; Mitchell, S. G.; Gabb, D.; Long, D. L.; Cronin, L. Investigating Cation Binding in the Polyoxometalate-Super-Crown [P 8W48O184]40-. *Chem. - A Eur. J.* **2011**, *17* (43), 12010–12014. https://doi.org/10.1002/chem.201101666.

(83) Contant, R.; Thouvenot, R. Hétéropolyanions de Type Dawson. 2. Synthèses de Polyoxotungstoarsénates Lacunaires Dérivant de l'octadécatungstodiarsénate. Étude Structurale Par RMN Du Tungstène-183 Des Octadéca(Mo1ybdotungstovanado)Diarsénates Apparentés. *Can. J. Chem.* **1991**, *69* (10), 1498–1506. https://doi.org/10.1139/v91-221.

(326) Contant, R.; Ciabrini, J. P. Stereospecific Preparations of New N-Molybdo-(18-n)-Tungsto-2-Phosphates and Related "Defect" Compounds (n = 2, 4 or 5). *J. Inorg. Nucl. Chem.* **1981**, *43* (7), 1525–1528. https://doi.org/10.1016/0022-1902(81)80330-2.

(327) Acerete, R.; Hammer, C. F.; Baker, L. C. W. Reinterpretations, Based on 183W NMR Spectra, of Several Heteropolytungstates Derived from the Wells-Dawson "2:18" Structure. Preparation and Structure Proof for the First γ-Isomer of a 2:18 Complex. *Inorg. Chem.* **1984**, *23* (10), 1478–1482. https://doi.org/10.1021/ic00178a034.

(328) Sugiarto, S.; Sadakane, M. Hexalacunary [A-H2P2W12O48]12– Wells-Dawson Anion: X-ray Crystal Structure Evidence and Oligomerization to WO(OH2)4+-Bridged Dimer and Trimer. *Chem. – A Eur. J.* **2023**, *29* (45), e202301051. https://doi.org/10.1002/chem.202301051.

(329) Malcolm, D.; Vilà-Nadal, L. Computational Study into the Effects of Countercations on the [P8W48O184]40– Polyoxometalate Wheel. *ACS Org. Inorg. Au* **2023**. https://doi.org/10.1021/acsorginorgau.3c00014.

(330) Kato, C.; Nishihara, S.; Tsunashima, R.; Tatewaki, Y.; Okada, S.; Ren, X.; Inoue, K.; Long, D.; Cronin, L. Quick and Selective Synthesis of Li6[Alpha-P2W18O62]28H2O Soluble in Various Organic Solvents. *Dalt. Trans.* **2013**, *42* (32), 11363–11366. https://doi.org/10.1039/c3dt51120k.

(331) Kaledin, A. L.; Yin, Q.; Hill, C. L.; Lian, T.; Musaev, D. G. Ion-Pairing in Polyoxometalate Chemistry: Impact of Fully Hydrated Alkali Metal Cations on Properties of the Keggin [PW12O40]3-Anion. *Dalt. Trans.* **2020**, *49* (32), 11170–11178. https://doi.org/10.1039/d0dt02239j.

(332) Pascual-Borràs, M.; López, X.; Poblet, J. M. Accurate Calculation of 31P NMR Chemical Shifts in Polyoxometalates. *Phys. Chem. Chem. Phys.* **2015**, *17* (14), 8723–8731. https://doi.org/10.1039/c4cp05016a.

Chapter 7: Improving Benchmarking of Polyoxometalate Frontier Orbitals using Hybrid Functionals

This chapter is based on the following publication: Malcolm, D., and Vilà-Nadal, L. **'Improving Benchmarking of Polyoxometalate Frontier Orbitals using Hybrid Functionals'.**

Within this chapter we aim to identify if there is a problem within the current library of frontier orbital POM literature, specifically with regards to computational modelling of the magnitude of the HOMO-LUMO gap, and to establish the level of DFT theory for accurate reporting of this commonly referenced property.

7.1 Introduction

UV-Vis spectroscopy is a common analytical technique for measuring absorption band energy values, characteristic for each species of compound. Within the visible light and UV regions of the electromagnetic spectrum (~800-200nm), valence electrons can be promoted to unoccupied or singly occupied energy levels when irradiated by specific wavelengths.

A UV-Vis spectrometer operates by exposing the dissolved compound to each wavelength in turn, observing which particular frequencies of light will trigger an absorption or emission. To use the Shimadzu 1800 spectrophotometer used later in this work as an example, the light from a tungsten-filament halogen (Visible light) and deuterium (UV light) lamp is exposed to the sample one wavelength at a time using a monochromator. After being filtered, the wavelength

of light is split into two beams using a mirror; one beam irradiates the dissolved sample whilst the other passes through a reference cuvette containing only the solvent. A silicon photodiode picks up any emission from the sample, with the diode discharging upon detection and recharging once light freely passes through the sample once more.

The highest wavelength absorption or lowest energy transition corresponds with the HOMO-LUMO transition or gap, which can be used as an identifying 'fingerprint' characteristic; this is due to each compound having a slightly different orbital composition, affecting the magnitude of the HOMO-LUMO gap.

The energies of POM frontier orbitals and the subsequent the HOMO-LUMO gap can be indicative of a number of electronic properties including POM reactivity and stability, catalytic ability, and redox potential. The magnitude of the HOMO-LUMO gap in particular directly determines a POM's suitability for use within a redox flow battery or molecular memory device, for example, charge transport and the ease with which redox reactions can be conducted are directly affected based on the difference in frontier orbital energies. Obtaining precise frontier orbital data for a given POM species will therefore allow for precise insight into how suitable the framework is for a given role.

Computational methods, predominantly Density Functional Theory (DFT), have been regularly used to establish frontier orbital properties for POMs for the last 20 years, as this is difficult to establish solely from empirical techniques; with DFT, it is straightforward to explain differences in relative isomeric stabilities and verify the HOMO-LUMO gap when compared with available UV-Vis absorption data. DFT can additionally generate theoretical UV-Vis spectra by calculating the full set of electronic transitions native to the POM species.

In order to ensure DFT is operating at an accurate level of theory, it is important to benchmark the results against empirical data and therefore ground our calculations in reality. After examining the literature, however, we have discovered that empirical benchmarking is seldom conducted to a sufficient standard to allow for proper utilization of DFT for the purposes

intended; there is either poor or no comparison between empirical and theoretical results, resulting in discrepancies between computationally determined HOMO-LUMO gaps and empirical absorption energy values. One notable exception is provided by Ravelli *et al*, who apply Time-Dependent DFT (TD-DFT) towards accurately predicting UV-Vis spectra for Lindqvist, Decatungstate, and Keggin species of POM ($[W_6O_{19}]^{2-}$, $[W_{10}O_{32}]^{4-}$, and $[PW_{12}O_{40}]^{3-}$ respectively).

We have also observed a distinct lack in usage of standard UV-Vis spectroscopy for determining the HOMO-LUMO gap empirically, despite their established accuracy and easiness with which their results can be compared between different works. We instead find Cyclic Voltammetry (CV) frequently utilised, despite the difficulty associated with reading the HOMO-LUMO gap from these methods' voltammogram, primarily the corrections involved which can vary significantly between different works. Additionally, CV merely provides one with the energy of the LUMO and not both HOMO and LUMO, preventing determination of the H-L gap.[333]

This lack of a standardized method by which the HOMO-LUMO gap is sourced further amplifies the disparity that exists between empirical and theoretical data, preventing reconciliation and critical verification between the two.

As such, this work aims to bridge this disparity by providing a rigorous benchmark with which to substantially improve our capabilities to accurately model frontier orbital energies of key POM species. To this end we shall present the findings of our extensive literature review, highlighting where sources of inaccuracy originate from, and conduct computational work in tandem with empirical methods to determine the HOMO-LUMO gap, utilizing a number of different functionals and DFT methods to achieve this.

7.2 Literature Review

As previously stated, we have conducted an extensive review of the available POM computational chemistry literature, reaching back to the advent of DFT usage in 2001.[237] Three of these early works are heavily cited,[237,238,239] and it is important we discuss them in detail in order to understand the issues we have with the literature as a whole; the first two papers simply report the theoretical HOMO-LUMO gap without empirical comparison to UV-Vis or CV spectra,[237,238] with the latter reporting differences in HOMO-LUMO gaps between isomers of the same POM species for Keggin and Wells-Dawson examples.[239] In the latter paper by Lopez *et al*, empirical benchmarking is conducted and the calculated HOMO-LUMO gaps are found to correspond to relative isomer stability, but we believe that, of no fault of this paper, from here a key misunderstanding is drawn by several later works.

To compare HOMO-LUMO gaps between isomers is valid at any level of theory, as only the absolute frontier orbital energies and not the relative differences in gap magnitude are affected. The mistake is to then report the magnitude of the HOMO-LUMO gap as empirically reproducible; to use an example, one may correctly observe that an apple is larger than a grape without having the means to accurately measure the diameter of either fruit, but this results in one being unable to then make assertions as to knowing the precise dimensions of the diameter. A number of other publications fall into this trap, with comparison in the frontier orbital energy gap between isomers being valid but where the size of said gap is never empirically verified.[334,62,95,69]

Most importantly, a highly cited 2003 review from Poblet *et al*[335] (1086 citations to date) references that the HOMO-LUMO gap was determined by Lopez *et al*,[239] but doesn't specify that the primary focus of the paper was explaining relative isomer stability. As such, subsequent researchers may read this review and conclude that they too can accurately report the HOMO-LUMO gap for a POM at the GGA-level of DFT theory. We believe these kinds of early

misunderstandings as to the level of accuracy provided by DFT calculations leads to mistakes being made by a multitude of other papers in the following years.

The main mistake we observe being made in the literature is putting too much reliance on previous works without regular benchmarks being conducted to provide one with a sanity check. One paper in particular by Mal S.S. *et al*[336] highlights this issue, with a number of previous computational works being referenced as justification for the level of theory used (**BP86/TZP/COSMO**)[237,238,334,335,62] but with no empirical benchmarking being carried out using the novel POM species described.

From our review of the available literature (**see Fig 7.1. and Appendix-3.1. for full collection of literature examined**), we have reason to believe the standard level of theory, GGA, is very inaccurate when compared to the empirical data. We thus decided to conduct our own benchmark to establish a more suitable level of theory to deploy in all subsequent computational work with POMs.

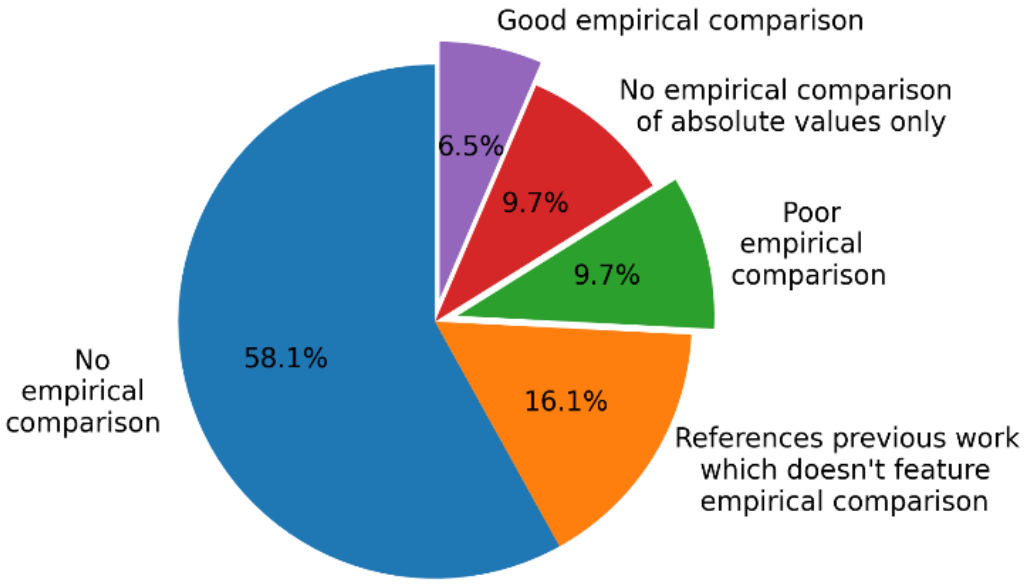

Figure 7.1. Analysis of literature examined over the course of this investigation. While the vast majority do not accurately replicate the empirical data, there are several different reasons for this discrepancy, illustrated here.

7.3 Results and Discussion

We were able to accurately replicate the UV-Vis data from the literature for the POM species $[P_2W_{18}O_{62}]^{6-}$ (Wells-Dawson) using DFT, with our predicted first absorption band relatively close to the value reported by the available literature. Using the BP86 functional, we observed a +32nm (-0.13eV) difference between the reported values and our own; results with PBE in lieu of BP86 provided us with a mean value of +14.7nm (-0.06eV). Both of these values, while in line with reported theoretical work, are still very inaccurate when compared against empirical data (**see Table A-3.3 for full list of computational data**).

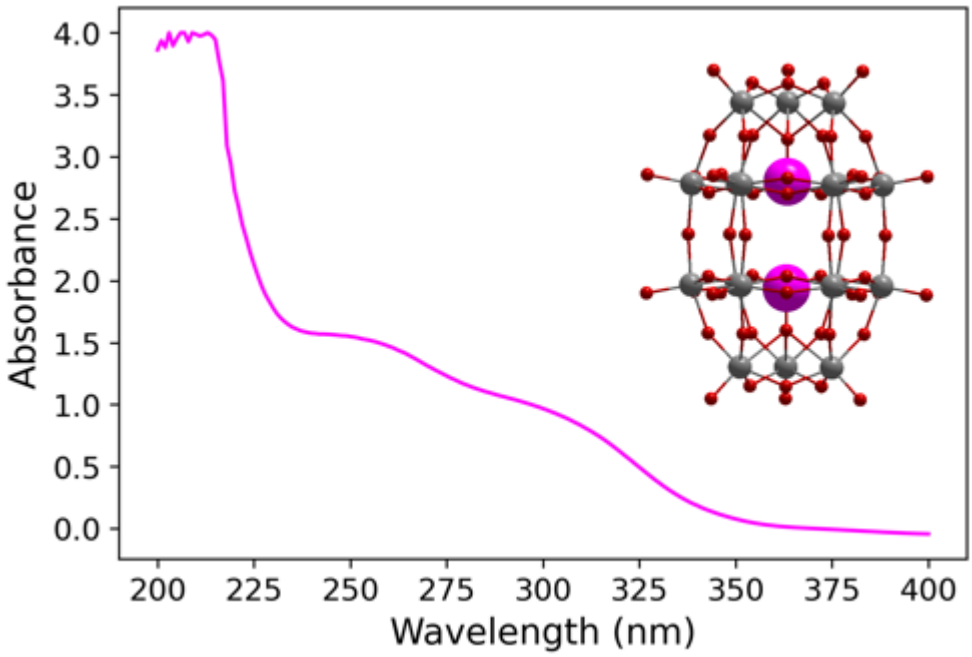

Figure 7.2. Experimental UV-Vis spectroscopy for $K_6[P_2W_{18}O_{62}]$ (310, 250nm), between the range of 200-400nm. The HOMO-LUMO gap or the lowest energy transition correlates with the absorption band with the greatest wavelength value (310nm).

Additionally, we synthesized and conducted UV-Vis spectroscopy using $K_6[P_2W_{18}O_{62}]$. Upon conducting our own UV-Vis spectroscopy, we observed that the WD POM displayed two absorption bands within the range of 200-400nm (~250nm, ~310nm). WD absorption bands can be difficult to read from UV-Vis spectra but can be read by observing the point in the

maxima with the smallest gradient. These absorption values are in good agreement with the two bands reported in the literature, the mean values for which are 254nm and 302.8nm respectively. (**see Fig. 7.2 and Table A-3.4**).

We then elected to run a series of calculations using several different functionals at varying levels of theory (GGA, GGA-D, Hybrid, Hybrid-D, and Range Separated), subsequently choosing to use the hybrid functional PBE0 moving forwards; though previous theoretical works operated at the GGA level,[334,337,180,323] we found that hybrid functionals were required to gain sufficient accuracy in our results when compared with the empirical data.[323,338,339,340,151] The PBE0 functional was able to replicate the absorption band energy to within 0.04eV (~3nm) of the empirical value, a marked increase over using functionals operating at a lower level of theory (**see Fig. 7.3 and Table A-3.5**).

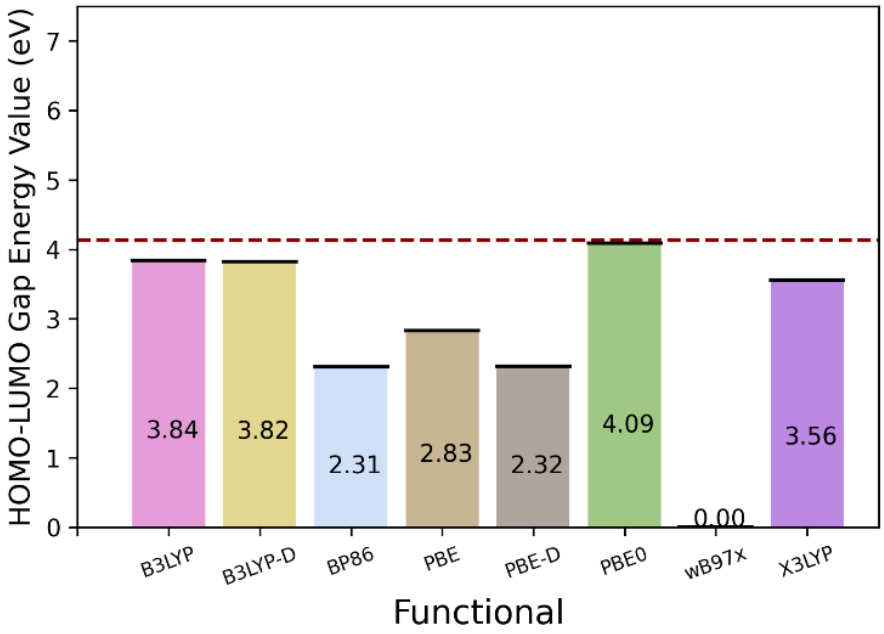

Figure 7.3. HOMO-LUMO gap energy values for $[\alpha\text{-}P_2W_{18}O_{62}]^{6-}$ across a range of functionals. A dashed red line is used to represent the empirical value for the HOMO-LUMO gap;[323] bars closer to the line will be considered more accurate. **(SP/{Functional}/TZP/SFC/COSMO)**

Upon establishing that PBE0 was a superior functional to use relative to PBE or BP86 in the case of WD, we set out to determine whether this held true across multiple different species of

POM. We next chose to examine the Keggin cluster $[XW_{12}O_{40}]^{n-}$, as, in addition to displaying a sufficient presence in the literature for our needs, Keggin is a small enough POM that we can feasibly include the cations in our model and still obtain an optimized structure.[338,339]

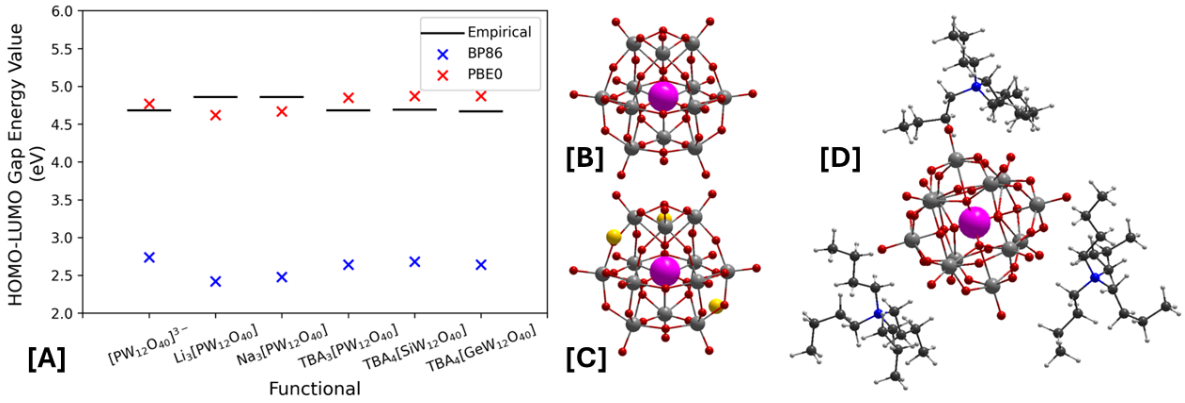

Figure 7.4. HOMO-LUMO gap energy values for $C_n[\alpha\text{-}XW_{12}O_{40}]^{m-}$, where C is the countercation atom/ molecule and X is the encapsulated heteroatom, across a range of different species of Keggin **[A]**. Geometries for $[PW_{12}O_{40}]^{3-}$ **[B]**, $Li_3[PW_{12}O_{40}]$ **[C]**, and $TBA_3[PW_{12}O_{40}]$ **[D]** are visualized. **(SP/{Functional}/TZP/SFC/COSMO)**

As with the WD, we observed that PBE0 was significantly more accurate at modelling the absorption band value than BP86 for Keggin, by a factor of almost 2.1eV (~195nm) in all species examined (**see Fig. 7.4**). The mean difference between the empirical and calculated band value was +2.14 for BP86 and -0.035 in the case of PBE0 and both groups of models were closely clustered around their respective mean values without outliers (standard deviation value of 0.11 for BP86 calculations and 0.099 with PBE0), see **Appendix-3.3**.

We also observed that the nature of countercation present had more of an effect on the absorption band value for the framework, with a maximum difference between models of +0.18eV where the cation was Li instead of TBA, than did the heteroatom of choice, with a mere +0.02eV difference between inclusion of the elements Si and Ge. Oddly, when it came to our DFT models we noticed the band gap values were reported as smaller than they should be relative to the empirical data when the only difference between models is inclusion and nature of the countercations; BP86, for example, reported a maximum difference of -0.23eV between different cation models, a relative error of -0.41eV.

There are clearly nuances regarding including countercations in DFT models that must be considered, with the easiest parameter to vary being that of difference between the POM and countercation. As has been reported previously,[331] there is a tendency for the frontier orbitals to be over stabilised if the calculation is left to optimize without any distance constraints, with the cations ending up closer to the POM than they would in the empirical structure.

Using our WD structure as an example, we observed that the optimized model preferred to place the cations at a distance of 6.3Å from the phosphorus heteroatoms when no distance constraints were included; this results in an over stabilising of the frontier orbitals by roughly -0.5eV in the case of the HOMO and LUMO as opposed to when no countercations are included in the model, with the HOMO-LUMO gap remaining at 4.34eV (**see Fig. 7.5**).

We believe this to be a limitation from our using an implicit solvation model, COSMO, instead of an explicit one. In solution, solvent molecules surround the POM cage and keep countercations at a distance of roughly 9.0Å due to electrostatic repulsion. When an implicit solvation model is used, there are no explicit solvent molecules to keep the countercations at an appropriate distance and, as a result, the optimized geometry features cations at a much closer distance to the POM. When COSMO and countercations are both present in our calculation, the distance between POM and cation must be constrained at the appropriate distance to deliver a more representative model of the species in solution.

Steadily increasing and constraining the distance between countercation and heteroatom gradually stabilized the absolute energies of the frontier orbitals, with change in the orbital energy being minimal after a distance of 9.0Å is enforced; as it becomes increasingly more difficult to converge the calculation as the constrained distance is increased, we recommend not going past 9.0Å.

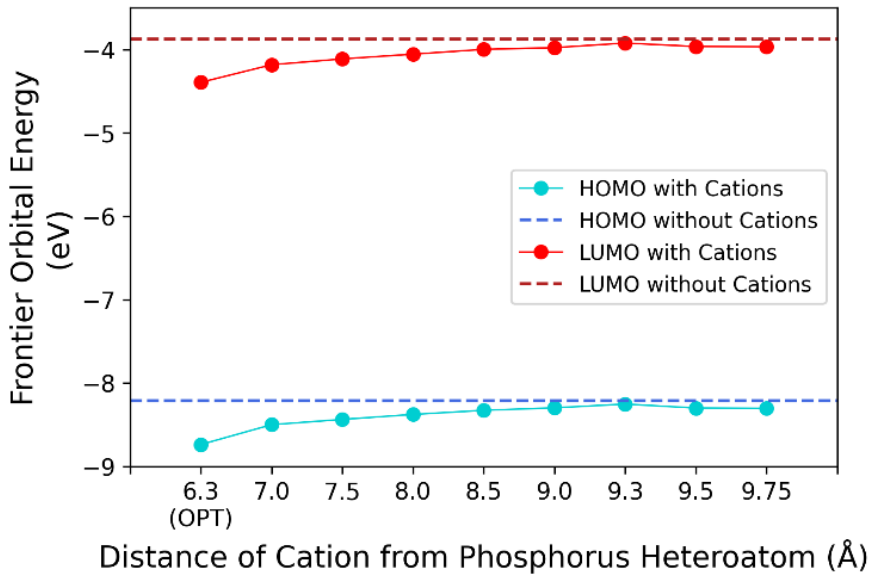

Figure 7.5. HOMO and LUMO absolute energy values for $K_n[\alpha\text{-}P_2W_{18}O_{62}]^{m-}$. Dashed line reports the frontier orbital energy when n=0, whilst solid lines display the energy when n=6, with each point representing a different distance between countercation and heteroatom (Å). **SP/PBE0/TZP/SFC/COSMO**

The HOMO-LUMO gap for all these calculations remains consistent when the UV Single Point calculation is run on top of an optimized geometry; results were naturally less consistent when a single point geometry was utilised. It is also worth noting that there is little difference between the H-L gap when countercations are included and when they are absent, with a standard deviation value of only 0.008 for the energy gap value of all models, cations included or not. Given this, we find no reason to included countercations in the structure for determining the absorption band gap energy value, see **Appendix 3.4**.

Widening our investigation, we conducted computational calculations to determine the absorption band energy value for $[W_6O_{19}]^{2-}$ Lindqvist, $[W_{10}O_{32}]^{4-}$ Decatungstate, and $[H_2W_{12}O_{40}]^{6-}$ Paratungstate frameworks, comparing our results with available literature data; we aimed to prove our new hybrid functional level of theory was applicable across a wide range of POM, including IsoPOMs as previously indicated by Ravelli D. *et al.*.[320]

What we found was most curious: for the WD and Keggin models, we had been comparing the difference between HOMO and LUMO energies using Time-Independent DFT (TI-DFT), reading the absolute energy values directly from the output file; these were in very good agreement with the empirically sourced lowest energy absorption band once we raised the level of theory we were working at. When we looked at the Decatungstate, Lindqvist, and Metatungstate models however, we found this method to be highly inaccurate when compared to both empirical and other computational works.[320] However, when we switched to Time-Dependent DFT (TD-DFT) we found the predicted lowest energy absorption band to be in close agreement with these small IsoPOMs but not for the original Keggin and WD HPOM species (**Fig. 7.6**).

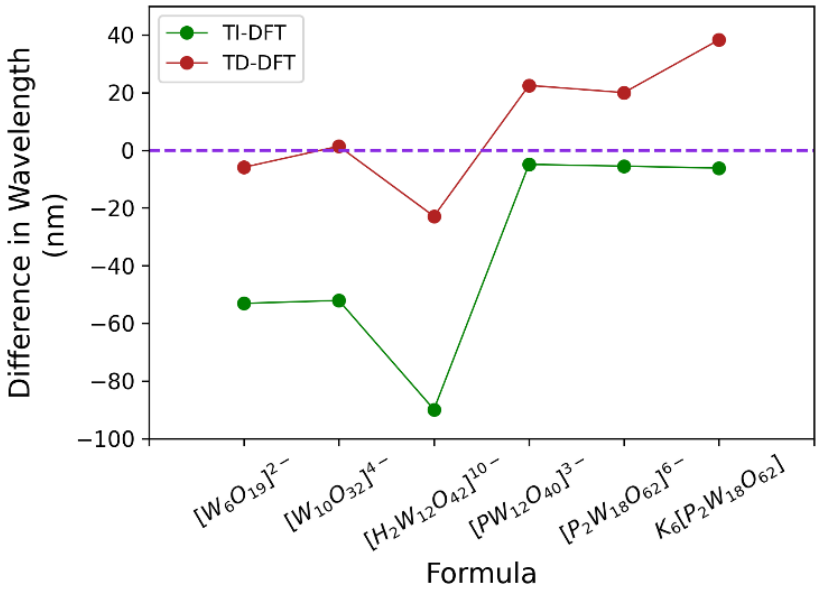

Figure 7.6. Discrepancies between empirical and computational wavelength values (nm) for the first UV-Vis absorption band. Dashed purple line signifies the position of the empirical value relative to the charted computational ones, whether they be time independent or time dependent DFT (TI-DFT or TD-DFT respectively). **SP/PBE0/TZP/SFC/COSMO**

We used several UV-Vis methods other than the default Davidson method that should improve the calculation results at the hybrid level of theory to attempt to reconcile this discrepancy, including Tamm-Dancoff Approximation (TDA),[341] simplified Tamm-Dancoff Approach (sTDA),[342] with and without Hybrid Diagonal Approximation (HDA),[343] and simplified Time-Dependent DFT (sTDDFT).[344] While some of these altered parameters improve absorption

band values for specific POM species, we didn't identify a method which improved band values across all the selected species.

Why one group of POMs requires TI-DFT and TD-DFT for a different group is unclear, but we have reason to believe the answer lies in the presence or absence of a heteroatom within the framework; the latter group of POMs we looked at were all IsoPOMs, with the former (Keggin and WD) both being HPOMs. Further work is clearly required to fully solve this mystery. See **Appendix-3.5** for TI-DFT and **Appendix-3.6** for TD-DFT results.

7.4 Conclusion

We have established over the course of this work that there exist discrepancies between the HOMO-LUMO gap reported by previous computational works and the empirical data. We have identified several recurring mistakes and their origins within the literature, predominantly incorrect understanding of referenced works and lacklustre benchmarking. This, combined with regular use of GGA-level functionals, has resulted in absorption band magnitudes of several different species of POMs being incorrectly reported.

By conducting our own empirical experiments and theoretical benchmarking process with $K_6[P_2W_{18}O_{62}]$, we have identified the hybrid functional PBE0 to report the HOMO-LUMO gap value to within 7nm (0.09eV) of the empirical value; this is a substantial improvement over the commonly reported, PBE sourced, difference of roughly 250nm (1.8eV). We repeated this process for several Keggin species, formulae $X_3[PW_{12}O_{40}]$ or $TBA_3[PW_{12}O_{40}]$, observing a similar increase in accuracy when PBE0 was used over the traditional BP86 functional; we also noted that results were further improved when the distance between cation and POM was constrained to 9Å.

Upon widening the scope of our investigation include a wider variety of POMs, we noticed that the HOMO-LUMO gap for IsoPOMs was only accurately modelled computationally when TD-DFT was deployed; the reverse was required for HPOMs, with TI-DFT proving more accurate. Why this distinction exists for DFT is unknown, but, with only a few examples of IsoPOMs and HPOMs respectively to work with, we need to expand our sample pool in order to either further validate our hypothesis or to offer insight into the true cause. One POM we would be keen to identify the true empirical HOMO-LUMO gap for is the IsoPOM $[W_{19}O_{62}]^{10-}$, which exists as the IsoPOM derivative of the WD cluster; determining if TI- or TD-DFT is more appropriate for modelling electronic properties would indicate if the size of the POM cluster or presence of a heteroatom is the source of discrepancy.

7.5 References

(62) López, X.; Poblet, J. M. DFT Study on the Five Isomers of PW12O403-: Relative Stabilization upon Reduction. *Inorg. Chem.* **2004**, *43* (22), 6863–6865. https://doi.org/10.1021/ic049119p.

(69) Fernández, J. A.; López, X.; Bo, C.; de Graaf, C.; Baerends, E. J.; Poblet, J. M. Polyoxometalates with Internal Cavities: Redox Activity, Basicity, and Cation Encapsulation in [Xn+P5W30O110](15-n)- Preyssler Complexes, with X = Na+, Ca2+, Y3+, La3+, Ce3+, and Th4+. *J. Am. Chem. Soc.* **2007**, *129* (3), 12244–12253. https://doi.org/10.1021/ja0737321.

(95) Long, D.-L.; Kögerler, P.; Cronin, L. Old Clusters with New Tricks: Engineering S···S Interactions and Novel Physical Properties in Sulfite-Based Dawson Clusters. *Angew. Chemie* **2004**, *116* (14), 1853–1856. https://doi.org/10.1002/ange.200352896.

(151) Kibler, A. J.; Souza, V. S.; Fernandes, J. A.; Lewis, W.; Argent, S. P.; Dupont, J.; Newton, G. N. A Cooperative Photoactive Class-I Hybrid Polyoxometalate With Benzothiadiazole–Imidazolium Cations. *Front. Chem.* **2021**, *8*, 1–10. https://doi.org/10.3389/fchem.2020.612535.

(180) Vilà-Nadal, L.; Peuntinger, K.; Busche, C.; Yan, J.; Lüders, D.; Long, D.; Poblet, J. M.; Guldi, D. M.; Cronin, L. Polyoxometalate {W18O56XO6} Clusters with Embedded Redox-Active Main-Group Templates as Localized Inner-Cluster Radicals. *Angew. Chemie* **2013**, *125*, 9877–9881. https://doi.org/ange.201303126.

(237) Maestre, J. M.; Lopez, X.; Bo, C.; Poblet, J. Electronic and Magnetic Properties of R -Keggin Anions : A DFT Study of [XM12O40]n-, (M = W, Mo; X = AlIII, SiIV, PV, FeIII, CoII, CoIII) and [SiM11VO40]m- (M = Mo and W). *J. Am. Chem. Soc.* **2001**, *123* (16), 3749–3758. https://doi.org/10.1021/ja003563j.

(238) López, X.; Maestre, J. M.; Bo, C.; Poblet, J. M. Electronic Properties of Polyoxometalates: A DFT Study of α/β-[XM12O40]n- Relative Stability (M=W, Mo and X a Main Group Element). *J. Am. Chem. Soc.* **2001**, *123* (39), 9571–9576. https://doi.org/10.1021/ja010768z.

(239) López, X.; Bo, C.; Poblet, J. M. Electronic Properties of Polyoxometalates: Electron and Proton Affinity of Mixed-Addenda Keggin and Wells-Dawson Anions. *J. Am. Chem. Soc.* **2002**, *124* (42), 12574–12582. https://doi.org/10.1021/ja020407z.

(320) Ravelli, D.; Dondi, D.; Fagnoni, M.; Albini, A.; Bagno, A. Predicting the UV Spectrum of Polyoxometalates by TD-DFT. *J. Comput. Chem.* **2011**, *32* (14), 2983–2987. https://doi.org/10.1002/jcc.21879.

(323) Chen, J. J.; Vilà-Nadal, L.; Solé-Daura, A.; Chisholm, G.; Minato, T.; Busche, C.; Zhao, T.; Kandasamy, B.; Ganin, A. Y.; Smith, R. M.; Colliard, I.; Carbó, J. J.; Poblet, J. M.; Nyman, M.; Cronin, L. Effective Storage of Electrons in Water by the Formation of Highly Reduced Polyoxometalate Clusters. *J. Am. Chem. Soc.* **2022**, *144* (20), 8951–8960. https://doi.org/10.1021/jacs.1c10584.

(331) Kaledin, A. L.; Yin, Q.; Hill, C. L.; Lian, T.; Musaev, D. G. Ion-Pairing in Polyoxometalate Chemistry: Impact of Fully Hydrated Alkali Metal Cations on Properties of the Keggin [PW12O40]3-Anion. *Dalt. Trans.* **2020**, *49* (32), 11170–11178. https://doi.org/10.1039/d0dt02239j.

(332) Pascual-Borràs, M.; López, X.; Poblet, J. M. Accurate Calculation of 31P NMR Chemical Shifts in Polyoxometalates. *Phys. Chem. Chem. Phys.* **2015**, *17* (14), 8723–8731. https://doi.org/10.1039/c4cp05016a.

(333) Elgrishi, N.; Rountree, K. J.; McCarthy, B. D.; Rountree, E. S.; Eisenhart, T. T.; Dempsey, J. L. A Practical Beginner's Guide to Cyclic Voltammetry. *J. Chem. Educ.* **2018**, *95* (2), 197–206.

https://doi.org/10.1021/acs.jchemed.7b00361.

(334) Lo, X.; Bo, C.; Poblet, J.; Sarasa, P.; Uni, C. Relative Stability in Alpha- and Beta-Wells–Dawson Heteropolyanions: A DFT Study of [P2M18O62]n- (M = W and Mo) and [P2W15V3O62]N-. *Inorg. Chem.* **2003**, *42* (8), 2634–2638. https://doi.org/10.1021/ic0262280.

(335) Poblet, J. M.; López, X.; Bo, C. Ab Initio and DFT Modelling of Complex Materials: Towards the Understanding of Electronic and Magnetic Properties of Polyoxometalates. *Chem. Soc. Rev.* **2003**, *32* (5), 297–308. https://doi.org/10.1039/b109928k.

(336) Mal, S. S.; Bassil, B. S.; Ibrahim, M.; Nellutla, S.; Van Tol, J.; Dalal, N. S.; Fernández, J. A.; López, X.; Poblet, J. M.; Biboum, R. N.; Keita, B.; Kortz, U. Wheel-Shaped Cu20-Tungstophosphate [Cu20X(OH) 24(H2O)12(P8W48O 184)]25- Ion (X = Cl, Br, I) and the Role of the Halide Guest. *Inorg. Chem.* **2009**, *48* (24), 11636–11645. https://doi.org/10.1021/ic901641f.

(337) López, X.; Fernández, J. A.; Poblet, J. M. Redox Properties of Polyoxometalates: New Insights on the Anion Charge Effect. *J. Chem. Soc. Dalt. Trans.* **2006**, *6* (9), 1162–1167. https://doi.org/10.1039/b507599h.

(338) Nomiya, K.; Sugie, Y.; Amimoto, K.; Miwa, M. Charge-Transfer Absorption Spectra of Some Tungsten(VI) and Molybdenum(VI) Polyoxoanions. *Polyhedron* **1987**, *6* (3), 519–524. https://doi.org/10.1016/S0277-5387(00)81018-9.

(339) Hiskia, A.; Mylonas, A.; Papaconstantinou, E. Comparison of the Photoredox Properties of Polyoxometallates and Semiconducting Particles. *Chem. Soc. Rev.* **2001**, *30* (1), 62–69. https://doi.org/10.1039/a905675k.

(340) Dhifallah, F.; Belkhiria, M. S.; Parent, L.; Leclerc, N.; Cadot, E. A Series of Octahedral First-Row Transition-Metal Ion Complexes Templated by Wells-Dawson Polyoxometalates: Synthesis, Crystal Structure, Spectroscopic, and Thermal Characterizations, and Electrochemical Properties. *Inorg. Chem.* **2018**, *57* (19), 11909–11919. https://doi.org/10.1021/acs.inorgchem.8b01207.

(341) Hirata, S.; Head-Gordon, M. Time-Dependent Density Functional Theory within the Tamm-Dancoff Approximation. *Chem. Phys. Lett.* **1999**, *314* (3–4), 291–299. https://doi.org/10.1016/S0009-2614(99)01149-5.

(342) Stefan Grimme. A Simplified Tamm-Dancoff Density Functional Approach for the Electronic Excitation Spectra of Very Large Molecules. *J. Chem. Phys.* **2013**, *138* (24), 244104. https://doi.org/10.1063/1.4811331.

(343) Medves, M.; Sementa, L.; Toffoli, D.; Fronzoni, G.; Fortunelli, A.; Stener, M. An Efficient Hybrid Scheme for Time Dependent Density Functional Theory. *J. Chem. Phys.* **2020**, *152* (18), 184104. https://doi.org/10.1063/5.0005954.

(344) Bannwarth, C.; Grimme, S. A Simplified Time-Dependent Density Functional Theory Approach for Electronic Ultraviolet and Circular Dichroism Spectra of Very Large Molecules. *Comput. Theor. Chem.* **2014**, *1040–1041*, 45–53. https://doi.org/10.1016/j.comptc.2014.02.023.

Chapter 8: Versatility of the Ugi Reaction: Experimental and Computational Study

Over the course of this work, we briefly delved into the field of organic chemistry; though this may seem random and unrelated to our work with POMs, the Ugi reaction proceeds by a comparable self-assembly process to POMs. While we were eventually unable to follow this project through to completion due to time constraints and choosing to focus more on our POM-related work, we include our results here to emphasize how inverse design can be utilized in the realm of organic chemistry.

8.1 Introduction

The Ugi reaction is a single-pot organic reaction whereby an aldehyde, amine, carboxylic acid, and isocyanide molecule are reacted together to form a synthetic peptide product, commonly referred to as a peptoid (**Figure 8.1**). The modular aspect of this reaction allows one to, in theory, easily synthesize an immense number of peptoid species by simply altering the combination of reactants involved.

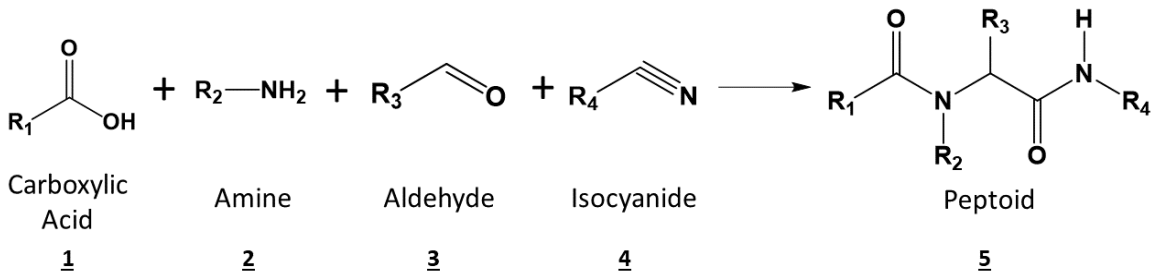

Figure 8.1. Ugi reaction mechanism. During this synthesis, the carboxylic acid (**1**), amine (**2**), aldehyde (**3**), and isocyanide (**4**) reactants self-assemble to form the final peptoid product (**5**).

Wender *et al*[345] described the ideal synthesis as a safe, single-pot reaction with a perfect atom economy and which is environmentally friendly. Whilst most chemical reactions breach at least one of these tenets, it is still an admirable goal to strive towards, especially when seeking to optimize or redesign an experimental procedure. The Ugi reaction, as a multi-component organic reaction that fulfils several of Wender *et al.*'s criteria, is the perfect example of a synthetic scheme to be promoted and utilised as much as possible in the design of new chemical species.[346]

As a result of the simplicity of the Ugi reaction scheme, it should be no surprise that there now exists an extensive library of peptoid molecules.[347] The new challenge is in determining the underlying reaction mechanism in each case, to both ensure that the peptoid can be replicated to a good degree of accuracy and to enhance our ability to design and successfully create novel peptoids. It is believed that there are at least two reaction pathways operating simultaneously in solution, with the mechanism progressing via either a nitrilium ion intermediate (**12)** or a hemiaminal ester-type (**13**); efforts to identify the intermediate formed suggests the nitrilium route is the more likely of the two.[348,349]

The consensus surrounding the mechanism, therefore, is that the starting reagent aldehyde **(3)** and amine **(2)** react to form an imine intermediate **(10)**, which then combines with the isocyanide reagent to form the nitrilium ion **(12)**.[350] Next, the carboxylic acid reagent **(11)** attacks the nitrilium ion, forming the imidate intermediate **(14)**. Finally, the imidate undergoes an irreversible Mumm-type rearrangement **(15)** to form the final peptoid product **(5)**.[351,352] See **Figure 8.2.** for the full reaction scheme.

The peptoid products created by the Ugi reaction allow for the incorporation of new functional groups into existing peptide structures, many of which are rare in nature.[353,354] These peptoids can be utilised in a range of applications, including usage in fluorescent cell imaging probes,[355] pH-sensitive probes,[346] photoaffinity scaffolds,[356] and OLEDs.[357] The Ugi reaction can also be

incorporated in pre-existing, robust peptide synthetic methods to yield a multifunctional peptoid within a more controlled environment.[358]

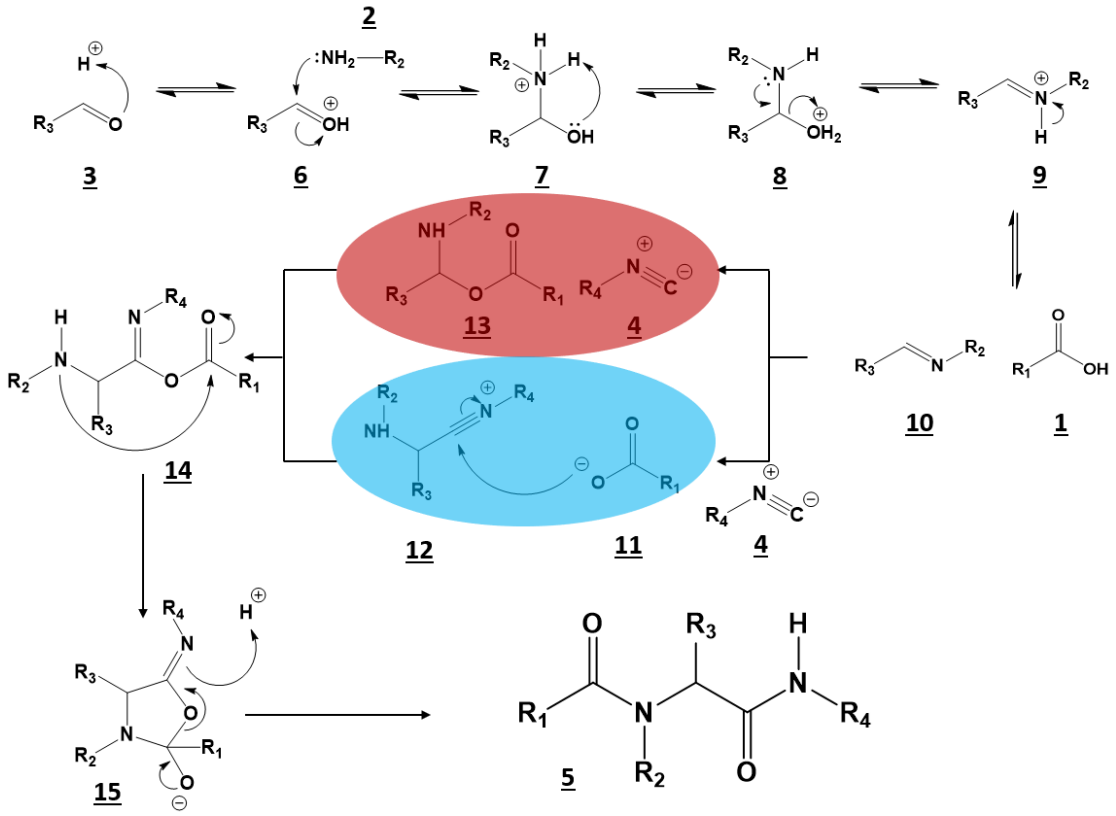

Figure 8.2. Detailed Ugi reaction mechanism. The red and blue spheres represent the two pathways by which the reaction can proceed to the final product, either by forming the hemiaminal ester or nitrilium ion intermediate respectively.

Cell imaging is an especially important field for peptoids; the ability for a non-toxic chemical to bind to the correct cellular component, feature an ideal half-life that allows for detection, and operate under a strict set of environmental conditions is vital for live-cell imaging viability.[355,359] Fluorescence in peptoids requires incorporation of a fluorophore functional group,[360] such as a coumarin.[361,362] The coumarin can be introduced as part of any of the starting reagents, despite its bulky size.[363,364,365]

Given that fluorescent peptoids are a relatively new sub-species with very promising applications, it is important to decipher the reaction mechanism to be able to continue to grow

the field and produce compounds with relevant properties. DFT is one tool that has been proven to offer insight both into transition state energies and reaction schemes for a variety of molecules;[366,367,368] transition state energies allow for identification of rate determining steps and possible sources of isomerisation or racemisation.

Modelling the synthetic mechanism using DFT will thereby allow for a more rational design of fluorescent peptoids, as it provides us with strategies and insights that improve stereoselectivity and methods to improve poor product yields. Understanding the underlying chemistry behind why, for instance, the specific fluorescent peptoids synthesized by Passos *et al.* would be of great value, as their fluorescent lifespan is an improvement over commercially available staining alternatives.[355]

We therefore present our replication in synthesizing and characterizing one of the peptoids created by Passos *et al*., both in terms of producing in the lab and modelling using DFT, and several novel peptoids using a similar set of reagents.

8.2 Ugi Results and Discussion

Following the synthetic procedure set out by Passos *et al*.,[355] we attempted to reproduce the peptoid referred to as 'P3' in that original work (**see Table 8.1. for our method of listing Ugi reactions and their products**). NMR of the resultant product indicated a very small amount of P3 was produced; the product signals were drowned out by the excess coumarin that remained unreacted in the solution. MS analysis corroborated the NMR data, with a visible peak at m/z 526.

Table 8.1. Designation of Ugi 'R' reactions, including the reagents and products involved in each one.

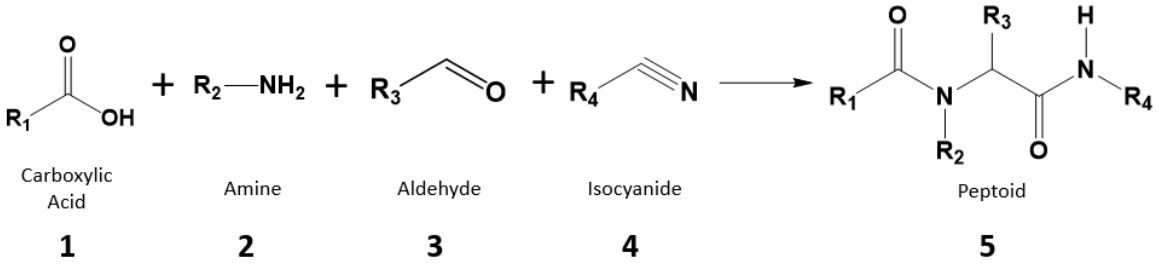

Reaction Designation	Carboxylic Acid Reagent	Amine Reagent	Aldehyde Reagent	Isocyanide Reagent	Peptoid Product Designation
R1	7-(diethylamino)coumarin-3-carboxylic acid	Aniline	Benzaldehyde	*n*-butyl isocyanide	P1
R2	7-(diethylamino)coumarin-3-carboxylic acid	Aniline	Piperonal	*n*-butyl isocyanide	P2
R3	7-(diethylamino)coumarin-3-carboxylic acid	Aniline	Benzaldehyde	*tert*-butyl isocyanide	P3
R4	7-(diethylamino)coumarin-3-carboxylic acid	Aniline	Piperonal	*tert*-butyl isocyanide	P4
R5	Coumarin 343	Aniline	Benzaldehyde	*n*-butyl isocyanide	P5
R6	Coumarin 343	Aniline	Benzaldehyde	*tert*-butyl isocyanide	P6
R7	Coumarin 343	Aniline	Piperonal	*n*-butyl isocyanide	P7
R8	Coumarin 343	Aniline	Piperonal	*tert*-butyl isocyanide	P8
R9	Coumarin 343	Aniline	Cinnamaldehyde	*tert*-butyl isocyanide	P9
R10	7-hydroxycoumarin-3-carboxylic acid	Aniline	Benzaldehyde	*n*-butyl isocyanide	P10
R11	7-hydroxycoumarin-3-carboxylic acid	Aniline	Benzaldehyde	*tert*-butyl isocyanide	P11
R12	7-hydroxycoumarin-3-carboxylic acid	Aniline	Piperonal	*n*-butyl isocyanide	P12
R13	7-hydroxycoumarin-3-carboxylic acid	Aniline	Piperonal	*tert*-butyl isocyanide	P13
R14	Coumarin-3-carboxylic acid	Aniline	Benzaldehyde	*n*-butyl isocyanide	P14
R15	Coumarin-3-carboxylic acid	Aniline	Benzaldehyde	*tert*-butyl isocyanide	P15
R16	Coumarin-3-carboxylic acid	Aniline	Piperonal	*n*-butyl isocyanide	P16
R17	Coumarin-3-carboxylic acid	Aniline	Piperonal	*tert*-butyl isocyanide	P17
R18	Coumarin-3-carboxylic acid	Aniline	Cinnamaldehyde	*tert*-butyl isocyanide	P18
R19	6,7-dihydroxycoumarin-3-carboxylic acid	Aniline	Benzaldehyde	*tert*-butyl isocyanide	P19
R20	6,7-dihydroxycoumarin-3-carboxylic acid	Aniline	Cinnamaldehyde	*tert*-butyl isocyanide	P20
R21	6,7-dihydroxycoumarin-3-carboxylic acid	Disperse Blue 1	Benzaldehyde	*tert*-butyl isocyanide	P21

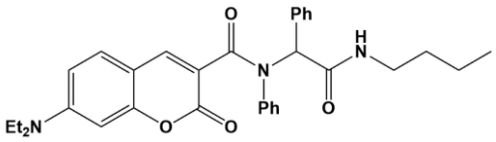

Product 1 (P1)

$C_{32}H_{35}N_3O_4$ – 525.64g mol^{-1}

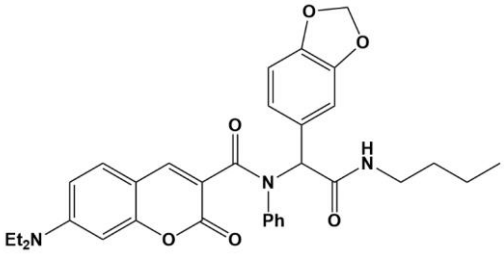

Product 2 (P2)

$C_{33}H_{35}N_3O_6$ – 569.65g mol^{-1}

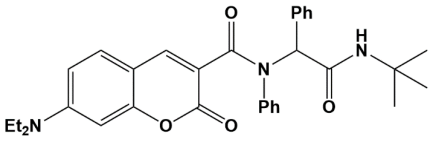

Product 3 (P3)

$C_{32}H_{35}N_3O_4$ – 525.64g mol^{-1}

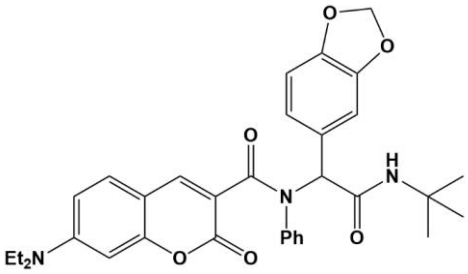

Product 4 (P4)

$C_{33}H_{35}N_3O_6$ – 569.65g mol^{-1}

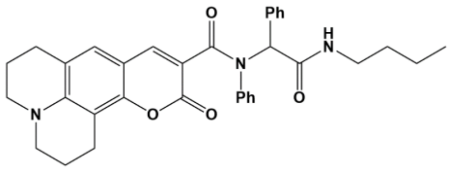

Product 5 (P5)

$C_{34}H_{35}N_3O_4$ – 549.66g mol^{-1}

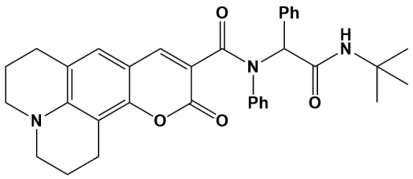

Product 6 (P6)

$C_{34}H_{35}N_3O_4$ – 549.66g mol^{-1}

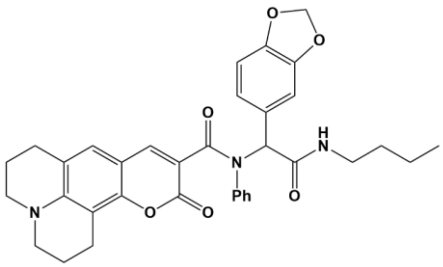

Product 7 (P7)

$C_{35}H_{35}N_3O_6$ – 593.67g mol^{-1}

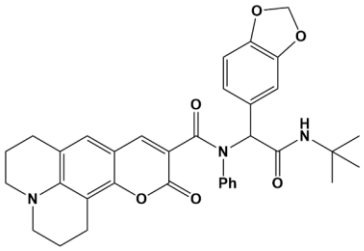

Product 8 (P8)

$C_{35}H_{35}N_3O_6$ – 593.67g mol^{-1}

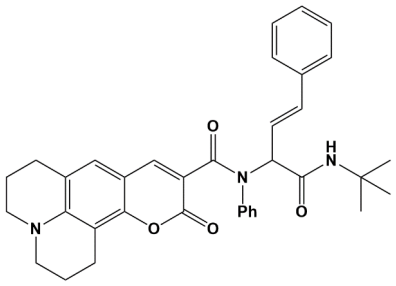

Product 9 (P9)

$C_{36}H_{37}N_3O_4$ – 575.70g mol^{-1}

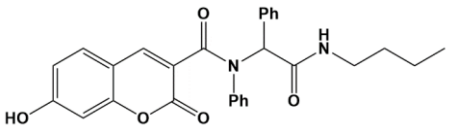

Product 10 (P10)

$C_{28}H_{26}N_2O_5$ – 470.52g mol^{-1}

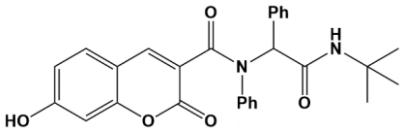

Product 11 (P11)

$C_{28}H_{26}N_2O_5$ – 470.52g mol^{-1}

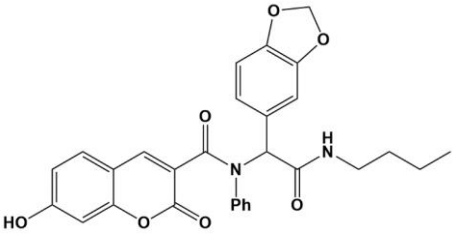

Product 12 (P12)

$C_{29}H_{26}N_2O_7$ – 514.52g mol^{-1}

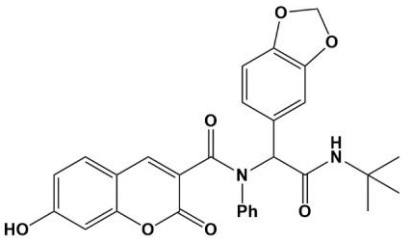

Product 13 (P13)

$C_{29}H_{26}N_2O_7$ – 514.52g mol^{-1}

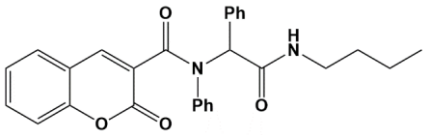

Product 14 (P14)

$C_{28}H_{26}N_2O_4$ – 454.52g mol^{-1}

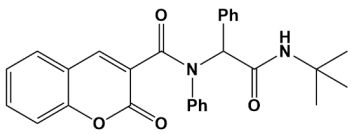

Product 15 (P15)

$C_{28}H_{26}N_2O_4$ – 454.52g mol^{-1}

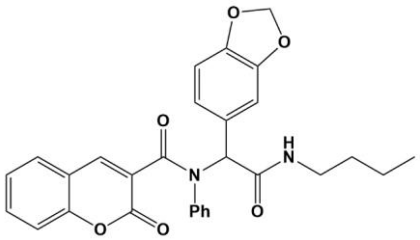

Product 16 (P16)

$C_{29}H_{26}N_2O_6$ – 498.53g mol^{-1}

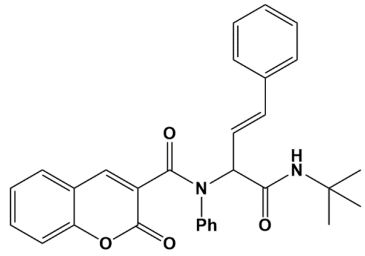

Product 17 (P17)

$C_{29}H_{26}N_2O_6$ – 498.53g mol^{-1}

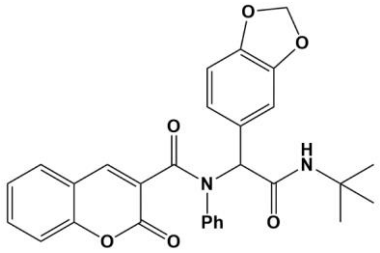

Product 18 (P18)

$C_{30}H_{28}N_2O_4$ – 480.55g mol^{-1}

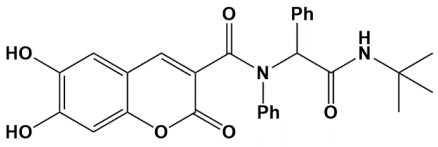

Product 19 (P19)

$C_{28}H_{26}N_2O_6$ – 486.51g mol^{-1}

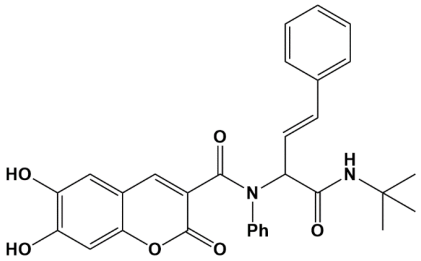

Product 20 (P20)

$C_{30}H_{28}N_2O_6$ – 512.55g mol^{-1}

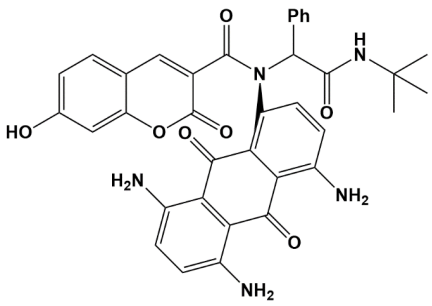

Product 21 (P21)

$C_{36}H_{30}N_5O_7$ – 644.65g mol^{-1}

In addition to P3, we ran several different UGI reactions, each varying in the combination of coumarin, amine, and/or aldehyde reagent used (**see Chapter 3.2 for the synthetic recipes used**). These are referred to in this work as R6, R9, R15, R18, R20, and R21. We were able to obtain MS spectra for R3, R6, R9, R15, R18, R20, R21, and NMR data for R3, R15, R20, R21. Product was observed for R15 and R20 only; the product for R15 is visible in both the NMR and MS spectra, whereas P20 was only present in the NMR (**see Appendix-4.2**).

Polar protic solvents, such as methanol, are the standard solvents used in Ugi reactions, although polar aprotic solvents and water can also be utilised.[369] Therefore, we optimized and ran a frequency calculation for each structure using a range of solvent species including methanol, dichloromethane, water, and hexane; hexane was included as a non-polar control.

In order to calculate the Standard Gibbs Free energy value for an Ugi reaction, we have to run frequency calculations on pre-optimized geometries. Frequency calculations calculate the modes of vibration available to a molecule at a specified temperature and pressure, which provides one with the Nuclear Internal Energy value. Using this value, the ADF software also determines the enthalpy (**eq. 8.1**) and entropy of the molecular system, allowing for easy computation of the Gibbs Free Energy value from there (**eq. 8.2**).

$$H = U + pV \qquad \text{(eq. 8.1)}$$

where:

H = enthalpy

U = Nuclear Internal Energy (kcal mol^{-1})

p = Pressure

V = volume

$$G = H - TS \qquad \textbf{(eq. 8.2)}$$

where:

G = Gibbs Free Energy

H = Enthalpy

T = Temperature

S = Entropy

From the electronic energies (kJ mol^{-1}) reported by our calculations, we calculated the Standard Gibbs Free energy value for Reactions 1-21 by subtracting the total energy values of the product(s) from those of the reactants (**eq. 8.3, 8.4**).

$$\Delta G_f^{\circ} = \sum(\text{Products}) - \sum(\text{Reactants}) \qquad \textbf{(eq. 8.3)}$$

$$\Delta G_f^{\circ} = \sum(\text{Peptoid} + \text{Water}) - \sum(\text{Carboxylic Acid} + \text{Amine} + \text{Aldehyde} + \text{Isocyanide}) \qquad \textbf{(eq. 8.4)}$$

We established that the energy was positive in every case (**Fig. 8.3**). This was unexpected, as Reactions 1-4 have been previously synthesized by Passos *et al*.[355] The frequency calculations were all conducted at room temperature (298.15K) and with methanol as the solvent, in line with the experimental data.

Repeating the process for the other solvents (dichloromethane, water, hexane) yielded the same results. Whilst the Gibbs Free Energy value for all these reactions is positive, the average Free Energy value across all solvents, including methanol, is roughly 71.89kJ mol^{-1}; most of these reactions should be feasible at just above room temperature.

The most favourable solvent for Ugi reactions appears to be Hexane, though as a non-polar, pH neutral solvent it would likely not be a viable option in the lab. There is clearly a problem with attempting to represent Ugi reactions in this manner and, in order to rectify this issue, we therefore attempted to model each transition state of the Ugi reaction separately, instead of

simply subtracting the total product energies from those of the reactant as we had previously done.

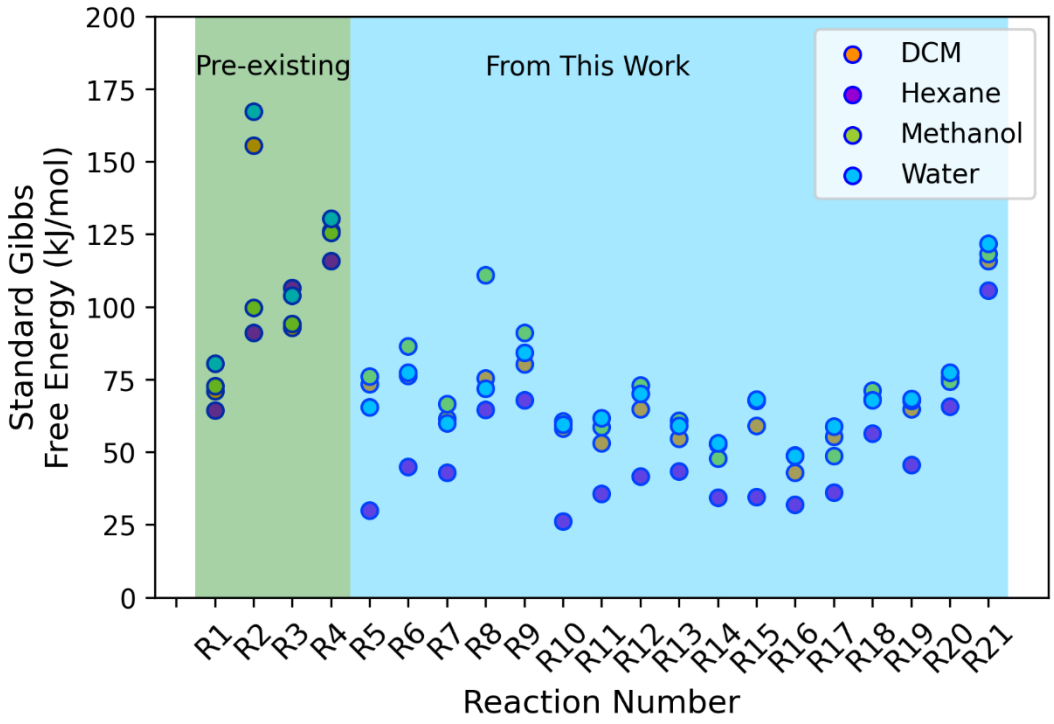

Figure 8.3. Gibbs Free Energy (kJ mol^{-1}) values for a number of different Ugi reactions. R1-R4 (green section have been previously reported in the literature,[355] with R5-R21 being devised as part of this work.

This, however proved beyond our ability to achieve for even a single reaction scheme; in attempting to apply this methodology to **R1**, we found that many of the Gibbs Free Energy of Formation values were positive at room temperature (**Fig. 8.4**). Additionally, we were unable

to converge a calculation for the TS of **Step 8** (**see Figure A-4.5.4**) due to steric hinderance from other sections of the molecule.

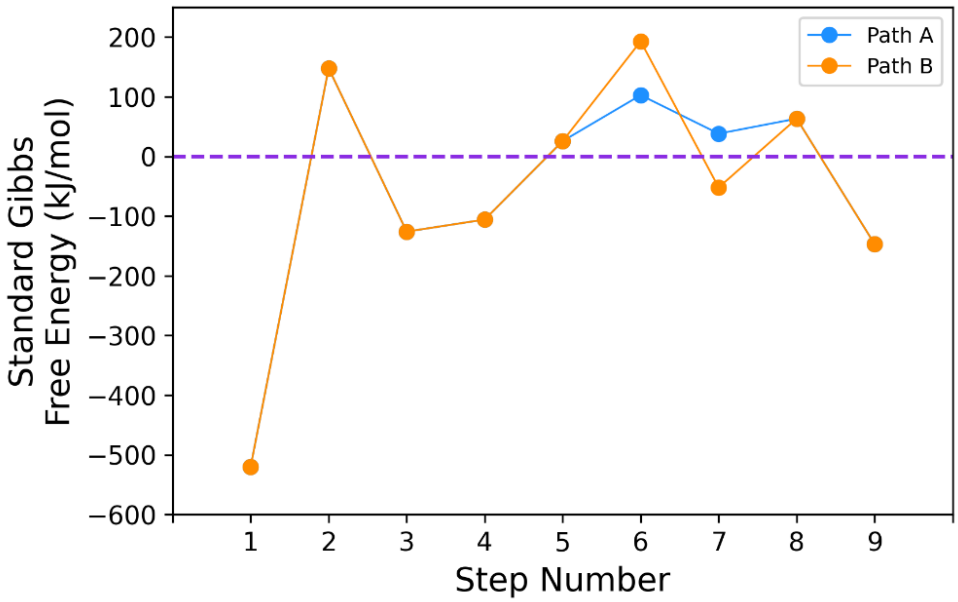

Figure 8.4. Gibbs Free Energy of Formation (kJ mol^{-1}) values for the R1 Ugi reaction, with each energy value calculated using ADF.

8.3 Ugi Conclusions

Over the course of our investigation, we attempted to replicate several known Ugi reaction methods, as well as conduct a few using novel reagents. We were able to observe formation of the peptoids referred to in this work as P3, P15, and P20 using NMR, though all in low concentrations and often drowned out by the overwhelming presence of unreacted reactants in the reaction mixture. We are unsure why such a large proportion of reactants were present in the final solution. If we were to continue with this project, our first port of call would be to alter the reaction conditions, temperature in particular, despite previous Ugi reactions being carried out at room temperature.

With respect to the computational work conducted, we still believe it worthwhile to try and model the Ugi reaction in full using intermediate and transition state structures. While we may not be able to model certain sections of the reaction mechanism, we can still assess earlier sections, thereby being able to ascertain the feasibility of particular species of aldehyde and amine as reactants for the wider Ugi reaction.

8.4 References

(345) Wender, P. A. Toward the Ideal Synthesis and Molecular Function through Synthesis-Informed Design. *Nat. Prod. Rep.* **2014**, *31* (4), 433–440. https://doi.org/10.1039/c4np00013g.

(346) Vázquez-Romero, A.; Kielland, N.; Arévalo, M. J.; Preciado, S.; Mellanby, R. J.; Feng, Y.; Lavilla, R.; Vendrell, M. Multicomponent Reactions for de Novo Synthesis of Bodipy Probes: In Vivo Imaging of Phagocytic Macrophages. *J. Am. Chem. Soc.* **2013**, *135* (43), 16018–16021. https://doi.org/10.1021/ja408093p.

(347) Barreto, A. D. F. S.; Vercillo, O. E.; Birkett, M. A.; Caulfield, J. C.; Wessjohann, L. A.; Andrade, C. K. Z. Fast and Efficient Microwave-Assisted Synthesis of Functionalized Peptoids via Ugi Reactions. *Org. Biomol. Chem.* **2011**, *9* (14), 5024–5027. https://doi.org/10.1039/c1ob05471f.

(348) El Kaïm, L.; Grimaud, L.; Oble, J. Phenol Ugi-Smiles Systems: Strategies for the Multicomponent N-Arylation of Primary Amines with Isocyanides, Aldehydes, and Phenols. *Angew. Chemie - Int. Ed.* **2005**, *44* (48), 7961–7964. https://doi.org/10.1002/anie.200502636.

(349) Iacobucci, C.; Reale, S.; De Angelis, F. Elusive Reaction Intermediates in Solution Explored by ESI-MS: Reverse Periscope for Mechanistic Investigations. *Angew. Chemie - Int. Ed.* **2016**, *55* (9), 2980–2993. https://doi.org/10.1002/anie.201507088.

(350) Ghashghaei, O.; Manna, C. A.; Vicente-García, E.; Revés, M.; Lavilla, R. Studies on the Interaction of Isocyanides with Imines: Reaction Scope and Mechanistic Variations. *Beilstein J. Org. Chem.* **2014**, *10*, 12–17. https://doi.org/10.3762/bjoc.10.3.

(351) Schwarz, J. S. . Preparation of Acyclic Isoimides and Their Rearrangement Rates to Imides. *J. Org. Chem* **1972**, *37* (18), 2906–2908. https://doi.org/10.7498/aps.51.2804.

(352) Iacobucci, C.; Reale, S.; Aschi, M.; Oomens, J.; Berden, G.; De Angelis, F. An Unprecedented Retro-Mumm Rearrangement Revealed by ESI-MS/MS, IRMPD Spectroscopy, and DFT Calculations. *Chem. Eur. J.* **2018**, *24* (27), 7026–7032. https://doi.org/10.1002/chem.201800347.

(353) Zhang, X.; Wang, S.; Liu, J.; Xie, Z.; Luan, S.; Xiao, C.; Tao, Y.; Wang, X. Ugi Reaction of Natural Amino Acids: A General Route toward Facile Synthesis of Polypeptoids for Bioapplications. *ACS Macro Lett.* **2016**, *5* (9), 1049–1054. https://doi.org/10.1021/acsmacrolett.6b00530.

(354) Tao, Y.; Wang, Z.; Tao, Y. Polypeptoids Synthesis Based on Ugi Reaction: Advances and Perspectives. *Biopolymers* **2019**, *110* (6). https://doi.org/10.1002/bip.23288.

(355) Passos, S. T. A.; Correa, J. R.; Soares, S. L. M.; Da Silva, W. A.; Neto, B. A. D. Fluorescent Peptoids as Selective Live Cell Imaging Probes. *J. Org. Chem.* **2016**, *81* (6), 2646–2651. https://doi.org/10.1021/acs.joc.6b00034.

(356) Bush, J. T.; Walport, L. J.; McGouran, J. F.; Leung, I. K. H.; Berridge, G.; van Berkel, S. S.; Basak, A.; Kessler, B. M.; Schofield, C. J. The Ugi Four-Component Reaction Enables Expedient Synthesis and Comparison of Photoaffinity Probes. *Chem. Sci.* **2013**, *4* (11), 4115–4120. https://doi.org/10.1039/c3sc51708j.

(357) Puthumana, S. S. E.; Damodaran, B. Multicomponent-Reaction- (MCR-) Assisted Synthesis of a Coumarin-Based Deep Blue Emitter for OLEDs and Related Applications. *ChemistrySelect* **2018**, *3* (11), 2951–2957. https://doi.org/10.1002/slct.201702989.

(358) Wu, H.; Yang, B.; Zhao, Y.; Wei, Y.; Wang, Z.; Wang, X.; Tao, L. Fluorescent Protein-Reactive Polymers via One-Pot Combination of the Ugi Reaction and RAFT Polymerization. *Polym. Chem.* **2016**, *7* (30), 4867–4872. https://doi.org/10.1039/c6py00781c.

(359) Ramírez-Ornelas, D. E.; Sola-Llano, R.; Bañuelos, J.; Arbeloa, I. L.; Martínez-Álvarez, J. A.; Mora-Montes, H. M.; Franco, B.; Peña-Cabrera, E. Synthesis, Photophysical Study, and Biological Application Analysis of Complex Borondipyrromethene Dyes. *ACS Omega* **2018**, *3* (7), 7783–7797.

https://doi.org/10.1021/acsomega.8b00753.

(360) Levi, L.; Müller, T. J. J. Multicomponent Syntheses of Functional Chromophores. *Chem. Soc. Rev.* **2016**, *45* (10), 2825–2846. https://doi.org/10.1039/c5cs00805k.

(361) He, L.; Xu, Q.; Liu, Y.; Wei, H.; Tang, Y.; Lin, W. Coumarin-Based Turn-On Fluorescence Probe for Specific Detection of Glutathione over Cysteine and Homocysteine. *ACS Appl. Mater. Interfaces* **2015**, *7* (23), 12809–12813. https://doi.org/10.1021/acsami.5b01934.

(362) Bu, M.; Li, H.; Wang, H.; Wang, J.; Lin, Y.; Ma, Y. Synthesis of Ergosterol Peroxide Conjugates as Mitochondria Targeting Probes for Enhanced Anticancer Activity. *Molecules* **2019**, *24* (18), 1–15. https://doi.org/10.3390/molecules24183307.

(363) Balalaie, S.; Bigdeli, M. A.; Sheikhhosseini, E.; Habibi, A.; Moghadam, H. P.; Naderi, M. Efficient Synthesis of Novel Coumarin-3-Carboxamides (=2-Oxo-2h-1- Benzopyran-3-Carboxamides) Containing Lipophilic Spacers. *Helv. Chim. Acta* **2012**, *95* (3), 528–535. https://doi.org/10.1002/hlca.201100238.

(364) Bay, S.; Müller, T. J. J. Phenothiazine-Aromatic Hydrocarbon Acceptor Dyads as Photo-Induced Electron Transfer Systems by Ugi Four-Component Reaction. *Zeitschrift fur Naturforsch. - Sect. B J. Chem. Sci.* **2014**, *69* (5), 541–553. https://doi.org/10.5560/ZNB.2014-4060.

(365) Afshari, R.; Ghasemi, V.; Shaabani, S.; Shaabani, A.; Aladaghlo, Z.; Fakhari, A. R. Post-modification of Phthalocyanines via Isocyanide-Based Multicomponent Reactions: Highly Dispersible Peptidomimetic Metallophthalocyanines as Potent Photosensitizers. *Dye. Pigment.* **2019**, *166* (July 2018), 49–59. https://doi.org/10.1016/j.dyepig.2019.03.018.

(366) Huang, S. P.; Shiota, Y.; Yoshizawa, K. DFT Study of the Mechanism for Methane Hydroxylation by Soluble Methane Monooxygenase (SMMO): Effects of Oxidation State, Spin State, and Coordination Number. *Dalt. Trans.* **2013**, *42* (4), 1011–1023. https://doi.org/10.1039/c2dt31304a.

(367) Yao, Y.; Zhang, X.; Ma, S. DFT Study on the: E -Stereoselective Reductive A3-Coupling Reaction of Terminal Alkynes with Aldehydes and 3-Pyrroline. *Org. Chem. Front.* **2020**, *7* (15), 2047–2054. https://doi.org/10.1039/d0qo00564a.

(368) Monreal-Corona, R.; Solà, M.; Pla-Quintana, A.; Poater, A. Stereoretentive Formation of Cyclobutanes from Pyrrolidines: Lessons Learned from DFT Studies of the Reaction Mechanism. *J. Org. Chem.* **2023**, *88* (7), 4619–4626. https://doi.org/10.1021/acs.joc.3c00080.

Chapter 9: Conclusions

Over the course of this work, we have conducted accurate, empirically benchmarked, computational modelling of hexalacunary and W_{48} POMs, primarily the $[P_2W_{12}O_{48}]^{14-}$ and $[P_8W_{48}O_{184}]^{40-}$ sub-species. We have achieved this by comparing our DFT optimized models against available crystallographic data, taking note of differences in distances and angles between various, specified atoms throughout the framework when various functionals are utilised. We also observed that the inclusion of counter cations in our models didn't improve the accuracy of said models when compared against the empirical data. This was consistent for both the hexalacunary **{W_{12}}** and POM wheel **{W_{48}}** species when examined against structural dimensions, and NMR and UV spectroscopy. The one exception is with regards to electron distribution throughout the POM, visualized with MEPs or by reviewing the MDC-q charge values; cations significantly alter electron localization when included and therefore including a fraction of the total number of cations, particularly protons over bulkier countercations, improves the accuracy with which we can identify regions of relative nucleo- or electrophilicity.

Additionally, we carried out extensive work into improving the accuracy of DFT-based prediction of UV-Vis absorption bands. We established that, contrary to the literature, hybrid functionals, specifically PBE0, are required to yield results comparable to empirically reported spectra across a wide range of POMs. Additionally, we discerned that, if a solvent method such as COSMO is included in the model, the inclusion of counter cations did not improve the accuracy of the calculated results; we hope this discovery in particular will save future researchers a lot of unnecessary time and frustration. Finally, we found that different sub-families of POMs required slight changes in the DFT method deployed to determine their electronic properties. HPOMs, such as Keggin and Wells-Dawson, require the use of TI-DFT to yield accurate results, whereas IsoPOM, including Lindqvist and Decatungstate, necessitated TD-DFT use.

9.1 Outlook

Given the rising interest in applying POMs to some of the most pertinent scientific problems of our times, especially with respect to their electronic properties, we predict that attempts to model these chemical frameworks using computational means will only increase in frequency. It is therefore more crucial than ever to establish well thought-out and standardized rules for modelling POMs, when we finally have the computational capabilities to replicate empirical properties to an excellent degree of accuracy which just 20 years ago remained tantalisingly out of reach of researchers.

Whilst sub-sections of extended POMzite networks are currently too complex for us to model using DFT, there is still an unexplored "no-man's land" where we can "build up" into using a bottom-up approach. By optimizing $[P_8W_{48}O_{184}]^{40-}$, it becomes a lot easier to do the same for $K_8[P_8W_{48}O_{184}]^{32-}$, followed by $K_{28}[P_8W_{48}O_{184}]^{12-}$, and so forth. This being said, we have established that, in most cases, omitting the K countercations provides the most accurate model for a fraction of the computational cost associated with including the full set of 28 cations. Being able to reduce the complexity of this model allows us to make the same assumption for the larger POMzite subsection, where being able to substantially reduce the complexity of the network is key to approaching a model, we can successfully converge using DFT calculations.

The goal moving forward would be to optimize small sub-sections of POMzites, for example a structure like $[(CoO_2)\{[P_8W_{48}O_{184}]\}_2]^{100-}$, which contains at least two **{W_{48}}** units connected by at least one TM linker unit; it is hoped that once we optimize a structure of this magnitude, we can freely interchange Co^{2+} with other TM linker elements and gain greater insight into the effect specific TM linker elements have on the configuration of the final POMzite material. This may require us initially attaching these TM linker units to smaller $[P_2W_{12}O_{48}]^{14-}$ or $[P_4W_{24}O_{94}]^{24-}$ POM structures but, now that we have good modelling principles for these types of POMs, we can immediately begin asking key questions which will lead us into modelling the desired POMzite subsections. We can additionally use the same structural dimensions

devised by our work with **{P_8W_{48}}** for work with POMzite networks; having established these basic modelling tenets for these structures, we hope to inspire more attempts at analysing POMzite networks using DFT moving forward.

While reporting optimized structures and making them readily available to researchers via deposition into accessible databases is useful, we believe our work into UV-Vis spectroscopy to be of special interest and importance to future researchers. Electronic properties, in particular the localization of and energy difference between the frontier orbitals (HOMO-LUMO gap), are incredibly important to determine accurately; the redox ability of a POM framework is very dependent on the magnitude of the HOMO-LUMO gap and is frequently reported in computational works. Our literature review highlights many of the misunderstandings and inaccuracies of previous works whilst rigorously justifying our own conclusions regarding appropriate levels of theory at which to operate at.

If we were to continue our work, we would ideally want to fully explore and explain the reason why certain POM sub-species require TI- or TD-DFT methods to produce accurate absorption band energy values, apparently based on the presence or absence of an encapsulated heteroatom within the framework. We are unclear as to whether this distinction in the theory between Iso- and HeteroPOMs is mathematically sound or is an oversight

Appendix-1: Chapter 5

Appendix-1.1: Benchmarking Results

Table A-1.1. List of functionals tested in this study, H-L values for the $[P_2W_{18}O_{62}]^{6-}$ Wells-Dawson. Frozen core options can be: Small (SFC), Large (LFC), or Not present (NFC)

Task	Functional	Basis Set	Frozen Core	No. of Cores (No. of Nodes)	Run Duration	Electronic Energy (Hartrees)	HOMO–LUMO (eV)
SP	PBE	TZP	SFC	20 (1)	10 minutes	−26.4997	2.32
SP	PBE	TZP	LFC	20 (1)	7 minutes	−26.0259	2.32
OPT	PBE	TZP	SFC	20 (2)	1 hour	−26.4997	2.32
OPT	PBE	TZP	LFC	20 (1)	1 hour	−26.0443	2.23
OPT	PBE	DZP	SFC	20 (1)	40 minutes	-26.4528	2.28
OPT	PBE	TZ2P	SFC	20 (1)	1 hour	−26.9075	2.43
OPT	PBE	QZ4P	SFC	20 (1)	7 hours	−26.8707	2.44
OPT	PBE−D	TZP	SFC	40 (1)	1 hour	−23.8266	0.62
OPT	PBE0	TZP	SFC	40 (1)	26 hours	−34.3282	4.34
OPT	BP86	TZP	SFC	40 (1)	35 minutes	−26.3361	2.32
OPT	BP86	TZP	LFC	20 (1)	1 hour	−25.8750	2.22
OPT	wB97x	TZP	NFC	20 (1)	72 hours	−45.8199	8.42
OPT	B3LYP	TZP	SFC	20 (2)	57 hours	−31.7635	3.82
OPT	B3LYP	TZP	LFC	20 (1)	55 hours	−31.2809	3.77
OPT	B3LYP−D	TZP	SFC	40 (1)	26 hours	−29.2849	1.13

Table A-1.2. Comparison between HOMO and LUMO energy values reported by Vilà-Nadal *et al*.[284] and those benchmarked by ourselves. **OPT/PBE/TZP/COSMO/Small Frozen Cores**

Species	Reported HOMO (eV)	Reported LUMO (eV)	Reported HOMO-LUMO (eV)	Benchmarked HOMO (eV)	Benchmarked LUMO (eV)	Benchmarked HOMO-LUMO (eV)
$[S_2Mo_{18}O_{60}]^{4-}$	-6.06	-5.18	0.88	-5.98	-5.29	0.69
$[S_2Mo_{18}O_{62}]^{4-}$	-6.77	-5.15	1.62	-6.87	-5.25	1.62
$[S_2W_{18}O_{60}]^{4-}$	-6.48	-4.61	1.87	-6.50	-4.87	1.63
$[S_2W_{18}O_{62}]^{4-}$	-6.89	-4.62	2.27	-7.12	-4.84	2.28

Table A-1.3. Comparison between HOMO and LUMO energy values reported by Cameron *et al.*[78] (TURBOMOLE) and those benchmarked by ourselves (ADF). **SP/B3LYP/TZP/COSMO/Small Frozen Cores**

Species	Reported HOMO (eV)	Reported LUMO (eV)	Reported HOMO-LUMO (eV)	Benchmarked HOMO (eV)	Benchmarked LUMO (eV)	Benchmarked HOMO-LUMO (eV)
$[P_2W_{12}O_{46}]^{14-}$	-4.41	-1.62	2.79	-3.55	-1.26	2.29
$[P_8W_{48}O_{176}]^{40-}$	-5.81	-1.97	3.83	-4.26	-1.80	2.46
$[Se_2W_{12}O_{46}]^{12-}$	-5.06	-2.16	2.90	-5.73	-1.57	4.16
$[Se_8W_{48}O_{176}]^{32-}$	-6.36	-2.53	3.82	-6.32	-2.38	3.94

For **Table A-1.4.** α-isomers were in very good agreement with the experimental data but the same is less so for the other isomers; this is attributed to the non-α-isomers being built within the ADF programme and not originating from an experimentally obtained xyz file. Manipulating structures to the extent of rotating sections tends to yield results further from the literature than those which are not.

Table A-1.4. Comparison between experimentally obtained HOMO and LUMO, and reduction energy values reported by Vilà-Nadal *et al.*[180] and those benchmarked by ourselves. **OPT/PBE/TZP/COSMO/Small Frozen Cores**

Species	Reported HOMO-LUMO (eV)	Reported Reduction Energy (eV) (E_f^o vs NHE)	Benchmarked HOMO-LUMO (eV)	Benchmarked Reduction Energy (eV)
α-$[P_2W_{18}O_{62}]^{6-}$	2.25	-4.22	2.32	-4.08
α-$[W_{19}O_{62}]^{10-}$	1.31	-3.68	1.36	-3.15
γ*-$[W_{19}O_{62}]^{10-}$	1.60	-3.68	1.92	-3.23
γ*-$[TeW_{18}]^{10-}$	1.65	-3.36	1.95	-3.10
β*-$[IW_{18}]^{9-}$	1.04	-3.36	1.63	-4.21

Finally, we come to **Table A-1.5.**, where bond lengths and angles for the classical WD framework are benchmarked. Though our calculations are slightly out of the expected range for a couple of properties, namely the P-P dimension, and tend to be at the greater extreme of the accepted range, they are generally within the boundaries for the sake of accuracy and provide a solid end to our benchmarking.

Table A-1.5. Comparison of bond lengths and other properties for $[P_2W_{18}O_{62}]^{6-}$ between values reported by a paper by Zhang *et al.*[64] and those benchmarked during the course of this work. **OPT/PBE/TZP/COSMO/Small Frozen Cores**

Species	LUMO (eV)	P-O_i (nm)	W-O_i (nm)	W-O_t (nm)	W-O_b (nm)	P-P (nm)	W-O_e-W (°)
Reported Experimental Data	N/A	1.531-1.569	2.306-2.408	1.679-1.743	1.863-1.940	3.986	159.7-163.4
Reported Calculation Data	-4.16	1.544-1.589	2.345-2.355	1.721-1.722	1.895-1.921	3.981	161.2
Benchmarked Calculation Data	-4.38	1.556	2.400	1.733	1.934	4.000	163.2

Based on the results displayed in **Tables A-1.2.** to **A-1.4.**, we can conclude that ADF at the PBE level accurately describes the HOMO-LUMO energy gap and reduction energy values for POMs. **Table A-1.2.** simply gave us a baseline to compare our ADF calculations with, whereas **Table A-1.3.** allowed for comparison with the TURBOMOLE software; the benchmarking against TURBOMOLE is poor but this is attributed to the differences between software packages, as well as the use of B3LYP which we have found to be overestimate POM properties relative to PBE.

Appendix-1.2: Selenium Heteroatom Configurations

Before detailing the specific HOMO and LUMO energy level values for the various WD, hexalacunary, and W_{48} strutures analyzed in this work, a quick word is necessary on our method of modelling the hexalacunary $[Se_2W_{12}O_{46}]^{14-}$ framework; towards the beginning of this investigation we used a xyz file from a paper by Cameron J.M. *et al* for our **{Se_8W_{48}}** wheel.[78] It was noticed that the oxygen atom missing from the structure due to the heteroatom anion being $[SeO_3]^{2-}$ (the oxygen is not missing when the anion is XO_4 or XO_6) was in a different position from that usually described for WD cages that contain a XO_3 anion (see **Figure A-1.1.**)[48,54,370]; unsure as to whether this was a special case or if a mistake had been made by this paper we made a geometry for the **{Se_2W_{12}}** where the vacant oxygen site was in the position

typically assumed to be correct, and a second WD structure where the site was in the more unusual location described by the paper. The aim was to identify if one configuration of site location yielded a more stable structure and thereby elucidate which was more suitable for modelling.

Our calculations found the 'normal' configuration to be the more stable of the two, but it's worth mentioning that there is not a large difference in either the electronic energy or the size of the HOMO−LUMO gap, thus we continued to use the standard configuration for the sake of consistency. As more hexalacunaries are synthesized and characterized, it would be prudent to determine which structure is correct when these oxo vacancies arise; it may be that the standard configuration is indeed correct and that a previously unknown rearrangement process occurs in an effort to stabilise the lacunary.

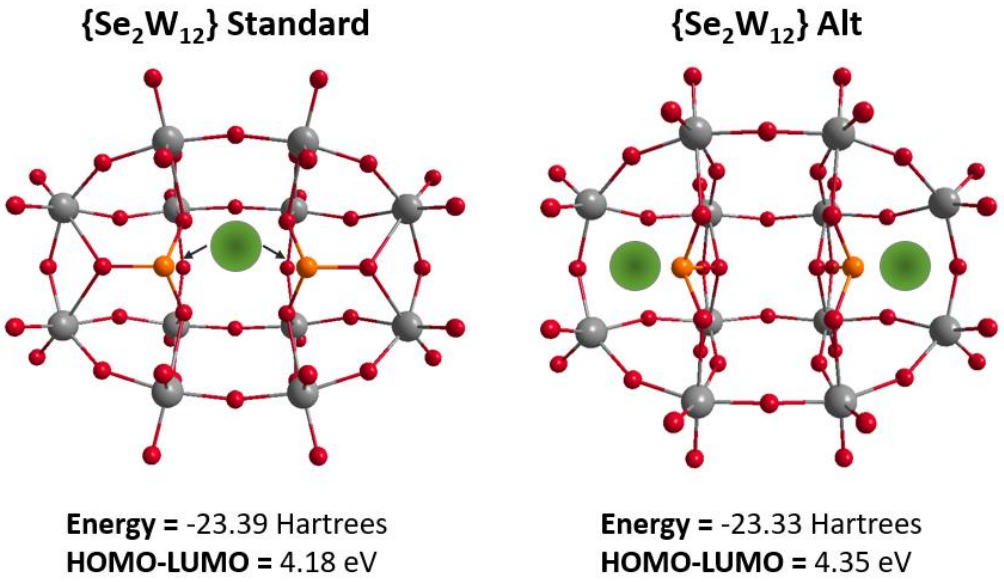

Figure A-1.1. Comparison between 'standard' and 'alternative' **{Se_2W_{12}}** quarter structures. A green sphere is used to illustrate where the vacant oxygen site is in each framework. **B3LYP/TZP/SFC/COSMO**

Appendix-1.3: POM HOMO-LUMO Energy Values

Table A-1.6. Electronic values for different species of WD frameworks obtained with PBE functional. **PBE/TZP/COSMO/Small Frozen Cores**

Species Formula	Heteroatom	E_{HOMO} (eV)	E_{LUMO} (eV)	ΔE_{H-L} (eV)
$[As_2W_{18}O_{62}]^{6-}$	AsO_4 (**V**)	−6.72	−4.41	2.31
$[P_2W_{18}O_{62}]^{6-}$	PO_4 (**V**)	−6.70	−4.38	2.32
$[Se_2W_{18}O_{60}]^{4-}$	SeO_3 (**IV**)	−7.01	−4.91	2.10
$[Se_2W_{18}O_{60}]^{4-}$ **ALT**	SeO_3 (**IV**)	−7.12	−4.85	2.27

Table A-1.7. Electronic values for different species of $[X_mW_{12}O_n]^{p-}$ lacunary POMs obtained with PBE functional. **PBE/TZP/COSMO/Small Frozen Cores**

Species Formula	Heteroatom	E_{HOMO} (eV)	E_{LUMO} (eV)	ΔE_{H-L} (eV)
$[As_2W_{12}O_{48}]^{14-}$	AsO_4 (**V**)	−4.37	−1.57	2.80
$[P_2W_{12}O_{48}]^{14-}$	PO_4 (**V**)	−4.42	−1.60	2.82
$[Se_2W_{12}O_{46}]^{12-}$	SeO_3 (**IV**)	−4.53	−1.96	2.57
$[Se_2W_{12}O_{46}]^{12-}$ **ALT**	SeO_3 (**IV**)	−4.84	−2.05	2.79

Table A-1.8. Electronic values for different species of $[X_8W_{48}O_n]^{p-}$ obtained with PBE functional. **PBE/TZP/COSMO/Small Frozen Cores**

Species Formula	Heteroatom	E_{HOMO} (eV)	E_{LUMO} (eV)	ΔE_{H-L} (eV)
$[As_8W_{48}O_{184}]^{40-}$	AsO_4 (**V**)	-4.69	-2.06	2.62
$[P_8W_{48}O_{184}]^{40-}$	PO_4 (**V**)	−4.78	−2.17	2.61
$[Se_8W_{48}O_{176}]^{32-}$	SeO_3 (**IV**)	−5.05	−2.64	2.41

Appendix-1.4: Benchmarking {P_8W_{48}} Pore Diameter

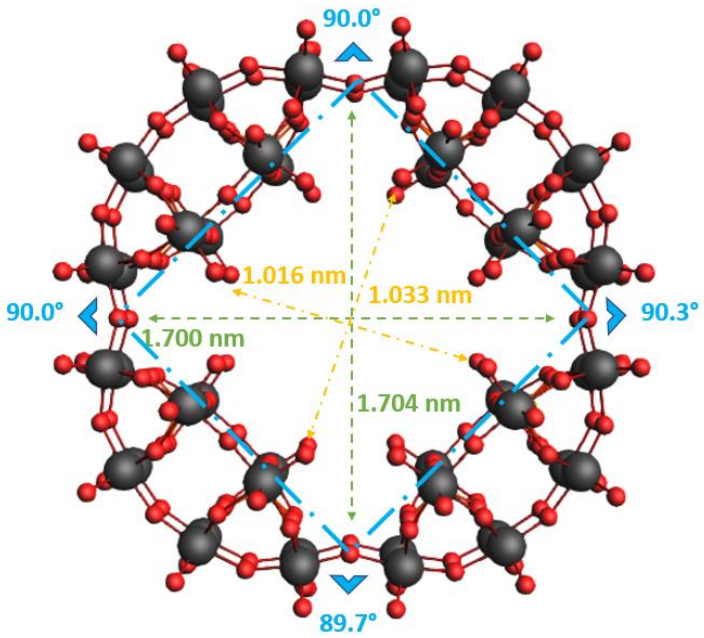

Figure A-1.2. Structure for $[P_8W_{48}O_{184}]^{40-}$, showing measurements for angles (blue), inner diameters (yellow), and outer diameters (green).

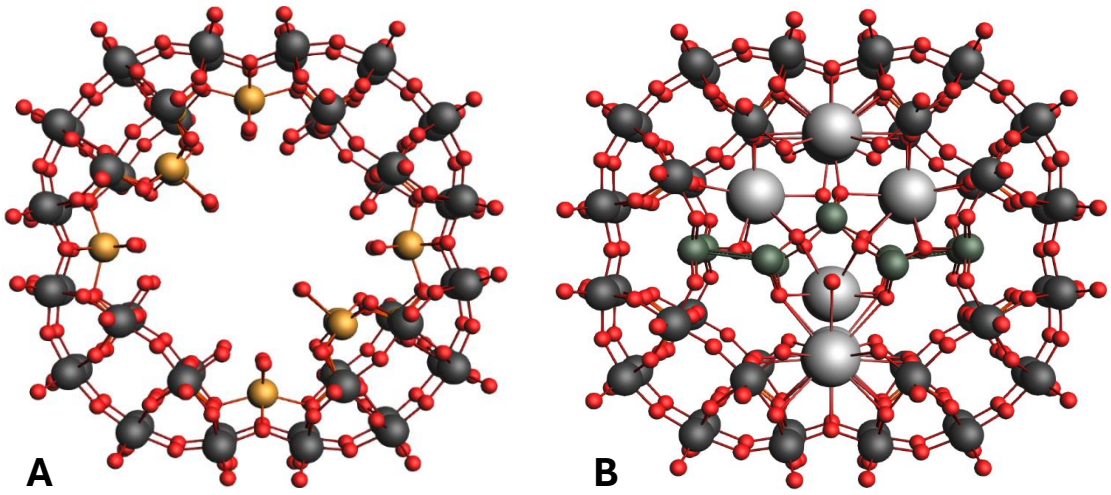

Figure A-1.3. Geometries of $Co_8[P_8W_{48}O_{196}]^{48-}$ (**A**) and $K_7As_{10}[P_8W_{48}O_{200}]^{15-}$ (**B**). Cations can occupy the central pore in many different configurations, some of which, such as $K_7As_{10}[P_8W_{48}O_{200}]^{15-}$, will cause the pore to stretch to unnatural dimensions.

Table A-1.9. Collection of empirical angle dimensions for **{P_8W_{48}}** structures, with a set of angles from a DFT structure for comparison. Included also is the crystal R-factor, which parameterizes the quality of the crystal. **PBE/TZP/COSMO/Small Frozen Cores**

Formula	Crystal R-factor (%)	Angle 1 (°)	Angle 2 (°)	Angle 3 (°)	Angle 4 (°)	Reference
$[P_8W_{48}O_{184}]^{40-}$		90.0	90.3	89.7	90.0	Calculated
$[P_8W_{48}O_{184}]^{40-}$	4.87	91.0	88.6	91.0	88.6	Yi, X. *et al.*[371]
$[P_8W_{48}O_{184}]^{40-}$	6.99	90.0	90.1	89.8	90.0	Jiao, Y.Q. *et al.*[372]
Mean		90.5	89.4	90.4	89.3	
$Co_8[P_8W_{48}O_{196}]^{48-}$	7.34	89.9	90.4	89.7	90.0	Sasaki, S. *et al.*[373]
$Cu_8[P_8W_{48}O_{196}]^{48-}$	7.72	89.9	90.2	89.8	90.0	Sasaki, S. *et al.*[373]
$K_7As_{10}[P_8W_{48}O_{200}]^{15-}$	7.63	81.3	98.7	81.3	98.8	Niu, Y. *et al.*[374]
$K_8[P_8W_{48}O_{184}]^{32-}$	6.96	90.0	90.0	90.0	90.0	Gabb, D. *et al.*[375]
$Mn_8[P_8W_{48}O_{196}]^{48-}$	7.40	90.0	90.1	89.8	90.1	Sasaki, S. *et al.*[373]
$Ni_8[P_8W_{48}O_{196}]^{48-}$	7.33	90.0	90.4	89.5	90.1	Sasaki, S. *et al.*[373]
$Zn_8[P_8W_{48}O_{196}]^{48-}$	7.18	90.0	90.2	89.7	90.1	Sasaki, S. *et al.*[373]
Mean		88.7	91.4	88.5	91.3	

Table A-1.10. Collection of empirical diameter dimensions for **{P_8W_{48}}** structures, with a set of diameter dimensions from a DFT structure for comparison. Also included is the Mean Absolute Error (MAE) and Standard Deviation (SD) value for each dimension, depending on if the structure contains countercations or not. **Figure A-1.2.** displays where the inner and outer ring diameters measure to and from within the pore. **PBE/TZP/COSMO/Small Frozen Cores**

Formula	Inner Ring Diameter 1 (nm)	Inner Ring Diameter 2 (nm)	Outer Ring Diameter 1 (nm)	Outer Ring Diameter 2 (nm)	Reference
$[P_8W_{48}O_{184}]^{40-}$	1.016	1.033	1.700	1.704	Calculated
$[P_8W_{48}O_{184}]^{40-}$	0.966	1.035	1.632	1.667	Yi, X. *et al.*[371]
$[P_8W_{48}O_{184}]^{40-}$	0.977	1.017	1.644	1.646	Jiao, Y.Q. *et al.*[372]
MAE	0.0445	0.0070	0.0620	0.0475	
STD	0.0055	0.0090	0.0060	0.0105	
$Co_8[P_8W_{48}O_{196}]^{48-}$	0.972	1.057	1.623	1.630	Sasaki, S. *et al.*[373]
$Cu_8[P_8W_{48}O_{196}]^{48-}$	0.978	1.069	1.617	1.620	Sasaki, S. *et al.*[373]
$K_7As_{10}[P_8W_{48}O_{200}]^{15-}$	0.932	1.094	1.790	1.536	Niu, Y. *et al.*[374]
$K_8[P_8W_{48}O_{184}]^{32-}$	0.999	0.999	1.653	1.653	Gabb, D. *et al.*[375]
$Mn_8[P_8W_{48}O_{196}]^{48-}$	0.975	1.071	1.633	1.630	Sasaki, S. *et al.*[373]
$Ni_8[P_8W_{48}O_{196}]^{48-}$	0.974	1.064	1.628	1.634	Sasaki, S. *et al.*[373]
$Zn_8[P_8W_{48}O_{196}]^{48-}$	0.974	1.064	1.621	1.625	Sasaki, S. *et al.*[373]
MAE	0.1540	0.1870	0.3350	0.3000	
STD	0.2372	0.5017	0.4717	0.3735	

Appendix-1.5: Benchmarking {As_8W_{48}} Pore Diameter

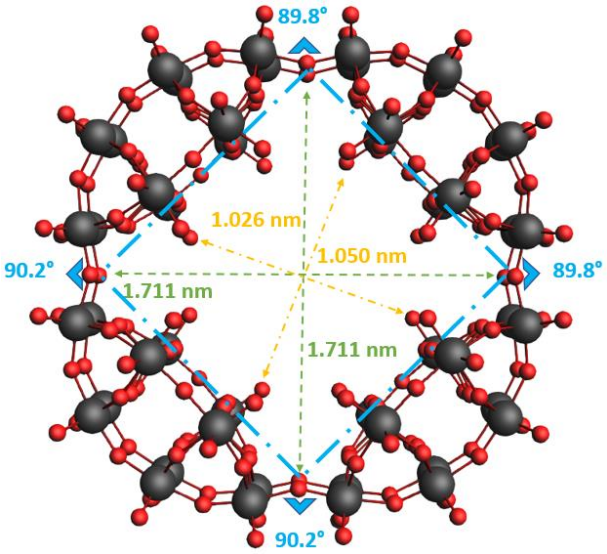

Figure A-1.4. Structure for $[As_8W_{48}O_{184}]^{40-}$, showing measurements for angles (blue), inner diameters (yellow), and outer diameters (green).

Table A-1.11. Collection of empirical angle dimensions for **{As_8W_{48}}** structures, with a set of angles from a DFT structure for comparison. Included also is the crystal R-factor, which parameterizes the quality of the crystal. **PBE/TZP/COSMO/Small Frozen Cores**

Formula	Crystal R-factor (%)	Angle 1 (°)	Angle 2 (°)	Angle 3 (°)	Angle 4 (°)	Reference
$[As_8W_{48}O_{184}]^{40-}$		89.8	89.8	90.2	90.2	Calculated
$K_8[As_8W_{48}O_{184}]^{32-}$	7.74	90.0	90.0	90.0	90.0	Mbomekallé, I.M. *et al.*[322]

Table A-1.12. Collection of empirical diameter dimensions for **{As_8W_{48}}** structures, with a set of angles from a DFT structure for comparison. Included also is the crystal R-factor, which parameterizes the quality of the crystal. **PBE/TZP/COSMO/Small Frozen Cores**

Formula	Inner Ring Diameter 1 (nm)	Inner Ring Diameter 2 (nm)	Outer Ring Diameter 1 (nm)	Outer Ring Diameter 2 (nm)	Reference
$[As_8W_{48}O_{184}]^{40-}$	1.026	1.050	1.711	1.711	Calculated
$K_8[As_8W_{48}O_{184}]^{32-}$	1.020	1.051	1.669	1.669	Mbomekallé, I.M. *et al.*[322]

Appendix-1.6: Benchmarking {Se_8W_{48}} Pore Diameter

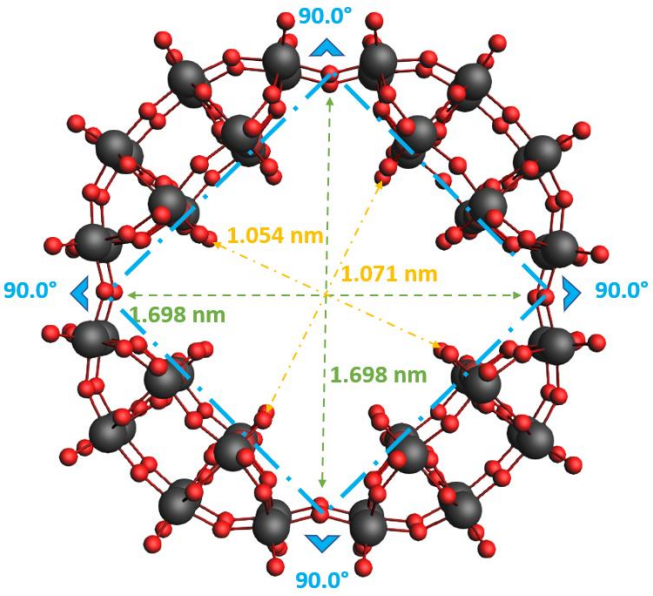

Figure A-1.5. Structure for $[Se_8W_{48}O_{176}]^{32-}$, showing measurements for angles (blue), inner diameters (yellow), and outer diameters (green).

Table A-1.13. Collection of empirical angle dimensions for **{Se_8W_{48}}** structures, with a set of angles from a DFT structure for comparison. Included also is the crystal R-factor, which parameterizes the quality of the crystal. **PBE/TZP/COSMO/Small Frozen Cores**

Formula	Crystal R-factor (%)	Angle 1 (°)	Angle 2 (°)	Angle 3 (°)	Angle 4 (°)	Reference
$[Se_8W_{48}O_{176}]^{32-}$		90.0	90.0	90.0	90.0	Calculated
$[Se_8W_{48}O_{176}]^{32-}$	5.05	90.1	89.9	89.9	90.1	Cameron, J.M. *et al.*[78]

Table A-1.14. Collection of empirical diameter dimensions for **{Se_8W_{48}}** structures, with a set of angles from a DFT structure for comparison. Included also is the crystal R-factor, which parameterizes the quality of the crystal. **PBE/TZP/COSMO/Small Frozen Cores**

Formula	Inner Ring Diameter 1 (nm)	Inner Ring Diameter 2 (nm)	Outer Ring Diameter 1 (nm)	Outer Ring Diameter 2 (nm)	Reference
$[Se_8W_{48}O_{176}]^{32-}$	1.054	1.071	1.698	1.698	Calculated
$[Se_8W_{48}O_{176}]^{32-}$	1.057	1.059	1.657	1.657	Cameron, J.M. *et al.*[78]

Appendix-1.7: K Countercations in {P_8W_{48}} Structure

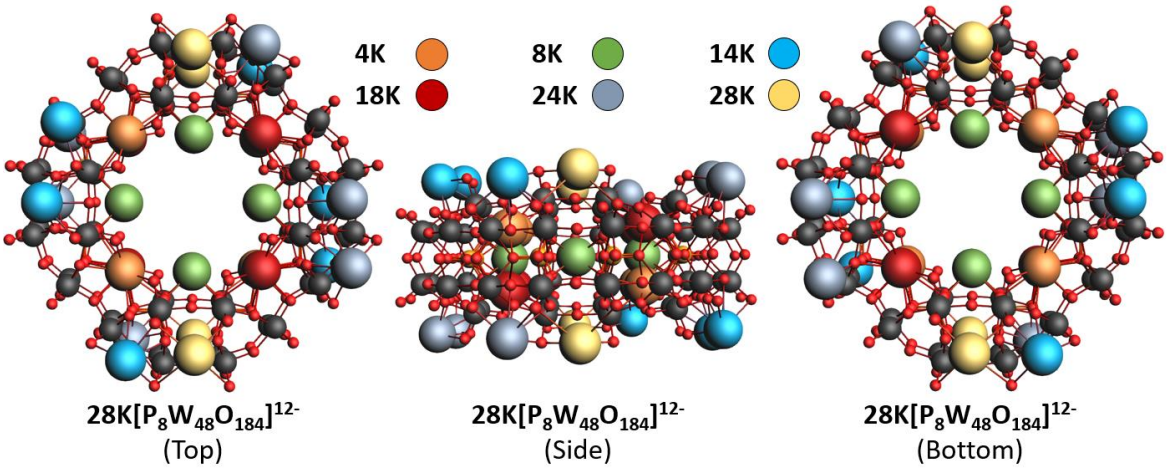

Figure A-1.6. Geometry of $K_{28}[P_8W_{48}O_{184}]^{12-}$ with K cations coloured in order of their addition to the initial $[P_8W_{48}O_{184}]^{40-}$ structure. The orange K atoms were added first, followed by the green, and so on; in this way $K_8[P_8W_{48}O_{184}]^{32-}$ contains the atoms coloured orange and green in the above image.

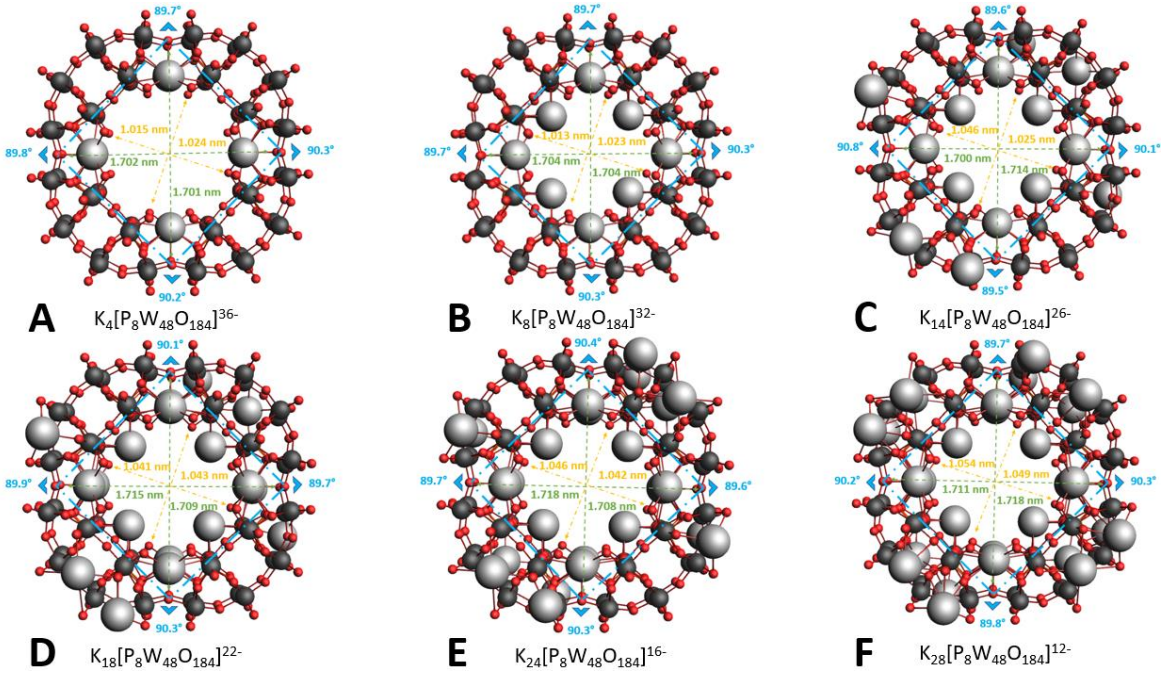

Figure A-1.7. Stepwise addition of K cations to **{P_8W_{48}}**. Angles (blue), inner diameters (green), and outer diameters (yellow) are all visualized

Table A-1.15. Collection of calculated angle dimensions for **$K_n\{P_8W_{48}\}$** structures, with a set of empirical angles for comparison. **PBE/TZP/COSMO/Small Frozen Cores**

Formula	Angle 1 (°)	Angle 2 (°)	Angle 3 (°)	Angle 4 (°)	Reference
$[P_8W_{48}O_{184}]^{40-}$	90.0	90.1	89.8	90.0	Yu, X. *et al.*[376]
$K_0[P_8W_{48}O_{184}]^{40-}$	90.0	90.3	89.7	90.0	
$K_4[P_8W_{48}O_{184}]^{36-}$	89.7	90.3	90.2	89.8	
$K_8[P_8W_{48}O_{184}]^{32-}$	89.7	90.3	90.3	89.7	
$K_{14}[P_8W_{48}O_{184}]^{26-}$	89.6	90.1	89.5	90.8	
$K_{18}[P_8W_{48}O_{184}]^{22-}$	90.1	89.7	90.3	89.9	
$K_{24}[P_8W_{48}O_{184}]^{16-}$	90.4	89.6	90.3	89.7	
$K_{28}[P_8W_{48}O_{184}]^{12-}$	89.7	90.3	89.8	90.2	

Table A-1.16. Collection of calculated inner diameter dimensions for **$K_n\{P_8W_{48}\}$** structures, with a set of empirical angles for comparison. **PBE/TZP/COSMO/Small Frozen Cores**

Formula	Inner Ring Diameter 1 (nm)	Inner Ring Diameter 2 (nm)	Mean Inner Ring Diameter (nm)	Reference
$[P_8W_{48}O_{184}]^{40-}$	0.977	1.017	0.997	Yu, X. *et al.*[376]
$K_0[P_8W_{48}O_{184}]^{40-}$	1.016	1.033	1.0245	
$K_4[P_8W_{48}O_{184}]^{36-}$	1.015	1.024	1.0195	
$K_8[P_8W_{48}O_{184}]^{32-}$	1.013	1.023	1.018	
$K_{14}[P_8W_{48}O_{184}]^{26-}$	1.046	1.025	1.0355	
$K_{18}[P_8W_{48}O_{184}]^{22-}$	1.041	1.043	1.042	
$K_{24}[P_8W_{48}O_{184}]^{16-}$	1.046	1.042	1.044	
$K_{28}[P_8W_{48}O_{184}]^{12-}$	1.054	1.049	1.0515	
MAE	0.1960	0.0600	0.1280	
STD	0.6081	0.4546	0.5301	

Table A-1.17. Collection of calculated outer diameter dimensions for **$K_n\{P_8W_{48}\}$** structures, with a set of empirical angles for comparison. **PBE/TZP/COSMO/Small Frozen Cores**

Formula	Outer Ring Diameter 1 (nm)	Outer Ring Diameter 2 (nm)	Mean Outer Ring Diameter (nm)	Reference
$[P_8W_{48}O_{184}]^{40-}$	1.644	1.646	1.645	Yu, X. *et al.*[376]
$K_0[P_8W_{48}O_{184}]^{40-}$	1.700	1.704	1.702	
$K_4[P_8W_{48}O_{184}]^{36-}$	1.702	1.701	1.7015	
$K_8[P_8W_{48}O_{184}]^{32-}$	1.704	1.704	1.704	
$K_{14}[P_8W_{48}O_{184}]^{26-}$	1.700	1.714	1.707	
$K_{18}[P_8W_{48}O_{184}]^{22-}$	1.715	1.709	1.712	
$K_{24}[P_8W_{48}O_{184}]^{16-}$	1.718	1.708	1.713	
$K_{28}[P_8W_{48}O_{184}]^{12-}$	1.711	1.718	1.7145	
MAE	0.2210	0.2180	0.2195	
STD	0.8862	0.8832	0.8847	

Table A-1.18. Standard Deviation data for $K_n[P_8W_{48}O_{184}]^{n-40}$ POMs. The full formula is abbreviated to the appropriate K_n value for the structure.

Formula	K_0	K_4	K_8	K_{14}	K_{18}	K_{24}	K_{28}
Total Charge	-40.00	-36.00	-32.00	-26.00	-22.00	-16.00	-12.00
SD Whole Molecule	1.194	1.185	1.175	1.164	1.152	1.142	1.135
SD Oxygen Only	0.046	0.046	0.047	0.038	0.034	0.034	0.036
SD Tungsten Only	0.019	0.023	0.018	0.016	0.018	0.016	0.012
SD Phosphorus Only	0.000	0.001	0.001	0.002	0.003	0.003	0.003
SD Potassium Only	N/A	0.001	0.074	0.081	0.088	0.091	0.088

Looking at the SD of atomic charge or electronic distribution throughout the POM as a whole (**Table A-1.18.**), we discovered that SD decreases as more potassium cations are added to the structure; this indicates a reduction in molecular reactivity and, therefore, an increase in stability. Examining SD by element doesn't provide much additional insight; oxygen and tungsten, the main constituent elements, become less polarised in an overall uniform manner as more cations are added. Phosphorus increases slightly, but this is due to potassium inclusion not being perfectly symmetrical with regard to these elements. It is worth noting that SD for

potassium increases sharply after addition of 4 cations; this is due to a reduction in symmetry from the K_4 structure, with more potassium cations being added in increasingly individual locations in order to balance the charge.

Table A-1.19. Mean Atomic Charge data for $K_n[P_8W_{48}O_{184}]^{n-40}$ POMs. The full formula is abbreviated to the appropriate K_n value for the structure.

Formula	K_0	K_4	K_8	K_{14}	K_{18}	K_{24}	K_{28}
Total Charge	-40.00	-36.00	-32.00	-26.00	-22.00	-16.00	-12.00
Mean Atomic Charge Oxygen Only	-0.823	-0.815	-0.807	-0.800	-0.791	-0.785	-0.780
Mean Atomic Charge Tungsten Only	2.045	2.042	2.040	2.029	2.025	2.017	2.010
Mean Atomic Charge Phosphorus Only	1.658	1.644	1.609	1.612	1.598	1.597	1.598
Mean Atomic Charge Potassium Only	N/A	0.694	0.720	0.781	0.755	0.783	0.791

Compared with SD, MAC gives us a more detailed image of what occurs when the W_{48} POM approaches a more charge neutral state (**Table A-1.19.**); it tells us that electron distribution becomes more evenly distributed throughout the molecule. Traditionally, anionic oxygens become less negatively charged, whilst tungsten and phosphorus become less cationic as they accept more of the negative contribution from surrounding oxygen atoms. Potassium becomes more cationic as more countercations are added to the structure; as more cations are included, not only is the electron distribution less polarised where potassium ions are positioned throughout the structure, but each potassium also bears a smaller individual load with regards to charge balancing.

Table A-1.20. Electronic values for different species of $K_n[P_8W_{48}O_{184}]^{n-40}$ **PBE/TZP/COSMO/Small Frozen Cores**

Formula	E_{HOMO} (eV)	E_{LUMO} (eV)	ΔE_{H-L} (eV)
$[P_8W_{48}O_{184}]^{40-}$	-4.782	-2.171	2.61
$K_4[P_8W_{48}O_{184}]^{36-}$	-4.799	-2.199	2.60
$K_8[P_8W_{48}O_{184}]^{32-}$	-4.931	-2.351	2.58
$K_{14}[P_8W_{48}O_{184}]^{26-}$	-5.253	-2.567	2.69
$K_{18}[P_8W_{48}O_{184}]^{22-}$	-5.560	-2.873	2.69
$K_{24}[P_8W_{48}O_{184}]^{16-}$	-5.778	-3.119	2.66
$K_{28}[P_8W_{48}O_{184}]^{12-}$	-5.979	-3.308	2.67

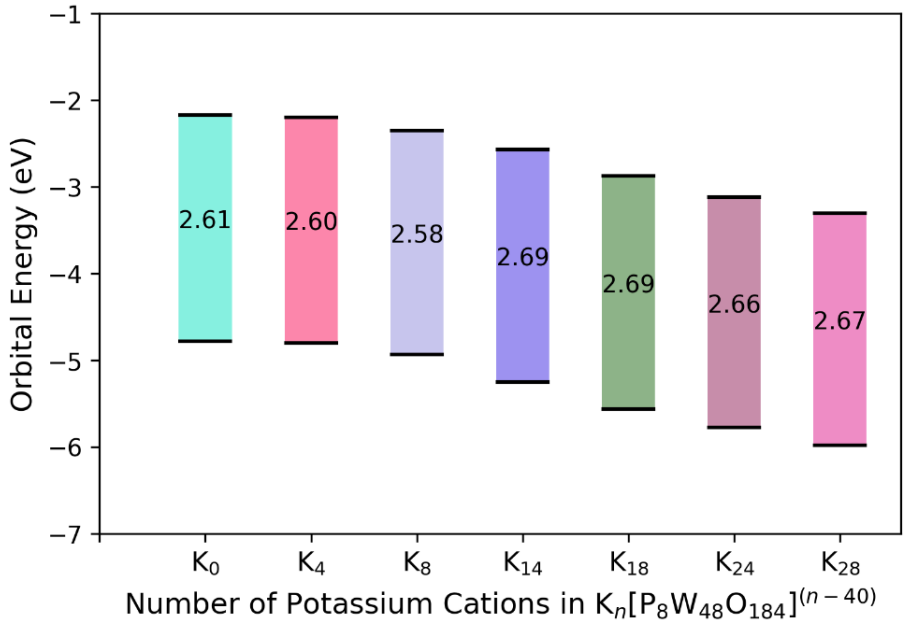

Figure A-1.8. Visualization of HOMO and LUMO stabilization as the number of K cations in the geometry increase **PBE/TZP/COSMO/Small Frozen Cores**

Appendix-1.8: Various Countercations in Hexalacunary and {P_8W_{48}} Structures

Table A-1.21. Frontier Orbital energy values for different species of $X_8[P_8W_{48}O_{184}]^{n-}$. Atomic Radii collected from Slater J.C.[377] **PBE/TZP/COSMO/Small Frozen Cores**

Formula	Cation	Cation Radius (Å)	E_{HOMO} (eV)	E_{LUMO} (eV)	ΔE_{H-L} (eV)
$Be_8[P_8W_{48}O_{184}]^{24-}$	Be^{2+} (Dication)	1.05	-5.823	-3.404	2.42
$Ca_8[P_8W_{48}O_{184}]^{24-}$	Ca^{2+} (Dication)	1.80	-5.722	-3.159	2.56
$K_8[P_8W_{48}O_{184}]^{32-}$	K^{+} (Monocation)	2.20	-4.931	-2.351	2.58
$Li_8[P_8W_{48}O_{184}]^{32-}$	Li^{+} (Monocation)	1.45	-5.212	-2.528	2.68
$Mg_8[P_8W_{48}O_{184}]^{24-}$	Mg^{2+} (Dication)	1.50	-5.806	-3.364	2.44
$Na_8[P_8W_{48}O_{184}]^{32-}$	Na^{+} (Monocation)	1.80	-5.163	-2.437	2.73
$Rb_8[P_8W_{48}O_{184}]^{32-}$	Rb^{+} (Monocation)	2.35	-5.041	-2.461	2.58

The SD values for W_{48} POMs containing a range of different elemental countercations (**Table A-1.22.**) correlate well with the literature in 2 key points; cations are required to stabilise the highly anionic POM wheel, see that the greatest SD value for the whole framework is for the POM with no cations present, and smaller cations are the most effective at stabilizing the structure as they exhibit the least polarization throughout the framework. This last point is represented by the tendency of smaller cations to trigger precipitation of the POM out of solution.

A lot of the difference in SD within the framework is tied to variation in the element used as cation. The dicationic species in particular have relatively high variance between individual atoms, which may explain why the HOMO-LUMO gaps for these POMs are smaller than their monocationic counterparts.

Table A-1.22. Standard Deviation (SD) values for $X_8[P_8W_{48}O_{184}]^{n-}$-type POMs. Each POM is abbreviated to only show the X_n countercation for that specific framework.

Formula	No Cation	Li_8	Na_8	K_8	Rb_8	Be_8	Mg_8	Ca_8
Total Charge	-40.00	-32.00	-32.00	-32.00	-32.00	-24.00	-24.00	-24.00
STD Whole Molecule	1.194	1.161	1.167	1.175	1.177	1.152	1.173	1.185
STD Oxygen Only	0.046	0.044	0.040	0.047	0.042	0.051	0.038	0.041
STD Tungsten Only	0.019	0.013	0.013	0.018	0.017	0.018	0.017	0.015
STD Phosphorus Only	0.000	0.002	0.001	0.001	0.001	0.473	0.003	0.000
STD 'X' Cation Only	N/A	0.032	0.085	0.074	0.061	0.025	0.120	0.124

It is worth mentioning that $Be_8[P_8W_{48}O_{184}]^{24-}$ has a strained structure, lacking the ordered symmetry of the other POM frameworks (**Table A-1.23, A-1.24**.) This may be due to beryllium being the smallest cation experimented with but regardless, it displays relatively anomalous results, such as a SD value for the phosphorus heteroatom that is two orders of magnitude bigger than the same property from the other POMs.

Table A-1.23. Collection of calculated inner diameter dimensions for **$K_n\{P_8W_{48}\}$** structures, with a set of empirical angles for comparison.

Formula	Inner Ring Diameter 1 (nm)	Inner Ring Diameter 2 (nm)	Mean Inner Ring Diameter (nm)	Reference
$[P_8W_{48}O_{184}]^{40-}$	0.977	1.017	0.997	Yu, X. *et al.*[376]
$Li_8[P_8W_{48}O_{184}]^{32-}$	1.061	1.013	1.037	
$Na_8[P_8W_{48}O_{184}]^{32-}$	1.0205	1.0495	1.035	
$K_8[P_8W_{48}O_{184}]^{32-}$	1.013	1.023	1.018	
$Rb_8[P_8W_{48}O_{184}]^{32-}$	1.017	1.028	1.0225	
$Be_8[P_8W_{48}O_{184}]^{24-}$	1.0485	1.061	1.055	
$Mg_8[P_8W_{48}O_{184}]^{24-}$	1.023	1.060	1.042	
$Ca_8[P_8W_{48}O_{184}]^{24-}$	1.031	1.029	1.030	

Table A-1.24. Collection of calculated outer diameter dimensions for **$K_n\{P_8W_{48}\}$** structures, with a set of empirical angles for comparison.

Formula	Outer Ring Diameter 1 (nm)	Outer Ring Diameter 2 (nm)	Mean Outer Ring Diameter (nm)	Reference
$[P_8W_{48}O_{184}]^{40-}$	1.644	1.646	1.645	Yu, X. *et al.*[376]
$Li_8[P_8W_{48}O_{184}]^{32-}$	1.680	1.673	1.6765	
$Na_8[P_8W_{48}O_{184}]^{32-}$	1.696	1.692	1.694	
$K_8[P_8W_{48}O_{184}]^{32-}$	1.704	1.704	1.704	
$Rb_8[P_8W_{48}O_{184}]^{32-}$	1.705	1.705	1.705	
$Be_8[P_8W_{48}O_{184}]^{24-}$	1.618	1.602	1.610	
$Mg_8[P_8W_{48}O_{184}]^{24-}$	1.659	1.659	1.659	
$Ca_8[P_8W_{48}O_{184}]^{24-}$	1.682	1.681	1.6815	

The data for mean atomic charge highlights how the smaller cation has a more stabilizing effect on the POM; $Li_8[P_8W_{48}O_{184}]^{32-}$ is the best example of this, with all the mean atomic charge values for the various elements within this POM being collectively closer to zero than the other examples (**Table A-1.25** and **Figure 5.23.**).

Table A-1.25. Mean atomic charge values for $X_8[P_8W_{48}O_{184}]^{n-}$-type POMs. Each POM is abbreviated to only show the X countercation, which varies between POMs, for that specific framework.

Formula	No Cation	Li_8	Na_8	K_8	Rb_8	Be_8	Mg_8	Ca_8
Total Charge	-40.00	-32.00	-32.00	-32.00	-32.00	-24.00	-24.00	-24.00
Mean Atomic Charge Oxygen Only	-0.823	-0.794	-0.802	-0.807	-0.809	-0.761	-0.781	-0.790
Mean Atomic Charge Tungsten Only	2.045	2.033	2.033	2.040	2.040	2.037	2.035	2.036
Mean Atomic Charge Phosphorus Only	1.658	1.597	1.602	1.609	1.623	1.135	1.575	1.586
Mean Atomic Charge 'X' Cation Only	N/A	0.466	0.638	0.720	0.754	0.677	1.173	1.360

Appendix-2: Chapter 6

Appendix-2.1: Wells-Dawson POM Benchmarking

Determining NMR peaks from our theoretical 31P NMR spectra in DFT required us to utilise the following equation devised by Pasucal-Borràs, *M. et al.*,[332] where $\sigma(X_{calc})$ is the raw, simulated peak and $\delta(X_{calc})$ is the converted peak which is appropriate to compare against empirical data:

$$\delta(X_{calc}) = |\sigma(PH_{3calc})| - |\sigma(X_{calc})| - 266.1$$

$$\sigma(PH_{3calc}) = -580.1312ppm$$

$$\delta(X_{calc}) = 314.0312 - \sigma(X_{calc})$$

See **Figure A-2.1** for our raw empirical spectroscopy and **Table A-2.2**, where we compare these peaks, as well as those found in the literature, with those of our calculations. We found $[P_2W_{18}O_{62}]^{6-}$ to be the model that most closely replicated the empirical data whilst also featuring the least complexity (no countercations).

Table A-2.1. Comparison in dimensions between empirical and theoretical $K_6[P_2W_{18}O_{62}]$ frameworks. Relevant atoms are labelled on the molecular diagram from Table 1. The empirical dimensions referred to can also be found in **Table 1**. The entry labelled 'No Constraint' features no constraints on cation-phosphorus distance; every other entry constrains the distance at the value shown. **OPT/PBE/TZP/SFC/COSMO**

Diameter Identifier (Å)	5.5Å	No Constraint	7.0Å	7.5Å	8.0Å	8.5Å	9.0Å	9.3Å	9.5Å	9.75Å	10.0Å
HEIGHT											
O_A-O_E	11.45	11.41	11.39	11.38	11.38	11.38	11.39	11.39	11.39	11.39	11.39
P-P	4.09	3.99	3.97	3.99	3.96	3.93	3.97	3.98	3.98	3.99	3.99
W_A-W_E	9.98	9.95	9.92	9.92	9.93	9.94	9.93	9.93	9.93	9.93	9.93
LENGTH											
O_B-O_D	7.37	7.44	7.42	7.39	7.41	7.40	7.39	7.39	7.39	7.38	7.38
W_C-W_D	7.11	7.14	7.14	7.14	7.14	7.14	7.14	7.14	7.14	7.14	7.14
WIDTH											
O_C-O_D	4.31	4.31	4.29	4.29	4.29	4.29	4.28	4.29	4.28	4.29	4.29
W_B-W_D	3.74	3.73	3.73	3.72	3.72	3.72	3.72	3.72	3.72	3.72	3.72
Theoretical - Empirical Difference											
HEIGHT											
O_A-O_E	+0.18	+0.14	+0.12	+0.11	+0.11	+0.11	+0.12	+0.12	+0.12	+0.12	+0.12
P-P	+0.11	+0.01	-0.01	+0.01	-0.02	-0.05	-0.01	0.00	0.00	+0.01	+0.01
W_A-W_E	+0.16	+0.13	+0.10	+0.10	+0.11	+0.12	+0.11	+0.11	+0.11	+0.11	+0.11
LENGTH											
O_B-O_D	+0.14	+0.21	+0.19	+0.16	+0.18	+0.17	+0.16	+0.16	+0.16	+0.15	+0.15
W_C-W_D	+0.05	+0.08	+0.08	+0.08	+0.08	+0.08	+0.08	+0.08	+0.08	+0.08	+0.08
WIDTH											
O_C-O_D	+0.06	+0.06	+0.04	+0.04	+0.04	+0.04	+0.03	+0.04	+0.03	+0.04	+0.04
W_B-W_D	+0.06	+0.05	+0.05	+0.05	+0.05	+0.05	+0.05	+0.05	+0.05	+0.05	+0.05
Mean Theoretical – Empirical Difference	+0.11	+0.10	+0.08	+0.08	+0.08	+0.07	+0.08	+0.08	+0.08	+0.08	+0.08

Table A-2.2. NMR data for $K_6[\alpha\text{-}P_2W_{18}O_{62}]$. Detailed is number of cations included in the theoretical model and the distance between cation and heteroatom (Å). The initial Wells-Dawson geometry was optimized using **B3LYP/TZP/SFC/COSMO**, upon which a **SP/PBE/TZP/SFC/COSMO/Spin-Orbit Relativity** NMR calculation was run.

Data Source	^{31}P Chemical Shift (ppm)	Reference
Empirical (literature)	-12.30	Graham, R.G. *et al.*[378]
	-12.50	Contant, R. *et al.*[379]
Empirical (carried out by LVN group)	-13.02	
Computational (No K cations)	-12.01	
Computational (6K, 6.3Å)	-11.45, -11.15	
Computational (6K, 9.0Å)	-11.89, -11.87	
Computational (6K, 10.0Å)	-12.87, -12.75	

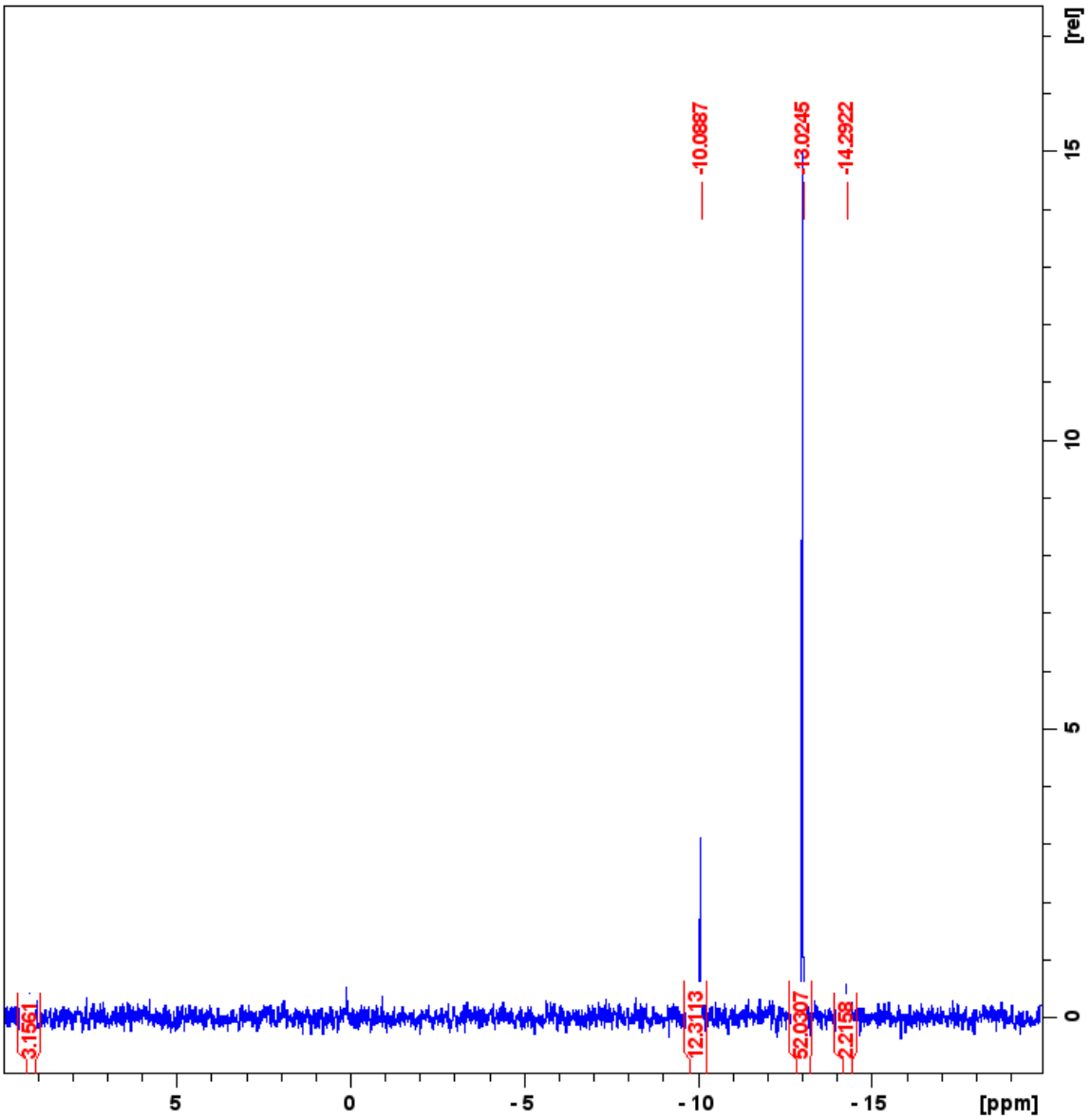

Figure A-2.1. ^{31}P NMR for $K_6[\alpha\text{-}P_2W_{18}O_{62}]\cdot 14H_2O$, following the synthetic method of Mbomekalle, I-M *et al.*[46] Primary peak at -13.02ppm is α-isomer.

With regards to UV-Vis spectroscopy, we found the functional utilised had a very big effect on the final HOMO-LUMO gap value. Based on the empirical data, we established that there are two characteristic peaks for $K_6[P_2W_{18}O_{62}]$: one at 300nm and the other between the range of 240-260nm. Past computational works have utilised GGA-level functionals to determine the HOMO-LUMO gap but, after reviewing the available UV-Vis data for $K_6[P_2W_{18}O_{62}]$, we believe this level of theory to underestimate the true empirical value. In **Table A-2.6** and **Figure A-2.2**, we can see that the calculated wavelength of emission using PBE or BP86 is more than 200nm off the reported data; this equates to a difference in energy of 2eV.

Additionally, the previously reported theoretical wavelength would indicate the base WD species is coloured blue, which is only true upon reduction.

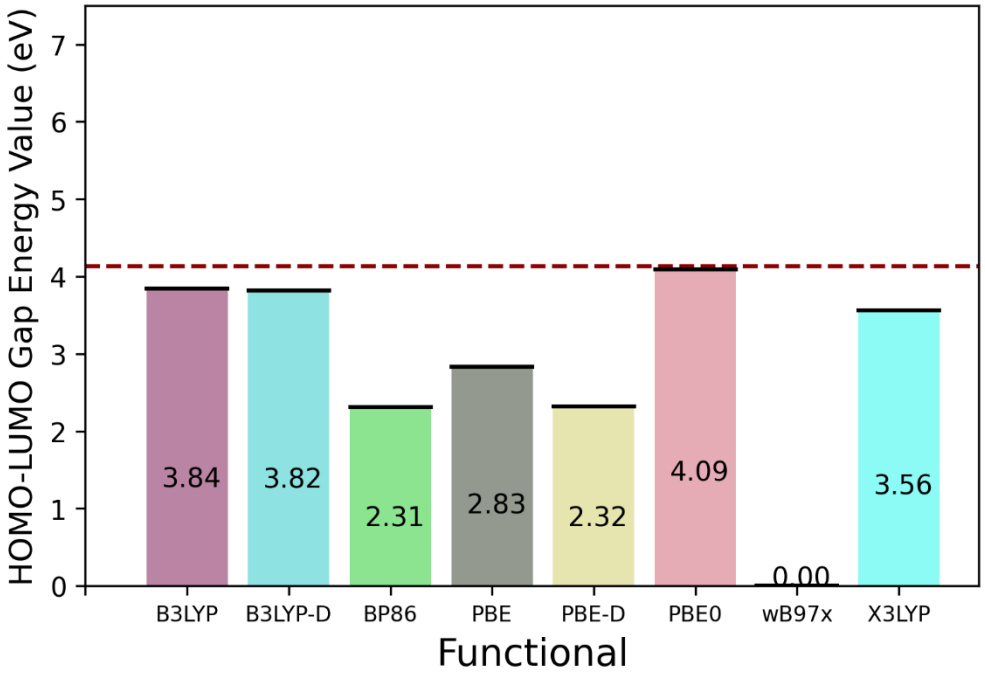

Figure A-2.2. HOMO-LUMO gap energy values for $[\alpha\text{-}P_2W_{18}O_{62}]^{6-}$ across a range of functionals. A dashed red line is used to represent the empirical value for the HOMO-LUMO gap (4.13eV); bars closer to the line will be considered more accurate. **SP/{Functional}/TZP/SFC/COSMO**

Table A-2.5. UV-Vis data for $K_n[\alpha\text{-}P_2W_{18}O_{62}]^{(n-6)}$. UV-vis calculations carried out by the LVN group are single point calculations which use pre-optimized geometries; both calculations use the same functional. Number of cations in the geometry and the distance between cation and heteroatom is specified. The calculation defined as '6K, OPT' has no cation-phosphorus distance constraints.

Functional/Basis Set/Frozen Cores	**HOMO-LUMO Energy Gap (eV)**			
	No K Cations	**6K, OPT**	**6K, (9.0Å)**	**6K, (10.0Å)**
B3LYP/TZP/SFC	3.84	3.83	3.82	3.82
B3LYP-D/TZP/SFC	3.82	3.74	3.82	3.82
BP86/TZP/SFC	2.31	2.32	2.29	2.29
PBE/TZP/SFC	2.83	2.34	2.30	2.30
PBE-D/TZP/SFC	2.32	2.34	2.30	2.30
PBE0/TZP/SFC	4.09	4.23	4.22	4.22
wB97x/TZP/NFC	-----	-----	-----	-----

Table A-2.6. UV-Vis data for $[\alpha\text{-}P_2W_{18}O_{62}]^{6-}$. UV-vis calculations carried out by the LVN group are single point calculations which use pre-optimized geometries; both calculations use the same functional.

Data Source	Functional/Basis Set/Frozen Core	First Transition Wavelength (nm)	First Transition Energy (eV)	Reference
Empirical (literature)	UV-Vis	~300	4.13	Chen, J.-J. *et al.*[323]
	UV-Vis	~267	4.64	Dhifallah, F. *et al.*[340]
	UV-Vis	~245, 300	5.06, 4.13	Hiskia, A. *et al.*[339]
	UV-Vis	250, 301.25	4.96, 4.12	Nomiya, K. *et al.*[338]
	CV	N/A	2.917	Kibler, A.J. *et al.*[151]
Theoretical (literature)	BP86/TZP	569	2.18	Chen, J.-J. *et al.*[323]
	PBE/TZVP	551	2.25	López, X. *et al.*[334]
	PBE/TZP	544	2.28	López, X. *et al.*[337]
	PBE/TZP	551	2.25	Vilà-Nadal, L. *et al.*[180]
Empirical (carried out by LVN group)	UV-Vis	310	4.00	
Theoretical (carried out by LVN group)	B3LYP/TZP/SFC	322.799	3.84	
	B3LYP-D/TZP/SFC	324.862	3.82	
	BP86/TZP/SFC	536.797	2.31	
	PBE/TZP/SFC	438.749	2.83	
	PBE-D/TZP/SFC	534.483	2.32	
	PBE0/TZP/SFC	302.912	4.09	
	wB97x/TZP/NFC	-----	-----	

Based on our findings from **Table A-2.5, A-2.6**, we found a DFT calculation which uses PBE0 as the functional provides the most accurate HOMO-LUMO energy gap value; for this, we assume the first transition in the empirical data to also be the HOMO-LUMO gap.

Appendix-2.2: Hexalacunary Benchmarking

Having established the appropriate level of theory required for accurate spectroscopic calculations of medium-sized POMs, we move on to the primary focus of this paper: DFT-modelling of $[P_2W_{12}O_{48}]^{14-}$. By changing the functional used in the optimization calculation, we found PBE to give the best results at the cheapest computational cost (**Table A-2.7**). Moving forward, we only used PBE for simple geometry optimization calculations.

Table A-2.7. Comparison in dimensions between empirical and theoretical $[P_2W_{12}O_{48}]^{14-}$ frameworks. **OPT/{Functional}/TZP/SFC/COSMO**

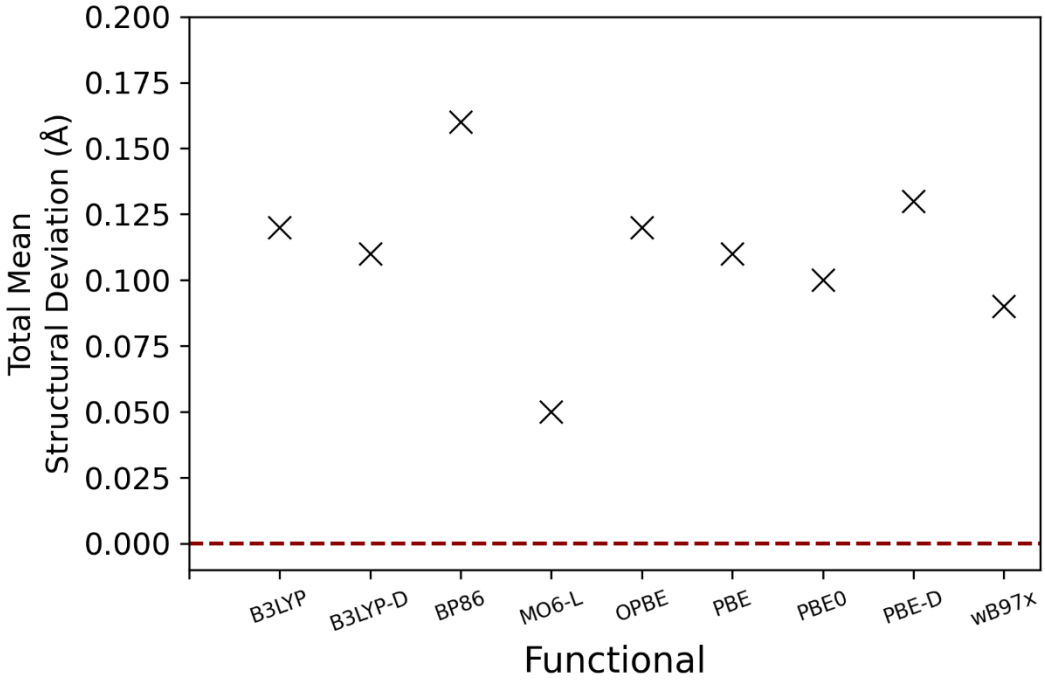

Diameter Identifier	Empirical Length {Sugiarto, S. *et al.*[328]} (Å)	B3LYP	B3LYP-D	BP86	MO6-L	OPBE	PBE	PBE0	PBE-D	wB97X
HEIGHT										
O_A-O_E	11.43	11.83	11.80	11.94	11.78	11.90	11.59	11.81	11.83	11.76
P-P	4.17	4.13	4.15	4.28	4.18	4.30	4.28	4.21	4.16	4.20
W_A-W_E	9.96	10.07	10.03	10.14	9.92	10.08	10.15	10.04	10.06	10.07
LENGTH										
O_B-O_D	6.83	7.06	7.02	7.02	6.97	6.95	7.00	6.95	7.05	6.92
W_C-W_D	6.73	6.82	6.88	6.87	6.77	6.81	6.87	6.82	6.89	6.86
WIDTH										
O_B-O_C	4.36	4.39	4.45	4.41	4.29	4.35	4.42	4.38	4.45	4.40
W_B-W_C	3.84	3.84	3.76	3.79	3.77	3.76	3.80	3.79	3.77	3.77
	Mean	+0.12	+0.11	+0.16	+0.05	+0.12	+0.11	+0.10	+0.13	+0.09

Using $[P_2W_{12}O_{48}]^{14-}$ and $[P_8W_{48}O_{184}]^{40-}$ as a control, we established that, with a couple exceptions, the dimensions of hexalacunaries tended to remain within a deviation of 0.2Å when sampled from a **{P_8W_{48}}**-type POM instead of as a separate POM species (**Table A-2.8** and **Figure 6.7**). We are therefore able to take a hexalacunary section from a **{X_8W_{48}}** wheel and treat it as a distinct, individual hexalacunary species, accurately modelling $[As_2W_{12}O_{48}]^{14-}$ and $[Se_2W_{12}O_{46}]^{12-}$ respectively.

Table A-2.8. Comparison in dimensions between empirical and theoretical $[P_2W_{12}O_{48}]^{14-}$ frameworks. Empirical data is split into $[P_2W_{12}O_{48}]^{6-}$ xyz and the $[P_2W_{12}O_{48}]^{6-}$ segment of a full $[P_8W_{48}O_{184}]^{40-}$ POM wheel. Relevant atoms are labelled on the molecular diagram.

Diameter Identifier (nm)	Empirical Length {Sugiarto, S. *et al.*[328]} (Å)	{P_2W_{12}} Fragment from {P_8W_{48}}	Theoretical Length (Å)	Theor. – Emp. Difference (Å)	Frag. – Emp. Difference (Å)	Theor. – Frag. Diff. (Å)
HEIGHT						
O_A-O_E	11.43	11.49	11.59	+0.16	+0.06	+0.10
P-P	4.17	4.18	4.28	+0.11	+0.01	+0.10
W_A-W_E	9.96	9.89	10.15	+0.19	-0.07	+0.26
LENGTH						
O_B-O_D	6.83	6.92	7.00	+0.17	+0.09	+0.08
W_C-W_D	6.73	6.75	6.87	+0.14	+0.02	+0.12
WIDTH						
O_B-O_C	4.36	4.29	4.42	+0.06	+0.07	+0.13
W_B-W_C	3.84	3.78	3.80	-0.04	-0.06	+0.02
			Mean	+0.11	+0.02	+0.12

We repeated this process for the $[As_2W_{12}O_{48}]^{14-}$ and $[Se_2W_{12}O_{46}]^{12-}$ hexalacunary variants, see **Table A-2.9**, **A-2.10** for arsenic and selenium respectively, and **Figure A-2.3** for the full results for all 3 hexalacunaries. We found the margin of error between the arsenic and selenium hexalacunaries and W_{48} wheels to be 0.17Å and 0.13Å respectively, comporable to the 0.12Å value for $[P_2W_{12}O_{48}]^{14-}$. We can therefore model theoretical arsenic and selenium based hexalacunary POMs to a good degree of accuracy, using existing the phosphorus counterpart as a reference point. We conclude that our hexalacunary models are in very good agreement with the empirical structure, allowing us to build ever more complex models off this solid base.

Apart from a couple outliers, the difference between empirical and theoretical dimension values for $[As_2W_{12}O_{48}]^{14-}$ and $[Se_2W_{12}O_{46}]^{12-}$ were of a similar magnitude with those for $[P_2W_{12}O_{48}]^{14-}$. We conclude that our hexalacunary models are in very good agreement with the empirical structure, allowing us to build ever more complex models off this solid base.

Table A-2.9. Comparison in dimensions between empirical and theoretical $[Se_2W_{12}O_{46}]^{12-}$ frameworks. **OPT/PBE/TZP/SFC/COSMO**

Diameter Identifier	Empirical Fragment Length {Cameron, J.M. *et al.*[78]} (Å)	Theoretical Length (Å)	Theor. – Emp. Difference (Å)
HEIGHT			
O_A-O_E	11.41	11.51	+0.10
Se-Se	3.86	3.99	+0.13
W_A-W_E	9.93	10.21	+0.28
LENGTH			
O_B-O_D	7.40	7.45	+0.05
W_C-W_D	6.91	6.96	+0.05
WIDTH			
O_B-O_C	3.28	3.51	+0.23
W_B-W_C	3.41	3.46	+0.05
		Mean	+0.13

Table A-2.10. Comparison in dimensions between empirical and theoretical $[As_2W_{12}O_{48}]^{14-}$ frameworks. **OPT/PBE/TZP/SFC/COSMO**

Diameter Identifier	Empirical Fragment Length {Mbomekallé, I.M. *et al.*[322]} (Å)	Theoretical Length (Å)	Theor. – Emp. Difference (Å)
HEIGHT			
O_A-O_E	11.50	11.60	+0.10
As-As	4.07	4.11	+0.04
W_A-W_E	9.40	10.13	+0.73
LENGTH			
O_B-O_D	7.24	7.36	+0.12
W_C-W_D	6.92	7.06	+0.14
WIDTH			
O_B-O_C	4.45	4.47	+0.02
W_B-W_C	3.77	3.80	+0.03
		Mean	+0.17

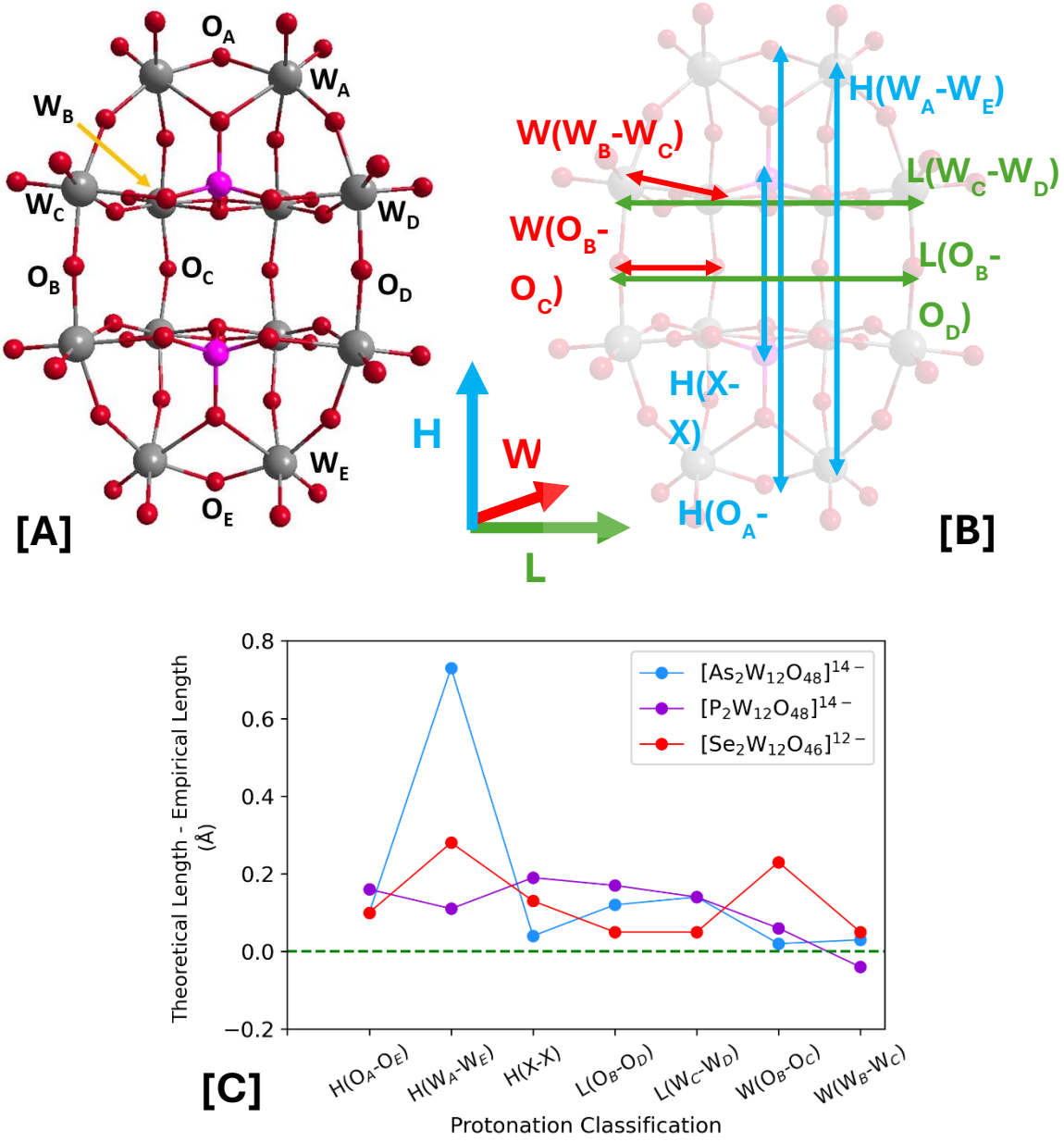

Figure A-2.3. Visual representation of hexalacunary $[As_2W_{12}O_{48}]^{14-}$, $[P_2W_{12}O_{48}]^{14-}$, and $[Se_2W_{12}O_{46}]^{12-}$ dimensions. Atoms are labelled **(A)** and the dimensions between them specified **(B)**. Using these specified dimensions, mean structural deviation is determined by subtracting the theoretical dimension from the empirical counterpart for the Arsenic-,[83] Phosphorus-,[328] and Selenium-containing[78] species **(C)**. A deviation of 0.0Å represents an identical value for both empirical and theoretical dimensions **OPT/PBE/TZP/SFC/COSMO**

Appendix-2.3: Countercation Structures

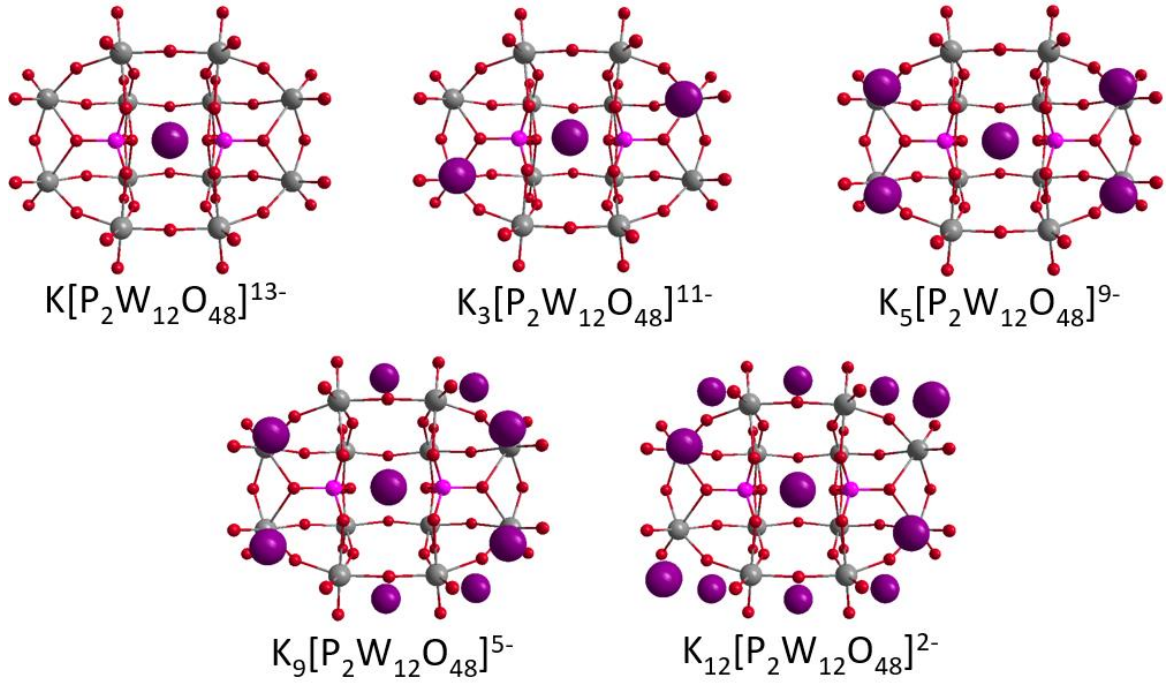

Figure A-2.4. Ball and stick models of the $[P_2W_{12}O_{48}]^{14-}$ hexalacunary framework, specifically highlighting the position of potassium countercations around the structure. In the instance of $K_{12}[P_2W_{12}O_{48}]^{2-}$, the twelfth cation is located at the 'back' of the hexalacunary and is thus obscured behind the central cation in this figure. (No cation distance constraints). Colour scheme: W: grey, O: red, P: pink, K: purple

Table A-2.11. Comparison in dimensions between empirical and theoretical $K_n[P_2W_{12}O_{48}]^{(n-14)}$ frameworks across a range of different n values for K. Cation to heteroatom distances are not constrained for these geometries. **OPT/PBE/TZP/SFC/COSMO**

Diameter Identifier	Empirical Length {Sugiarto, S. *et al.*[328]} (Å)	K_0	K_1	K_3	K_5	K_9	K_{12}
HEIGHT							
O_A-O_E	11.43	11.59	11.61	11.58	11.59	11.60	11.59
P-P	4.17	4.28	4.35	4.29	4.38	4.40	4.34
W_A-W_E	9.96	10.15	10.17	10.17	10.21	10.22	10.28
LENGTH							
O_B-O_D	6.83	7.00	6.96	6.99	7.09	6.98	6.95
W_C-W_D	6.73	6.87	6.86	6.89	7.00	6.93	6.84
WIDTH							
O_B-O_C	4.36	4.42	4.41	4.41	4.36	4.37	4.55
W_B-W_C	3.84	3.80	3.80	3.81	3.78	3.80	3.87
Theoretical - Empirical Difference							
HEIGHT							
O_A-O_E		+0.16	+0.18	+0.15	+0.16	+0.17	+0.16
P-P		+0.11	+0.18	+0.12	+0.21	+0.23	+0.17
W_A-W_E		+0.19	+0.21	+0.21	+0.25	+0.26	+0.32
LENGTH							
O_B-O_D		+0.17	+0.13	+0.16	+0.26	+0.15	+0.12
W_C-W_D		+0.14	+0.13	+0.16	+0.27	+0.20	+0.11
WIDTH							
O_B-O_C		+0.06	+0.05	+0.05	0.00	+0.01	+0.19
W_B-W_C		-0.04	-0.04	-0.03	-0.06	-0.04	+0.03
Mean Theoretical – Empirical Difference		+0.11	+0.12	+0.12	+0.16	+0.14	+0.16

Table A-2.12. Comparison in dimensions between empirical and theoretical $K_n[P_2W_{12}O_{48}]^{(n-14)}$ frameworks across a range of different n values for K. Cation to heteroatom distances are constrained at 9.0Å for these geometries. **OPT/PBE/TZP/SFC/COSMO**

Diameter Identifier	Empirical Length {Sugiarto, S. *et al.*[328]} (Å)	0K	1K	3K	5K	9K	12K
HEIGHT							
O_A-O_E	11.43	11.59	11.58	11.58	11.58	11.58	11.58
P-P	4.17	4.28	4.26	4.25	4.24	4.24	4.24
W_A-W_E	9.96	10.15	10.15	10.14	10.14	10.14	10.14
LENGTH							
O_B-O_D	6.83	7.00	7.01	7.02	7.02	7.03	7.10
W_C-W_D	6.73	6.87	6.88	6.88	6.88	6.93	6.97
WIDTH							
O_B-O_C	4.36	4.42	4.41	4.41	4.41	4.41	4.39
W_B-W_C	3.84	3.80	3.80	3.80	3.80	3.80	3.80
Theoretical - Empirical Difference							
HEIGHT							
O_A-O_E		+0.16	+0.15	+0.15	+0.15	+0.15	+0.15
P-P		+0.11	+0.09	+0.08	+0.07	+0.07	+0.07
W_A-W_E		+0.19	+0.19	+0.18	+0.18	+0.18	+0.18
LENGTH							
O_B-O_D		+0.17	+0.18	+0.19	+0.19	+0.20	+0.27
W_C-W_D		+0.14	+0.15	+0.15	+0.15	+0.20	+0.24
WIDTH							
O_B-O_C		+0.06	+0.05	+0.05	+0.05	+0.05	+0.03
W_B-W_C		-0.04	-0.04	-0.04	-0.04	-0.04	-0.04
Mean Theoretical – Empirical Difference		+0.11	+0.11	+0.11	+0.11	+0.12	+0.13

Deviation is slightly greater for the arsenic and significantly greater selenium counterparts, maxing out at +0.20Å and +0.30Å respectively when the POM-cation distance was constrained ay 9.0Å (see **Figure 6.11** and **Tables A-2.13, A-2.14** for arsenic and **Figure 6.12** and **Tables A-2.15, A-2.16** for selenium). As with the models without countercations, the constrained model almost always deviates less from the empirical xyz crystal than the unconstrained model; this is to be expected as the countercations are further from the POM in the constrained version.

Table A-2.13. Comparison in dimensions between empirical and theoretical $K_n[As_2W_{12}O_{48}]^{(n-14)}$ frameworks across a range of different n values for K. Cation to heteroatom distances are not constrained for these geometries. **OPT/PBE/TZP/SFC/COSMO**

Diameter Identifier	Empirical Fragment Length {Mbomekallé, I.M. *et al.*[322]} (Å)	0K	1K	3K	5K	9K	12K
HEIGHT							
O_A-O_E	11.50	11.60	11.61	11.58	11.59	11.60	11.66
As-As	4.07	4.11	4.35	4.29	4.38	4.40	4.26
W_A-W_E	9.40	10.13	10.17	10.17	10.20	10.22	10.24
LENGTH							
O_B-O_D	7.24	7.36	6.96	6.99	7.09	6.98	7.25
W_C-W_D	6.92	7.06	6.86	6.89	7.00	6.93	7.01
WIDTH							
O_B-O_C	4.45	4.47	4.41	4.40	4.36	4.37	4.50
W_B-W_C	3.77	3.80	3.80	3.81	3.79	3.80	3.83
Theoretical - Empirical Difference							
HEIGHT							
O_A-O_E		+0.10	+0.11	+0.08	+0.09	+0.10	+0.16
As-As		+0.04	+0.28	+0.22	+0.31	+0.33	+0.19
W_A-W_E		+0.73	+0.77	+0.77	+0.80	+0.82	+0.84
LENGTH							
O_B-O_D		+0.12	-0.28	-0.25	-0.15	-0.26	+0.01
W_C-W_D		+0.14	-0.06	-0.03	+0.08	+0.01	+0.09
WIDTH							
O_B-O_C		+0.02	-0.04	-0.05	-0.09	-0.08	+0.05
W_B-W_C		+0.03	+0.03	+0.04	+0.02	+0.03	+0.06
Mean Theoretical – Empirical Difference		+0.17	+0.12	+0.11	+0.15	+0.14	+0.20

Table A-2.14. Comparison in dimensions between empirical and theoretical $K_n[As_2W_{12}O_{48}]^{(n-14)}$ frameworks across a range of different n values for K. Cation to heteroatom distances are constrained at 9.0Å for these geometries. **OPT/PBE/TZP/SFC/COSMO**

Diameter Identifier	Empirical Fragment Length {Mbomekallé, I.M. *et al.*[322]} (Å)	0K	1K	3K	5K	9K	12K
HEIGHT							
O_A-O_E	11.50	11.60	11.63	11.62	11.62	11.64	11.64
As-As	4.07	4.11	4.17	4.14	4.14	4.19	4.20
W_A-W_E	9.40	10.13	10.16	10.16	10.16	10.19	10.18
LENGTH							
O_B-O_D	7.24	7.36	7.32	7.34	7.33	7.41	7.45
W_C-W_D	6.92	7.06	7.05	7.05	7.05	7.12	7.13
WIDTH							
O_B-O_C	4.45	4.47	4.46	4.47	4.46	4.44	4.42
W_B-W_C	3.77	3.80	3.82	3.82	3.82	3.81	3.82
Theoretical - Empirical Difference							
HEIGHT							
O_A-O_E		+0.10	+0.13	+0.12	+0.12	+0.14	+0.14
As-As		+0.04	+0.10	+0.07	+0.07	+0.12	+0.13
W_A-W_E		+0.73	+0.76	+0.76	+0.76	+0.79	+0.78
LENGTH							
O_B-O_D		+0.12	+0.08	+0.10	+0.09	+0.17	+0.21
W_C-W_D		+0.14	+0.13	+0.13	+0.13	+0.20	+0.21
WIDTH							
O_B-O_C		+0.02	+0.01	+0.02	+0.01	-0.01	-0.03
W_B-W_C		+0.03	+0.05	+0.05	+0.05	+0.04	+0.05
Mean Theoretical – Empirical Difference		+0.17	+0.18	+0.18	+0.18	+0.21	+0.21

Table A-2.15. Comparison in dimensions between empirical and theoretical $K_n[Se_2W_{12}O_{46}]^{(n-12)}$ frameworks across a range of different n values for K. Cation to heteroatom distances are not constrained for these geometries. **OPT/PBE/TZP/SFC/COSMO**

Diameter Identifier	Empirical Fragment Length {Cameron, J.M. *et al.*[78]} (Å)	0K	1K	3K	5K	9K	10K Front	10K Side	10K Top
HEIGHT									
O_A-O_E	11.41	11.51	11.53	11.58	11.52	11.57	11.47	11.47	11.46
Se-Se	3.86	3.99	4.12	4.29	4.19	4.29	4.08	4.13	4.12
W_A-W_E	9.93	10.21	10.13	10.17	10.15	10.20	10.17	10.18	10.16
LENGTH									
O_B-O_D	7.40	7.45	7.15	6.99	7.22	6.93	7.53	7.47	7.67
W_C-W_D	6.91	6.96	7.03	6.89	7.14	6.97	7.34	7.34	7.44
WIDTH									
O_B-O_C	3.28	3.51	4.48	4.40	4.47	4.52	4.38	4.41	4.42
W_B-W_C	3.41	3.46	3.85	3.81	3.82	3.81	3.82	3.82	3.80
Theoretical - Empirical Difference									
HEIGHT									
O_A-O_E		+0.10	+0.12	+0.17	+0.11	+0.16	+0.06	+0.06	+0.05
Se-Se		+0.13	+0.26	+0.43	+0.33	+0.43	+0.22	+0.27	+0.26
W_A-W_E		+0.28	+0.20	+0.24	+0.22	+0.27	+0.24	+0.25	+0.23
LENGTH									
O_B-O_D		+0.05	-0.25	-0.41	-0.18	-0.47	+0.13	+0.07	+0.27
W_C-W_D		+0.05	+0.12	-0.02	+0.23	+0.06	+0.43	+0.43	+0.53
WIDTH									
O_B-O_C		+0.23	+1.20	+1.12	+1.19	+1.24	+1.10	+1.13	+1.14
W_B-W_C		+0.05	+0.44	+0.40	+0.41	+0.40	+0.41	+0.41	+0.39
Mean Theoretical – Empirical Difference		+0.13	+0.30	+0.28	+0.33	+0.30	+0.37	+0.37	+0.41

Table A-2.16. Comparison in dimensions between empirical and theoretical $K_n[Se_2W_{12}O_{46}]^{(n-12)}$ frameworks across a range of different n values for K. Cation to heteroatom distances are constrained at 9.0Å for these geometries. **OPT/PBE/TZP/SFC/COSMO**

Diameter Identifier	Empirical Fragment Length {Cameron, J.M. *et al.*[78]} (Å)	0K	1K	3K	5K	9K	10K Front	10K Side	10K Top
HEIGHT									
O_A-O_E	11.41	11.51	11.56	11.53	11.53	11.53	11.51	11.52	11.49
Se-Se	3.86	3.99	4.07	4.08	4.07	4.05	4.02	4.11	3.99
W_A-W_E	9.93	10.21	10.12	10.13	10.13	10.12	10.12	10.12	10.11
LENGTH									
O_B-O_D	7.40	7.45	7.17	7.16	7.17	7.14	7.23	7.20	7.22
W_C-W_D	6.91	6.96	7.03	7.04	7.04	7.10	7.14	7.12	7.10
WIDTH									
O_B-O_C	3.28	3.51	4.49	4.47	4.46	4.49	4.44	4.44	4.46
W_B-W_C	3.41	3.46	3.85	3.85	3.85	3.85	3.85	3.85	3.85
Theoretical - Empirical Difference									
HEIGHT									
O_A-O_E		+0.10	+0.15	+0.12	+0.12	+0.12	+0.10	+0.11	+0.08
Se-Se		+0.13	+0.21	+0.22	+0.21	+0.19	+0.16	+0.25	+0.13
W_A-W_E		+0.28	+0.19	+0.20	+0.20	+0.19	+0.19	+0.19	+0.18
LENGTH									
O_B-O_D		+0.05	-0.23	-0.24	-0.23	-0.26	-0.17	-0.20	-0.18
W_C-W_D		+0.05	+0.12	+0.13	+0.13	+0.19	+0.23	+0.21	+0.19
WIDTH									
O_B-O_C		+0.23	+1.21	+1.19	+1.18	+1.21	+1.16	+1.16	+1.18
W_B-W_C		+0.05	+0.44	+0.44	+0.44	+0.44	+0.44	+0.44	+0.44
Mean Theoretical – Empirical Difference		+0.13	+0.30	+0.29	+0.29	+0.29	+0.30	+0.31	+0.29

Appendix-2.4: Protonation of Phosphorus Hexalacunary

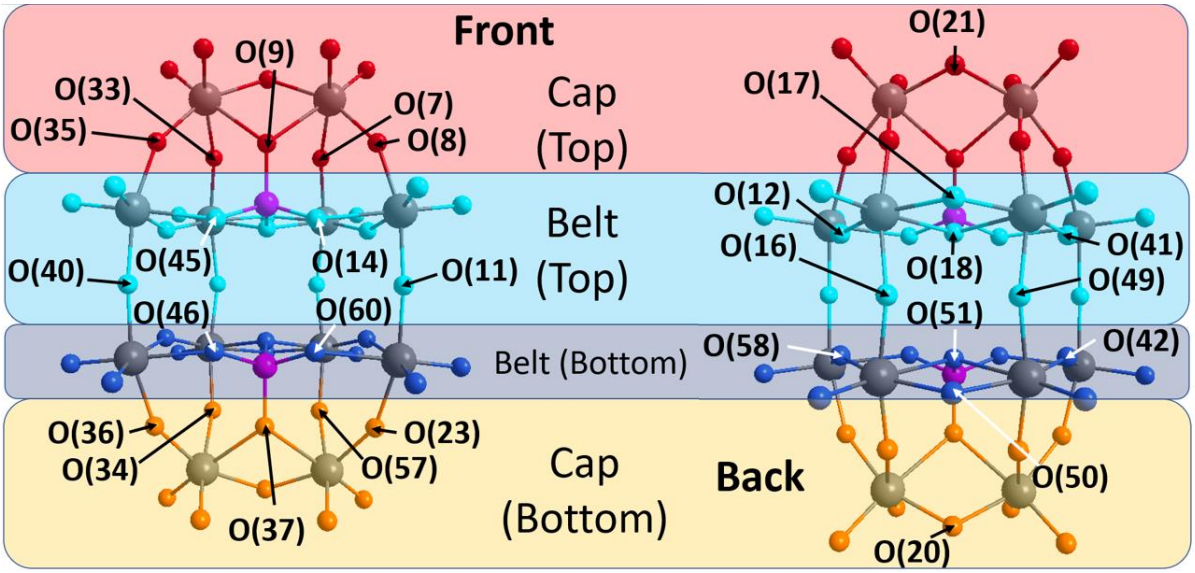

Figure A-2.5. Oxygen atom numbering guide for $[H_2P_2W_{12}O_{48}]^{12-}$ configurations. A configuration of O7,16, for example, will have protons bound to the O7 and O16 atoms respectively. Colour scheme: W: grey, O: red, cyan, indigo, orange, P: pink

There are two types of oxygens within a POM framework: terminal (W=O) and bridging (W-O-W). Taking into account that only bridging oxygens are suitable for protonation,[2] the total number of possible configurations amounts to 112; see **Figure A-2.5.** for the guide on how to assign each configuration and **Table A-2.17** and **Figure A-2.6** for the full list of protonation configurations studied. The range of electronic energies across the different configuration is surprisingly high, with a 48.4kcal mol^{-1} difference between the highest and lowest energy values, **see Figure 6.16B.**

Table A-2.17. Full list of protonated geometries, ordered in ascending order of electronic energy. All energies are relative to the lowest electronic energy, which is associated with the configuration O12,42 (-13098.149kcal mol^{-1}).

Geometry Configuration Number	Protonated Atom Numbers	POM Regions Protonated		Electronic Energy Difference (kcal mol^{-1})	HOMO-LUMO Gap (eV)
Geometry 1	O12, O42	Belt, Belt		0.000	3.04

Geometry 2	O12, O49	Belt, Belt		+0.230	3.30
Geometry 3	O12, O41	Belt, Belt		+1.925	2.97
Geometry 4	O12, O16	Belt, Belt		+2.058	3.28
Geometry 5	O16, O49	Belt, Belt		+6.112	3.40
Geometry 6	O7, O41	Cap, Belt		+7.165	3.09
Geometry 7	O7, O49	Cap, Belt		+7.465	3.29
Geometry 8	O12, O18	Belt, Belt		+8.649	3.02
Geometry 9	O12, O51	Belt, Belt		+9.114	2.98
Geometry 10	O12, O14	Belt, Belt		+9.139	3.01
Geometry 11	O7, O58	Cap, Belt		+10.373	3.04
Geometry 12	O12, O50	Belt, Belt		+10.851	3.26
Geometry 13	O7, O12	Cap, Belt		+11.590	3.12
Geometry 14	O16, O17	Belt, Belt		+11.854	3.32
Geometry 15	O16, O18	Belt, Belt		+12.242	3.30
Geometry 16	O12, O58	Belt, Belt		+13.101	3.08
Geometry 17	O7, O34	Cap, Cap		+13.357	3.12
Geometry 18	O7, O57	Cap, Cap		+13.884	2.79
Geometry 19	O7, O33	Cap, Cap		+14.483	3.15
Geometry 20	O12, O21	Cap, Belt		+14.540	2.95
Geometry 21	O8, O42	Cap, Belt		+15.440	2.85
Geometry 22	O8, O49	Cap, Belt		+15.641	3.03
Geometry 23	O8, O41	Cap, Belt		+16.043	2.84
Geometry 24	O11, O41	Belt, Belt		+16.236	2.92
Geometry 25	O11, O49	Belt, Belt		+16.536	3.23
Geometry 26	O12, O20	Cap, Belt		+17.149	2.95
Geometry 27	O8, O58	Cap, Belt		+17.304	2.89
Geometry 28	O12, O17	Belt, Belt		+17.636	3.09
Geometry 29	O7, O35	Cap, Cap		+17.771	2.94
Geometry 30	O7, O36	Cap, Cap		+17.777	2.89
Geometry 31	O11, O16	Belt, Belt		+17.823	3.20
Geometry 32	O16, O20	Cap, Belt		+18.264	3.15
Geometry 33	O8, O16	Cap, Belt		+18.278	2.97
Geometry 34	O17, O18	Belt, Belt		+18.693	3.27
Geometry 35	O8, O12	Cap, Belt		+19.059	2.99
Geometry 36	O7, O50	Cap, Belt		+19.309	3.16
Geometry 37	O7, O51	Cap, Belt		+19.389	2.99
Geometry 38	O17, O51	Belt, Belt		+19.627	3.20
Geometry 39	O14, O18	Belt, Belt		+19.666	2.89
Geometry 40	O12, O46	Belt, Belt		+19.759	2.92
Geometry 41	O8, O11	Cap, Belt		+20.057	2.90
Geometry 42	O14, O17	Belt, Belt		+20.256	3.20
Geometry 43	O12, O60	Belt, Belt		+20.366	2.97
Geometry 44	O7, O18	Cap, Belt		+20.516	3.06
Geometry 45	O12, O45	Cap, Cap		+20.608	2.95
Geometry 46	O7, O17	Cap, Belt		+20.901	3.14
Geometry 47	O7, O21	Cap, Cap		+20.936	2.95
Geometry 48	O17, O50	Belt, Belt		+21.070	3.43
Geometry 49	O14, O49	Belt, Belt		+21.162	3.17
Geometry 50	O11, O12	Belt, Belt		+21.205	2.92
Geometry 51	O7, O23	Cap, Cap		+21.254	2.67
Geometry 52	O7, O42	Cap, Belt		+21.410	3.05
Geometry 53	O14, O16	Belt, Belt		+21.625	3.19
Geometry 54	O7, O20	Cap, Cap		+21.711	2.86
Geometry 55	O7, O40	Cap, Belt		+23.320	2.95
Geometry 56	O9, O42	Cap, Belt		+23.503	2.94
Geometry 57	O18, O21	Cap, Belt		+23.590	2.86
Geometry 58	O9, O12	Cap, Belt		+23.771	3.00
Geometry 59	O9, O16	Cap, Belt		+25.063	3.21
Geometry 60	O17, O21	Cap, Belt		+25.222	3.11
Geometry 61	O7, O8	Cap, Cap		+25.728	2.93
Geometry 62	O8, O51	Cap, Belt		+25.875	2.74
Geometry 63	O18, O20	Cap, Belt		+25.919	2.83
Geometry 64	O11, O18	Belt, Belt		+26.103	2.86
Geometry 65	O8, 50	Cap, Belt		+26.296	2.99
Geometry 66	O8, O18	Cap, Belt		+26.547	2.79
Geometry 67	O17, O20	Cap, Belt		+26.927	3.14

Geometry 68	O8, O36	Cap, Cap		+27.380	2.73
Geometry 69	O7, O46	Cap, Belt		+27.797	2.90
Geometry 70	O7, O60	Cap, Belt		+28.322	2.88
Geometry 71	O7, O11	Cap, Belt		+28.713	2.93
Geometry 72	O11, O17	Belt, Belt		+28.974	3.15
Geometry 73	O7, O45	Cap, Belt		+29.525	2.96
Geometry 74	O8, O17	Cap, Belt		+29.556	2.96
Geometry 75	O14, O51	Belt, Belt		+29.564	2.84
Geometry 76	O20, O21	Cap, Cap		+29.979	2.72
Geometry 77	O7, O14	Cap, Belt		+30.451	2.95
Geometry 78	O14, O50	Belt, Belt		+30.834	3.11
Geometry 79	O8, O9	Cap, Cap		+31.597	2.84
Geometry 80	O7, O37	Cap, Cap		+32.132	2.93
Geometry 81	O8, O35	Cap, Cap		+32.510	2.75
Geometry 82	O14, O46	Belt, Belt		+32.722	2.88
Geometry 83	O8, O20	Cap, Cap		+32.974	2.67
Geometry 84	O8, O40	Cap, Belt		+33.018	2.75
Geometry 85	O11, O40	Cap, Cap		+33.217	2.80
Geometry 86	O11, O20	Cap, Belt		+34.049	2.84
Geometry 87	O9, O50	Cap, Belt		+34.091	3.11
Geometry 88	O11, O14	Belt, Belt		+34.391	2.87
Geometry 89	O8, O23	Cap, Cap		+34.945	2.56
Geometry 90	O9, O17	Cap, Belt		+35.246	3.30
Geometry 91	O9, O51	Cap, Belt		+35.298	2.88
Geometry 92	O11, O45	Belt, Belt		+35.352	2.81
Geometry 93	O14, O21	Cap, Belt		+35.362	2.88
Geometry 94	O7, O9	Cap, Cap		+35.474	3.02
Geometry 95	O8, O14	Cap, Belt		+35.494	2.85
Geometry 96	O8, O46	Cap, Belt		+35.704	2.72
Geometry 97	O14, O20	Cap, Belt		+35.732	2.78
Geometry 98	O8, O45	Cap, Belt		+36.066	2.79
Geometry 99	O9, O20	Cap, Cap		+36.109	2.78
Geometry 100	O8, O60	Cap, Belt		+36.229	2.70
Geometry 101	O8, O21	Cap, Cap		+36.274	2.85
Geometry 102	O9, O21	Cap, Cap		+36.643	2.94
Geometry 103	O18, O51	Belt, Belt		+37.874	2.91
Geometry 104	O14, O60	Belt, Belt		+38.338	2.80
Geometry 105	O8, O37	Cap, Cap		+38.857	2.73
Geometry 106	O9, O18	Cap, Belt		+41.937	2.93
Geometry 107	O9, O11	Cap, Belt		+42.487	2.86
Geometry 108	O9, O46	Cap, Belt		+43.036	2.81
Geometry 109	O9, O14	Cap, Belt		+43.912	2.96
Geometry 110	O9, O37	Cap, Cap		+47.404	2.83
Geometry 111	O14, O45	Belt, Belt		+48.405	2.83
Geometry 112	O7, O16	Cap, Belt		+99.875	3.12

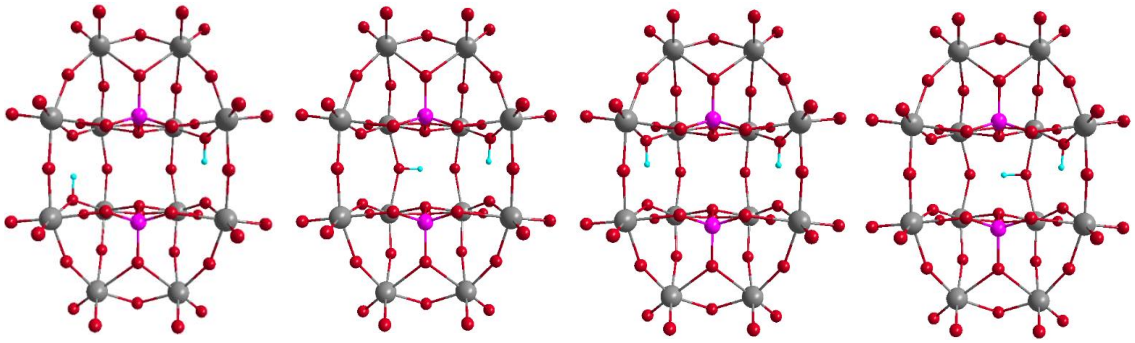

Geometry 1
O12, O42

Geometry 2
O12, O49

Geometry 3
O12, O41

Geometry 4
O12, O16

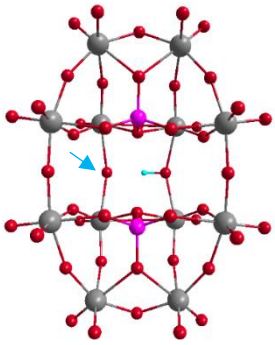

Geometry 5
O16, O49

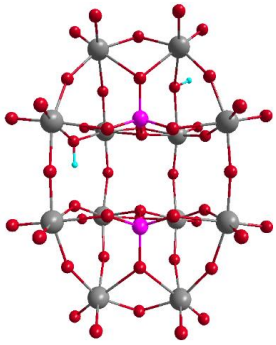

Geometry 6
O7,O41

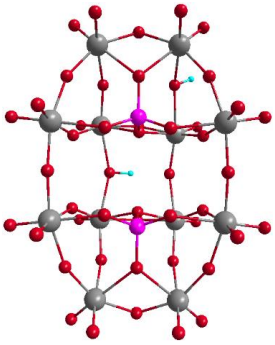

Geometry 7
O7, O49

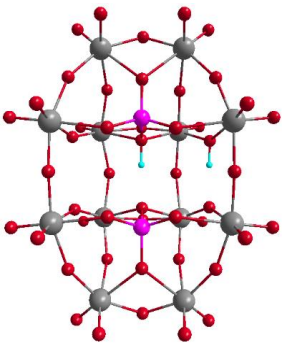

Geometry 8
O12, O18

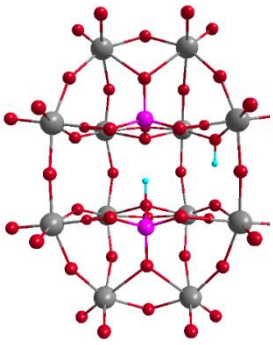

Geometry 9
O12, O51

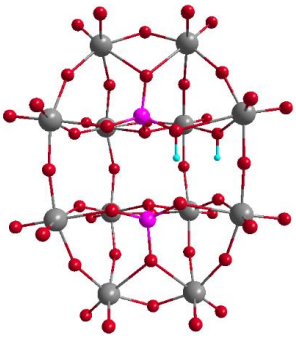

Geometry 10
O12, O14

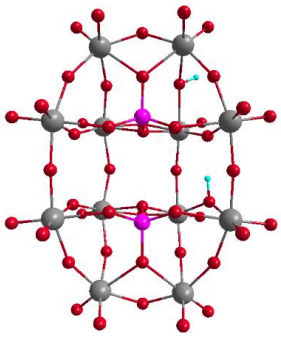

Geometry 11
O7, O58

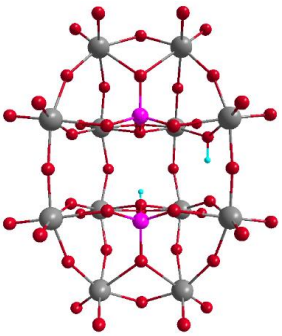

Geometry 12
O12, O50

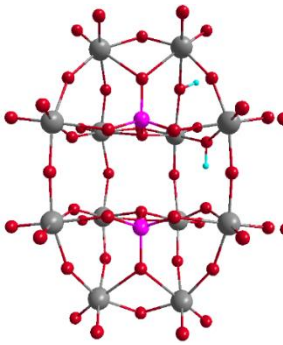

Geometry 13
O7, O12

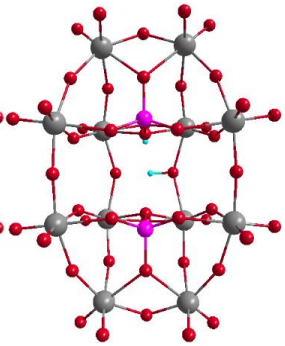

Geometry 14
O16, O17

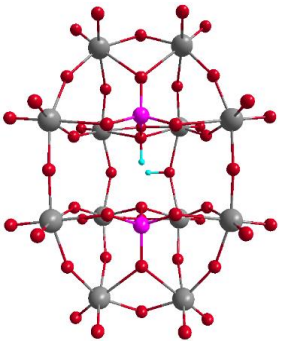

Geometry 15
O16, O18

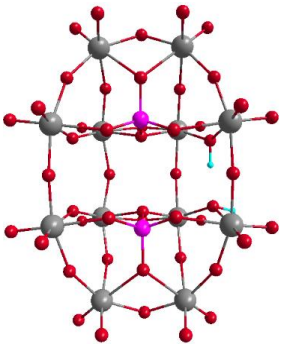

Geometry 16
O12, O58

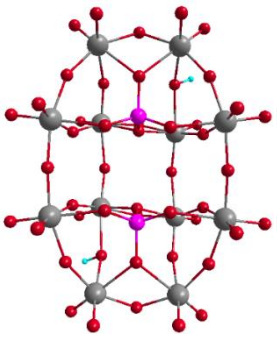

Geometry 17
O7, O34

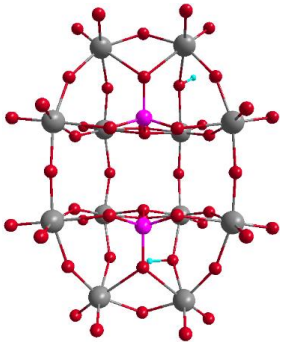

Geometry 18
O7, O57

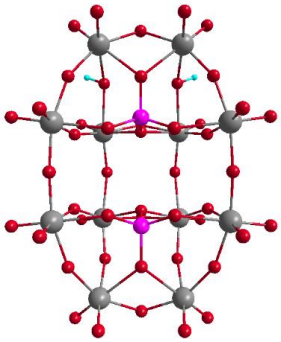

Geometry 19
O7, O33

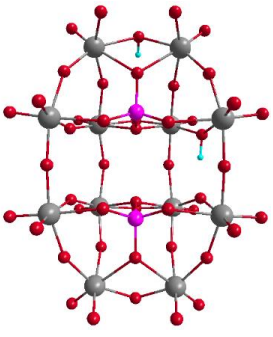

Geometry 20
O12, O21

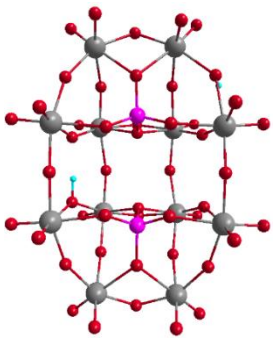

Geometry 21
O8, O42

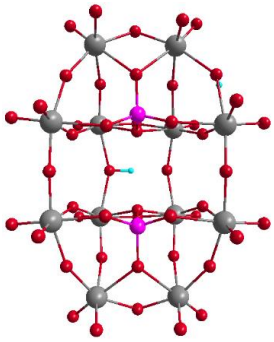

Geometry 22
O8, O49

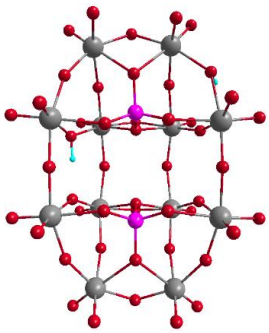

Geometry 23
O8, O41

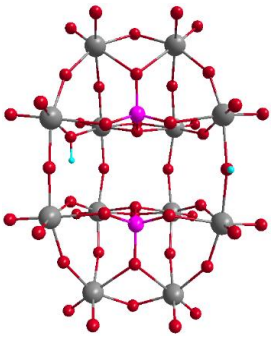

Geometry 24
O11, O41

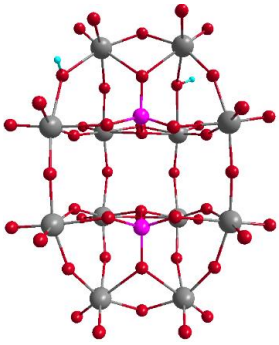

Geometry 25
O11, O49

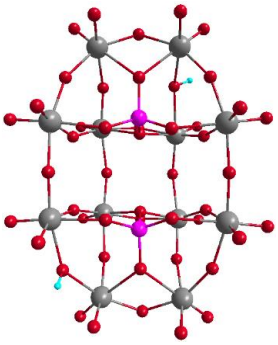

Geometry 26
O12, O20

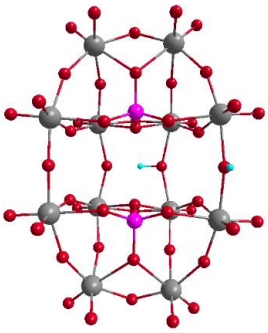

Geometry 27
O8, O58

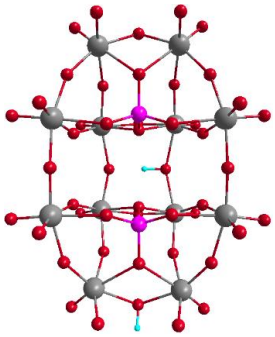

Geometry 28
O12, O17

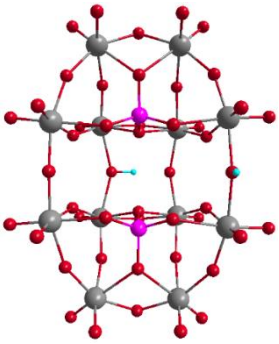

Geometry 29
O7, O35

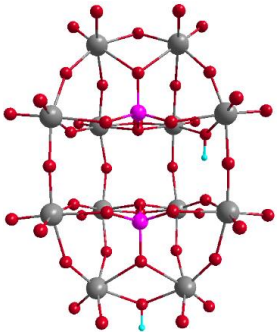

Geometry 30
O7, O36

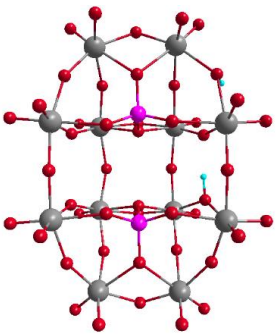

Geometry 31
O11, O16

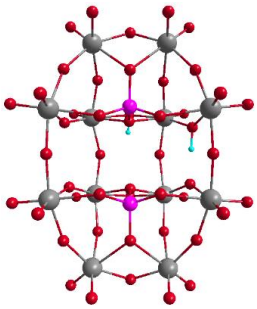

Geometry 32
O16, O20

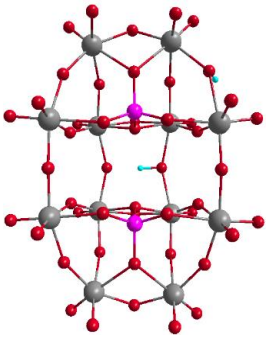

Geometry 33
O8, O16

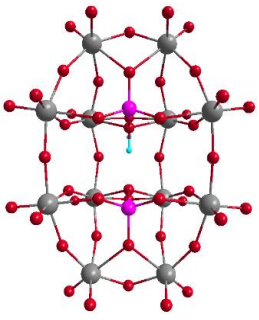

Geometry 34
O17, O18

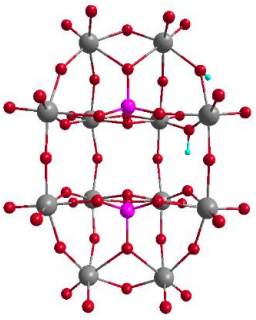

Geometry 35
O8, O12

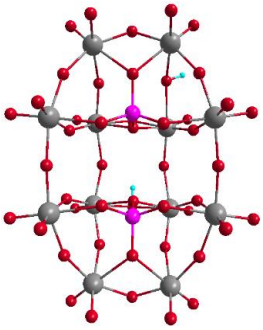

Geometry 36
O7, O50

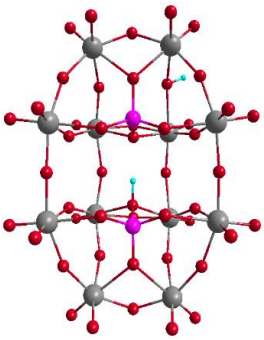

Geometry 37
O7, O51

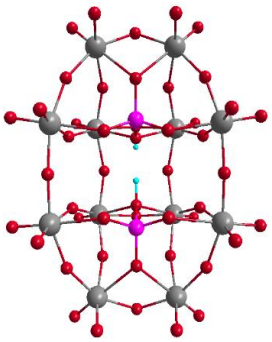

Geometry 38
O17, O51

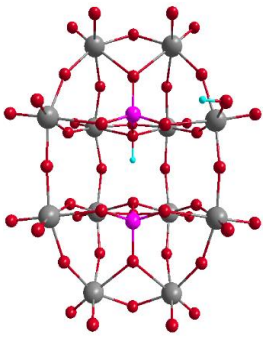

Geometry 39
O14, O18

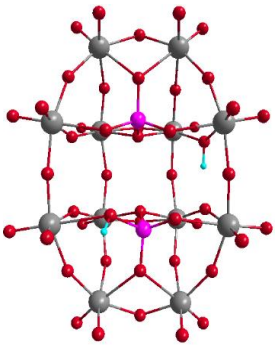

Geometry 40
O12, O46

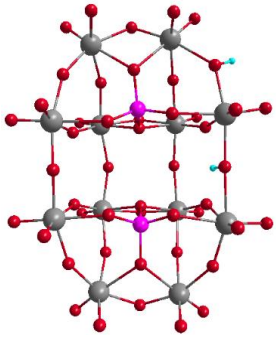

Geometry 41
O8, O11

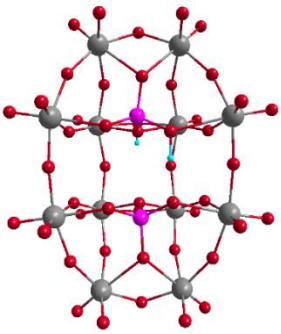

Geometry 42
O14, O17

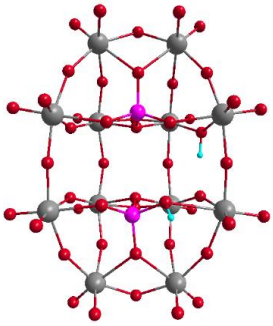

Geometry 43
O12, O60

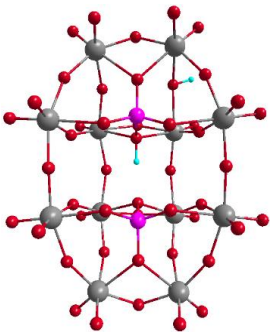

Geometry 44
O7, O18

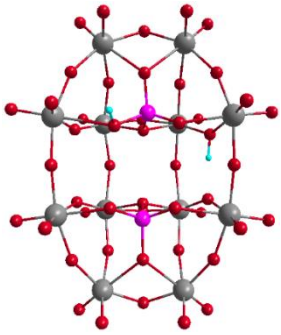

Geometry 45
O12, O45

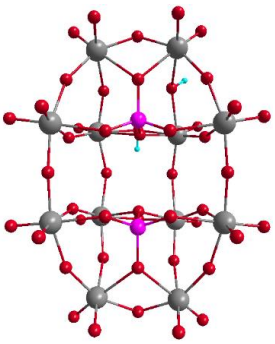

Geometry 46
O7, O17

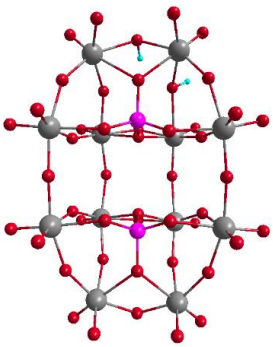

Geometry 47
O7, O21

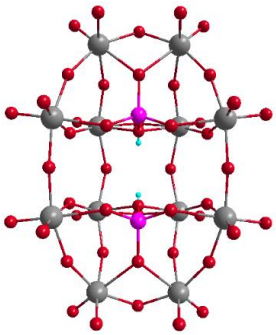

Geometry 48
O17, O50

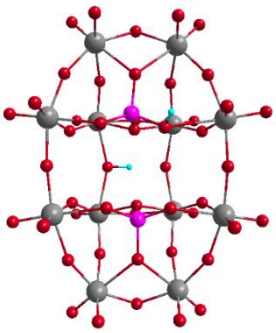

Geometry 49
O14, O49

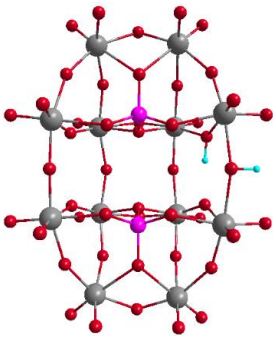

Geometry 50
O11, O12

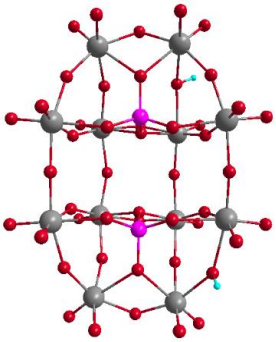

Geometry 51
O7, O23

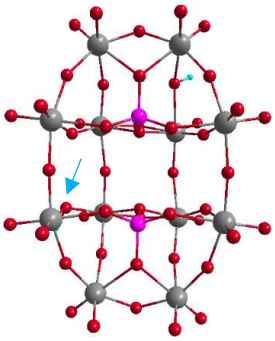

Geometry 52
O7, O42

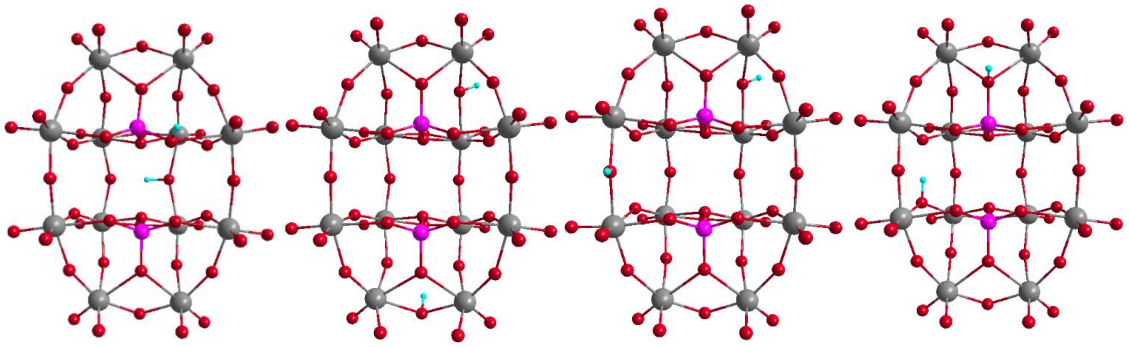

Geometry 53
O14, O16

Geometry 54
O7, O20

Geometry 55
O7, O40

Geometry 56
O9, O42

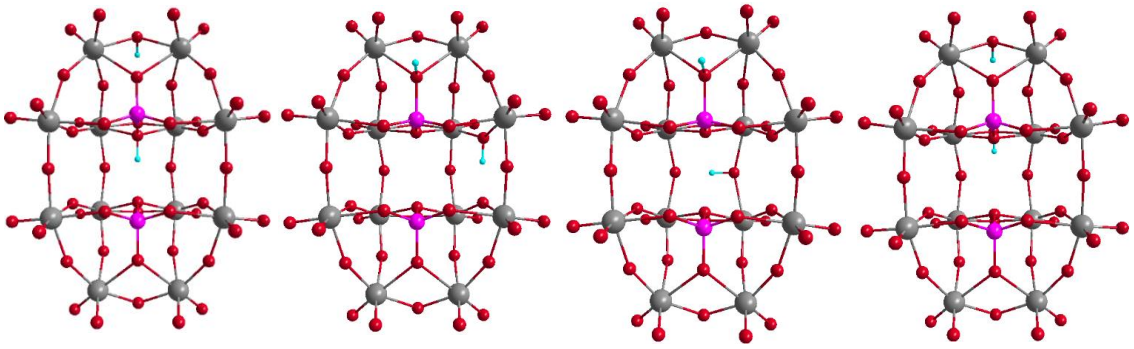

Geometry 57
O18, O21

Geometry 58
O9, O12

Geometry 59
O9, O16

Geometry 60
O17, O21

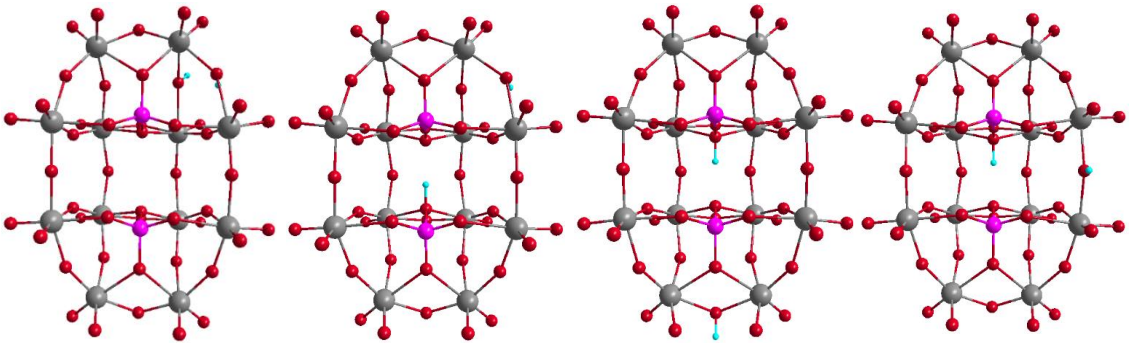

Geometry 61
O7, O8

Geometry 62
O8, O51

Geometry 63
O18, O20

Geometry 64
O11, O18

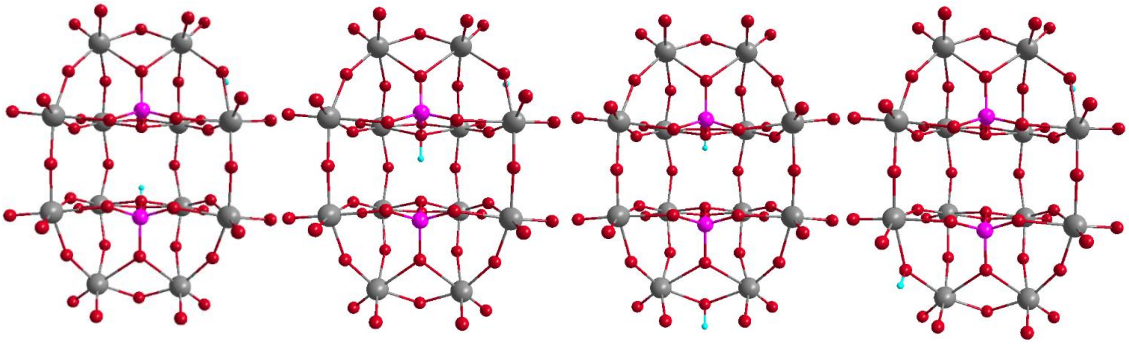

Geometry 65
O8, O50

Geometry 66
O8, O18

Geometry 67
O17, O20

Geometry 68
O8, O36

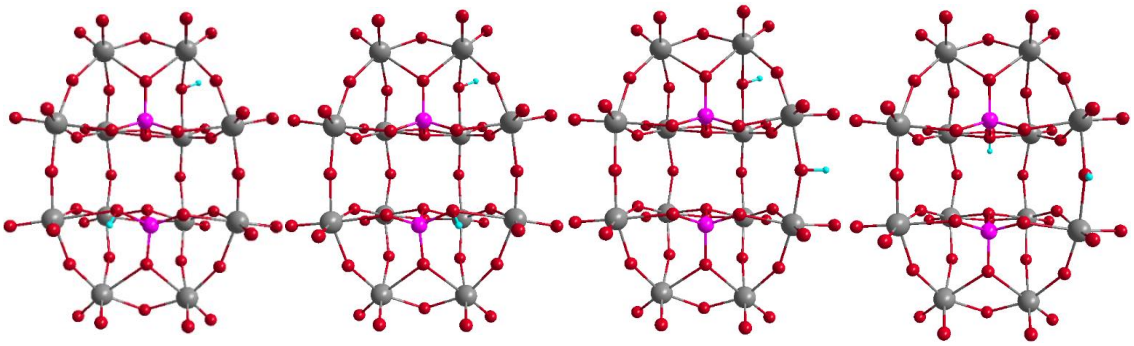

Geometry 69
O7, O46

Geometry 70
O7, O60

Geometry 71
O7, O11

Geometry 72
O11, O17

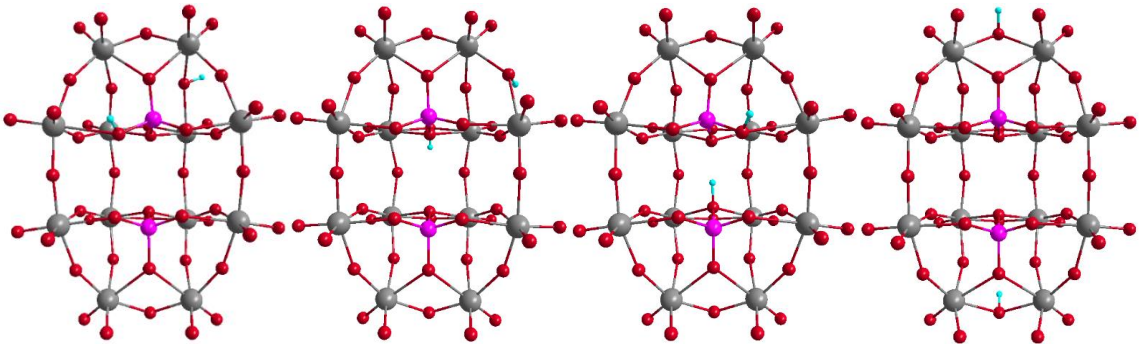

Geometry 73
O7, O45

Geometry 74
O8, O17

Geometry 75
O14, O51

Geometry 76
O20, O21

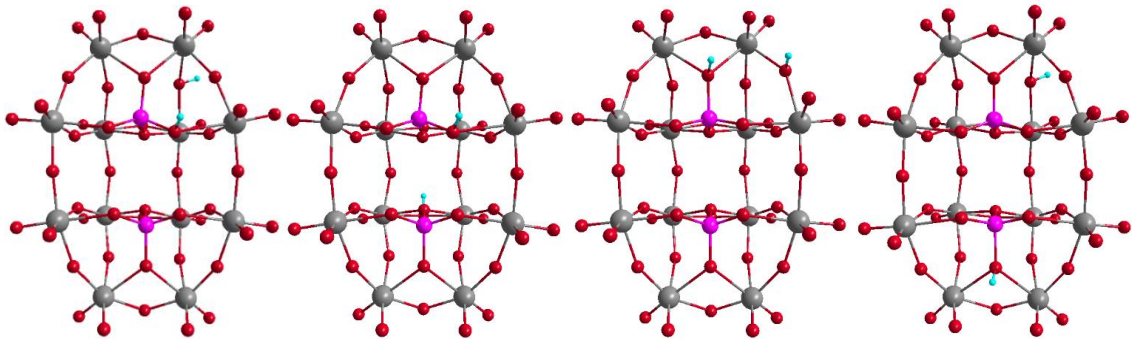

Geometry 77
O7, O14

Geometry 78
O14, O50

Geometry 79
O8, O9

Geometry 80
O7, O37

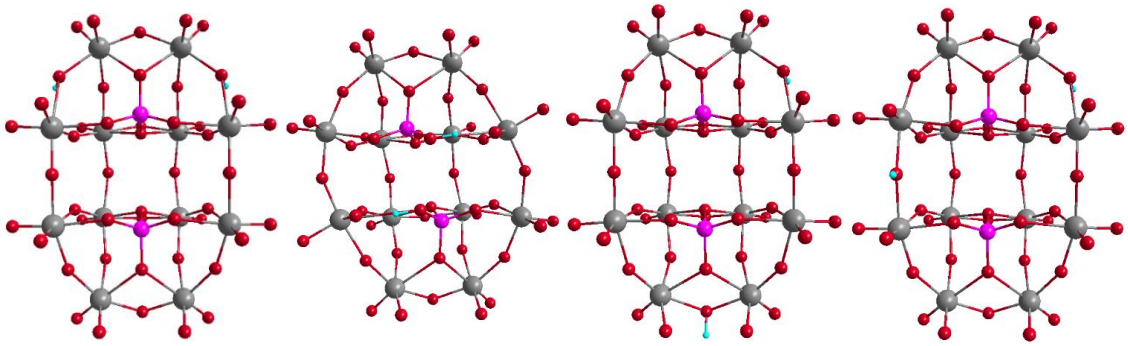

Geometry 81
O8, O35

Geometry 82
O14, O45

Geometry 83
O8, O20

Geometry 84
O8, O40

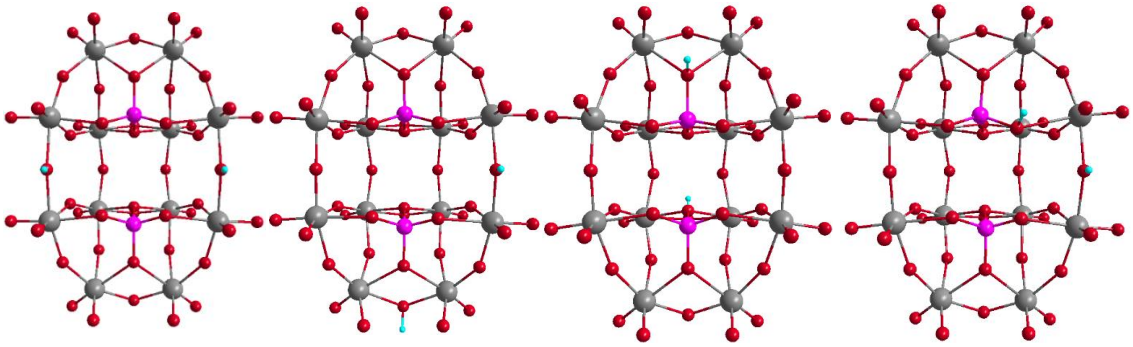

Geometry 85 O11, O40 | **Geometry 86** O11, O20 | **Geometry 87** O9, O50 | **Geometry 88** O11, O14

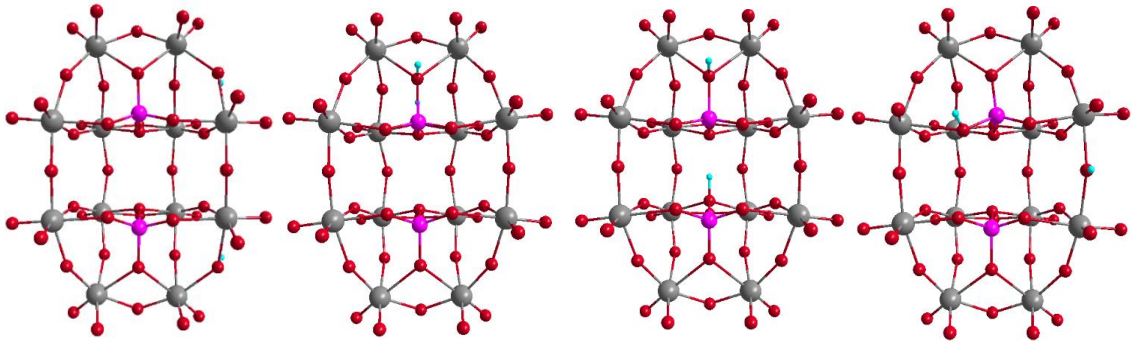

Geometry 89 O8, O23 | **Geometry 90** O9, O17 | **Geometry 91** O9, O51 | **Geometry 92** O11, O45

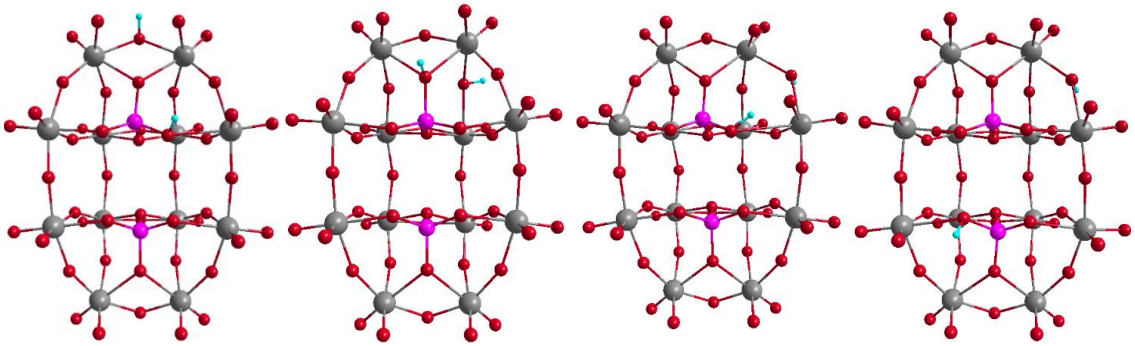

Geometry 93 O14, O21 | **Geometry 94** O7, O9 | **Geometry 95** O8, O14 | **Geometry 96** O8, O46

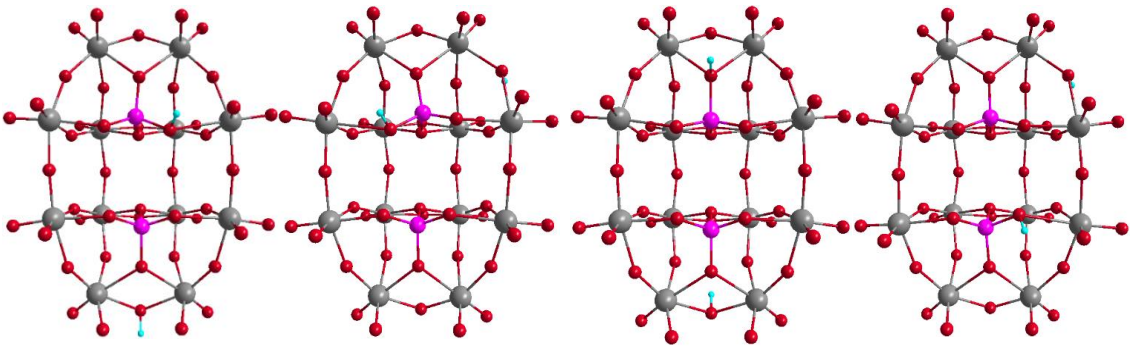

Geometry 97 O14, O20 | **Geometry 98** O8, O45 | **Geometry 99** O9, O20 | **Geometry 100** O8, O60

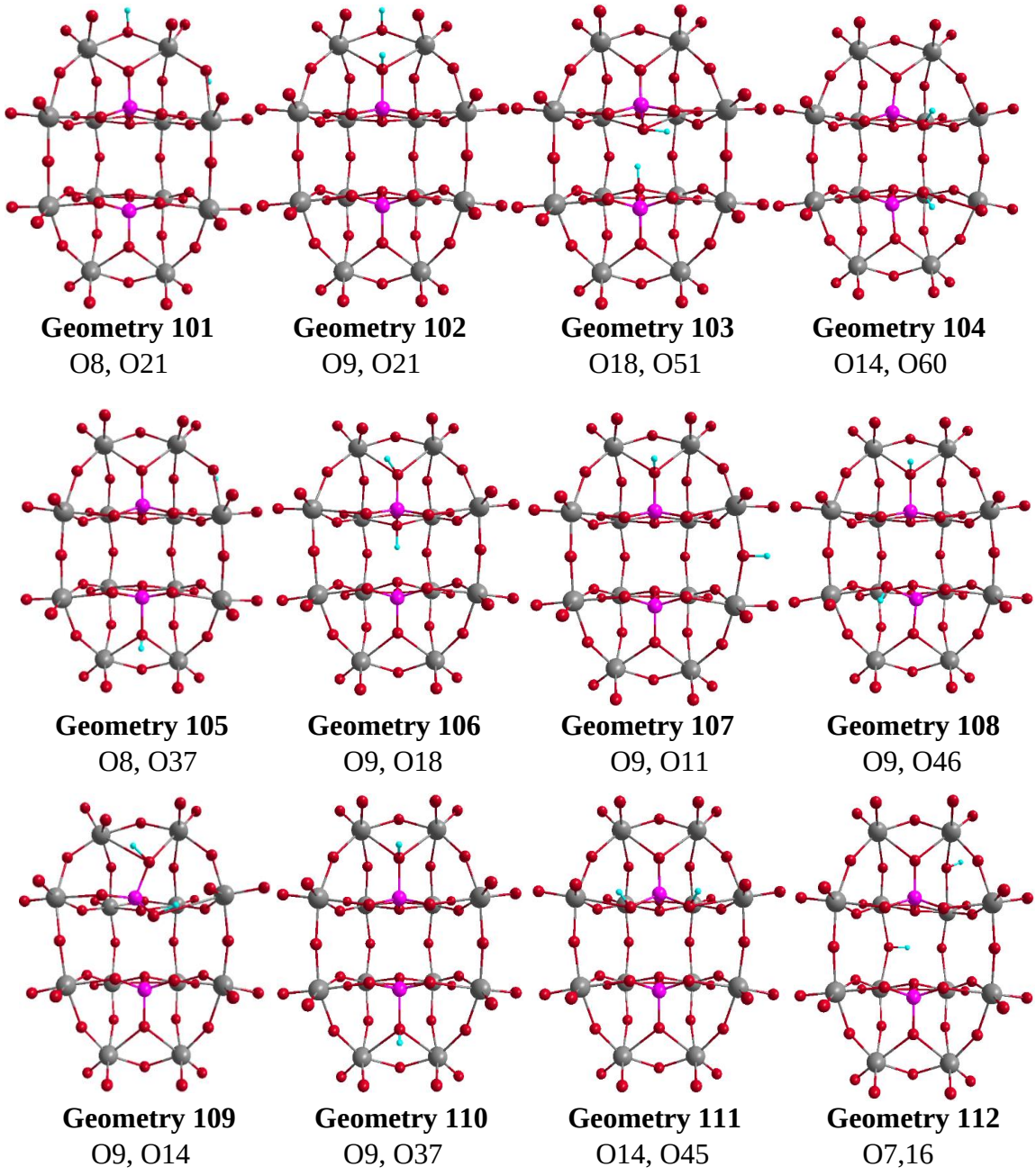

Figure A-2.6. Ball and stick geometries for all ($O_{bridging}$ - $O_{bridging}$) $[H_2P_2W_{12}O_{48}]^{12-}$ configurations. Hydrogen atoms are visualized as cyan to make them easier to spot in the geometry. Colour scheme: W: grey, O: red, P: pink, H: cyan

In **Table A-2.18**, we collected the protonated configurations with the top 10 lowest electronic energy and largest HOMO-LUMO gap values respectively. From these, we selected the 4 configurations ranked highest in both their individual rankings. These were: **O12,49**, **O16,49**, **O12,16**, and **O7,49**. Repeating this for the bottom 10 configurations gave us the following

selection: **O8,37**, **O8,60**, **O9,20**, and **O7,16**. This should enable us to compare relatively stable and unstable configurations, to see if they have any trends within their respective groups. We collected all the highlighted configurations in **Table A-2.19**.

Table A-2.18. 10 selected $[H_2P_2W_{12}O_{48}]^{12-}$ configurations with either the lowest electronic energy (left column) or the largest HOMO-LUMO gap value (right column). The configurations highlighted bold are the 4 which share both a low electronic energy and large HOMO-LUMO gap.

Configuration	Group	Energy (kcal mol^{-1})	Configuration	Group	HOMO-LUMO Gap (eV)
O12,42	Belt-Belt	-13098.149	O17,50	Belt-Belt	3.43
O12,49	Belt-Belt	-13097.919	**O16,49**	Belt-Belt	3.40
O12,41	Belt-Belt	-13096.224	O16,17	Belt-Belt	3.32
O12,16	Belt-Belt	-13096.091	O9,17	Cap-Belt	3.30
O16,49	Belt-Belt	-13092.037	**O12,49**	Belt-Belt	3.30
O7,41	Cap-Belt	-13090.984	O16,18	Belt-Belt	3.30
O7,49	Cap-Belt	-13090.684	**O7,49**	Cap-Belt	3.29
O12,18	Belt-Belt	-13089.500	**O12,16**	Belt-Belt	3.28
O12,51	Belt-Belt	-13089.035	O17,18	Belt-Belt	3.27
O12,14	Belt, Belt	-13089.010	O12,50	Belt-Belt	3.26

Table A-2.19. List of 8 $[H_2P_2W_{12}O_{48}]^{12-}$ configurations which are regarded as existing at opposite ends of the geometry's 'spectrum'. The top 4 geometries in the table (**O7,49**, **O12,16**, **O12,49**, and **O16,49**) are at one end of the spectrum, and the bottom 4, (**O7,16**, **O8,37**, **O8,60**, and **O9,20**) are at the other. Electronic standard deviation measures the standard deviation in electron density for every atom in the molecule

Configuration	Group	HOMO (eV)	LUMO (eV)	HOMO-LUMO Gap (eV)
O7,49	Cap-Belt	-5.166	-1.880	3.29
O12,16	Belt-Belt	-5.117	-1.841	3.28
O12,49	Belt-Belt	-5.165	-1.865	3.30
O16,49	Belt-Belt	-5.194	-1.795	3.40
…				
O7,16	Cap-Belt	-5.166	-1.881	3.29
O8,37	Cap-Cap	-4.892	-2.159	2.73
O8,60	Cap-Belt	-4.866	-2.166	2.70
O9,20	Cap-Cap	-4.876	-2.101	2.78

Though geometries with at least 1 proton located in the belt region tended to have a more negative electronic energy and a larger HOMO-LUMO gap, there is little correlation between the location of the proton with relation to the cap or belt, how far apart the protons are from each other, or in how negative the electronic energy value ties with the size of the HOMO-LUMO gap, see **Figure A-2.7.**

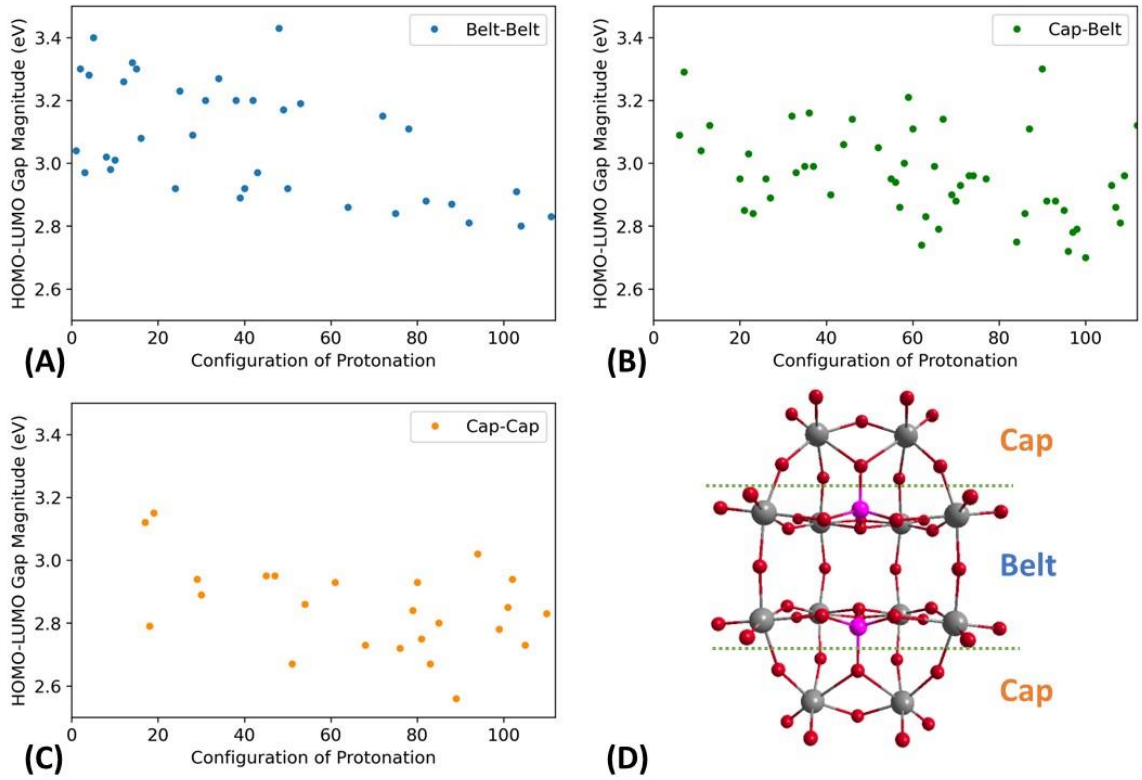

Figure A-2.7. HOMO-LUMO gap values for $[H_2P_2W_{12}O_{48}]^{12-}$ frameworks in ascending order of electronic energy. All energies are relative to the lowest electronic energy, which is associated with the configuration O12,42. Different configurations are collected into three separate groups based on the type of bridging atoms the protons are bound to: Belt-Belt **(A)**, Cap-Belt **(B)**, and Cap-Cap **(C)**. Configurations are coloured according to their respective group **(D)**

When comparing the HOMO-LUMO gaps for the selected protonated geometries, we found that the gap could vary by 0.9eV, a not inconsiderable deviation, though variance was mostly confined to a roughly 0.3eV window ranging from 2.85-3.12eV, see **Table A-2.18**. This wide range in potential HOMO-LUMO gap values has little to no difference on the dimensions of the hexalacunary structure; we observed that the mean difference in structural dimensions between the large and small H-L groups respectively was 0.0025Å – a truly miniscule value, even on a molecular scale. Despite this, there is great variance in frontier orbital localization, see **Figure A-2.8**, again affirming that it is crucial our models correctly reflect the empirical data in order to grant us the level of understanding into electronic POM properties we desire.

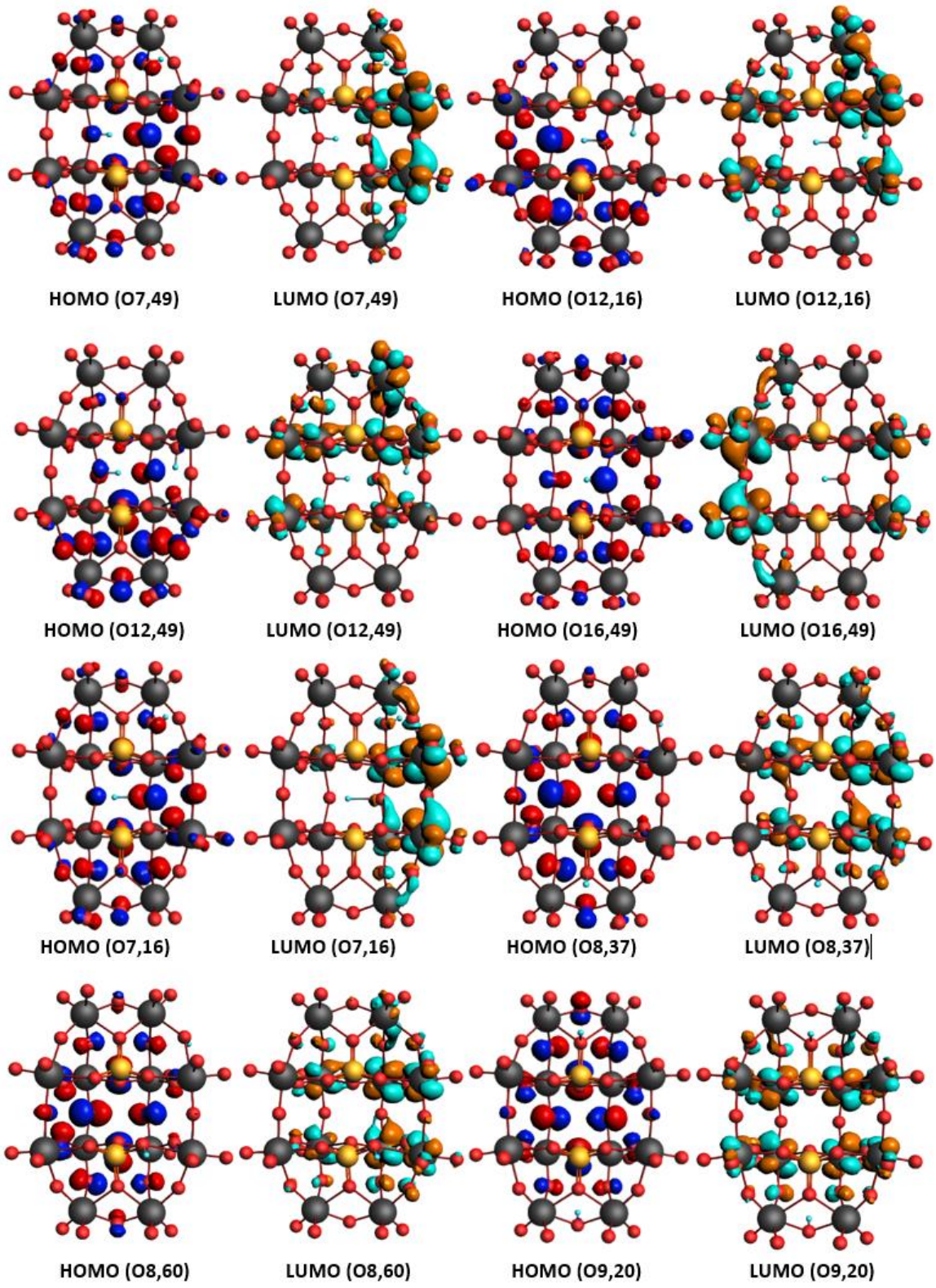

Figure A-2.8. Visualization of HOMO and LUMO frontier orbitals for selected protonated configurations of $[H_2P_2W_{12}O_{48}]^{12-}$ frameworks. Hydrogen atoms are coloured cyan to improve visibility. Colour scheme: W: grey, O: red, P: pink, H: cyan

Determining the handful of protonation configurations the structure is most likely to adopt is therefore more dependent on having the empirical HOMO and LUMO orbital energies than it is on the framework dimensions, sourced from crystallographic data. Without UV-Vis spectroscopy, we can only speculate as to the geometry configurations featured by the hexalacunary when in solution.

Whilst the difference in HOMO-LUMO gap varies dramatically based on the protonation configuration, the degree of structural deviation of the computational model from the empirical dimensions is relatively small, never exceeding a mean value for the framework of 0.2Å, see **Table A-2.19**. These mean values are also closely grouped together, with a standard deviation value of only 0.023

Table A-2.19. Comparison in dimensions between empirical $K_{12}[H_2P_2W_{12}O_{48}]$ and theoretical $[H_2P_2W_{12}O_{48}]^{12-}$ frameworks for a selection of different protonation configurations. **OPT/PBE/TZP/SFC/COSMO**

Diameter Identifier (Å)	O7,16	O7,49	O8,37	O8,60	O9,20	O12,16	O12,49	O16,49
HEIGHT								
O_A-O_E	11.72	11.72	11.64	11.64	11.52	11.55	11.56	11.73
P-P	4.28	4.28	4.17	4.34	4.14	4.26	4.25	4.28
W_A-W_E	10.30	10.30	10.25	10.22	10.14	10.20	10.20	10.31
LENGTH								
O_B-O_D	7.00	7.01	7.02	7.15	7.07	6.97	6.97	7.00
W_C-W_D	6.85	6.85	6.96	7.01	6.96	6.85	6.84	6.85
WIDTH								
O_B-O_C	4.49	4.48	4.44	4.41	4.40	4.55	4.55	4.51
W_B-W_C	3.81	3.81	3.81	3.80	3.81	3.87	3.87	3.79
Theoretical - Empirical Difference (Å)								
HEIGHT								
O_A-O_E	+0.29	+0.29	+0.21	+0.21	+0.09	+0.12	+0.13	+0.30
P-P	+0.11	+0.11	0.00	+0.17	-0.03	+0.09	+0.08	+0.11
W_A-W_E	+0.34	+0.34	+0.29	+0.26	+0.18	+0.24	+0.24	+0.35
LENGTH								
O_B-O_D	+0.17	+0.18	+0.19	+0.32	+0.24	+0.14	+0.14	+0.17
W_C-W_D	+0.12	+0.12	+0.23	+0.28	+0.23	+0.12	+0.11	+0.12
WIDTH								
O_B-O_C	+0.13	+0.12	+0.08	+0.05	+0.04	+0.19	+0.19	+0.15
W_B-W_C	-0.03	-0.03	-0.03	-0.04	-0.03	+0.03	+0.03	-0.05
Mean Deviation (Å)	+0.16	+0.16	+0.14	+0.18	+0.10	+0.13	+0.13	+0.16

To avoid running more than 100 protonation geometries for As and Se hexalacunary structures, we elected to run calculations for the selected top and bottom 4 geometries where As and Se are the respective heteroatoms; if the magnitude of difference in HOMO-LUMO gap between the top and bottom configurations is like that of P hexalacunaries, we can assume the trend for P-based protonation holds true for As- and Se-based protonation as well. We generally found this to be true, so continued using the same set of configurations for all hexalacunaries.

This trend mostly follows for Arsenic and Selenium, with large variance in the HOMO-LUMO gap value and small deviation in the structural dimensions, see **Table A-2.20** and **Table A-2.22** for arsenic electronic properties and dimension data respectively, and **Table A-2.21** and **Table A-2.23** for the same properties with regards to selenium. It is worth noting that deviation between theoretical and empirical dimensions is greater in the Selenium-containing hexalacunary, with an XO_3 heteroatom, than the Arsenic- or Phosphorus-containing species, both with XO_4 heteroatoms; this is true whether the cations or protons are present or absent.

We theorise this to be caused by the oxidation state of the heteroatom species; the two missing oxygen atoms would usually aid in holding the structure together, but without them stretching of the POM cage becomes a greater factor. While this warping is still relatively small, it may partially explain why **{Se_2W_{12}}** has yet to be isolated, as it is less structurally robust than its **{As_2W_{12}}** and **{P_2W_{12}}** counterparts.

The collected results from all 3 families of hexalacunary can be found in **Figures A-2.25, A-2.26**.

Table A-2.20. List of 8 $[H_2As_2W_{12}O_{48}]^{12-}$ configurations which are regarded as existing at opposite ends of the geometry's 'spectrum'. Electronic standard deviation measures the standard deviation in electron density for every atom in the molecule. Difference is calculated by subtracting the Arsenic hexalacunary value from the corresponding Phosphorus hexalacunary configuration.

Configuration	Group	HOMO-LUMO Gap (eV)	HOMO-LUMO Gap Difference w/ P	Standard Deviation	Standard Deviation Difference w/ P
O7,49	Cap-Belt	3.29	0.00	1.186	+0.006
O12,16	Belt-Belt	3.28	0.00	1.201	+0.022
O12,49	Belt-Belt	3.30	0.00	1.205	+0.026
O16,49	Belt-Belt	3.42	+0.02	1.208	+0.026
...					
O7,16	Cap-Belt	3.08	+0.01	1.189	+0.009
O8,37	Cap-Cap	2.73	0.00	1.209	+0.026
O8,60	Cap-Belt	2.70	0.00	1.206	+0.026
O9,20	Cap-Cap	2.77	-0.01	1.208	+0.026

Table A-2.21. List of 8 $[H_2Se_2W_{12}O_{46}]^{10-}$ configurations which are regarded as existing at opposite ends of the geometry's 'spectrum'. Electronic standard deviation measures the standard deviation in electron density for every atom in the molecule. Difference is calculated by subtracting the Selenium hexalacunary value from the corresponding Phosphorus hexalacunary configuration.

Configuration	Group	HOMO-LUMO Gap (eV)	HOMO-LUMO Gap Difference w/ P	Standard Deviation	Standard Deviation Difference w/ P
O7,49	Cap-Belt	3.42	+0.13	1.158	-0.022
O12,16	Belt-Belt	3.45	+0.17	1.155	-0.024
O12,49	Belt-Belt	3.38	+0.08	1.155	-0.024
O16,49	Belt-Belt	3.60	+0.20	1.160	-0.022
...					
O7,16	Cap-Belt	3.23	+0.16	1.158	-0.022
O8,37	Cap-Cap	2.76	+0.03	1.162	-0.021
O8,60	Cap-Belt	2.75	+0.05	1.158	-0.022
O9,20	Cap-Cap	2.84	+0.06	1.161	-0.021

Table A-2.22. Comparison in dimensions between empirical $K_{12}[H_2As_2W_{12}O_{48}]$ and theoretical $[H_2As_2W_{12}O_{48}]^{12-}$ frameworks for a selection of different protonation configurations. **OPT/PBE/TZP/SFC/COSMO**

Diameter Identifier (Å)	O7,16	O7,49	O8,37	O8,60	O9,20	O12,16	O12,49	O16,49
HEIGHT								
O_A-O_E	11.71	11.78	11.64	11.64	11.52	11.60	11.56	11.73
As-As	4.17	4.17	4.17	4.34	4.14	4.14	4.25	4.28
W_A-W_E	10.28	10.32	10.25	10.22	10.14	10.21	10.20	10.31
LENGTH								
O_B-O_D	7.31	7.30	7.02	7.15	7.07	7.29	6.97	7.00
W_C-W_D	7.03	7.03	6.96	7.06	6.96	7.03	6.84	6.85
WIDTH								
O_B-O_C	4.58	4.54	4.44	4.41	4.40	4.63	4.55	4.51
W_B-W_C	3.83	3.82	3.81	3.80	3.81	3.88	3.87	3.79
Theoretical - Empirical Difference (Å)								
HEIGHT								
O_A-O_E	+0.21	+0.28	+0.14	+0.14	+0.02	+0.10	+0.06	+0.23
As-As	+0.10	+0.10	+0.10	+0.27	+0.07	+0.07	+0.18	+0.21
W_A-W_E	+0.88	+0.92	+0.85	+0.82	+0.74	+0.81	+0.80	+0.91
LENGTH								
O_B-O_D	+0.07	+0.06	-0.22	-0.09	-0.17	+0.05	-0.27	-0.24
W_C-W_D	+0.11	+0.11	-0.04	-0.14	-0.04	+0.11	-0.08	-0.07
WIDTH								
O_B-O_C	+0.13	+0.09	-0.01	-0.04	-0.05	+0.18	+0.10	+0.06
W_B-W_C	+0.06	+0.05	+0.04	+0.03	+0.04	+0.11	+0.10	+0.02
Mean Deviation (Å)	+0.22	+0.23	+0.12	+0.14	+0.09	+0.20	+0.13	+0.16

Table A-2.23. Comparison in dimensions between empirical $K_{10}[H_2Se_2W_{12}O_{46}]$ and theoretical $[H_2Se_2W_{12}O_{46}]^{10-}$ frameworks for a selection of different protonation configurations. **OPT/PBE/TZP/SFC/COSMO**

Diameter Identifier (Å)	O7,16	O7,49	O8,37	O8,60	O9,20	O12,16	O12,49	O16,49
HEIGHT								
O_A-O_E	11.62	11.62	11.57	11.57	11.47	1.153	1.156	1.171
Se-Se	4.06	3.90	3.90	4.19	3.86	0.407	0.407	0.403
W_A-W_E	10.27	10.23	10.20	10.20	10.08	1.020	1.022	1.031
LENGTH								
O_B-O_D	7.03	6.92	7.17	7.28	7.19	0.707	0.706	0.701
W_C-W_D	6.97	6.97	7.15	7.21	7.16	0.701	0.698	0.696
WIDTH								
O_B-O_C	4.59	4.61	4.49	4.46	4.47	0.457	0.459	0.455
W_B-W_C	3.87	3.87	3.82	3.83	3.88	0.394	0.394	0.385
Theoretical - Empirical Difference (Å)								
HEIGHT								
O_A-O_E	+0.21	+0.21	+0.16	+0.16	+0.06	+0.12	+0.15	+0.30
Se-Se	+0.20	+0.04	+0.04	+0.33	0.00	+0.21	+0.21	+0.17
W_A-W_E	+0.34	+0.30	+0.27	+0.27	+0.15	+0.27	+0.29	+0.38
LENGTH								
O_B-O_D	-0.37	-0.48	-0.23	-0.12	-0.21	-0.33	-0.34	-0.39
W_C-W_D	+0.06	+0.06	+0.24	+0.30	+0.25	+0.10	+0.07	+0.05
WIDTH								
O_B-O_C	+1.31	+1.33	+1.21	+1.18	+1.19	+1.29	+1.31	+1.27
W_B-W_C	+0.46	+0.46	+0.41	+0.42	+0.47	+0.53	+0.53	+0.44
Mean Deviation (Å)	+0.32	+0.27	+0.30	+0.36	+0.27	+0.31	+0.32	+0.32

Appendix-2.5: Combining Protonation and Countercation Models

For this section, where we combine our established cation and proton geometries, we created 2 families of structures, these being hexalacunaries which are completely charge neutral, $K_{12}[H_2P_2W_{12}O_{48}]$, and those which learn from the findings of earlier sections of this paper; the latter features only 3 potassium cations as this was earlier established to be the ideal number, $K_3[H_2P_2W_{12}O_{48}]^{9-}$. All the structures within each family share the same number of potassium countercations, the only difference is in the proton configurations utilised; these are the **O7,16**, **O7,49**, **O12,49**, and **O16,49** configs already described, see **Figure A-2.9.**

With respect to deviation in molecular dimensions between the theoretical and empirical structures for **{K_3H_2}** and **{$K_{12}H_2$}** hexalacunaries, there is minimal difference in deviation. We found there to be little point including all 12 potassium cations as this does not lead to a substantial improvement in this deviation value, see **Tables A-2.24** to **A-2.29** and **Figure A-2.10**

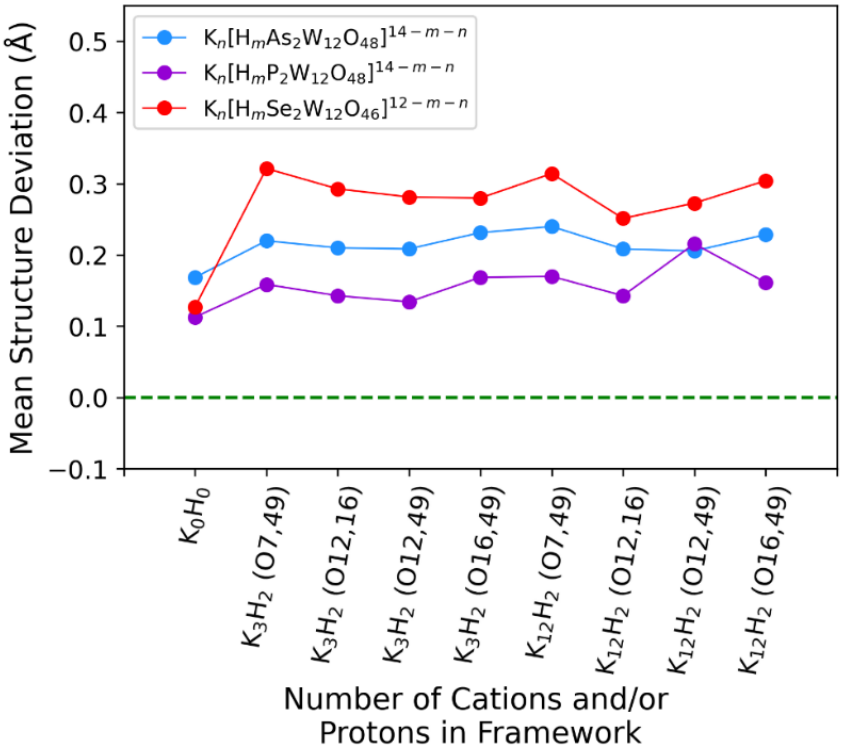

Figure A-2.9. Differences in the mean structure deviation value for $[P_2W_{12}O_{48}]^{14-}$, $[As_2W_{12}O_{48}]^{14-}$, and $[Se_2W_{12}O_{46}]^{12-}$ with and without protons and cations. Proton configuration is included where appropriate. **OPT/PBE/TZP/SFC/COSMO**

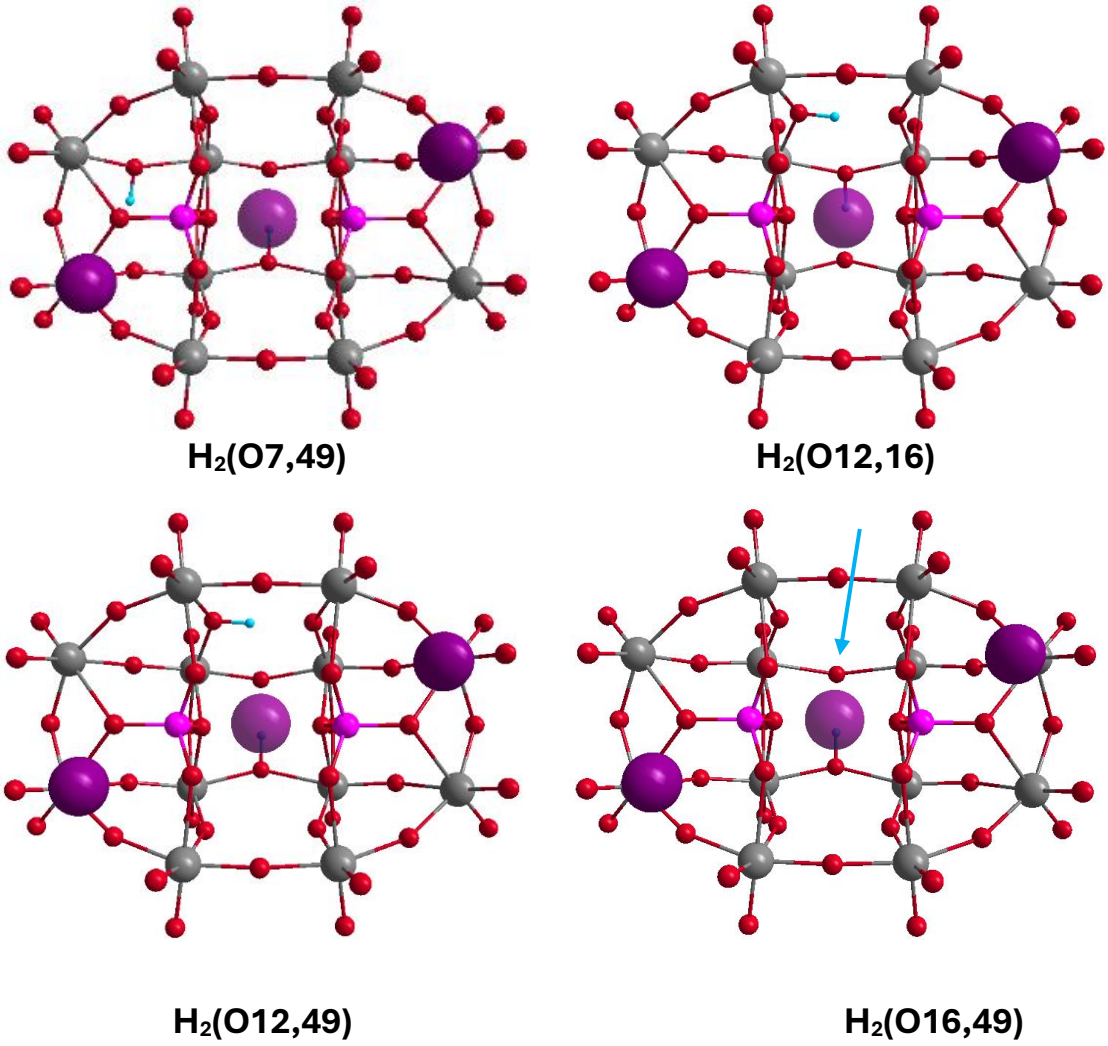

Figure A-2.10. Ball and stick geometries for $K_3[H_2P_2W_{12}O_{48}]^{9-}$ structures across 4 different protonation configurations. Hydrogen atoms are visualized cyan. The central potassium cation is slightly transparent to enable the hydrogen behind the cation to be visible. The second hydrogen in H_2(O16,49) – $K_3[H_2P_2W_{12}O_{48}]^{9-}$ is not visible from the front of the framework but its position is indicated using a cyan arrow. Colour scheme: W: grey, O: red, P: pink, K: purple, H: cyan **OPT/PBE/TZP/SFC/COSMO**

Table A-2.24. Comparison in dimensions between empirical $K_{12}[H_2P_2W_{12}O_{48}]$ and theoretical $K_3[H_2P_2W_{12}O_{48}]^{9-}$ frameworks for a selection of different protonation configurations. The distance between cation and heteroatom is constrained at 9.0Å. **OPT/PBE/TZP/SFC/COSMO**

Diameter Identifier (Å)	O7,49	O12,16	O12,49	O16,49
HEIGHT				
O_A-O_E	11.70	11.54	11.56	11.73
P-P	4.27	4.29	4.24	4.28
W_A-W_E	10.30	10.22	10.20	10.32
LENGTH				
O_B-O_D	6.99	6.95	6.97	7.00
W_C-W_D	6.85	6.88	6.84	6.85
WIDTH				
O_B-O_C	4.48	4.55	4.55	4.51
W_B-W_C	3.82	3.87	3.88	3.79
Theoretical - Empirical Difference (Å)				
HEIGHT				
O_A-O_E	+0.27	+0.11	+0.13	+0.30
P-P	+0.10	+0.12	+0.07	+0.11
W_A-W_E	+0.34	+0.26	+0.24	+0.36
LENGTH				
O_B-O_D	+0.16	+0.12	+0.14	+0.17
W_C-W_D	+0.12	+0.15	+0.11	+0.12
WIDTH				
O_B-O_C	+0.12	+0.19	+0.19	+0.15
W_B-W_C	0.00	+0.05	+0.06	-0.03
Mean Deviation (Å)	+0.16	+0.14	+0.13	+0.17

Table A-2.25. Comparison in dimensions between empirical $K_{12}[H_2As_2W_{12}O_{48}]$ and theoretical $K_3[H_2As_2W_{12}O_{48}]^{9-}$ frameworks for a selection of different protonation configurations. The distance between cation and heteroatom is constrained at 9.0Å. **OPT/PBE/TZP/SFC/COSMO**

Diameter Identifier (Å)	O7,49	O12,16	O12,49	O16,49
HEIGHT				
O_A-O_E	11.74	11.61	11.61	11.77
P-P	4.10	4.13	4.10	4.15
W_A-W_E	10.29	10.21	10.21	10.33
LENGTH				
O_B-O_D	7.33	7.30	7.32	7.32
W_C-W_D	7.05	7.03	7.05	7.02
WIDTH				
O_B-O_C	4.55	4.64	4.62	4.58
W_B-W_C	3.83	3.89	3.89	3.80
Theoretical - Empirical Difference (Å)				
HEIGHT				
O_A-O_E	+0.24	+0.11	+0.11	+0.27
P-P	+0.03	+0.06	+0.03	+0.08
W_A-W_E	+0.89	+0.81	+0.81	+0.93
LENGTH				
O_B-O_D	+0.09	+0.06	+0.08	+0.08
W_C-W_D	+0.13	+0.11	+0.13	+0.10
WIDTH				
O_B-O_C	+0.10	+0.19	+0.17	+0.13
W_B-W_C	+0.06	+0.13	+0.13	+0.03
Mean Deviation (Å)	+0.22	+0.21	+0.21	+0.23

Table A-2.26. Comparison in dimensions between empirical $K_{10}[H_2Se_2W_{12}O_{46}]$ and theoretical $K_3[H_2Se_2W_{12}O_{46}]^{7-}$ frameworks for a selection of different protonation configurations. The distance between cation and heteroatom is constrained at 9.0Å. **OPT/PBE/TZP/SFC/COSMO**

Diameter Identifier (Å)	O7,49	O12,16	O12,49	O16,49
HEIGHT				
O_A-O_E	11.66	11.49	11.50	11.64
P-P	4.04	3.98	3.92	3.89
W_A-W_E	10.27	10.17	10.18	10.26
LENGTH				
O_B-O_D	7.03	7.06	6.99	6.94
W_C-W_D	6.98	7.02	7.02	6.99
WIDTH				
O_B-O_C	4.59	4.59	4.62	4.59
W_B-W_C	3.88	3.94	3.94	3.85
Theoretical - Empirical Difference (Å)				
HEIGHT				
O_A-O_E	+0.25	+0.08	+0.09	+0.23
P-P	+0.18	+0.12	+0.06	+0.03
W_A-W_E	+0.34	+0.24	+0.25	+0.33
LENGTH				
O_B-O_D	-0.37	-0.34	-0.41	-0.46
W_C-W_D	+0.07	+0.11	+0.11	+0.08
WIDTH				
O_B-O_C	+1.31	+1.31	+1.34	+1.31
W_B-W_C	+0.47	+0.53	+0.53	+0.44
Mean Deviation (Å)	+0.32	+0.29	+0.28	+0.28

Table A-2.27. Comparison in dimensions between empirical and theoretical $K_{12}[H_2P_2W_{12}O_{48}]$ frameworks for a selection of different protonation configurations. The distance between cation and heteroatom is constrained at 9.0Å. **OPT/PBE/TZP/SFC/COSMO**

Diameter Identifier (Å)	O7,49	O12,16	O12,49	O16,49
HEIGHT				
O_A-O_E	11.70	11.54	11.58	11.69
P-P	4.27	4.24	4.09	4.28
W_A-W_E	10.31	10.19	10.21	10.32
LENGTH				
O_B-O_D	7.01	6.98	7.33	7.03
W_C-W_D	6.88	6.91	7.10	6.92
WIDTH				
O_B-O_C	4.48	4.55	4.60	4.37
W_B-W_C	3.82	3.87	3.88	3.80
Theoretical - Empirical Difference (Å)				
HEIGHT				
O_A-O_E	+0.27	+0.11	+0.15	+0.26
P-P	+0.10	+0.07	-0.08	+0.11
W_A-W_E	+0.41	+0.29	+0.31	+0.42
LENGTH				
O_B-O_D	+0.14	+0.11	+0.46	+0.16
W_C-W_D	+0.15	+0.18	+0.37	+0.19
WIDTH				
O_B-O_C	+0.12	+0.19	+0.24	+0.01
W_B-W_C	0.00	+0.05	+0.06	-0.02
Mean Deviation (Å)	+0.17	+0.14	+0.22	+0.16

Table A-2.28. Comparison in dimensions between empirical and theoretical $K_{12}[H_2As_2W_{12}O_{48}]$ frameworks for a selection of different protonation configurations. The distance between cation and heteroatom is constrained at 9.0Å. **OPT/PBE/TZP/SFC/COSMO**

Diameter Identifier (Å)	O7,49	O12,16	O12,49	O16,49
HEIGHT				
O_A-O_E	11.76	11.58	11.58	11.78
P-P	4.15	4.09	4.09	4.19
W_A-W_E	10.33	10.20	10.21	10.37
LENGTH				
O_B-O_D	7.37	7.33	7.33	7.32
W_C-W_D	7.08	7.11	7.10	7.08
WIDTH				
O_B-O_C	4.51	4.62	4.60	4.39
W_B-W_C	3.83	3.88	3.88	3.82
Theoretical - Empirical Difference (Å)				
HEIGHT				
O_A-O_E	+0.26	+0.08	+0.08	+0.28
P-P	+0.08	+0.02	+0.02	+0.12
W_A-W_E	+0.93	+0.80	+0.81	+0.97
LENGTH				
O_B-O_D	+0.13	+0.09	+0.09	+0.08
W_C-W_D	+0.16	+0.19	+0.18	+0.16
WIDTH				
O_B-O_C	+0.06	+0.17	+0.15	-0.06
W_B-W_C	+0.06	+0.11	+0.11	+0.05
Mean Deviation (Å)	+0.24	+0.21	+0.21	+0.23

Table A-2.29. Comparison in dimensions between empirical and theoretical $K_{10}[H_2Se_2W_{12}O_{46}]$ frameworks for a selection of different protonation configurations. The distance between cation and heteroatom is constrained at 9.0Å. **OPT/PBE/TZP/SFC/COSMO**

Diameter Identifier (Å)	O7,49	O12,16	O12,49	O16,49
HEIGHT				
O_A-O_E	11.66	11.38	11.50	11.74
P-P	4.00	3.80	3.88	4.02
W_A-W_E	10.30	10.08	10.14	10.36
LENGTH				
O_B-O_D	7.20	6.98	6.93	7.18
W_C-W_D	7.10	7.12	7.07	7.10
WIDTH				
O_B-O_C	4.22	4.61	4.62	4.02
W_B-W_C	3.90	3.95	3.95	3.89
Theoretical - Empirical Difference (Å)				
HEIGHT				
O_A-O_E	+0.25	-0.03	+0.09	+0.33
P-P	+0.14	-0.06	+0.02	+0.16
W_A-W_E	+0.37	+0.15	+0.21	+0.43
LENGTH				
O_B-O_D	-0.20	-0.42	-0.47	-0.22
W_C-W_D	+0.21	+0.23	+0.18	+0.21
WIDTH				
O_B-O_C	+0.94	+1.35	+1.34	+0.74
W_B-W_C	+0.49	+0.54	+0.54	+0.48
Mean Deviation (Å)	+0.31	+0.25	+0.27	+0.30

Appendix-2.6: Charge Distribution

Table A-2.30. Electronic standard deviation for $K_n[As_2W_{12}O_{48}]^{n-14}$, $K_n[P_2W_{12}O_{48}]^{n-14}$, and $K_n[Se_2W_{12}O_{46}]^{n-12}$ hexalacunary structures. A smaller deviation value indicates more delocalisation and a smaller degree of polarisation throughout the framework.

Formula	Total Standard Deviation (electrons)	Formula	Total Standard Deviation (electrons)	Formula	Total Standard Deviation (electrons)
$[As_2W_{12}O_{48}]^{14-}$	1.223	$[P_2W_{12}O_{48}]^{14-}$	1.213	$[Se_2W_{12}O_{46}]^{12-}$	1.197
$K[As_2W_{12}O_{48}]^{13-}$	1.232	$K[P_2W_{12}O_{48}]^{13-}$	1.206	$K[Se_2W_{12}O_{46}]^{11-}$	1.178
$K_3[As_2W_{12}O_{48}]^{11-}$	1.214	$K_3[P_2W_{12}O_{48}]^{11-}$	1.191	$K_3[Se_2W_{12}O_{46}]^{9-}$	1.164
$K_5[As_2W_{12}O_{48}]^{9-}$	1.201	$K_5[P_2W_{12}O_{48}]^{9-}$	1.178	$K_5[Se_2W_{12}O_{46}]^{7-}$	1.151
$K_9[As_2W_{12}O_{48}]^{5-}$	1.172	$K_9[P_2W_{12}O_{48}]^{5-}$	1.150	$K_9[Se_2W_{12}O_{46}]^{3-}$	1.123
$K_{12}[As_2W_{12}O_{48}]^{2-}$	1.133	$K_{12}[P_2W_{12}O_{48}]^{2-}$	1.129	$K_{10}[Se_2W_{12}O_{46}]^{2-}$ **Front**	1.146
				$K_{10}[Se_2W_{12}O_{46}]^{2-}$ **Side**	1.143
				$K_{10}[Se_2W_{12}O_{46}]^{2-}$ **Top**	1.149

Table A-2.31. Electronic standard deviation for $[H_2As_2W_{12}O_{48}]^{12-}$, $[H_2P_2W_{12}O_{48}]^{12-}$, and $[H_2Se_2W_{12}O_{46}]^{10-}$ hexalacunary structures. A smaller deviation value indicates more delocalisation and a smaller degree of polarisation throughout the framework

Formula	Total Standard Deviation (electrons)	Formula	Total Standard Deviation (electrons)	Formula	Total Standard Deviation (electrons)
$[As_2W_{12}O_{48}]^{14-}$	1.223	$[P_2W_{12}O_{48}]^{14-}$	1.213	$[Se_2W_{12}O_{46}]^{12-}$	1.197
$[H_2As_2W_{12}O_{48}]^{12-}$ (O7,16)	1.189	$[H_2P_2W_{12}O_{48}]^{12-}$ (O7,16)	1.180	$[H_2Se_2W_{12}O_{46}]^{10-}$ (O7,16)	1.158
$[H_2As_2W_{12}O_{48}]^{12-}$ (O7,49)	1.186	$[H_2P_2W_{12}O_{48}]^{12-}$ (O7,49)	1.180	$[H_2Se_2W_{12}O_{46}]^{10-}$ (O7,49)	1.158
$[H_2As_2W_{12}O_{48}]^{12-}$ (O8,37)	1.209	$[H_2P_2W_{12}O_{48}]^{12-}$ (O8,37)	1.183	$[H_2Se_2W_{12}O_{46}]^{10-}$ (O8,37)	1.162
$[H_2As_2W_{12}O_{48}]^{12-}$ (O8,60)	1.206	$[H_2P_2W_{12}O_{48}]^{12-}$ (O8,60)	1.180	$[H_2Se_2W_{12}O_{46}]^{10-}$ (O8,60)	1.158
$[H_2As_2W_{12}O_{48}]^{12-}$ (O9,20)	1.208	$[H_2P_2W_{12}O_{48}]^{12-}$ (O9,20)	1.182	$[H_2Se_2W_{12}O_{46}]^{10-}$ (O9,20)	1.161
$[H_2As_2W_{12}O_{48}]^{12-}$ (O12,16)	1.184	$[H_2P_2W_{12}O_{48}]^{12-}$ (O12,16)	1.179	$[H_2Se_2W_{12}O_{46}]^{10-}$ (O12,16)	1.155
$[H_2As_2W_{12}O_{48}]^{12-}$ (O12,49)	1.205	$[H_2P_2W_{12}O_{48}]^{12-}$ (O12,49)	1.179	$[H_2Se_2W_{12}O_{46}]^{10-}$ (O12,49)	1.155
$[H_2As_2W_{12}O_{48}]^{12-}$ (O16,49)	1.208	$[H_2P_2W_{12}O_{48}]^{12-}$ (O16,49)	1.182	$[H_2Se_2W_{12}O_{46}]^{10-}$ (O16,49)	1.160

Table A-2.32. Calculated Standard Deviation values for electron distribution around $K_n[H_mP_2W_{12}O_{48}]^{n+m-12}$, $K_n[H_mAs_2W_{12}O_{48}]^{n+m-12}$, and $K_n[H_mSe_2W_{12}O_{46}]^{n+m-10}$ structures

Formula	Total Standard Deviation (electrons)	Formula	Total Standard Deviation (electrons)	Formula	Total Standard Deviation (electrons)
$[As_2W_{12}O_{48}]^{14-}$	1.223	$[P_2W_{12}O_{48}]^{14-}$	1.213	$[Se_2W_{12}O_{46}]^{12-}$	1.197
$K_3[H_2As_2W_{12}O_{48}]^{9-}$ **(O7,49)**	1.182	$K_3[H_2P_2W_{12}O_{48}]^{9-}$ **(O7,49)**	1.176	$K_3[H_2Se_2W_{12}O_{46}]^{7-}$ **(O7,49)**	1.154
$K_3s_2W_{12}O_{48}]^{9-}$ **(O12,16)**	1.183	$K_3[H_2P_2W_{12}O_{48}]^{9-}$ **(O12,16)**	1.176	$K_3[H_2Se_2W_{12}O_{46}]^{7-}$ **(O12,16)**	1.153
$K_3[H_2As_2W_{12}O_{48}]^{9-}$ **(O12,49)**	1.182	$K_3[H_2P_2W_{12}O_{48}]^{9-}$ **(O12,49)**	1.176	$K_3[H_2Se_2W_{12}O_{46}]^{7-}$ **(O12,49)**	1.152
$K_3[H_2As_2W_{12}O_{48}]^{9-}$ **(O16,49)**	1.186	$K_3[H_2P_2W_{12}O_{48}]^{9-}$ **(O16,49)**	1.179	$K_3[H_2Se_2W_{12}O_{46}]^{7-}$ **(O16,49)**	1.157
$K_{12}[H_2As_2W_{12}O_{48}]$ **(O7,49)**	1.162	$K_{12}[H_2P_2W_{12}O_{48}]$ **(O7,49)**	1.156	$K_{10}[H_2Se_2W_{12}O_{46}]$ **(O7,49)**	1.142
$K_{12}[H_2As_2W_{12}O_{48}]$ **(O12,16)**	1.166	$K_{12}[H_2P_2W_{12}O_{48}]$ **(O12,16)**	1.160	$K_{10}[H_2Se_2W_{12}O_{46}]$ **(O12,16)**	1.141
$K_{12}[H_2As_2W_{12}O_{48}]$ **(O12,49)**	1.166	$K_{12}[H_2P_2W_{12}O_{48}]$ **(O12,49)**	1.160	$K_{10}[H_2Se_2W_{12}O_{46}]$ **(O12,49)**	1.143
$K_{12}[H_2As_2W_{12}O_{48}]$ **(O16,49)**	1.166	$K_{12}[H_2P_2W_{12}O_{48}]$ **(O16,49)**	1.161	$K_{10}[H_2Se_2W_{12}O_{46}]$ **(O16,49)**	1.142

Appendix-2.7: Spectroscopy

Table A-2.33. Empirical $K_{12}[H_2P_2W_{12}O_{48}]$ and theoretical $[P_2W_{12}O_{48}]^{14-}$ NMR spectra. The initial Hexalacunary geometry was optimized using **B3LYP/TZP/SFC/COSMO**, upon which a **SP/PBE/TZP/SFC/COSMO/Spin-Orbit Relativity** NMR calculation was run.

Data Source	^{31}P Chemical Shift (ppm)	Reference
Empirical (literature)	-9.69	Sugiarto, S. *et al.*[328]
Empirical (carried out by LVN group)	-10.12	
Computational ($[P_2W_{12}O_{48}]^{14-}$)	-3.58	

Table A-2.34. Empirical $K_{12}[H_2P_2W_{12}O_{48}]$ and theoretical $K_n[P_2W_{12}O_{48}]^{(n-14)}$ ^{31}P NMR spectra. Detailed is number of cations included in the theoretical model and whether the distance between cation and heteroatom is constrained or not. The initial Hexalacunary geometry was optimized using **B3LYP/TZP/SFC/COSMO**, upon which a **SP/PBE/TZP/SFC/COSMO/Spin-Orbit Relativity** NMR calculation was run.

Data Source	^{31}P Chemical Shift (ppm)	Reference
Empirical (literature)	-9.69	Sugiarto, S. *et al.*[328]
Empirical (carried out by LVN group)	-10.12	
Computational (No K cations)	-3.58	
Computational (1K, No Constraint)	1.02, 1.89	
Computational (1K, 9.0Å)	3.29, 3.41	
Computational (3K, No Constraint)	-3.04, -2.99	
Computational (3K, 9.0Å)	3.28, 3.40	
Computational (5K, No Constraint)	0.75, 1.54	
Computational (5K, 9.0Å)	3.28, 3.40	
Computational (9K, No Constraint)	0.85, 1.30	
Computational (9K, 9.0Å)	3.38	
Computational (12K, No Constraint)	0.79, 1.89	
Computational (12K, 9.0Å)	3.24, 3.36	

Table A-2.35. Empirical $K_{12}[H_2P_2W_{12}O_{48}]$ and theoretical $[H_2P_2W_{12}O_{48}]^{12-}$ ^{31}P NMR spectra. The initial Hexalacunary geometry was optimized using **B3LYP/TZP/SFC/COSMO**, upon which a **SP/PBE/TZP/SFC/COSMO/Spin-Orbit Relativity** NMR calculation was run.

Data Source	^{1}H Chemical Shift (ppm)	^{31}P Chemical Shift (ppm)	Reference
Empirical (literature)		-9.69	Sugiarto, S. *et al.*[328]
Empirical (carried out by LVN group)		-10.12	
Computational (No Protons)		-3.58	
Computational (O7,16)	4.36, 10.13	90.87, 94.99	
Computational (O7,49)	3.19, 7.04	-1.74, 0.15	
Computational (O8,37)	4.01, 5.24	-5.44, 1.23	
Computational (O8,60)	3.87, 5.48	1.88, 2.85	
Computational (O9,20)	4.76, 5.22	-5.37, 3.86	
Computational (O12,16)	7.07, 8.04	-0.57, 0.77	
Computational (O12,49)	9.44, 9.47	-0.67, -0.05	
Computational (O16,49)	1.87, 8.69	0.06, 0.07	

Table A-2.36. Empirical $K_{12}[H_2P_2W_{12}O_{48}]$ and theoretical $K_n[H_2P_2W_{12}O_{48}]^{(n-12)}$ ^{31}P NMR spectra. The initial Hexalacunary geometry was optimized using **B3LYP/TZP/SFC/COSMO**, upon which a **SP/PBE/TZP/SFC/COSMO/Spin-Orbit Relativity** NMR calculation was run.

Data Source	^{1}H Chemical Shift (ppm)	^{31}P Chemical Shift (ppm)	Reference
Empirical (literature)		-9.69	Sugiarto, S. *et al.*[328]
Empirical (carried out by LVN group)		-10.12	
Computational (No K cations)		-3.58	
Computational (**O7,49**, $K_3[H_2P_2W_{12}O_{48}]^{9-}$)	4.97, 7.42	-1.20, 0.23	
Computational (**O12,16**, $K_3[H_2P_2W_{12}O_{48}]^{9-}$)	9.65, 11.32	-0.33, -0.00	
Computational (**O12,49**, $K_3[H_2P_2W_{12}O_{48}]^{9-}$)	9.37, 9.44	-0.33, -0.26	
Computational (**O16,49**, $K_3[H_2P_2W_{12}O_{48}]^{9-}$)	1.76, 8.74	-0.37, 0.39	
Computational (**O7,49**, $K_{12}[H_2P_2W_{12}O_{48}]$)	4.83, 7.63	6.82, 6.95	
Computational (**O12,16**, $K_{12}[H_2P_2W_{12}O_{48}]$)	9.63, 11.46	6.48, 7.51	
Computational (**O12,49**, $K_{12}[H_2P_2W_{12}O_{48}]$)	8.73, 9.29	6.36, 7.46	
Computational (**O16,49**, $K_{12}[H_2P_2W_{12}O_{48}]$)	5.40, 8.64	0.55, 1.22	

We ultimately found that no molecular structure was able to replicate the ^{31}P NMR data to a sufficiently good degree of accuracy, regardless of the number of countercations or protons included.

Appendix-2.8: Summation

Given the immense body of data presented in this Appendix section, we thought it prudent to summarise our results and explain which model(s) we believe to present the model most in line with the empirical structure.

Formula	Core Hours (Minutes)	Formula	Core Hours (Minutes)	Formula	Core Hours (Minutes)
$[As_2W_{12}O_{48}]^{14-}$	2,120	$[P_2W_{12}O_{48}]^{14-}$	210	$[Se_2W_{12}O_{46}]^{12-}$	1,250
$K[As_2W_{12}O_{48}]^{13-}$	1,380	$K[P_2W_{12}O_{48}]^{13-}$	1,040	$K[Se_2W_{12}O_{46}]^{11-}$	1,320
$[H_2As_2W_{12}O_{48}]^{12-}$ **(O7,49)**	2,070	$[H_2P_2W_{12}O_{48}]^{12-}$ **(O7,49)**	5,140	$[H_2Se_2W_{12}O_{46}]^{10-}$ **(O7,49)**	3,460
$[H_2As_2W_{12}O_{48}]^{12-}$ **(O12,16)**	740	$[H_2P_2W_{12}O_{48}]^{12-}$ **(O12,16)**	2,830	$[H_2Se_2W_{12}O_{46}]^{10-}$ **(O12,16)**	1,400
$[H_2As_2W_{12}O_{48}]^{12-}$ **(O12,49)**	3,840	$[H_2P_2W_{12}O_{48}]^{12-}$ **(O12,49)**	3,080	$[H_2Se_2W_{12}O_{46}]^{10-}$ **(O12,49)**	1,450
$[H_2As_2W_{12}O_{48}]^{12-}$ **(O16,49)**	8,750	$[H_2P_2W_{12}O_{48}]^{12-}$ **(O16,49)**	2,270	$[H_2Se_2W_{12}O_{46}]^{10-}$ **(O16,49)**	1,420
$K_3[As_2W_{12}O_{48}]^{11-}$	13,120	$K_3[P_2W_{12}O_{48}]^{11-}$	5,970	$K_3[Se_2W_{12}O_{46}]^{9-}$	4,430
$K_3[H_2As_2W_{12}O_{48}]^{9-}$ **(O7,49)**	15,130	$K_3[H_2P_2W_{12}O_{48}]^{9-}$ **(O7,49)**	3,950	$K_3[H_2Se_2W_{12}O_{46}]^{7-}$ **(O7,49)**	1,830
$K_3[H_2As_2W_{12}O_{48}]^{9-}$ **(O12,16)**	5,050	$K_3[H_2P_2W_{12}O_{48}]^{9-}$ **(O12,16)**	10,630	$K_3[H_2Se_2W_{12}O_{46}]^{7-}$ **(O12,16)**	4,340
$K_3[H_2As_2W_{12}O_{48}]^{9-}$ **(O12,49)**	15,050	$K_3[H_2P_2W_{12}O_{48}]^{9-}$ **(O12,49)**	7,740	$K_3[H_2Se_2W_{12}O_{46}]^{7-}$ **(O12,49)**	28,140
$K_3[H_2As_2W_{12}O_{48}]^{9-}$ **(O16,49)**	6,830	$K_3[H_2P_2W_{12}O_{48}]^{9-}$ **(O16,49)**	8,090	$K_3[H_2Se_2W_{12}O_{46}]^{7-}$ **(O16,49)**	19,600
$K_5[As_2W_{12}O_{48}]^{9-}$	9,500	$K_5[P_2W_{12}O_{48}]^{9-}$	6,470	$K_5[Se_2W_{12}O_{46}]^{7-}$	11,220
$K_9[As_2W_{12}O_{48}]^{5-}$	36,500	$K_9[P_2W_{12}O_{48}]^{5-}$	12,830	$K_9[Se_2W_{12}O_{46}]^{3-}$	21,400
$K_{12}[As_2W_{12}O_{48}]^{2-}$	38,930	$K_{12}[P_2W_{12}O_{48}]^{2-}$	13,450	$K_{10}[Se_2W_{12}O_{46}]^{2-}$ **(Front)**	22,680
$K_{12}[H_2As_2W_{12}O_{48}]$ **(O7,49)**	14,760	$K_{12}[H_2P_2W_{12}O_{48}]$ **(O7,49)**	34,320	$K_{10}[H_2Se_2W_{12}O_{46}]$ **(O7,49) (Front)**	47,680
$K_{12}[H_2As_2W_{12}O_{48}]$ **(O12,16)**	13,040	$K_{12}[H_2P_2W_{12}O_{48}]$ **(O12,16)**	9,960	$K_{10}[H_2Se_2W_{12}O_{46}]$ **(O12,16) (Front)**	32,800
$K_{12}[H_2As_2W_{12}O_{48}]$ **(O12,49)**	32,560	$K_{12}[H_2P_2W_{12}O_{48}]$ **(O12,49)**	5,040	$K_{10}[H_2Se_2W_{12}O_{46}]$ **(O12,49) (Front)**	35,700
$K_{12}[H_2As_2W_{12}O_{48}]$ **(O16,49)**	30,560	$K_{12}[H_2P_2W_{12}O_{48}]$ **(O16,49)**	27,940	$K_{10}[H_2Se_2W_{12}O_{46}]$ **(O16,49) (Front)**	52,040

Table A-2.37. Core hours required to converge $K_n[H_mAs_2W_{12}O_{48}]^{14-m-n}$, $K_n[H_mP_2W_{12}O_{48}]^{14-m-n}$, and $K_n[H_mSe_2W_{12}O_{46}]^{12-m-n}$ hexalacunary structures. The number of core hours is defined by the number of cores utilised multiplied by the total job time in minutes.

Table A-2.38. HOMO and LUMO orbital energy values for $K_n[H_mP_2W_{12}O_{48}]^{m+n-14}$, as well as the energy gap between them, commonly referred to as the HOMO-LUMO gap.

Data Source	HOMO (eV)	LUMO (eV)	HOMO-LUMO Gap (eV)
$[P_2W_{12}O_{48}]^{14-}$	-4.416	-1.601	2.815
$K[P_2W_{12}O_{48}]^{13-}$	-4.445	-1.632	2.813
$[H_2P_2W_{12}O_{48}]^{12-}$ (**07,49**)	-5.166	-1.880	3.286
$[H_2P_2W_{12}O_{48}]^{12-}$ (**012,16**)	-5.117	-1.841	3.276
$[H_2P_2W_{12}O_{48}]^{12-}$ (**012,49**)	-5.165	-1.865	3.300
$[H_2P_2W_{12}O_{48}]^{12-}$ (**016,49**)	-5.194	-1.795	3.399
$K_3[P_2W_{12}O_{48}]^{11-}$	-4.461	-1.646	2.815
$K_3[H_2P_2W_{12}O_{48}]^{9-}$ (**07,49**)	-5.256	-1.953	3.303
$K_3[H_2P_2W_{12}O_{48}]^{9-}$ (**012,16**)	-5.156	-1.876	3.280
$K_3[H_2P_2W_{12}O_{48}]^{9-}$ (**012,49**)	-5.214	-1.909	3.305
$K_3[H_2P_2W_{12}O_{48}]^{9-}$ (**016,49**)	-5.238	-1.833	3.405
$K_5[P_2W_{12}O_{48}]^{9-}$	-4.494	-1.682	2.812
$K_9[P_2W_{12}O_{48}]^{5-}$	-4.551	-1.744	2.807
$K_{12}[P_2W_{12}O_{48}]^{2-}$	-4.531	-1.765	2.766
$K_{12}[H_2P_2W_{12}O_{48}]$ (**07,49**)	-5.427	-2.137	3.290
$K_{12}[H_2P_2W_{12}O_{48}]$ (**012,16**)	-5.260	-1.999	3.261
$K_{12}[H_2P_2W_{12}O_{48}]$ (**012,49**)	-5.282	-2.006	3.276
$K_{12}[H_2P_2W_{12}O_{48}]$ (**016,49**)	-5.328	-1.966	3.362

Table A-2.39. HOMO and LUMO orbital energy values for $K_n[H_mAs_2W_{12}O_{48}]^{m+n-14}$, as well as the energy gap between them, commonly referred to as the HOMO-LUMO gap.

Data Source	HOMO (eV)	LUMO (eV)	HOMO-LUMO Gap (eV)
$[As_2W_{12}O_{48}]^{14-}$	-4.371	-1.569	2.802
$K[As_2W_{12}O_{48}]^{13-}$	-4.474	-1.662	2.812
$[H_2As_2W_{12}O_{48}]^{12-}$ (**07,49**)	-5.186	-1.895	3.291
$[H_2As_2W_{12}O_{48}]^{12-}$ (**012,16**)	-5.141	-1.857	3.284
$[H_2As_2W_{12}O_{48}]^{12-}$ (**012,49**)	-5.191	-1.878	3.313
$[H_2As_2W_{12}O_{48}]^{12-}$ (**016,49**)	-5.211	-1.829	3.382
$K_3[As_2W_{12}O_{48}]^{11-}$	-4.480	-1.663	2.817
$K_3[H_2As_2W_{12}O_{48}]^{9-}$ (**07,49**)	-5.272	-1.949	3.323
$K_3[H_2As_2W_{12}O_{48}]^{9-}$ (**012,16**)	-5.188	-1.906	3.282
$K_3[H_2As_2W_{12}O_{48}]^{9-}$ (**012,49**)	-5.225	-1.908	3.317
$K_3[H_2As_2W_{12}O_{48}]^{9-}$ (**016,49**)	-5.259	-1.873	3.386
$K_5[As_2W_{12}O_{48}]^{9-}$	-4.517	-1.702	2.815
$K_9[As_2W_{12}O_{48}]^{5-}$	-4.609	-1.820	2.789
$K_{12}[As_2W_{12}O_{48}]^{2-}$	-4.590	-1.836	2.754
$K_{12}[H_2As_2W_{12}O_{48}]$ (**07,49**)	-5.383	-2.153	3.230
$K_{12}[H_2As_2W_{12}O_{48}]$ (**012,16**)	-5.285	-2.008	3.277
$K_{12}[H_2As_2W_{12}O_{48}]$ (**012,49**)	-5.338	-2.043	3.295
$K_{12}[H_2As_2W_{12}O_{48}]$ (**016,49**)	-5.427	-1.990	3.437

Table A-2.40. HOMO and LUMO orbital energy values for $K_n[H_mSe_2W_{12}O_{46}]^{m+n-12}$, as well as the energy gap between them, commonly referred to as the HOMO-LUMO gap.

Data Source	HOMO (eV)	LUMO (eV)	HOMO-LUMO Gap (eV)
$[Se_2W_{12}O_{46}]^{12-}$	-4.531	-1.957	2.574
$K[Se_2W_{12}O_{46}]^{11-}$	-4.848	-1.953	2.895
$[H_2Se_2W_{12}O_{46}]^{10-}$ (**O7,49**)	-5.613	-2.189	3.424
$[H_2Se_2W_{12}O_{46}]^{10-}$ (**O12,16**)	-5.654	-2.202	3.452
$[H_2Se_2W_{12}O_{46}]^{10-}$ (**O12,49**)	-5.697	-2.321	3.376
$[H_2Se_2W_{12}O_{46}]^{10-}$ (**O16,49**)	-5.703	-2.100	3.606
$K_3[Se_2W_{12}O_{46}]^{9-}$	-4.875	-1.971	2.904
$K_3[H_2Se_2W_{12}O_{46}]^{7-}$ (**O7,49**)	-5.745	-2.293	3.452
$K_3[H_2Se_2W_{12}O_{46}]^{7-}$ (**O12,16**)	-5.706	-2.221	3.485
$K_3[H_2Se_2W_{12}O_{46}]^{7-}$ (**O12,49**)	-5.617	-2.369	3.248
$K_3[H_2Se_2W_{12}O_{46}]^{7-}$ (**O16,49**)	-5.674	-2.166	3.508
$K_5[Se_2W_{12}O_{46}]^{7-}$	-4.895	-1.993	2.902
$K_9[Se_2W_{12}O_{46}]^{3-}$	-4.972	-2.052	2.920
$K_{10}[Se_2W_{12}O_{46}]^{2-}$ (**Front**)	-4.965	-2.076	2.889
$K_{10}[Se_2W_{12}O_{46}]^{2-}$ (**Side**)	-4.960	-2.074	2.886
$K_{10}[Se_2W_{12}O_{46}]^{2-}$ (**Top**)	-4.981	-2.101	2.880
$K_{10}[H_2Se_2W_{12}O_{46}]$ (**O7,49**)	-5.812	-2.501	3.311
$K_{10}[H_2Se_2W_{12}O_{46}]$ (**O12,16**)	-5.575	-2.315	3.260
$K_{10}[H_2Se_2W_{12}O_{46}]$ (**O12,49**)	-5.628	-2.559	3.069
$K_{10}[H_2Se_2W_{12}O_{46}]$ (**O16,49**)	-5.804	-2.305	3.499

Appendix-3: Chapter 7

Appendix-3.1: Literature Review

Table A-3.1. Collection of literature papers we examined as part of our investigation.

Reference	Year Published	Cited by	Computational Details	Reason for Inaccuracy
Maestre, J.M. *et al* [237]	2001	208	**PBE/TZP**	No empirical comparison
López, X. *et al* [238]	2001	172	**PBE/TZP**	No empirical comparison
López, X. *et al* [239]	2002	312	**PBE/TZP/COSMO**	Relative H-L gap between Keggin isomers empirically verified, but not the size of the gaps themselves via UV-Vis. Same for WD
Zhan, C.G. *et al* [380]	2003	1086		No problem, just no POMs referenced here. Rabbit hole paper?
Lo, X. *et al* [334]	2003	38	**PBE/TZP**	Relative H-L gap between Keggin isomers empirically verified, but not the size of the gaps themselves via UV-Vis. Same for WD
Poblet, J.M. *et al* [335]	2003	252		Refs previous works [238,239] Review
López, X. *et al* [62]	2004	65	**BP86/TZP**	Relative H-L gap between Keggin isomers empirically verified, but not the size of the gaps themselves via UV-Vis. Same for WD
López, X. *et al* [95]	2004	149	**BP86/TZVP**	Relative H-L gap between WD isomers examined, and gap magnitude reported. Work justifies empirical observations but no UV-Vis data to verify
Goubin, F. *et al* [381]	2004	17	SAMOA package	No empirical comparison
Chiang, M.-H. *et al* [382]	2004	21		
López, X. *et al* [337]	2006	94	**BP86/TZP/COSMO**	No empirical comparison
Zhang, G. *et al* [383]	2007	673		Refs previous works [380] States GGA is more accurate than Hybrids in specific cases for small, organic molecules
Fernández, J.A. *et al* [69]	2007	147	**BP86/TZP/COSMO**	Refs previous works [337]

				Relative H-L gaps for different countercations examined, and gap magnitude reported. Work tries to justify empirical observations but no UV-Vis data to verify
Yan, L. *et al* [21]	2008	102	**BP86/TZP/COSMO**	Refs previous works [337] Several different transitions calculated using TD-DFT but no empirical comparison
Mal, S. *et al* [336]	2009	59	**BP86/TZP/COSMO**	Refs previous works [237,238,334, 335,62] No empirical comparison
Sartorel, A. *et al* [236]	2009	188	**BP86/TZP/COSMO**	No real issue here, doesn't try to determine gap size empirically or theoretically
López, X. *et al* [20]	2010	6		No real issue here, not relevant to our work
López, X. *et al* [384]	2011	69		Refs previous works [62] Summarizes recent DFT work on frontier orbitals, no mention of how it relates to UV-Vis spectra, just relative observations. No hard, absolute energy values
Zhang, F. *et al* [64]	2011	33	**KT2/TZP/COSMO**	Refs previous works [382,337,69] No empirical comparison
Bo, C. *et al* [385]	2011	19		Refs previous works [237] Reports previous H-L gap which is not empirically compared
Vilà-Nadal, L. *et al* [65]	2012	24	**BP86/TZP/COSMO**	No empirical comparison, arguably beyond scope of paper though
López, X. *et al* [231]	2012	368		Review, no empirical comparison
Miró, P. *et al* [283]	2012	33	**BP86/TZVP/COSMO**	No issue, visualizes frontier orbitals only
Vilà-Nadal, L. *et al* [180]	2013	26	**BP86/TZP/COSMO**	No empirical comparison
Vilà-Nadal, L. *et al* [284]	2013	62	**PBE/TZP/COSMO**	No empirical comparison for H-L gap
Cameron, J.M. *et al* [78]	2014	41	**B3LYP/TZVP/COSMO (TURBOMOLE)**	No empirical comparison
Busche, C. *et al* [176]	2014	294	**B3LYP/TZVP/COSMO (TURBOMOLE)**	Attempt to empirically benchmark using CV
Chen, W.-C. *et al* [386]	2014	38	**BP86/TZP/COSMO**	No empirical comparison, just stating the gap is within the bounds of reason
Minato, T. *et al* [47]	2014	43	**B3LYP/63++G**/CPCM (GAUSS)**	No issue, visualizes frontier orbitals only
Cameron, J.M. *et al* [285]	2017	40	**B3LYP/6-31++G**/CDCM (GAUSS)**	Refs **10.1039/c2cs35168d** No empirical comparison, relies on previous studies to justify validity of results
Li, C. *et al* [387]	2018	54	**B3LYP/6-31++G**/CDCM (GAUSS)**	Empirical work done but no absolute energy comparison to theoretical work
Kibler, A.J. *et al* [41]	2018	37		Review, no comment of accuracy of previous comp work
Xu, J. *et al* [152]	2018	59	**PBEh-3c/COSMO (TURBOMOLE)**	No issue, geometry optimization only
Ueda, T. *et al* [181]	2018	120		Review, doesn't realise inaccuracy of previous works
Chen, X. *et al* [57]	2019	38	**PBE/**	Empirical work done but no absolute energy comparison to theoretical work
Solé-Daura, A. *et al* [235]	2019	18	**B3LYP/TZ2P/COSMO**	No empirical comparison
McAllister, J. *et al* [233]	2019	99	**PBE-D3/TZ2P/COSMO**	No empirical comparison

Babaei, S. *et al* [388]	2020	8	**B3LYP/6-31++G** (GAUSS)**	No empirical comparison
Gao, Y. *et al* [389]	2020	11	**B3LYP/6-31G(d)/CPCM (GAUSS)**	No issues, good paper
Kaledin, A.L. *et al* [331]	2020	5	**M06L/6-31++G(d,p)/PCM (GAUSS)**	No empirical comparison
Steffler, F. *et al* [60]	2020	9	**CAM-B3LYP/LanL2DZ (GAUSS)**	Good empirical and theoretical comparison
Lapham, P. *et al* [318]	2021	24	**BP86/DZP (QuantumATK-2019.12)**	No empirical comparison, uses **10.1021/jp061633o** as a justification of theory
Chen, J.-J. *et al* [323]	2022	13	**BP86/TZP/COSMO**	Empirical comparison made, but computed H-L gap doesn't match empirical when converted to wavelength
Amin, S.S. *et al* [321]	2022	1	**BP86/CRENBL/PCM (Q-Chem)**	Empirical comparison made, good agreement with comp data
Malcolm, D. *et al* [329]	2023	0	**PBE/TZP/COSMO**	No empirical comparison, uses previous works as a justification of theory [64,180,284,78]
Kibler, A.J. *et al* [390]	2023	1	**BP86/CRENBL/PCM (Q-Chem)**	Relative gap in good agreement with empirical data, but not absolute energies
Yang, M. *et al* [162]	2023	5	**B3LYP/SVP/SMD (GAUSS)**	No empirical comparison

Table A-3.2: Evaluation of literature from **Table SI-1**

Reason for Inaccuracy	**Number of Publications**
No empirical comparison	18
Uses a previous publication as justification for operating at a specific level of theory, despite that work not using empirical comparison	3
Empirical comparison made, but computed H-L gap doesn't match empirical when converted to wavelength	3
Relative H-L gap in good agreement with empirical data, but not absolute energies	5
Empirical comparison made, good agreement with comp data	2

Appendix-3.2: Wells-Dawson UV-Vis Spectra

Table A-3.3: DFT UV-Vis results for $[P_2W_{18}O_{62}]^{6-}$. Calculations with the reference 'LVN Group' were carried out by us during this investigation.

Functional/ Basis Set	Transition Wavelength (nm)	Transition Energy (eV)	Reference
BP86/TZP	569	2.18	Chen, J.-J. *et al.*[323]
PBE/TZVP	551	2.25	López, X. *et al.*[334]
PBE/TZP	544	2.28	López, X. *et al.*[337]
PBE/TZP	551	2.25	Vilà-Nadal, L. *et al.*[180]
BP86/TZP	537	2.31	LVN Group
PBE/TZP	534	2.32	LVN Group

Table A-3.4: Empirical UV-Vis results for $[P_2W_{18}O_{62}]^{6-}$. Data samples with the reference 'LVN Group' were carried out by us during this investigation.

Transition Wavelength (nm)	Transition Energy (eV)	Reference
~300	4.13	Chen, J.-J. *et al.*[323]
~267	4.64	Dhifallah, F. *et al.*[340]
~245, 300	5.06, 4.13	Hiskia, A. *et al.*[339]
250, 301.25	4.96, 4.12	Nomiya, K. *et al.*[338]
~310	4.00	Kibler, A.J. *et al.*[151]
~250, ~310	4.96, 4.00	LVN Group

Past computational works have utilised GGA-level functionals to determine the HOMO-LUMO gap but, after reviewing the available UV-Vis data for $K_6[P_2W_{18}O_{62}]$, we believe this level of theory to underestimate the true empirical value. By comparing **Table A-3.3** and **A-3.4.**, we can see that the calculated wavelength of emission is more than 200nm off the reported data; this equates to a difference in energy of 2eV. Additionally, the calculated wavelength would indicate the WD is coloured blue, when it is in fact white.

Table A-3.5: Comparison between empirical and computational results for lowest energy absorption bands. This band is assumed to be the HOMO-LUMO gap when calculated from TI-DFT. **SP/PBE0/TZP/SFC/COSMO**

POM Species	Empirical Absorption Wavelength (nm)	Empirical Absorption Energy (eV)	Computational Absorption Energy (eV)	Computational Absorption Wavelength (nm)
$[P_2W_{18}O_{62}]^{6-}$	310	4.00	4.09	303

Appendix-3.3: Keggin UV-Vis Spectra

Given that WD spectra often gives off a broad peak, we decided to conduct a benchmark using Keggin compounds as these POMs are associated with a sharper, and therefore easier to identify, peak. Using available empirical data, we carried out 2 sets of UV-Vis calculations: one at the GGA level used in previous works and the other at the hybrid level we believe to be more accurate.

Table A-3.6: Comparison between empirical and computational UV-Vis data samples for $C_n[\alpha\text{-}XW_{12}O_{40}]^{m-}$, where C is the countercation atom or molecule and X is the encapsulated heteroatom. Data with the reference source 'LVN Group' refers to work carried out by Dr. Jake Thompson within the group, currently being submitted for publication. Where cation distance is reported as 'varied', there are no constraints on the cation distance from X. **SP/BP86/TZP/SFC/COSMO**

Cluster	Cation Distance (Angstrom)	Emp. λ (nm)	Emp. Gap (eV)	Calc. λ (nm)	Calc. Gap (eV)	Diff. λ (nm)	Diff. Gap (eV)	Reference
$[PW_{12}O_{40}]^{3-}$	N/A	265	4.68	453	2.74	+188	-1.94	Hiskia, A. *et al.*[339]
$Li_3[PW_{12}O_{40}]$	4.20	255	4.86	512	2.42	+257	-2.44	LVN Group
$Na_3[PW_{12}O_{40}]$	4.82	255	4.86	500	2.48	+245	-2.38	LVN Group
$TBA_3[PW_{12}O_{40}]$	Varied	265	4.68	470	2.64	+205	-2.04	LVN Group
$TBA_3[PW_{12}O_{40}]$	Varied	265	4.68	470	2.64	+205	-2.04	Nomiya, K. *et al.*[338]
$TBA_4[SiW_{12}O_{40}]$	Varied	264	4.69	463	2.68	+199	-2.01	Nomiya, K. *et al.*[338]
$TBA_4[GeW_{12}O_{40}]$	Varied	266	4.67	470	2.64	+204	-2.03	Nomiya, K. *et al.*[338]

Table A-3.7: Comparison between empirical and computational UV-Vis data samples for $C_n[\alpha\text{-}XW_{12}O_{40}]^{m-}$, where C is the countercation atom or molecule and X is the encapsulated heteroatom. Where cation distance is reported as 'varied', there are no constraints on the cation distance from X. **SP/PBE0/TZP/SFC/COSMO**

Cluster	Cation Distance (Angstrom)	Emp. λ (nm)	Emp. Gap (eV)	Calc. λ (nm)	Calc. Gap (eV)	Diff. λ (nm)	Diff. Gap (eV)	DOI
$[PW_{12}O_{40}]^{3-}$	N/A	265	4.68	260	4.77	-5	+0.09	Hiskia, A. *et al.*[339]
$Li_3[PW_{12}O_{40}]$	4.15	255	4.86	268	4.62	+13	-0.24	LVN Group
$Na_3[PW_{12}O_{40}]$	4.82	255	4.86	265	4.67	+10	-0.19	LVN Group
$TBA_3[PW_{12}O_{40}]$	Varied	265	4.68	256	4.85	-9	+0.17	LVN Group
$TBA_3[PW_{12}O_{40}]$	Varied	265	4.68	256	4.85	-9	+0.17	Nomiya, K. *et al.*[338]
$TBA_4[SiW_{12}O_{40}]$	Varied	264	4.69	255	4.87	-9	+0.18	Nomiya, K. *et al.*[338]
$TBA_4[GeW_{12}O_{40}]$	Varied	266	4.67	255	4.87	-11	+0.20	Nomiya, K. *et al.*[338]

Based on work previously undertaken by this group,[329] the hybrid functional PBE0 operates at a more appropriate level of theory; the error in energy between a PBE0 optimization and the common 300nm emission is only 0.2eV. From this point onwards, we will therefore be using PBE to optimize our geometries and PBE0 for determining likely UV-Vis emission spectra for both the WD and Hexalacunary POMs.

Appendix-3.4: Countercation Calculations

Table A-3.8: Reported frontier orbital eigenvalues for $K_n[P_2W_{18}O_{62}]^{n-6}$, where the HOMO-LUMO gap value for each POM species is compared against the value supplied by Chen, J.-J. *et al* [323]. **OPT/PBE0/TZP/COSMO/Small Frozen Cores**

Molecular Formula	P-K Distance (Å)	HOMO (eV)	LUMO (eV)	HOMO-LUMO (eV)	HOMO-LUMO Difference
$[P_2W_{18}O_{62}]^{6-}$	N/A	-8.210	-3.875	4.34	0.21
$K_6[P_2W_{18}O_{62}]$	OPT	-8.736	-4.394	4.34	0.21
$K_6[P_2W_{18}O_{62}]$	7.0	-8.498	-4.183	4.32	0.19
$K_6[P_2W_{18}O_{62}]$	7.5	-8.435	-4.113	4.32	0.19
$K_6[P_2W_{18}O_{62}]$	8.0	-8.375	-4.056	4.32	0.19
$K_6[P_2W_{18}O_{62}]$	8.5	-8.326	-3.999	4.33	0.20
$K_6[P_2W_{18}O_{62}]$	9.0	-8.296	-3.978	4.32	0.19
$K_6[P_2W_{18}O_{62}]$	9.3	-8.251	-3.923	4.33	0.20
$K_6[P_2W_{18}O_{62}]$	9.5	-8.298	-3.964	4.33	0.20
$K_6[P_2W_{18}O_{62}]$	9.75	-8.303	-3.967	4.34	0.21

Table A-3.9: Reported frontier orbital eigenvalues for $K_n[P_2W_{18}O_{62}]^{n-6}$, where the HOMO-LUMO gap value for each POM species is compared against the value supplied by Chen, J.-J. *et al* [323]. **SP/PBE0/TZP/COSMO/Small Frozen Cores**

Molecular Formula	P-K Distance (Å)	HOMO (eV)	LUMO (eV)	HOMO-LUMO (eV)	HOMO-LUMO Difference
$[P_2W_{18}O_{62}]^{6-}$	N/A	-8.210	-3.875	4.34	0.21
$K_6[P_2W_{18}O_{62}]$	OPT	-9.129	-4.988	4.14	0.01
$K_6[P_2W_{18}O_{62}]$	7.0	-8.568	-4.367	4.20	0.07
$K_6[P_2W_{18}O_{62}]$	7.5	-8.501	-4.297	4.20	0.07
$K_6[P_2W_{18}O_{62}]$	8.0	-8.441	-4.240	4.20	0.07
$K_6[P_2W_{18}O_{62}]$	8.5	-8.393	-4.186	4.21	0.08
$K_6[P_2W_{18}O_{62}]$	9.0	-8.300	-4.083	4.22	0.09
$K_6[P_2W_{18}O_{62}]$	9.3	-8.361	-4.144	4.22	0.09
$K_6[P_2W_{18}O_{62}]$	9.5	-8.360	-4.144	4.22	0.09
$K_6[P_2W_{18}O_{62}]$	9.75	-8.365	-4.147	4.22	0.09
$K_6[P_2W_{18}O_{62}]$	10.0	-8.366	-4.149	4.22	0.09

When cations are included in the Wells-Dawson model, the optimized model tends to favour placing the cations at 6.3 Å. This is too close to the POM, however, and results in over-stabilization of the HOMO and LUMO energy levels; in solution, there are many solvent molecules which surround each cation and act to repel the cations further away from the POM. These molecules are omitted from the model for the sake of reducing complexity, as implicitly including all the solvent molecules would result in the calculation never converging with the available computational power; we should still aim to take them into account as much as possible, almost 'pretend' that the solvent molecules are there even when omitted to develop a model that more closely reflects the empirical chemical system.

By running several single point calculations, with the potassium cations at different distances each time, we aimed to find the optimum distance that would result in the HOMO-LUMO energy gap most closely reflecting that reported in the literature.

Based on the above data, we have determined the optimum cation distance between heteroatom and cations to be 9.0 Å.

Table A-3.10. UV-Vis data for $K_n[\alpha\text{-}P_2W_{18}O_{62}]^{(n-6)}$. UV-vis calculations carried out by the LVN group are single point calculations which use pre-optimized geometries; both calculations use the same functional. Number of cations in the geometry and the distance between cation and heteroatom is specified. The calculation defined as '6K, OPT' has no cation-phosphorus distance constraints.

Functional/Basis Set/Frozen Cores	No K Cations	6K, OPT	6K, (9.0Å)	6K, (10.0Å)
B3LYP/TZP/SFC	3.84	3.83	3.82	3.82
B3LYP-D/TZP/SFC	3.82	3.74	3.82	3.82
BP86/TZP/SFC	2.31	2.32	2.29	2.29
PBE/TZP/SFC	2.83	2.34	2.30	2.30
PBE-D/TZP/SFC	2.32	2.34	2.30	2.30
PBE0/TZP/SFC	4.09	4.23	4.22	4.22
wB97x/TZP/NFC	-----	-----	-----	-----

Appendix-3.5: Time-Independent DFT Results

Table A-3.11. Frontier orbital energy gap values for various POM species, calculated using TI-DFT **SP/PBE0/TZP/COSMO/Small Frozen Cores**

POM Species	H-L Gap (eV)	Gap difference with empirical absorbance band (eV)	Reference
$[W_6O_{19}]^{2-}$	5.49	+1.05	Ravelli, D. *et al.*[320]
$[W_{10}O_{32}]^{4-}$	4.58	+0.74	Ravelli, D. *et al.*[320]
$[H_2W_{12}O_{42}]^{10-}$	5.39	+1.51	Fait, M.J.G *et al.*[391]
$[PW_{12}O_{40}]^{3-}$	4.77	+0.09	Hiskia, A. *et al.*[339]
$[P_2W_{18}O_{62}]^{6-}$	4.21	+0.08	Chen, J.-J. *et al.*[323]
$K_6[P_2W_{18}O_{62}]$	4.22	+0.09	Chen, J.-J. *et al.*[323]
$[P_5W_{30}O_{110}]^{15-}$	4.47	+0.04	Bamoharram, F.F. *et al.*[392]

Appendix-3.6: Time-Dependent DFT Results

Table A-3.12. Simulated UV-Vis spectroscopy for various POM species, calculated using TD-DFT **SP/PBE0/TZP/COSMO/Small Frozen Cores**

POM Species	First Transition Energy (eV)	Gap difference with empirical absorbance band (eV)	Transition	Specific Orbitals	Reference
$[W_6O_{19}]^{2-}$	4.59	+0.10	6t1.g -> 3e.u (97.0%)	HOMO -> LUMO	Ravelli, D. *et al.*[320]
$[W_{10}O_{32}]^{4-}$	3.82	-0.02	8a2.g -> 8a1.u (97.5%)	HOMO+1 -> LUMO	Ravelli, D. *et al.*[320]
$[H_2W_{12}O_{42}]^{10-}$	4.17	+0.29	299A -> 301A (38.3%)	HOMO+1 -> LUMO	Fait, M.J.G *et al.*[391]
$[PW_{12}O_{40}]^{3-}$	4.31	-0.37	43t2 -> 25e (79.4%)	HOMO+2 -> LUMO	Hiskia, A. *et al.*[339]
$[P_2W_{18}O_{62}]^{6-}$	3.88	-0.25	29AA2 -> 30AAA1 (47.6%)	HOMO+11 -> LUMO	Chen, J.-J. *et al.*[323]
$K_6[P_2W_{18}O_{62}]$	3.67	-0.46	474A -> 479A (66.2%)	HOMO+4 -> LUMO	Chen, J.-J. *et al.*[323]

Appendix-4: Chapter 8

Appendix-4.1: Experimental Spectra

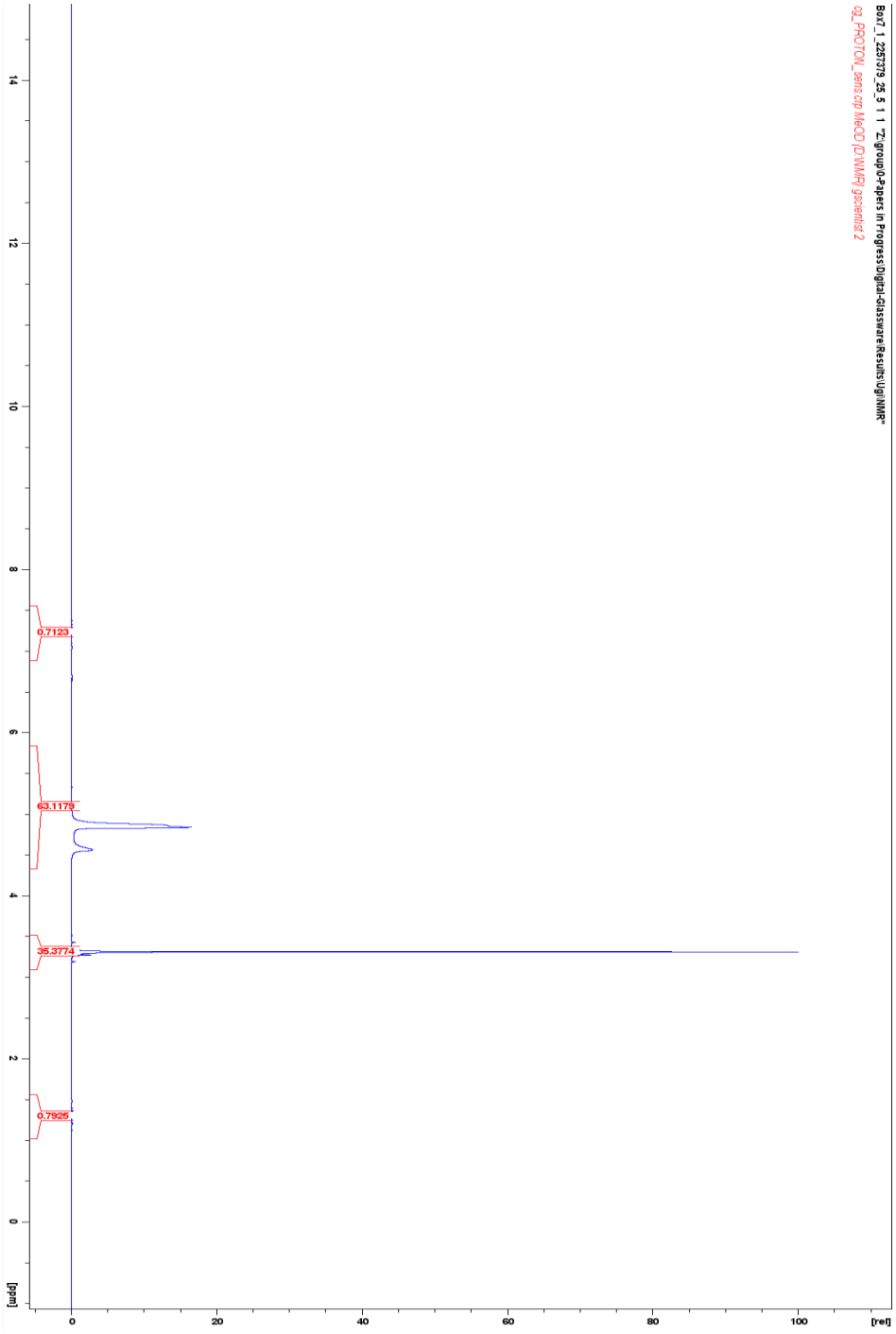

Figure A-4.1. NMR Results for the **R3** Ugi reaction. Characteristic aromatic (7-8ppm), and amine and methyl (1-1.5ppm) peaks are indicative of **P3** formation, albeit in very small quantities. Sharp peak at roughly 3.3ppm is attributed to unreacted 7-(diethylamino)coumarin-3-carboxylic acid in the solution. Results were as follows; H(200 MHz; MeOH), δ 3.19 (s), 3.27 (s), 3.31 (s), 3.42 (s), 4.56 (s), 4.82 (s), 4.83 (s).

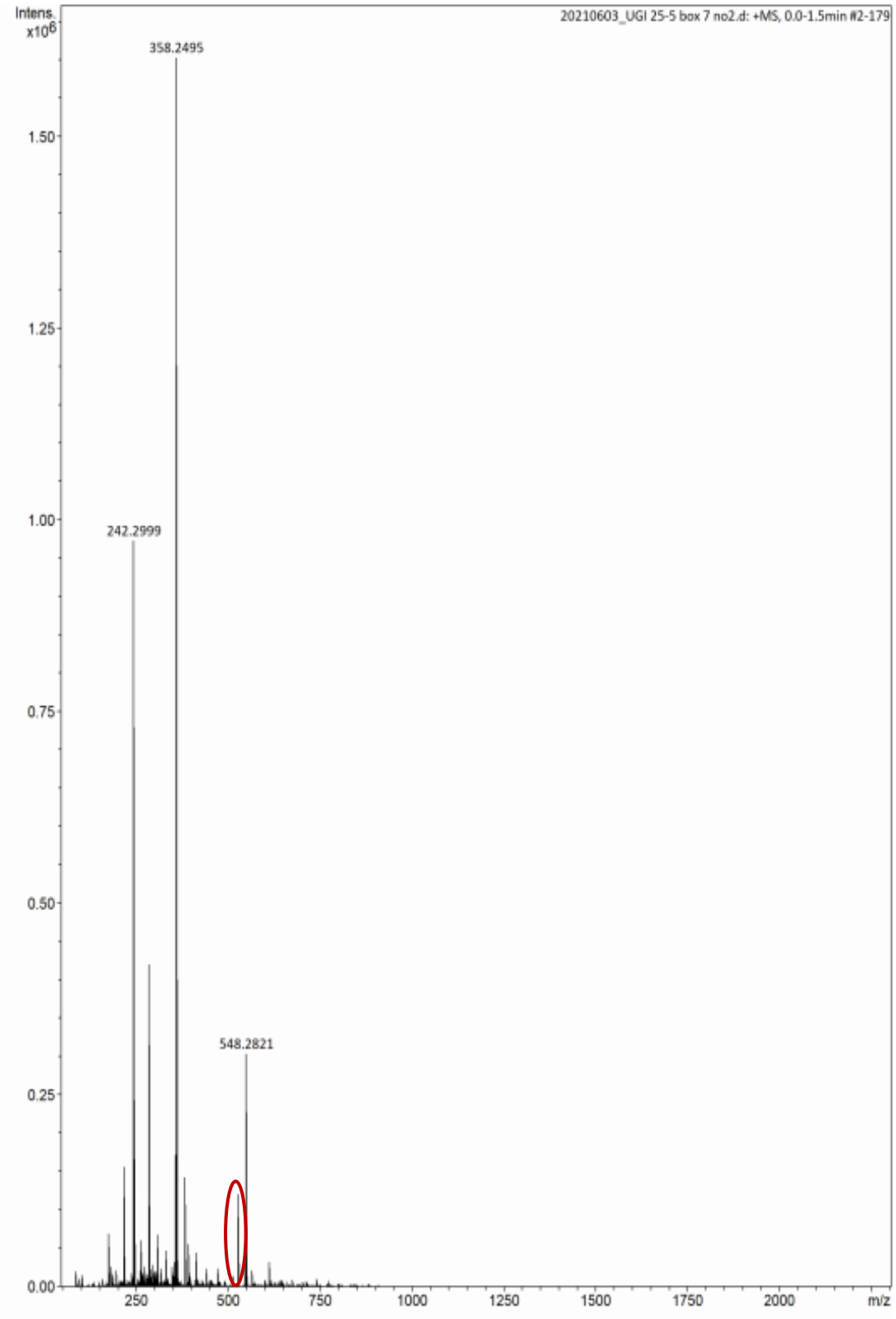

Figure A-4.2. MS results for the **P3** Ugi reaction. The circled peak at m/z 526 indicates presence of the product.

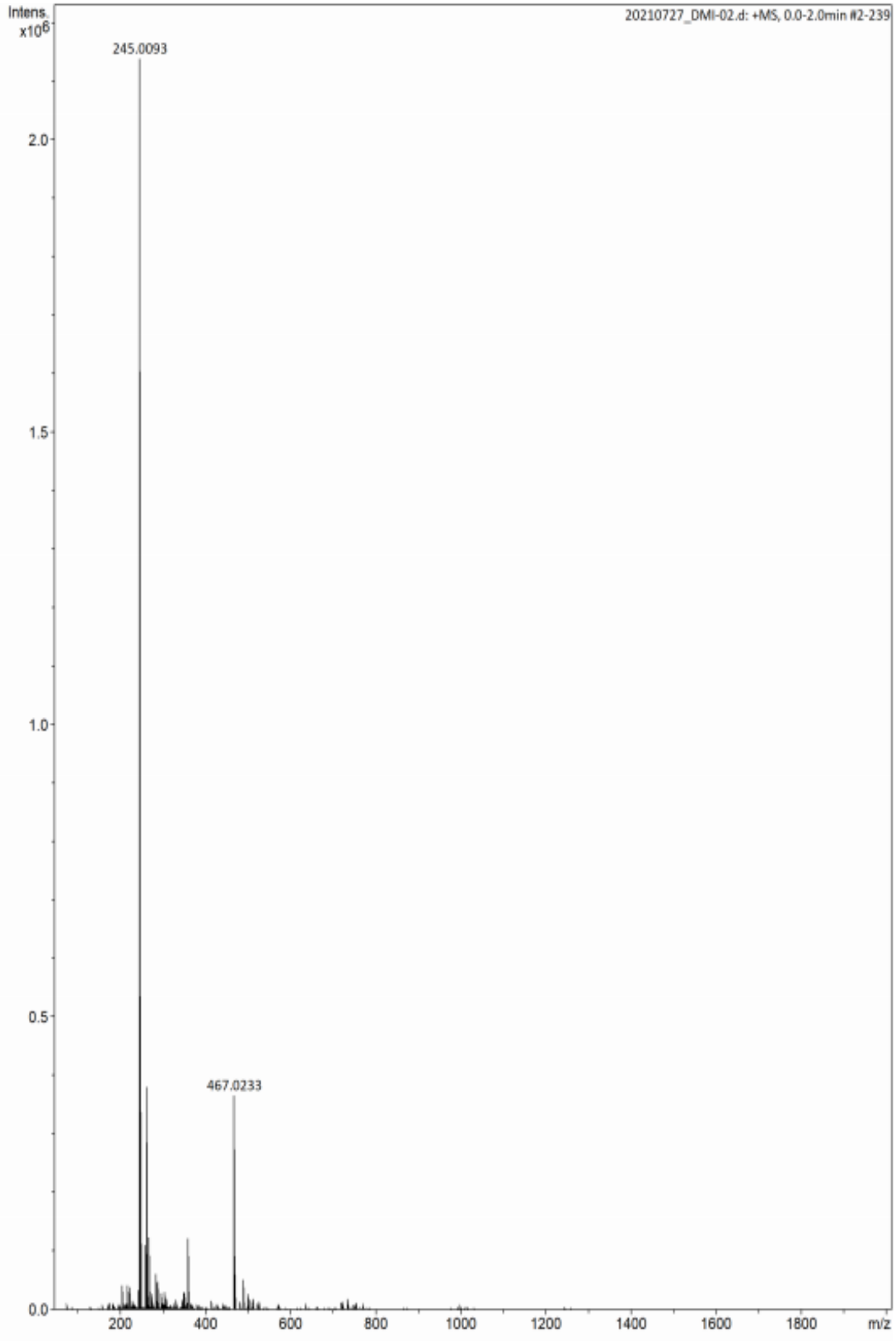

Figure A-4.3. First fraction MS results for the **P6** Ugi reaction. No product is visible.

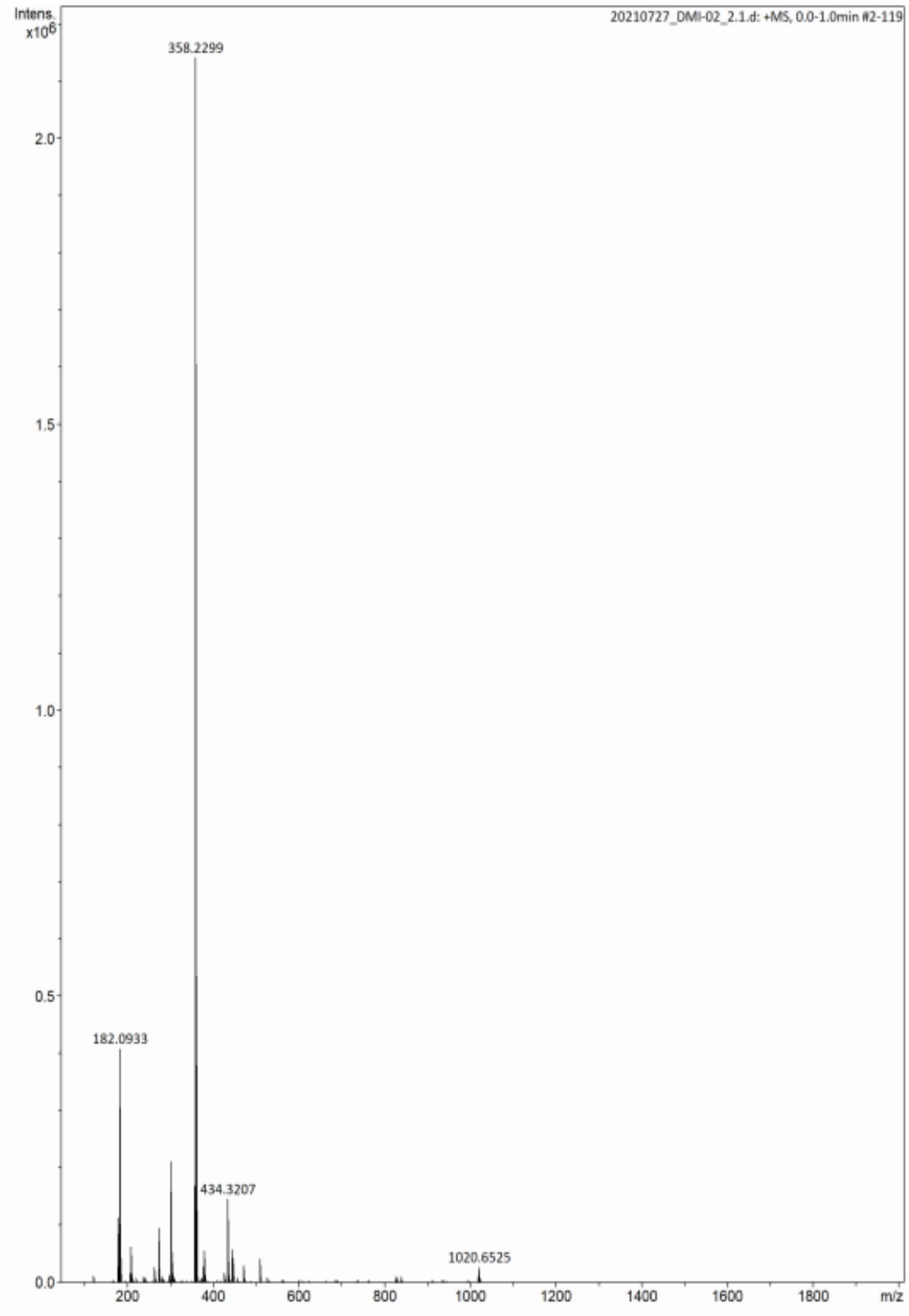

Figure A-4.4. Second fraction MS results for the **P6** Ugi reaction. No product is visible.

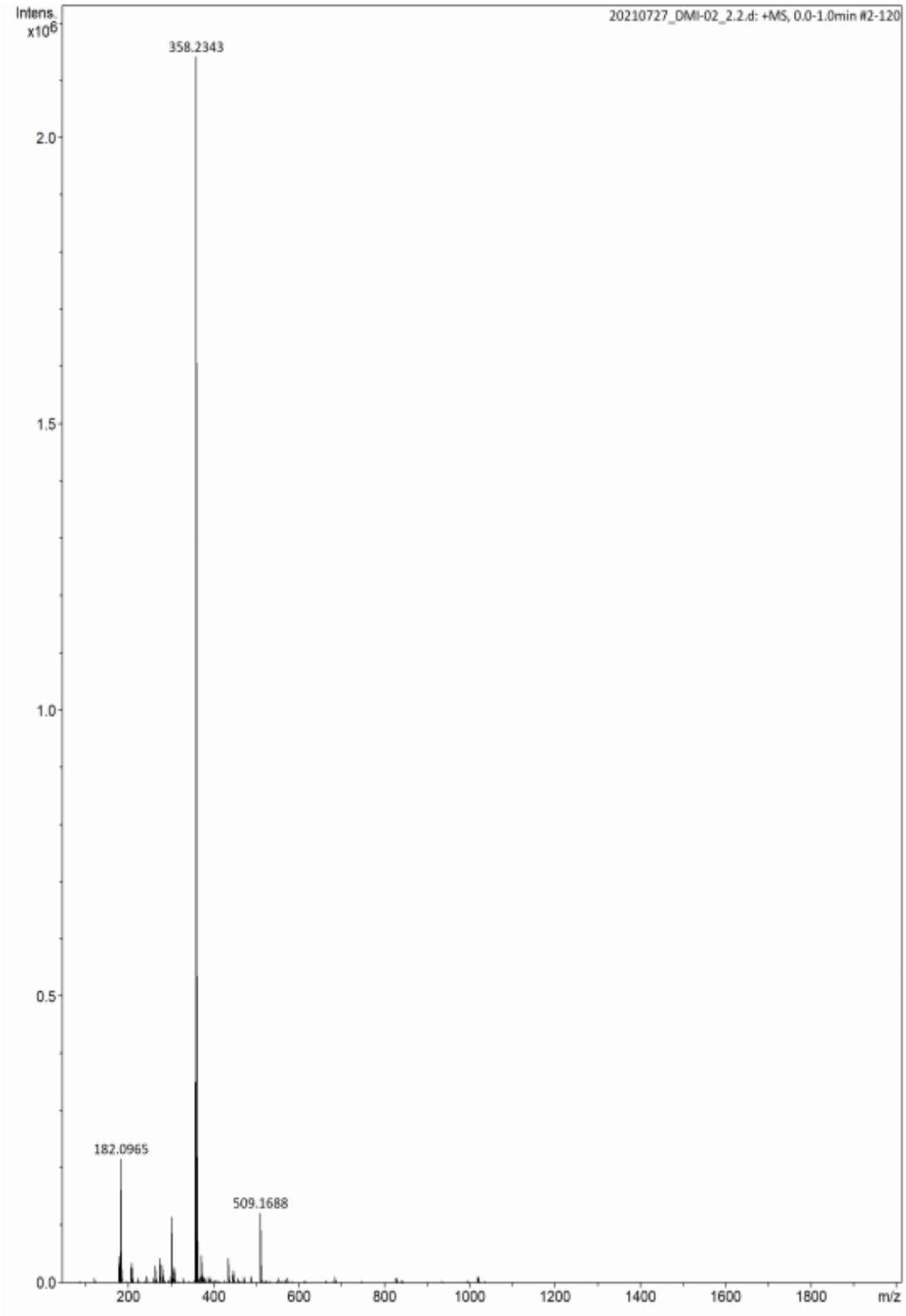

Figure A-4.5. Third fraction MS results for the **P6** Ugi reaction. No product is visible.

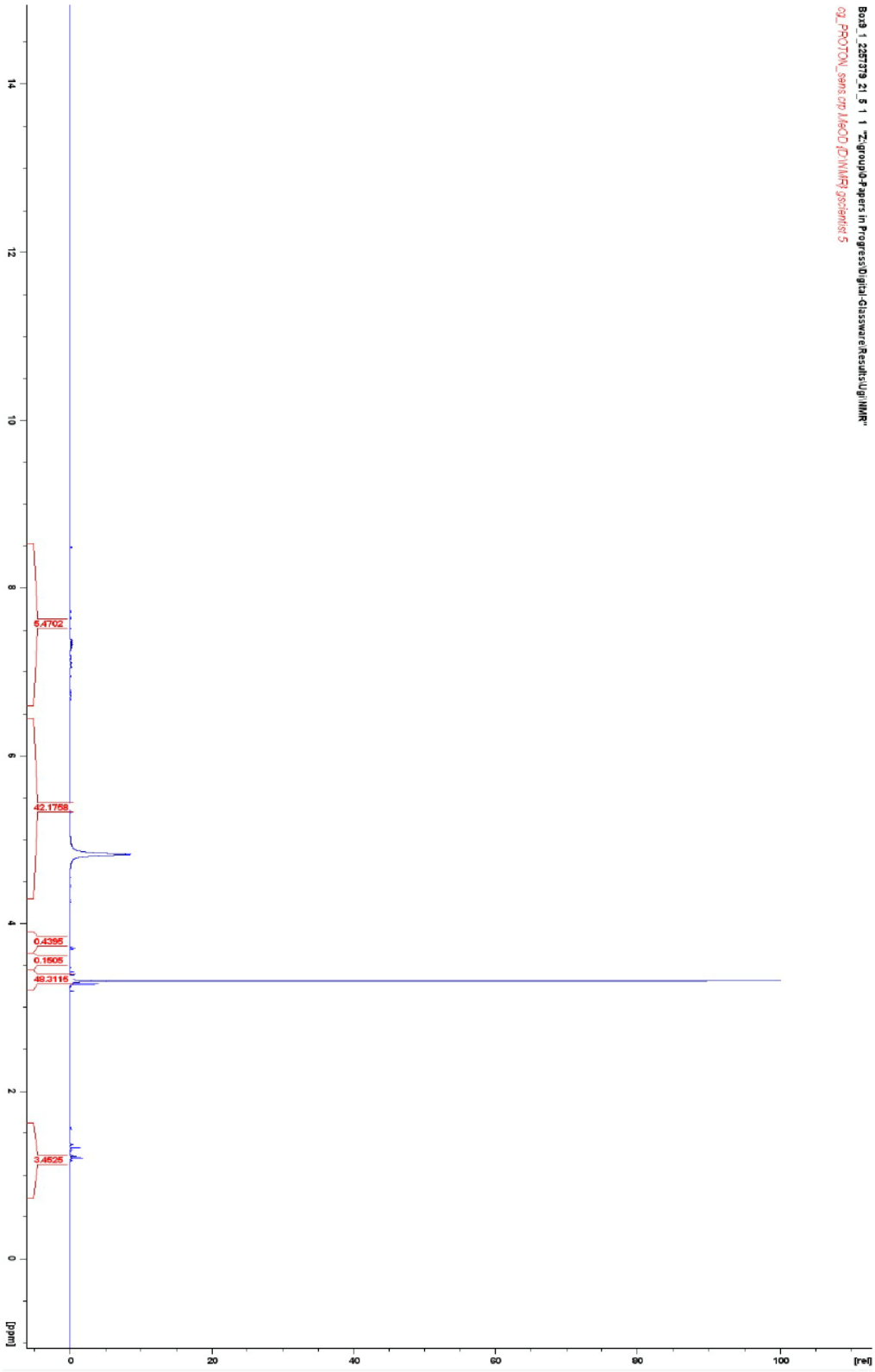

Figure A-4.6. NMR Results for the **R6** Ugi reaction. Characteristic aromatic (7-8ppm), and amine and methyl (1-1.5ppm) peaks are indicative of **P6** formation, albeit in very small quantities. Results were as follows; H(200 MHz; MeOH), δ 1.17-1.22 (t), 1.30-1.36 (t), 3.19-3.42 (m), 3.69-3.71 (d), 4.82 (s), 5.33 (s), 7.06 (t), 7.31-7.38 (m)

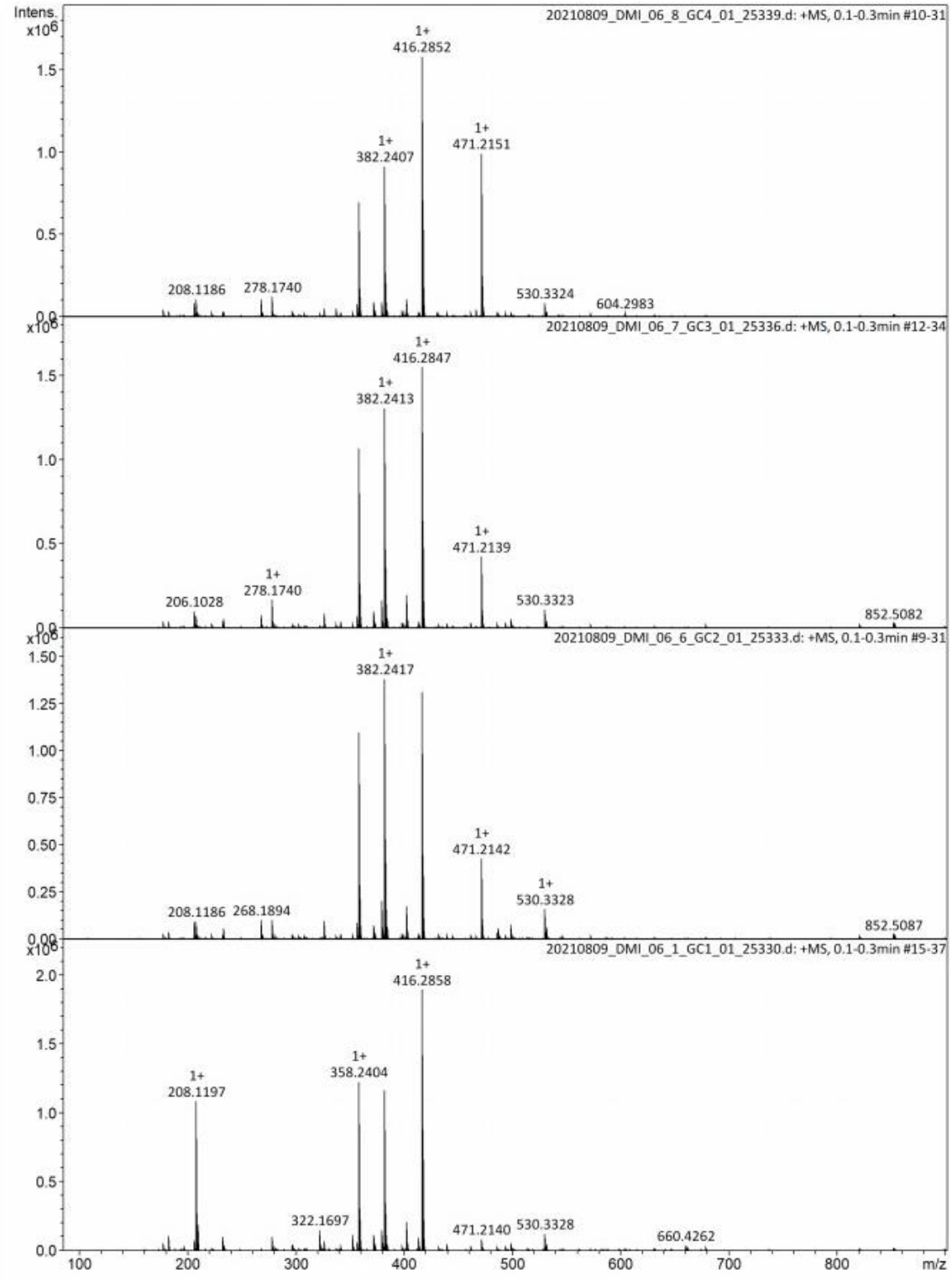

Figure A-4.7. MS results for the **P9** Ugi reaction, split into four fractions. No product is visible.

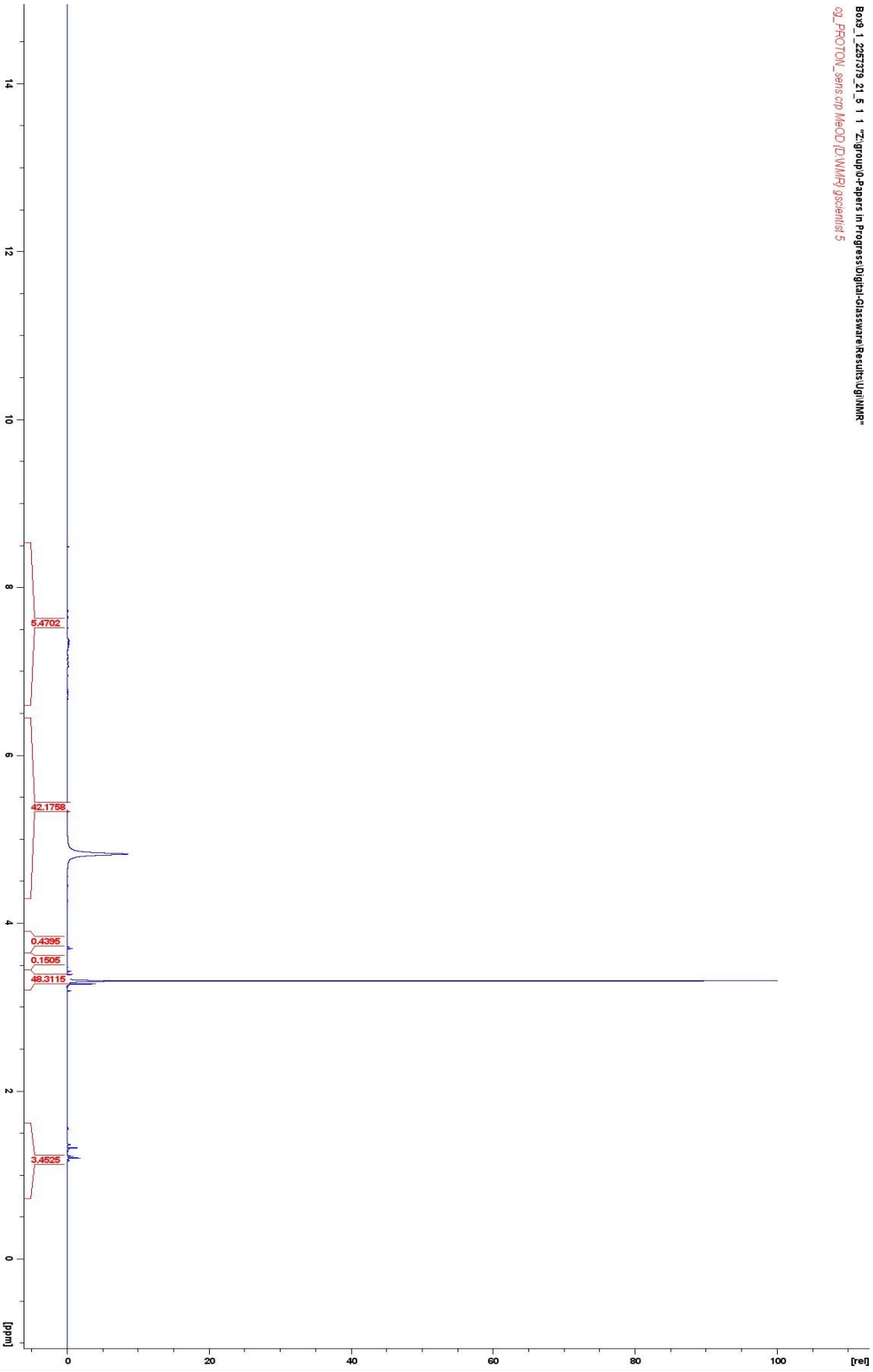

Figure A-4.8 NMR Results for the **R15** Ugi reaction. The starting materials for **R15** were coumarin-3-carboxylic acid, aniline, benzaldehyde, and *tert*-butyl isocyanide. Results were as follows; H(200 MHz; MeOH), δ 1.35 (s), 1.55 (s), 3.19 (s), 3.27 (t), 3.31 (s), 3.42 (s), 4.84 (s).

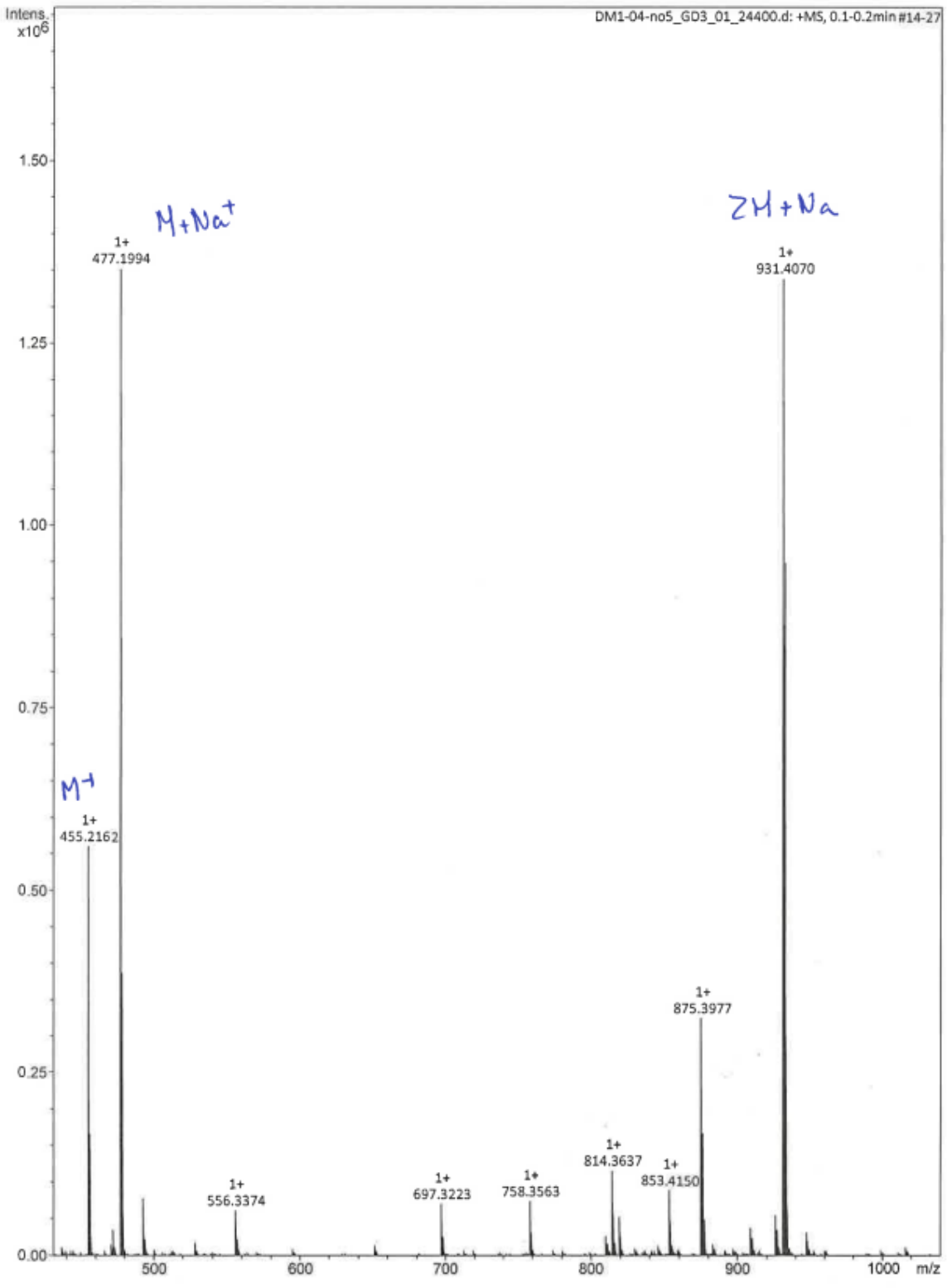

Figure A-4.9. MS results for the **P15** Ugi reaction. Product is present as three distinct peaks: 455.2162 ($[C_{28}H_{26}O_4N_2]^+$), 477.1994 ($Na[C_{28}H_{26}O_4N_2]^+$), and 931.407 ($Na[C_{28}H_{26}O_4N_2]_2^+$)

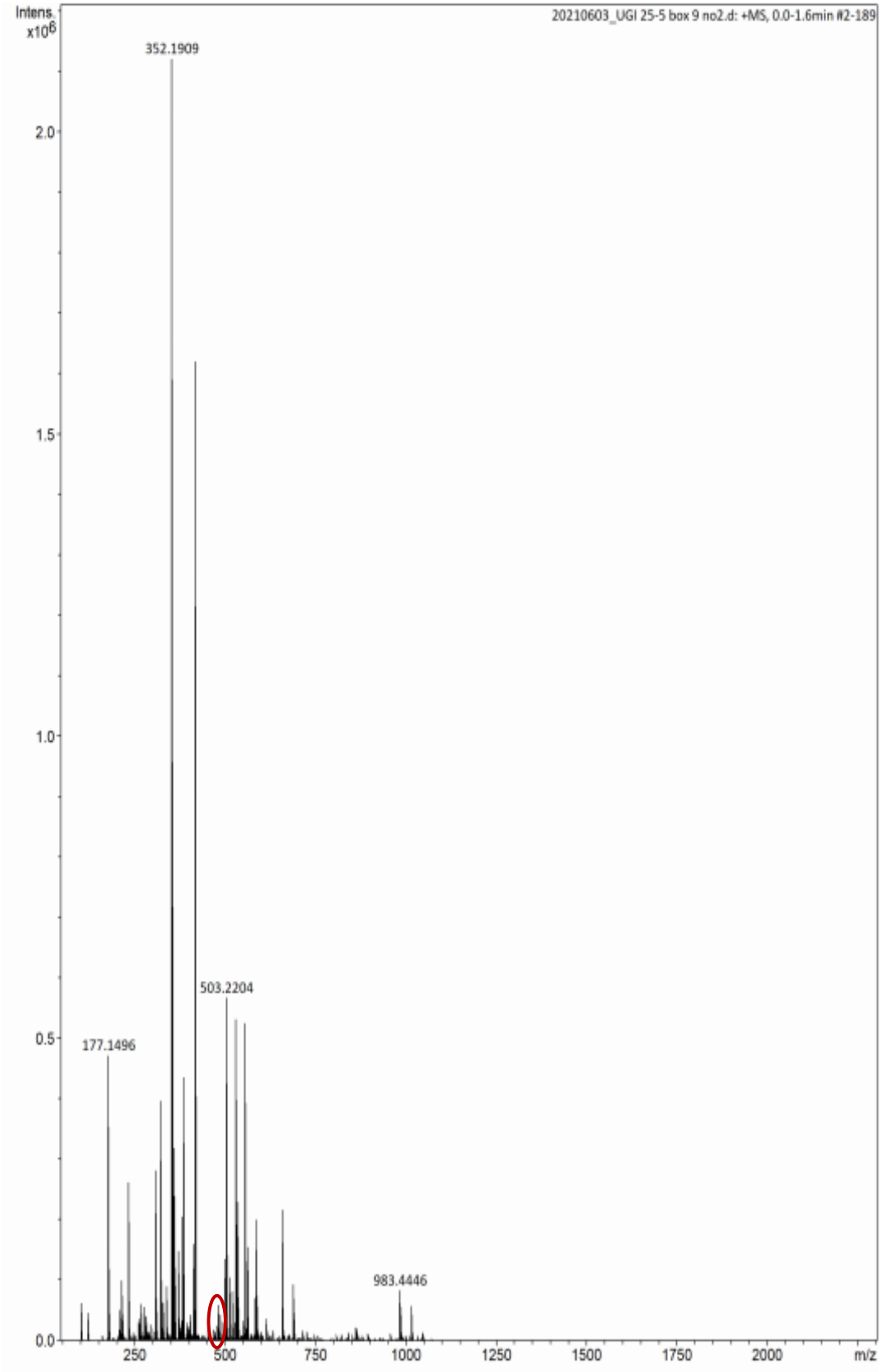

Figure A-4.10. MS results for the **P18** Ugi reaction. The circled peak at m/z 481 indicates presence of the product.

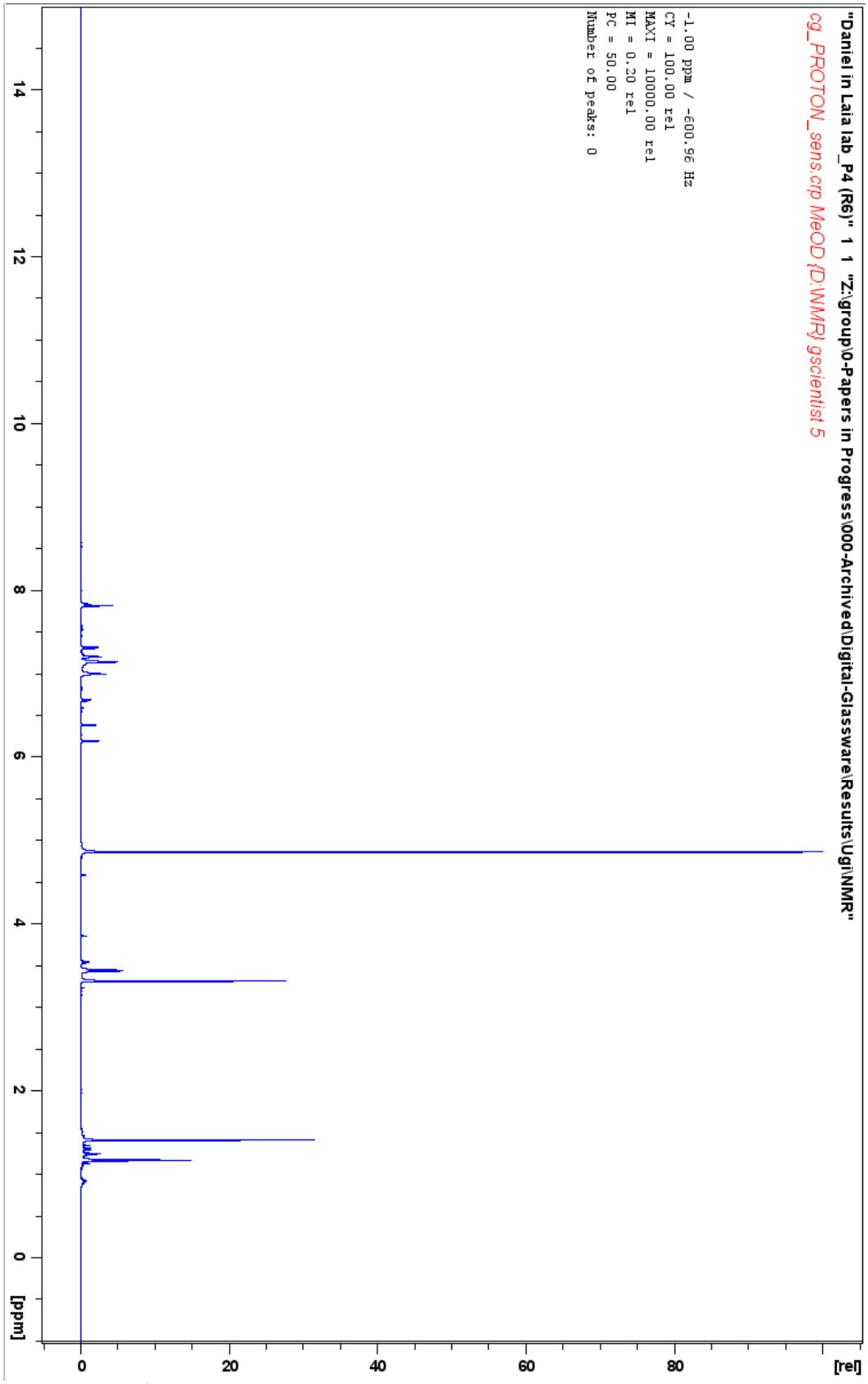

Figure A-4.11. H^1 NMR Results for the **R18** Ugi reaction. Characteristic aromatic (7-8ppm), and amine and methyl (1-1.5ppm) peaks are indicative of **P18** formation, albeit in very small quantities. Results were as follows; H(200 MHz; MeOH), δ 0.91-0.93 (m), 1.12 (s), 1.15-1.18 (t), 1.22-1.25 (t), 1.29-1.34 (m), 1.40 (s), 3.23 (s), 3.31 (s), 3.42-3.45 (q), 3.52-3.55 (q), 3.85 (s), 4.58 (s), 4.86 (s), 6.19 (s), 6.38 (d), 6.58 (d), 6.67-6.68 (dd), 6.99 (d), 7.13-7.14 (dd), 7.19-7.21 (dd), 7.30 (d), 7.52 (m), 8.56 (m)

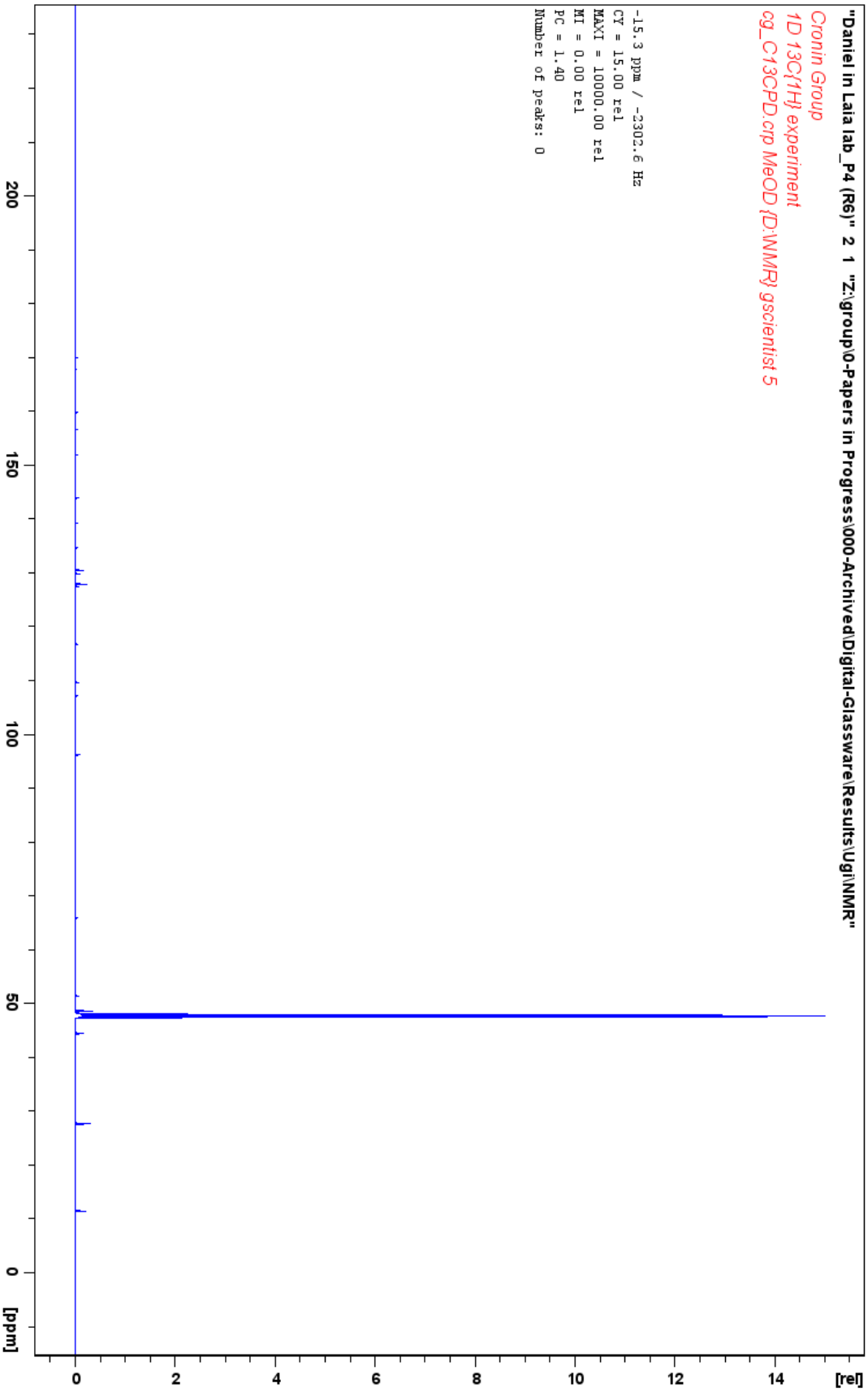

Figure A-4.12. C^{13} NMR Results for the **R18** Ugi reaction. Results were as follows; H(200 MHz; MeOH), δ 11.22-11.27 (m), 27.52 (s), 47.17-48.44 (sept), 127.35 (s), 127.72 (d), 129.73 (s), 130.30 (d)

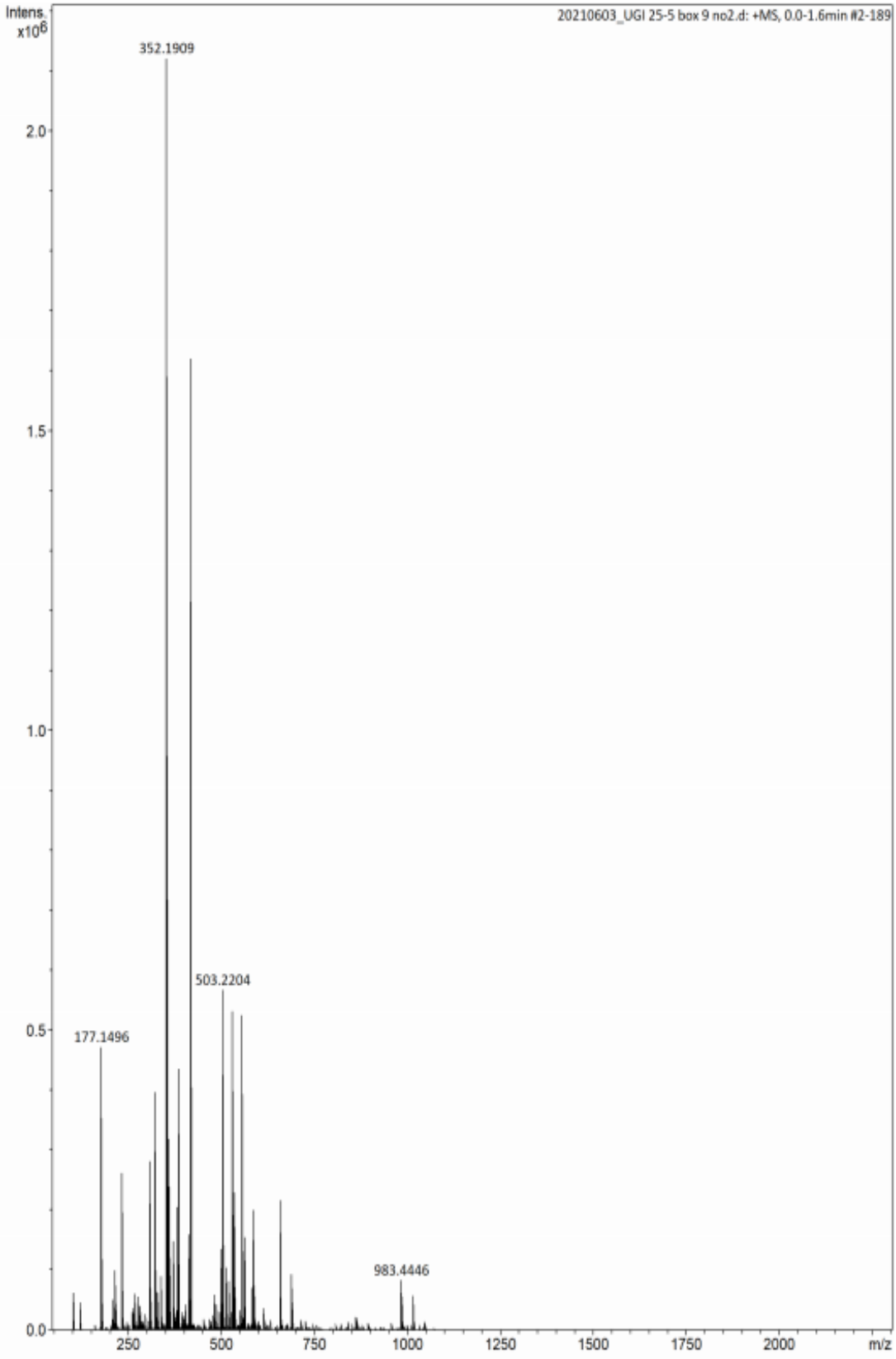

Figure A-4.13. MS results for the **P19** Ugi reaction. No product is visible.

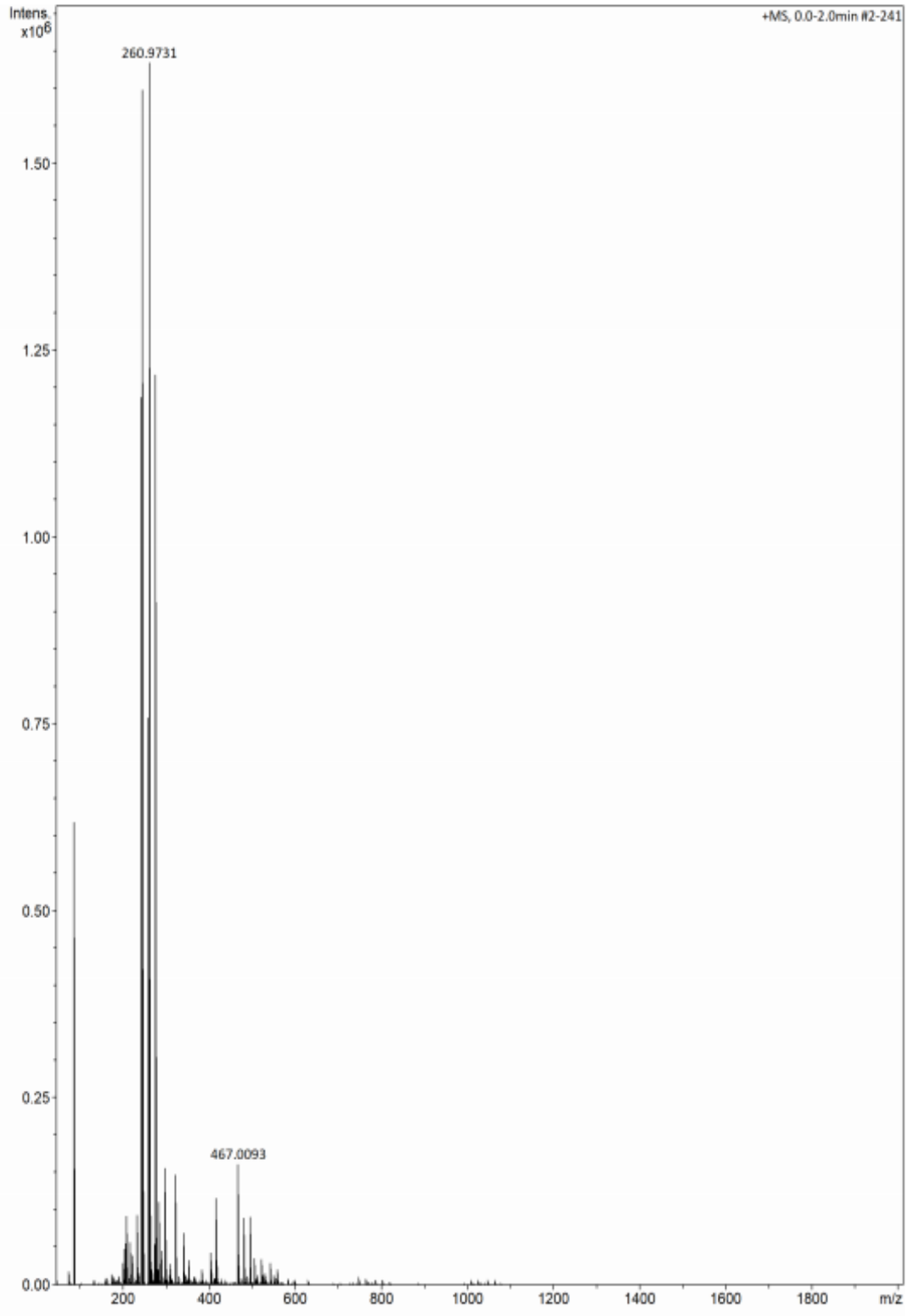

Figure A-4.14. MS results for the **P20** Ugi reaction. No product is visible.

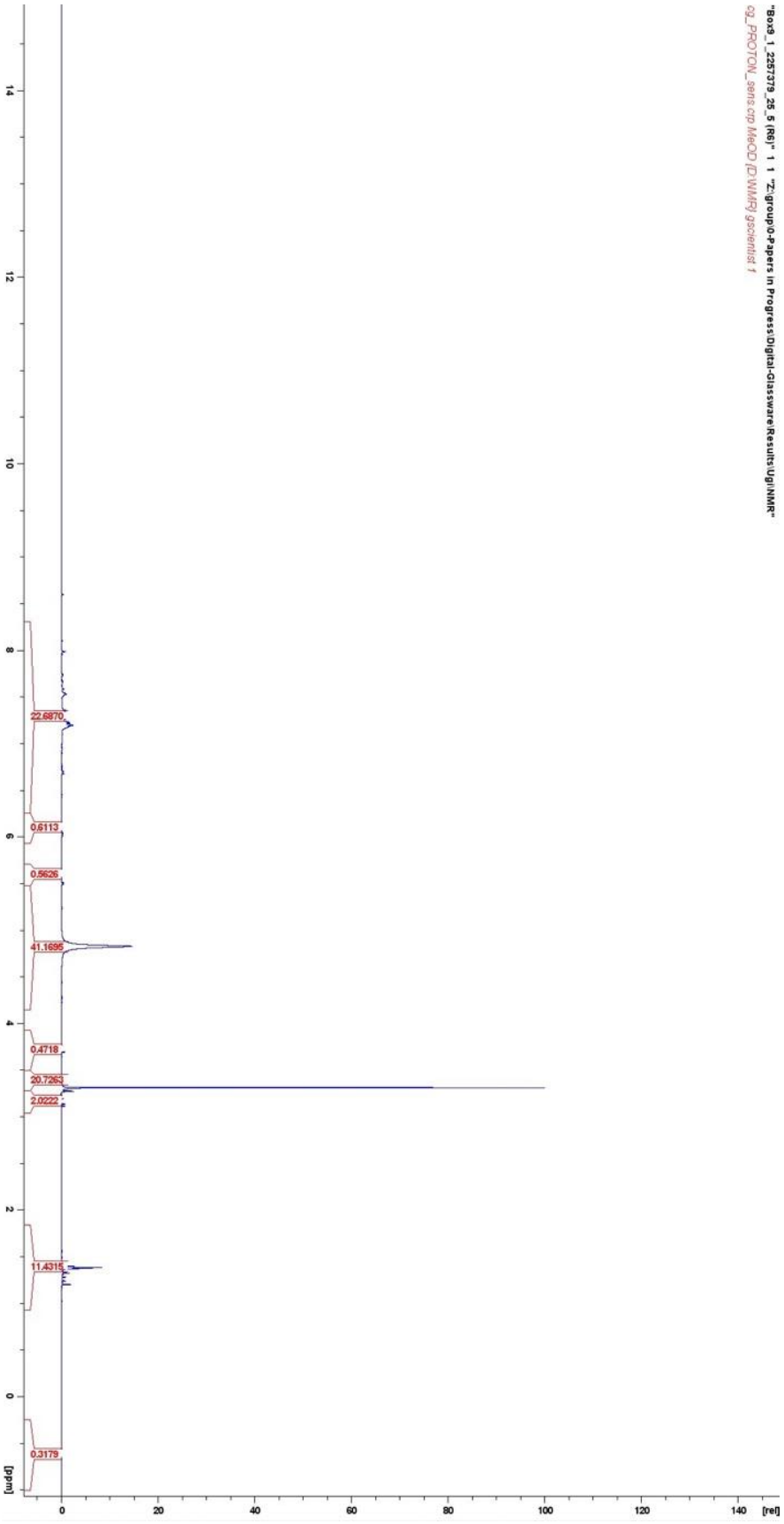

Figure A-4.15. NMR Results for the **R20** Ugi reaction. Characteristic aromatic (7-8ppm), and amine and methyl (1-1.5ppm) peaks are indicative of **P20** formation, albeit in very small quantities.

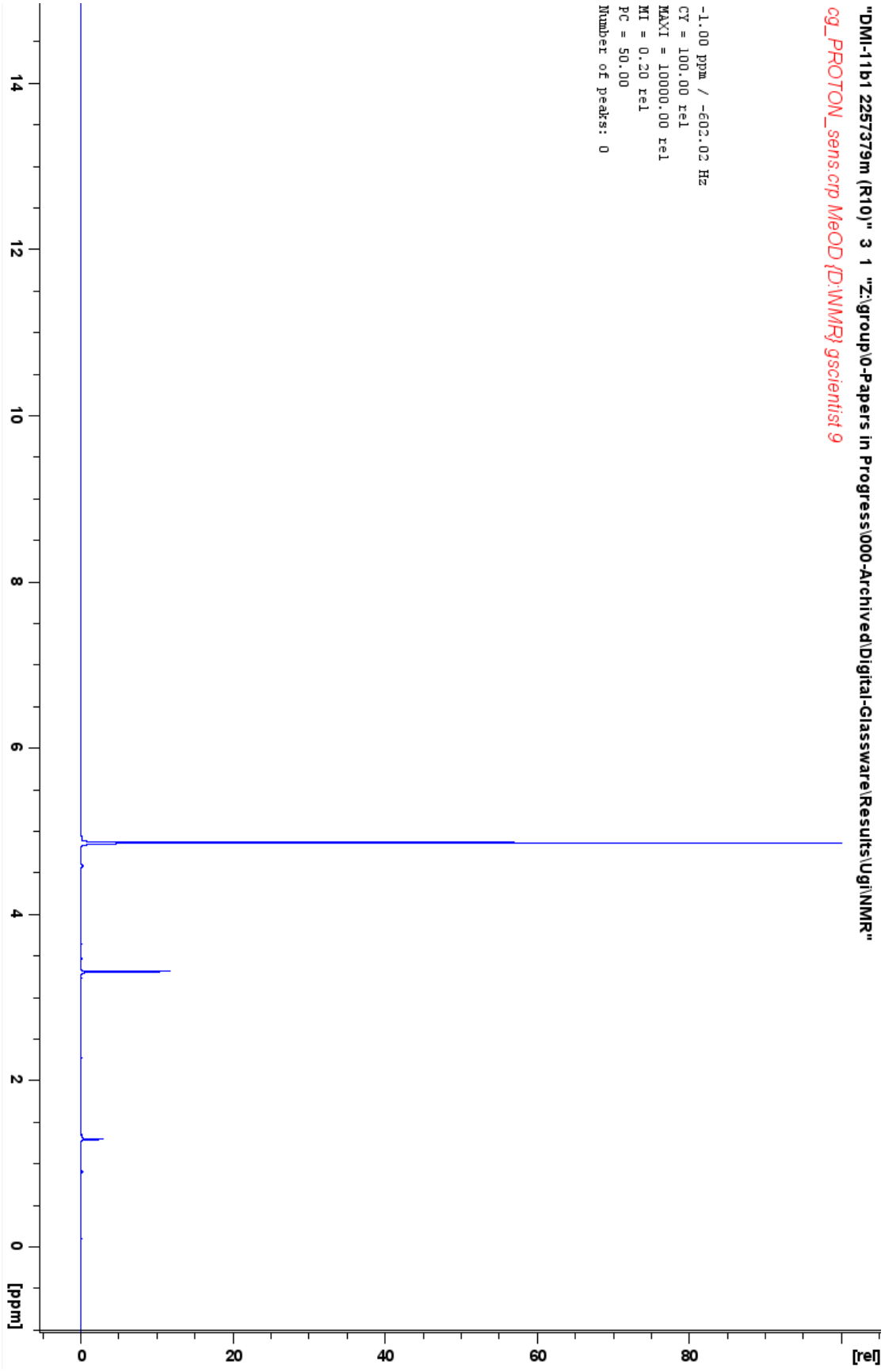

Figure A-4.16. NMR Results for the **R21** Ugi reaction. Results were as follows; H(200 MHz; MeOH), δ 0.90 (t), 1.29 (s), 3.30-3.32 (quin), 4.58 (s), 4.86 (s)

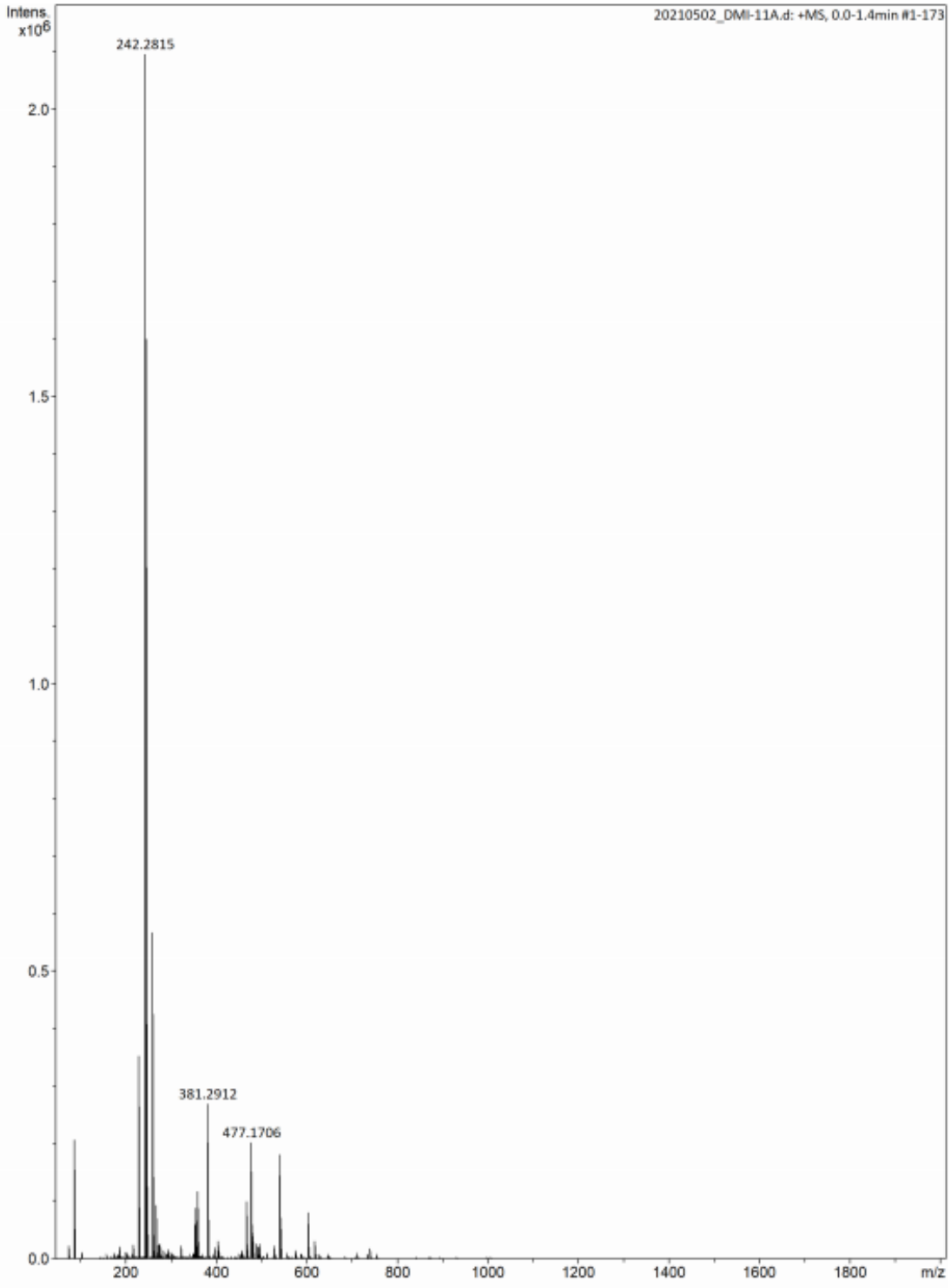

Figure A-4.17. MS results for the **P21** Ugi reaction. No product is visible.

Appendix-4.3: Theoretical Spectra

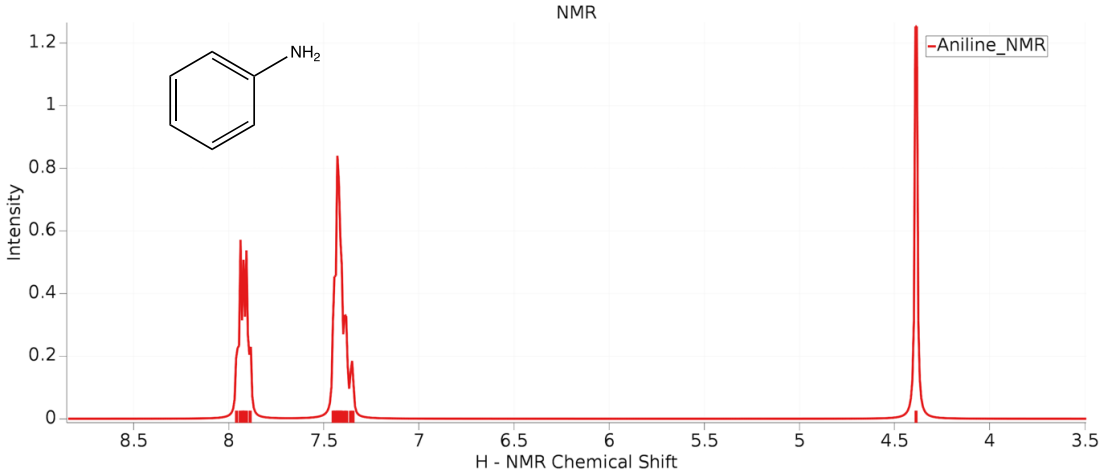

Figure A-4.18. Computationally modelled NMR of aniline. Results were as follows; H(200 MHz; MeOH), δ 4.39 (2H, s, N**H**$_2$), 7.35-7.50 (3H, m, 3 x C**H**), 7.92 (2H, dt, *J* 6.6, 3.8, 2 x C**H**).

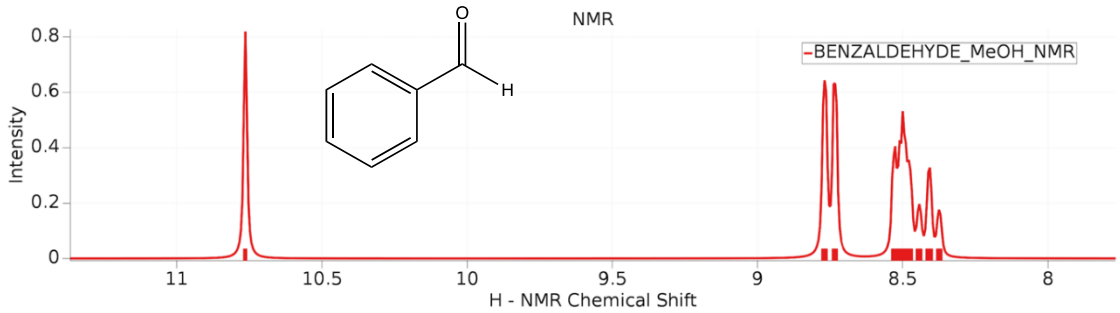

Figure A-4.19. Computationally modelled NMR of benzaldehyde. Results were as follows; H(200 MHz; MeOH), δ 8.37-8.45 (1H, m, C**H**), 8.47-8.52 (1H, m, C**H**), 8.49-8.53 (1H, m, C**H**), 8.7 (2H, d, *J* 6.9, 2 x C**H**), 10.77 (1H, s, C**H**O).

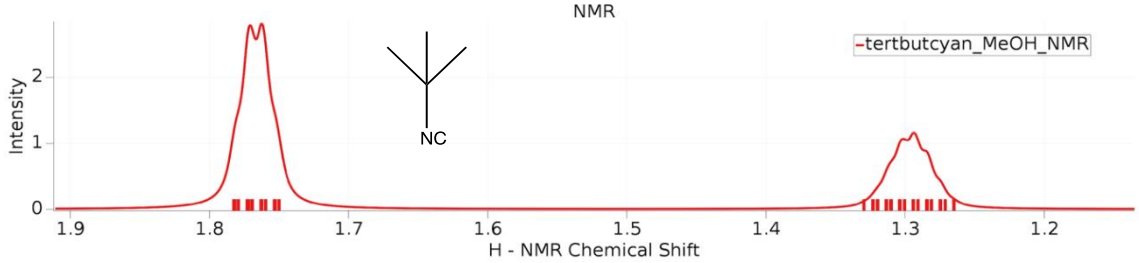

Figure A-4.20. Computationally modelled NMR of *tert*-butyl isocyanide. Results were as follows; H(200 MHz; MeOH), δ 1.26-1.32 (3H, m, 3 x C**H**), 1.76 (6H, 3 x C**H**$_2$).

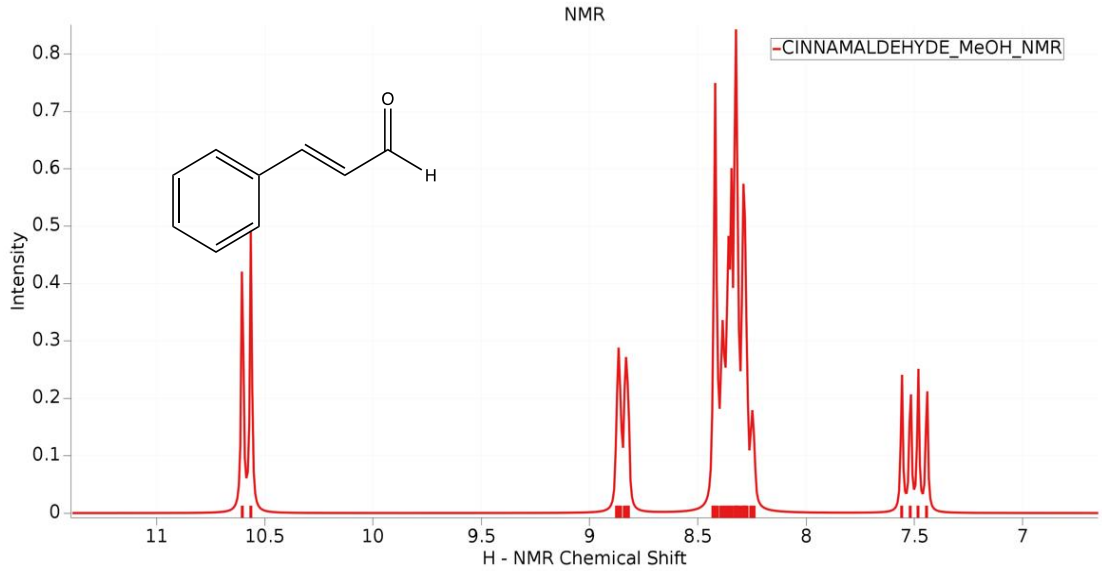

Figure A-4.21. Computationally modelled NMR of cinnamaldehyde. Results were as follows; H(200 MHz; MeOH), δ 7.50 (1H, dd, *J* 15.1, 8.0, C**H**), 8.24-8.32 (1H, m, C**H**), 8.29-8.36 (1H, m, C**H**), 8.29-8.36 (1H, m, C**H**), 8.34-8.42 (1H, m, C**H**), 8.38-8.43 (1H, m, C**H**), 8.85 (1H, dt, *J* 7.2, 2.2, C**H**), 10.58 (1H, d, *J* 8.0, C**H**O).

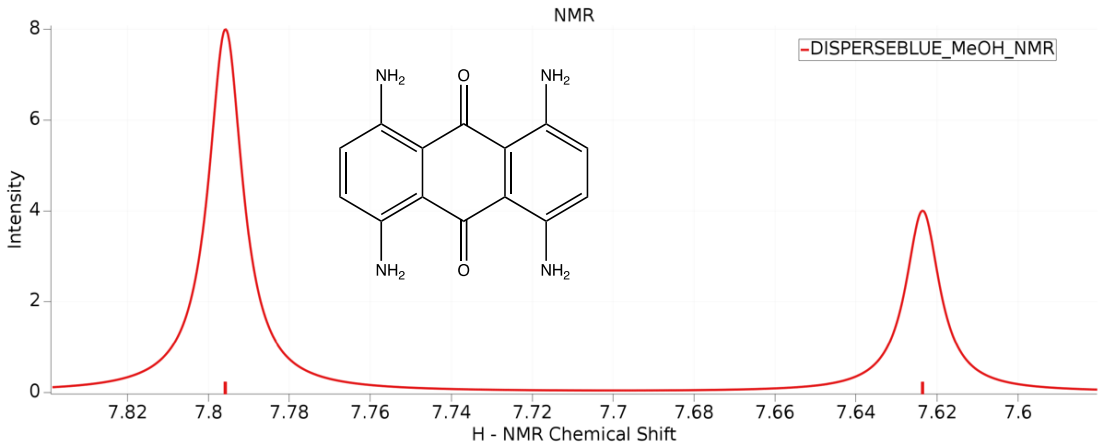

Figure A-4.22. Computationally modelled NMR of disperse blue 1. Results were as follows; H(200 MHz; MeOH), δ 7.62 (4H, s, 4 x C**H**), 7.80 (8H, s, 4 x N**H**$_2$).

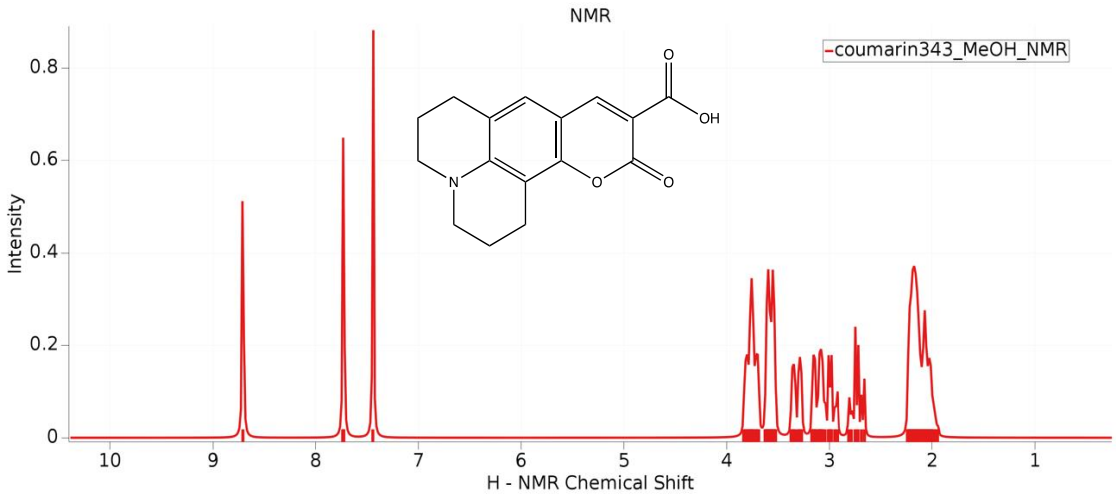

Figure A-4.23. Computationally modelled NMR of Coumarin 343. Results were as follows; H(200 MHz; MeOH), δ 1.95-2.24 (4H, m, 2 x C**H**$_2$), 2.73 (1H, td, *J* 12.2, 5.3, C**H**$_2$), 3.00 (1H, td, *J* 12.2, 5.3, C**H**$_2$), 3.12 (1H, dt, *J* 3.5, 2.2, C**H**$_2$), 3.32 (1H, dt, *J* 3.5, 2.2, C**H**$_2$), 3.57-3.58 (2H, m, C**H**$_2$), 3.75-3.77 (2H, m, C**H**$_2$), 7.44 (1H, s, O**H**), 7.73 (1H, s, C**H**), 8.71 (1H, s, C**H**).

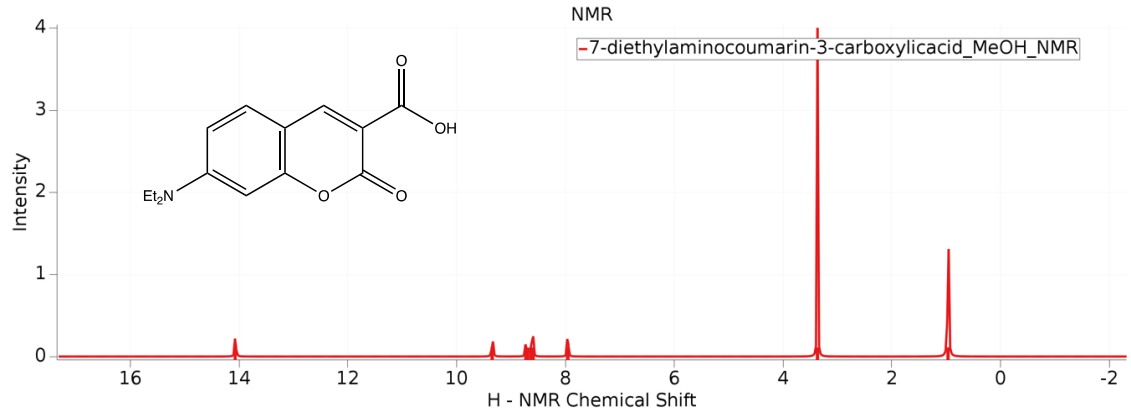

Figure A-4.24. Computationally modelled NMR of 7-(diethylamino)coumarin-3-carboxylic acid. Results were as follows; H(200 MHz; MeOH), δ 0.97 (6H, s, 2 x C**H**$_3$), 3.37 (4H, s, 2 x C**H**$_2$), 7.96 (1H, s, C**H**), 8.62 (1H, dd, *J* 7.6, 2.2, C**H**), 8.71 (1H, d, *J* 7.6, C**H**), 9.35 (1H, s, C**H**), 14.07 (1H, s, O**H**).

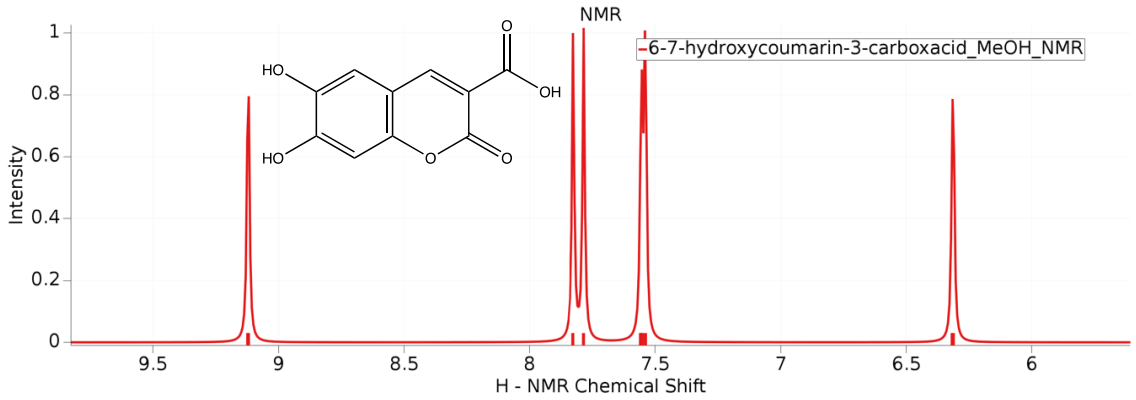

Figure A-4.25. Computationally modelled NMR of 6,7-dihydroxycoumarin-3-carboxylic acid. Results were as follows; H(200 MHz; MeOH), δ 6.31 (1H, s, O**H**), 7.54 (1H, s, O**H**), 7.55 (1H, s, C**H**), 7.78 (1H, s, O**H**), 7.83 (1H, s, C**H**), 9.12 (1H, s, C**H**).

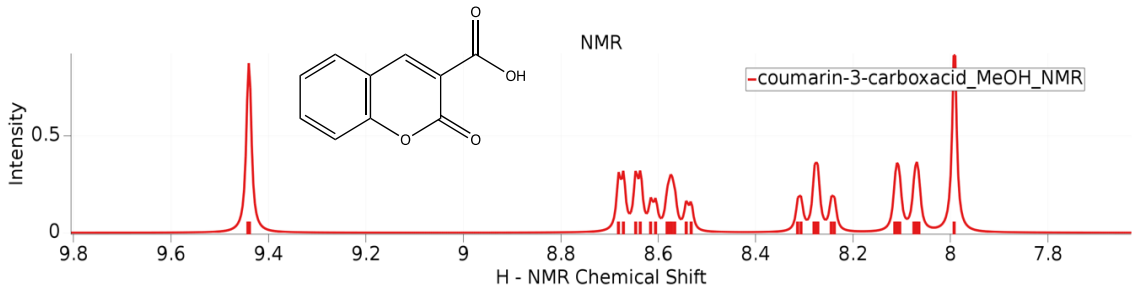

Figure A-4.26. Computationally modelled NMR of coumarin-3-carboxylic acid. Results were as follows; H(200 MHz; MeOH), δ 7.99 (1H, s, O**H**), 8.09 (1H, d, *J* 7.9, C**H**), 8.28 (1H, t, *J* 7.0, C**H**), 8.57 (1H, td, *J* 7.9, 6.7, C**H**), 8.66 (1H, dd, *J* 7.0, 2.0), 9.44 (1H, s, C**H**).

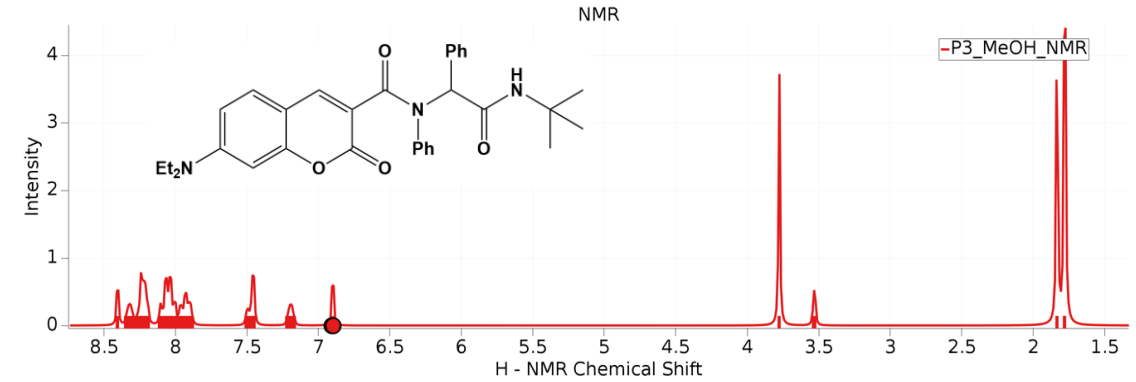

Figure A-4.27. Computationally modelled NMR of P3. The starting materials for R3 were 7-(diethylamino)coumarin-3-carboxylic acid, aniline, benzaldehyde, and *tert*-butyl isocyanide. Results were as follows; H(200 MHz; MeOH), δ 1.78 (9H, s, 3 x C**H**$_3$), 1.83 (6H, s, 2 x C**H**$_3$), 3.53 (1H, s, N**H**), 3.78 (4H, s, 2 x C**H**$_2$), 6.90 (1H, s, C**H**), 7.17-7.22 (1H, m, C**H**), 7.45-7.46 (1H, m, C**H**), 7.45-7.51 (1H, m, C**H**), 7.88-7.96 (6H, m, 6 x C**H**), 8.19-8.25 (3H, m, 3 x C**H**), 8.29-8.35 (1H, m, C**H**), 8.40 (1H, s, C**H**)

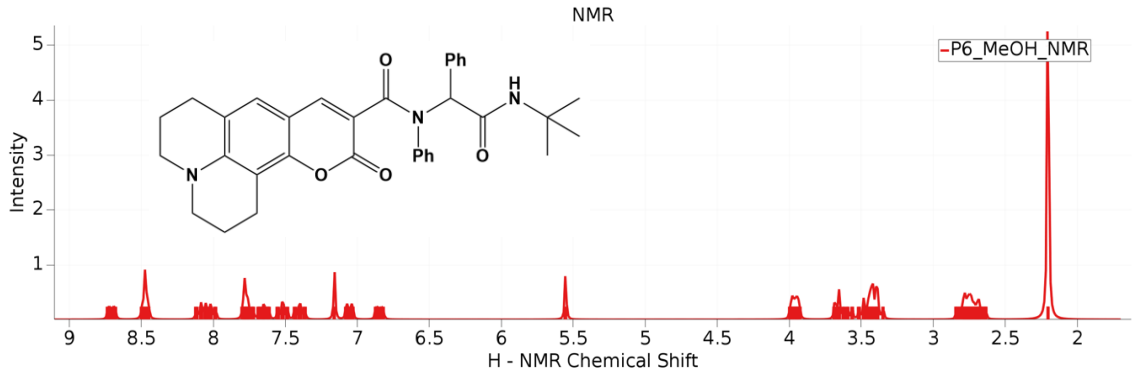

Figure A-4.28. Computationally modelled NMR of P6. The starting materials for R6 were Coumarin 343, aniline, benzaldehyde, and *tert*-butyl isocyanide. The results were as follows; H(200 MHz; MeOH), δ 2.20 (9H, s, 3 x C**H**$_3$), 2.63-2.84 (4H, m, 4 x C**H**), 3.35-3.44 (4H, m, 4 x C**H**), 3.56-3.69 (2H, m, 2 x C**H**$_2$), 3.93-4.00 (2H, m, 2 x C**H**$_2$), 5.56 (1H, s, N**H**), 6.85 (1H, dq, *J* 7.1, 2.7, C**H**), 7.06 (1H, dt, *J* 6.7, 2.3, C**H**), 7.16 (1H, s, C**H**), 7.40 (1H, td, *J* 6.7, 2.3, C**H**), 7.52 (1H, td, *J* 6.7, 2.3, C**H**), 7.65 (1H, tt, *J* 6.7, 2.3, C**H**), 7.76 (1H, tt, *J* 6.6, 1.5, C**H**), 7.78 (1H, s, C**H**), 8.02 (1H, td, *J* 7.0, 2.0, C**H**), 8.09 (1H, td, *J* 7.0, 2.0, C**H**), 8.47 (1H, dq, *J* 6.6, 2.3, C**H**), 8.47 (1H, s, C**H**), 8.71 (1H, dq, *J* 7.0, 2.7, C**H**).

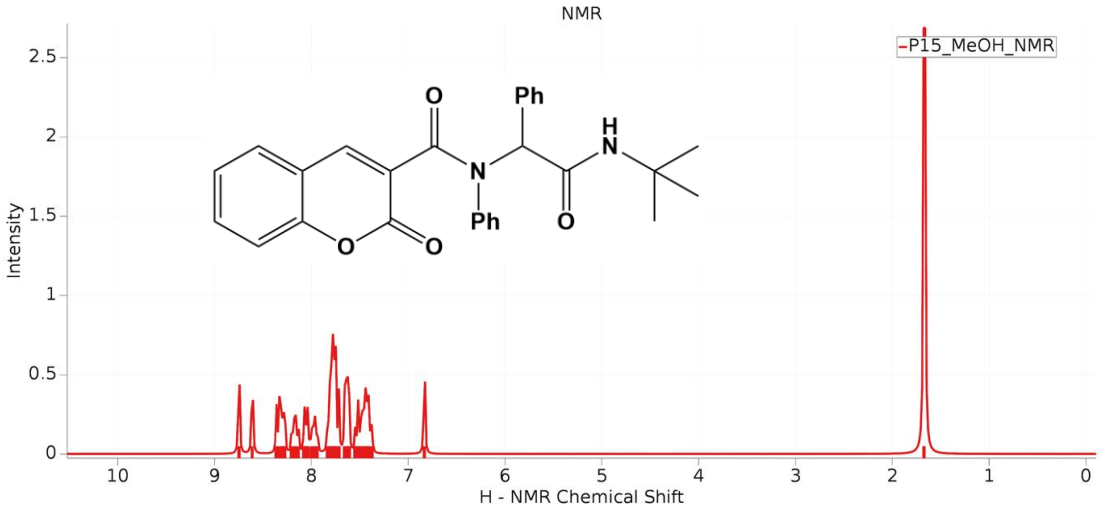

Figure A-4.29. Computationally modelled NMR of P15. The starting materials for R15 were coumarin-3-carboxylic acid, aniline, benzaldehyde, and *tert*-butyl isocyanide. Results were as follows; H(200 MHz; MeOH), δ 1.67 (6H, s, 3 x C**H**$_3$), 6.84 (1H, s, C**H**), 7.41 (1H, td, *J* 6.1, 5.9, C**H**), 7.43-7.47 (1H, m, C**H**), 7.52 (1H, t, *J* 5.9, C**H**), 7.63 (1H, dt, *J* 5.9, 1.3, C**H**), 7.62-7.67 (1H, m, C**H**), 7.74 (1H, d, *J* 7.0, C**H**), 7.74-7.80 (1H, m, C**H**), 7.75-7.82 (1H, m, C**H**). 7.77-7.84 (1H, m, C**H**), 7.97 (1H, t, *J* 6.1, C**H**), 8.06 (1H, d, *J* 6.1, C**H**), 8.17 (1H, td, *J* 7.0, 5.7, C**H**), 8.30 (1H, d, *J* 7.0, 5.7, C**H**), 8.35 (1H, dd, *J* 7.0, 5.7, C**H**), 8.61 (1H, s, N**H**), 8.75 (1H, s, C**H**).

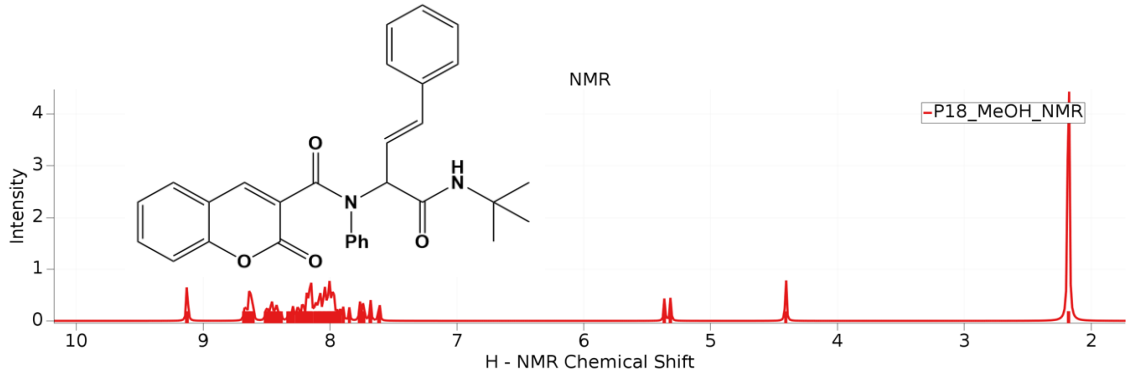

Figure A-4.30. Computationally modelled NMR of P18. The starting materials for R18 were coumarin-3-carboxylic acid, aniline, cinnamaldehyde, and *tert*-butyl isocyanide. The results were as follows; H(200 MHz; MeOH), δ 2.18 (9H, s, 3 x C**H**$_3$), 4.41 (1H, s, N**H**), 5.34 (1H, d, *J* 9.5, C**H**), 7.65 (1H, d, *J* 13.95, C**H**), 7.75 (1H, d, *J* 5.3, C**H**), 7.91 (1H, dd, *J* 13.9, 9.5, C**H**), 7.94-8.25 (8H, m, 8 x C**H**), 8.29 (1H, td, *J* 7.0, 2.0, C**H**), 8.39-8.51 (2H, m, 2 x C**H**), 8.61-8.68 (2H, m, 2 x C**H**), 9.13 (1H, s, C**H**).

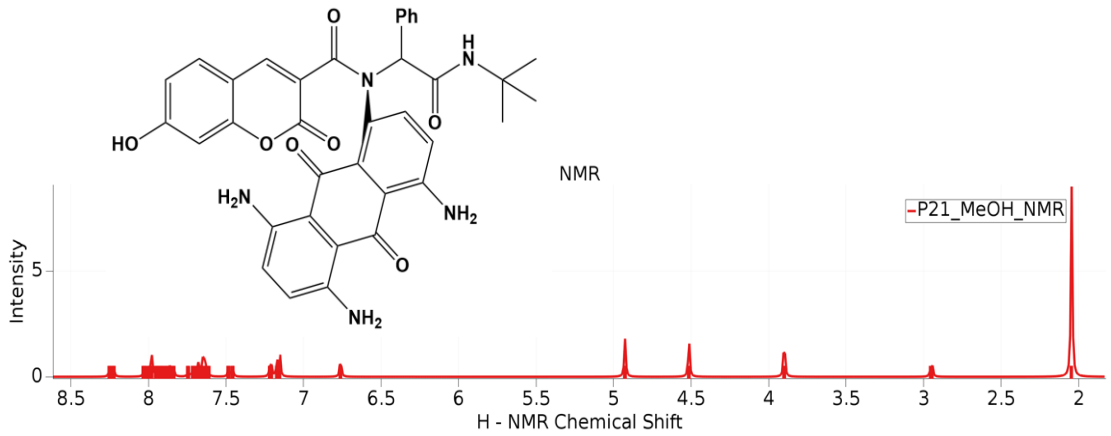

Figure A-4.31. Computationally modelled NMR of P21. The starting materials for R21 were 6,7-dihydroxycoumarin-3-carboxylic acid, disperse blue 1, benzaldehyde, and *tert*-butyl isocyanide. The results were as follows; H(200 MHz; MeOH), δ 2.05 (9H, s, 3 x C**H**$_3$), 2.95 (1H, d, *J* 2.4, N**H**), 3.90 (2H, s, N**H**$_2$), 4.51 (2H, s, N**H**$_2$), 4.93 (2H, s, N**H**$_2$), 6.76 (1H, s, O**H**), 7.15 (1H, s, O**H**), 7.17 (1H, s, C**H**), 7.21 (1H, d, *J* 2.4, C**H**), 7.47 (1H, d, *J* 5.3, C**H**), 7.61-7.69 (1H, m, C**H**), 7.64 (1H, s, C**H**), 7.71 (1H, td, *J* 6.6, 1.5, C**H**), 7.84-7.96 (3H, m, 3 x C**H**), 7.98 (1H, s, C**H**), 8.01 (1H, dq, *J* 6.9, 2.3, C**H**), 8.24 (1H, d, *J* 5.0, C**H**).

Appendix-4.4: R1 Transition States

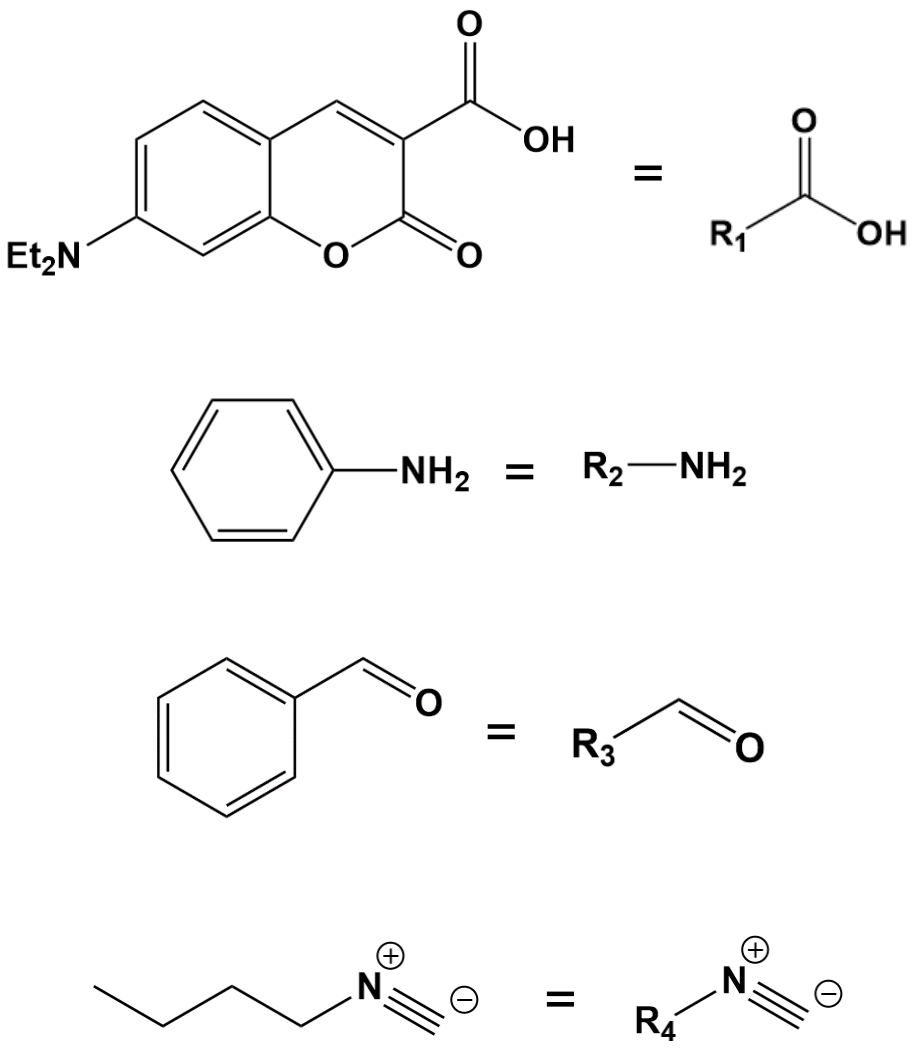

Figure A-4.32. Reactants used in **R1**. Shorthand molecular structure included on the right.

Appendix-4.5: R1 Reaction Mechanism

Appendix-4.5.1: Imine Formation

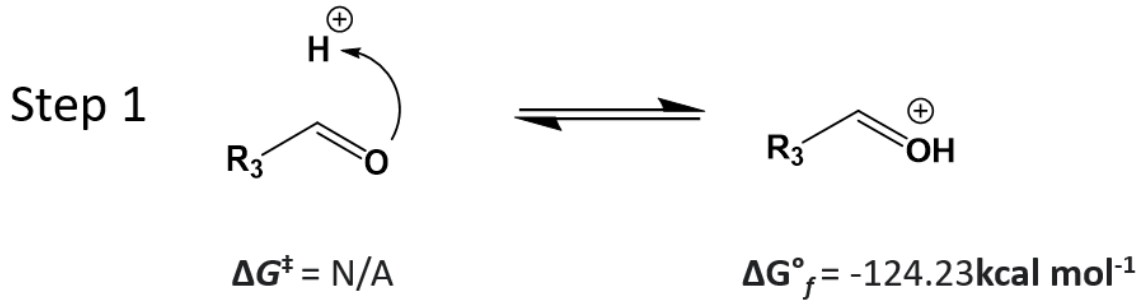

Figure A-4.33. Protonation of benzaldehyde, alongside associated Gibbs Activation Energy ($\Delta G^{\ddagger}$) (kcal mol^{-1}) and Gibbs Free Energy of Formations (ΔG^{o}_{f}) (kcal mol^{-1}) for the reaction

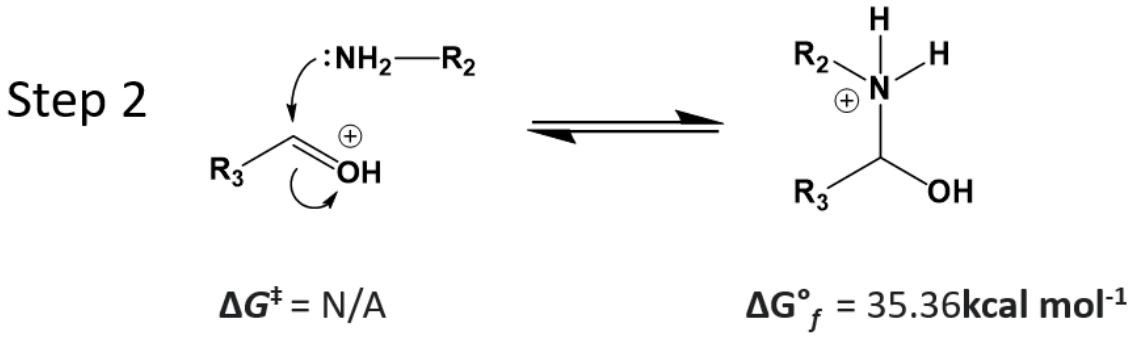

Figure A-4.34. Nucleophilic attack of protonated benzaldehyde by amine, alongside associated Gibbs Activation Energy ($\Delta G^{\ddagger}$) (kcal mol^{-1}) and Gibbs Free Energy of Formations (ΔG^{o}_{f}) (kcal mol^{-1}) for the reaction

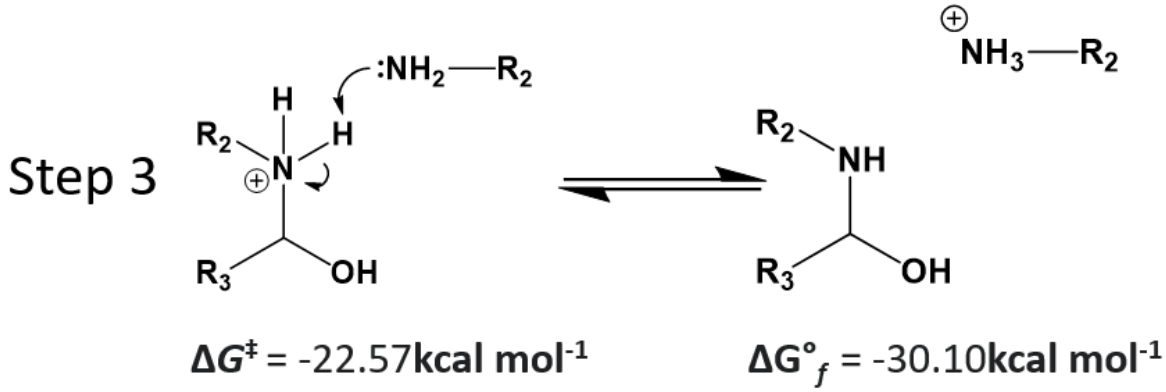

Figure A-4.35. Deprotonation of Benzaldehyde-Amine transition state, alongside associated Gibbs Activation Energy ($\Delta G^{\ddagger}$) (kcal mol^{-1}) and Gibbs Free Energy of Formations (ΔG^{o}_{f}) (kcal mol^{-1}) for the reaction

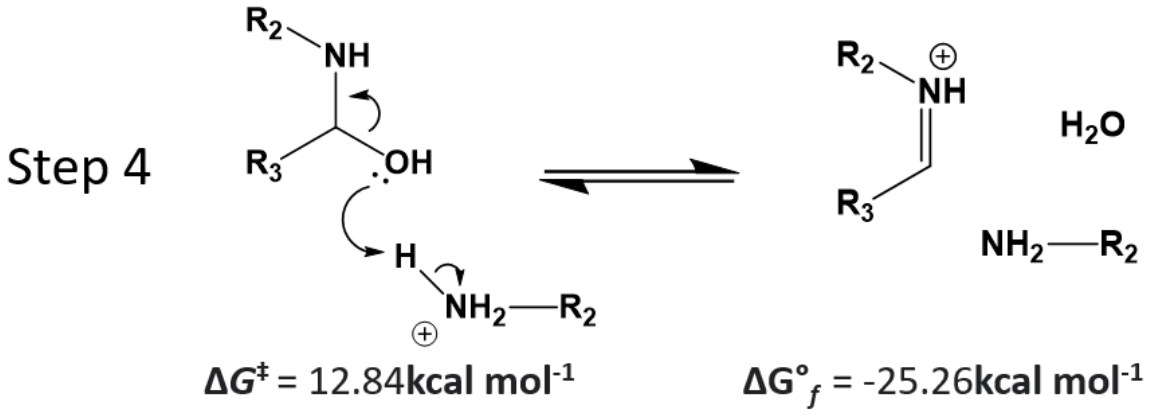

Figure A-4.36. Formation of proto-Imine transition state by condensation reaction, alongside associated Gibbs Activation Energy ($\Delta G^{\ddagger}$) (kcal mol^{-1}) and Gibbs Free Energy of Formations (ΔG^{o}_{f}) (kcal mol^{-1}) for the reaction

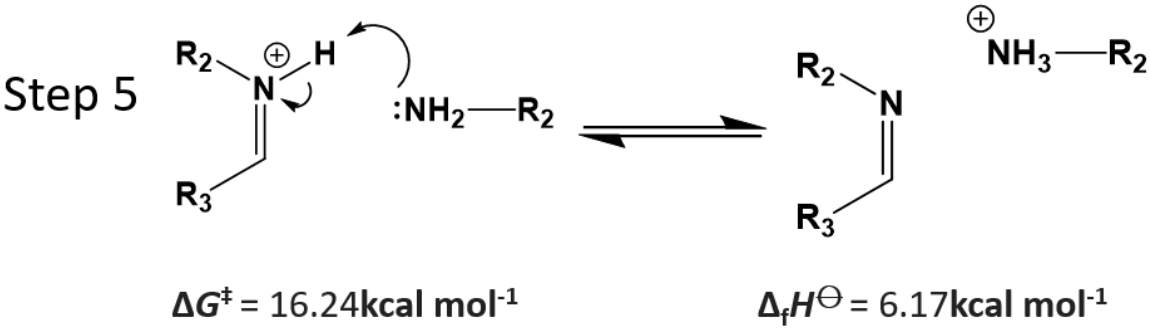

Figure A-4.37. Formation of Imine transition state, alongside associated Gibbs Activation Energy ($\Delta G^{\ddagger}$) (kcal mol^{-1}) and Gibbs Free Energy of Formations (ΔG^{o}_{f}) (kcal mol^{-1}) for the reaction

Appendix-4.5.2: Imidate Formation via Hemiaminal Ester

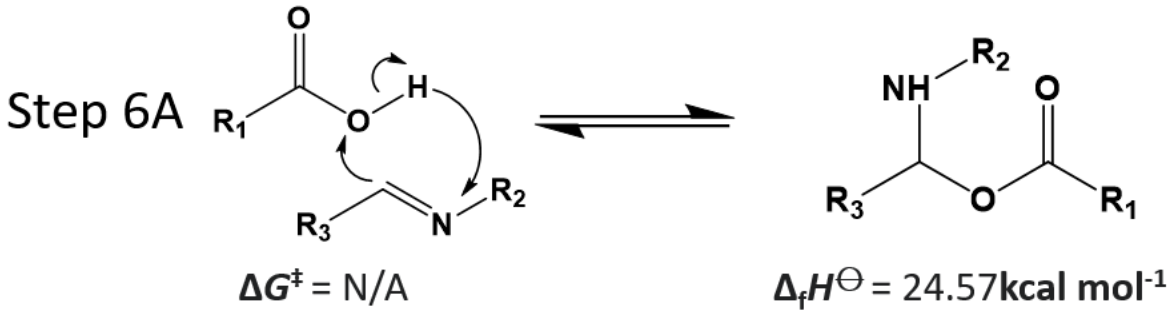

Figure A-4.38. Formation of Hemiaminal Ester, alongside associated Gibbs Activation Energy ($\Delta G^{\ddagger}$) (kcal mol^{-1}) and Gibbs Free Energy of Formations (ΔG^{o}_{f}) (kcal mol^{-1}) for the reaction

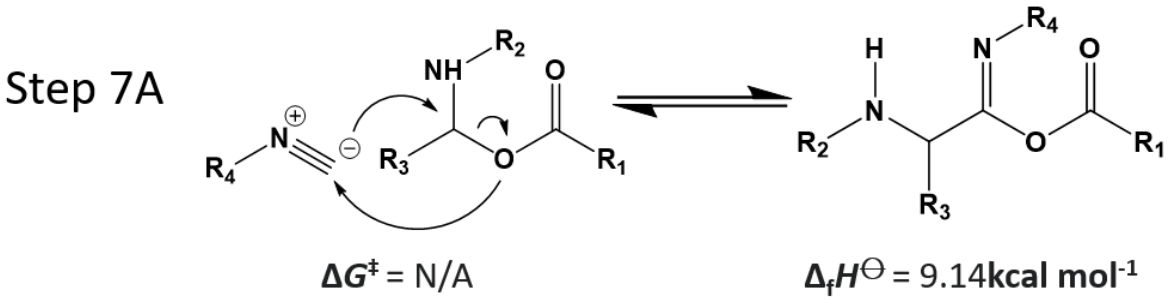

Figure A-4.39. Formation of Imidate intermediate from Hemiaminal Ester, alongside associated Gibbs Activation Energy ($\Delta G^{\ddagger}$) (kcal mol^{-1}) and Gibbs Free Energy of Formations (ΔG^{o}_{f}) (kcal mol^{-1}) for the reaction

Appendix-4.5.3: Imidate Formation via Nitrilium Ion

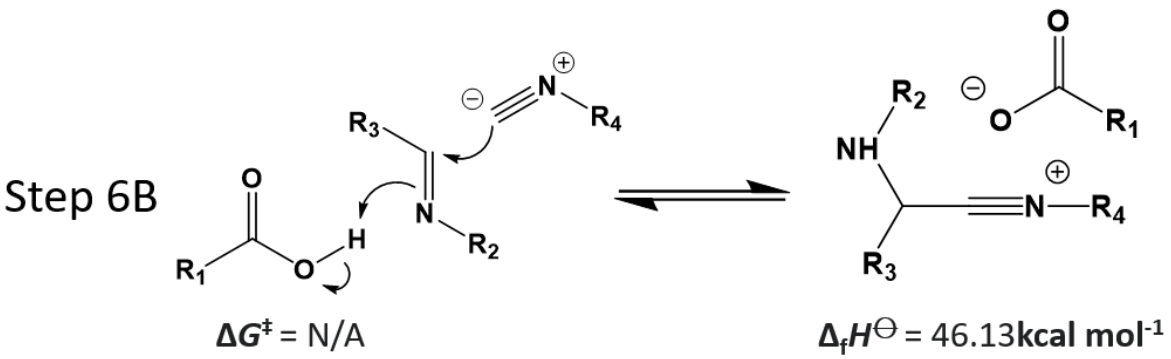

Figure A-4.40. Formation of Nitrilium ion, alongside associated Gibbs Activation Energy ($\Delta G^{\ddagger}$) (kcal mol^{-1}) and Gibbs Free Energy of Formations (ΔG^{o}_{f}) (kcal mol^{-1}) for the reaction

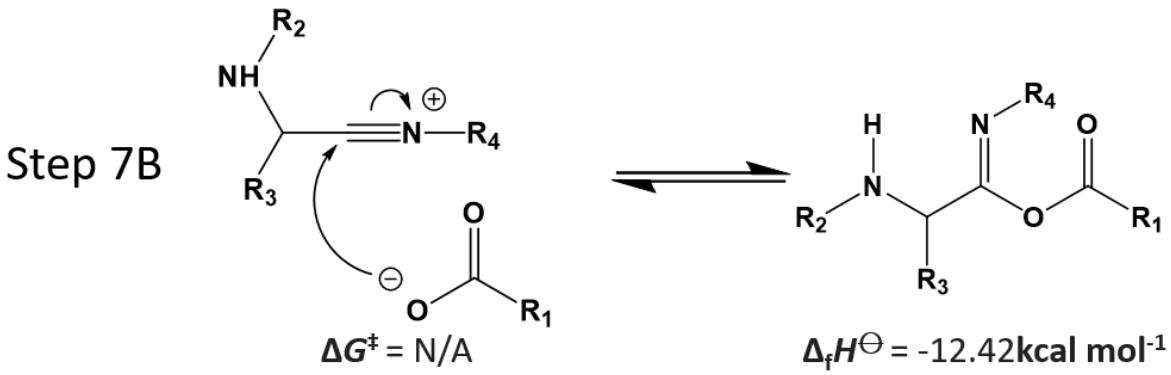

Figure A-4.41. Formation of Imidate intermediate from Nitrilium Ion, alongside associated Gibbs Activation Energy ($\Delta G^{\ddagger}$) (kcal mol^{-1}) and Gibbs Free Energy of Formations (ΔG^{o}_{f}) (kcal mol^{-1}) for the reaction

Appendix-4.5.4: Peptoid Formation

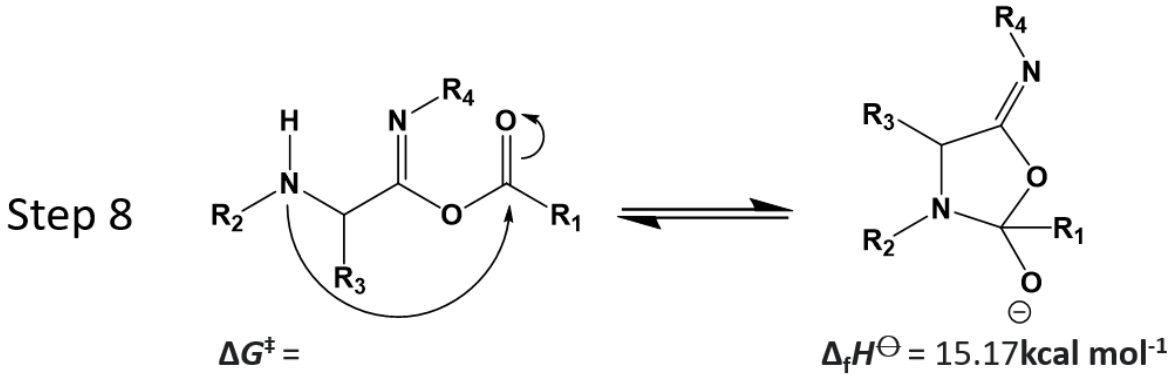

Figure A-4.42. Mumm rearrangement, alongside associated Gibbs Activation Energy (**ΔG**‡) (kcal mol^{-1}) and Gibbs Free Energy of Formations (**ΔG°$_f$**) (kcal mol^{-1}) for the reaction

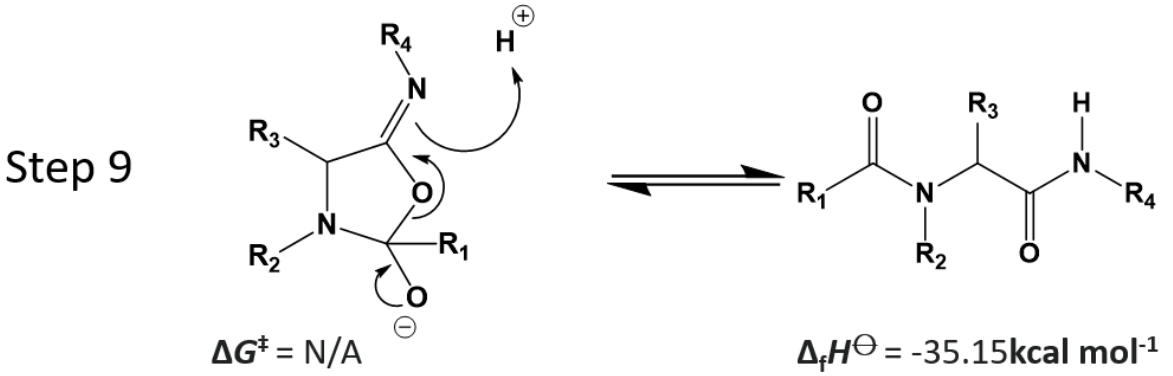

Figure A-4.43. Formation of peptoid, alongside associated Gibbs Activation Energy (**ΔG**‡) (kcal mol^{-1}) and Gibbs Free Energy of Formations (**ΔG°$_f$**) (kcal mol^{-1}) for the reaction

Appendix-5: Appendices References

(2) Pope, M. T. *Heteropoly and Isopoly Oxometalates*, 1st ed.; Springer Berlin, Heidelberg, 1983.

(20) López, X.; Vilà-Nadal, L.; Aparicio-Anglès, X.; Poblet, J. M. Theoretical View on the Origin and Implications of Structural Distortions in Polyoxometalates. *Phys. Procedia* **2010**, *8*, 94–103. https://doi.org/10.1016/j.phpro.2010.10.018.

(21) Yan, L.; López, X.; Carbó, J. J.; Sniatynsky, R.; Duncan, D. C.; Poblet, J. M. On the Origin of Alternating Bond Distortions and the Emergence of Chirality in Polyoxometalate Anions. *J. Am. Chem. Soc.* **2008**, *130* (26), 8223–8233. https://doi.org/10.1021/ja711008n.

(41) Kibler, A. J.; Newton, G. N. Tuning the Electronic Structure of Organic–Inorganic Hybrid Polyoxometalates: The Crucial Role of the Covalent Linkage. *Polyhedron* **2018**, *154*, 1–20. https://doi.org/10.1016/j.poly.2018.06.027.

(47) Minato, T.; Suzuki, K.; Kamata, K.; Mizuno, N. Synthesis of α-Dawson-Type Silicotungstate [α-Si 2W18O62]8- and Protonation and Deprotonation inside the Aperture through Intramolecular Hydrogen Bonds. *Chem. - A Eur. J.* **2014**, *20* (20), 5946–5952. https://doi.org/10.1002/chem.201400390.

(48) Long, D. L.; Abbas, H.; Kögerler, P.; Cronin, L. Confined Electron-Transfer Reactions within a Molecular Metal Oxide "Trojan Horse." *Angew. Chemie - Int. Ed.* **2005**, *44* (22), 3415–3419. https://doi.org/10.1002/anie.200500541.

(50) Miras, H. N.; Stone, D.; Long, D. L.; McInnes, E. J. L.; Kögerler, P.; Cronin, L. Exploring the Structure and Properties of Transition Metal Templated {VM17(VO4)2} Dawson-like Capsules. *Inorg. Chem.* **2011**, *50* (17), 8384–8391. https://doi.org/10.1021/ic200943s.

(57) Chen, X.; Huang, P.; Zhu, X.; Zhuang, S.; Zhu, H.; Fu, J.; Nissimagoudar, A. S.; Li, W.; Zhang, X.; Zhou, L.; Wang, Y.; Lv, Z.; Zhou, Y.; Han, S. T. Keggin-Type Polyoxometalate Cluster as an Active Component for Redox-Based Nonvolatile Memory. *Nanoscale Horizons* **2019**, *4* (3), 697–704. https://doi.org/10.1039/c8nh00366a.

(60) Steffler, F.; De Lima, G. F.; Duarte, H. A. The Effect of the Heteroatom (X=P, As, Si and Ge) on the Geometrical and Electronic Properties of α-Keggin Polyoxometalates (M=Mo, W and Nb) – A DFT Investigation. *J. Mol. Struct.* **2020**, *1213*, 1–6. https://doi.org/10.1016/j.molstruc.2020.128159.

(62) López, X.; Poblet, J. M. DFT Study on the Five Isomers of PW12O403-: Relative Stabilization upon Reduction. *Inorg. Chem.* **2004**, *43* (22), 6863–6865. https://doi.org/10.1021/ic049119p.

(64) Zhang, F. Q.; Guan, W.; Yan, L. K.; Zhang, Y. T.; Xu, M. T.; Hayfron-Benjamin, E.; Su, Z. M. On the Origin of the Relative Stability of Wells-Dawson Isomers: A DFT Study of α-, β-, γ-, A*-, B*-, and Γ*-[(PO4)2W18O54] 6-Anions. *Inorg. Chem.* **2011**, *50* (11), 4967–4977. https://doi.org/10.1021/ic200203s.

(65) Vilà-Nadal, L.; Mitchell, S. G.; Long, D. L.; Rodríguez-Fortea, A.; López, X.; Poblet, J. M.; Cronin, L. Exploring the Rotational Isomerism in Non-Classical Wells-Dawson Anions {W 18X}: A Combined Theoretical and Mass Spectrometry Study. *Dalt. Trans.* **2012**, *41* (8), 2264–2271. https://doi.org/10.1039/c2dt11919f.

(69) Fernández, J. A.; López, X.; Bo, C.; de Graaf, C.; Baerends, E. J.; Poblet, J. M. Polyoxometalates with Internal Cavities: Redox Activity, Basicity, and Cation Encapsulation in [Xn+P5W30O110](15-n)- Preyssler Complexes, with X = Na+, Ca2+, Y3+, La3+, Ce3+, and Th4+. *J. Am. Chem. Soc.* **2007**, *129* (3), 12244–12253. https://doi.org/10.1021/ja0737321.

(74) Bamoharram, F. F.; Heravi, M. M.; Roshani, M.; Tavakoli, N. N-Oxidation of Pyridine Carboxylic Acids Using Hydrogen Peroxide Catalyzed by a Green Heteropolyacid Catalyst: Preyssler's Anion, [NaP5W30O110]14-. *J. Mol. Catal. A Chem.* **2006**, *252* (1–2), 219–225. https://doi.org/10.1016/j.molcata.2006.02.059.

(78) Cameron, J. M.; Gao, J.; Vilà-Nadal, L.; Long, D. L.; Cronin, L. Formation, Self-Assembly and Transformation of a Transient Selenotungstate Building Block into Clusters, Chains and Macrocycles. *Chem. Commun.* **2014**, *50* (17), 2155–2157. https://doi.org/10.1039/c3cc49293a.

(83) Contant, R.; Thouvenot, R. Hétéropolyanions de Type Dawson. 2. Synthèses de Polyoxotungstoarsénates Lacunaires Dérivant de l'octadécatungstodiarsénate. Étude Structurale Par RMN Du Tungstène-183 Des Octadéca(Mo1ybdotungstovanado)Diarsénates Apparentés. *Can. J. Chem.* **1991**, *69* (10), 1498–1506. https://doi.org/10.1139/v91-221.

(95) Long, D.-L.; Kögerler, P.; Cronin, L. Old Clusters with New Tricks: Engineering S···S Interactions and Novel Physical Properties in Sulfite-Based Dawson Clusters. *Angew. Chemie* **2004**, *116* (14), 1853–1856. https://doi.org/10.1002/ange.200352896.

(151) Kibler, A. J.; Souza, V. S.; Fernandes, J. A.; Lewis, W.; Argent, S. P.; Dupont, J.; Newton, G. N. A Cooperative Photoactive Class-I Hybrid Polyoxometalate With Benzothiadiazole–Imidazolium Cations. *Front. Chem.* **2021**, *8*, 1–10. https://doi.org/10.3389/fchem.2020.612535.

(152) Xu, J.; Volfova, H.; Mulder, R. J.; Goerigk, L.; Bryant, G.; Riedle, E.; Ritchie, C. Visible-Light-Driven "on"/"Off" Photochromism of a Polyoxometalate Diarylethene Coordination Complex. *J. Am. Chem. Soc.* **2018**, *140* (33), 10482–10487. https://doi.org/10.1021/jacs.8b04900.

(162) Yang, M.; Wang, X.; Gómez-García, C. J.; Jin, Z.; Xin, J.; Cao, X.; Ma, H.; Pang, H.; Tan, L.; Yang, G.; Kan, Y. Efficient Electron Transfer from an Electron-Reservoir Polyoxometalate to Dual-Metal-Site Metal-Organic Frameworks for Highly Efficient Electroreduction of Nitrogen. *Adv. Funct. Mater.* **2023**, *33* (28), 1–13. https://doi.org/10.1002/adfm.202214495.

(176) Busche, C.; Vilà-Nadal, L.; Yan, J.; Miras, H. N.; Long, D. L.; Georgiev, V. P.; Asenov, A.; Pedersen, R. H.; Gadegaard, N.; Mirza, M. M.; Paul, D. J.; Poblet, J. M.; Cronin, L. Design and Fabrication of Memory Devices Based on Nanoscale Polyoxometalate Clusters. *Nature* **2014**, *515* (7528), 545–549. https://doi.org/10.1038/nature13951.

(180) Vilà-Nadal, L.; Peuntinger, K.; Busche, C.; Yan, J.; Lüders, D.; Long, D.; Poblet, J. M.; Guldi, D. M.; Cronin, L. Polyoxometalate {W18O56XO6} Clusters with Embedded Redox-Active Main-Group Templates as Localized Inner-Cluster Radicals. *Angew. Chemie* **2013**, *125*, 9877–9881. https://doi.org/ange.201303126.

(181) Ueda, T. Electrochemistry of Polyoxometalates: From Fundamental Aspects to Applications. *ChemElectroChem* **2018**, *5* (6), 823–838. https://doi.org/10.1002/celc.201701170.

(231) López, X.; Carbó, J. J.; Bo, C.; Poblet, J. M. Structure, Properties and Reactivity of Polyoxometalates: A Theoretical Perspective. *Chem. Soc. Rev.* **2012**, *41* (22), 7537–7571. https://doi.org/10.1039/c2cs35168d.

(233) McAllister, J.; Bandeira, N. A. G.; McGlynn, J. C.; Ganin, A. Y.; Song, Y. F.; Bo, C.; Miras, H. N. Tuning and Mechanistic Insights of Metal Chalcogenide Molecular Catalysts for the Hydrogen-Evolution Reaction. *Nat. Commun.* **2019**, *10* (1). https://doi.org/10.1038/s41467-018-08208-4.

(235) Solé-Daura, A.; Notario-Estévez, A.; Carbó, J. J.; Poblet, J. M.; De Graaf, C.; Monakhov, K. Y.; López, X. How Does the Redox State of Polyoxovanadates Influence the Collective Behavior in Solution? A Case Study with [I@V 18 O 42] q- (q = 3, 5, 7, 11, and 13). *Inorg. Chem.* **2019**, No. Md. https://doi.org/10.1021/acs.inorgchem.8b03508.

(236) Sartorel, A.; Miró, P.; Salvadori, E.; Romain, S.; Carraro, M.; Scorrano, G.; Di Valentin, M.; Llobet, A.; Bo, C.; Bonchio, M. Water Oxidation at a Tetraruthenate Core Stabilized by Polyoxometalate Ligands: Experimental and Computational Evidence to Trace the Competent Intermediates. *J. Am. Chem. Soc.* **2009**, *131* (44), 16051–16053. https://doi.org/10.1021/ja905067u.

(237) Maestre, J. M.; Lopez, X.; Bo, C.; Poblet, J. Electronic and Magnetic Properties of R -Keggin Anions : A DFT Study of [XM12O40]n-, (M = W, Mo; X = AlIII, SiIV, PV, FeIII, CoII, CoIII) and [SiM11VO40]m- (M = Mo and W). *J. Am. Chem. Soc.* **2001**, *123* (16), 3749–3758. https://doi.org/10.1021/ja003563j.

(238) López, X.; Maestre, J. M.; Bo, C.; Poblet, J. M. Electronic Properties of Polyoxometalates: A DFT Study of α/β-[XM12O40]n- Relative Stability (M=W, Mo and X a Main Group Element). *J. Am. Chem. Soc.* **2001**, *123* (39), 9571–9576. https://doi.org/10.1021/ja010768z.

(239) López, X.; Bo, C.; Poblet, J. M. Electronic Properties of Polyoxometalates: Electron and Proton Affinity of Mixed-Addenda Keggin and Wells-Dawson Anions. *J. Am. Chem. Soc.* **2002**, *124* (42), 12574–12582. https://doi.org/10.1021/ja020407z.

(283) Miro, P.; Ling, J.; Qiu, J.; Burns, P. C.; Gagliardi, L.; Cramer, C. J. Experimental and Computational Study of a New Wheel-Shaped {[W5O21]3[(UVIO2)2(M-O2)]3}30− Polyoxometalate. *Inorg. Chem.* **2012**, *2*, 8784–8790. https://doi.org/10.1021/ic3005536.

(284) Vilà-Nadal, L.; Mitchell, S. G.; Markov, S.; Busche, C.; Georgiev, V.; Asenov, A.; Cronin, L. Towards Polyoxometalate-Cluster-Based Nano-Electronics. *Chem. - A Eur. J.* **2013**, *19* (49), 16502–16511. https://doi.org/10.1002/chem.201301631.

(285) Cameron, J. M.; Fujimoto, S.; Kastner, K.; Wei, R. J.; Robinson, D.; Sans, V.; Newton, G. N.; Oshio, H. H. Orbital Engineering: Photoactivation of an Organofunctionalized Polyoxotungstate. *Chem. - A Eur. J.* **2017**, *23* (1), 47–50. https://doi.org/10.1002/chem.201605021.

(318) Lapham, P.; Vilà-Nadal, L.; Cronin, L.; Georgiev, V. P. Influence of the Contact Geometry and Counterions on the Current Flow and Charge Transfer in Polyoxometalate Molecular Junctions: A Density Functional Theory Study. *J. Phys. Chem. C* **2021**, *125* (6), 3599–3610. https://doi.org/10.1021/acs.jpcc.0c11038.

(320) Ravelli, D.; Dondi, D.; Fagnoni, M.; Albini, A.; Bagno, A. Predicting the UV Spectrum of Polyoxometalates by TD-DFT. *J. Comput. Chem.* **2011**, *32* (14), 2983–2987. https://doi.org/10.1002/jcc.21879.

(321) Amin, S. S.; Cameron, J. M.; Winslow, M.; Davies, E. S.; Argent, S. P.; Robinson, D.; Newton, G. N. A Mixed-Addenda Mo/W Organofunctionalised Hybrid Polyoxometalate. *Eur. J. Inorg. Chem.* **2022**, *2022* (10). https://doi.org/10.1002/ejic.202200019.

(322) Mbomekallé, I. M.; Bassil, B. S.; Suchopar, A.; Keita, B.; Nadjo, L.; Ammam, M.; Haouas, M.; Taulelle, F.; Kortz, U. Improved Synthesis, Structure, and Solution Characterization of the Cyclic 48-Tungsto-8-Arsenate(V), [H4As8W48O184]36-. *J. Clust. Sci.* **2014**, *25* (1), 277–285. https://doi.org/10.1007/s10876-013-0656-2.

(323) Chen, J. J.; Vilà-Nadal, L.; Solé-Daura, A.; Chisholm, G.; Minato, T.; Busche, C.; Zhao, T.; Kandasamy, B.; Ganin, A. Y.; Smith, R. M.; Colliard, I.; Carbó, J. J.; Poblet, J. M.; Nyman, M.; Cronin, L. Effective Storage of Electrons in Water by the Formation of Highly Reduced Polyoxometalate Clusters. *J. Am. Chem. Soc.* **2022**, *144* (20), 8951–8960. https://doi.org/10.1021/jacs.1c10584.

(328) Sugiarto, S.; Sadakane, M. Hexalacunary [A-H2P2W12O48]12– Wells-Dawson Anion: X-ray Crystal Structure Evidence and Oligomerization to WO(OH2)4+-Bridged Dimer and Trimer. *Chem. – A Eur. J.* **2023**, *29* (45), e202301051. https://doi.org/10.1002/chem.202301051.

(329) Malcolm, D.; Vilà-Nadal, L. Computational Study into the Effects of Countercations on the [P8W48O184]40– Polyoxometalate Wheel. *ACS Org. Inorg. Au* **2023**. https://doi.org/10.1021/acsorginorgau.3c00014.

(331) Kaledin, A. L.; Yin, Q.; Hill, C. L.; Lian, T.; Musaev, D. G. Ion-Pairing in Polyoxometalate Chemistry: Impact of Fully Hydrated Alkali Metal Cations on Properties of the Keggin [PW12O40]3-Anion. *Dalt. Trans.* **2020**, *49* (32), 11170–11178. https://doi.org/10.1039/d0dt02239j.

(334) Lo, X.; Bo, C.; Poblet, J.; Sarasa, P.; Uni, C. Relative Stability in Alpha- and Beta-Wells–Dawson Heteropolyanions: A DFT Study of [P2M18O62]n- (M = W and Mo) and [P2W15V3O62]N-. *Inorg. Chem.* **2003**, *42* (8), 2634–2638. https://doi.org/10.1021/ic0262280.

(335) Poblet, J. M.; López, X.; Bo, C. Ab Initio and DFT Modelling of Complex Materials: Towards the Understanding of Electronic and Magnetic Properties of Polyoxometalates. *Chem. Soc. Rev.* **2003**, *32* (5), 297–308. https://doi.org/10.1039/b109928k.

(336) Mal, S. S.; Bassil, B. S.; Ibrahim, M.; Nellutla, S.; Van Tol, J.; Dalal, N. S.; Fernández, J. A.; López, X.; Poblet, J. M.; Biboum, R. N.; Keita, B.; Kortz, U. Wheel-Shaped Cu20-Tungstophosphate [Cu20X(OH) 24(H2O)12(P8W48O 184)]25- Ion (X = Cl, Br, I) and the Role of the Halide Guest. *Inorg. Chem.* **2009**, *48* (24), 11636–11645. https://doi.org/10.1021/ic901641f.

(337) López, X.; Fernández, J. A.; Poblet, J. M. Redox Properties of Polyoxometalates: New Insights on the Anion Charge Effect. *J. Chem. Soc. Dalt. Trans.* **2006**, *6* (9), 1162–1167. https://doi.org/10.1039/b507599h.

(338) Nomiya, K.; Sugie, Y.; Amimoto, K.; Miwa, M. Charge-Transfer Absorption Spectra of Some Tungsten(VI) and Molybdenum(VI) Polyoxoanions. *Polyhedron* **1987**, *6* (3), 519–524. https://doi.org/10.1016/S0277-5387(00)81018-9.

(339) Hiskia, A.; Mylonas, A.; Papaconstantinou, E. Comparison of the Photoredox Properties of Polyoxometallates and Semiconducting Particles. *Chem. Soc. Rev.* **2001**, *30* (1), 62–69. https://doi.org/10.1039/a905675k.

(340) Dhifallah, F.; Belkhiria, M. S.; Parent, L.; Leclerc, N.; Cadot, E. A Series of Octahedral First-Row Transition-Metal Ion Complexes Templated by Wells-Dawson Polyoxometalates: Synthesis, Crystal Structure, Spectroscopic, and Thermal Characterizations, and Electrochemical Properties. *Inorg. Chem.* **2018**, *57* (19), 11909–11919. https://doi.org/10.1021/acs.inorgchem.8b01207.

(370) Ozawa, Y.; Sasaki, Y. Synthesis and Crystal Structure of [(CH3)4N]6[H3BiW18O60]. *Chem. Lett.* **1987**, *16* (5), 923–926. https://doi.org/10.1246/cl.1987.923.

(371) Yi, X.; Izarova, N. V.; Kögerler, P. Organoarsonate Functionalization of Heteropolyoxotungstates. *Inorg. Chem.* **2017**, *56* (22), 13822–13828. https://doi.org/10.1021/acs.inorgchem.7b01928.

(372) Jiao, Y. Q.; Qin, C.; Wang, X. L.; Wang, C. G.; Sun, C. Y.; Wang, H. N.; Shao, K. Z.; Su, Z. M. Three Cobalt(II)-Linked {P8W48} Network Assemblies: Syntheses, Structures, and Magnetic and Photocatalysis Properties. *Chem. - An Asian J.* **2014**, *9* (2), 470–478. https://doi.org/10.1002/asia.201300856.

(373) Sasaki, S.; Yonesato, K.; Mizuno, N.; Yamaguchi, K.; Suzuki, K. Ring-Shaped Polyoxometalates Possessing Multiple 3d Metal Cation Sites: [{M2(OH2)2}2{M(OH2)2}4P8W48O176(OCH3)8]16- (M = Mn, Co, Ni, Cu, Zn). *Inorg. Chem.* **2019**, *58* (12), 7722–7729. https://doi.org/10.1021/acs.inorgchem.9b00061.

(374) Niu, Y.; Ding, Y.; Sheng, H.; Sun, S.; Chen, C.; Du, J.; Zang, H. Y.; Yang, P. Space-Confined Nucleation of Semimetal-Oxo Clusters within a [H7P8W48O184]33-Macrocycle: Synthesis, Structure, and Enhanced Proton Conductivity. *Inorg. Chem.* **2022**, *61* (51), 21024–21034. https://doi.org/10.1021/acs.inorgchem.2c03543.

(375) Gabb, D.; Pradeep, C. P.; Boyd, T.; Mitchell, S. G.; Miras, H. N.; Long, D. L.; Cronin, L. A General Route for the Transfer of Large, Highly-Charged Polyoxometalates from Aqueous to Organic Phase. *Polyhedron* **2013**, *52*, 159–164. https://doi.org/10.1016/j.poly.2012.10.015.

(376) Yu, X.; Zhang, X.; Zhao, J.; Xu, L.; Yan, J. Flower-like Shaped Bi12TiO20/g-C3N4 Heterojunction for Effective Elimination of Organic Pollutants: Preparation, Characterization, and Mechanism Study. *Appl. Organomet. Chem.* **2020**, *34* (8), 1–13. https://doi.org/10.1002/aoc.5702.

(377) Slater, J. C. Atomic Radii in Crystals. *J. Chem. Phys.* **1964**, *41* (10), 3199–3204.

(378) Graham, C. R.; Finke, R. G. The Classic Wells-Dawson Polyoxometalate, K6[α-P 2W18O62]·14H2O. Answering an 88 Year-Old Question: What Is Its Preferred, Optimum Synthesis? *Inorg. Chem.* **2008**, *47* (9), 3679–3686. https://doi.org/10.1021/ic702295y.

(379) Contant, R. *Inorganic Synthesis*, 1st ed.; Ginsberg, A., Ed.; Wiley-Interscience: New York, 1990. https://doi.org/10.1002/9780470132586.

(380) Zhan, C. G.; Nichols, J. A.; Dixon, D. A. Ionization Potential, Electron Affinity, Electronegativity, Hardness, and Electron Excitation Energy: Molecular Properties from Density Functional Theory Orbital Energies. *J. Phys. Chem. A* **2003**, *107* (20), 4184–4195. https://doi.org/10.1021/jp0225774.

(381) Goubin, F.; Guénée, L.; Deniard, P.; Koo, H. J.; Whangbo, M. H.; Montardi, Y.; Jobic, S. Synthesis, Optical Properties and Electronic Structures of Polyoxometalates K 3P(Mo 1-XW x) 12O 40 (0≤x≤1). *J. Solid State Chem.* **2004**, *177* (12), 4528–4534. https://doi.org/10.1016/j.jssc.2004.08.046.

(382) Chiang, M. H.; Antonio, M. R.; Soderholm, L. Energetics of the Preyssler Anion's Molecular Orbitals: Quantifying the Effect of the Encapsulated-Cation's Charge. *Dalt. Trans.* **2004**, No. 21, 3562–3567. https://doi.org/10.1039/b412337a.

(383) Zhang, G.; Musgrave, C. B. Comparison of DFT Methods for Molecular Orbital Eigenvalue Calculations. *J. Phys. Chem. A* **2007**, *111* (8), 1554–1561. https://doi.org/10.1021/jp061633o.

(384) López, X.; Miró, P.; Carbó, J. J.; Rodríguez-Fortea, A.; Bo, C.; Poblet, J. M. Current Trends in the Computational Modelling of Polyoxometalates. *Theor. Chem. Acc.* **2011**, *128* (4), 393–404. https://doi.org/10.1007/s00214-010-0820-9.

(385) Bo, C.; Poblet, J. M. Electronic Properties and Molecular Simulations of Polyoxometalates. *Isr. J. Chem.* **2011**, *51* (2), 228–237. https://doi.org/10.1002/ijch.201100017.

(386) Chen, W. C.; Yan, L. K.; Wu, C. X.; Wang, X. L.; Shao, K. Z.; Su, Z. M.; Wang, E. B. Assembly of Keggin-/Dawson-Type Polyoxotungstate Clusters with Different Metal Units and SeO32- Heteroanion Templates. *Cryst. Growth Des.* **2014**, *14* (10), 5099–5110. https://doi.org/10.1021/cg500719q.

(387) Li, C.; Suzuki, K.; Mizuno, N.; Yamaguchi, K. Polyoxometalate LUMO Engineering: A Strategy for Visible-Light-Responsive Aerobic Oxygenation Photocatalysts. *Chem. Commun.* **2018**, *54* (52), 7127–7130. https://doi.org/10.1039/c8cc03519a.

(388) Babaei, S.; Niad, M. Chemical Reactivity Descriptors as a Tool of Prediction in the Synthesis of Sandwich Type Polyoxometalate Organic–Inorganic Hybrid Compounds. *Polyhedron* **2020**, *188*, 114710. https://doi.org/10.1016/j.poly.2020.114710.

(389) Gao, Y.; Guan, W.; Yan, L. K.; Su, Z. M. A Theoretical Investigation on Promising Acceptor Groups for POM-Based Dyes: From Electronic Structure to Photovoltaic Conversion Efficiency. *J. Mater. Chem. C* **2019**, *8* (1), 219–227. https://doi.org/10.1039/c9tc04025k.

(390) Kibler, A. J.; Tsang, N.; Winslow, M.; Argent, S. P.; Lam, H. W.; Robinson, D.; Newton, G. N. Electronic Structure and Photoactivity of Organoarsenic Hybrid Polyoxometalates. *Inorg. Chem.* **2023**, *62* (8), 3585–3591. https://doi.org/10.1021/acs.inorgchem.2c04249.

(391) Fait, M. J. G.; Lunk, H. J. Thermal Decomposition of Ammonium Paratungstate Tetrahydrate Traced by in Situ UV/Vis Diffuse Reflectance Spectroscopy. *Eur. J. Inorg. Chem.* **2012**, *3* (2), 213–216. https://doi.org/10.1002/ejic.201100838.

(392) Bamoharram, F. F. Synthesis and Characterization of Two Novel Organic-Inorganic Compounds Based on Tetrahexyl and Tetraheptyl Ammonium Ions and the Preyssler Anion and Their Catalytic Activities in the Synthesis of 4-Aminopyrazolo[3,4-d]- Pyrimidines. *Molecules* **2010**, *15* (4), 2509–2519. https://doi.org/10.3390/molecules15042509.